From ambient to metamorphic conditions: Deciphering fluid evolution and ore-forming processes through mineralogy, geochemistry, and thermodynamic modelling

Dissertation

der Mathematisch-Naturwissenschaftlichen Fakultät

der Eberhard Karls Universität Tübingen

zur Erlangung des Grades eines

Doktors der Naturwissenschaften

(Dr. rer. nat.)

vorgelegt von

Manuel Scharrer, M. Sc.

aus Chiang Mai, Thailand

Tübingen

2021

Gedruckt mit Genehmigung der Mathematisch-Naturwissenschaftlichen Fakultät der Eberhard Karls Universität Tübingen.

Tag der mündlichen Qualifikation:	18.08.2021
Dekan:	Prof. Dr. Thilo Stehle
1. Berichterstatter:	Prof. Dr. Gregor Markl
2. Berichterstatter:	Prof. Dr. Jochen Kolb
3. Berichterstatter:	Prof. Mag. rer. nat. Dr. mont. Frank Melcher

Acknowledgements

My first and special thanks are due to Prof. Dr. Gregor Markl for granting me this doctorate position, for being my primary supervisor, and for demonstrating his confidence in me. I am also grateful to him for making my Fulbright Scholarship a possiblity, as enabling a scholarship for my first one and a half years as a doctorate, before my DFG project was accepted. It was our numerous discussions, his guidance, and feedback that enabled and refined this work. I would also like to kindly thank Prof. Dr. Jochen Kolb for being the second referee for my Doctoral Thesis.

Furthermore, I would like to thank PD Dr. Thomas Wenzel for his role as the secondary supervisor, his helpful insights on the electron microprobe and other analytical inquires, and his unwavering support – as well as for exhilarating and helpful conversations, also outside of this doctoral thesis. Thirdly, I would like to express my gratitude to Dr. Philippe Blanc and the associated Team from the BRGM that maintains the Thermoddem database for the fruitful cooperation, the willingness to implement the thermodynamic data additions and the extrapolation of the thermodynamic data to higher temperature and pressure conditions.

I would like to express my sincere appreciation to Dr. Udo Neumann and Dr. Sebastian Staude for insightful discussions, input, and the supply of publications concerning ore mineral, economic, geological, and microscopic matters. Dr. Udo Neumann is further thanked for his mentoring and trust placed in me while I assisted him during his practical seminars on reflected light microscopy over the years. Additional thanks are addressed to Dr. Sebastian Staude for repeatedly letting me join his excursions and field work as a co-supervisor. A special thanks is also due for Associate Prof. Dr. Katarina Pfaff and all involved personnel from the Colorado School of Mines, who made my international research exchange though the Fulbright Scholarship a reality.

I would like to thank all present and past members of the Department of Petrology and Mineral Resources at the Eberhard Karls University of Tübingen that I have had the chance to work with, all collaborators in my research, and all co-authors of the manuscripts presented here. You all have helped me become the scientist I am today. Not yet named above, I would like to thank PD Dr. Michael Marks for his critical discussions that have helped me to further investigate specific aspects of this thesis. Furthermore, I want to acknowledge and thank Dr. Benjamin Walter and Dr. Mathias Burisch for a continuous productive cooperation as well as for fruitful discussions and feedback. Furthermore, I would like to thank Simone Schafflick for her willingness to help me, all the numerous timely sample preparations, and her help and guidance therewith.

I would like to express my exceptional gratitude and appreciation to my co-workers Dr. Tatjana Epp, Dr. Sebastian Staude, Rebekka Reich, Frieder Lauxmann, Dr. Simon Braunger, Isaac Simon, Dr. Stefan Kreißl, Dr. Maximilian Keim, Thomas Binder, Curtis Rooks, Dr. Johannes Giebel, Katharina Sandritter, Christian Dietzel, Johannes Hecker, and Rainer Babiel, that made this time a memorable experience both in and outside of work. For proofreading of this thesis, I would like to acknowledge Samuel Scharrer, Dr. Tatjana Epp, Dr. Simon Braunger, and Thomas Binder.

Last but not least, I would like to express my gratitude to my family and friends who have supported me and have always been there for me.

Abstract

The formation of hydrothermal ore deposits depends on both the fertility of the involved fluids and the precipitation mechanism. The groundwork for understanding these two aspects is best laid by a detailed mineralogical and geochemical investigation, and supplemented by a geological-framework-considering qualitative model. However, in order to fully understand the involved processes, and to verify the qualitative model, an at least semi-quantitative thermodynamic model is essential. This requires the time-consuming task of compiling, and estimating where appropriate, thermodynamic data for all important mineral species involved. In this thesis, this approach is applied to various aqueous settings from ambient to metamorphic conditions. The thesis is subdivided to cover four different settings: (I) groundwater brines, (II) the fertility and evolution of basement brines and the process of fluid mixing, (III) As- and Ni- bearing hydrothermal brines and the process of fluid reduction and (IV) metamorphic fluids and the process of hydrothermal Ni-remobilization under reducing conditions as well as cooling of Sb-rich fluids.

(I) Surficial water can drastically change its fluid composition through fluid-rock interaction. This is an important process that occurs anywhere between surficial and deep-seated crustal settings. Furthermore, ligands such as Cl play a vital role in the ability of such fluids to mobilize elements. At Buggingen, SW Germany, groundwater partially dissolved evaporitic salts and subsequently reacted with mafic magmatic dikes. Progressive desiccation due to H_2O consumption by clay mineral formation and swelling, the fluid ultimately reached the point of halite saturation.

(II) Surficial fluids can infiltrate deeper into the crust and form fertile hydrothermal fluids, and if certain conditions are met, form hydrothermal veins. In the study area of the Black Forest, this occurred over the past ~300 Ma in the basinal and rift-related setting of SW Germany. The trace element distribution between primary and alteration mineral reveal that basement aquifer fluid-rock interactions can liberate both major and trace elements into the fluid during host rock alteration. Temporally resolved fluid inclusion analyses by microthermometry and LA-ICP-MS on three hydrothermal veins which, in total, formed over a period of 150 Ma, were done to attain a better understanding of the basement aquifer evolution. This revealed a transition with depth and time from a NaCl to a $CaCl_2$-richer basement aquifer. Based on aquifer host rock mineralogy, Na-Ca-K thermometry, Na-K thermometry, compositional trends, and thermodynamic modelling, this evolution and transition with depth can be traced back to the preferred alteration and consumption of Ca-rich feldspar during infiltration of the basement by saline fluids. Fluid mixing from various depths along this transition results in the formation of the Triassic to Cretaceous fluorite-quartz-barite veins in the Black Forest. The formation of the base metal sulfides further requires an influx of sulfide into this otherwise binary mixing scenario. The shift in hydrothermal regime to the subsequent post-Cretaceous veins due to

the opening of the Upper Rhine Graben reflects a gradual transition. This has been observed for the siderite-chalcopyrite-gersdorffite veins in the Black Forest.

(III) The Black Forest also presents a rare but characteristic occurrence of native As±native Ag±arsenide±antimonide-bearing ore shoots that formed cogenetic with the Triassic to Cretaceous veins. The same mineralization type, typically known as native element-arsenide, five element, or Bi-Co-Ni association, is also found as independent veins worldwide. Based on both a local study of the ore shoots and a comprehensive global literature compilation, the previously proposed formation mechanism by reduction is reinforced and refined. Novel thermodynamic modelling of the Ni-Co-Fe-As-Sb-Ag-Bi system reveals that reduction suffices to produce the characteristic and nearly ubiquitous general mineral sequence: native Ag / native Bi → Ni-arsenides → Co-arsenides → Fe-arsenides → native As. The relative abundance of the precipitated minerals is correlated to the fluid composition. When Sb is present in the fluid, the Ni-mono- and -sulfantimonide quickly become stable over their respective As counterpart. Textural information, sulfur isotopic investigation, and experimental literature data supplemented by thermodynamic modelling reveal a redox disequilibrium between sulfate and sulfide which enables the fluid to maintain a low sulfide activity during reduction. This is required for the arsenides and native As to form. The formation of native As is further aided by low temperatures and the presence of sulfide-binding elements such as Pb or Zn. Thus, a reduction of a moderately oxidized fluid (increased solubility of most elements involved) forms these arsenide-bearing associations.

(IV) However, it is also possible to mobilize minor amounts of Ni in reduced, low-saline, near-neutral fluids, if higher temperature/metamorphic conditions prevail. This was studied at Kambalda, Western Australia, where the Ni mobilization at these conditions from primary magmatic Ni-sulfide bodies resulted in the rare formation of several types of hydrothermal pentlandite-rich veins. The “more typical” regional metamorphic hydrothermal fluid is, however, not rich in Ni. A more common scenario is the presence of reduced, Sb-, Fe-, and sulfide-rich fluids, that occasionally are Au-bearing. The formation of hydrothermal veins from such fluids is found in veins all over the Black Forest. Mineralogical, textural, fluid inclusion analysis, and oxygen isotopes augmented by thermodynamic modelling reveal a formation of these Sb-Pb-Ag±Au veins by cooling of a metamorphic fluid and subsequent remobilization stages due to the influx of new basinal brines.

Concluding, the studies presented in this thesis show the applicability and fruitfulness of fluid-mineral system thermodynamic modeling from ambient to metamorphic conditions. Specifically, when it is based on a well-founded mineralogical and geochemical groundwork. Although this multimethod approach is not novel, it is not commonly applied to such an extent as shown here.

Zusammenfassung

Die Bildung von hydrothermalen Erzlagerstätten ist sowohl von der Ergiebigkeit der beteiligten Fluide als auch vom Ausfällungsmechanismus abhängig. Um diese beiden Aspekte zu untersuchen, ist ein qualitatives Modell unter Einbeziehung des geologischen Rahmens und einer detaillierten mineralogischen und geochemischen Studie eine essenzielle Grundlage. Um jedoch die beteiligten Prozesse vollständig zu verstehen und um das qualitative Modell zu verifizieren, ist eine thermodynamische Modellierung essenziell. Dies beinhaltet die zeitintensive Aufgabe, thermodynamische Daten für alle wichtigen beteiligten Spezies zusammenzustellen und gegebenenfalls zu extrapolieren. In dieser Arbeit wurde dieser Ansatz auf verschiedene wässrige Milieus angewandt, von Normalzustandsbedingungen bis hin zu metamorphen Bedingungen. Die Arbeit ist insgesamt in vier verschiedene Teilaspekte unterteilt: (I) Grundwasser-Gestein Wechselwirkungen, (II) die Ergiebigkeit und Entwicklung von Grundgebirgssolen und der Prozess der Fluidmischung, (III) Erzausbildung durch Reduktion von As- und Ni-haltigen Fluiden (IV) metamorphe Fluide und der Prozess der hydrothermalen Ni-Remobilisierung unter reduzierenden Bedingungen sowie die Abkühlung von Sb-reichen Fluiden.

(I) Oberflächenwasser können durch die Wechselwirkung zwischen Fluid und Gestein ihre Fluidzusammensetzung erheblich verändern. Dies ist ein bedeutsamer Prozess, der überall von oberflächlichen nah bis tief in der Kruste auftritt. Dabei spielen Liganden wie Cl eine wichtige Rolle verschiedene Elemente zu mobilisieren und transportieren. In Buggingen, SW-Deutschland, führte Grundwasser zur partiellen Auflösung von Salzen und zur anschließenden Reaktion mit magmatischen mafischen Gängen. Die bei der Alteration fortschreitende Austrocknung aufgrund des H_2O-Verbrauchs durch Tonmineralbildung und Quellung führte bis hin zur Sättigung und Ausfällung von Halit.

(II) Oberflächenfluide können durch Infiltration der Kruste zu metallreichen hydrothermalen Fluiden umgewandelt werden und, wenn die Bedingungen gegeben sind, hydrothermale Mineralisationen bilden. Im Untersuchungsgebiet, SW Deutschland, geschah dies in den letzten ~300 Ma in der durch Becken- und Grabenbildung geprägten Umgebung. Die Spurenelementverteilung zwischen Primär- und Alterationsmineral im Grundgebirge zeigt, dass die Wechselwirkungen zwischen Fluid und Wirtsgestein sowohl Haupt-, als auch Spurenelemente in das Fluid freisetzen können. Zeitlich aufgelöste Fluideinschluss-Analysen mittels Mikrothermometrie und LA-ICP-MS an drei hydrothermalen Gängen, die sich insgesamt über einen Zeitraum von 150 Ma gebildet haben, wurden durchgeführt, um ein besseres Verständnis für die Entwicklung des Grundwasserleiters zu gewinnen.

(III) Der Schwarzwald weist auch ein seltenes, aber charakteristisches Vorkommen von gediegenem As±gediegenem Ag±Arsenid±Antimonid-führenden Erzgängen auf, die sich kogenetisch mit den triassischen bis kreidezeitlichen Gängen gebildet haben. Derselbe

Mineralisierungstyp, der typischerweise als gediegenes Element-Arsenid, Fünf-Element oder Bi-Co-Ni-Assoziation bekannt ist, wird auch als unabhängige Erzgänge weltweit vorgefunden. Basierend sowohl auf einer lokalen Untersuchung der Erzgänge als auch auf einer umfassenden globalen Literaturzusammenstellung, wird der in der Literatur vorgeschlagene Bildungsmechanismus durch Reduktion bekräftigt und im Detail erklärt. Eine erstmalige thermodynamische Modellierung des Ni-Co-Fe-As-Sb-Ag-Bi-Systems zeigt, dass eine Reduktion ausreicht, um die charakteristische und nahezu weltweit allgegenwärtige Mineralsequenz zu erzeugen: natives Ag/natives Bi → Ni-Arsenide → Co-Arsenide → Fe-Arsenide → natives As. Die relative Häufigkeit der Minerale ist dabei durch die Fluidzusammensetzung gesteuert. Wenn Sb in der Flüssigkeit vorhanden ist, werden die Ni-Mono- und Ni-Sulfantimonide stabiler als ihr jeweiliges As-Äquivalent. Texturinformationen, Schwefelisotopenuntersuchungen und experimentelle Literaturdaten, ergänzt durch thermodynamische Modellierung, zeigen ein Redox-Ungleichgewicht zwischen Sulfat und Sulfid, das es dem Fluid ermöglicht, während der Reduktion eine niedrige Sulfidaktivität beizubehalten. Dies ist für die Bildung der Arsenide und des gediegen As erforderlich. Die Bildung von gediegenem As wird durch niedrige Temperaturen und das Vorhandensein von sulfidbindenden Elementen wie Pb oder Zn weiter begünstigt. So bildet die Reduktion eines mäßig oxidierten Fluids diese arsenidhaltigen Verbindungen.

(IV) Es ist jedoch auch möglich, geringe Mengen an Ni schon direkt bei reduzierten Bedingungen und nahezu neutralen pH zu mobilisieren, wenn höhere Temperatur- und Metamorphosebedingungen vorherrschen. Dies wurde in Kambalda, Westaustralien, untersucht, wo die Ni-Mobilisierung unter diesen Bedingungen aus primären magmatischen Ni-Sulfid-Körpern zur seltenen Bildung mehrerer Typen von hydrothermalen pentlanditreichen Gängen führte. Regional metamorphe hydrothermale Fluid sind jedoch arm an Ni. Häufiger ist das Vorhandensein von reduzierten, teils Sb-, Fe- und sulfidreichen Fluiden, die gelegentlich auch Au-haltig sein können. Die Bildung von hydrothermalen Gängen aus solchen Fluiden ist in Gängen im gesamten Schwarzwald zu finden. Mineralogische, texturelle, Fluid-Einschluss-Analysen und Sauerstoff-Isotope, ergänzt durch thermodynamische Modellierung, zeigen eine Bildung dieser Sb-Pb-Ag±Au-Adern durch Abkühlung und anschließende Remobilisierungsprozesse, initiiert durch den Zufluss metallführender hochsalinarer Fluide.

Zusammenfassend zeigen die in dieser Arbeit vorgestellten Studien die Anwendbarkeit und den Nutzen der thermodynamischen Modellierung von Fluid-Mineral-Systemen von Bedingungen nahe der Erdoberfläche bis zu metamorphen Bedingungen. Im Besonderen wird darauf eingegangen, wenn eine solche Modellierung mit einer detaillierten mineralogischen und geochemischen Untersuchung kombiniert wird. Obwohl dieser Multimethoden-Ansatz nicht grundsätzlich neu ist, wird er gewöhnlich nicht in so einem Umfang wie in dieser Arbeit angewandt.

List of publications and personal contribution

The following depicts a list of publications included in this thesis along with a table that explains the author's respective contributions.

Study 1

Braunger, S., **Scharrer, M.**, Marks, M. A. W., Wenzel, T., & Markl, G. (accepted). Interaction between mafic dyke rocks and salt deposits in the Rhine graben (SW Germany). The Canadian Mineralogist.
Status of the publication process: accepted

Author		Scientific ideas (%)	Data generation (%)	Analysis and interpretation (%)	Paper writing (%)
Braunger, S.	1	50	90	60	75
Scharrer, M.	**2**	**15**	**0**	**20**	**5**
Marks, M. A. W.	3	10	0	10	10
Wenzel, T.	4	0	10	0	5
Markl, G.	5	25	0	10	5

Study 2

Walter, B. F., Kortenbruck, P., **Scharrer, M.**, Zeitvogel, C., Wälle, M., Mertz-Kraus, R., & Markl, G. (2019). Chemical evolution of ore-forming brines – Basement leaching, metal provenance, and the redox link between barren and ore-bearing hydrothermal veins. A case study from the Black Forest mining district in SW-Germany. Chemical Geology, 506, 126-148.
Status of the publication process: published

Author		Scientific ideas (%)	Data generation (%)	Analysis and interpretation (%)	Paper writing (%)
Walter, B. F.	1	40	30	35	60
Kortenbruck, P.	2	10	15	15	0
Scharrer, M.	**3**	**20**	**20**	**20**	**20**
Zeitvogel, C.	4	10	15	15	0
Wälle, M.	5	0	10	0	0
Mertz-Kraus, R.	6	0	10	0	0
Markl, G.	7	20	0	15	20

Study 3

Scharrer, M., Reich, R., Fusswinkel, T., Walter, B. F., & Markl, G. (2021). Basement aquifer evolution and the formation of unconformity-related hydrothermal vein deposits: LA-ICP-MS analyses of single fluid inclusions in fluorite from SW Germany. Chemical Geology, 575, 120260.
Status of the publication process: published

Author		Scientific ideas (%)	Data generation (%)	Analysis and interpretation (%)	Paper writing (%)
Scharrer, M.	**1**	**70**	**45**	**75**	**60**
Reich, R.	2	0	40	10	5
Fusswinkel, T.	3	5	10	5	5
Walter, B. F.	4	10	0	0	5
Markl, G.	5	15	0	10	25

Study 4

Walter, B. F., **Scharrer, M.**, Burisch, M., Apukthina, O., & Markl, G. (2020). Limited availability of sulfur promotes copper-rich mineralization in hydrothermal Pb-Zn veins: A case study from the Black Forest, SW Germany. Chemical Geology, 532, 119358.
Status of the publication process: published

Author		Scientific ideas (%)	Data generation (%)	Analysis and interpretation (%)	Paper writing (%)
Walter, B. F.	1	45	60	40	50
Scharrer, M.	**2**	**25**	**10**	**30**	**20**
Burisch, M.	3	5	0	10	10
Apukthina, O.	4	10	30	5	0
Markl, G.	5	15	0	5	20

Study 5

Scharrer, M., Epp, T., Walter, B. F., Pfaff, K., Vennemann, T., & Markl, G. (accepted). The formation of (Ni-Co-Sb)-Ag-As ore shoots in hydrothermal galena-sphalerite-fluorite veins
Status of the publication process: published

Author		Scientific ideas (%)	Data generation (%)	Analysis and interpretation (%)	Paper writing (%)
Scharrer, M.	**1**	**65**	**65**	**65**	**60**
Epp, T.	2	0	20	5	5
Walter, B. F.	3	5	0	10	5
Pfaff, K.	4	10	0	0	5
Vennemann, T.	5	0	15	0	0
Markl, G.	6	20	0	20	25

Study 6

Scharrer, M., Sandritter, K., Walter, B. F., Neumann, U., & Markl, G. (2020). Formation of native arsenic in hydrothermal base metal deposits and related supergene U^{6+} enrichment: The Michael vein near Lahr, SW Germany. American Mineralogist: Journal of Earth and Planetary Materials, 105(5), 727-744.
Status of the publication process: published

Author		Scientific ideas (%)	Data generation (%)	Analysis and interpretation (%)	Paper writing (%)
Scharrer, M.	**1**	**35**	**25**	**65**	**70**
Sandritter, K.	2	15	75	15	5
Walter, B. F.	3	10	0	5	5
Neumann, U.	4	10	0	5	0
Markl, G.	5	20	0	5	20

Study 7

Scharrer, M., Kreissl, S., & Markl, G. (2019). The mineralogical variability of hydrothermal native element-arsenide (five-element) associations and the role of physicochemical and kinetic factors concerning sulfur and arsenic. Ore Geology Reviews, 113, 103025.
Status of the publication process: published

Author		Scientific ideas (%)	Data generation (%)	Analysis and interpretation (%)	Paper writing (%)
Scharrer, M.	**1**	**40**	**65**	**50**	**45**
Kreissl, S.	2	30	35	40	30
Markl, G.	3	30	0	10	25

Study 8

Staude, S., Simon, I., **Scharrer, M.**, Blanc, P., Pfaff, K., & Markl, G., (in preparation). Vein-type pentlandite, $(Ni,Fe)_9S_8$: formation conditions and its implication for orogenic gold deposits
Status of the publication process: in preparation

Author		Scientific ideas (%)	Data generation (%)	Analysis and interpretation (%)	Paper writing (%)
Staude, S.	1	40	10	20	40
Simon, I.	2	20	40	30	5
Scharrer, M.	**3**	**20**	**30**	**20**	**20**
Pfaff, K.	5	10	0	10	5
Blanc, P.	4	0	20	0	5
Monecke, T.	6	0	0	20	5
Markl, G.	7	10	0	0	20

Study 9

Epp, T., Walter, B. F., **Scharrer, M.**, Lehmann, G., Henze, K., Heimgärtner, C., & Markl, G. (2019). Quartz veins with associated Sb-Pb-Ag±Au mineralization in the Black Forest, SW Germany: a record of metamorphic cooling, tectonic rifting, and element remobilization processes in the Variscan belt. Mineralium Deposita, 54(2), 281-306.
Status of the publication process: published

Author		Scientific ideas (%)	Data generation (%)	Analysis and interpretation (%)	Paper writing (%)
Epp, T.	1	30	30	40	60
Walter, B. F.	2	20	20	15	10
Scharrer, M.	**3**	**15**	**10**	**20**	**10**
Lehmann, G.	4	0	15	5	0
Henze, K.	5	0	10	5	0
Heimgärtner, C.	6	0	10	5	0
Bach, W.	7	0	5	0	5
Markl, G.	8	35	0	10	15

Table of content

1. Introduction

Fluid-fluid and/or fluid-rock interactions are crucial processes in all types of geologic environments. They range from atmospheric processes, biological processes, surface weathering, diagenesis, and hydrothermal interactions to subduction and mantle-related processes (e.g., Chapin et al., 2011; Landeweert et al., 2001; Liebscher and Heinrich, 2007; Navon et al., 1988; Peacock, 1990; Smith et al., 2003). Furthermore, specifically concerning economic geology, fluids are involved in nearly all types of ore deposits worldwide. They can both play an essential part in the formation of the ore, and subsequently overprint the ore which may enrich or deplete its economic value (e.g., Cathelineau et al., 2017; Fanlo et al., 2010; Horton et al., 2001; Keim et al., 2019; Marshall et al., 2000).

For most geologic fluid-involving processes, these cannot be studied in situ but have to be deducted from the resulting mineral assemblage. For this, mineralogical and geochemical investigations provide the groundwork for a, at least qualitative, model. However, to fully understand the fluid-involved processes, it is vital to fully characterize all involved species, identify the formation conditions, and to verify (or further interpret) the results using thermodynamic modelling (Bethke, 2007). Therefore, one needs to constrain as many parameters as possible, such as identifying the fluid sources, the mechanism of precipitation and the prevailing conditions.

This, already widespread but not sufficiently applied multiapproach procedure is the baseline of this thesis. It is used to further understand various fluid-fluid and fluid-mineral processes in several settings over a large pressure and temperature range. These include (I) groundwater brine-host rock interactions, (II) the fertility and evolution of basement brines and the process of fluid mixing, (III) As- and Ni- bearing hydrothermal brines and the process of fluid reduction and (IV) metamorphic fluids and the process of hydrothermal Ni-remobilization under reducing conditions as well as cooling of Sb-rich systems.

1.1. Hydrothermal fundamentals

In hydrothermal systems, the fluids involved are typically of magmatic, metamorphic, meteoric, seawater, connate origin, or a mixture of these (e.g., Pirajno, 2012; Robb, 2020). They are originally in equilibrium with their respective host rock, and the type of fluid source can, in some cases, be distinguished using isotope or compositional tracers (e.g., Barnes, 1997; Robb, 2020). Every system has an equilibrium state at each given conditions. A change in one or more of these parameters leads to a disequilibrium, which in turn will be compensated by reactions to reach a new equilibrium state (e.g., Gyftopoulos and Beretta, 2005; Henley et al., 1984). This causes minerals to precipitate, minerals to dissolve, aqueous species to interchange, and/or fluids to segregate due to immiscibility (Barnes, 1997).

There are various geological processes that can lead to a change in one or more of the equilibrium-defining parameters (pressure, temperature, composition, redox state, pH). The most common ones are

- fluid mixing (e.g., Bons et al., 2014; Bouch et al., 2006; Canals and Cardellach, 1993; Fusswinkel et al., 2013; Walter et al., 2018a; Wilkinson et al., 2005),
- fluid rock-interaction (e.g., Einaudi and Burt, 1982; Hu et al., 2015; Kreissl et al., 2018; Meinert, 1992)
- fluid cooling (e.g., Burisch et al., 2017b; Goldfarb and Groves, 2015; Wagner and Cook, 2000)
- fluid boiling or fluid segregation (e.g., Canet et al., 2011; Cunningham, 1978; Korges et al., 2018; Ruggieri et al., 1999),
- and a sudden drop in pressure due to e.g., fracturing (lithostatic to hydrostatic) (e.g., Cunningham, 1978; Monecke et al., 2018; Rusk and Reed, 2002; Weis et al., 2012).

Typically, not just one, but several of these occur at the same time. However, one is usually the predominating mechanism that causes a hydrothermal mineral to precipitate.

1.2. Mineralogical and geochemical approach

To understand both the fluid source and formation process of a hydrothermal deposit, a detailed mineralogical study must be the foundation. A clear textural analysis and interpretation thereof provides information on the temporal evolution and mineral paragenetic sequence of a mineralization (e.g., Bastin, 1950; Ramdohr, 2013; Schwartz, 1951; Spry, 2013). Combining this information with geochemical and fluid inclusion analyses yields the necessary information to construct a qualitative, and in rare cases even a quantitative formation model (e.g., Li and Naldrett, 1993; Phillips and Powell, 2009; Tao et al., 2007).

1.3. Fluid compositional approach

Although some information on the fluid may be inferred from the mineralogy and mineral composition, the most effective way to identify the fluid composition is by fluid inclusion analyses (e.g., Bodnar, 1994; Fusswinkel et al., 2018; Goldstein and Reynolds, 1994; Van den Kerkhof and Hein, 2001; Wilkinson, 2001). Microthermometry with the corresponding petrography provides homogenization temperature and other phase transition temperatures (Van den Kerkhof and Hein, 2001; Wilkinson, 2001). These can, given certain constrains and models, be used to constrain formation temperatures, pressures and major fluid compositions (e.g., Driesner and Heinrich, 2007; Roedder and Bodnar, 1980; Steele-MacInnis et al., 2011). For this, the fluid inclusions are typically classified into secondary, pseudosecondary and primary fluid inclusions, while only the latter two provide information on the conditions during mineral precipitation (e.g., Goldstein and Reynolds, 1994; Van den Kerkhof and Hein, 2001).

The textural correlation of the fluid inclusions relative to the mineralization can further inform about the temporal evolution of the fluid conditions (e.g., Catchpole et al., 2011; Evans, 1995). Furthermore, the gas-to-liquid ratio in the fluid inclusion can be examined to identify fluid boiling or post-depositional inclusion leakage (Wilkinson, 2001). Using Raman or IR spectroscopy, gaseous and aqueous species may be identified and, in some instances, quantified (e.g., Guillaume et al., 2003; Pironon et al., 2001; Seitz et al., 1987).

To gain further insight into the fluid composition, crush leach (e.g., Banks and Yardley, 1992; Bottrell et al., 1988) or in situ LA-ICP-MS can be used (Allan et al., 2005; Audetat et al., 1998; Fusswinkel et al., 2018). The latter is superior, as individual fluid inclusions with their known textural relation are analyzed. Crush leach is a bulk analysis which may only provide reliable fluid compositions for samples containing just one type of fluid, or for samples in which the amount of secondary inclusions is minimal. Both of these methods provide relative concentrations which are normed on the major fluid composition and/or host mineral, commonly the NaCl and/or $CaCl_2$ content provided by microthermometry (e.g., Guillong et al., 2008).

1.4. Thermodynamic modelling

Although detailed mineralogical and geochemical approaches are crucial to infer both qualitative and quantitative formation processes, there still exists a need for thermodynamic validation. Furthermore, when the mineralogy and the geochemistry do not suffice to deduce a formation model, thermodynamic modelling may provide further constraints and insights on the processes involved (e.g., Bethke, 2007). This, in combination with the increase in computational resources, made thermodynamic approaches more and more popular over the years. A wide range of thermodynamic software applications is available, specialized not only for hydrothermal but also for magmatic and/or metamorphic environments, such as – but not limited to – GEM-Selektor, The Geochemist's Workbench (GWB), PHREEQC, OpenCalphad, Bingo-Antidote, Thermo-Calc, HCh, Perple_X, and MELTS. Many of these have seen a recent surge in development with regard to both usability and applicability (e.g., Duesterhoeft and Lanari, 2020; Kulik et al., 2013; Sundman et al., 2015). These programs rely either on the principle of minimizing the Gibbs free energy of formation (dG_f^0), or on the principle of the reaction constant (logK equilibria). The latter is more commonly applied to low-temperature fluids and hydrothermal environments (e.g., Bethke, 1998; Bethke, 2007; Parkhurst, 1995), whereas the principle of minimizing dGf is generally used for all settings (e.g., Duesterhoeft and Lanari, 2020; Kulik et al., 2013). By definition, the logK principle is merely a simplified variant of the dGf principle.

The potential applications of these thermodynamic models are mostly limited by the available quantity and/or quality of thermodynamic data, and not by the software itself. There is a general

scarcity of good regularly updated, publicly-available thermodynamic data for unusual minerals and species, and it is a tedious task to compile these while ensuring quality control. This is further complicated by the problematic nature of the internal consistency of thermodynamic databases and data implementation (Arthur, 2001). Thus, most users refer to one of the precompiled thermodynamic databases available (e.g., Barin, 1995; Blanc et al., 2012; Gamsjäger et al., 2005; Helgeson, 1969; Holland and Powell, 2011; Naumov et al., 1971b; Sehmel, 1989). However, these are not always up to date, while newer, updated or novel thermodynamic data for specific substances may be available. This hinders many from applying thermodynamic modelling.

Considering many geological processes of interest, empirically predicted/extrapolated thermodynamic constants can be precise enough for rough thermodynamic modelling (e.g., Craig and Barton, 1973). Thus, if some thermodynamic constants are lacking, they may reasonably be interpolated or extrapolated using a number of different empirical approaches (e.g., Craig and Barton, 1973; Glasser, 2013; Jenkins and Glasser, 2003; Leitner et al., 2010; Van Hinsberg et al., 2005).

As the basis of this thesis, the regularly updated thermodynamic database “Thermoddem” was used (Blanc, 2008; Blanc, 2017; Blanc and Gaboreau, 2013; Blanc and Lassin, 2013; Blanc et al., 2012). In this study, in cooperation with the Bureau de recherches géologiques et minières (BRGM) team working on maintaining this database, several additions and changes were made by integrating data from other sources and/or extrapolating constants. These include the aqueous Sb-, Bi-, and Ni-system, several Ag- and Pb-sulfosalts, several arsenides, several uranyl-bearing minerals, as well as an increase in applicability up to 600 °C and higher pressures (up to 5 kbar). For this, in each respective study, the choice of thermodynamic data as well as the methods of extrapolation for missing data is well elaborated.

1.5. Stability diagrams for aqueous systems

The focus of the individual studies in this thesis is not on the thermodynamic calculations themselves, but on the application of these to serve the different research questions. These are typically the development of novel processes or confining unknown parameters to further understand preexisting processes. Typical unknown or variable parameters in hydrothermal systems are for example, composition, temperature, pH, and redox conditions. Thus, it is customary to parameterize the thermodynamic model of the investigated system with regards to these variables. The resulting diagrams are commonly activity-activity or activity-temperature diagrams.

A popular method of visualization are stability diagrams that show relative stabilities of mineral assemblages. Common ones are log(fS_2)-temperature (sulfidation state) diagrams (e.g., Barton Jr, 1970; Einaudi et al., 2003) and log(fO_2)-temperature diagrams. For these, most

aqueous and gaseous species are typically not considered, but they are applied not only to magmatic and metamorphic but also to hydrothermal environments (Brenan, 2003; Einaudi et al., 2003).

Also popular are so-called “predominance stability diagrams” based on the designation of one major species. Modelling programs such as GWB(Act2) and PhreeqC calculate these according to one major and several minor species, while all solid, gaseous, and aqueous species can be considered and speciated (Bethke and Yeakel, 2013; Parkhurst, 1995). The equations involving the major element are balanced according to that element, and not on the respective limiting reagent. This simplification can be problematic, especially in complex multicomponent fluid systems. Furthermore, a maximum of one mineral at each condition is allowed to be stable, and this must include the main element (Bethke and Yeakel, 2013). This limits the applicability of such diagrams, as for example a scenario where chalcopyrite and pyrite form a stable paragenesis cannot be calculated this way. The main benefit of these simple predominance diagrams is the reduced computing power needed, which is why these were the diagrams of choice throughout most of the history of thermodynamic modelling.

A more complex approach used in this thesis, is that of true stability – here on called “true assemblage stability diagrams”. For these, at each condition in the activity-activity diagram, the abundance of all gaseous, aqueous, and solid species of all involved elements are considered in the calculation of the stability fields (Bethke and Yeakel, 2021). This diagram type eliminates some major drawbacks of the classic predominance stability diagrams, such as the inability of modelling mineral assemblages. Furthermore, the actual stability fields of minerals can be presented, and not only the predominance fields. In an assemblage stability diagram, the following points are considered:

- Which elements are in excess or in short supply (concerning their activity)?
- Which species are present at each condition?
- What are the absolute and relative individual species activities?

Consequently, true assemblage stability diagrams can deviate significantly from the stability diagrams based on one designated major species, and the resulting interpretations can also diverge. The benefits of these true assemblage stability diagrams are demonstrated by their recent implementation into GWB by the program GWB(Phase2). This implementation by the GWB development team occurred independently of, and in parallel to our rudimentary in-house development of this technique using a script and the program GWB(React).

When enough parameters are known or can be estimated, equilibrium conditions can be fairly easily calculated and depicted in true assemblage stability diagrams. However, thermodynamic modelling only predicts how stable a phase is in one state versus another (Gyftopoulos and Beretta, 2005). For determining which phases do form in nature, another important factor is kinetics, which defines how quickly or slowly species react (Bethke, 2007;

Lothenbach et al., 2010; Machlin, 2010). Thus, just because a specific substance is thermodynamically stable, does not mean it forms at the given conditions in the time available. A substance for which kinetics play a crucial role is sulfur, specifically the transformation from an oxidized to a reduced state or vice versa (Ohmoto and Lasaga, 1982). Sulfur is of importance in many hydrothermal systems, and is present in most of the studied assemblages throughout all studies in this thesis.

2. Choice of study sites and site characteristics

This thesis addresses several fluid-involving environments from ambient to metamorphic conditions. Thus, one study site does not suffice to investigate these. The ones selected for the respective studies of this thesis are described below.

2.1. Black Forest and SW Germany

Most studies (study 1, 2, 3, 4, 5, 6 and 9) were performed within the Black Forest mining district or surrounding region in SW Germany. This district provides an ideal natural laboratory to investigate various hydrothermal processes and fluid-rock interactions. It is rich in hydrothermal mineralogical diversity (Markl, 2015; Markl, 2016; Markl, 2017a; Markl, 2017b), which can be traced back to various ore-forming events that occurred in the past > 300 Ma (e.g., Baatartsogt et al., 2007; Walter et al., 2016; Walter et al., 2018b). The small-scale nature of most hydrothermal veins enables the investigation of involved processes without the need of large sample sets. Furthermore, the abundant already-published research on various geological aspects of the region presents ideal background knowledge and boundary conditions for further research. These include studies on fluid inclusions (e.g., Baatartsogt et al., 2007; Behr et al., 1987; Fusswinkel et al., 2013; Fusswinkel et al., 2014; Schwinn et al., 2006; Staude et al., 2012; Walter et al., 2018a; Walter et al., 2016; Walter et al., 2017), radiogenic and stable isotopes (e.g., Schwinn et al., 2006; Staude et al., 2011), mineral composition (e.g., Pfaff et al., 2011; Staude et al., 2010), paleo fluid models (e.g., Bons et al., 2014; Staude et al., 2009) as well as leaching and alteration of the basement (Burisch et al., 2016).

The region comprises an exhumed Variscan basement (mainly gneisses and granites) overlain by Permian to Jurassic sediments, including sandstones, shales, carbonates and evaporites (Geyer et al., 2011). The present-day structural setting is marked by rifting to the west since the Paleogene, resulting in the formation of the Upper Rhine Graben (Geyer et al., 2011). Simultaneous lifting of the rift shoulders and consequent erosion resulted in the erosional window of the Black Forest (Rupf and Nitsch, 2008).

There has been a history of long lasting (~300 Ma) continuous hydrothermal activity and vein formation in the region (Walter et al., 2018b). According to Walter et al. (2016) and Walter et al. (2018b), five hydrothermal maxima can be distinguished: (i) Carboniferous, (ii) Permian, (iii) Triassic to Early Jurassic, (iv) Middle Triassic to Cretaceous, and (v) post-Cretaceous. The first hydrothermal group (I) comprising quartz-tourmaline veins, is of carboniferous age, and is related to magmatic processes. The second (II) is of Permian age, quartz-dominated, rich in Sb±Ag±Au-sulfide ore, and related to the late Variscan orogenic regime. The third group of hydrothermal veins (III) formed during a period from the Triassic to the Jurassic. These quartz-hematite veins are characterized by a low Cl/Br fluid ratio and fluid inclusion homogenization

temperatures of 100-200 °C. The fourth vein group (IV), formed from the Triassic to Cretaceous (Walter et al., 2018b), is characterized by fluorite-quartz-barite and barite-quartz veins that developed from fluids with a high salinity of 20-30 wt.% NaCl eq., a variable fluid Cl/Br ratio (< 100-1000), and fluid inclusion homogenization temperatures between 50 and 200 °C. The ore mineralogy is largely variable between veins, but generally rich in Pb- and Zn-sulfides (Metz et al., 1957) or Fe- and Mn-ores (Walter et al., 2016). In addition, some veins are arsenide-bearing and can be categorized either as five element associations (Staude et al., 2007; Staude et al., 2012). The last hydrothermal maxima (IV) occurred post-Cretaceous, formed quartz-barite-fluorite veins with a variable sulfide mineralogy and are characterized by a highly variable fluid inclusion salinity (0-25 wt.% NaCl eq.) and fluid inclusion homogenization temperatures of 50-200 °C.

2.2. Kambalda (Western Australia)

Hydrothermal pentlandite that formed from metamorphic fluids is of scientific interest as it is a rare occurrence and thus indicates very specific and unique conditions that favor the transport of Ni and then the precipitation of pentlandite. Since of hydrothermal pentlandite is absent in the Black Forest, the conditions required for its formation were studied at Kambalda, Western Australia. Kambalda is part of the Kalgoorlie Terrane in the Archean Yilgarn Crateon (Goscombe et al., 2009). It consists of a ~ 2700 Ma old sedimentary-volcanic sequence that includes komatiite, chert layers, and basalts (Barnes et al., 2007; Gresham and Loftus-Hills, 1981; Kositcin et al., 2008). This sequence also includes magmatic sulfide ore bodies at the base of the komatiite, which represent several major Ni-deposits (Barnes et al., 2007).

After deposition of the volcanic and sedimentary units, the whole region was intruded by intermediate to felsic dikes, sills, and stocks, whereas the centre of the present-day Kambalda Dome is made up of a trondhjemite pluton. Furthermore, regional metamorphism and folding at 2680 and 2665-2655 Ma overprinted the whole region (Mueller et al., 2016). However, many pre-metamorphic textures are still preserved and enable interpretation thereof (e.g., Staude et al., 2016). There are various types of pre-, syn- and post-metamorphic hydrothermal veins in the Kambalda region. These, among others, include gold-bearing (Neumayr et al., 2008) and pentlandite bearing veins.

2.3. Worldwide comparison

The processes investigated in this thesis are meant to improve their universal understanding and are not focused on describing local processes. Thus, most studies also cover global aspect by comparison to similar, worldwide occurrences. Furthermore, study 7 is based not only on an individual occurrence, but on a worldwide literature review of the investigated ore association.

3. Objective

The topic of this dissertation is fairly broad, and covers various fluid-rock- and fluid-fluid-involving, non-magmatic processes from ambient to metamorphic conditions. The main goal throughout all of the sub-studies (manuscripts) is the mineralogical, textural, and geochemical study of specific mineral assemblages supplemented by thermodynamic modelling in order to investigate certain fluid evolution and mineral formation processes. Variations in settings and mineralogical assemblages between the studies provide unique views and additional information that is mutually supportive in further understanding different aspects of these processes.

3.1. Groundwater brines (I)

When meteoric water or seawater starts to penetrate into the crust, the primary processes (excluding biological processes) that alter the fluid composition are low temperature fluid rock interactions (e.g., Coogan and Gillis, 2018; Musgrove and Banner, 2004). The degree of interaction, and the resulting fluid composition strongly depends on the pre-existing fluid composition, the ambient conditions, and the reacting rock. Such processes were investigated at the Buggingen salt deposit in the Upper Rhine Graben (study 1). There, groundwater reacted with the salt deposits to form a brine, which in turn reacted with the mafic volcanic dikes present at the locality. However, to understand the low-temperature fluid alteration processes, one must first characterize the primary rocks involved. Thus, the focus of this study was:

- characterization of the magmatic mineralogy and magmatic textures, as well as possible magmatic host rock interactions
- identifying and texturally classifying fluid-rock interactions
- developing a qualitative formation model for the alteration of the magmatic dyke rocks and the halite formation in spheroidal textures previously described
- investigating the formation of datolite, a rare boron silicate that has been found in these dykes

3.2. Basement brines and fluid mixing (II)

When meteoric water, seawater, or groundwater penetrates deeper into the crust, fluid-rock interactions occur at elevated conditions. Such an infiltration of fluids into the underlying rocks of the crust is fairly typical in basinal environments (e.g., Bons et al., 2014) and present in the Black Forest, where we studied these processes. The heightened temperature at depth promotes reactions and transport of most species (e.g., Krumgalz, 2017; Krumgalz, 2018a; Krumgalz, 2018b), which in turn enables the formation of fertile hydrothermal fluids. The mixing of these fluids with each other or with surficial fluids can then lead to the formation of

hydrothermal veins. Several studies of this thesis, based on such hydrothermal vein samples of the Black Forest, and on mineralogy, texture, mineral composition, as well as fluid inclusion composition aim to address the following aspects:

- brine fertility and the liberation of trace elements by fluid alteration of biotite to chlorite and feldspars to clay minerals (study 2)
- temporal and spatial transition and evolution of a shallow seawater/groundwater brine to a deep-seated basement brine (study 3)
- transition from a basement brine hydrothermal regime to a dominantly sedimentary brine hydrothermal regime due to a change in tectonic setting (study 4)
- the temporal and spatial aspect of fluid mixing and the thus-resulting textures in the hydrothermal veins (study 3)
- the difference between barren and sulfide ore-bearing veins, and the requirement for sulfide precipitation (study 3, 4 & 5)

3.3. As- and Ni-bearing fluids and fluid reduction (III)

Interestingly, a few veins of the Black Forest show a cogenetic formation of fluorite-quartz-barite-sulfide-galena veins and native As±arsenide±antimonide±native Ag-rich ore pockets with the same gangue mineralogy. These ore pockets are herein referred to as ore shoots, and are classified as native element-arsenide associations, also known as five element association or Bi-Co-Ni associations. The arsenides are typically Ni-, Co-, and Fe-arsenides. These have been attributed to a number of formation conditions (e.g., Kissin, 1993; Marshall et al., 2000; Ondrus et al., 2003), but the more recent literature has emphasized the importance of oxidizing conditions during mobility and reduction during deposition (e.g., Burisch et al., 2017a; Kreissl et al., 2018; Markl et al., 2016; Naumov et al., 1971a). This thesis studies such unique arsenide and native-element rich associations in the Black Forest (study 5 & 6) and by a comprehensive worldwide literature review (study 7) with a specific focus on:

- the formation mechanism by fluid reduction (study 5 & 7)
- the required conditions for native As formation (study 6)
- the presence of a universally typical mineral sequence and how it is controlled (study 7)
- the impact of variations in fluid compositions and prevailing conditions (study 5 & 7)
- the impact of sulfide and the sulfide-sulfate disequilibrium on the mineralogy of these hydrothermal associations (study 5 & 7)

3.4. Metamorphic fluids and metal mobility (IV)

Although these native element-arsenide associations are commonly rich in Ni-arsenides, their global contribution to Ni-ore is negligible as most worldwide Ni-ore resources are of magmatic

or secondary enrichment origin (www.usgs.gov). There, it is typically bound as sulfides, mainly pentlandite, $Ni_{4.5}Fe_{4.5}S_8$ (Mishra, 2001). Although pentlandite can also precipitate from an aqueous solution, its hydrothermal origin is very rare worldwide. The reasons for this must be related to the low solubility of Ni under most conditions and the unique conditions required for its mobility and/or precipitation. Thus, these conditions and involved processes have been investigated at a location where hydrothermal pentlandite-rich veins formed. Such a location is Kambalda, WA, where hydrothermal pentlandite veins formed around magmatic sulfide bodies (Simon, 2019; study 8). The main points of focus were:

- source of the fluids and investigating the Ni uptake from the magmatic sulfide ore body
- conditions favoring Ni-mobility
- constraining conditions (pH, Temp, fluid composition) present at vein formation by mineral assemblage
- the relation of these conditions to the fact that some of these veins are gold-bearing, while others are gold-barren

The Ni-bearing reduced fluids responsible for the pentlandite vein formation at Kambalda are fairly atypical for most metamorphic-hydrothermal or orogenic fluids. Such fluids more typically form sulfide-poor, quartz- and/or carbonate-rich veins that can also be rich in silicates, Al-phases and/or graphite (e.g., Robert et al., 1995; Rumble et al., 1986; Yardley, 1983). However, there are other types of sulfide-bearing, orogenically induced or metamorphic hydrothermal systems that even produce economically important deposits. An example for this are mesothermal Sb±Au-deposits (e.g., Goldfarb et al., 2005; Goldfarb and Groves, 2015; Lentz et al., 2002; Neiva et al., 2008). Such a mineralization type, on a smaller scale, is also present in many areas of exposed Variscan basement in Europe. There, they typically form polystage Sb-Pb-Ag±Au-bearing quartz veins. To investigate their formation and involved remobilization processes, the veins exposed in the Black Forest, SW Germany, are subject to this study (study 9). The main focus was put on:

- the occurrence of both invisible Au and discrete native Au grains
- refining their formation model and investigation on the thermodynamic control of the metamorphic-hydrothermal ore deposition and its relation to the observed mineral sequence
- the impact of remobilization processes during subsequent influxes of hydrothermal fluids with varying composition
- identifying the large-scale tectonic events related to each remobilization event

4. Individual studies

In the following sub-sections, each individual study conducted during this thesis is summarized. A specific focus is put on the outcomes and conclusions of each studies.

4.1. Groundwater brines (I)

Title of publication: Interaction between mafic dyke rocks and salt deposits in the Rhine graben (SW Germany). (Study 1)

The mafic rocks, olivine melilitites, and monchiquites intruded into the sediment at Buggingen containing a potash salt deposit. Although a large chemical contrast exits between the magmatic and salt-hosting rocks, no primary chemical interaction occurred during dyke emplacement. However, a detailed mineralogical and mineral-chemical characterization (EPMA) revealed a low-temperature overprint of the magmatic dykes. Due to the large unknown impact of kinetics and sorption processes involved, regrettably thermodynamic modelling was not possible in the timeframe and scope of the study.

Typical dyke rock textures are spheroids that, depending on whether they adjoin the salt rocks or the bituminous Fish Shale, show a contrasting mineralization. Those associated with the salt layers mainly consist of smectite, calcite, halite, and sometimes anhydrite, while those associated with the Fish Shale comprise smectite, calcite, zeolite, and analcime. Spheroidal textures are present independent of the host rock. Thus, the halite inclusions are interpreted to not illustrate salt-magma mingling, or salt-liquid immiscibility caused by intense magmatic assimilation with the salt rocks as one might expect. The lack of rock-melt interactions is likely a result of the high melting point of halite and possibly a low orthomagmatic water content of the primitive melts. The latter inhibited intense magmatic fluid exsolution and a consequent dissolution of the salt. Small-scale dykes, such as the ones investigated, presumably cooled too fast to reach the melting point of the salt, which would have enabled liquid mingling and/or assimilation processes (Knipping, 2006).

The two types of halite-bearing textures are interpreted as amygdules and hydrothermally altered ocelli. Meteoric water/groundwater interacting with the salt layers formed saline, NaCl-rich fluids. These subsequently reacted with the groundmass of the dyke rocks to form smectites and zeolites, thereby increasing the Na concentration of the fluid and cementing the fluid paths. The absence of halite in the groundmass indicates that the initial fluid could not have been halite-saturated. Upon entering a vesicle or an ocellus, from which the calcite-bearing interior (Hurrle, 1973) was previously dissolved, smectite formation continues. This forms a clay-rich layer on the marginal areas, and traps the fluid in the vesicle. Continued water extraction by clay mineral formation and/or swelling finally led to the precipitation of halite.

Datolite, a rare boron silicate, is present in some pseudomorphs after olivine, associated with halite or with serpentine/smectite. The boron is most likely sourced from the clay-rich layers of the host rock (e.g., Garrett, 1998) and was incorporated/adsorbed into serpentine/smectite during alteration of olivine. The later breakdown of serpentine/smectite liberates and provides the Si and B needed for the formation of datolite.

4.2. Basement brines and fluid mixing (II)

4.2.1. Basement brine fertility and fluid mixing

Title of publication: Chemical evolution of ore-forming brines – Basement leaching, metal provenance, and the redox link between barren and ore-bearing hydrothermal veins. A case study from the Black Forest mining district in SW-Germany. (Study 2)

Over geological timeframes, surface- and groundwaters can penetrate and permeate deep into the crust in basinal settings (Bucher and Stober, 2010; Harrison, 1989; Stober and Bucher, 2004). There, these are transformed into metal-bearing fertile hydrothermal fluids that can act as a source for hydrothermal ore deposits. This study addresses two subjects: One is the metal provenance of such basinal brines, and the other is to investigate the ore formation (Pb and Zn-sulfides) in unconformity-related hydrothermal veins. For this, the Black Forest mining district, SW Germany, was selected as a case study area.

To investigate the metal provenance, LA-ICPMS trace element analyses of primary minerals (feldspars and biotites) and alteration products (chlorite and clay minerals) in both granites and paragneisses were conducted. A previous experimental study on these rocks had determined the release of Pb, Zn, Cu and W by felsic minerals and Ni, As, Zn and Cu by biotite during their alteration by aqueous fluids at elevated temperatures (Burisch et al., 2016). Our average values of non-altered and alteration minerals at least partially replicate these findings. Furthermore, the dominant provenance for Pb, Zn, As, Sb, Ba, Tl, Mo, Fe and Mn are probably paragneisses, while Co, Cu and Ni are probably predominantly sourced from S-type granites. Due to the natural variability, and since these alterations are not volume- or mass-constant, these results have to be treated with care. However, the elemental content of the primary minerals reveals the presence of abundant trace elements that, when liberated, suffice for the formation of the occurring hydrothermal veins in the Black Forest.

To investigate the ore forming process (sulfide precipitation), six independent hydrothermal veins of Jurassic-Cretaceous and Cenozoic age in the Black Forest mining district, SW Germany were studied by microthermometry and LA-ICP-MS on single fluid inclusions. As numerous previous studies have shown, these are formed by fluid mixing of a basement brine and a sedimentary sourced fluid (e.g., Baatartsogt et al., 2007; Schwinn et al., 2006; Staude et al., 2011; Walter et al., 2016). The investigated veins include both barren and galena-

sphalerite-bearing veins. Since these strongly overlap regarding their fluid composition, their mineralogical difference cannot be a cause of large variations in fluid sources. Thermodynamic equilibrium modelling based on the measured fluid salinity and trace element composition indicates the need for a reducing or sulfide rich phase. Thus, whether a barren or galena-sphalerite-bearing vein forms is dependent on the availability of sulfide in addition to the two major fluids. Furthermore, mineralogical variations may also be influenced by variations in fluid mixing ratios between the metal-richer basement brine and the sedimentary cover.

4.2.2. Basement brine evolution and fluid mixing

Basement aquifer evolution and the formation of unconformity-related hydrothermal vein deposits: LA-ICP-MS analyses of single fluid inclusions in fluorite from SW Germany. (Study 3)

The previous study has shown that a saline fluid can assimilate trace elements during alteration of the primary basement, and in turn is transformed into a fertile hydrothermal fluid. However, the temporal aspect of this uptake and the fluid evolution during penetration of a surface fluid into the basement was not yet investigated. This, in combination with the temporal and spatial aspect of hydrothermal vein formation in basinal unconformity related settings, is addressed in this study. Three similar unconformity-related vein systems in the Black Forest, SW Germany, are selected on the basis that the main ore stage of all three veins spans a ~150 Ma period of hydrothermal activity.

To provide a robust statistical basis, over 1650 fluid inclusions were analyzed by microthermometry. Of these, a total of 108 fluid inclusions (mainly in fluorite) were successfully analyzed by LA-ICP-MS. The resulting fluid compositional data confirm the binary mixing as described by several prior publications (e.g., Baatartsogt et al., 2007; Schwinn et al., 2006; Staude et al., 2011; Walter et al., 2016). The source fluids for mineralization are

- fluid A, a $CaCl_2$-dominated, KCl-poor, deeper seated modified bittern brine with a salinity of ~25 wt% $CaCl_2$+NaCl, and
- fluid B, a NaCl-dominated and KCl-richer bittern/halite dissolution brine situated at shallower depths in the crystalline basement with salinities of ~22 wt% NaCl+$CaCl_2$.

Both fluids are transition metal-bearing (e.g., up to ~100 mg/kg Ba, Pb, Zn, Ni, and up to 10 mg/kg Ag), show high As (up to 1000 mg/kg), and low S (below the detection limit in most analyses). The analyses do not suffice to provide a statistical difference between fluid A and B concerning the above-mentioned elements. However, Fusswinkel et al. (2013) demonstrated a higher transition metal content for fluid A for a different hydrothermal vein in the region.

Both fluid A and subsequently fluid B were originally derived from seawater, and modified prior to and during penetration of the basement. The high Cl/Br ratios in the investigated fluid

inclusions indicate the influence of halite dissolution in the sedimentary cover for both fluids (Walter et al., 2016). To decipher further modification processes within the basement, the Na-Ca-K and Na-K geothermometers, Rb/Cs and Cl/Br systematics, and thermodynamic modelling were applied. These conclude that fluid A is characterized by the presence of Na-, K-, and Ca-bearing feldspars. These are abundantly present in the granitic and gneissic host rocks (Geyer et al., 2011). Progressive alteration of predominantly Ca-rich plagioclase led to its consumption and clay mineral formation. Accordingly, fluid B that entered the basement subsequently to fluid A is mainly in equilibrium with K-rich and Na-rich feldspars and with clay minerals. This scenario produced a gradual shift in fluid composition from a deep, $CaCl_2$-rich to a shallow NaCl-dominated aquifer.

The fluid inclusions further indicate a change from a $CaCl_2$-rich to an NaCl-dominated fluid system. This is a result of, either a change in fluid mixing ratios, or more likely, a change in composition of the reservoir fluid. The downward fluid flow pushes the shift from a shallow NaCl-dominated to a deep $CaCl_2$-rich fluid aquifer to greater depth over time. Thus, if the source reservoir depth (3-7 km, depending on the assumed geothermal gradient) is fairly constant over time, an evolutionary shift to more NaCl rich environment is given.

The aquifer temperature (~250 °C) and the temperature of vein formation (100-170 °C) indicate fluid cooling prior to fluid mixing. The latter resulted in the formation of the major gangue minerals fluorite, quartz, barite, and calcite. The great diversity of fluid compositions (including ones close to the mixing endmembers) trapped within the same crystal, as well as compositional variations even within individual fluid inclusion trails indicated that fluid mixing is a rapid and turbulent process.

4.2.3. Fluid mixing and transition of hydrothermal regimes

Title of publication: Limited availability of sulfur promotes copper-rich mineralization in hydrothermal Pb-Zn veins: A case study from the Black Forest, SW Germany. (Study 4)

The mixing of a deeper and a shallower basement brine, both sedimentary and/or seawater sourced, provides a viable way to form unconformity-related hydrothermal veins in the region as has been shown by Study 3 and previous authors (e.g., Baatartsogt et al., 2007; Schwinn et al., 2006; Staude et al., 2011; Walter et al., 2016). Through the evolution of these fluids (study 3) and/or the involvement of new fluids, the resulting mineralogy can also be affected. The galena-sphalerite-fluorite-barite veins, typical of the Black Forest region, commonly show a late-stage change in mineralogy of both ore and gangue minerals. An example of this is the occurrence of late-stage siderite-chalcopyrite-gersdorffite associations. The required change in parameters and processes needed for the transition from a Pb-Zn- to a Cu-Ni-stage is studied on 28 hydrothermal veins in the Black Forest.

The mineralogy, mineral abundance and mineral composition (of sphalerite, gersdorffite, pyrite, arsenopyrite, fahlore and galena) record a gradual transition from the Pb-Zn- to the Cu-Ni-stage. The gradual nature is explained by systematic step-by-step variations in mixing ratios. However, the change in mineralogy of the Cu-Ni-stage contrasts to the Pb-Zn-stage, which is formed by a fluid mixing of two basement aquifers (study 3). A change in parameters such as fO_2, pH, and temperature is either not present, or does not suffice to explain this change in mineralogy of both ore and gangue minerals. Thus, a further fluid source is required. This is most likely attributed to the opening of the Upper Rhine Graben and the therewith related juxtaposition of various aquifers (e.g., Walter et al., 2016).

This transition in hydrothermal stages is also reflected by the fluid composition. Through direct quantitative (LA-ICP-MS) and indirect qualitative (trace element composition of minerals) analyses, the early-basement-derived fluid system is determined to have been rich in Pb, Zn, Ag, and Sb. The subsequently entrapped fluid of the Cu-Ni-stage is significantly richer in Cu. However, its composition still indicates a significant portion of at least one of these basement fluids to be involved. Ba, Pb, and Zn are still present in the mixed fluid of the Cu-Ni-stage. In order to form chalcopyrite without abundant barite, galena, or sphalerite, thermodynamic modelling constrains its formation to very low-sulfur-species activity. Furthermore, the formation of the observed pyrite → chalcopyrite + pyrite → chalcopyrite sequence at the given conditions and fluid compositional range also requires an increase in Cu/Fe ratio over time. In summary, the change in mineralogy from the Pb-Zn-stage to the Cu-Ni-stage reflects a gradual transition from a hydrothermal regime of long-term stable deep fluid reservoirs towards shallower and perturbed fluid reservoirs during rifting of the Upper Rhine Graben.

4.3. As- and Ni-bearing brines and fluid reduction (III)

4.3.1. Reduction of an As-bearing hydrothermal fluid (local study)

Title of publication: The formation of (Ni-Co-Sb)-Ag-As ore enrichment zones in hydrothermal galena-sphalerite-fluorite veins. (Study 5)

A sharp or gradual change in mineralogy is typically coherent with a unidirectional transition in hydrothermal stage and hydrothermal fluid regime, as shown in study 3. However, the main hydrothermal stage of three hydrothermal vein systems in the Black Forest, SW Germany, incorporates native As-bearing hydrothermal ore enrichment zones (here called “ore shoots”). Their textural occurrence implies that they formed syngenetic with their host base metal sulfide-fluorite-barite-quartz veins with a short-termed change in mineralogy. The ore shoots are decimeters to tens of meters large, and classified as native element-arsenide associations, also known as five element association. They contain native arsenic, arsenides, antimonides, sulfides, and sulfosalts, which are otherwise absent in the vein. The focus of this study is (a)

the physical change from a “normal” hydrothermal regime to one producing ore shoots, and (b) the chemical pre-requisites for their formation. Furthermore, the three localities vary with regard to ore shoot mineralogy and composition, which is (1) Ag-As-rich in the Münstertal, (2) Ag-Ni-As-rich at Urberg, and (3) Ag-Ni-As-Sb-rich at Wieden.

Based on detailed fluid inclusion investigations, the formation of the vein’s gangue minerals is the result of a binary mixing between a NaCl- and a $CaCl_2$-rich brine (both ~20 wt% NaCl eq). This mixing correlation, major and minor fluid composition (by microthermometry and LA-ICP-MS), formation temperature (~150 °C), pressure (< ~500 bar), and sulfur isotopic signature are identical (within the margin of variability) in ore shoot and host vein. As a consequence, supported by thermodynamic modelling, ore shoot formation must have resulted from a change in redox conditions by a local influx of a volumetrically minor reducing agent in an otherwise undisturbed hydrothermal system. The elemental content and the mineralogy of each ore shoot reflects the metal content of the binary mixed, hydrothermal fluid. The mineralogical textures and successions or assemblages are then thermodynamically and (concerning sulfur) kinetically controlled. The sulfide required for both the vein sulfides and the ore shoot sulfides is likely sourced from the host rock because of matching isotope signatures and because sulfide transport in the vein-forming (and metal-bearing) fluids can be disregarded based on thermodynamic and kinetic reasons. The same holds true for sulfate reduction.

The final (present-day) ore shoot textures are also strongly influenced by hydrothermal remobilization processes of As and Ag, which formed several sulfosalts. Although the fluid system is As dominated, the predominant stability of the Sb-endmember sulfosalts allows them to form.

4.3.2. Conditions required for native As formation

Title of publication: Formation of native arsenic in hydrothermal base metal deposits and related supergene U^{6+} enrichment: The Michael vein near Lahr, SW Germany. American Mineralogist. (Study 6)

Some native element-arsenide associations such as the ore shoots investigated in study 5 are known for their massive aggregates of native As. It also forms in other unique hydrothermal environments, but is generally rare compared to other hydrothermal ore minerals. This is surprising, as arsenic is a common constituent of upper crustal fluids. Thus, the prerequisites required for its formation must be distinctive. To study these, the Michael vein near Lahr, SW Germany, has been selected because native As is a major gangue constituent and previous studies provide sufficient background conditions of hydrothermal activity in the region (e.g., Baatartsogt et al., 2007; Geyer et al., 2011; Pfaff et al., 2011; Walter et al., 2018a; Walter et al., 2016) to decipher favorable conditions of native As formation.

The native As-bearing stage (sphalerite-native arsenic-quartz stage) of the Michael vein is the second hydrothermal stage succeeding a galena-barite stage. Its formation comprises the generalized mineral succession: pyrite → sphalerite±jordanite-gratonite solid solution → galena → native As. Microthermometry, sulfide isotopic equilibrium, and thermodynamic modelling indicate that the native As-bearing stage formed by cooling of a ~130 °C hot saline fluid accompanied by reduction due to admixing of a sulfide- and reducing agent-bearing fluid. Based on thermodynamic calculations, the formation of native arsenic is constrained to reduced conditions in combination with very low concentrations of the transition metals Fe, Co, and Ni, as well as low sulfide concentrations. A “typical” hydrothermal solution does not fulfill these criteria, because it can contain significant amounts of at least Fe and sulfide. Thus, the sulfarsenides and As-bearing sulfides are considerably more common. In the case at hand, the scarcity of pyrite, sulfarsenides, and arsenides records the low Fe, Co, and Ni content of the fluid. The still available Fe is further consumed by the formation of Fe-poor but Fe-bearing sphalerite. Furthermore, the lack of As-sulfides (e.g. realgar) is a result of abundant Zn and Pb in the fluid, stabilizing sphalerite and galena. Sulfur must be the limiting agent in this precipitation reaction: When it is exhausted, native As can form.
A specialty of the Michael vein is the presence of secondary uranyl-bearing arsenates without the presence of any primary hydrothermal uranium-bearing minerals. These are hügelite, hallimondite, zeunerite, heinrichite or novacekite. Sourced from the surrounding host rock, U^{6+}-bearing oxidized fluids infiltrated the vein structure where native As acted as a trap for uranium during supergene weathering processes. However, native As did not act as a reducing agent to the U^{6+}, but rather as an arsenate supply to stabilize these quite unusual assemblages.

4.3.3. Reduction of As-, Ni- and Co-bearing hydrothermal fluids (global study)

Title of publication: The mineralogical variability of hydrothermal native element-arsenide (five-element) associations and the role of physicochemical and kinetic factors concerning sulfur and arsenic. (Study 7)

Native element-arsenide associations, also known as five element association, do not only occur as locally constrained ore shoots, as is the case in study 4. They more commonly form as spate veins or as an individual hydrothermal stage commonly comprising Ni-, Co-, and Fe-arsenides and -sulfarsenides. These typically form characteristic overgrowth textures on skeletal native silver and/or bismuth aggregates. Depending on locality, native arsenic, native antimony, antimony-arsenic-silver alloys, and uraninite may also be present. The most common associated gangue minerals are carbonates. Famous deposits of this type include Bou Azzer, Morocco; Cobalt, Ontario; Jáchymov, Czech Republic; Kongsberg, Norway; and Schneeberg, Germany.

To develop, or in this case refine and improve, the formation model by Markl et al. (2016) for native element-arsenide associations, it is vital to not only investigate individual occurrences but to consider the broad spectrum of both similarities and the observed mineralogical and textural diversity. Thus, this contribution is based on a comprehensive literature review, on which it builds by means of thermodynamic modelling. This includes novel calculated stability relations of native elements (Ag, Bi, As), Ni-, Co- and Fe-mono-, di- and -sulfarsenides, and -sulfides/sulfosalts. For this, missing thermodynamic data was estimated according to several preexisting and unique extrapolation methods, and the resulting values were weighted according to several parameters.

Considering all available literature data, the physicochemical conditions of formation (e.g. p, T, fluid composition) and of the host rocks are variable. The only unifying features are the reduced conditions required for their formation, and the more oxidized conditions required for their aqueous transport. Thus, this study supports the theory by Markl et al. (2016) of a formation by a geologically fast reduction process of a Ni-, Co-, Fe-, As-bearing fluid by e.g., methane, graphite or Fe^{2+}. Furthermore, the nearly ubiquitous and characteristic sequence of Ni- → Co- → Fe-diarsenides can be thermodynamically explained by the continuous reduction of a metal- and arsenic-bearing aqueous solution. This sequence is reasonably robust against variations in fluid composition, as three orders of magnitude differences between Fe, Co, and Ni concentrations in the fluid are needed to change this sequence at neutral pH. Therefore, it is nearly omnipresent. The mineralogical sequence is, however, not only dependent on the process of reduction and differences in reducing agents, but also on dissolution reactions, initial pH, fluid/rock ratio, and the crystallization in contained microenvironments. A combination of these can explain all observed local variations. At a higher pH, the typical Ni → Co → Fe sequence changes to Co → Ni → Fe. Such a sequence has been observed only at two localities worldwide. Furthermore, the prevalence of mono- versus diarsenides is also pH-dependent.

Although sulfide is commonly only present in minor amounts during the arsenide ore stage, the stability of dissolved sulfide plays a crucial role in five-element mineralogy, as Co- and Fe-arsenides would not form in the presence of appreciable amounts of sulfide. The lack of abundant sulfide in the mineralogy is either a consequence of an absence of sulfur, or a thermodynamic disequilibrium between sulfate and sulfide; both cases occur in nature. The latter is explained by slow reaction kinetics for the sulfate-sulfide (Ohmoto and Lasaga, 1982) compared to the arsenite/arsenate-arsenide conversion (Allin, 2019). In such a case, formation of arsenides and native metals is kinetically controlled, which is supported by the common skeletal textures in this type of ore. At some occurrences of native element-arsenide associations, sulfarsenides and/or sulfides are present, but generally are only common in late

assemblages. This indicates either a late-stage sulfide influx or attainment of thermodynamic equilibrium with regards to sulfur.

4.4. Metamorphic fluids and metal mobility (IV)

4.4.1. Hydrothermal Ni-remobilization under reduced metamorphic conditions

Title of publication: Vein-type pentlandite, $(Ni,Fe)_9S_8$: formation conditions and its implication for orogenic gold deposits. (Study 8)

Although native element-arsenide associations are typically rich in Ni, the overall occurrence of hydrothermal Ni-ore is not very common. Their rarity is especially puzzling, considering that with an average of 47 ppm in the crust (~2000 ppm in ultramafic rocks), Ni is an abundant trace element (González-Álvarez et al., 2013). However, its mobility is what is driving the lack of hydrothermal Ni-ore occurrences (González-Álvarez et al., 2013). When these do form, Ni is not only bound to arsenides as it is the case for native element-arsenide associations (study 5, 6 and 7). More typically, Ni-is present as sulfides such as millerite or pentlandite. The latter is abundantly common in magmatic Ni-ore, whereas the worldwide hydrothermal portion of pentlandite is negligible. A rare case where Ni is hydrothermally mobilized and redeposited as pentlandite is at Kambalda, Western Australia. The aim is to further understand the conditions required for hydrothermal transport of Ni and for the deposition of pentlandite.

Three distinct types of hydrothermal pentlandite occurrences have been found in Kambalda, all closely associated with magmatic Ni-sulfide ore bodies. These are (1) pentlandite-rich veins with biotite, quartz, and an albite alteration in the host rock, (2) pentlandite-bearing quartz-scheelite veins, and (3) pentlandite-poor carbonate veins with arsenides, base metal sulfides, and gold associated with magnetite alteration within a magmatic sulfide body. In all of these cases, pentlandite is associated with pyrrhotite. The presence of hydrothermal pentlandite within these veins and associated alteration is constrained to a region of less than 10 m from the magmatic Ni-ore bodies. This is in accordance with all documented hydrothermal pentlandite occurrences worldwide as these are almost exclusively associated with the close presence of magmatic sulfides or ultramafic rocks. The mineral compositional data from Kambalda show that hydrothermal pentlandite can be distinguished from its neighboring magmatic pentlandite by a higher Fe- and lower Co-content. When present, the associated sulfarsenides also vary in composition to their magmatic counterparts. The hydrothermal ones are typically richer in Ni and poorer in Co.

The hydrothermal pentlandite formed from a fluid originally sourced from one of the various host rocks in the region (felsic to ultramafic), which then interacted with the magmatic sulfide body and was coherently enriched in Ni, Fe, and sulfide. The high temperature, near peak metamorphic conditions, assumed for the vein formation enabled the mobility and transport of

Ni. Novel high-temperature hydrothermal modelling of pentlandite and the Ni-system (up to 600 °C) reveals that the mobility of Ni increases with increasing temperature and salinity. However, metamorphic fluids that are not associated with evaporitic rocks generally have a low to moderate salinity (e.g., Phillips, 1993; Yardley and Graham, 2002; Yardley, 2005). Under such metamorphic conditions, the stability of pentlandite is confined to reduced conditions at a near neutral pH. The absence of pure Ni-sulfides such as millerite further restrict the system to reducing conditions. Thus, in a Fe-Ni-S fluid system, the mobility of abundant Ni is constrained to a low pH as long as reducing conditions prevail. The pentlandite-associated minerals thus restrict the precipitation mechanism to a process of increasing pH likely associated to the intense fluid-rock interaction with the felsic host rock. Fluid cooling may have further supported the precipitation.

The assemblage pentlandite, pyrrhotite, and biotite is confined to a narrow stability field that also overlaps with a local increase (in the fO_2-pH space) in Au solubility. This is due to the stability of Au-sulfide-complexes, which inhibits the deposition of Au in veins with this association. However, when pentlandite is associated with arsenides instead of biotite, their overlapping stability field is larger. Thus, gold can more easily precipitate. This is visible in the Kambalda samples, where the arsenide-bearing veins are also associated with gold.

4.4.2. Cooling of Sb-rich metamorphic fluids

Title of publication: Quartz veins with associated Sb-Pb-Ag±Au mineralization in the Black Forest, SW Germany: a record of metamorphic cooling, tectonic rifting, and element remobilization processes in the Variscan belt. (Study 9)

Concerning the formation of Au-bearing hydrothermal associations, it is fairly common for these to form under very late to post-peak metamorphic conditions (Goldfarb and Groves, 2015 and references therin). However, the close association of Au to Ni in a metamorphic-hydrothermal setting, as is the case in study 8, is rather atypical. More common is the association with Fe- and As- or Sb-bearing sulfides such as pyrite, arsenopyrite, and stibnite in vein-type settings. An example of such a mineralization type is present in exposed Variscan basement rocks throughout Europe (e.g., Dill, 1993). In the following study, a total of 38 Au-bearing and Au-barren, stibnite-rich quartz-veins in the Black Forest are investigated. These veins are classified as a polymetallic Sb-Pb-Ag±Au-W-Sn-As-Zn, multistage hydrothermal mineralization. Based on textural, isotopic, fluid inclusion, and compositional data complemented by thermodynamic modelling, the genetic model for this fairly common and important type of Sb-mineralization is refined. Since the veins in question also display a regional diversity with regard to mineralogy and mineral abundance, this study also aims to investigate this discrepancy between these veins

Four texturally distinct hydrothermal stages are distinguished: (I) an Fe-As(-Sb±Au)-stage, (II) a Pb-Zn-Cu-stage, (III) a Pb-Sb-stage, and (IV) an Ag-Sb-stage. During the first stage, fluid cooling of a Permian low-salinity metamorphic mesothermal fluid (of initially more than 400°C) precipitated quartz, associated with a sulfide mineral sequence of pyrrhotite → pyrite + arsenopyrite → berthierite → stibnite. This fluid-cooling-driven mineralogical sequence has been thermodynamically verified. In the model, a pure H_2O fluid at neutral pH and a salinity of 5 wt% NaCl was injected with sulfur and antimony, and equilibrated with the granitic host rock at 400 °C. Subsequent cooling of this fluid produced the observed mineralogy and mineral sequence. The relative abundance of pyrite is strongly dependent on the degree of fluid-host rock interaction during fluid cooling. The sulfides of this stage incorporated invisible gold (up to 0.2 wt%), which was partially remobilized and reprecipitated as discrete electrum grains at the end of stage I.

The subsequent two stages (II & III) formed due to mixing of high-salinity, mid- and upper-crustal fluids (up to 27 wt% NaCl+$CaCl_2$) from the Jurassic to the Cretaceous. Typical homogenization temperatures are 50-250 °C. The third stage, specifically, is characterized by abundant Pb-sulfosalts that predominantly formed by the remobilization of preexisting stage I minerals. Through the estimation of the thermodynamic sulfosalt stability, their formation could also be thermodynamically verified.

The last hydrothermal ore stage (IV) formed due to the opening of the Upper Rhine Graben. This last stage is mainly found along NE-SW-oriented veins, which reflects the tectonic setting during the Tertiary. The percolating fluids were specifically rich in Ag, and thus resulted in the formation of Ag-rich minerals such as miargyrite, pyrargyrite, and stephanite. Furthermore, the Ag-content of fahlore significantly increased relative to earlier-stage fahlore. The replacement of minerals from prior ore stages are a common feature. The mineralogical sequence present in the samples reveal an overall enrichment in Ag content of the minerals over time.

5. Conclusion and implication

Fluid-fluid and fluid-mineral involving processes are essential in defining mineralogy, textures, and geochemistry over a large range of conditions. In turn, when mineralogy, textures, and geochemistry are studied and supplemented by thermodynamic modelling, these processes can be reconstructed. Although this approach is not novel, the increase in computational capacity and advances in modelling software enable sophisticated techniques such as the modelling of true assemblage stability diagrams, reaction path modelling, and reactive transport modelling. In prior literature, these techniques are often still not sufficiently or adequately applied.

We have shown that when applied, they can provide essential input in understanding some geological processes. Surficial water such as meteoric or seawater penetrates into the crust, and fluid-mineral interactions characterize the evolution of both the host rock and aquifer. This occurs from shallow environments (study 1) to deeper seated upper crustal environments (study 2 & 3). The fluid evolution of a NaCl-bearing brine in a granitic aquifer host during crustal infiltration progressively leads to an increase in $CaCl_2$ and trace element content of the fluid. This is related to feldspar (mainly Ca-rich plagioclase) and mica alteration. Such a fluid evolution during progressive fluid penetration to greater depths, results in a gradual transition from a shallow NaCl-rich to a deeper $CaCl_2$-rich aquifer. Mixing of fluids from different depths (study 3) or with sedimentary fluids (study 4) explains the presence of hydrothermal veins in basinal settings such as the Black Forest. There, it is clear that for the formation of the base metal-sulfides, an influx of sulfide during the volumetrically mainly binary fluid mixing is essential.

If instead, or in addition to, fluid mixing, such fertile metal-bearing brines are reduced, a texturally and mineralogically unique mineralization type – the native element-arsenide association – can form (study 5-7). This mineralization type incorporates a characteristic mineral sequence that is controlled by thermodynamic stability of the respective minerals during progressive reduction. Furthermore, sulfide must be largely absent from the liquid for its formation. This can occur due to an absence of sulfur, or due to the sulfate-sulfide disequilibrium present at lower epithermal conditions prohibiting a sufficiently fast reduction of sulfate. Besides the abundant Ni-Co- and Fe-arsenides, native As is a common mineral in several native element-arsenide associations worldwide. Native As, although not common, also forms in other unique hydrothermal environments. Reducing conditions are a prerequisite for its formation; low temperatures and low-sulfide environments are also advantageous.

In an As- or S-bearing environment, the Ni mobility is mostly constrained to oxidizing, highly acidic, or highly alkaline conditions. However, Ni can also be transported over short distances at high-temperature, reducing, and near-neutral conditions (study 8). This has been shown by equilibrium modelling of hydrothermal pentlandite veins that are spatially confined to around

magmatic sulfide ore bodies at Kambalda. Locally, these metamorphic veins also comprise native Au. Its solubility and precipitation conditions are in accordance to the thermodynamic stability of the hosting vein minerals.

There are, however, other mineralized mesothermal orogenically driven hydrothermal associations. Mesothermal Sb±Au-associations are one example. These typically comprise stibnite-rich quartz-carbonate veins and are found all over the world. Their formation in the Black Forest is primarily linked to fluid cooling of a metamorphic fluid. This has been verified by fluid inclusion microthermometry oxygen stable isotopes and thermodynamic modeling of the mineralogical sequence during cooling. Multiple influxes of new compositionally unique fluids (basement brines and formation fluids) resulted in subsequent remobilization events that overprinted the primary mineralization and formed numerous sulfosalts.

Our studies have demonstrated the importance of thermodynamic modelling in a variety of different natural settings, from ambient to metamorphic. Commonly, the most complex aspect of this is the compilation or extrapolation of both thermodynamic parameters and boundary conditions to constrain the models. Thus, this is a research area that still requires attention in the future. Many of the processes investigated here could be further refined by improving the underlying thermodynamic data. Furthermore, experimental approaches to confirm the formation mechanisms or processes proposed here would be a future area of interest.

References

Allan, M.M. et al., 2005. Validation of LA-ICP-MS fluid inclusion analysis with synthetic fluid inclusions. American Mineralogist, 90(11-12): 1767-1775.

Allin, N., 2019. Experimental Investigation of the Thermochemical Reduction of Arsenite and Sulfate: Low Temperature Hydrothermal Copper, Nickel, and Cobalt Arsenide and Sulfide Ore Formation. MSc Thesis Thesis.

Arthur, R.C., 2001. Comment on the internal consistency of thermodynamic databases supporting repository safety assessments, Swedish Nuclear Power Inspectorate.

Audetat, A., Günther, D., Heinrich, C.A., 1998. Formation of a magmatic-hydrothermal ore deposit: Insights with LA-ICP-MS analysis of fluid inclusions. Science, 279(5359): 2091-2094.

Baatartsogt, B. et al., 2007. Contrasting paleofluid systems in the continental basement: a fluid inclusion and stable isotope study of hydrothermal vein mineralization, Schwarzwald district, Germany. Geofluids, 7(2): 123-147.

Banks, D., Yardley, B., 1992. Crush-leach analysis of fluid inclusions in small natural and synthetic samples. Geochimica et Cosmochimica Acta, 56(1): 245-248.

Barin, I., 1995. Thermochemical data of pure substances, 304. Wiley-VCH, New York, 1885 pp.

Barnes, H.L., 1997. Geochemistry of hydrothermal ore deposits. John Wiley & Sons.

Barnes, S.J., Barnes, S., Perring, C., 2007. Komatiite-hosted nickel sulfide deposits: Geology, geochemistry, and genesis. SPECIAL PUBLICATION-SOCIETY OF ECONOMIC GEOLOGISTS, 13: 51.

Barton Jr, P., 1970. Sulfide petrology: Mineralogical Society of America Special Paper, v. 3.

Bastin, E.S., 1950. Interpretation of ore textures, 45. Geological Society of America.

Behr, H.-J., Horn, E., Frentzel-Beyme, K., Reutel, C., 1987. Fluid inclusion characteristics of the Variscan and post-Variscan mineralizing fluids in the Federal Republic of Germany. Chemical Geology, 61(1-4): 273-285.

Bethke, C.M., 1998. The geochemist's workbench. Users Guide, 184.

Bethke, C.M., 2007. Geochemical and biogeochemical reaction modeling. Cambridge University Press, 564 pp.

Bethke, C.M., Yeakel, S., 2013. GWB Essentials Guide, Aqueous Solutions, LLC Champaign, Illinois.

Bethke, C.M., Yeakel, S., 2021. GWB Reaction Modeling Guide, Aqueous Solutions, LLC Champaign, Illinois.

Blanc, P., 2008. Sélection de propriétés thermodynamiques pour les principales espèces aqueuses et minérales porteuses de fer. RP-56587-FR, BRGM, http://thermoddem.brgm.fr/.

Blanc, P., 2017. Update for the 2017 version. RP-66811-FR, BRGM, http://thermoddem.brgm.fr/.

Blanc, P., Gaboreau, S., 2013. Sélection de propriétés thermodynamiques pour les principales espèces aqueuses et minérales porteuses de nickel. RP-61871-FR, BRGM, http://thermoddem.brgm.fr/.

Blanc, P., Lassin, A., 2013. Sélection de propriétés thermodynamiques pour les principales espèces aqueuses et minérales porteuses d'arsenic. RP-62585-FR, BRGM, http://thermoddem.brgm.fr/.

Blanc, P. et al., 2012. Thermoddem: A geochemical database focused on low temperature water/rock interactions and waste materials. Applied Geochemistry, 27(10): 2107-2116.

Bodnar, R., 1994. Interpretation of microthermometric data for H_2O-NaCl fluid inclusions. in. Fluid inclusions in minerals: methods and applications: 117-130.

Bons, P.D. et al., 2014. Fluid mixing from below in unconformity-related hydrothermal ore deposits. Geology, 42(12): 1035-1038.

Bottrell, S., Yardley, B.W., Buckley, F., 1988. A modified crush-leach method for the analysis of fluid inclusion electrolytes. Bulletin de minéralogie, 111(3): 279-290.

Bouch, J.E. et al., 2006. Direct evidence of fluid mixing in the formation of stratabound Pb–Zn–Ba–F mineralisation in the Alston Block, North Pennine Orefield (England). Mineralium Deposita, 41(8): 821-835.

Brenan, J.M., 2003. Effects of fO2, fS2, temperature, and melt composition on Fe-Ni exchange between olivine and sulfide liquid: implications for natural olivine–sulfide assemblages. Geochimica et Cosmochimica Acta, 67(14): 2663-2681.

Bucher, K., Stober, I., 2010. Fluids in the upper continental crust. Geofluids, 10(1-2): 241-253.

Burisch, M. et al., 2017a. Methane and the origin of five-element veins: Mineralogy, age, fluid inclusion chemistry and ore forming processes in the Odenwald, SW Germany. Ore Geology Reviews, 81: 42-60.

Burisch, M., Marks, M.A., Nowak, M., Markl, G., 2016. The effect of temperature and cataclastic deformation on the composition of upper crustal fluids - An experimental approach. Chemical Geology, 433: 24-35.

Burisch, M., Walter, B.F., Markl, G., 2017b. Silicification of Hydrothermal Gangue Minerals in Pb-Zn-Cu-fluorite-quartz-baryte Veins. The Canadian Mineralogist, 55(3): 501-514.
Canals, A., Cardellach, E., 1993. Strontium and sulphur isotope geochemistry of low-temperature barite-fluorite veins of the Catalonian Coastal Ranges (NE Spain): a fluid mixing model and age constraints. Chemical Geology, 104(1-4): 269-280.
Canet, C., Franco, S.I., Prol-Ledesma, R.M., González-Partida, E., Villanueva-Estrada, R.E., 2011. A model of boiling for fluid inclusion studies: Application to the Bolaños Ag–Au–Pb–Zn epithermal deposit, Western Mexico. Journal of Geochemical Exploration, 110(2): 118-125.
Catchpole, H., Kouzmanov, K., Fontboté, L., Guillong, M., Heinrich, C.A., 2011. Fluid evolution in zoned Cordilleran polymetallic veins—insights from microthermometry and LA-ICP-MS of fluid inclusions. Chemical Geology, 281(3-4): 293-304.
Cathelineau, M. et al., 2017. Multistage crack seal vein and hydrothermal Ni enrichment in serpentinized ultramafic rocks (Koniambo massif, New Caledonia). Mineralium Deposita, 52(7): 945-960.
Chapin, F.S., Matson, P.A., Vitousek, P., 2011. Principles of terrestrial ecosystem ecology. Springer Science & Business Media.
Coogan, L.A., Gillis, K.M., 2018. Low-temperature alteration of the seafloor: Impacts on ocean chemistry. Annual Review of Earth and Planetary Sciences, 46: 21-45.
Craig, J.R., Barton, P.B., 1973. Thermochemical approximations for sulfosalts. Economic Geology, 68(4): 493-506.
Cunningham, C.G., 1978. Pressure gradients and boiling as mechanisms for localizing ore in porphyry systems. US department of the interior, 6(6): 745-754.
Dill, H.G., 1993. Die Antimonvorkommen der mitteleuropäischen Alpiden und Varisziden. Z Dtsch Geol Ges, 144: 434-450.
Driesner, T., Heinrich, C.A., 2007. The system H2O–NaCl. Part I: Correlation formulae for phase relations in temperature–pressure–composition space from 0 to 1000 C, 0 to 5000 bar, and 0 to 1 XNaCl. Geochimica et Cosmochimica Acta, 71(20): 4880-4901.
Duesterhoeft, E., Lanari, P., 2020. Iterative thermodynamic modelling—Part 1: A theoretical scoring technique and a computer program (Bingo-Antidote). Journal of Metamorphic Geology, 38(5): 527-551.
Einaudi, M.T., Burt, D.M., 1982. Introduction; terminology, classification, and composition of skarn deposits. Economic geology, 77(4): 745-754.
Einaudi, M.T., Hedenquist, J.W., Inan, E.E., 2003. Sulfidation state of fluids in active and extinct hydrothermal systems: Transitions from porphyry to epithermal environments. Special Publication-Society of Economic Geologists, 10: 285-314.
Evans, M.A., 1995. Fluid inclusions in veins from the Middle Devonian shales: A record of deformation conditions and fluid evolution in the Appalachian Plateau. Geological Society of America Bulletin, 107(3): 327-339.
Fanlo, I., Subías, I., Mateo, E., 2010. Supergene enrichment of primary Cu-Ag assemblages in Ag at the Padros deposit, Iberian range, Spain. The Canadian Mineralogist, 48(2): 415-430.
Fusswinkel, T. et al., 2018. Combined LA-ICP-MS microanalysis of iodine, bromine and chlorine in fluid inclusions. Journal of Analytical Atomic Spectrometry, 33(5): 768-783.
Fusswinkel, T. et al., 2013. Fluid mixing forms basement-hosted Pb-Zn deposits: Insight from metal and halogen geochemistry of individual fluid inclusions. Geology, 41(6): 679-682.
Fusswinkel, T., Wagner, T., Wenzel, T., Wälle, M., Lorenz, J., 2014. Red bed and basement sourced fluids recorded in hydrothermal Mn–Fe–As veins, Sailauf (Germany): A LA-ICPMS fluid inclusion study. Chemical Geology, 363: 22-39.
Gamsjäger, H., Bugajski, J., Gajda, T., Lemire, R.J., Preis, W., 2005. Chemical thermodynamics of Nickel. Elsevier Science
Garrett, D.E., 1998. Borates: Handbook of deposits, processing, properties, and use. Elsevier.
Geyer, O.F., Gwinner, M.P., Geyer, M., Nitsch, E., Simon, T., 2011. Geologie von Baden-Württemberg. Schweizerbart.
Glasser, L., 2013. Single-Ion values for ionic solids of both formation enthalpies, Δf H (298) ion, and gibbs formation energies, Δf G (298) ion. Inorganic Chemistry, 52(2): 992-998.
Goldfarb, R. et al., 2005. Distribution, character and genesis of gold deposits in metamorphic terranes. Society of Economic Geologists.
Goldfarb, R.J., Groves, D.I., 2015. Orogenic gold: Common or evolving fluid and metal sources through time. Lithos, 233: 2-26.
Goldstein, H., Reynolds, T., 1994. Systematics of fluid inclusions in diagenetic minerals. SEPM short course, 31: 199.
González-Álvarez, I., Pirajno, F., Kerrich, R., 2013. Hydrothermal nickel deposits: Secular variation and diversity. Elsevier.

Goscombe, B., Blewett, R., Czarnota, K., Groenewald, P., Maas, R., 2009. Metamorphic evolution and integrated terrane analysis of the eastern Yilgarn Craton; rationale, methods, outcomes and interpretation. Geoscience Australia Record, 23: 270.
Gresham, J., Loftus-Hills, G., 1981. The geology of the Kambalda nickel field, Western Australia. Economic Geology, 76(6): 1373-1416.
Guillaume, D., Teinturier, S., Dubessy, J., Pironon, J., 2003. Calibration of methane analysis by Raman spectroscopy in H2O–NaCl–CH4 fluid inclusions. Chemical Geology, 194(1-3): 41-49.
Guillong, M., Meier, D.L., Allan, M.M., Heinrich, C.A., Yardley, B.W., 2008. Appendix A6: SILLS: A MATLAB-based program for the reduction of laser ablation ICP-MS data of homogeneous materials and inclusions. Mineralogical Association of Canada Short Course, 40: 328-333.
Gyftopoulos, E.P., Beretta, G.P., 2005. Thermodynamics: foundations and applications. Courier Corporation.
Harrison, W.J., 1989. Modeling fluid/rock interactions in sedimentary basins, SEG Technical Program Expanded Abstracts 1989. Society of Exploration Geophysicists, pp. 595-598.
Helgeson, H.C., 1969. Thermodynamics of hydrothermal systems at elevated temperatures and pressures. American journal of science, 267(7): 729-804.
Henley, R.W., Truesdell, A., Barton, P., Whitney, J., 1984. Fluid-mineral equilibria in hydrothermal systems, 1. Society of Economic Geologists Littleton, CO.
Holland, T., Powell, R., 2011. An improved and extended internally consistent thermodynamic dataset for phases of petrological interest, involving a new equation of state for solids. Journal of Metamorphic Geology, 29(3): 333-383.
Horton, T.W., Becker, J., Craw, D., Koons, P., Chamberlain, C.P., 2001. Hydrothermal arsenic enrichment in an active mountain belt: Southern Alps, New Zealand. Chemical Geology, 177(3-4): 323-339.
Hu, H. et al., 2015. Reequilibration processes in magnetite from iron skarn deposits. Economic Geology, 110(1): 1-8.
Hurrle, H., 1973. Ocelli-und Mandelbildung der Melilithankaratrite im Kalisalzlager Buggingen und im Kristallin des Schwarzwaldes.
Jenkins, H.D.B., Glasser, L., 2003. Entropy, standard absolute S0 298, values from volume or density. Inorganic Chemistry 42(26): 8702-8706.
Keim, M.F. et al., 2019. Polyphase enrichment and redistribution processes in silver-rich mineral associations of the hydrothermal fluorite-barite-(Ag-Cu) Clara deposit, SW Germany. Mineralium Deposita, 54(2): 155-174.
Kissin, S.A., 1993. The geochemistry of transport and deposition in the formation of five-element (Ag-Ni-Co-As-Bi) veins, Eight Quadrennial International Association on the Genesis of Ore Deposits Symposium. Schweizerbart'sche Verlagsbuchhandlung, pp. 14.
Knipping, B.J., 2006. Basalt intrusions in evaporites, 24. Springer.
Korges, M., Weis, P., Lüders, V., Laurent, O., 2018. Depressurization and boiling of a single magmatic fluid as a mechanism for tin-tungsten deposit formation. Geology, 46(1): 75-78.
Kositcin, N. et al., 2008. SHRIMP U-Pb zircon age constraints on the Late Archaean tectonostratigraphic architecture of the Eastern Goldfields superterrane, Yilgarn craton, Western Australia. Precambrian Research, 161(1-2): 5-33.
Kreissl, S. et al., 2018. Reconstruction of a >200 Ma multi-stage “five element” Bi-Co-Ni-Fe-As-S system in the Penninic Alps, Switzerland. Ore Geology Reviews, 95: 746-788.
Krumgalz, B., 2017. Temperature dependence of mineral solubility in water. Part I. Alkaline and alkaline earth chlorides. Journal of Physical and Chemical Reference Data, 46(4): 043101.
Krumgalz, B., 2018a. Temperature dependence of mineral solubility in water. Part 2. Alkaline and alkaline earth bromides. Journal of Physical and Chemical Reference Data, 47(1): 013101.
Krumgalz, B., 2018b. Temperature dependence of mineral solubility in water. Part 3. Alkaline and alkaline earth sulfates. Journal of Physical and Chemical Reference Data, 47(2): 023101.
Kulik, D.A. et al., 2013. GEM-Selektor geochemical modeling package: revised algorithm and GEMS3K numerical kernel for coupled simulation codes. Computational Geosciences, 17(1): 1-24.
Landeweert, R., Hoffland, E., Finlay, R.D., Kuyper, T.W., van Breemen, N., 2001. Linking plants to rocks: ectomycorrhizal fungi mobilize nutrients from minerals. Trends in ecology & evolution, 16(5): 248-254.
Leitner, J., Voňka, P., Sedmidubský, D., Svoboda, P.J.T.A., 2010. Application of Neumann–Kopp rule for the estimation of heat capacity of mixed oxides. 497(1-2): 7-13.
Lentz, D.R., Thorne, K., Yang, X.-M., 2002. Preliminary analysis of the controls on the various episodes of gold mineralization at the Lake George antimony deposit, New Brunswick. Current research: 02-1.

Li, C., Naldrett, A., 1993. Sulfide capacity of magma; a quantitative model and its application to the formation of sulfide ores at Sudbury, Ontario. Economic Geology, 88(5): 1253-1260.
Liebscher, A., Heinrich, C.A., 2007. Fluid–fluid interactions in the Earth's lithosphere. Reviews in Mineralogy and Geochemistry, 65(1): 1-13.
Lothenbach, B., Damidot, D., Matschei, T., Marchand, J., 2010. Thermodynamic modelling: state of knowledge and challenges. Advances in cement research, 22(4): 211-223.
Machlin, E., 2010. An introduction to aspects of thermodynamics and kinetics relevant to materials science. Elsevier.
Markl, G., 2015. Schwarzwald, Vol. 1, Nordschwarzwald and Grube Clara. Bode Verlag, Lauenstein, 672 pp.
Markl, G., 2016. Schwarzwald, Vol. 2, Mittlerer Schwarzwald Teil 1. Bode Verlag, Lauenstein, 648 pp.
Markl, G., 2017a. Schwarzwald, Vol. 3, Mittlerer Schwarzwald Teil 2. Bode Verlag, Lauenstein, 640 pp.
Markl, G., 2017b. Schwarzwald, Vol. 4, Südlicher Schwarzwald. Bode Verlag, Lauenstein, 880 pp.
Markl, G., Burisch, M., Neumann, U., 2016. Natural fracking and the genesis of five-element veins. Mineralium Deposita, 51(6): 703-712.
Marshall, B., Vokes, F., Larocque, A., 2000. Regional metamorphic remobilization: upgrading and formation of ore deposits. Reviews in Economic Geology, 11(1): 19-38.
Meinert, L.D., 1992. Skarns and skarn deposits. Geoscience Canada.
Metz, R., Richter, M., Schürenberg, 1957. Die Blei-Zink-Erzgänge des Schwarzwaldes. Beihefte zum Geologischen Jahrbuch. Amt für Bodenforschung, Hannover, 153 pp.
Mishra, B., 2001. Cobalt and nickel production. Encyclopedia of Materials: Science and Technology (Second Edition): 1288-1294.
Monecke, T. et al., 2018. Quartz solubility in the H2O-NaCl system: A framework for understanding vein formation in porphyry copper deposits. Economic Geology, 113(5): 1007-1046.
Mueller, A.G., Hagemann, S.G., McNaughton, N.J., 2016. Neoarchean orogenic, magmatic and hydrothermal events in the Kalgoorlie-Kambalda area, Western Australia: constraints on gold mineralization in the Boulder Lefroy-Golden Mile fault system. Mineralium Deposita, 55(4): 633-663.
Musgrove, M., Banner, J.L., 2004. Controls on the spatial and temporal variability of vadose dripwater geochemistry: Edwards Aquifer, central Texas. Geochimica et Cosmochimica Acta, 68(5): 1007-1020.
Naumov, G.B., Motorina, Z.M., Naumov, V.B., 1971a. Conditions of formation of carbonates in veins of the lead-cobalt-nickel-silver-uranium type (translation from Geokhimiya, No 8, pp. 938-948, 1971). Geochemistry International, 8: 590-598.
Naumov, G.B., Ryzhenko, B.N., Khodakovsky, I.L., 1971b. Handbook of thermodynamic data (in Russian). Moscow Atomizdat., Moscow 239 pp.
Navon, O., Hutcheon, I., Rossman, G., Wasserburg, G., 1988. Mantle-derived fluids in diamond micro-inclusions. Nature, 335(6193): 784-789.
Neiva, A.M., Andráš, P., Ramos, J., 2008. Antimony quartz and antimony–gold quartz veins from northern Portugal. Ore Geology Reviews, 34(4): 533-546.
Neumayr, P. et al., 2008. Oxidized and reduced mineral assemblages in greenstone belt rocks of the St. Ives gold camp, Western Australia: vectors to high-grade ore bodies in Archaean gold deposits? Mineralium Deposita, 43(3): 363-371.
Ohmoto, H., Lasaga, A.C., 1982. Kinetics of reactions between aqueous sulfates and sulfides in hydrothermal systems. Geochimica et Cosmochimica Acta, 46(10): 1727-1745.
Ondrus, P. et al., 2003. Ore-forming processes and mineral parageneses of the Jáchymov ore district. Journal of GEOsciences, 48(3-4): 157-192.
Parkhurst, D.L., 1995. User's guide to PHREEQC: A computer program for speciation, reaction-path, advective-transport, and inverse geochemical calculations. US Department of the Interior, US Geological Survey.
Peacock, S.A., 1990. Fluid processes in subduction zones. Science, 248(4953): 329-337.
Pfaff, K. et al., 2011. Trace and minor element variations and sulfur isotopes in crystalline and colloform ZnS: Incorporation mechanisms and implications for their genesis. Chemical Geology, 286(3-4): 118-134.
Phillips, G.N., 1993. Metamorphic fluids and gold. Mineralogical Magazine, 57(388): 365-374.
Phillips, G.N., Powell, R., 2009. Formation of gold deposits: Review and evaluation of the continuum model. Earth-Science Reviews, 94(1-4): 1-21.
Pirajno, F., 2012. Hydrothermal mineral deposits: principles and fundamental concepts for the exploration geologist. Springer Science & Business Media.
Pironon, J. et al., 2001. FT-IR measurements of petroleum fluid inclusions: methane, n-alkanes and carbon dioxide quantitative analysis. Geofluids, 1(1): 2-10.

Ramdohr, P., 2013. The ore minerals and their intergrowths. Elsevier.
Robb, L., 2020. Introduction to ore-forming processes. John Wiley & Sons.
Robert, F., Boullier, A.M., Firdaous, K., 1995. Gold-quartz veins in metamorphic terranes and their bearing on the role of fluids in faulting. Journal of Geophysical Research: Solid Earth, 100(B7): 12861-12879.
Roedder, E., Bodnar, R., 1980. Geologic pressure determinations from fluid inclusion studies. Annual review of earth and planetary sciences, 8(1): 263-301.
Ruggieri, G., Cathelineau, M., Boiron, M.-C., Marignac, C., 1999. Boiling and fluid mixing in the chlorite zone of the Larderello geothermal system. Chemical Geology, 154(1-4): 237-256.
Rumble, I., Douglas, Duke, E.F., Hoering, T.L., 1986. Hydrothermal graphite in New Hampshire: Evidence of carbon mobility during regional metamorphism. Geology, 14(6): 452-455.
Rupf, I., Nitsch, E., 2008. Das Geologische Landesmodell von Baden-Württemberg: Datengrund lagen, technische Umsetzung und erste geologische Ergebnisse, Regierungspräsidium Freiburg: Landesamt für Geologie, Rohstoffe und Bergbau.
Rusk, B., Reed, M., 2002. Scanning electron microscope–cathodoluminescence analysis of quartz reveals complex growth histories in veins from the Butte porphyry copper deposit, Montana. Geology, 30(8): 727-730.
Schwartz, G.M., 1951. Classification and definitions of textures and mineral structures in ores. Economic Geology, 46(6): 578-591.
Schwinn, G., Wagner, T., Baatartsogt, B., Markl, G., 2006. Quantification of mixing processes in ore-forming hydrothermal systems by combination of stable isotope and fluid inclusion analyses. Geochimica et Cosmochimica Acta, 70(4): 965-982.
Sehmel, G., 1989. Cyanide and antimony thermodynamic database for the aqueous species and solids for the EPA-MINTEQ geochemical code. PNL-6835, Pacific Northwest Lab., Richland, WA (USA).
Seitz, J.C., Pasteris, J.D., Wopenka, B., 1987. Characterization of CO2□ CH4□ H2O fluid inclusions by microthermometry and laser Raman microprobe spectroscopy: Inferences for clathrate and fluid equilibria. Geochimica et Cosmochimica Acta, 51(6): 1651-1664.
Simon, I., 2019. Characterization of pentlandite-bearing quartz veins of Kambalda, Western Australia. MSc Thesis Thesis, Colorado School of Mines.
Smith, K.A. et al., 2003. Exchange of greenhouse gases between soil and atmosphere: interactions of soil physical factors and biological processes. European journal of soil science, 54(4): 779-791.
Spry, A., 2013. Metamorphic textures. Elsevier.
Staude, S., Barnes, S.J., Le Vaillant, M., 2016. Evidence of lateral thermomechanical erosion of basalt by Fe-Ni-Cu sulfide melt at Kambalda, Western Australia. Geology, 44(12): 1047-1050.
Staude, S., Bons, P.D., Markl, G., 2009. Hydrothermal vein formation by extension-driven dewatering of the middle crust: An example from SW Germany. Earth and Planetary Science Letters, 286(3-4): 387-395.
Staude, S. et al., 2011. Deciphering fluid sources of hydrothermal systems: a combined Sr-and S-isotope study on barite (Schwarzwald, SW Germany). Chemical Geology, 286(1-2): 1-20.
Staude, S., Mordhorst, T., Neumann, R., Prebeck, W., Markl, G., 2010. Compositional variation of the tennantite–tetrahedrite solid-solution series in the Schwarzwald ore district (SW Germany): the role of mineralization processes and fluid source. Mineralogical Magazine, 74(2): 309-339.
Staude, S., Wagner, T., Markl, G., 2007. Mineralogy, mineral compositions and fluid evolution at the Wenzel hydrothermal deposit, Southern Germany: Implications for the formation of Kongsberg-type silver deposits. The Canadian Mineralogist, 45(5): 1147-1176.
Staude, S. et al., 2012. Multi-stage Ag–Bi–Co–Ni–U and Cu–Bi vein mineralization at Wittichen, Schwarzwald, SW Germany: geological setting, ore mineralogy, and fluid evolution. Mineralium Deposita, 47(3): 251-276.
Steele-MacInnis, M., Bodnar, R., Naden, J., 2011. Numerical model to determine the composition of H2O–NaCl–CaCl2 fluid inclusions based on microthermometric and microanalytical data. Geochimica et Cosmochimica Acta, 75(1): 21-40.
Stober, I., Bucher, K., 2004. Fluid sinks within the earth's crust. Geofluids, 4(2): 143-151.
Sundman, B., Kattner, U.R., Palumbo, M., Fries, S.G., 2015. OpenCalphad-a free thermodynamic software. Integrating Materials and Manufacturing Innovation, 4(1): 1-15.
Tao, L., Gao, J.-g., Luo, Q.-l., Zang, X.-b., He, R., 2007. Establishing Quantitative Information Model of Comprehensive Ore-Formation and Forecasting Lancang Lead-Deposit in Yunnan. Journal of Kunming University of Science and Technology (Science and Technology), 2.
Van den Kerkhof, A.M., Hein, U.F., 2001. Fluid inclusion petrography. Lithos, 55(1-4): 27-47.

Van Hinsberg, V., Vriend, S., Schumacher, J.J.J.o.m.G., 2005. A new method to calculate end-member thermodynamic properties of minerals from their constituent polyhedra I: enthalpy, entropy and molar volume. 23(3): 165-179.
Wagner, T., Cook, N., 2000. Late-Variscan antimony mineralisation in the Rheinisches Schiefergebirge, NW Germany: evidence for stibnite precipitation by drastic cooling of high-temperature fluid systems. Mineralium Deposita, 35(2-3): 206-222.
Walter, B.F. et al., 2018a. Multi-reservoir fluid mixing processes in rift-related hydrothermal veins, Schwarzwald, SW-Germany. Journal of Geochemical Exploration, 186: 158-186.
Walter, B.F., Burisch, M., Markl, G., 2016. Long-term chemical evolution and modification of continental basement brines–a field study from the Schwarzwald, SW Germany. Geofluids, 16(3): 604-623.
Walter, B.F., Burisch, M., Marks, M.A., Markl, G., 2017. Major element compositions of fluid inclusions from hydrothermal vein-type deposits record eroded sedimentary units in the Schwarzwald district, SW Germany. Mineralium Deposita, 52(8): 1191-1204.
Walter, B.F. et al., 2018b. The connection between hydrothermal fluids, mineralization, tectonics and magmatism in a continental rift setting: Fluorite Sm-Nd and hematite and carbonates U-Pb geochronology from the Rhinegraben in SW Germany. Geochimica et Cosmochimica Acta, 240: 11-42.
Weis, P., Driesner, T., Heinrich, C.A., 2012. Porphyry-copper ore shells form at stable pressure-temperature fronts within dynamic fluid plumes. Science, 338(6114): 1613-1616.
Wilkinson, J., 2001. Fluid inclusions in hydrothermal ore deposits. Lithos, 55(1-4): 229-272.
Wilkinson, J.J., Eyre, S.L., Boyce, A.J., 2005. Ore-forming processes in Irish-type carbonate-hosted Zn-Pb deposits: Evidence from mineralogy, chemistry, and isotopic composition of sulfides at the Lisheen Mine. Economic Geology, 100(1): 63-86.
Yardley, B., Graham, J., 2002. The origins of salinity in metamorphic fluids. Geofluids, 2(4): 249-256.
Yardley, B.W., 1983. Quartz veins and devolatilization during metamorphism. Journal of the Geological Society, 140(4): 657-663.
Yardley, B.W., 2005. 100th Anniversary Special Paper: metal concentrations in crustal fluids and their relationship to ore formation. Economic Geology, 100(4): 613-632.

Appendix

Table of content

Appendix I

Accepted manuscript

Study 1

Braunger, S., Scharrer, M., Marks, M. A. W., Wenzel, T., & Markl, G. (accepted). Interaction between mafic dyke rocks and salt deposits in the Rhine graben (SW Germany). The Canadian Mineralogist.

INTERACTION BETWEEN MAFIC DYKE ROCKS AND SALT DEPOSITS IN THE RHINE GRABEN (SW GERMANY)

SIMON BRAUNGER[§], MANUEL SCHARRER, MICHAEL A.W. MARKS, THOMAS WENZEL, AND GREGOR MARKL

Department of Geosciences, Eberhard-Karls-Universität Tübingen, Schnarrenbergstraße 94-96, 72076 Tübingen, Germany

[§] *Corresponding author e-mail address: simonbraunger@hotmail.com*

ABSTRACT

Dykes of primitive olivine melilitites and monchiquites intruded into an Oligocene (Rupelian) potash salt deposit near Buggingen (SW Germany). Ocelli and amygdules reveal distinct mineral assemblages, depending on whether the dyke rocks are in direct contact to the potash layer or to bituminous shales (*Fish Shale*). Samples in contact with the potash salt layer show roundish textures that contain smectite±talc±chlorite, calcite, and in cases anhydrite and halite, while those close to the bituminous shale mainly comprising smectite, calcite, zeolites and analcime.

No textural or mineralogical evidence for high-temperature (magmatic) interaction between the dyke rocks and the evaporites was observed. This is presumably related to (i) a very low magmatic water activity in the magma, which prevented exsolution of aqueous fluids and appreciable dissolution of the salt, and (ii) fast cooling of the magmas, inhibiting melting of the salt deposits and potential liquid mingling and/or assimilation processes. Halite formation in the dyke rocks is rather related to later, post-magmatic hydrothermal fluids that previously interacted with the salt-rich host rocks. Alteration of the initially glassy groundmass to smectites and zeolites caused an enrichment of Na in the residual fluid, but halite saturation was not reached, as recorded by the absence of groundmass halite. Only fluid rock interaction in mm-sized vugs caused halite-precipitation via desiccation by swelling of previously formed clay minerals. Locally, the boron-silicate datolite formed in pseudomorphs after olivine. Its precipitation was controlled by Si and B supply provided by the breakdown of serpentine and smectite.

Keywords: Oligocene potash salt deposit, Buggingen, clay minerals, hydration, olivine melilitite, monchiquite

INTRODUCTION

Little is known about the interaction between silicate magmas and salt rocks, where the large chemical contrast provides potential for intense magmatic and hydothermal processes. Studies on basaltic rocks that intruded into the Zechstein evaporites (Upper Permian) of the Werra-Fulda region (Central Germany) report peperite textures and glassy halite inclusions that were interpreted to indicate carnallite ($KMgCl_3 \cdot 6H_2O$)-magma mingling (Schofield *et al.*, 2014) and partial melting of salts (Koch & Vogel, 1980). Hydrothermal redistribution of the

salt is demonstrated by halite-bearing amygdules (= former gas bubbles/vesicles infilled by hydrothermal mineral phases) and altered ocelli (= spherulitic mineral structures that typically form by magmatic liquid-liquid immiscibility; e.g. Koch, 1978, Knipping, 1989). Besides the Werra-Fulda region, primitive dyke rocks that contain halite-bearing amgydules/ocelli were also reported from the potash salt deposit at Buggingen in southwest Germany (e.g. Wimmenauer, 1951, Braitsch *et al.*, 1964, Hurrle, 1973, Esslinger, 1976, Hurrle, 1976). Despite a detailed petrographic investigation of the dyke rocks by Hurrle (1973), the precipitation mechanism for such salt textures was not investigated so far. Especially intriguing and not understood is the fact that salt crystals do not occur in the groundmass but are restricted to amygdules/ocelli. We shed light on this peculiarity based on a detailed textural, mineralogical and mineral chemical characterization of monchiquitic dyke rocks (feldspar-free lamprophyres) and olivine melilititic dyke rocks (ultramafic volcanic rocks with > 10 % modal olivine, respectively melilite) at the Buggingen salt deposit.

GEOLOGY

The potash salt deposit near Buggingen is situated in the Upper Rhine Graben, about 25 km southwest of Freiburg, southwest Germany (Fig. 1a). The Upper Rhine Graben formed as a consequence of the stress regime induced by the Alpine orogeny and led to the emplacement of alkaline rocks along deep-reaching zones of weakness (Edel *et al.*, 1975, Dèzes *et al.*, 2004, Edel *et al.*, 2006). Due to the rift formation and eustatic sea level fluctuations, the paleoenvironment changed several times from continental to marine (Fig. 1b; Sissingh, 1998). The 4.5 m thick potash salt deposit formed at brackish-evaporitic conditions and was mined from 1928 to 1973 at a depth level of 800 to 1000 m below surface (Esslinger, 1976). The deposit is of Oligocene age (Rupelian, 34 to 28 Ma; Braitsch *et al.*, 1964, Sissingh, 1998). It is situated near the base of the ~600-900 m thick Upper Saliferous Zone, which consists of sylvite,

halite, anhydrite and marl (Fig. 1b&c). It is underlain by brackish-marine calcite- and dolomite-bearing marls of the ~100 m thick Middle Saliferous Zone (Zone fossilifère). A progression of the Paratethys and a subsequent regression is indicated by the uppermost layers which consist of bituminous marine marls and shales (Foraminifera Marls and Fish Shale; total thickness of ~20 m), marine-brackish marls (Meletta Beds; ~300 m thick) and limnic marls (Cyrena Marls; < 100 m tick). Unconformable Quaternary sediments (sands and gravel; < 100 m thick) cover the sequence. Alkaline magmatism of the Upper Rhine Graben and outside to the east at Urach and Hegau is part of the European Cenozoic Volcanic Province (Fig. 1a; Wilson & Downes, 1991). The Miocene Kaiserstuhl volcano with its broad spectrum of different rock types, such as olivine nephelinites, tephrites, phonolites, melilitites, haüynites and carbonatites (e.g. Braunger *et al.*, 2018, Walter *et al.*, 2018, Giebel *et al.*, 2019) is only 20 km away. The first dyke rocks at Buggingen were discovered during underground mining in 1936 and intruded along two fault zones: The dyke system is N-S-trending and consists of several, up to 4 m thick olivine melilitites, with additional monchiquites in its western part (Esslinger, 1976). A rough estimate of the dyke rock age is given by the nearby, mineralogically similar olivine nephelinites at Eichstetten, Lehen and Mahlberg, which indicate an age of ~13-19 Ma (based on whole rock K-Ar, and U-Pb in perovskite; Baranyi *et al.*, 1976; Binder, personal communication).

SAMPLE LOCALITIES

The investigated samples were provided by the Regierungspräsidium Freiburg, Landesamt für Geologie, Rohstoffe und Bergbau (Geological Survey of Baden-Württemberg) and were collected in the 1950´s and 1960´s. Samples from the western dyke zone were taken from the 793 m working horizon within the potash salt deposit and comprise olivine melilitites

and monchiquites. At the eastern dyke zone, olivine melilitites in contact to the Fish Shale Zone were sampled in the shaft Heitersheim at a depth of 185-190 meters (Fig. 1c).

METHODS

The investigated thin sections were prepared and polished completely dry (water-free) in order to prevent dissolution and redistribution of halite and sylvite. Mineral compositions were analyzed using a JEOL JXA8900 electron microprobe (EPMA) in wave-length dispersive mode at the Department of Geosciences, University of Tübingen (Germany) with an acceleration voltage of 15 kV (clinopyroxene, amphibole, mica) or 20 kV (olivine, spinel group minerals, garnet, titanite, perovskite), and a beam current of 20 nA (see supplementary file 1 for a compilation of the WDS configurations). Peak counting times for major elements were 16 s and between 30 and 60 s for minor elements while the background counting times were half as long. Natural and synthetic standards were used for calibration. Peak overlap corrections involving Ba-Ti, Ti-Ba, V-Ti, V-Cr, Al-Ba, F-Fe, Sm-Ce and Pr-La were implemented and the internal ZAF (for spinel group minerals, garnet, perovskite and titanite) or φρz correction was applied for the raw data (Armstrong, 1991). Measurements were done with a 2 µm beam spot except for olivine, clinopyroxene and spinel group minerals which were measured with a focused beam.

MINERALOGY AND PETROGRAPHY

According to the guidelines of the International Union of Geological Sciences, Subcommission on the Systematics of Igneous Rocks (Le Maitre *et al.*, 2002), the two types of dyke rocks at Buggingen are monchiquites and olivine melilitites (formerly also described as ankaratrites, a biotite-bearing variety of olivine nephelinites). In the following, the general

mineral assemblages of the two dyke rock types as well as the mineralogical differences between dyke rocks associated with the Fish Shale and the potash salt layer are described in more detail. Paragenetic schemes summarize the crystallization sequence for olivine melilitites and monchiquites (Fig. 2) and representative mineral compositions for olivine, clinopyroxene, spinel group minerals, amphibole, biotite, garnet, titanite and perovskite are given in Tables 1-4 (see supplementary file 2 for a compilation of all EPMA data). The composition of clinopyroxene is additionally shown in Fig. 3.

General mineral assemblages

Olivine melilitite Precursor olivine macrocrysts of up to 1 mm in size are completely altered (Fig. 4a) and replaced by serpentine minerals and smectites (nontronite-saponite based on X-ray diffraction analyses of Hurrle, 1973). Clinopyroxene with 50-80 mol % diopside end member (Fig. 3a&b; see appendix of Marks *et al.* (2008) for the calculation scheme) typically forms small needles and is only rarely present as phenocrysts (Fig. 4b). Chromian spinel (up to 1.1 wt.% Cr_2O_3) occurs as inclusions in olivine pseudomorphs (Fig. 4c) and in the groundmass, where it commonly shows a sieve-like texture (Fig. 4d) frequently overgrown by magnetite (<0.5 apfu Ti; Fig. 4c). In sample M110 and M156, some magnetites show an atoll-shaped texture with a core of garnet (schorlomite-morimotoite-grossular solid solutions) or titanite (Fig. 4e). Groundmass melilite is completely altered to chlorite (Fig. 4f). Fresh haüyne was not observed but in some samples, purple pseudomorphs presumably after haüyne were found that consist of a very fine-grained mixture of unidentified secondary minerals (Fig. 4g). Further groundmass constituents are apatite needles and interstitial biotite (Fig. 4h). The latter can be distinguished into a Mg-rich (X_{Mg}=0.7-0.8) and a Fe-rich (X_{Mg}=0.0-0.6) variety (Table 3). Much of the formerly glassy groundmass consists of very fine-grained secondary minerals including smectites, zeolites, calcite and chlorite. Based on whole-rock

analyses, Wimmenauer (1951) suggested that the fine-grained groundmass originally consisted of melilite, leucite and nepheline.

Monchiquite Monchiquites contain up to 3 mm large, sub- to anhedral and partly rounded olivine macrocrysts (Fig. 5a) that are heavily altered and commonly replaced by serpentine minerals and smectites (nontronite; Hurrle, 1973). The olivine relicts tend to higher forsterite components (Fo_{92} to Fo_{83}), higher Ni (0.28-0.37 wt.% NiO) and lower Ca (0.02-0.12 wt.% CaO) concentrations compared to olivine microphenocrysts of the groundmass (Fo_{87} to Fo_{84}; 0.17-0.32 wt.% NiO; 0.1-0.3 wt.% CaO; Fig. 5b). Diopsidic clinopyroxene (50-80 mol %; Fig. 3&b) forms several mm large, euhedral to subhedral macrocrysts, which typically consist of a bright sieved core, a plain transitional zone and a brown rim (Fig. 5c). Occasionally, there is an irregularly shaped bright clinopyroxene generation within the sieved core (Fig. 5d) which reveals the highest enstatite component (7-20 mol %; Fig. 3c) and the highest Cr concentrations (up to 1.65 wt.% Cr_2O_3). Green core clinopyroxenes are rare (Fig. 5e). The groundmass is dominated by brown elongated clinopyroxene grains. Chromian spinel (up to 1.1 wt.% Cr_2O_3) occurs as inclusions in olivine, the bright sieved clinopyroxene and within the groundmass where it sometimes reveals a sieve texture. Titanomagnetite (up to 0.6 apfu Ti) only is present in the groundmass. The groundmass additionally comprises partly altered glass (fine-grained zeolites, calcite, chlorite, talc), apatite, small tabular kaersutite and biotite (X_{Mg}=0.4-0.6; Fig. 5b; Table 3). Notable are roundish areas consisting of chlorite, talc and calcite which are surrounded by a zone of amphiboles and biotite grains (Fig. 5f).

Textural and mineralogical differences of the dyke rocks depending on the host rock (bituminous shales versus potash salt layers)

Both olivine melilitites and monchiquites contain roundish textures (Fig. 6). In olivine melilitites, the spheroidal to sometimes lobate textures contain abundant carbonate and minor

diopside, perovskite, melilite, and nepheline (see above and Hurrle, 1973). Hence, these spheroids are interpreted as ocelli that may represent immiscible droplets of a "proto-carbonatitic" melt (that is a carbonate-rich mafic silicate melt). However, some roundish textures in these rocks do not show any indication for primary magmatic mineral phases and presumably represent refilled amygdules. The spheroids in monchiquites show a concentric texture and lack evidence for magmatic mineral phases. Consequently, they are interpreted as amygdules (c.f. Hurrle, 1973, Hurrle, 1976). Other roundish areas that are surrounded by seams of biotite and amphibole resemble vitreous melt residues that have subsequently been altered.

Mineralization associated with the Fish Shale At the contact to the bituminous and pyrite-bearing Fish Shale (Böcker & Littke, 2014, Eichentopf *et al.*, 2017), the ocelli of the olivine melilitite comprise variable amounts of irregularly distributed aggregates of smectite, natrolite and small amounts of calcite (Fig. 7a&b). Biotite may additionally occur at the ocelli rim. The amygdules typically consist of a marginal zone of smectite and a centre with variable amounts of tabular or needle-shaped natrolite (Fig. 7b&c), euhedral analcime and late-stage calcite (Fig. 7d). In some amygdules, marginal smectite is missing (Fig. 7f). Pyrite may occur at the rim of the ocelli (Fig. 7e), but also replaces parts of the groundmass (Fig. 7f).

Mineralization associated with the potash salt layer Ocelli of the olivine melilitite associated with the potash salt deposit consist of marginal smectite and sometimes biotite, while the central parts of the ocelli are dominated by halite (Fig. 8a). Hematite was rarely found but then typically grew on top of the smectite seam (Fig. 8b). Tabular anhydrite grains and barite are particularly common in sample M67 and M156 with the latter sample additionally comprising small amounts of celestine (Fig. 8b). Notably, the ocelli margins of sample M156 also contain isometric garnet with inclusions of small needle-shaped

clinopyroxene (Fig. 8c) and dark green aegirine needles replacing diopside (Fig. 3a&b; Fig. 8a). Furthermore, sample M156 is characterized by halite pseudomorphs after olivine (Fig. 8d). Datolite grains occur in altered olivine, either associated with halite (Fig. 8d) or serpentine and smectite (Fig. 8e). Amygdules generally consist of a small rim of smectite minerals, marginal calcite, sometimes anhydrite, and a core of halite (Fig. 8f).

The amygdules of the monchiquites have a concentric succession from rim to core consisting of chlorite, smectite, talc, calcite and halite. A thin seam of pyrite sometimes occurs between talc and halite (Fig. 8g). In some amygdules, halite is missing (Fig. 8h), which, however, may be a 3-D-effect.

DISCUSSION

Crystallization conditions

The anhedral olivine macrocrysts in monchiquites (forsterite content up to 92 %) show high Ni (≥0.3 wt % NiO) and low Ca (≤0.1 wt. % CaO) concentrations that are typical of mantle xenocrysts (Foley *et al.*, 2013, Bussweiler *et al.*, 2015). Moreover, depth estimates were obtained by the clinopyroxene barometer of Nimis & Ulmer (1998) which was applied to the various diopsidic to augitic clinopyroxene types of the monchiquites (Fig. 3 & Fig. 9). White core clinopyroxenes demonstrate high crystallization depths roughly between 40 and 20 km (depth estimates below 10 km are based on altered clinopyroxenes) and may represent mantle xenocrysts or early magmatic crystals. Green core clinopyroxenes presumably demonstrate the involvement of percolative melts at lower crustal conditions (Pilet *et al.*, 2002). The sieve-like textured clinopyroxenes (Fig. 5c) and spinels indicate a partial resorption of the macrocrysts during magma ascent (e.g. Qi *et al.*, 1995, Shaw *et al.*, 2006). Groundmass clinopyroxenes (transitional/brown clinopyroxenes) typically show values below those expected by an

overburden of ~1000 m (approximately 0.3 kbar) which may be related to the high uncertainty of the calculated values (σ=1.75 kbar) and the fact that the barometer was initially calibrated for anhydrous systems. However, groundmass amphibole and mica in the monchiquites provide prove of a considerable water concentration of the melt at late stage conditions. Pressure estimates therefore are underestimated by ~1 kbar per wt.% H_2O in the melt (Nimis & Ulmer, 1998). Based on coexisting olivine microphenocrysts and brown clinopyroxene, the groundmass temperature could be determined to approximately 950 °C (Andersen *et al.*, 1993).

Reason for the absence of salt rock-magma interactions

The large chemical contrast between the mafic dykes and the potash salts provide potential for intense assimilation and metasomatic processes. However, no textural or chemical differences in the magmatic mineral phases could be observed between the olivine melilitites in contact to the Fish Shale and those surrounded by the potash salt layer. Note, that slightly elevated Cl concentrations in biotite associated with the salt deposit (Table 3) may be caused by Cl diffusion into magmatically formed biotite (high X_{Mg}) during interaction with the NaCl-rich fluid, or may hint to a hydrothermal formation of biotite (low X_{Mg}). Sodium- and chlorine-rich mineral phases such as sodalite, which could be expected to form during magmatic interaction between a silica-undersaturated magma and salt rocks, are absent. Since spheroidal textures occur in all investigated dyke rocks, independent of the surrounding host rock, we exclude the possibility that the halite textures in these spheroidal structures demonstrate a salt-magma mingling, or even a salt-liquid immiscibility due to intense magmatic assimilation of the halite-bearing host rock. Since all investigated dykes crosscut salt-rich layers, we also exclude the possibility that the halite-bearing spheroids formed as a result of salt interaction/assimilation during ascent rather than during emplacement of the magma. We suggest that the absence of salt rock-melt interactions is mainly related to two facts:

i) monchiquites and olivine melilitites are characterized by the absence of OH-bearing phenocryst minerals. Thus, the melts presumably had a rather low water activity during the magmatic stage which prevented the exsolution of large amounts of fluids and a subsequent dissolution of the salt rock. Moreover, carnallite, a hydrous salt mineral that already decomposes at low temperatures <170 °C (Braitsch, 1971) is relatively rare in the salt deposit of Buggingen, and hence could not provide significant amounts of water (Braitsch & Herrmann, 1964). Note that the amount of primary brines in the host rock is uncertain.

ii) the dyke magma cooled rapidly. Knipping (1989) calculated the temperature for halite- and sylvite-bearing salt rocks that were intruded by basaltic magmas in the Werra Fulda region. He assumed a dyke thicknesses of 0.3, 1.0 and 1.8 m, a magma temperature of 1150 °C, and a wall rock temperature of 50 °C. These parameters can also be applied to our study, where the dike widths vary between a few cm to a maximum of 4 m (Esslinger, 1976), the magma temperature is estimated to be above 950 °C, and the reported air temperature of the mine at 1000 m depth was about 50 °C (Markl, 2017; we assume little erosion of the overburden since the intrusion of the dyke rocks). Based on these input parameters, the calculated wall-rock temperature at the contact to the dyke always remained below 790 °C, which prevented melting of halite, and presumably also of sylvite (melting point of ~804 °C and 750-790 °C, respectively; Warren, 2006). Indeed, no evidence of salt melting is reported from Buggingen. At the Werra-Fulda region in Central Germany, Schofield *et al.* (2014) described a lot of peperite structures at the contact between salt and dyke rocks which indicate a magmatic interaction. This process was caused by heating and dehydration of carnallite, which is rare at Buggingen (Braitsch & Herrmann, 1964). Likewise, Schofield *et al.* (2014) suggest that the heat flow of the dyke magma was not sufficient to melt the halite layers in the Werra-Fulda region. However, at branching dykes, between (almost) contemporaneously emplaced intrusions, or if salt fragments got entrapped into the magma, heat could act from more than one side and the halite may locally have reached the melting temperature, as suggested by Koch & Vogel (1980).

Fluid conditions

The minimum temperature of the fluid responsible for the precipitation of halite in amygdules and ocelli was estimated to ~50 °C based on the current temperature of the mine at ~1000 m depth. Evidence for a somewhat higher minimum temperature of a hydrothermal event is shown by sample M156, where the presence of garnet and aegirine-rich clinopyroxene in the ocelli illustrates temperatures of at least 200 °C (Easton *et al.*, 1977, Decarreau *et al.*, 2004). Moreover, the core of atoll-shaped magnetite in sample M110 and M156 consists of garnet or titanite, and may demonstrate a replacement of Ti-rich magnetite by relatively hot fluids (>200 °C) that penetrated the grain along cracks. However, a direct link between these relatively hot fluids and the halite-bearing spheroids is uncertain. While textural observations of Wimmenauer (1951) suggest that the salt layer in contact to the dyke rock is almost completely impoverished in KCl, Braitsch *et al.* (1964) demonstrated by chemical analyses that the contact zones still contain high KCl concentrations of up to 40 wt.%. We therefore suggest that the hydrothermal fluid contained a mixture of dissolved KCl and NaCl. Due to the high variations of the KCl concentration in the salt layers (between 3 and 40 wt.% KCl; Braitsch *et al.*, 1964), and the high temperature dependence of the KCl solubility (Braitsch, 1971), we omit a quantitative calculation for the salt content of the fluid. Sulfate-bearing mineral phases in some ocelli (Fig. 8b) demonstrate that the fluid also passed through anhydrite-bearing layers.

The hydrothermal fluid that interacted with halite-free olivine melilitites most likely equilibrated in the bituminous, pyrite-bearing and marly Fish Shale (Böcker & Littke, 2014, Eichentopf *et al.*, 2017). This is consistent with the high amounts of zeolite, analcime and calcite in the ocelli and amygdule fillings, as well as with the presence of pyrite in the groundmass.

The crystallization process for halite-bearing amygdules and ocelli

Evaporation can be excluded as the precipitation mechanism for the hydrothermal formation of halite because the mafic dyke rocks were sampled at depth. In the following, we discuss a possible crystallization process for the halite-bearing spheroids (Fig. 10a). Due to the complex cation incorporation and adsorption capacity of smectites (e.g. Kloprogge *et al.*, 1999), the importance of kinetics (Gysi & Stefánsson, 2011) and the large number of uncertain parameters (e.g. fluid composition; fluid/dyke rock temperature; groundmass mineralogy of pristine dyke rocks), we chose not to construct a thermodynamic model of the fluid evolution Instead, we present a qualitative approach with focus on the Na concentration, the H_2O concentration and the NaCl saturation degree of the fluid (Fig. 10b).

Assuming that the fine-grained groundmass of the monchiquites and the olivine melilitites mainly consisted of nepheline (as being typical of most silica-undersaturated primitive rocks), the hydrothermal alteration to clay minerals ± zeolites (Fig. 10a-1) should result in an increase of the sodium concentration of the fluid. Indeed, whole-rock analyses (after subtracting halite and anhydrite) of the heavily altered dyke rocks at Buggingen have lower Na concentrations than relatively fresh rock samples (Wimmenauer, 1951, Hurrle, 1973). In contrast, the K concentration of hydrothermally strongly overprinted rock samples is higher compared to the rather fresh dyke rocks (see also supplementary figure 3 for a compilation of the whole rock data). This also conforms with chemical analyses of the clay minerals, which typically consist of K-bearing smectites (Hurrle, 1973). Such a groundmass alteration process typically releases more Na than it consumes K, as shown in the simplified reaction 1,

$$2.33\ NaAlSiO_4\ (Nepheline) + 0.33\ K^+ + 1.34\ Si^{4+} + 2.66\ H_2O =$$

$$K_{0.33}Al_2Si_{3.67}Al_{0.33}O_{10}(OH)_2\ (K\text{-smectite}) + 2.33\ Na^+ + 3.34\ H^+ \quad \text{(reaction 1)}.$$

The uptake of sodium into a salt-saturated fluid should immediately lead to the precipitation of halite. However, as no halite was observed in the groundmass (note that the thin sections were

prepared completely dry, hence excluding a preparation-based salt dissolution), we suggest that the initial fluid (brine from the wall rock) was not saturated with halite before penetrating the dyke rock, possibly due to mixing and diluting with meteoric water. During interaction with the groundmass, the Na concentration of the fluid steadily increased (while the K concentration decreased) but obviously did not yet reach NaCl saturation. As soon as the fluid entered an amygdule, smectites formed at the rim and the fluid became trapped (Fig. 10a-2). The Na concentration of the fluid further increased during interaction with the marginal zone while the salt-rich fluids finally desiccated in the vugs due to swelling of smectites (e.g. Usuki *et al.*, 1993). Consequently, NaCl saturation was reached and halite precipitated in the vugs (Fig. 10a-3). In the amygdules, the crystallization of talc additionally removed H_2O from the fluid and drove it towards NaCl saturation. A similar halite precipitation process can be assumed for the ocelli. In two olivine melilitites, Hurrle (1973) found ocelli with only partly altered nepheline and a core of calcite, which possibly demonstrates the primary magmatic ocelli filling. We assume that calcite dissolved during interaction with the fluid, while smectites formed at the ocelli rim by alteration of the marginal mineral assemblage of the ocelli (Fig. 11). Subsequent desiccation of the trapped fluids by clay mineral swelling led to the crystallization of halite.

Smectite and zeolite formation in the groundmass presumably cemented possible fluid paths (Fig. 10a-3), which would indicate that the salt-rich spheroids formed by a single hydrothermal event. In amygdules, halite comprises up to ~12-20 vol.%, which is in the same order of magnitude as the 16.5 vol.% halite that can precipitate from an NaCl-saturated (~30 wt.% NaCl) fluid at ~50 °C, assuming equimolar Na^+ and Cl^- (Driesner & Heinrich, 2007). As a consequence, we suggest that the fluid was near NaCl saturation when it got trapped in the vugs and finally desiccated by clay mineral swelling. Due to the uncertainty about the dissolved amount of former mineral phases in the ocelli, we omit similar calculations for this spheroid type.

343 The effect of closed-system clay mineral swelling is also illustrated by the mineral proportions
344 in the ocelli/amygdules. Based on the simplified assumption, that the OH-bearing mineral
345 phases of the ocelli/amygdules have an average volume of 140 cm^3/mol (halite 30 cm^3/mol;
346 Blanc *et al.*, 2012 and references therein), and only contain 1 OH-group per formula unit (no
347 interlayer water), the observed amount of smectite in the amygdules/ocelli (~85 vol.%) that
348 formed due to the interaction between the spheroid rim and the NaCl-saturated fluid, is
349 approximately 9 times too low. The absence of a prominent clay rim in some amygdules (Fig.
350 8f) implies that nearby clay minerals of the groundmass additionally bound H_2O in their
351 interlayers. Indeed, the lack of OH-bearing minerals at the amygdule rims is restricted to the
352 olivine melilitites, which in contrast to the monchiquites, contain much more smectite minerals
353 in the groundmass.

354

355 *Crystallization of datolite*

356 Datolite [$CaB(SiO_4)(OH)$] only occurs in one olivine melilitite sample (M156) as
357 pseudomorphs after olivine, either associated with serpentine and smectite (Fig. 8e) or halite
358 (Fig. 8d), but it is never present within ocelli. The required boron presumably derived from
359 ocean-related sedimentary rocks (e.g. Leeman & Sisson, 1996, Garrett, 1998). The salt rocks at
360 Buggingen are unlikely to represent the source of the boron since the concentrations are very
361 low (< 10 ppm; Braitsch *et al.*, 1964), but the clay-rich layers of the salt horizon contain up to
362 600 ppm boron. Braitsch *et al.* (1964) did not believe in this boron source in the country rocks
363 and suggested a magmatic origin since they could not detect significant variations in the boron
364 content between the clay-rich layers in contact to the dyke rocks and those further away.
365 However, we suggest that boron-leaching of the wall rock would have too little effect to be
366 detectable, since boron is adsorbed by clays and should have been balanced again by circulating
367 fluids over the course of the years. The high Ca concentration of the fluid required for the

crystallization of datolite most likely derived from the anhydrite-rich parts of the host rock, which is consistent with high amounts of anhydrite in ocelli of sample M156 (Fig. 8b).

The formation of datolite presumably was caused by a two-step process. This is in accordance with the restriction of datolite to only one rock sample of the present study (it has been found more often in other sample suites, though; Braitsch *et al.*, 1964, Markl, 2017), since clay mineral and zeolite precipitation generally cement the fluid paths. However, in case of sample M156, new cracks possibly formed due to tectonic stress (Wimmenauer, 1951). The first fluid batch equilibrated with the dyke rock by the alteration of olivine to serpentine and Mg-rich smectites (e.g. saponite; Hurrle, 1973). Boron thereby was incorporated into serpentine (e.g. Pabst *et al.*, 2011) and was adsorptively bound in the clay minerals (e.g. Gu & Lowe, 1990, Goldberg *et al.*, 1993, Karahan *et al.*, 2006). A second fluid batch which then was in disequilibrium with the olivine alteration phases dissolved serpentine and Mg-rich smectite. The high amounts of released boron and silica finally led to the crystallization of datolite grains. In contrast to the ocelli and amygdules, anhydrite is absent as presumably all available Ca was incorporated in datolite.

SUMMARY AND CONCLUSION

No evidence for a magmatic interaction between the primitive dyke magma and the salt layers at Buggingen in SW Germany was observed. This is presumably related to (i) relatively dry magmatic melt conditions which prevented a dissolution of the water-soluble salt, and to (ii) a too fast cooling of the dyke. Apparently, the heat flow of the dyke magma was not sufficient to reach the melting point of halite and sylvite (~800 °C). The hydrous salt carnallite decomposes already at 170 °C, but in contrast to the Werra-Fulda region in Central Germany, where plenty of carnallite-magma interaction structures were reported, it is very rare at Buggingen. Instead of a magmatic interaction, halite-bearing spheroids in the olivine melilitites

and the monchiquites represent amygdules, respectively hydrothermally altered ocelli. Low temperature NaCl-bearing fluids from the surrounding salt layers reacted with the dyke rock groundmass, thereby forming smectites and zeolites. During alteration of the groundmass, the NaCl concentration of the fluid steadily increased but remained below NaCl saturation. As soon as the fluid entered a vug, smectites formed at the margin and the fluid got trapped. Clay mineral swelling gradually consumed water from the fluid and finally led to the precipitation of halite. The presence of datolite is restricted to pseudomorphs after olivine. Serpentine/smectite breakdown provided the required Si and boron for its formation.

ACKNOWLEDGMENTS

We would like to thank the Landesamt für Geologie, Rohstoffe und Bergbau (Geological Survey for Baden-Württemberg) in Freiburg for providing the rock samples studied here. Constructive comments by Nick Schofield and an anonymous reviewer on an earlier version of this contribution are gratefully acknowledged, as well as the handling of the manuscript by editor Lee Andrew Groat and associate editor Luca Medici. This work was supported by the Deutsche Forschungsgemeinschaft (grant number MA2563/12–1).

REFERENCES

ANDERSEN, D. J., LINDSLEY, D. H. & DAVIDSON, P. M. (1993). Quilf - a Pascal Program to Assess Equilibria among Fe-Mg-Mn-Ti Oxides, Pyroxenes, Olivine, and Quartz. *Computers & Geosciences* **19**, 1333-1350.

ARMSTRONG, J. T. (1991). Quantitative elemental analysis of individual microparticles with electron beam instruments. *Electron probe quantitation*: Springer, 261-315.

BARANYI, I., LIPPOLT, H. & TODT, W. (1976). Kalium-Argon-Altersbestimmungen an tertiären Vulkaniten des Oberrheingraben-Gebietes: II Die Alterstraverse vom Hegau nach Lothringen. *Oberrhein. Geol. Abh* **25**, 41-62.

419 BLANC, P., LASSIN, A., PIANTONE, P., AZAROUAL, M., JACQUEMET, N., FABBRI, A. & GAUCHER,
420 E. C. (2012). Thermoddem: A geochemical database focused on low temperature
421 water/rock interactions and waste materials. *Applied Geochemistry* **27**, 2107-2116.

422 BÖCKER, J. & LITTKE, R. (2014). Source rock characterisation and thermal maturity of the
423 Rupelian Fish Shale (Bodenheim Fm./Hochberg Subfm.) in the central Upper Rhine
424 Graben. *Zeitschrift der Deutschen Gesellschaft für Geowissenschaften* **165**, 247-273.

425 BRAITSCH, O. (1971). *Salt deposits their origin and composition*. Berlin-Heidelberg-New York:
426 Springer Verlag.

427 BRAITSCH, O., GUNZERT, G., WIMMENAUER, W. & THIEL, R. (1964). Über ein
428 Datolithvorkommen am Basaltkontakt im Kaliwerk Buggingen (Südbaden). *Beiträge*
429 *zur Mineralogie und Petrographie* **10**, 111-124.

430 BRAITSCH, O. & HERRMANN, A. G. (1964). Zur Geochemie des Broms in salinaren Sedimenten
431 Teil II: Die Bildungstemperaturen primärer Sylvin- und Carnallit-Gesteine. *Geochimica*
432 *et Cosmochimica Acta* **28**, 1081-1109.

433 BRAUNGER, S., MARKS, M. A. W., WALTER, B. F., NEUBAUER, R., REICH, R., WENZEL, T.,
434 PARSAPOOR, A. & MARKL, G. (2018). The Petrology of the Kaiserstuhl Volcanic
435 Complex, SW Germany: The Importance of Metasomatized and Oxidized Lithospheric
436 Mantle for Carbonatite Generation. *Journal of Petrology* **59**, 1731-1762.

437 BUSSWEILER, Y., FOLEY, S. F., PRELEVIC, D. & JACOB, D. E. (2015). The olivine macrocryst
438 problem: New insights from minor and trace element compositions of olivine from Lac
439 de Gras kimberlites, Canada. *Lithos* **220**, 238-252.

440 DECARREAU, A., PETIT, S., VIEILLARD, P. & DABERT, N. (2004). Hydrothermal synthesis of
441 aegirine at 200°C. *European Journal of Mineralogy* **16**, 85-90.

442 DÈZES, P., SCHMID, S. M. & ZIEGLER, P. A. (2004). Evolution of the European Cenozoic Rift
443 System: interaction of the Alpine and Pyrenean orogens with their foreland lithosphere.
444 *Tectonophysics* **389**, 1-33.

445 DRIESNER, T. & HEINRICH, C. A. (2007). The system H2O–NaCl. Part I: Correlation formulae
446 for phase relations in temperature–pressure–composition space from 0 to 1000°C, 0 to
447 5000bar, and 0 to 1 XNaCl. *Geochimica et Cosmochimica Acta* **71**, 4880-4901.

448 EASTON, A. J., HAMILTON, D., KEMPE, D. R. C., SHEPPARD, S. M. F. & AGRELL, S. O. (1977).
449 Low-Temperature Metasomatic Garnets in Marine Sediments [and Discussion].
450 *Philosophical Transactions of the Royal Society of London. Series A, Mathematical and*
451 *Physical Sciences* **286**, 253-271.

452 EDEL, J.-B., WHITECHURCH, H. & DIRAISON, M. (2006). Seismicity wedge beneath the Upper
453 Rhine Graben due to backwards Alpine push? *Tectonophysics* **428**, 49-64.

454 EDEL, J. B., FUCHS, K., GELBKE, C. & PRODEHL, C. (1975). Deep Structure of Southern
455 Rhinegraben Area from Seismic Refraction Investigations. *Journal of Geophysics-*
456 *Zeitschrift Fur Geophysik* **41**, 333-356.

EICHENTOPF, H., BÖCKER, J. & LITTKE, R. (2017). Source rock characterisation of the Rupelian Fish Shale (Bodenheim Fm./Hochberg Sbfm.)–An organic geochemical profile from the clay pit. *Zeitschrift der Deutschen Gesellschaft für Geowissenschaften* **168**, 217-232.

ESSLINGER, G. (1976). Vorkommen und Tektonik der Basalte im Kalisalzlager Buggingen (Südbaden). *Jahresheft des Geologischen Landesamtes in Baden-Württemberg* **18**, 7-18.

FOLEY, S. F., PRELEVIC, D., REHFELDT, T. & JACOB, D. E. (2013). Minor and trace elements in olivines as probes into early igneous and mantle melting processes. *Earth and Planetary Science Letters* **363**, 181-191.

GARRETT, D. E. (1998). *Borates: Handbook of deposits, processing, properties, and use*: Elsevier.

GIEBEL, R. J., PARSAPOOR, A., WALTER, B. F., BRAUNGER, S., MARKS, M. A. W., WENZEL, T. & MARKL. (2019). Evidence for magma – wall rock interaction in carbonatites from the Kaiserstuhl Volcanic Complex (Southwest Germany). *Journal of Petrology*.

GOLDBERG, S., FORSTER, H. S. & HEICK, E. L. (1993). Boron Adsorption Mechanisms on Oxides, Clay Minerals, and Soils Inferred from Ionic Strength Effects. *Soil Science Society of America Journal* **57**, 704-708.

GU, B. & LOWE, L. E. (1990). STUDIES ON THE ADSORPTION OF BORON ON HUMIC ACIDS. *Canadian Journal of Soil Science* **70**, 305-311.

GYSI, A. P. & STEFÁNSSON, A. (2011). CO2–water–basalt interaction. Numerical simulation of low temperature CO2 sequestration into basalts. *Geochimica et Cosmochimica Acta* **75**, 4728-4751.

HURRLE, H. (1973). Ocelli-und Mandelbildung der Melilithankaratrite im Kalisalzlager Buggingen und im Kristallin des Schwarzwaldes. *Geoscience*. Freiburg: Albert Ludwigs University, Freiburg i. Br., 129.

HURRLE, H. (1976). Ocelli-und Mandelbildung der ultrabasischen Basalte im Kalisalzlager Buggingen und im Kristallin des Schwarzwaldes. *Jh. geol. Landesamt Baden-Württemberg* **18**, 19-37.

KARAHAN, S., YURDAKOÇ, M., SEKI, Y. & YURDAKOÇ, K. (2006). Removal of boron from aqueous solution by clays and modified clays. *Journal of Colloid and Interface Science* **293**, 36-42.

KLOPROGGE, J. T., KOMARNENI, S. & AMONETTE, J. E. (1999). Synthesis of Smectite Clay Minerals: A Critical Review. *Clays and Clay Minerals* **47**, 529-554.

KNIPPING, B. J. (1989). Basalt Intrusions in Evaporites. *Lecture Notes in Earth Sciences, Berlin Springer Verlag* **24**.

KOCH, K. (1978). Zur Entstehung von Tonmineralen im Kontaktbereich Basalt-Salinar. *Z. geol. Wiss* **6**, 733-747.

KOCH, K. & VOGEL, J. (1980). Zu den Beziehungen von Tektonik, Silvinitbildung und Basaltintrusion im Werra-Kaligebiet (DDR): mit 2 Tabellen. Dt. Verlag für Grundstofindustrie.

LE MAITRE, R., STRECKEISEN, A., ZANETTIN, B., LE BAS, M., BONIN, B., BATEMAN, P., BELLIENI, G., DUDEK, A., EFREMOVA, A. & KELLER, J. (2002). Igneous rocks. A classification and glossary of terms. Recommendations of the IUGS Subcomission on the Systematics of Igneous Rocks. Cambridge University Press, Cambridge.

LEEMAN, W. & SISSON, V. (1996). Geochemistry of boron and its implications for crustal and mantle processes. Boron: mineralogy, petrology and geochemistry. *Rev. Mineral.* **33**, 645-708.

MARKL, G. (2017). *Schwarzwald-Lagerstätten und Mineralien aus vier Jahrhunderten-Band 4-Südlicher Schwarzwald*. Salzhemmendorf-Lauenstein, Germany: Bodeverlag.

MARKS, M. A., SCHILLING, J., COULSON, I. M., WENZEL, T. & MARKL, G. (2008). The alkaline–peralkaline Tamazeght complex, High Atlas Mountains, Morocco: mineral chemistry and petrological constraints for derivation from a compositionally heterogeneous mantle source. *Journal of Petrology* **49**, 1097-1131.

NIMIS, P. & ULMER, P. (1998). Clinopyroxene geobarometry of magmatic rocks Part 1: An expanded structural geobarometer for anhydrous and hydrous, basic and ultrabasic systems. *Contributions to Mineralogy and Petrology* **133**, 122-135.

OBERTI, R., SMITH, D. C., ROSSI, G. & CAUCIA, F. (1981). The crystal-chemistry of high-aluminium titanites. *European Journal of Mineralogy*, 777-792.

PABST, S., ZACK, T., SAVOV, I. P., LUDWIG, T., ROST, D. & VICENZI, E. P. (2011). Evidence for boron incorporation into the serpentine crystal structure. *American Mineralogist* **96**, 1112-1119.

PILET, S., HERNANDEZ, J. & VILLEMANT, B. (2002). Evidence for high silicic melt circulation and metasomatic events in the mantle beneath alkaline provinces: the Na–Fe-augitic green-core pyroxenes in the Tertiary alkali basalts of the Cantal massif (French Massif Central). *Mineralogy and Petrology* **76**, 39-62.

QI, Q. U., TAYLOR, L. A. & ZHOU, X. (1995). Petrology and Geochemistry of Mantle Peridotite Xenoliths from SE China. *Journal of Petrology* **36**, 55-79.

SCHOFIELD, N., ALSOP, I., WARREN, J., UNDERHILL, J. R., LEHNÉ, R., BEER, W. & LUKAS, V. (2014). Mobilizing salt: Magma-salt interactions. *Geology* **42**, 599-602.

SHAW, C. S. J., HEIDELBACH, F. & DINGWELL, D. B. (2006). The origin of reaction textures in mantle peridotite xenoliths from Sal Island, Cape Verde: the case for "metasomatism" by the host lava. *Contributions to Mineralogy and Petrology* **151**, 681.

SISSINGH, W. (1998). Comparative Tertiary stratigraphy of the Rhine Graben, Bresse Graben and Molasse Basin: correlation of Alpine foreland events. *Tectonophysics* **300**, 249-284.

USUKI, A., KAWASUMI, M., KOJIMA, Y., OKADA, A., KURAUCHI, T. & KAMIGAITO, O. (1993). Swelling behavior of montmorillonite cation exchanged for ω-amino acids by ∈-caprolactam. *Journal of Materials Research* **8**, 1174-1178.

WALTER, B. F., PARSAPOOR, A., BRAUNGER, S., MARKS, M. A. W., WENZEL, T., MARTIN, M. & MARKL, G. (2018). Pyrochlore as a monitor for magmatic and hydrothermal processes in carbonatites from the Kaiserstuhl volcanic complex (SW Germany). *Chemical geology* **498**, 1-16.

WARREN, J. K. (2006). *Evaporites: sediments, resources and hydrocarbons*. Berlin+Heidelberg: Springer Science & Business Media.

WILSON, M. & DOWNES, H. (1991). Tertiary—Quaternary extension-related alkaline magmatism in western and central Europe. *Journal of Petrology* **32**, 811-849.

WIMMENAUER, W. (1951). Petrographische Untersuchungen über das Ankaratrit-Vorkommen, im Kalisalzlager von Buggingen in Baden. Mitt. *Bl. bad. geol. Landesamt*, 117-128.

Figure captions

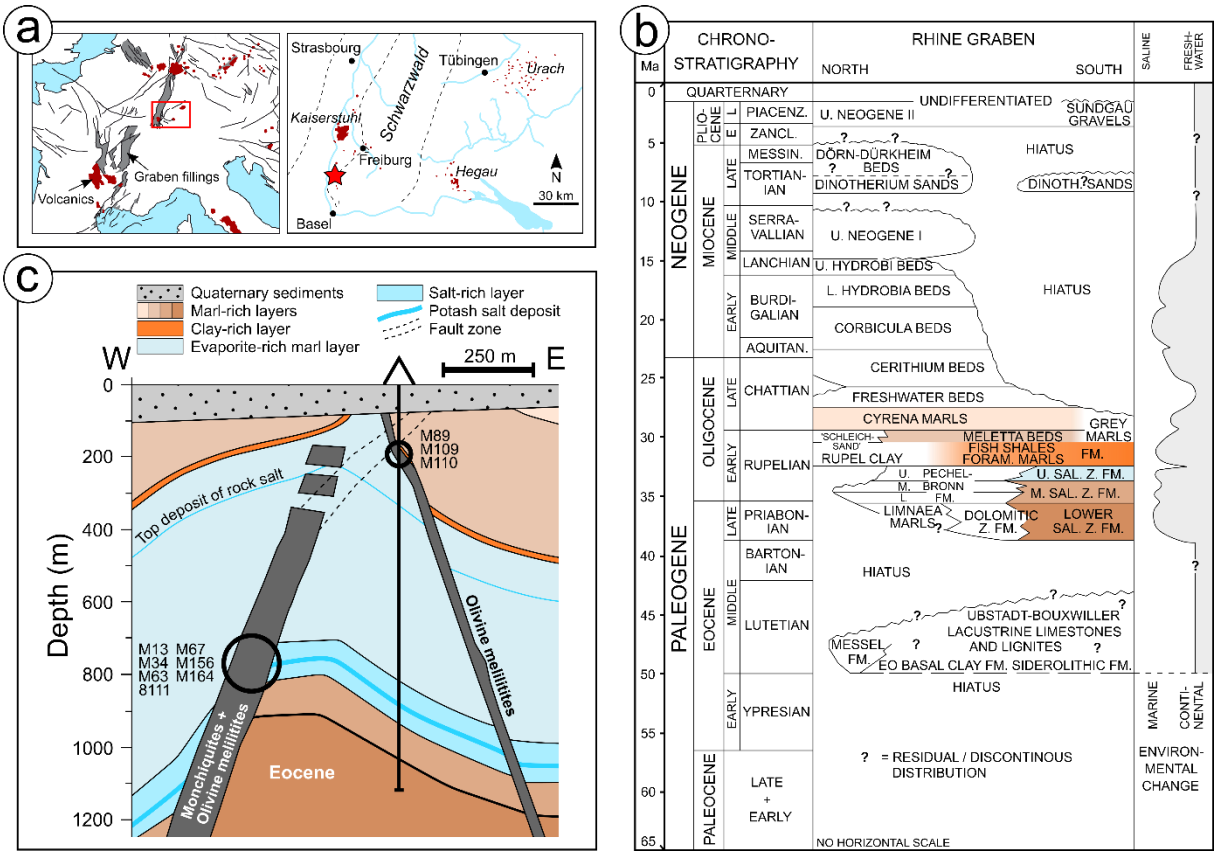

Fig. 1: Geology of Buggingen. a) Overview map of the European Cenozoic Volcanic Province and the Cenozoic magmatic occurrences in southwest Germany (modified after Dèzes *et al.*, 2004). Buggingen is located at the red star. b) Stratigraphic diagram showing the lithostratigraphy of the Rhine Graben (after Sissingh, 1998). c) Cross-section showing the geology of Buggingen and the sample sites (modified after Esslinger, 1976). The dark grey areas represent dyke zones which consist of several smaller dykes. Colors correspond to those of the lithostratigraphic units.

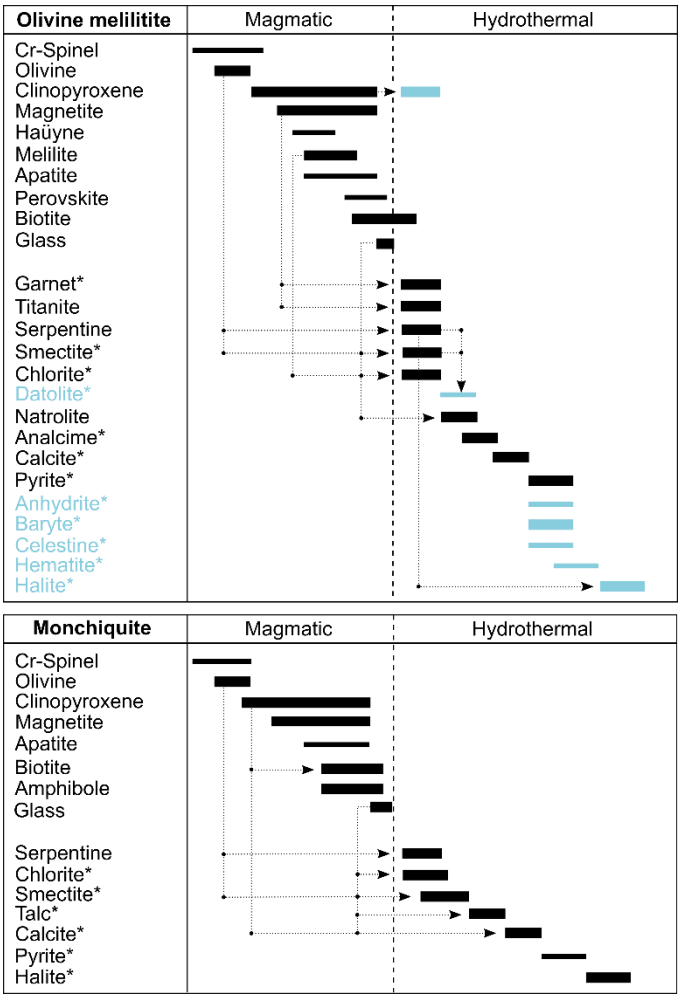

555

556 Fig. 2: Paragenetic scheme for the olivine melilitites and the monchiquites from Buggingen. Alteration processes
557 are indicated by arrows. Mineral phases of the olivine melilitite that only occur in association with the salt layer
558 are indicated in blue. Mineral phases highlighted by the star are present in ocelli/amygdules.

559

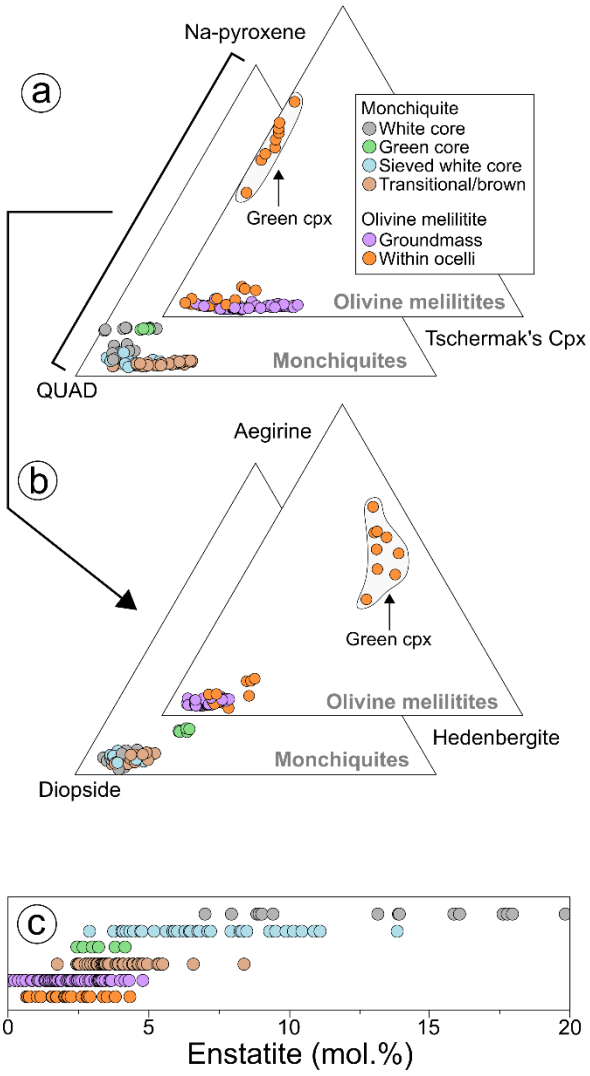

560

561 Fig. 3: Clinopyroxene composition for the olivine melilitites and the monchiquites from Buggingen. a) Na-
562 pyroxene ($NaFeSi_2O_6$+$NaAlSi_2O_6$)-QUAD ($CaMgSi_2O_6$+$CaFeSi_2O_6$)-Tschermak's pyroxene
563 ($CaFeFeSiO_6$+$CaTiAl_2O_6$+$CaAlAlSiO_6$) triangles. b) Diopside–hedenbergite–aegirine triangles. c) Enstatite
564 component (in mol %).

565

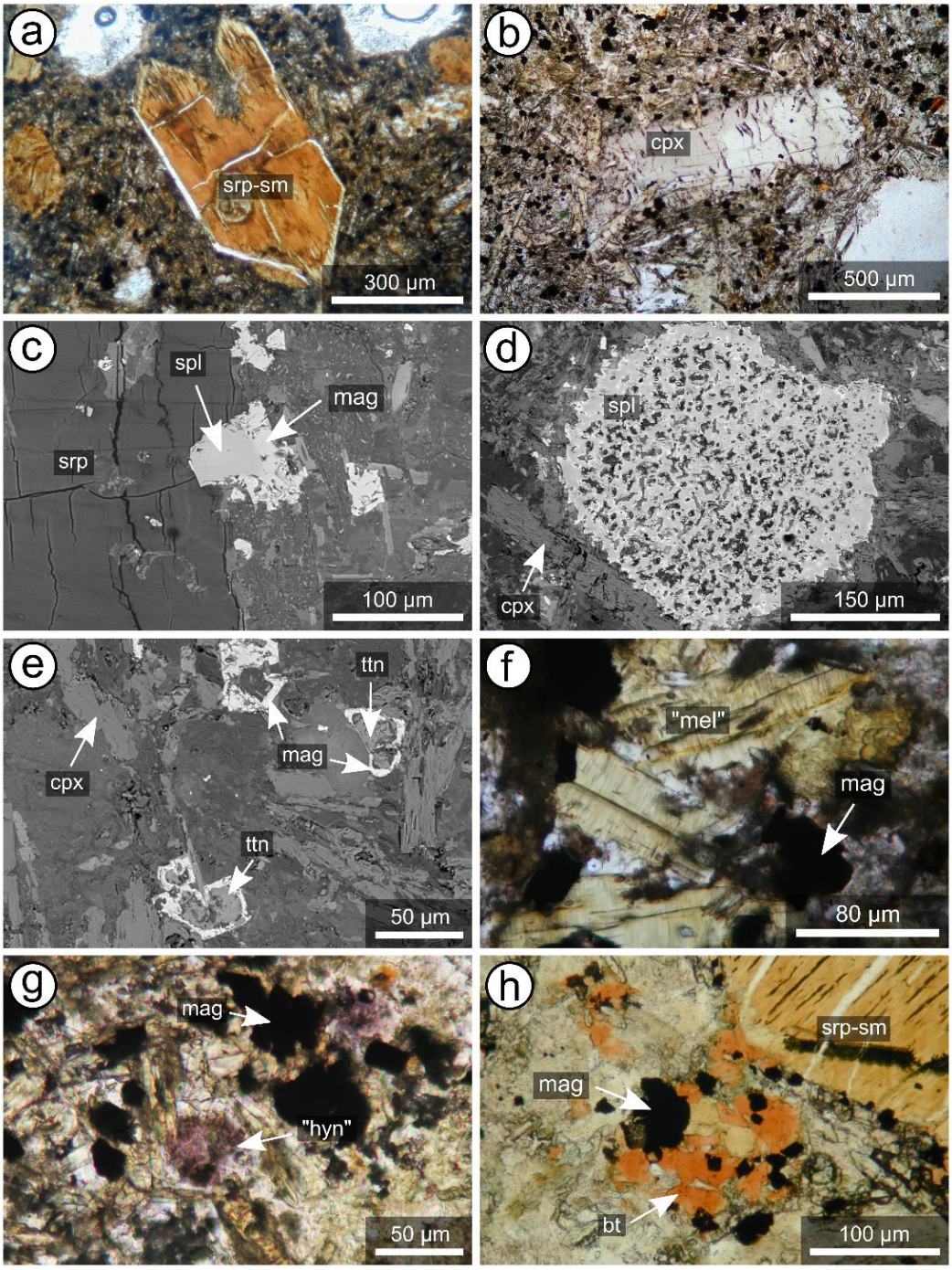

Fig. 4: Mineral textures in the olivine melilitites from Buggingen (transmitted light microscopy and BSE images [c,d,e]). a) Euhedral olivine macrocryst totally replaced by serpentine (srp) and smectite (sm) minerals. b) Clinopyroxene (cpx) macrocryst in a groundmass consisting of plenty clinopyroxene needles. c) Spinel (spl) at the rim of an serpentinized olivine. Those parts of the spinel that are not enclosed by former olivine are surrounded by magnetite (mag). d) Spinel showing a sieve texture. e) Atoll-shaped magnetite with a core of titanite (ttn). f) Melilite (mel) being totally altered to chlorite. g) Purple pseudomorphs after haüyne (hyn) consisting of a mixture of fine-grained secondary minerals. e) Interstitial biotite (bt).

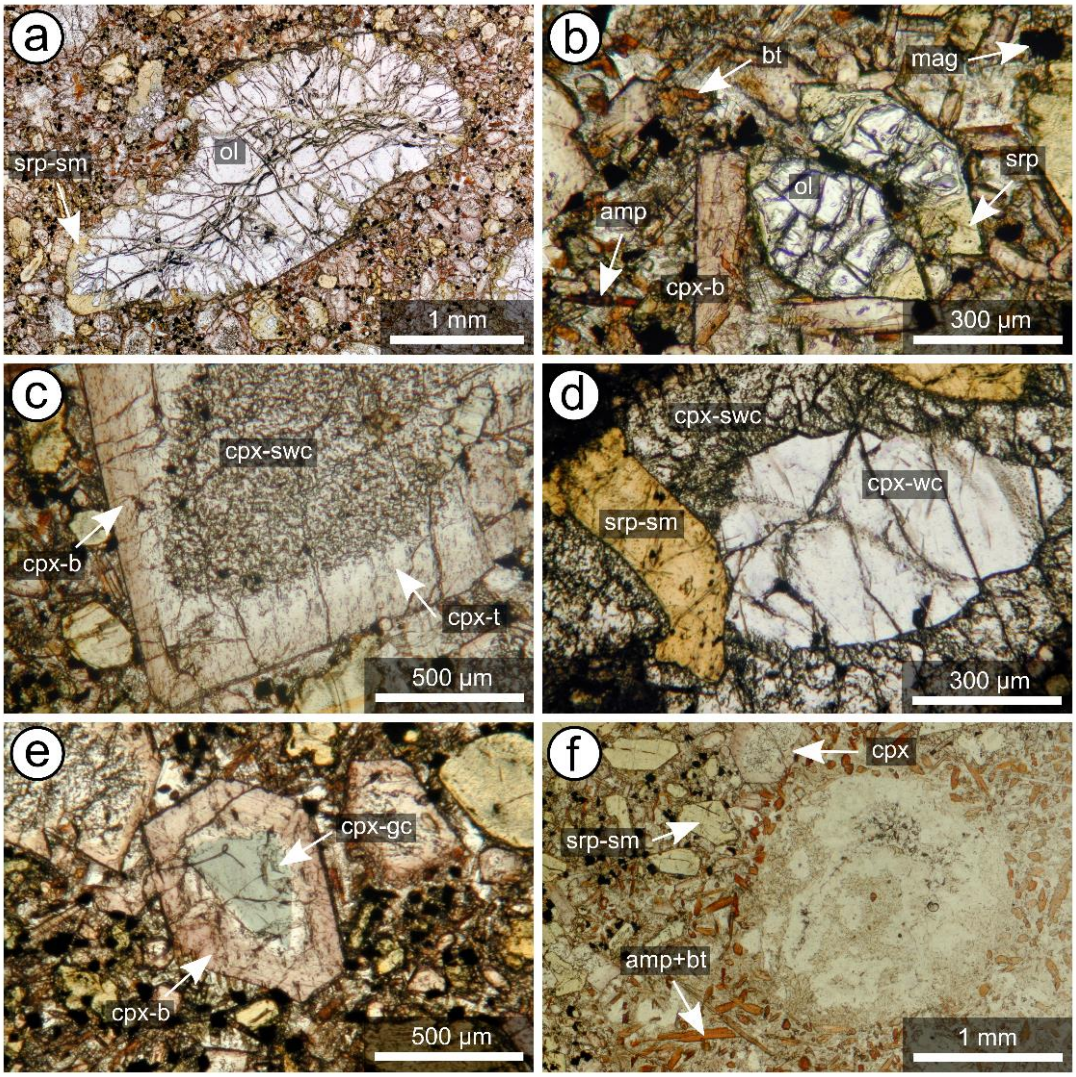

574

575 Fig. 5: Mineral textures in the monchiquites from Buggingen (transmitted light microscopy images). a) Large,
576 rounded olivine (ol) macrocryst partly replaced by serpentine and smectite minerals. b) Euhedral olivine, brown
577 clinopyroxene needles and small tabular amphibole (amp) and biotite constitute the groundmass. c) Clinopyroxene
578 consisting of a sieved white core (cpx-swc), a plain transitional zone (cpx-t) and a brown rim (cpx-b). d)
579 Clinopyroxene with an irregularly shaped white core (cpx-wc), surrounded by sieved white clinopyroxene and
580 olivine that is completely replaced by serpentine and smectite minerals. e) Green-core clinopyroxene (cpx-gc)
581 rimmed by brown clinopyroxene. f) Roundish zone consisting of a fine-grained mixture of chlorite, talc and calcite,
582 surrounded by amphiboles and biotite.

583

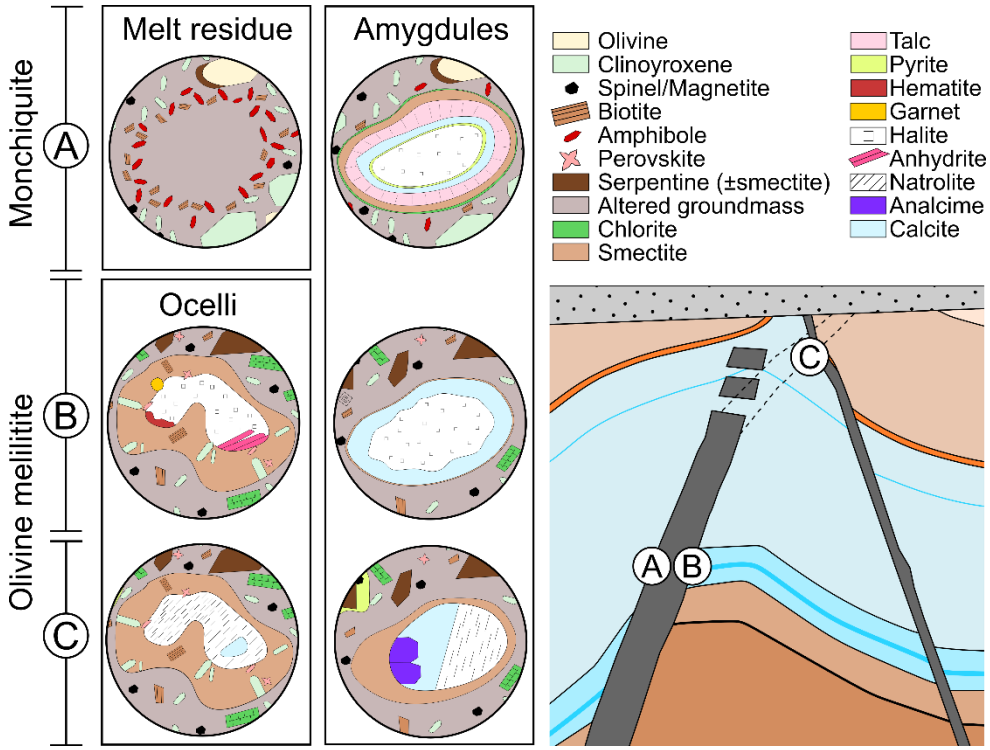

584

585 Fig. 6: Schematic overview of the spheroidal textures in the monchiquites and the olivine melilitites.

586

587

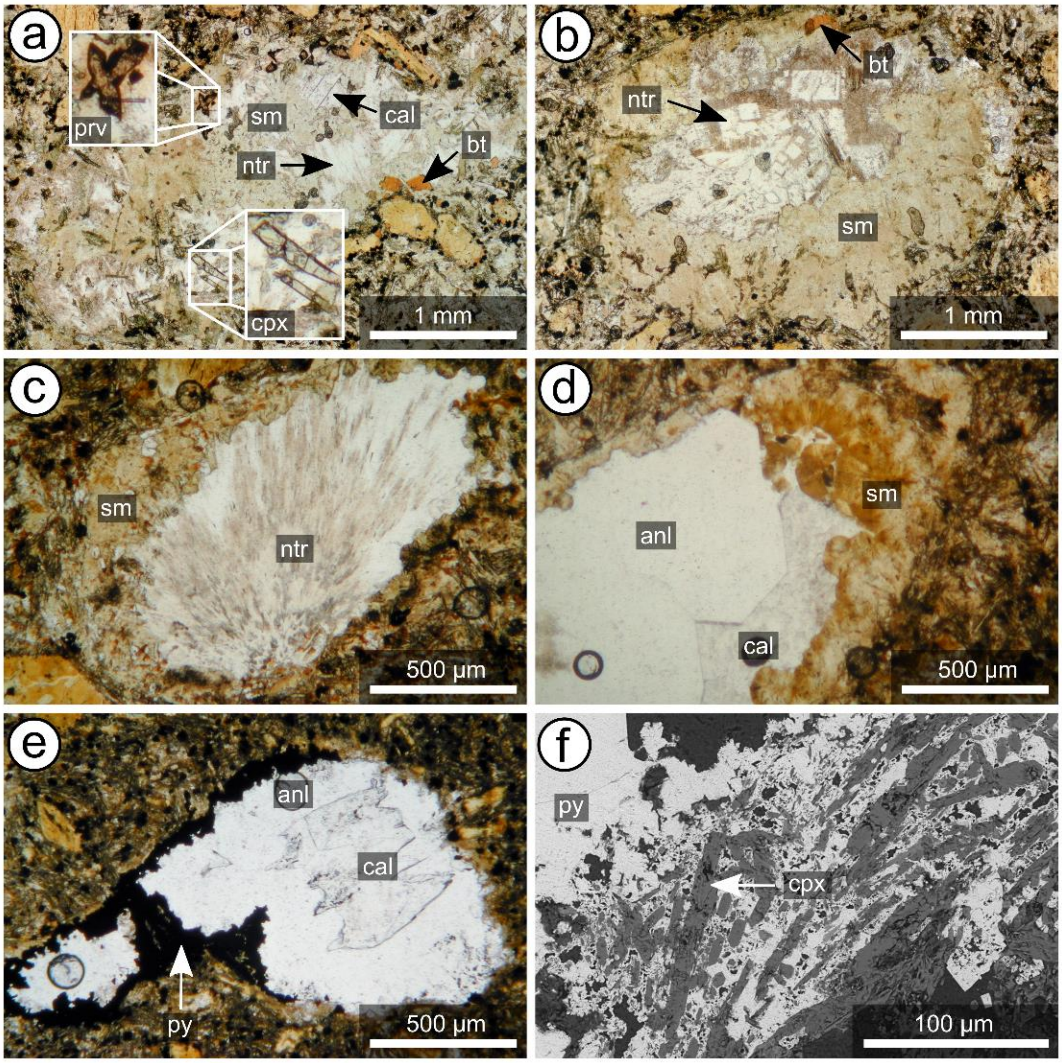

Fig. 7: Mineral textures of the ocelli in the olivine melilitites associated with the Fish Shale (transmitted light microscopy images. a) Biotite, clinopyroxene and perovskite (prv) sometimes occur at the rim of ocelli. Calcite (cal), smectite and natrolite are further common constituents. b) Ocellus with a rim mainly consisting of smectite and rare biotite, and a core of natrolite (ntr). c) Ocellus with marginal smectite minerals and a core of natrolite. d) Ocellus consisting of smectites, calcite and analcime (anl). e) Ocellus with marginal pyrite (py), analcime and calcite. f) Parts of the groundmass are replaced by pyrite.

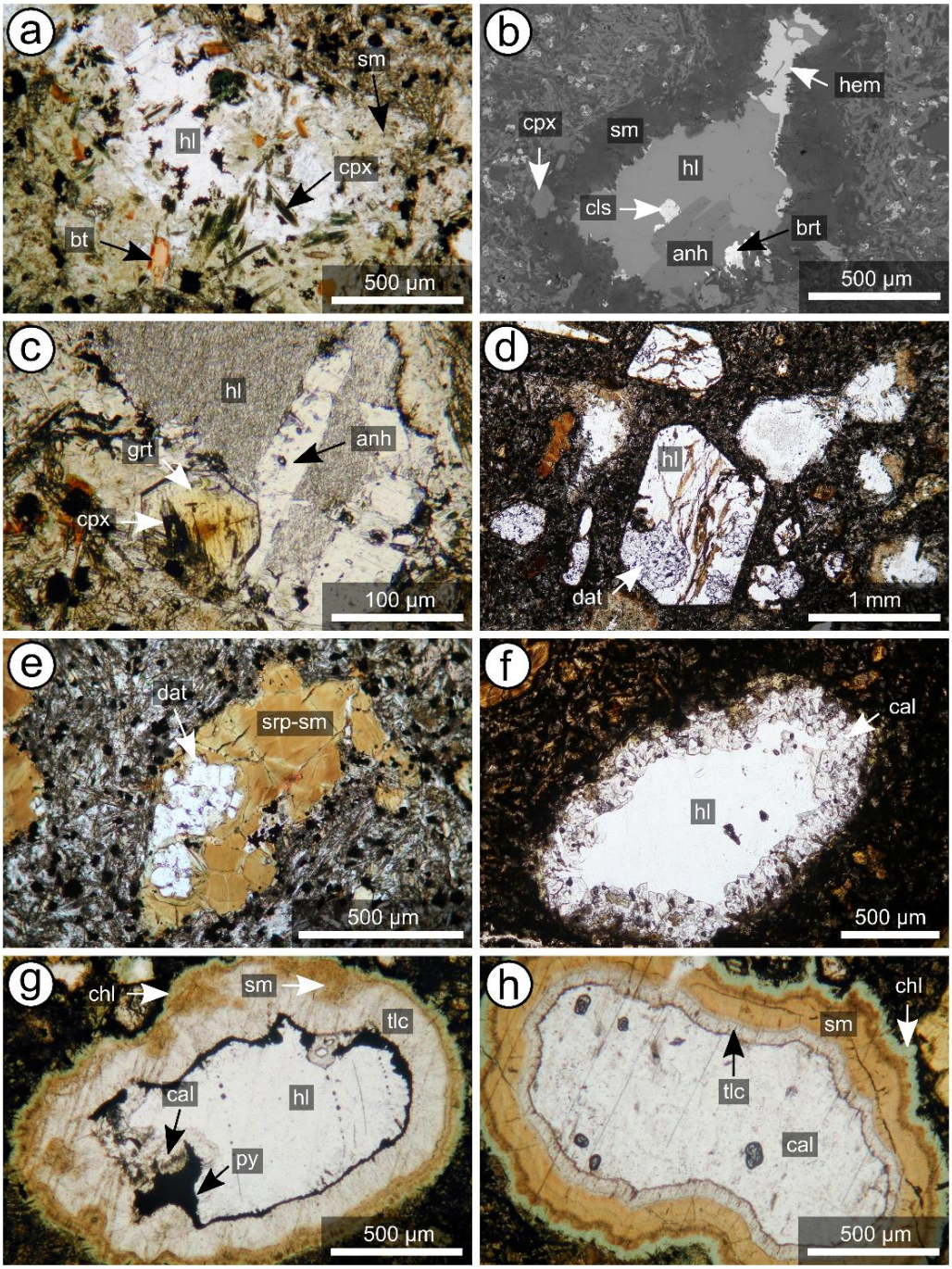

596

597 Fig. 8: Mineral textures of the ocelli and amygdules in the olivine melilitites and the monchiquites associated with
598 the potash salt layer (transmitted light microscopy and BSE images [b]). a) Ocellus with a rim of biotite, aegirine
599 and smectites, and a core of halite. b) Ocellus consisting of smectites, hematite (hem), barite (brt), anhydrite (anh),
600 celestine (cls) and halite. c) In sample M156, euhedral garnet (grt) with inclusions of clinopyroxene sometimes
601 occur at the rim of ocelli. d) Halite and datolite (dat) pseudomorph after olivine. e) Serpentine, smectite and datolite
602 pseudomoprh after olivine. f) Amygdule consisting of marginal calcite and a core of halite. g) Amygdule with a
603 concentric succession of chlorite (chl), smectite, talc (tlc), calcite, pyrite (py) and halite. h) Amygdule showing a
604 concentric succession of chlorite, smectite, talc and calcite.

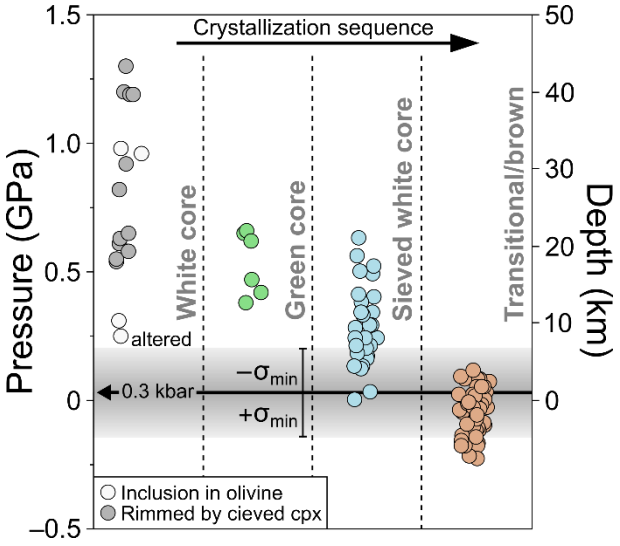

Fig. 9: Crystallization depth for the various clinopyroxene types in the monchiquites from Buggingen. Pressure estimates are based on Nimis & Ulmer (1998) and indicate a minimum uncertainty of σ=1.75 kbar. The negative pressure estimates for many of the transitional/brown clinopyroxenes might additionally be caused by the fact that the barometer is calibrated for anhydrous systems (note that late-stage clinopyroxenes coexist with amphibole and mica). The line at 0.3 kbar demonstrates the expected minimum pressure during groundmass crystallization due to an overburden of ~1000 m.

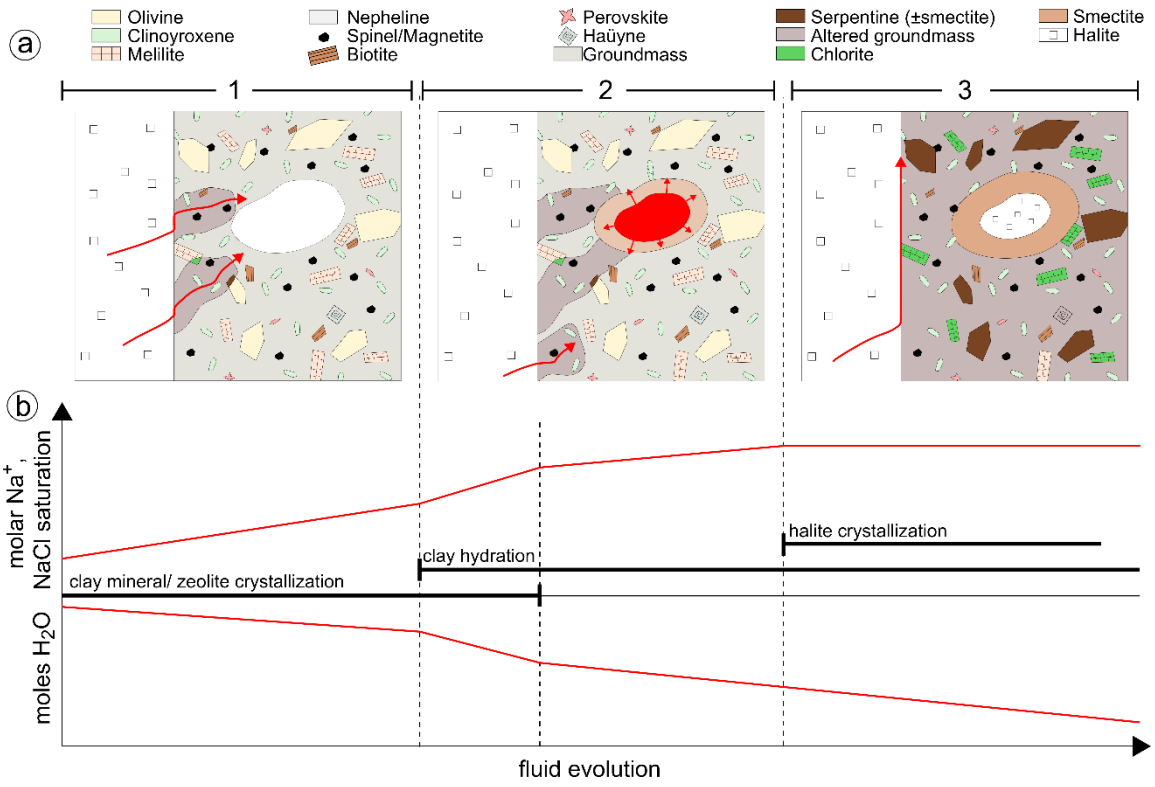

614

615 Fig. 10: Precipitation mechanism for the halite-bearing amygdules/ocelli. a) Schematic evolution of the dyke rock
616 mineral assemblage. 1) NaCl-saturated fluid (red arrow) interacts with the groundmass, thereby producing Na- and
617 OH-bearing alteration phases (smectites and zeolites). 2.) Fluid enters a vug, forms marginal smectite minerals
618 and gets trapped. 3) Gradual removal of H_2O from the fluid by clay mineral swelling results in NaCl precipitation.
619 The formation of smectites and zeolites cements possible fluid paths and prevents further fluids from entering the
620 dyke rock (blue arrow). b) Schematic evolution of the fluid composition. The upper two xy-diagram demonstrate
621 the evolution of the molar Na^+, respectively H_2O concentration of the fluid with respect to the initial fluid
622 composition. The lower xy-diagram demonstrates the NaCl saturation degree during fluid evolution.

623

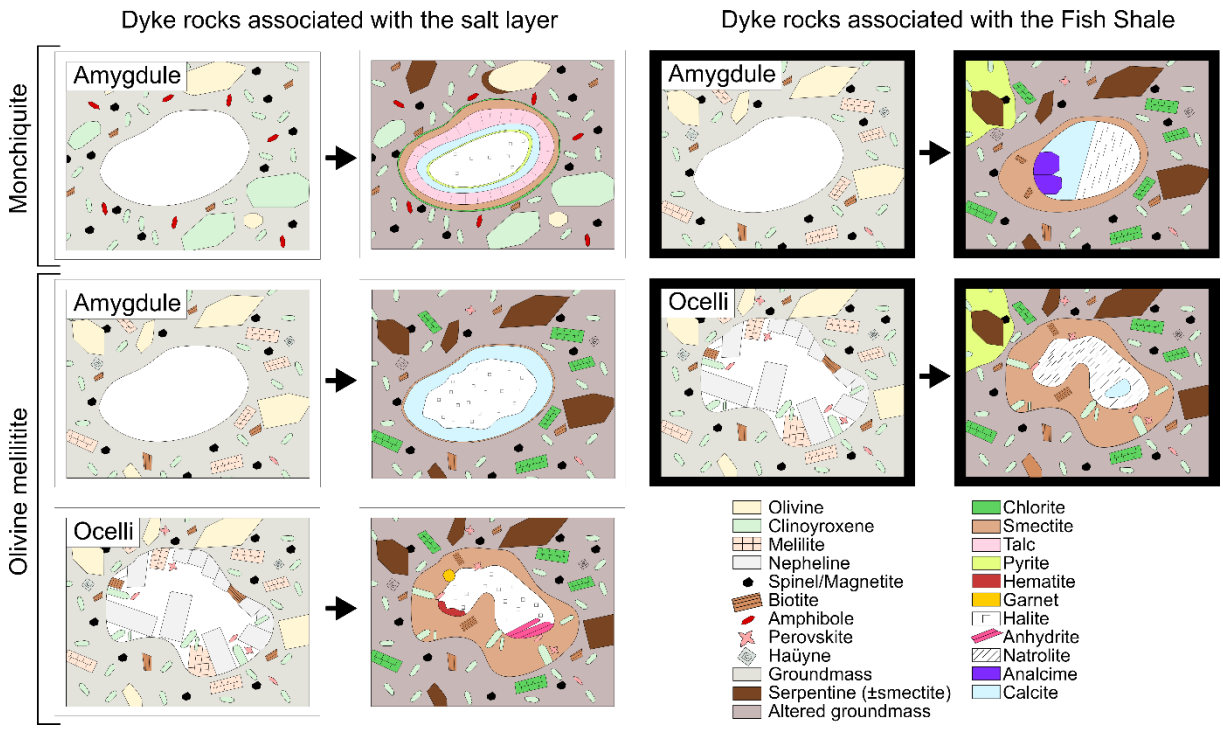

624

625 Fig. 11: Schematic diagram illustrating the mineral assemblage of amygdules and ocelli before and after the

626 hydrothermal overprint.

Appendix II

Accepted publication

Study 2

Walter, B. F., Kortenbruck, P., Scharrer, M., Zeitvogel, C., Wälle, M., Mertz-Kraus, R., & Markl, G. (2019). Chemical evolution of ore-forming brines – Basement leaching, metal provenance, and the redox link between barren and ore-bearing hydrothermal veins. A case study from the Black Forest mining district in SW-Germany. Chemical Geology, 506, 126-148.

Chemical Geology 506 (2019) 126–148

Contents lists available at ScienceDirect

Chemical Geology

journal homepage: www.elsevier.com/locate/chemgeo

Chemical evolution of ore-forming brines – Basement leaching, metal provenance, and the redox link between barren and ore-bearing hydrothermal veins. A case study from the Schwarzwald mining district in SW-Germany

Benjamin F. Walter[a,*], Philipp Kortenbruck[a], Manuel Scharrer[a], Christine Zeitvogel[a], Markus Wälle[b], Regina Mertz-Kraus[c], Gregor Markl[a]

[a] University of Tübingen, Department of Geoscience, Wilhelmstraße 56, 72074 Tübingen, Germany
[b] Memorial University of Newfoundland and Labrador, Core Research Equipment and Instrument Training Network (CREAIT), St. John's, Canada
[c] Johannes Gutenberg-Universität Mainz, Institut für Geowissenschaften, J.-J.-Becher-Weg 21, D-55128 Mainz, Germany

ARTICLE INFO

Editor: E. B Michael

Keywords:
Ore deposits
LA-ICPMS analyses on single fluids
Metal transport
Metal provenance
Fluid mixing
Trace elements
Basement rocks

ABSTRACT

Six mineralogically exemplary barren and mineralized hydrothermal veins (with Pb and Zn ores) of Jurassic-Cretaceous and Cenozoic age in the Schwarzwald mining district, SW Germany were chosen to shed light on the origin of their mineralogical diversity. The selection of the veins was guided by the fact that they represent the largest number of veins in the region, are very well known mineralogically and geochemically, and they provide nice examples of barren and mineralized veins of similar age. Fluid inclusion data from the individual veins overlap implying their diverse mineralogy is not caused by different fluid compositions participating during fluid mixing. LA-ICPMS data of single fluid inclusions indicate no systematic variations in major elements, but significant changes in fluid mixing ratios which caused variable trace element concentrations of different fluid inclusion assemblages in one sample. We suggest that different ore-gangue-assemblages can be produced by mixing of identical fluid endmembers, but variable mixing ratios. LA-ICPMS analyses of single fluid inclusions in barren and mineralized veins record similar base metal and sulfur concentrations. Hence, sulfide mineralization in the veins appears not to be controlled by metal solubility. Thermodynamic modeling based on the fluid data indicates that the presence of a reducing phase during fluid mixing is required for sulfide mineralization to precipitate.

LA-ICPMS trace element analyses of feldspars, biotites, chlorites and clay minerals in granites and paragneisses which are the source of the metal content in the ore-forming fluids demonstrate that the dominant provenance for Pb, Zn, As, Sb, Ba, Tl, Mo, Fe and Mn are probably paragneisses, while Co, Cu and Ni are probably sourced from S-type granite. A rough quantification indicates that < 1 m^3 paragneiss or granite has to be altered (10% alteration) to supply sufficient Zn to 1 l of hydrothermal fluid reaching a concentration of 2 g/l Zn. Hence, this study confirms that ore fluids can be produced from any lithology in the upper crust that contains at least some trace metals (μg/g level is sufficient).

1. Introduction

In the last two decades, significant progress has been made in the understanding of the origin of hydrothermal vein type deposits related to the interface between sedimentary cover rocks and crystalline basement. Typically, fluid inclusions (Wilkinson, 2010), stable and radiogenic isotopes (Bau et al., 2003; Kessen et al., 1981; Shouakar-Stash et al., 2007; Staude et al., 2011; Wilkinson et al., 2005), trace element studies of fluids, ores and gangue mineralogy (Fusswinkel et al., 2013; Pfaff et al., 2011; Fusswinkel et al., 2014) or paleo-hydrological modeling (Garven et al., 1999) are used as tools to decipher ore-forming processes. Suitable field areas such as the South East Basin in France (Aquilina et al., 2011), the Moroccan Anti Atlas district (Essarraj et al., 2016, 2017), the Irish Midlands (Banks et al., 2002), the Alaskan Brooke Range (Leach et al., 2004), the Athabasca Basin in Canada (Richard et al., 2016; Martz et al., 2018), the Pyrenees

* Corresponding author.
E-mail address: benjamin.walter@uni-tuebingen.de (B.F. Walter).

https://doi.org/10.1016/j.chemgeo.2018.12.038
Received 28 August 2018; Received in revised form 17 December 2018; Accepted 28 December 2018
Available online 03 January 2019

(Crognier et al., 2018),the Massif Central in France (Boiron et al., 2010), the Catalan Coastal Ranges in Spain (Grandia et al., 2003), the St. Lawrence Rift System in Canada (Carignan et al., 1997), the Otavi Mountainland in Namibia (Deane, 1995) and the Schwarzwald mining district in SW Germany (Walter et al., 2018a, 2018b and references therein) have been studied to decipher ore-forming processes in time and space. Numerous authors agree that (besides cooling) fluid mixing between hot basement brines (or basinal brines) and cooler, sediment-derived fluids with contrasting fluid chemistry from the overburden sequence is the dominant process for the formation of hydrothermal vein-type base metal deposits (e.g. Hoeve and Sibbald, 1978; Duane and De Wit, 1988; Tornos et al., 1991; Carignan et al., 1997; McCaig et al., 2000; Wilkinson, 2010; Fusswinkel et al., 2013; Fusswinkel et al., 2014; Bons et al., 2014; Walter et al., 2015, 2016, 2017a; Richard et al., 2016). In numerous contributions, evidence is presented that the metals originate from the crystalline basement by the alteration of micas and feldspars (see also Burisch et al., 2016a and references therein). It has remained difficult to quantify the importance of basement leaching due to the lack of trace metal data in primary minerals and alteration products in the source rocks. Burisch et al. (2016a) supplied such data for the Schwarzwald mining district.

Over the last years, geomodels for deep fluid mixing processes were significantly refined by the introduction of a two-component or multi-component fluid “mixing from below” model (Bons et al., 2014; Walter et al., 2018a, 2018b). The models can be applied to complex geological settings such as the Schwarzwald and adjacent Rhinegraben rift, where chemically different basement and sedimentary strata generate and contain fluids of diverse compositions (Bons et al., 2014; Walter et al., 2017b, 2018a, 2018b). Multi-component fluid mixing models may thus help to constrain the diversity of fluid compositions and mineralization in hydrothermal vein type deposits related to rifts and unconformities (e.g. Athabasca Basin; Richard et al., 2016; Yukon Territory, Rio Grande Rift, Newfoundland, Sardinia; Van Alstine, 1976).

Barren veins in numerous mining districts occur in close proximity to mineralized (i. e., containing base-metal ores) veins (e.g. Beaudoin et al., 1992; Hein, 1993; Sun et al., 2017 and references therein). In hydrothermal Pb-Zn vein type deposits (Walter et al., 2018a, and references therein), orogenic gold deposits (Naden and Shepherd, 1989; Cox et al., 1991; Sherlock et al., 1993; Mavrogenes et al., 1995; Wilde et al., 2001) and 5-element veins (Markl et al., 2016; Burisch et al., 2017; Kreissl et al., 2018), the presence or absence of CH_4 and H_2S was recognized as the driving force to suppress or permit ore mineralization because a reduced environment is necessary for metal transport (gold) and/or precipitation (e.g. galena and sphalerite). However, the process of locally generating ore mineralization in an otherwise barren vein (system) is still under debate (e.g. Mavrogenes et al., 1995; Wilde et al., 2001 and references therein).

In this contribution, fluid inclusions from mineralized and barren veins are analyzed from the Schwarzwald district to find evidence if barren veins are either precipitated from a “barren, metal-poor fluid” or if there is a difference in the mineralization process (e.g. presence or absence of a reducing phase) that could explain the presence or absence of base metal sulfides. A common observation is that hydrothermal veins in the center of granitic complexes are typically barren, while paragneiss-hosted veins (e. g., Schauinsland, Schwarzwaldsegen, Wenzel or Kropbach) or veins in the vicinity of the granite-paragneiss contacts show extensive sulfide ore mineralization.

Hence, the focus of the present contribution lies on the following three aspects which are not sufficiently addressed in previous contributions (e.g. Walter et al., 2016, 2017a, 2017b, 2018a, 2018b):

- an integrated study of ore-forming fluids using microthermometry, Raman micro spectroscopy and Laser ablation inductively coupled plasma mass spectrometry (LA-ICPMS) analyses of various types of hydrothermal mineralization (barren fluorite-barite veins, barren quartz veins, calcite veins with Pb-Zn mineralization and fluorite-barite-quartz veins with Pb-Zn mineralization) across the Schwarzwald mining district;
- the comparison of fluid compositions from barren and from mineralized veins;
- the metal budget of the country rocks and how much leached country rock volume is required to produce an ore fluid.

The Schwarzwald mining district in SW-Germany is bordered by the Cenozoic Rhinegraben rift and is chosen as an unusually well-studied and typical example for a region that has vein-hosted ore deposits associated with several tectonic events (for details see below) and several hundreds of hydrothermal veins of diverse mineralogy (e.g. Metz et al., 1957; Bliedtner and Martin, 1986; Baatartsogt et al., 2007; Staude et al., 2009) which occur in sedimentary (Lower Triassic sandstone) and crystalline basement host rocks (paragneisses, orthogneisses and granites). The chemistry of hydrothermal fluids that has given rise to vein-hosted mineral assemblages in the Schwarzwald have been related to various types of sedimentary and basement rocks (Walter et al., 2016, 2017a, 2017b, 2018a). Hence, by the choice of this district, it is possible to study host rock-dependent chemical variations in hydrothermal fluids.

1.1. Regional geology

Variscan paragneisses, migmatites and granites form the crystalline basement of the Schwarzwald mining district are covered by Permian to Upper Jurassic terrestrial and marine sedimentary rock successions (Fig. 1). Syn- to post-tectonic S-type granites intruded between 335 and 315 Ma into the Variscan paragneisses (Altherr et al., 2000; Hann et al., 2003; Kalt et al., 2000; Todt, 1976). During the Permian the Variscan orogen became deeply eroded and local sedimentary basins were filled by proximal red bed arkoses and conglomerates (Geyer and Gwinner, 2011; Jenkner, 1986; Nitsch and Zedler, 2009). In the Lower Triassic, quartz sandstone units with a thickness up to 400 m were deposited and separated from crystalline basement rocks and Permian-aged sedimentary rocks by a prominent erosional unconformity (basement-cover unconformity). In the Middle Triassic, the area became a marine environment and limestones (Muschelkalk) and evaporites (Walter et al., 2017a) reached a thickness of up to 220 m. During the Upper Triassic (Keuper), evaporitic units and clastic sediments reached a maximum thickness of about 300 m (Geyer and Gwinner, 2011). About 1000 m of clastic and evaporitic sediments and (mainly) limestones were deposited on the shallow continental Tethys shelf during the Jurassic. Cretaceous sediments are completely lacking in SW Germany (Geyer and Gwinner, 2011).

Since the breakup of the Upper Rhinegraben rift (Paleogene) up to 4000 m of clastic sediments and evaporites (gypsum, anhydrite, dolomite, Na-K-Mg halides) were deposited in the rift valley (Geyer and Gwinner, 2011; Rupf and Nitsch, 2008). During opening of the rift, alkaline magmatism produced several volcanic fields (e.g. Kaiserstuhl, Hegau, Urach; Braunger et al., 2018; Walter et al., 2018c and references therein). Contemporaneous with the ongoing rifting, the rift shoulders were uplifted about three kilometers (Geyer and Gwinner, 2011). Uplift of the shoulders and erosion rates were much stronger in the south relative to the middle and northern Schwarzwald. Due to this asymmetric exhumation the basement-cover unconformity is still preserved in the middle and northern Schwarzwald, while the southern Schwarzwald is exhumed to a total depth of about 3.5–4 km below the Upper Jurassic land surface (Rupf and Nitsch, 2008; Walter et al., 2017a).

1.2. Hydrothermal veins in the Schwarzwald

> 1000 hydrothermal veins are known in the Schwarzwald mining district. These are either mineralized with base metal sulfide ores (Table 1) or contain sulfide-free assemblages of quartz, barite, fluorite

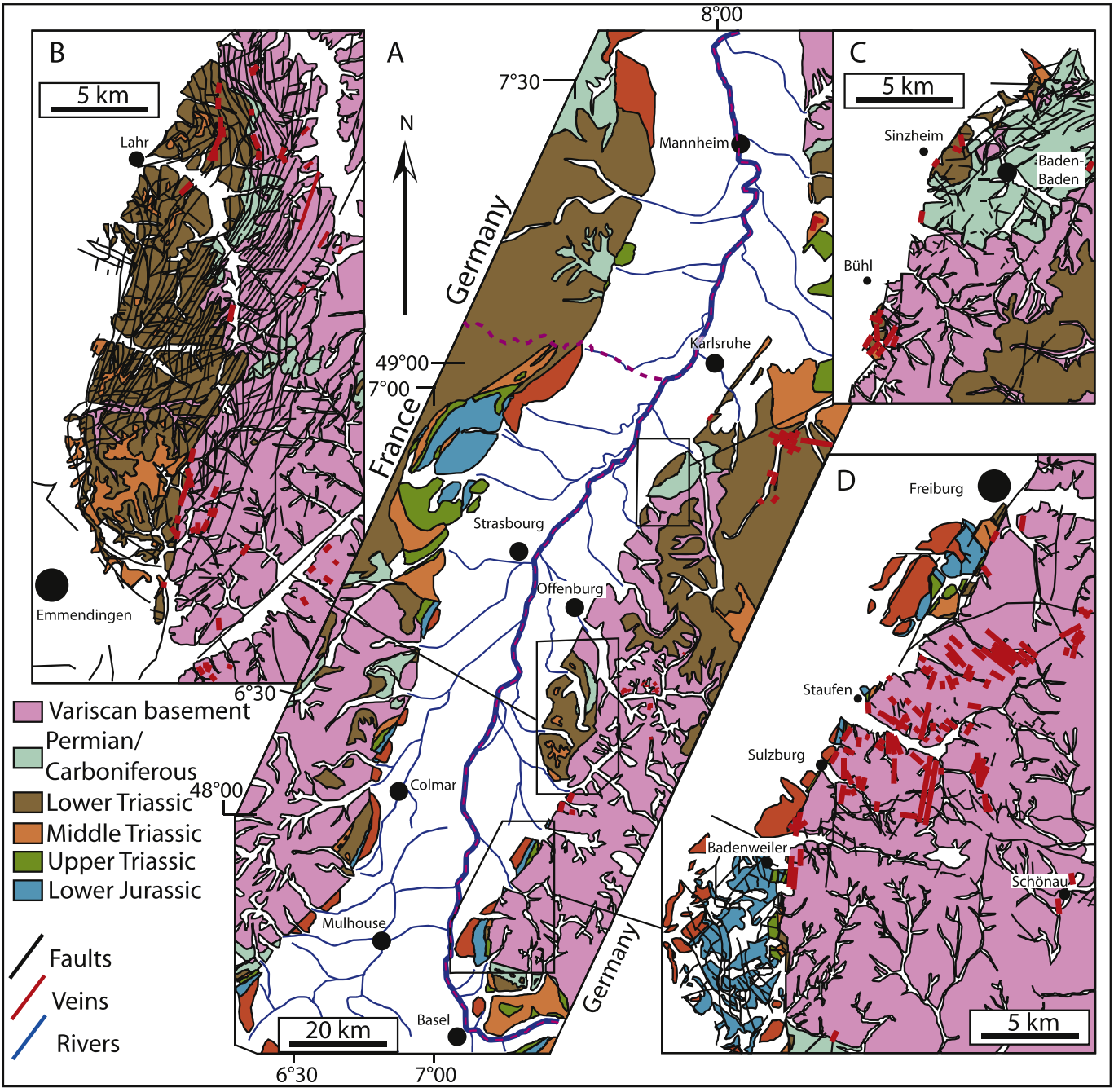

Fig. 1. (A) Geological and structural map of the Upper Rhinegraben modified after the data of Beccaletto et al. (2010). Adopted from Walter et al. (2017b, 2018a). (B–D) close ups of rift related mining districts with veins following the Graben structures.

or carbonate. The latter are referred to as "barren" in the context of this contribution. Mineralized and barren veins formed in basement and lower Triassic host rocks from lower Permian until geologically recent times, with discrete maxima of hydrothermal activity related to the late stages of the Variscan orogeny around 280–300 Ma, the Jurassic and Cretaceous breakup of the North Atlantic Ocean between 190 and 110 Ma and during Rhinegraben formation between 40 and 0 Ma (Pfaff et al., 2009 and references therein; Staude et al., 2009; Loges et al., 2012; Walter et al., 2016; Burisch et al., 2018; Walter et al., 2018b). Numerous studies were done to investigate the variable vein mineralogy and the related physico-chemical processes through space and time. Aspects of fluid flow and hydrothermal vein formation were in the focus of various contributions, including studies on microthermometry (e.g. Behr and Gerler, 1987; Behr et al., 1987; Burisch et al., 2016a; Staude et al., 2009, 2012a; Fusswinkel et al., 2013; Bons et al., 2014; Walter et al., 2015, 2016, 2017a, 2017b, 2018a). Stable and radiogenic isotopes (O, C, H, S, Sr, Pb, Cu, Fe, Mg) were analyzed to decipher fluid sources and redox conditions of the hydrothermal veins (e.g. Staude et al., 2011, 2012b; Walter et al., 2015 and references therein). Additionally, trace element distribution in fahlore and sphalerite (Staude et al., 2010b; Pfaff et al., 2011), geochemical evolution of various deposits with specific mineralization (Staude et al., 2007, 2012b), paleofluid models (Pfaff et al., 2010; Staude et al., 2011; Fusswinkel et al., 2013; Bons et al., 2014; Walter et al., 2015, 2018a), geochemistry of modern thermal and mineral waters from spas (Stober and Bucher, 1999; Loges et al., 2012; Göb et al., 2013) and alteration experiments on basement and cover rocks (Bucher and Stober, 2002; Burisch et al., 2016b) were performed to shed light on fluid sources, fluid pathways

Table 1
Types of veins and fluid signatures of the Schwarzwald ore district modified after Walter et al. (2016) and references therein.

Group	Age	Mineralogy	Mineralization	Structural position	Age constraints	Fluid type	Salinity in wt% ($NaCl + CaCl_2$)	T_h in °C	Cl/Br mass ratio
i	Carboniferous	Quartz-tourmaline	W-Sn	Spatially associated and genetically related to specific granites	U-Pb age of host granite	H_2O-NaCl ± (CO_2 ± CH_4)	0–4	130–390 °C	48–146
ii	Permian	Quartz	Sb ± Ag ± Au	Only in basement rocks (granite and gneiss)	High fluid temperatures > 250 °C never reached again after Permian times by the SW German basement at shallow depths; comparison with very similar veins from the Taunus	H_2O-NaCl-KCl	< 5	99–300 °C	94
iii	Triassic-Jurassic	Quartz-hematite	Fe	Only in basement rocks (granite and gneiss)	(U-Th)/He age	H_2O-NaCl-KCl & H_2O-NaCl-$CaCl_2$	0.7–3.3 & 23.3–25.8	121–224 °C	60–112
iv	Jurassic-Cretaceous	Fluorite-quartz-barite barite-quartz	Pb-Zn-Cu-Ag & U-Bi-Co-Ni-Ag & Fe-Mn	From > 2000 m below the basement/cover unconformity up to the boundary between Lower and Middle Triassic sediments	Rb-Sr and U-Pb age-dating	H_2O-NaCl-$CaCl_2$	20–28	50–180 °C	49–824
v	Post-Cretaceous	Quartz-barite-fluorite	Pb-Zn-Cu-Ag & Cu-Ni-Bi-Ag	Spatially closely associated with Upper Rhinegraben faults or tributary fault systems	Structural position on Rhinegraben-related faults	H_2O-NaCl-$CaCl_2$ ± (SO_4 ± CO_2 ± HCO_3)	0–25	50–194 °C	2–144

and metal sources. Microstructural studies were done on breccias in the hydrothermal veins that provide evidence for hydraulic fracturing, tectonic forces or a combination of both to be involved in the generation of fluid pathways (e.g. Sprengel, 2014). Moreover, numerous contributions are available on the regional geology (Geyer and Gwinner, 2011 and references therein). Hence, this extensive dataset of the various geochemical parameters renders it possible to decipher the chemical evolution of fluids responsible for the different vein formation processes and the mechanisms of base metal sulfide ore precipitation over the last 300 Ma (Table 1).

The contributions of Behr and Gerler (1987), Behr et al. (1987), Staude et al. (2009), Pfaff et al. (2009, 2010), Burisch et al. (2016b) and Walter et al. (2015, 2016, 2017a, 2017b, 2018a, 2018b) reported evidence for five maxima of hydrothermal activity in the Schwarzwald mining district based on structural, mineralogical, age-dating and fluid inclusion data (Table 1): (i) Carboniferous (ii) Permian, (iii) Triassic-Early Jurassic, (iv) Middle Jurassic-Cretaceous and (v) post-Cretaceous. In this contribution, only veins of stage iv and v are analyzed, as they represent the largest number of veins in the region, are very well known mineralogically and geochemically, and they provide nice examples of barren and mineralized veins of similar age. The following paragraphs explain in detail what we know about the Jurassic-Cretaceous and post-Cretaceous veins.

Veins of Jurassic and Cretaceous age (stage iv) are mineralogically very diverse containing variable modal amounts of fluorite, barite, quartz and carbonates with significant Ag-Bi-Co-Ni-U, Fe-Mn or Pb-Zn-Cu mineralization (e.g., Mertz et al., 1986; Wernicke and Lippolt, 1993, 1997; Werner et al., 2002; Pfaff et al., 2009; Staude et al., 2009, 2011, 2012a, 2012b; Werner, 2011; Walter et al., 2015, 2016, 2017a). The formation of these veins relates to a binary fluid mixing process between a deep-seated, metal-rich, highly saline (originally surface-derived) basement brine (20–28 wt% salinity) and a sulfate-rich, metal-poor highly saline brine (20–25 wt%) derived from Middle Triassic evaporite-bearing limestone. This brine was mobilized during tectonic activity and mixed with colder Middle Triassic formation waters with Cl/Br and Ca/Na signatures of halite or sulfate dissolution prior to vein formation (Staude et al., 2009, 2010a, 2010b, 2011, 2012b; Fusswinkel et al., 2013; Walter et al., 2015, 2016, 2017a, 2017b, 2018a). Fluid cooling was only of minor significance (Burisch et al., 2017) for mineralization and no evidence for boiling was found.

During the Paleogene and Neogene, the breakup of the Upper Rhinegraben rift and subsequent strike-slip tectonics generated or reactivated Upper Rhinegraben-parallel NE-SW to NNE-SSW-striking fault systems. Rift-related hydrothermal veins of group (v) formed in some of these fault zones (Pfaff et al., 2009 and references therein; Staude et al., 2012b and references therein). Typical of group (v) veins is the occurrence of large amounts of barite and quartz, only some veins contain fluorite and carbonates with Pb and, rarely, As, Zn, Cu, Bi and Ni ore minerals (Staude et al., 2009; Walter et al., 2017a). The fluid chemistry (salinity 1–23 wt% $NaCl + CaCl_2$) of these post-Cretaceous veins is heterogeneous due to multi-component, multi-aquifer fluid mixing processes caused by a juxtaposition of different aquifers by Neogene rift tectonics (Walter et al., 2015, 2016, 2017b, 2018a). The last mineralization stages are characterized by sulfate-carbonate assemblages that document the transition from a deep to a shallow geothermal system which is still active today (Burisch et al., 2018).

2. Samples and methods

2.1. Sample material

To shed light on a hydrothermal system, a holistic sample collection based on ten country rocks (source rocks for the metals in the fluid) and gangue minerals of representative six hydrothermal veins (which bear the ore forming, metal rich brine in fluid inclusions) were used.

2.1.1. Country rocks

In order to investigate the metal provenance in the hydrothermal fluids, the trace element budget of representative country rock samples was determined. The crystalline basement of the Schwarzwald dominantly consists of paragneisses, orthogneisses and S-type granites, and hence, four paragneisses, one orthogneiss and five granite bodies were selected. To include the trace metal budget of clay minerals formed during hydrothermal alteration of K-feldspar, plagioclase and biotite, samples showing various degrees of hydrothermal alteration were selected.

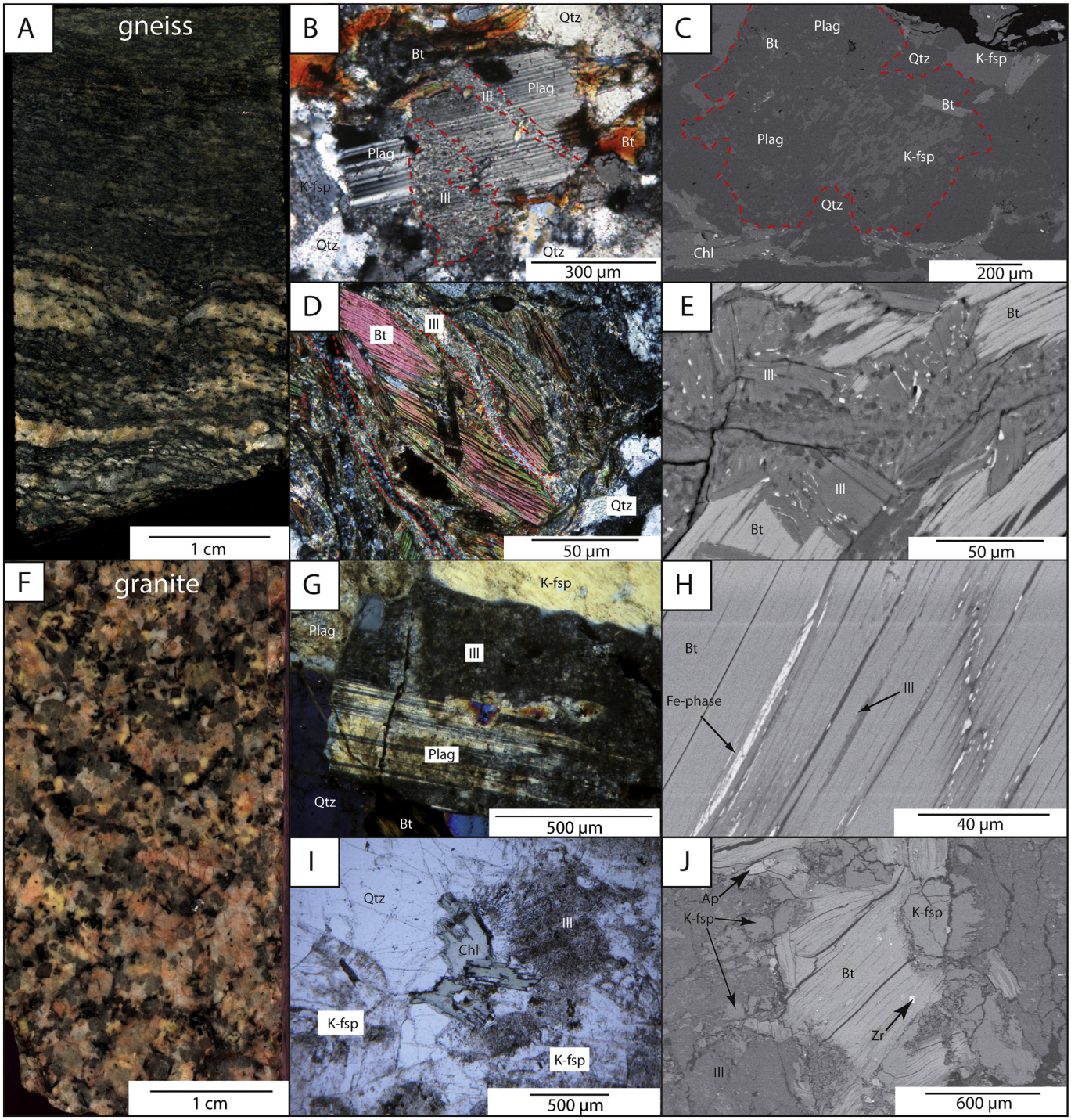

Fig. 2. Samples (A–F) are gneisses and (F–J) granites from representative gneiss and granite bodies in the Schwarzwald (A) Sample MB2 from the Hechtsberg quarry contains a relative unaltered paragneiss. (B) Plagioclase (Plg) is often altered to illite (Ill) and kaolinite in gneisses. Red lines indicate the contact between alteration mineral and host rock mineral. (C) BSE image of a gneiss sample where the plagioclase is replaced by chlorite (Chl). (D) Biotite (Bt) from gneiss altered to illite. (E) BSE image of a gneiss sample. Note replacement of biotite by illite (F) Strongly altered granite sample from the Rappenfelsen quarry (MB3). Note reddish color. (G) In this sample the micas and feldspars are strongly affected by alteration. (H) In numerous granite samples, biotite shows alteration to illite and secondary Fe-phases (presumably goethite or limonite) along cleavage planes. (I) Plagioclase in granite samples are altered to illite and rarely to chlorite whereas the K-feldspar (K-fsp) remains unaffected by alteration. (J) BSE image of an altered granite sample. Note strong alteration of biotite to illite. (For interpretation of the references to color in this figure legend, the reader is referred to the web version of this article.)

Table 2
Modal fractions of the minerals in the source rocks. Modal amounts are presented in Vol%.

Rock	Paragneiss	Granite	Orthogneiss	Paragneiss	Paragneiss	Paragneiss	Granite	Granite	Granite
Sample	MB2	MB3	MB4	CK-C-2	(CK-TG-2A)	(CK-SeG-2)	LM41-1	CK-SG-2	CK-WI-1B CK-WB-2C
Location	Hechtsberg	Rappenfelsen	Hechtsberg	Caroline mine	Teufelsgrund	Segen Gottes	Tiefenstein	Silbergründle	Wittichen
Region	Central Schwarzwald	Central Schwarzwald	Central Schwarzwald	Southern Schwarzwald	Southern Schwarzwald	Central Schwarzwald	Southern Schwarzwald	Central Schwarzwald	Central Schwarzwald
coordinates	48°16′48.2″N 8°08′06.2″E	48°14′41.3″N 8°22′41.7″E	48°16′48.2″N 8°08′06.2″E	48°07′31.6″N 7°55′10.1″E	47°50′43.7″N 7°49′11.8″E	48°17′28.9″N 8°05′03.1″E	47°37′00.7″N 8°05′22.6″E	48°34′49.5″N 8°10′06.0″E	48°20′11.9″N 8°20′29.4″E
Plg	32%	14%	21–64%	60%	50%	48%	35%	24%	12%
Bt	42%	7%	3–23%	20%	17%	21%	14%	5%	5%
Qtz	14%	31%	12–38%	13%	18%	16%	25%	33%	30%
K-Fsp	7%	44%	0–41%	5%	3%	8%	24%	30%	42%
Amph			0–13%	3%	3%	3%			
Accessory	2%	2%		2%	2%	2%	1%	4%	3%
Alteration and clay minerals.	3%	2%	3%	2%	7%	2%	1%	4%	8%

An unaltered paragneiss and orthogneiss sample (Fig. 2A) were taken at the Hechtsberg quarry (MB2a, MB4a; Burisch et al., 2016b). The paragneisses in the vicinity of the Caroline mine (CK-C-2), Segen Gottes (CK-SeG-2) and Teufelsgrund mine (CK-TG-2A) contain medium to strongly altered feldspars and micas. Granite samples from the Tiefenstein quarry (LM41–1), Rappenfelsen quarry (MB3a) and from the country rocks of the Silbergründle mine (CK-SG-2) show only a weak hydrothermal alteration whereas granites from the Wittichen mining district (CK-WI-1B, CK-WI-2C) are strongly hydrothermally altered. Modal compositions (determined by petrography) of the samples and coordinates are presented in Table 2. For details on the XRD analyses for clay mineral identification in the paragneisses, the orthogneiss and the granites the reader is referred to the electronic Supplement ES1.

The paragneisses contain medium-grained biotite (< 250 μm) (Fig. 2A) with inclusions of apatite and zircon. In the strongly hydrothermally overprinted samples, the biotite is typically altered to illite and kaolinite (and occasionally to chlorite) (Fig. 2B–E). Furthermore, medium to coarse-grained quartz (< 200 μm) and plagioclase (< 700 μm) are present, the latter often altered to chlorite (and rarely to illite or kaolinite) to a high degree (Fig. 2B–E). Quartz may contain micro-inclusions of apatite and garnet.

The granites are medium-grained (< 1.5 cm; Fig. 2F). The biotite contains inclusions of apatite and zircon partially altered to illite (Fig. 2G–J). The plagioclase commonly shows polysynthetic twinning and often strong alteration to illite, whereas K-feldspar with Karlsbad twins is typically only weakly altered (Fig. 2G–J). Quartz occurs as anhedral grains, muscovite is rare and, hence, was not considered in this study.

2.1.2. Samples used for LA-ICPMS analyses on single fluid inclusions

This section presents the description only of those samples in which single fluid inclusions were analyzed by LA-ICPMS. Six veins were studied to decipher the processes relevant for understanding the formation of vein-hosted mineral assemblages. The six sampled veins occur along N-S and SSW-NNE trending, vertical fractures (Fig. 3A, B) initiated during Jurassic-Cretaceous (n = 4) or post-Cretaceous times (n = 2) in the central and southern parts of the Schwarzwald mining district. The selection of these veins was primarily guided by their mineralogical composition - covering the most common vein mineral assemblages in the district, their sample quality (large, euhedral crystals with large fluid inclusions that allow detailed fluid petrography and LA-ICPMS analyses, for details please refer to ES2) and their known structural positions. The same samples were used in former studies for fluid inclusion analyses and therefore, the authors of this contribution were confident to find fluid inclusions that fulfill the criteria for LA-ICPMS analyses (see Walter et al., 2017a, 2017b, 2018a). The selected quartz, fluorite and calcite samples contain primary fluid inclusions in macroscopically visible growth zones of centimeter-sized individual crystals. Quartz from the Ottenhöfen locality occurs as late-stage precipitate in a barren vein. Similarly, the Nonnenmattweiher fluorite comes from a barren (i.e., devoid of sulfides) fluorite vein. Fluorite from the Brenden and Schwarzwaldsegen mines and calcite from the Gottesehre mine are co-genetic to abundant Pb-Zn-Cu sulfides. Calcite from the Wenzel mine occurs in close association with Ag-Sb sulfide mineralization.

Sample BW105 is derived from the Ottenhöfen vein (TF35) in the sandpit “Galli” near the town of Achern. It represents one of the many barren quartz veins (typical in terms of textures, structural position and fluid inclusion inventory) (Fig. 3C) located on a north-south striking fault in the sulfide-poor and weakly altered Oberkirch S-type granite, close to the basement-cover unconformity to Lower Triassic Buntsandstein sandstones.

Two samples of the calcite-barite vein in the Wenzel mine (Oberwolfach, Fig. 3D) and from the fluorite-calcite-quartz vein in the Gottesehre mine (Urberg, Fig. 3E) (BW90 and 270) contain large subhedral to euhedral calcite crystals with Ag-Sb and Pb-Zn-Cu mineralization, respectively. The Wenzel mine is hosted in a strongly altered graphite- and sulfide-rich paragneisses and orthogneisses, the Gottesehre vein crosscuts medium altered graphite- and sulfide-rich migmatites with some amphibolite lenses.

The paragneiss-hosted fluorite-barite-quartz veins with Pb-Zn-Cu mineralization of Brenden (near Birkendorf, GS20, Fig. 3F) and the Schwarzwaldsegen mine (close to the town of St. Blasien, BW50, Fig. 3G) contain large anhedral to euhedral crystals of fluorite. The investigated ore-stage fluorite contains micro-inclusions of galena, sphalerite and chalcopyrite. Both veins crosscut a strongly altered graphite- and sulfide-rich paragneiss. The granite-hosted Nonnenmattweiher fluorite-barite-quartz vein (FP19, Fig. 3H) close to the village of Neuenweg is barren, as is the granite-hosted quartz vein from Ottenhöfen.

2.2. Methods

2.2.1. EMPA and LA-ICPMS on minerals of the country rocks

Major elements of the host rock minerals in the paragneisses, the orthogneiss and the granites were analyzed by EMPA using a JEOL JXA-8900RL Superprobe at Department for Geoscience, University of Tübingen applying a beam current of 20 nA and an acceleration voltage of 15 kV in connection with a 10–20 μm beam. For calibration on biotite, chlorite and clay minerals, diopside was used for Mg, albite for Na, hematite for Fe, rhodonite for Mn, $SrTiO_3$ for Ti, plagioclase for Al and Ca, barite for Ba, sanidine for K, tugtupite for Cl, and topaz for F. Counting times on the peak were 16 s for Ca, 30 s for Sr, Mg, Na, Fe, Mn, Ti, Al, Ba, K, and Cl and 60 s for F. Background counting times (upper

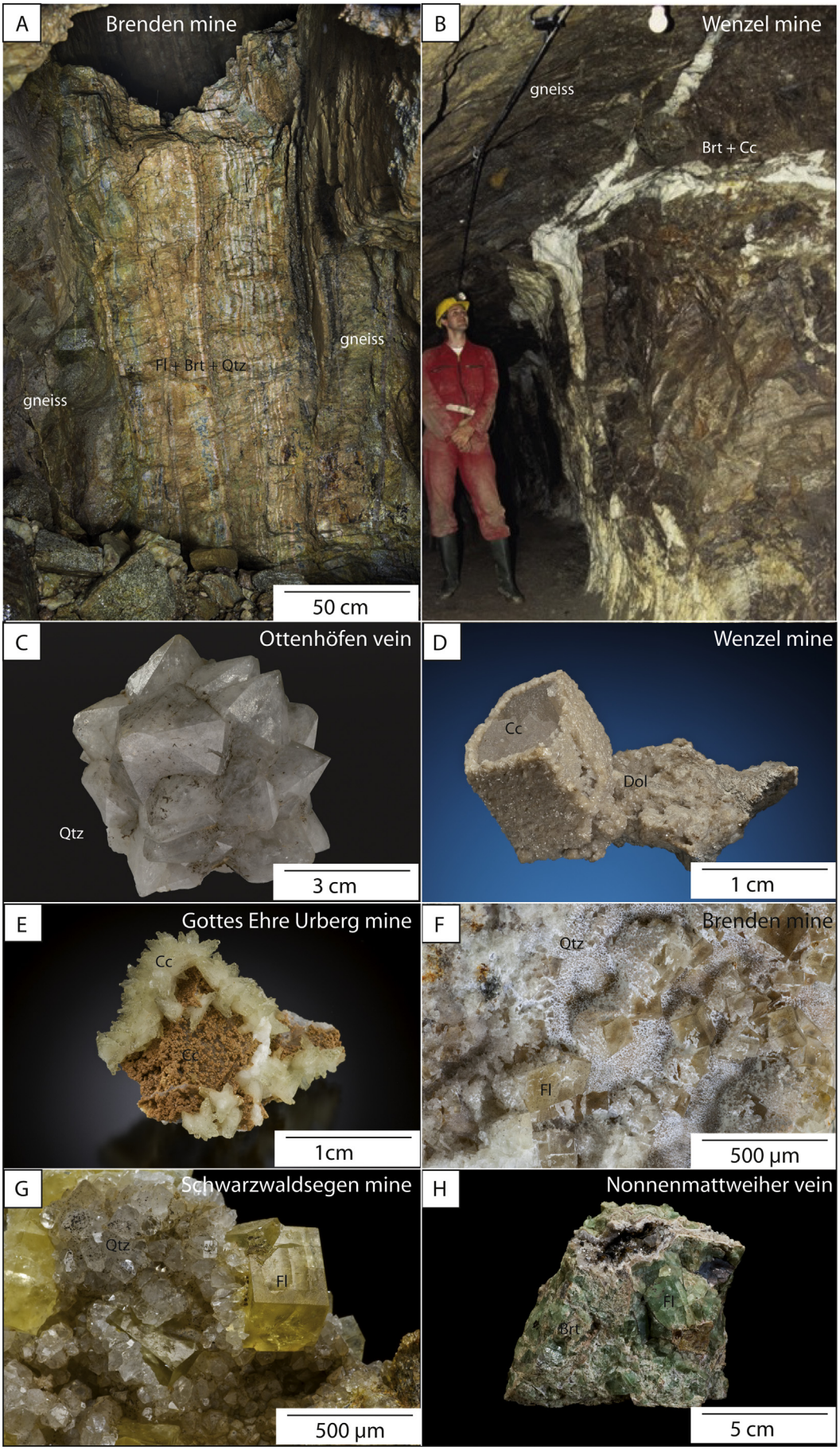

(caption on next page)

Fig. 3. (A) The hydrothermal vein in the Brenden mine contains multiple generations of fluorite, barite and quartz. (B) The hydrothermal vein of the Wenzel mine is discontinuous and mainly consists of carbonates and barite (C) Large euhedral quartz crystals are typical from the barren Ottenhöfen vein (sample BW105). (D) Ore-stage calcite is overgrown from late-stage ankerite and dolomite in the Wenzel mine (sample BW90). (E) Euhedral fluorite is overgrown by late-stage dolomite and calcite in the Gottes Ehre Urberg mine (sample 270). (F) In the Brenden mine, euhedral fluorites are overgrown by barite and carbonates (sample GS20). (G) Euhedral quartz overgrows yellow fluorite in the Schwarzwaldsegen mine (sample BW50). (H) Green fluorite and quartz are common in the barren Nonnenmattweiher vein (sample FP19).

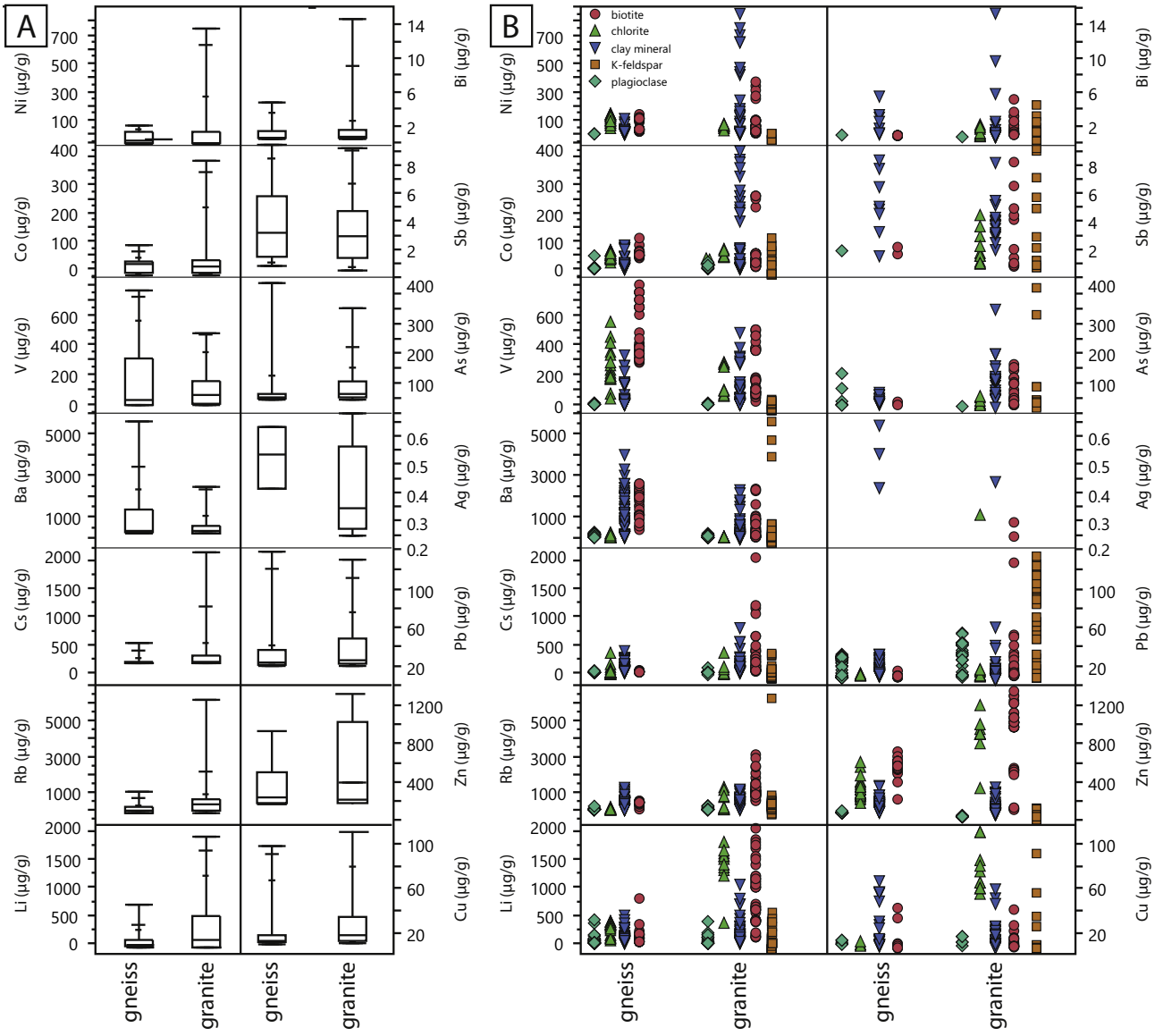

Fig. 4. Trace element contents of the rock forming minerals in the crystalline basement determined by LA-ICPMS. (A) Box-plot illustrating the trace element composition sorted after rock type and (B) trace element composition of individual minerals. Note: Due to the similarity in the trace element contents, the para-gneisses and the one orthogneiss sample are summarized as gneiss.

and lower) where half the peak times. For the calibration on feldspars, albite was used for Na, Si and Al, plagioclase for Ca, barite for Ba, $SrTiO_3$ for Sr, sanidine for K and hematite for Fe. Counting times on the peak were 16 s for Ca, 30s for Sr, K, Na, Fe, Al, Ba and K. Data reduction was performed using the internal ZAF matrix correction software of JEOL (Bence and Albee, 1968; Armstrong, 1991). The results are presented in the electronic Supplement ES3 together with typical standard deviations and detection limits for the individual elements.

LA-ICPMS microanalyses of the country rock minerals were performed at the Institute for Geosciences of the Johannes Gutenberg University Mainz using a 7500ce Agilent Technology ICP-MS quadrupole connected to an ESINWR 193 ArF Excimer laser ablation system. An energy density of 3.0 J/cm^2 with a laser repetition rate of 10 Hz and a beam size of 45 µm was used. Background was recorded for ~20 s prior to the start of the 40 s of ablation followed by 20 s wash out time. The following isotopes were monitored: ^{6}Li, ^{7}Li, ^{29}Si, ^{30}Si, ^{43}Ca, ^{44}Ca, ^{51}V, ^{59}Co, ^{60}Ni, ^{62}Ni, ^{63}Cu, ^{65}Cu, ^{66}Zn, ^{67}Zn, ^{75}As, ^{85}Rb, ^{86}Sr, ^{88}Sr, ^{107}Ag, ^{109}Ag, ^{121}Sb, ^{123}Sb, ^{133}Cs, ^{135}Ba, ^{137}Ba, ^{208}Pb und ^{209}Bi.

For calibration, the multi-element synthetic glass NIST SRM 610 is used applying the preferred values reported in the GeoReM database (http://georem.mpch-mainz.gwdg.de/; Application version of 21, January 2017) (Jochum et al., 2005, 2011) as the “true” concentrations to calculate the element concentrations of the samples. We also analyzed NIST SRM 612, USGS BCR-2G and MPI-DING StHs6/80-G during

Table 3
Averages of trace elements in the host rock minerals.

Rock	Biotite (in µg/g)		Chlorite (in µg/g)		K-feldspar (in µg/g)		Plagioclase (in µg/g)		Clay minerals (in µg/g)	
	Gneiss	Granite	Gneiss	Granite	Gneiss	Granite	Gneiss	Granite	Gneiss	Granite
Li	120	850	250	1390	150	70	40	12	90	200
V	480	200	240	160	20	10	2	b.d.l.	50	100
Co	55	55	45	45	65	20	4	5	20	130
Ni	65	75	100	55	4	3	2	b.d.l.	20	200
Cu	8	7	4	75	4	20	4	b.d.l.	20	15
Zn	500	790	275	880	20	30	4	2	75	70
As	10	60	b.d.l.	20	160	20	35	b.d.l.	20	70
Rb	400	1200	20	380	240	690	15	15	380	490
Ag	b.d.l.	b.d.l.	b.d.l.	b.d.l.	b.d.l.	b.d.l.	b.d.l.	b.d.l.	1	1
Sb	1	3	b.d.l.	2	4	4	1	b.d.l.	5	4
Cs	20	300	8	85	25	70	5	1	75	130
Ba	1650	540	60	10	1070	260	100	7	1010	410
Pb	3	12	1	5	50	50	15	25	8	7
Bi	b.d.l.	1	b.d.l.	1	2	1	b.d.l.	b.d.l.	2	2

each analytical session as quality control materials (QCMs) to monitor precision and accuracy of the measurements as well as calibration strategy. Signals were monitored in time-resolved mode and processed using the SILLS software package (Guillong et al., 2008). Applying the SiO_2 concentration determined by electron microprobe, ^{29}Si was used as internal standard. Element compositions, detection limits and uncertainties for the individual elements are presented in the electronic Supplement ES3. Results on the QCMs are given in the electronic Supplement ES3. For quantification of the whole rock concentrations, the following average densities were used: Biotite 3.1 g/cm^3, chlorite 3.0 g/cm^3, K-feldspar 2.65 g/cm^3, plagioclase 2.6 g/cm^3 and clay minerals 2.8 g/cm^3.

2.2.2. Microthermometry

Microthermometric analyses prior to LA-ICPMS data was carried out using a Linkam THMS600 heating-freezing stage at the University of Tübingen for internal standardization of the fluid inclusions. For fluid petrographic analyses, two doubly-polished thick sections (200 to 400 µm) were prepared representing a cross-section through each vein. The fluid inclusion petrography of each fluid inclusion assemblage was carefully documented by optical and cathodoluminescence microscopy following the method by Goldstein and Reynolds (1994). The observed fluid inclusion assemblages (FIA) were genetically classified as primary inclusions which are situated on growth zones (p), pseudo-secondary (ps), secondary (s), isolated inclusions with no genetic relationship (iso) or clusters of inclusions with no geometrical relation to former crystal surfaces or fractures which, however, depict areas of a former crystal in the host mineral (c) (Walter et al., 2015). For each analysis, three repeated heating and freezing cycles were conducted to measure the initial and final melting temperature of ice ($T_{m,ice}$) and hydrohalite ($T_{m,hh}$) and the homogenization temperature (T_h). For interpretation and LA-ICPMS calibration, only fluid inclusions were used, for which triple analyses showed a variability < 0.1 °C for $T_{m,ice}$ and $T_{m,hh}$ and < 1 °C for T_h. For some inclusions, the resulted microthermometry data indicated a metastable absence of hydrohalite due to the system-related phase diagram NaCl-H_2O-$CaCl_2$ (e.g. Steele-MacInnis et al., 2011). Data of these inclusions were excluded from the interpretation and further LA-ICPMS measurements. Synthetic quartz-hosted H_2O, H_2O-NaCl and H_2O-CO_2 fluid inclusion reference materials (SynFlinc Standard collection) were used for temperature correction of the measured data once a day.

Single fluid inclusions within one FIA that strongly deviate in salinity and T_h from the majority of the same assemblage were neglected to exclude possible post-entrapment modifications. The salinity and molar Ca/(Na + Ca) ratios in the ternary NaCl-$CaCl_2$-H_2O system were calculated using the Excel–based calculation program of Steele-MacInnis et al. (2011). The volume fraction of each fluid inclusion was visually estimated based on published volume proportion tables (e.g. Shepherd et al., 1985). For data presentation, the volume fraction notation is used, which is based on the phase assemblage at room temperature (Lx, numerical subscription refers to the volume percentage of aqueous liquid), carbonic liquid (Lc), vapor (V) and solid (S) (Shepherd et al., 1985; Bakker and Diamond, 2006). Pressure correction of the T_h values was performed following the approach of Bodnar and Vityk (1994), assuming hydrostatic conditions with a depth of the water column inferred from the cumulated overburden lithology thicknesses and resulting paleo-depth (Geyer and Gwinner, 2011; Walter et al., 2017a). Hydrostatic conditions are assumed because of the vein geometry that contains vertical fractures with even recent water flow in the center of the veins and a probable connection to the surface which is indicated by the modern geothermal system that surficially feeds the numerous geothermal spas in the study area. The uncertainties of the method are discussed in the Appendix of Walter et al. (2015). However, the pressure correction has only a minor effect on the trapping temperature (< 7 °C, see also Keim et al., 2018). Hence, in our study we did not make a pressure correction and only considered T_h.

2.2.3. LA-ICPMS microanalyses of single fluid inclusions

LA-ICPMS microanalyses of single fluid inclusions were performed at the ETH Zürich using a Perkin Elmer Elan 6100DRC quadrupole ICP-MS connected to an ETH-GeoLas 193 nm ArF Excimer laser system. An energy density of 15–20 J/cm^2 with a laser pulse frequency of 10 Hz and a variable beam size was used. Background was recorded for ~30 s prior to the start of the ablation. The following isotopes were monitored: ^7Li, ^{11}B, ^{23}Na, ^{24}Mg, ^{32}S, ^{35}Cl, ^{39}K, ^{44}Ca (not quantified in fluorite and calcite but used for matrix correction), ^{55}Mn, ^{57}Fe, ^{59}Co, ^{60}Ni, ^{63}Cu, ^{66}Zn, ^{75}As, ^{79}Br, ^{85}Rb, ^{88}Sr, ^{95}Mo, ^{107}Ag, ^{121}Sb, ^{133}Cs, ^{137}Ba, ^{182}W, ^{205}Tl, ^{208}Pb, ^{209}Bi and ^{28}Si (for the quartz host correction).

The synthetic reference material NIST SRM 610 was used for calibration for all measured elements with exception of Cl and Br, for which the scapolite reference material Sca 17 (Seo et al., 2011) was used. The Na concentration determined by microthermometry in the $CaCl_2$-NaCl-H_2O system (Steele-MacInnis et al., 2011) was taken as internal standard (Steele-MacInnis et al., 2017). Data reduction, background correction and signal deconvolution of the fluid inclusion signal from the host was performed using the procedure of Heinrich et al. (2003) with application by the SILLS software package (Guillong et al., 2008). For quantification, it is assumed that any Si content is a contribution from the quartz host mineral. The Ca concentration determined from microthermometry was used as a second internal standard in the case of fluorite and calcite inclusions. Na, Cl and K were used as tracer to identify the interval of the fluid inclusions in the time-resolved LA-ICPMS signal. Fluid inclusions were analyzed up to 50 µm below the sample surface. The composition of the host was determined from the

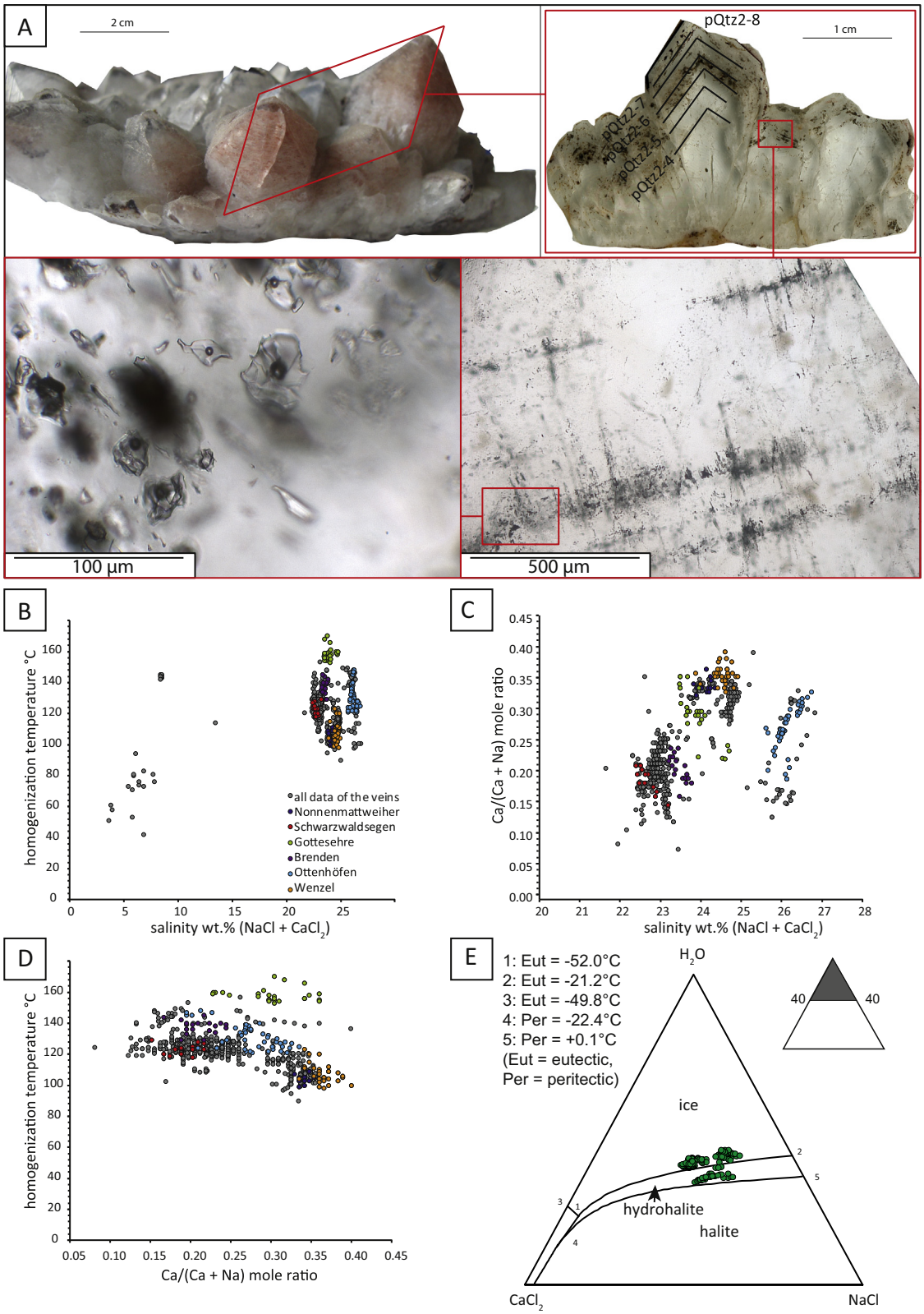

Fig. 5. (A) Fluid inclusion petrography of the Ottenhöfen quartz vein. (B) homogenization temperatures (°C) versus salinity of the analyzed samples. The literature reference data are taken from Walter et al. (2017a, 2017b, 2018a). (C) Ca/(Ca + Na) mole ratios of the fluid versus salinity. (D) Homogenization temperatures versus Ca/(Ca + Na) mole ratios of the fluid. (E) Phase diagram of the relevant NaCl-$CaCl_2$-H_2O system.

signal shortly before and after the inclusion signal if possible.

2.2.4. Raman micro-spectroscopy

Raman micro-spectroscopy measurements were carried out with a confocal Raman spectrometer Renishaw InVia Reflex at the Eberhard Karls University of Tübingen to identify volatile phases, solid phases, and dissolved polyatomic ions (e.g. carbonate, sulfate) in selected fluid inclusion assemblages. All measurements were carried out with a laser

Table 4
Medians of the microthermometric data sorted after samples.

Location	Wenzel	Ottenhöfen	Brenden	Gottesehre	Schwarzwaldsegen	Nonnenmattweiher
Sample	BW-90	BW-105	GS 20	270	BW50	FP19
No of inclusions	35	47	20	26	14	14
Mineral	calcite	quartz	fluorite	calcite	fluorite	fluorite
T_{ice} in °C	−25.4 (−24.2to −26.0)	−25.4 (−26.7 to −24.2)	−22.6 (−23.0 to −22.3)	−23.8 (−24.6 to −23.3)	−21.3 (−21.9 to −21.0)	−24.6 (−24.9 to −24.0)
T_{hh} in °C	−26.4 (−25.9 to −27.0)	−14.3 (−18.0 to −9.8)	−24.1 (−24.5 to −23.4)	−25.4 (−26.3 to −22.9)	−23.9 (−24.1 to −23.2)	−26 (26.5–25.8)
T_h in °C	106 –(98 to 123)	129 (121 to 148)	139 (129 to 145)	158 (153 to 170)	124 (118–129)	105 (99–111)
Volume fraction	0.95	0.95	0.95	0.95	0.95	0.95
R_{wt} NaCl/(NaCl + CaCl2)	0.5 (0.4–0.5)	0.6 (0.5–0.7)	0.7 (0.6–0.7)	0.5 (0.5–0.6)	0.7 (0.7)	0.5 (0.5)
S_{wt} (NaCl + $CaCl_2$)	24.6 (23.9–24.9)	26.1 (25.6–26.7)	23.4 (23.2–23.8)	23.9 (23.5–24.7)	22.6 (22.4–23.2)	24.1 (23.8–24.4)
wt% NaCl	11.8 (10.9–12.6)	15.1 (13.7–17.9)	15.5 (14.4–17.0)	13.1 (11.4–15.8)	15.3 (14.7–17.3)	12.1 (11.4–12.4)
wt% $CaCl_2$	12.7 (12.0–13.7)	10.9 (8.2–13.1)	7.9 (6.5–8.9)	10.7 (8.7–12.2)	7.3 (5.9–7.7)	12.0 (11.5–12.7)
Mole Ca	1.15 (1.1–1.3)	0.98 (0.7–1.2)	0.71 (0.6–0.8)	0.97 (0.8–1.1)	0.66 (0.5–0.7)	1.08 (1.0–1.2)
Mole Na	2.02 (1.9–2.2)	2.59 (2.3–3.1)	2.65 (2.5–2.9)	2.24 (2.0–2.7)	2.62 (2.5–3.0)	2.08 (2.0–2.1)
Ca/(Na + Ca) mole	0.36 (0.34–0.4)	0.27 (0.2–0.3)	0.21 (0.17–0.24)	0.30 (0.23–0.36)	0.20 (0.15–0.22)	0.34 (0.33–0.37)

wavelength of 532 nm (green) using a laser output of 10–50%. The use of a 50× objective results in a numerical aperture of 0.55 with an opening angle of 66.7°. The regulation and correction of the slit diaphragm was done automatically. The focus diameter was approximately 2–5 µm, the measurement time was 30 s with five accumulations. For matrix correction, analyses of the host mineral were performed under identical orientations and conditions. For larger inclusions, both liquid and vapor analyses were done. The Raman database for fluid inclusions of Frezzotti et al. (2012) was used for phase determination.

2.2.5. Cathodoluminescence microscopy

Cathodoluminescence microscopy (CL) of calcite, fluorite and quartz (in which fluid inclusions were analyzed by LA-ICPMS) was performed to assist fluid petrography to obtain detailed textural information on the petrographic relationship and age-constraints of the FIAs (e.g. Kolchugin et al., 2016; Walter et al., 2018a; Kreissl et al., 2018). A 'hot cathode' CL microscope (type HC1-LM) at the University of Tübingen was used with an average acceleration voltage of about 14 kV and a beam current density of approximately 9 µA mm^{-2} on the sample surface (Neuser et al., 1995).

2.2.6. Thermodynamic calculations

Thermodynamic modeling was carried out using the Geochemist's Workbench 12® (Bethke, 2007) in combination with the internally consistent Thermoddem thermodynamic database version of 2017. Due to the significant difference between the stability boundary and the predominance boundary and the aim of discussing stability regions of minerals during fluid mixing, we used the application Phase2 and P2plot to produce real stability diagrams (and no predominance diagrams). All calculations were carried out at 150 °C as an approximation of the general formation temperature; concentrations were selected to best represent the fluids according to thermodynamics, literature data and fluid inclusion data from this study, and no minerals or aqueous species where suppressed during calculations.

3. Results

3.1. Mineral chemistry of minerals in country rocks

In the 9 basement rock samples (Table 2), 84 LA-ICPMS analyses were carried out on biotite, 32 on chlorite, 57 on K-feldspar, 91 on plagioclase and 102 on clay minerals (Table 3, ES3). Boxplots (Fig. 4) illustrate the average and maximum trace element contents of the paragneisses together with the orthogneisses and granites. The trace element contents are similar in the paragneisses and the orthogneiss. Therefore, they will be presented and discussed together as gneisses. Ag, As, Sb and Bi are often close to or below the detection limit.

In biotite, average (gneiss/granite) trace element contents are high for V (~480/~200 µg/g), Zn (~500/~790 µg/g), Rb (~400/~1200 µg/g), Cs (~20/300 µg/g) and Ba (~1650/~540 µg/g), but medium to low for Co (~55/~55 µg/g), Ni (~65/~75 µg/g), Cu (~8/~7 µg/g), As (~10/~60 µg/g), Ag (b.d.l./b.d.l. µg/g), Sb (~1/ < ~3 µg/g), Pb (~3/~12 µg/g) and Bi (b.d.l./~1 µg/g).

In chlorite (gneiss/granite), average concentrations are for high for Ni (~100/~55 µg/g), Cu (~4/~75 µg/g) and moderate to low for V (~240/~160 µg/g), Co (~45/~45 µg/g), Zn (~275/~ 880 µg/g), As (b.d.l./20 µg/g), Rb (~20/~380 µg/g), Ag (b.d.l./b.d.l. µg/g), Sb (b.d.l./~2 µg/g), Cs (~8/85 µg/g), Ba (~60/~10 µg/g), Pb (~1/~5 µg/g) and Bi (b.d.l./~1 µg/g). As, Ag, Sb and Bi in chlorites of the gneisses are below detection limit.

K-feldspar only occurs in granite (with exception of very rare crystals in one paragneiss sample MB2a) in a significant amount. Due to the insignificance of K-feldspar in gneisses, only data for granite are presented and used for interpretation. Trace element average contents are high for Zn (~30 µg/g) and Rb (~690 µg/g) and moderate to low for V (~10 µg/g), Co (~20 µg/g), Ni (~3 µg/g), Cu (~20 µg/g), As (~20 µg/g), Sb (~4 µg/g), Cs (~70 µg/g), Ba (~260 µg/g), Pb (~50 µg/g) and Bi (~1 µg/g). Ag is again below detection limit.

Averages of all elements in plagioclase of gneiss and granite samples are relatively low in comparison to the other host rock minerals with V (~2 µg/g/b.d.l.), Co (~4/~5 µg/g), Ni (~2 µg/g/b.d.l.), Cu (4/b.d.l. µg/g), Zn (~4/~2 µg/g), As (~35 µg/g/b.d.l.), Rb (~15/~15 µg/g), Ag (b.d.l./b.d.l.), Sb (~1 µg/g/b.d.l.), Cs (~5/~1 µg/g), Ba (~100/~7 µg/g), Pb (~15/~25 µg/g) and Bi (b.d.l./b.d.l.). With the exception of As and Ba in gneiss, most concentrations are close or below the detection limit.

The trace element content of the clay minerals is typically related to the altered precursor mineral K-feldspar, plagioclase or biotite. Averages (gneiss/granite) of V (~50/~100 µg/g), Co (~20/~130 µg/g), Ni (~20/~200 µg/g), Cu (~20/~15 µg/g), Zn (~75/~70 µg/g), As (~20/~70 µg/g), Rb (~380/~490 µg/g), Ag (~1/~1 µg/g), Sb (~5/~4 µg/g), Cs (~75/130 µg/g), Ba (~1010/~410 µg/g), Pb (~8/~7 µg/g) and Bi (~2/~2 µg/g) were measured. K-feldspar and biotite alteration results in relatively high trace element concentrations of the alteration minerals. If plagioclase is altered, trace element concentrations in the associated clay mineral are lower than those of K-feldspar and biotite alteration products. With exception of Ba in gneiss and Rb in granite, average concentrations in clay minerals are generally lower for all trace elements.

3.2. Fluid inclusion analyses by microthermometry

Fluid inclusion petrography was performed to classify the observed FIAs in the context of their relative age (Fig. 5A). Primary inclusions

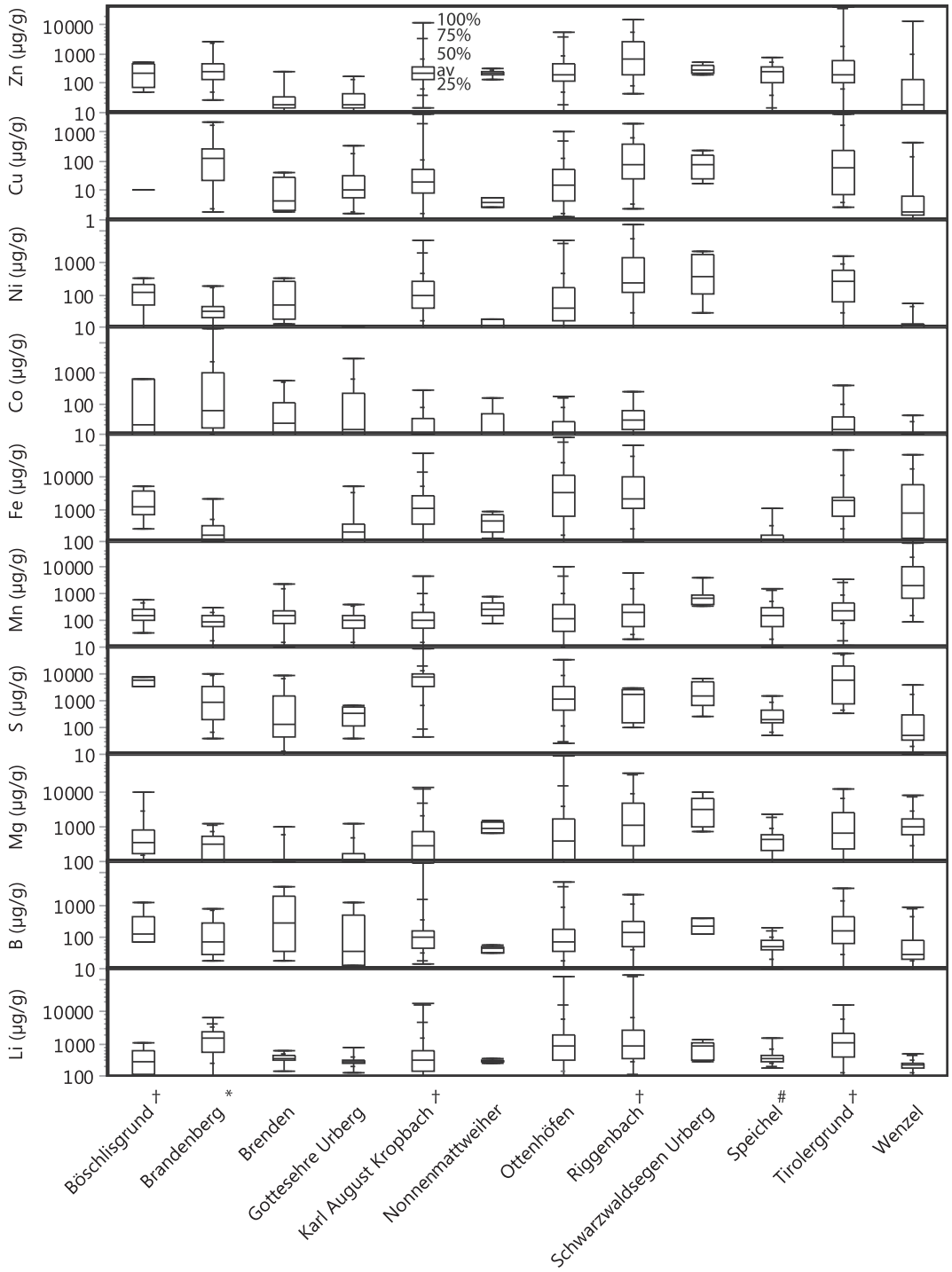

Fig. 6. Boxplots are illustrating the range of trace element concentrations (part 1) measured by LA-ICPMS. For comparison, the previously published LA-ICPMS results are added to the figure (data taken from Fusswinkel et al., 2013 (#); Burisch et al., 2016a (*); Walter et al., 2018a (†)).

occur along crystal growth zones as inclusions with relatively small size (< 5–40 µm). Primary inclusions (p) show irregular and angular inclusion shapes. Pseudosecondary (ps), secondary FIAs (s), isolated (iso) and inclusion cluster (c) are typically larger (< 5–90 µm) and show rounded or negative crystal shapes. S and ps inclusions are related to healed cracks and, hence, are younger than the fluid inclusions on primary growth zones they crosscut. Fluid inclusion data of all genetic positions (p, s, ps, iso, c) were brought into a relative time sequence following the approach of Goldstein and Reynolds (1994) and were classified after Walter et al. (2015). Fluid inclusion evidence for boiling (fluid immiscibility, heterogeneous trapping) was never observed. The samples were studied by optical and CL-microscopy in order to understand the fluid petrography and to determine overprinting events.

Sample BW105 (Ottenhöfen) contains growth zones in a clear euhedral quartz crystal (Fig. 5; ES2). On these growth zones, primary fluid inclusions occur with variable shapes and sizes. Numerous secondary cracks with secondary inclusions crosscut the growth zones pQtz2–4 to pQtz2–9. A pseudosecondary trail (psQtz2-(8–9)) shows a similar direction like the secondary ones, however, the trail stops at growth zone pQtz2–9. Sample BW90 (Wenzel mine) contains euhedral calcite crystals which were filled by clusters of large fluid inclusions (up to 100 µm). However, the genetic relation of these fluid inclusions is

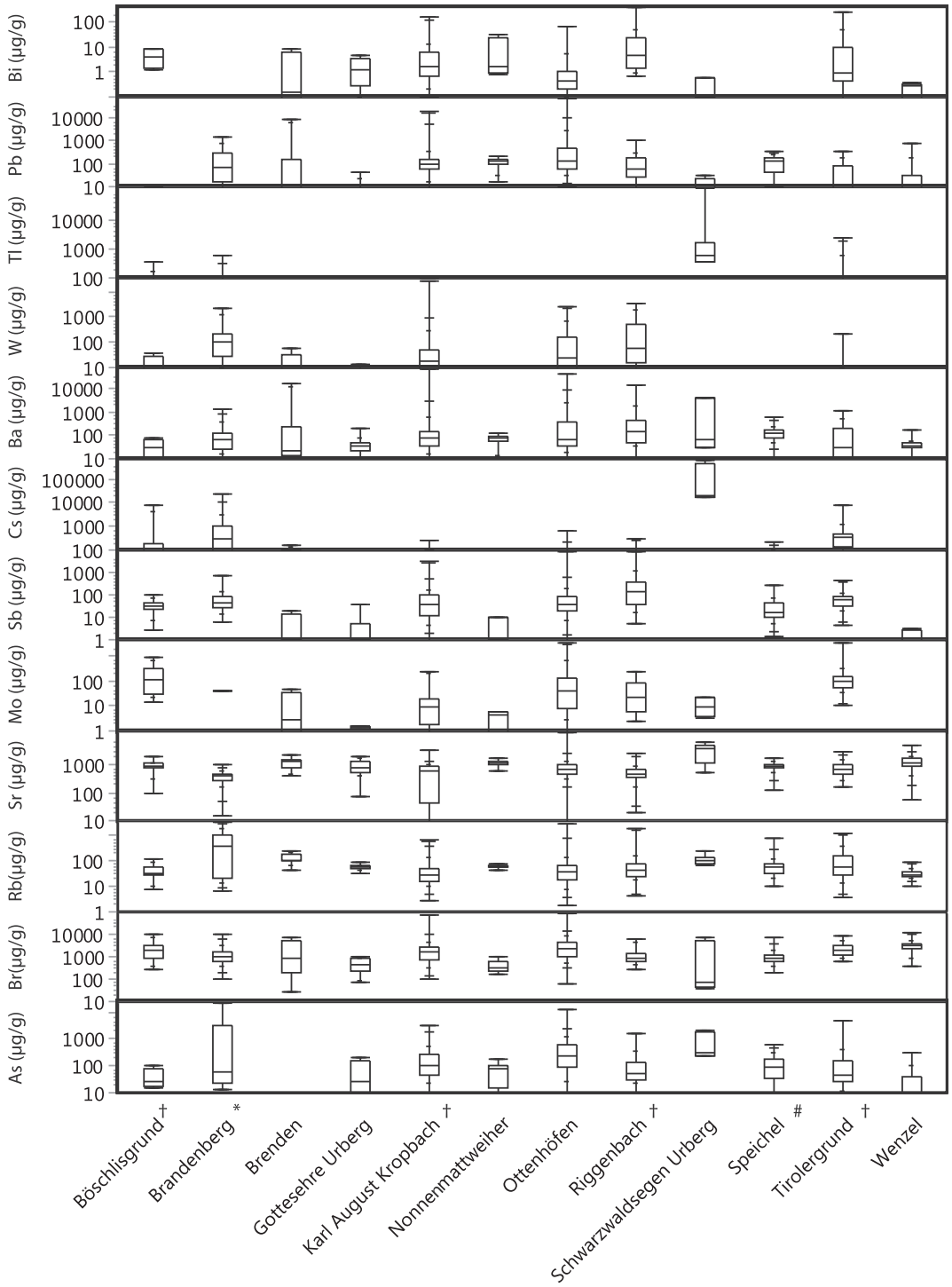

Fig. 7. Boxplots illustrating the range of trace element concentrations (part 2) measured by LA-ICPMS. For comparison, the previously published LA-ICPMS results are added to the figure (data taken from Fusswinkel et al., 2013(#); Burisch et al., 2016a(*); Walter et al., 2018a (†)).

unclear. Only one growth zone was recognized with primary fluid inclusions (pCc1-1; ES2). Similarly, sample 270 from the Gottesehre mine only contains one growth zone with primary fluid inclusions (pCc1-1). The fluid inclusion cluster cCc1-1 is older than the primary growth zone. Furthermore, the primary growth zone is crosscut by a pseudosecondary FIA (psCc1-1) and a secondary inclusion trail (sCc1-1). In the clear fluorite 2 in sample GS20 (Brenden mine), a growth zone with primary inclusions (pFl2-2) is crosscut by a pseudosecondary FIA (psFl2-1; ES2). Sample BW50 contains a clear fluorite with eight growth zones. However, only the inclusions on zone pFl1-2 were large enough to be analyzed by LA-ICPMS. Moreover, primary fluid inclusions were recognized on two growth zones of the green fluorite 1 and 2 generation of sample FP19 (Nonnenmattweiher, ES2).

The fluid inclusions in all FIAs record the first visible/apparent melting between −49 and − 54 °C which suggests a eutectic temperature at −52.0 °C which therefore refers to the ternary NaCl-$CaCl_2$-H_2O system (Table 4, ES4). Ice and hydrohalite both occur as last dissolving phases. The final melting temperature of ice is between −21.7 and − 26.7 °C and for hydrohalite in the range of −9.8 to −27.5 °C which results in calculated salinities (after Steele-MacInnis et al., 2011)

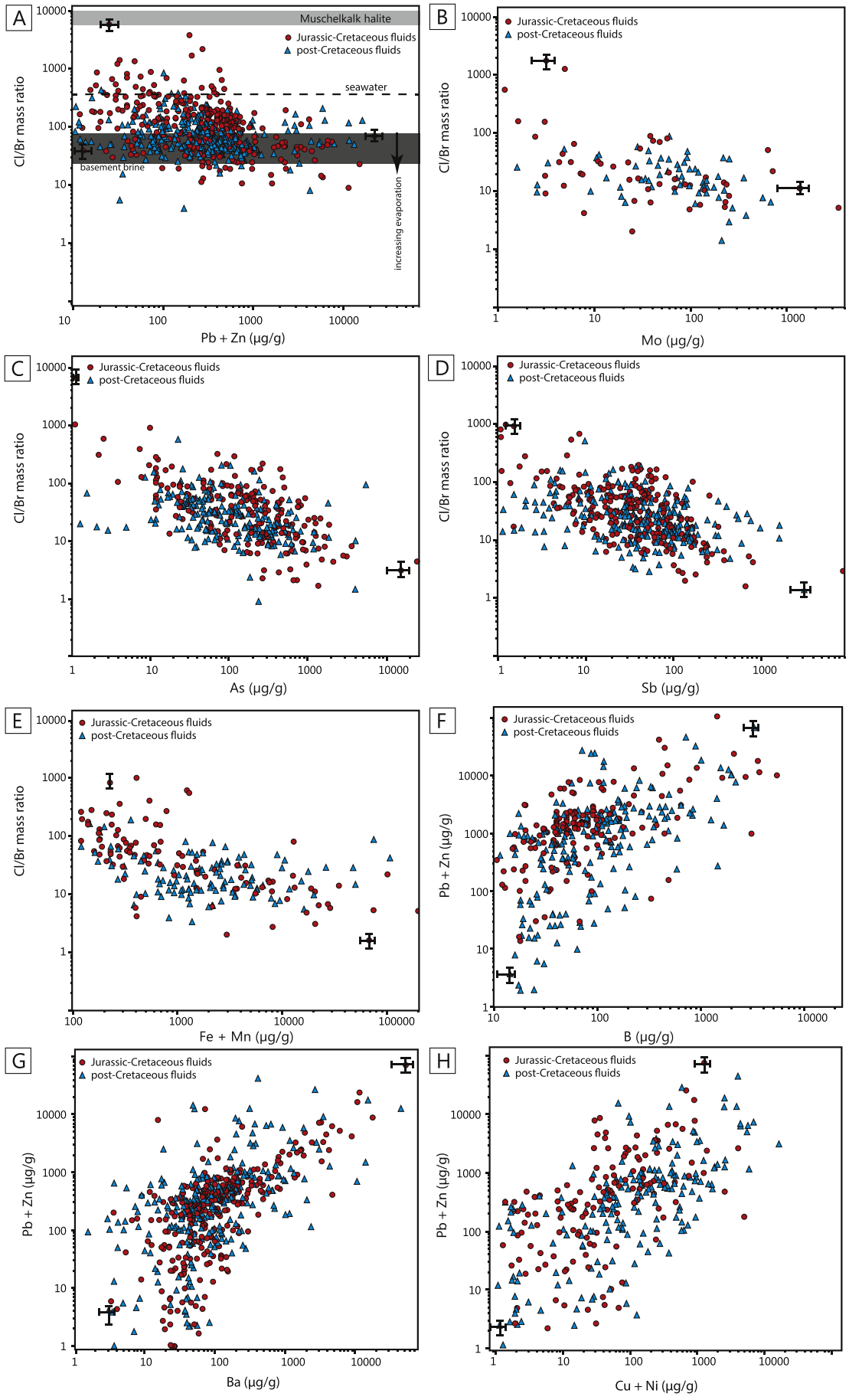

(caption on next page)

Fig. 8. (A-F) Cl/Br mass ratios plotted versus selected element concentrations in the fluid as determined by LA-ICPMS. Seawater ratio of Cl/Br (288) from McCaffrey et al. (1987). The basement brine Cl/Br ratio of ~80 and the Muschelkalk Cl/Br ratio of 9900 originates from Walter et al. (2016) and references therein. (F-H) Pb + Zn content plotted versus B, Ba and (Cu + Ni) content of the fluid.

of 22.4–26.7 wt% $NaCl + CaCl_2$. Homogenization temperatures to the vapor are variable between 98 and 170 °C. No systematic compositional variations were observed between p, ps, s, iso and c FIAs. Within a defined FIA, salinity (± 1 wt%) is almost constant and T_h (± 10 °C) shows minor variations, but typically vary between different assemblages even within a single crystal. The inclusions contain volume fractions between $L_{85}V_{15}$ and $L_{95}V_5$. The new fluid inclusion data fits well to the preexisting data of the six samples (Walter et al., 2017a, 2017b, 2018a). Raman micro-spectroscopic analysis shows only H_2O as Raman-active phase in all FIAs of the six veins. However, NaCl-dependent variations of the H_2O spectrum were observed (Dubessy et al., 2002; Baumgartner and Bakker, 2009; Caumon et al., 2013, 2015). Hence, there is no evidence for further volatile species in the gas phase or further daughter minerals on the inclusion walls which is in agreement with the microscopic observations.

3.3. LA-ICPMS on single fluid inclusions

LA-ICPMS analyses of single fluid inclusions were performed on 327 primary or pseudosecondary fluid inclusions from one quartz sample, two calcite samples and three fluorite samples (see Section 2.2; Figs. 6 and 7, ES5). Fluids in a single FIA are homogeneous in salinity, but trace metal concentrations show a significant spread within a given sample and within a given FIA, respectively. A systematic variation between trace metal content and the relative age of an FIA was not observed. In general, the trace element variation resembles previous data from the Schwarzwald mining district (Fusswinkel et al., 2013; Burisch et al., 2016b; Walter et al., 2018a). The new data contributed by this study is presented in electronic Supplement ES5.

Trace element contents of single quartz-hosted fluid inclusions show a higher spread of Li (up to 17,600 µg/g), B (up to 5420 µg/g), S (up to 34,900 µg/g), Ni (up to 4980), Cu (up to 1010 µg/g), As (up to 12,700 µg/g), Sb (up to 860 µg/g), Cs (up to 600 µg/g), Ba (up to 47,100 µg/g), W (up to 2470 µg/g), Pb (up to 63,500 µg/g) and Bi (up to 70 µg/g) compared to the fluid inclusions hosted in fluorite or calcite. Highest values of Mn (up to 16,000 µg/g), Zn (up to 13,300 µg/g) and Fe (up to 83,500 µg/g) in calcite are regarded as a contamination effect from the carbonate host mineral. The content of Co (up to 3220 µg/g) is relatively high, which is probably related to contamination effects due to the common incorporation of Co into the crystal lattice of calcite. In all other trace elements, the fluids trapped in calcite are depleted relative to those trapped in quartz.

Trace element concentrations in fluorite-hosted fluid inclusions are in the same range as the calcite-hosted ones, but show higher contents of Sr (380–6040 µg/g), Cs (up to 59,100 µg/g) and Ba (up to 15,900 µg/g). In all samples, the base-metal content is positively correlated with the Cl-concentration in the fluid, similar to trends reported for other systems by Yardley (2005) and Walter et al. (2017a, 2017b, 2018a). Interestingly, the barren Nonnenmattweiher and Ottenhöfen veins show similar base-metal concentrations as the other four veins that contain sulfide mineralization.

4. Discussion

The following discussion combines the microthermometric and LA-ICPMS results of this study with previously published data of Fusswinkel et al. (2013), Burisch et al. (2016b) and Walter et al. (2015, 2016, 2017a, 2017b, 2018a). LA-ICPMS data from the Karl August vein near Kropbach, a typical quartz vein with Pb-Zn mineralization (Walter et al., 2018a) were also included to compare barren and mineralized veins. The fluid and LA-ICPMS data of this contribution are in excellent agreement with results of Staude et al. (2010a, 2010b, 2011, 2012a, 2012b), Fusswinkel et al. (2013), Bons et al. (2014) and Walter et al. (2015, 2016, 2017a, 2017b, 2018a). The combination of trace element analyses in hydrothermally altered basement rocks and in ore-forming fluids (LA-ICPMS on single FI) renders it possible to quantify basement leaching processes and to decode the metal provenance in a complex hydrothermal system.

4.1. Evidence for long-term stability of fluid reservoirs and metal provenance

Metal provenance are among the most pertinent factors to form ore deposits. In Fig. 8A–E, the Pb + Zn, As, Sb and Fe + Mn contents from LA-ICPMS data of single fluid inclusions are presented. This data does not reveal any significant difference between fluids present in primary and secondary fluid inclusions of Jurassic-Cretaceous and post-Cretaceous veins. All these elements are negatively correlated with the Cl/Br mass ratio (Fig. 8A–E). This implies that the main source of these elements is the crystalline basement – because the sediment-derived fluid has high Cl/Br ratios (Walter et al., 2015, 2016, 2017a, 2017b, 2018a; Burisch et al., 2016b). Similarly, Cu + Ni, B and Ba (Fig. 8F–H) are correlated with high Pb + Zn concentrations; their source is also seen in leached feldspars and biotites of crystalline basement rocks (Burisch et al., 2016b). Accordingly, the data indicate that all mineralogically different types of veins can be produced by mixing from the same fluid endmembers. Furthermore, since the earliest record of basement leaching by a high salinity brine during the Middle Triassic (Walter et al., 2016, 2017a) the fluid mixing ratios (and hence the element concentrations) remain rather consistent (Fig. 8A–H). Clay-mineral K-Ar and Ar-Ar age data suggest that major alteration of the rock-forming minerals happened during the Jurassic (Meyer et al., 2000; Brockamp and Clauer, 2005; Walter et al., 2016 and references therein). This observation perfectly matches the first occurrence of hydrothermal Pb-Zn mineralization in the investigated area (Pfaff et al., 2009; Walter et al., 2016, 2018b). In summary, the scatter of metal concentrations in fluid inclusions from Jurassic-Cretaceous and post-Cretaceous veins (Fig. 8) indicate leaching of basement rocks by high salinity fluids. This process is regarded as the dominant source of metals for hydrothermal vein deposits in the Schwarzwald at least for the last ~200 Ma (Bons et al., 2014; Burisch et al., 2016a, 2016b, 2017, 2018; Walter et al., 2016, 2017a, 2017b, 2018a, 2018b).

4.2. The source of Pb and Zn in the context of vein formation depth

The data presented in Fig. 9A indicates a variation in fluid inclusion geochemistry from Jurassic-Cretaceous veins with their formation depth. This is not observed for the studied post-Cretaceous veins which are probably related to the complex tectonic setting of the rift. Highest Pb and Zn concentrations with low Cl/Br mass ratios occur in veins of the central Schwarzwald, which were emplaced at shallower depths than those of the southern Schwarzwald (Walter et al., 2017a). Interestingly, Pb and Zn concentrations in fluid inclusions are higher in the shallow central compared to the deeper southern Schwarzwald veins, although the latter show the higher proportion of basement fluid in calculated mixing ratios (Staude et al., 2011; Walter et al., 2015). According to the arguments presented in Section 4.1, the dominant source of Pb and Zn should be the crystalline basement rocks. This may tentatively be explained by variable degrees of alteration and leaching in the basement in combination with salinity variations. The exemplary sampled gneisses and granites of the central Schwarzwald (e.g. MB2, MB3, MB4, CK-SeG-2) generally show a higher clay mineral content

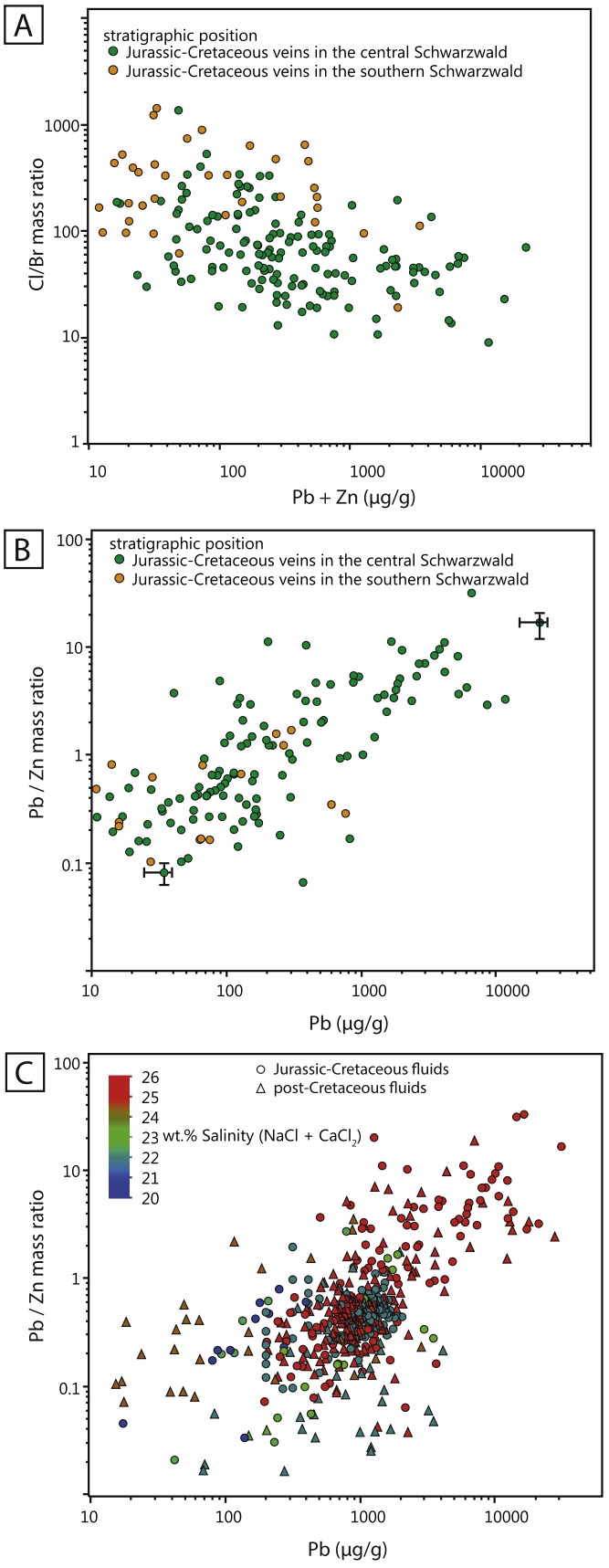

Fig. 9. (A) Cl/Br mass ratio versus Pb + Zn concentration in the fluid. Note: systematic variations between central and southern Schwarzwald. (B) Pb/Zn mass ratio versus Pb content of the fluid, sorted after vein group. (C) Pb/Zn mass ratio versus Pb content of the fluid, sorted vein group and colored after wt % salinity.

(Table 2) than those of the southern Schwarzwald (e.g. CK-C-2, CK-TG-2A, LM41-1) while the trace element contents in the primary rock-forming minerals are similar (ES3). In addition, the fluids in Jurassic-Cretaceous veins of the central Schwarzwald are more saline than those of the southern Schwarzwald as explained by Walter et al. (2017a). Hence the most plausible explanation is a higher release and uptake of metals (here specifically: Pb and Zn) by the basement brine due to their higher salinity in areas with more strongly altered country rocks (i. e. in the central Schwarzwald).

Pb and Zn are very similar in their geochemical behavior and the solubility product of galena and sphalerite is similarly low (pK_{sp} ~26.7 and pK_{gal} ~25.6; Ball and Nordstrom, 1991). This should result in only slight variations of Pb/Zn-ratios in response to concurrent galena and sphalerite precipitation. However, the LA-ICPMS data of the fluids show a significant variation in their Pb/Zn ratios and hence, imply a process that fractionates Pb from Zn (Fig. 9B and C). Importantly, Jurassic-Cretaceous and post-Cretaceous veins show similar scatter. The Jurassic-Cretaceous veins show higher Pb/Zn ratios as well as higher Pb concentrations and higher salinity in fluid inclusions from the central Schwarzwald (Fig. 9B and C).

The explanation for this result is similar to Section 4.2. The higher salinity brines lead to an increasing alteration in the basement and hence, fractionation of Pb and Zn occurred during variable alteration rates of biotite and K-feldspar in granite. However, although the K-feldspar (only in granite) is the major host for Pb in the basement, it is typically not strongly affected by alteration. Also the variation of the Pb/Zn ratio with the stratigraphic depth cannot be explained by this process.

An alternative and more probable interpretation would involve an additional source of Pb, which would have to be sought at shallow depth, because the Pb content and Pb/Zn ratio in the mixed fluid increases with decreasing depth (Fig. 9B). Previous studies indicated mixing between Muschelkalk and basement fluid (Fusswinkel et al., 2013; Bons et al., 2014; Walter et al., 2016, 2017a) as the dominant process for mineralization in Jurassic-Cretaceous veins. The Muschelkalk (and Keuper) limestones, however, are well-known for some galena-rich layers ("Bleiglanzbank", Walther, 1982; Geyer and Gwinner, 2011) which could be an additional (albeit minor) source of Pb in the mixed fluid. The Pb input would have to be enough to shift the Pb/Zn ratio, but not the trend in Fig. 8A. This assumption is in agreement with the calculated mixing ratios for the central Schwarzwald: ~70–90% basement brine and ~10–30% Muschelkalk fluid (Staude et al., 2011; Walter et al., 2015).

Judging from the data in Fig. 4B, an element-specific fractionation between fluid and clay minerals appears to exist, which is different in granites and gneisses. Some elements are preferentially stored in clay minerals (Ba, Cu, Ag, Sb and Bi in granites and gneisses, Co, Ni, As only in granites) while Li, Zn and Pb are preferentially released into the fluid. This feature could be an effect of element-specific adsorption on clay mineral surfaces. In this case, leaching of the host rocks would be no congruent process and there could be a (clay) mineralogical or a fluid chemical control (e.g. complexation) on the trace element budget of the leaching solution in the different rocks. This preliminary interpretation, however, is only a first step in the understanding of adsorption processes during host rock alteration.

4.3. Estimates on the leached volume of basement rocks

To shed light on the extent of water-rock interaction in the root zone of the studied veins, a simplified mass balance calculation was carried out. The host rock data (Table 2) were used as input and combined with the highest Pb and Zn content found in fluid inclusions (ES5). The following assumptions had to be made:

- the highest Zn content of the fluid inclusions is close to the basement brine endmember concentration

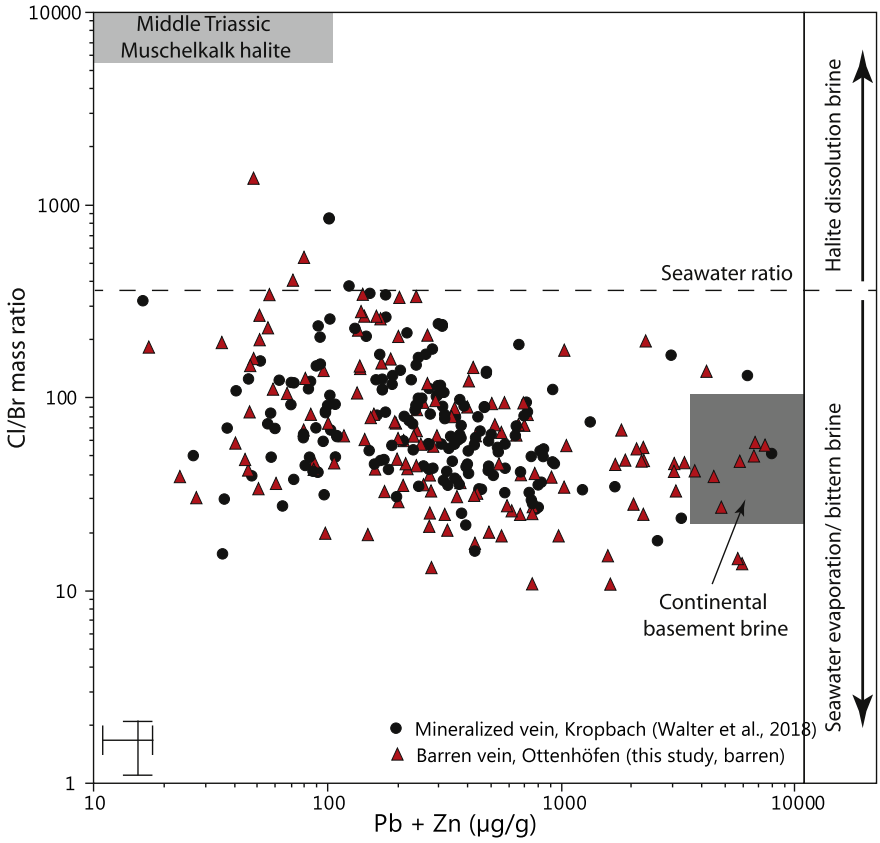

Fig. 10. Cl/Br mass ratios versus Pb + Zn (µg/g) content of LA-ICPMS data from the Ottenhöfen vein and Karl August mine near Kropbach (Walter et al., 2018a).

- no phases were precipitated from this fluid prior to trapping
- $C^{average}_{metal\ in\ biotite} + C^{average}_{metal\ in\ feldspar} - C^{average}_{metal\ in\ claymineral}$ is the amount of metals released to the fluid (C = concentration of a trace metal in the host mineral)
- alteration of plagioclase and biotite is ~10% (in accordance with textural observations)
- faults and fractures are negligible
- alteration by fluids is facilitated by open porosity in the rocks

The calculation sheet is reported in the electronic Supplement ES6. It is assumed that an average gneiss of the Schwarzwald contains ~60% plagioclase and ~15% biotite with ~10% alteration. Based on the above assumptions, 17 g Zn from biotite with a content of 510 µg/g (Zn release from plagioclase is negligible) would be released from 1 m^3 gneiss (density 2.7 g/cm^3). Accordingly, ~40 m^3 gneiss have to be leached for 1 kg of precipitated sphalerite. The Schauinsland mine in the southern Schwarzwald, which was the largest Zn mine in the area, produced about 180.000 t of sphalerite between 1909 and 1957 (Metz et al., 1957) for which leaching of 7.017.000.000 m^3 gneiss would be required. This would correspond to a gneiss cube with a side length of about 2000 m. This rough quantification shows that ore fluids can be produced by (highly saline) fluid-rock interaction of almost every country rock with trace metal concentrations in the µg/g level. Accordingly, no pre-enrichment is required and a fertile source rock can be seen in almost all crystalline basement rocks.

4.4. Barren and ore-bearing veins: the redox potential of the country rocks

Following the previous section, it appears most likely that the formation of barren vs. sulfide mineralized veins of all ages in the Schwarzwald is not a source, but a precipitation phenomenon. This notion is corroborated by the fact that the metal contents in the fluid inclusions from barren and from ore-bearing veins are in the same range (Fig. 10). Additionally, barren and ore-bearing veins may form in close spatial and temporal proximity.

To decipher this aspect in more detail, LA-ICPMS trace element data of single fluid inclusions from the barren Ottenhöfen quartz vein are compared to the sphalerite-bearing Karl August quartz vein near Kropbach/Münstertal (data for the latter are taken from Walter et al., 2018a) where multi-component fluid mixing between a Muschelkalk fluid, a meteoric fluid and a basement brine has been identified as the driving force for ore formation based on Cl/Br mass ratios and Pb + Zn concentrations (Walter et al., 2018a). Fig. 10 shows no significant differences in base metal or Cl/Br mass ratios between the barren Ottenhöfen and the ore-bearing Kropbach fluids (Figs. 11 and 12). In both veins, however, the trace element concentrations in different FIAs may vary significantly (sometimes several orders of magnitude). These variations may be related to changing mixing ratios.

In both veins, which were precipitated by fluid mixing of the same fluid endmembers; concentrations of base metals and sulfur (probably as SO_4^{2-}; direct evidence is lacking in this study but indirect evidence is discussed in Walter et al., 2017b; Walter et al., 2018a and ES7) were evidently similar. The presence and abundance of sulfides is then dependent on the concentration of sulfide and hence on the redox conditions (see also Göb et al., 2013; Markl et al., 2016; Burisch et al., 2017 and Walter et al., 2017b, 2018a). As the solubility product of most sulfides is much too low to transport aqueous sulfides with Pb, Zn or Cu in the same fluid (Allison et al., 1991; Ball and Nordstrom, 1991; Walter et al., 2018a), addition of a reducing phase like CH_4, other hydrocarbons, graphite or H_2S (with the intermediate reaction steps of CO_2 which immediately reacts to dissolved HCO_3^-) is required to reduce the sulfate present in the metal-bearing fluid. Such a process was previously suggested for orogenic gold deposits (Naden and Shepherd, 1989; Wilde et al., 2001; Cox et al., 1991; Bell et al., 2017 and references therein), for MVT deposits (e.g. Liu et al., 2017 and references therein) and for 5-element veins (Markl et al., 2016; Burisch et al., 2017; Kreissl et al.,

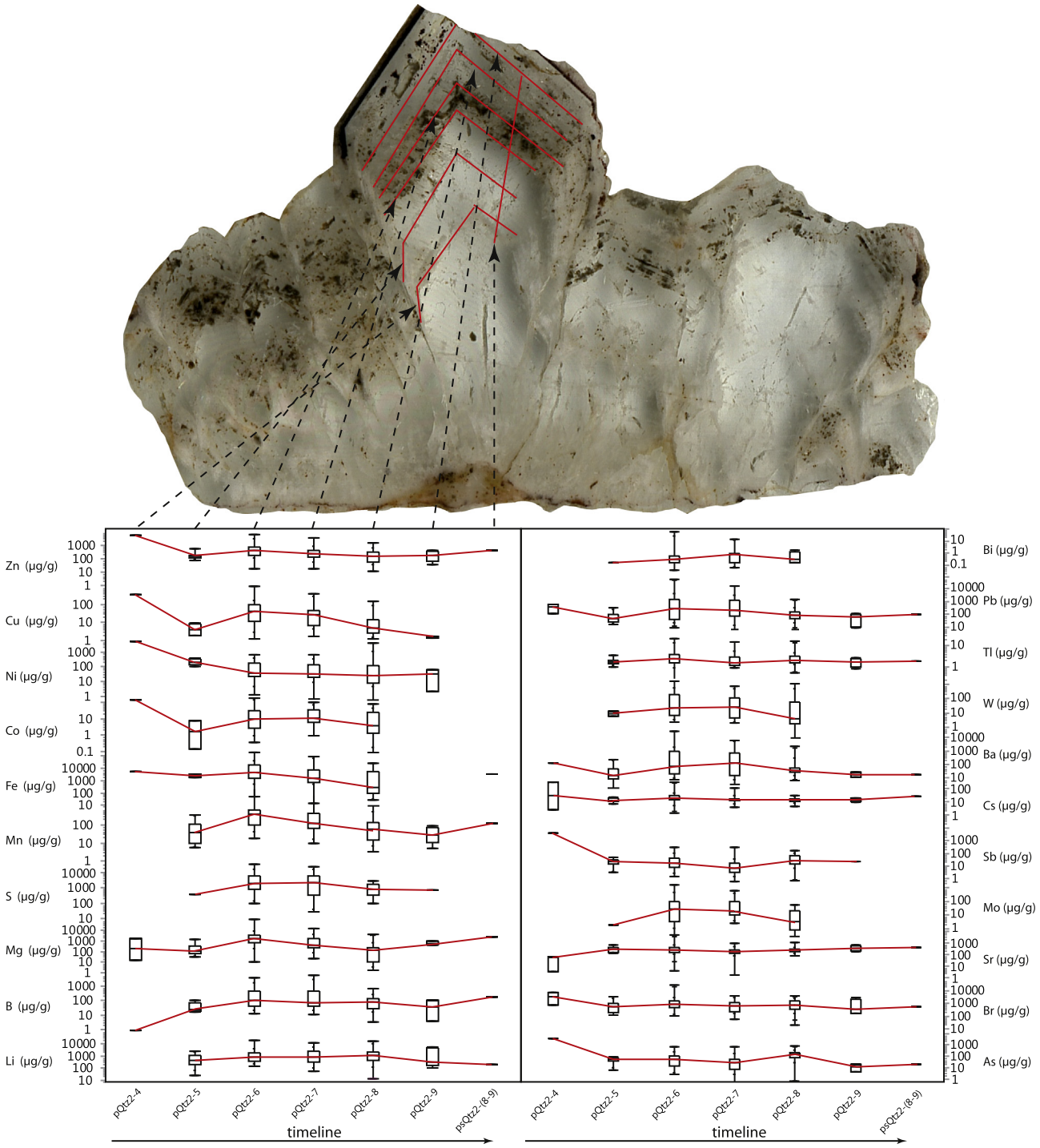

Fig. 11. Trace element variations between the different FIAs of the barren Ottenhöfen vein. Note: significant variations in base metals between the FIAs.

2018 and references therein). Hence, it appears that the "natural fracking" model developed for 5-element veins (Markl et al., 2016; Burisch et al., 2017; Kreissl et al., 2018) can be also used to explain nugget sulfide ore mineralization in ordinarily barren unconformity-related vein type deposits. Interestingly, hydrocarbons were found in crushed sphalerite from the Schauinsland mine in the southern Schwarzwald (Werner et al., 2002), which supports their presence during the precipitation process. Furthermore, fluid inclusion Raman micro-spectroscopy data from further veins (not studied by LA-ICPMS on single inclusions) provides first evidence of H_2S and CH_4 in some of the Schwarzwald veins' fluid inclusions (see figure in ES7).

Unfortunately, no fluid inclusion Raman micro-spectroscopic evidence was found for CH_4 (and CO_2) or H_2S in the six samples of this contribution. This may be explained by a complete consumption of CH_4 and oxidation to CO_2, which would be immediately converted to dissolved HCO_3^- (Burisch et al., 2016b and references therein). The negative charge balance in numerous crush-leach analyses from the Schwarzwald veins (Walter et al., 2016, 2017a, 2017b, 2018a) indicates a significant HCO_3^- component in the fluid, but the source of this species remains unclear (e.g. produced by CH_4 oxidation or from an external source). The measured high metal content in our fluid data support the assumption that the availability of the reducing agent is the

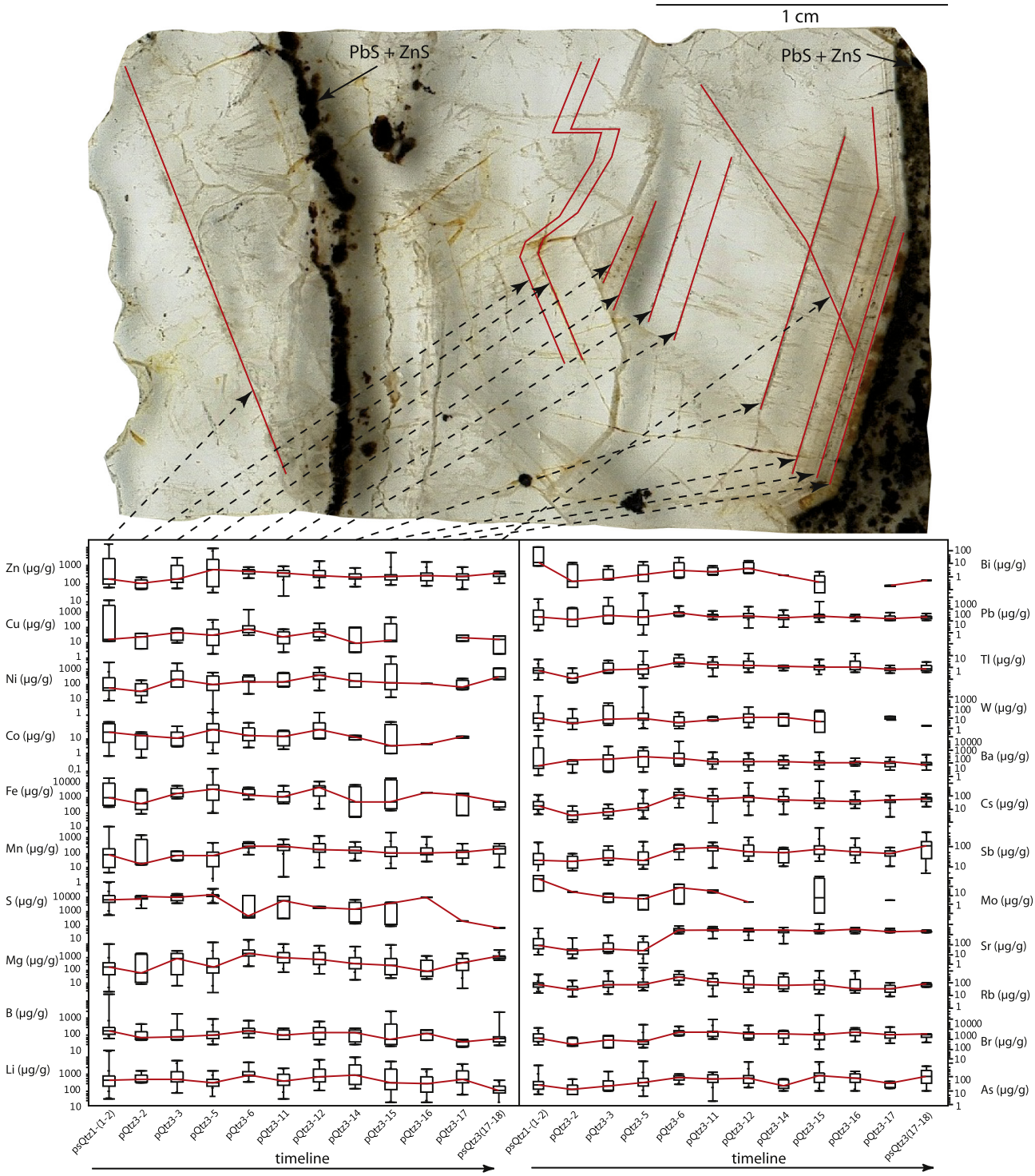

Fig. 12. Trace element variations between the different FIAs of the mineralized Karl August mine, near Kropbach. Data are taken from Walter et al. (2018a). Note: significant variations in base metals between the FIAs.

limitation for sulfide precipitation. In the present high salinity fluid at neutral conditions (e.g. pH of 5.82 at 150 °C), the dominant species are: HCO_3^-, H_2S/SO_4^{2-}, Ba^{2+}, $ZnCl^+$ und $PbCl_2$. Therefore, we suggest the following precipitation mechanism for barite without sulfide ores:

$$Ba^{2+}_{(aq)} + SO_4^{2-}{}_{(aq)} = BaSO_4 \quad (1)$$

This process occurs due to a simple mixing of a metal-rich, oxidized basement brine, and a sulfate-rich, metal-poor, oxidized Muschelkalk brine (Fig. 13a). However, for the precipitation of sulfides, more reduced conditions (Fig. 13b), i.e., a reducing agent like CH_4, is required (Fig. 13a), which is to be oxidized (reaction (2)–(4)) so that sulfate is in turn reduced to sulfide (reaction (3))

oxidation of CH_4: $CH_{4(g)} + 2\,O_{2(aq)} = HCO_3^- + H^+ + H_2O$ (2)

reduction of SO_4: $SO_4^{2-} + 2H^+ = H_2S_{(aq)} + 2\,O_{2(aq)}$ (3)

Hence, the following precipitation mechanism for galena and sphalerite can be assumed:

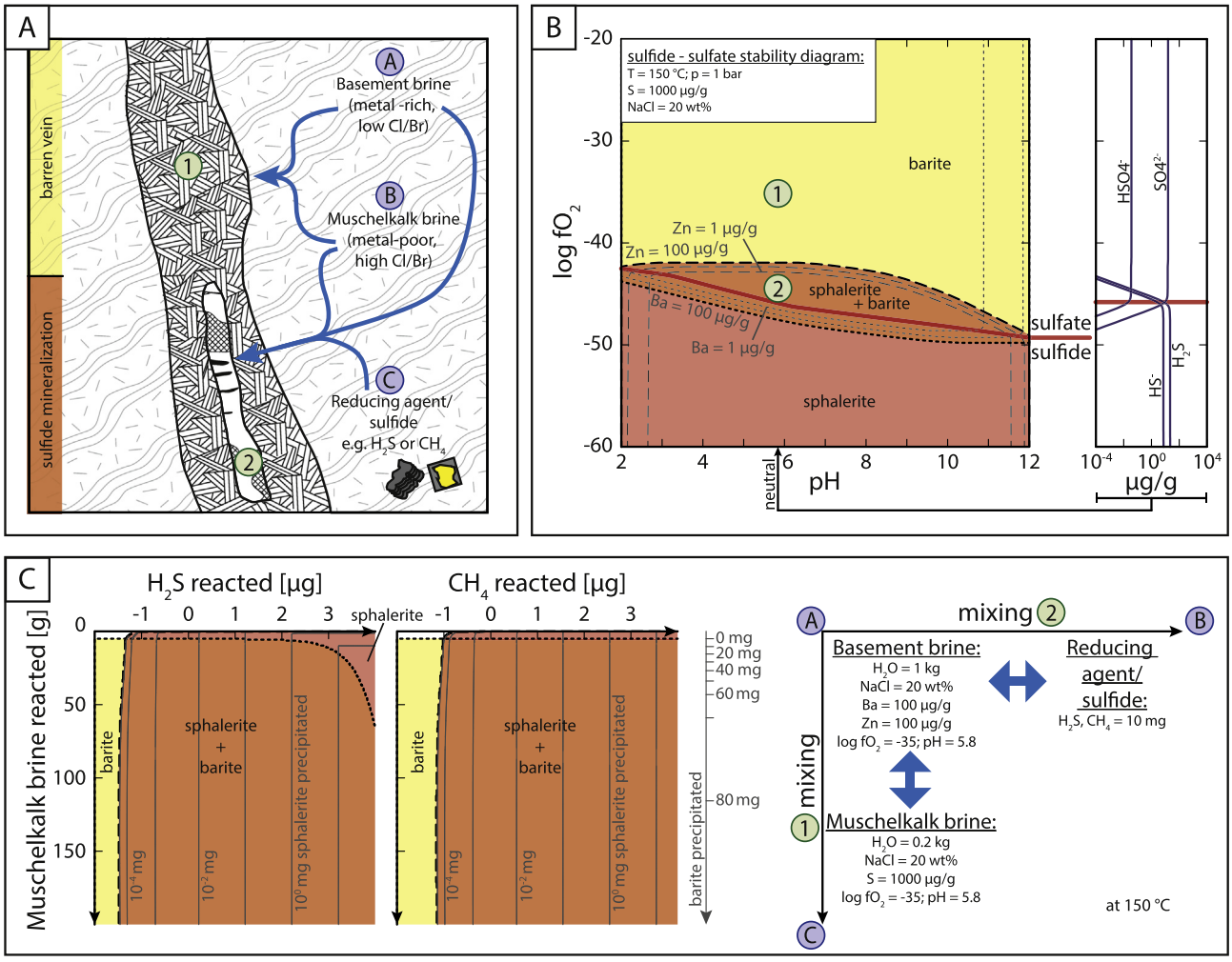

Fig. 13. For all thermodynamic modeling, charge balancing was reached by adding Cl^-. The modeled fluid composition and input parameters are presented within each diagram. (A) Simplified model explaining the occurrence for sulfide mineralization in barren veins. Note: The alteration of graphite and sulfides could be the driving process to generate a redox agent which is required for sulfide precipitation. (B & C) Stability field relation between sphalerite and barite at 150 °C. Galena is not presented here due to simplification of the diagram, however, the difference between galena and sphalerite stability is negligible. Dashed lines represent variable element composition of the fluid as indicated. (C) Mineral stability diagram of the ternary fluid mixing model between a metal bearing basement fluid, a sulfate and metal deprived Muschelkalk fluid and a reducing agent (H_2S and CH_4).

$$PbCl_{2(aq)} + SO_4^{2-} + CH_{4(aq)} = PbS + 2Cl^- + H^+ + HCO_3^- + H_2O \quad (4)$$

$$ZnCl^+ + SO_4^{2-} + CH_{4(aq)} = ZnS + Cl^- + H^+ + HCO_3^{2-} + H_2O \quad (5)$$

If H_2S is introduced instead of CH_4, it can directly react with the aqueous Pb and Zn to form sulfides. Fig. 13c shows that during the mixing of a metal-bearing oxidized brine with a sulfate-bearing oxidized brine, only small quantities (< 1 µg per 1 l fluid) of CH_4 or H_2S are needed for sphalerite (equivalent to galena) supersaturation. However, to produce significant quantities of these sulfides, as are present in naturally occurring barite veins, H_2S and/or CH_4 is required in the order of mg per 1 l metal-bearing fluid. In the case of methane as the reducing agent, the resulting HCO_3^{2-} content often results in late stage carbonate precipitation (similar to the process of 5-element precipitation; Markl et al., 2016):

$$HCO_3^- + Ca^{2+} = CaCO_3 + H^+ \quad (6)$$

In the Schwarzwald mining district, numerous multi-stage veins contain carbonates as the last precipitating mineral of each stage (Metz et al., 1957; Burisch et al., 2018).

The Ottenhöfen vein is hosted by a sulfide-poor weakly altered S-type granite, while the Karl August vein is situated in a strongly altered graphite- and sulfide-rich paragneisses. Hence, it seems plausible that the alteration of graphite and/or sulfides in the paragneiss produced H_2S and/or CH_4 which were released into fractures and participated during mixing (Fig. 13a; see also Markl et al., 2016; Burisch et al., 2017 and Walter et al., 2018a). Furthermore, veins in the center of granitic complexes are commonly barren (e. g., Ottenhöfen), while gneiss-hosted veins (e. g., Schauinsland, Schwarzwaldsegen, Wenzel or Kropbach) or veins close to granite-gneiss contacts (e. g., Wittichen, Igelschlatt, Brenden) show extensive ore mineralization (Metz et al., 1957). In conclusion, the question of sulfide mineralization is directly linked to the redox potential of a vein's host and/or the fluid's source rock. Hence, if all parameters are favorable for mineralization, ore formation would be simply a question of reduction.

5. Conclusions

The present study sheds light on different stages of ore deposition, specifically on element uptake during basement alteration and mineral precipitation. Fluids in disequilibrium with the crystalline basement alter igneous biotite and feldspars to sheet silicates. This process releases metals to the fluid, especially Pb and Zn. Not yet understood adsorption phenomena appear to retard the mobilization of elements such as Ag, Co, Ni or Cu relative to Pb and Zn. Our new data imply that

the source for almost all metals are the rocks of the crystalline basement. A rough mass balance calculation shows that about 8 km^3 country rock with 10% alteration is required to produce an ore deposit containing 180.000 t of sphalerite if 50% of the metals in the fluids are precipitated. If all parameters are favorable, ore fluids can be produced from most basement lithologies of the upper crust because traces of metals at the µg/g level are ubiquitous.

Precipitation of minerals in veins in the investigated area dominantly occurred during fluid mixing. Fluid mixing ratios vary during crystal growth and ore formation; this is recorded by strong variations of trace element concentrations in analyzed fluid inclusions from the same vein and the same FIA. Sulfide ores form only if fluid mixing and reduction occur concurrently. This requires the addition of a reducing agent like methane or higher hydrocarbons to the mixing aqueous fluids. If the reducing agent is lacking veins containing little or no sulfide will form. The presence and abundance of the reducing agent is probably linked to redox-sensitive processes like graphite or sulfide oxidation in the host rocks immediately adjacent to the veins.

Supplementary data to this article can be found online at https://doi.org/10.1016/j.chemgeo.2018.12.038.

Acknowledgments

We thank S. Schafflick for sample preparation. Furthermore, we thank Alexandre Tarantola and an anonymous reviewer for their detailed reviews. Moreover, Michael Böttcher is thanked for his editorial guidance. Mathias Burisch, Sebastian Staude, Max Keim and Stefan Kreissl are thankfully acknowledged for fruitful discussions. Furthermore, we thank Jens Gutzmer for his detailed critique on a previous version of the manuscript. His suggestions significantly improved the manuscript. This study was supported by the German Science Foundation (DFG), grant MA 2135/20-1.

References

Allison, J.D., Brown, D.S., Novo-Gradac, K.J., 1991. MINTEQA2/PRODEFA2, A Geochemical Assessment Model for Environmental Systems, Version 3.0, User's Manual, EPA/600/3-91/021.
Altherr, R., Holl, A., Hegner, E., Langer, C., Kreuzer, H., 2000. High-potassium, calc-alkaline I-type plutonism in the European Variscides: northern Vosges (France) and northern Schwarzwald (Germany). Lithos 50, 51–73.
Aquilina, L., Boulvais, P., Mossmann, J.-R., 2011. Fluid migration at the basement/sediment interface along the margin of the Southeast basin (France): implications for Pb–Zn ore formation. Mineral. Deposita 46, 959–979.
Armstrong, J.T., 1991. Quantitative elemental analysis of individual microparticles with electron beam instruments. In: Electron Probe Quantitation. Springer, US, pp. 261–315.
Baatartsogt, B., Schwinn, G., Wagner, T., Taubald, H., Beitter, T., Markl, G., 2007. Contrasting paleofluid systems in the continental basement: a fluid inclusion and stable isotope study of hydrothermal vein mineralization, Schwarzwald district, Germany. Geofluids 7, 123–147.
Bakker, R.J., Diamond, L.W., 2006. Estimation of volume fractions of liquid and vapor phases in fluid inclusions, and definition of inclusion shapes. Am. Mineral. 91, 635–657.
Ball, J.W., Nordstrom, D.K., 1991. WATEQ4F – user's manual with revised thermodynamic data base and test cases for calculating speciation of major, trace and redox elements in natural waters. In: U.S.G.S. Open-File Report, pp. 90–129.
Banks, D.A., Boyce, A.J., Samson, I.M., 2002. Constraints on the origins of fluids forming Irish Zn-Pb-Ba deposits: evidence from the composition of fluid inclusions. Econ. Geol. 97 (3), 471–480.
Bau, M., Romer, R.L., Lüders, V., Dulski, P., 2003. Tracing element sources of hydrothermal mineral deposits: REE and Y distribution and Sr-Nd-Pb isotopes in fluorite from MVT deposits in the Pennine Orefield, England. Mineral. Deposita 38, 992–1008.
Baumgartner, M., Bakker, R.J., 2009. Raman spectroscopy of pure H2O and NaCl-H2O containing synthetic fluid inclusions in quartz—a study of polarization effects. Mineral. Petrol. 95 (1–2), 1–15.
Beaudoin, G., Taylor, B.E., Sangster, D.F., 1992. Silver-lead-zinc veins and crustal hydrology during Eocene extension, southeastern British Columbia, Canada. Geochim. Cosmochim. Acta 56 (9), 3513–3529.
Beccaletto, L., Capar, L., Cruz-Mermy, D., Rupf, I., Nitsch, E., Oliviero, G., Elsass, P., Perrin, A., Stephane, M., 2010. The GeORG project – Geological Potential of the Upper Rhine Graben - Situation, Goals and First Scientific Results. – Abstractes, 23ème Réunion des Science. Bordeaux, France, HAL Id: hal-00642768.
Behr, H.J., Gerler, J., 1987. Inclusions of sedimentary brines in post-Variscan mineralizations in the Federal Republic of Germany—a study by neutron activation analysis. Chem. Geol. 61 (1–4), 65–77.
Behr, H.J., Horn, E.E., Frentzel-Beyme, K., Reutel, C., 1987. Fluid inclusion characteristics of the Variscan and post-Variscan mineralizing fluids in the Federal Republic of Germany. Chem. Geol. 61 (1–4), 273–285.
Bell, R.M., Kolb, J., Waight, T.E., Bagas, L., Thomsen, T.B., 2017. A Palaeoproterozoic multi-stage hydrothermal alteration system at Nalunaq gold deposit, South Greenland. Mineral. Deposita 52, 383–404.
Bence, A.E., Albee, A.L., 1968. Empirical correction factors for the electron microanalysis of silicates and oxides. J. Geol. 76 (4), 382–403.
Bethke, C.M., 2007. Geochemical and Biogeochemical Reaction Modeling. Cambridge University Press.
Bliedtner, M., Martin, M., 1986. Erz- und Minerallagerstätten des Mittleren Schwarzwaldes. Geologisches Landesamt Baden-Württemberg, Freiburg im Breisgau, Germany. (782p).
Bodnar, R.J., Vityk, M.O., 1994. Interpretation of microthermometric data for H_2O-NaCl fluid inclusions. In: De Vivo, B., Frezzotti, M.L. (Eds.), Fluid Inclusions in Minerals, Methods and Applications. Virginia Tech, Blacksburg, pp. 117–130.
Boiron, M.C., Cathelineau, M., Richard, A., 2010. Fluid flows and metal deposition near basement/cover unconformity: lessons and analogies from Pb–Zn–F–Ba systems for the understanding of Proterozoic U deposits. Geofluids 10, 270–292.
Bons, P.D., Fusswinkel, T., Gomez-Rivas, E., Markl, G., Wagner, T., Walter, B., 2014. Fluid mixing from below in unconformity-related hydrothermal ore deposits. Geology 42 (12), 1035–1038.
Braunger, S., Marks, M.A.W., Walter, B.F., Neubauer, R., Reich, R., Wenzel, T., Parsapoor, A., Markl, G., 2018. The petrology of the Kaiserstuhl Volcanic Complex, SW Germany: the importance of metasomatized and oxidized lithospheric mantle for carbonatite generation. J. Petrol. 498, 1–1632.
Brockamp, O., Clauer, N., 2005. A km-scale illite alteration zone in sedimentary wall rocks adjacent to a hydrothermal fluorite vein deposit. Clay Miner. 40, 245–260.
Bucher, K., Stober, I., 2002. Water-rock reaction experiments with Black Forest gneiss and granite. Water Sci. Technol. 40, 61–95.
Burisch, M., Marks, M.A., Nowak, M., Markl, G., 2016a. The effect of temperature and cataclastic deformation on the composition of upper crustal fluids — an experimental approach. Chem. Geol. 433, 24–35.
Burisch, M., Walter, B.F., Wälle, M., Markl, G., 2016b. Tracing fluid migration pathways in the root zone below unconformity-related hydrothermal veins: insights from trace element systematics of individual fluid inclusions. Chem. Geol. 429, 44–50.
Burisch, M., Gerdes, A., Walter, B.F., Neumann, U., Fettel, M., Markl, G., 2017. Methane and the origin of five-element veins: mineralogy, age, fluid inclusion chemistry and ore forming processes in the Odenwald, SW Germany. Ore Geol. Rev. 81, 42–61.
Burisch, M., Walter, B.F., Gerdes, A., Lanz, M., Markl, G., 2018. Hydrothermal anhydrite-gypsum-siderite-dolomite-calcite assemblages record the transition from a deep to a shallow hydrothermal system in the Schwarzwald mining district, SW Germany. Geochim. Cosmochim. Acta 223, 259–278.
Carignan, J., Gariépy, C., Hillaire-Marcel, C., 1997. Hydrothermal fluids during Mesozoic reactivation of the St. Lawrence rift system, Canada: C, O, Sr and Pb isotopic characterization. Chem. Geol. 137, 1–21.
Caumon, M.C., Dubessy, J., Robert, P., Tarantola, A., 2013. Fused-silica capillary capsules (FSCCs) as reference synthetic aqueous fluid inclusions to determine chlorinity by Raman spectroscopy. Eur. J. Mineral. 25 (5), 755–763.
Caumon, M.C., Tarantola, A., Mosser-Ruck, R., 2015. Raman spectra of water in fluid inclusions: I. Effect of host mineral birefringence on salinity measurement. J. Raman Spectrosc. 46 (10), 969–976.
Cox, S.F., Wall, V.J., Etheridge, M.A., Potter, T.F., 1991. Deformational and metamorphic processes in the formation of mesothermal vein-hosted gold deposits—examples from the Lachlan Fold Belt in central Victoria, Australia. Ore Geol. Rev. 6 (5), 391–423.
Crognier, N., Hoareau, G., Aubourg, C., Dubois, M., Lacroix, B., Branellec, M., Vennemann, T., 2018. Syn-orogenic fluid flow in the Jaca basin (South Pyrenean Fold and Thrust Belt) from fracture and vein analyses. Basin Res. 30 (2), 187–216.
Deane, J., 1995. The Structural Evolution of the Kombat Deposits, Otavi Mountainland, Namibia: Communications of the Geological Survey of Namibia. 10. pp. 99–107.
Duane, M.J., De Wit, M.J., 1988. Pb-Zn ore deposits of the northern Caledonides: products of continental-scale fluid mixing and tectonic expulsion during continental collision. Geology 16 (11), 999–1002.
Dubessy, J., Lhomme, T., Boiron, M.C., Rull, F., 2002. Determination of chlorinity in aqueous fluids using Raman spectroscopy of the stretching band of water at room temperature: application to fluid inclusions. Appl. Spectrosc. 56 (1), 99–106.
Essarraj, S., Boiron, M.C., Cathelineau, M., Tarantola, A., Leisen, M., Boulvais, P., Maacha, L., 2016. Basinal brines at the origin of the imiter Ag-Hg deposit (Anti-Atlas, Morocco): evidence from LA-ICP-MS data on fluid inclusions, halogen signatures, and stable isotopes (H, C, O). Econ. Geol. 111 (7), 1753–1781.
Essarraj, S., Boiron, M.C., Cathelineau, M., Tarantola, A., Leisen, M., Hibti, M., 2017. Mineralogy and ore fluid chemistry of the Roc Blanc Ag deposit, Jebilet Hercynian massif, Morocco. J. African Earth Sci. 127, 175–193.
Frezzotti, M.L., Tecce, F., Casagli, A., 2012. Raman spectroscopy for fluid inclusion analysis. J. Geochem. Explor. 112, 1–20.
Fusswinkel, T., Wagner, T., Wälle, M., Wenzel, T., Heinrich, C.A., Markl, G., 2013. Fluid mixing forms basement-hosted Pb-Zn deposits: insight from metal and halogen geochemistry of individual fluid inclusions. Geology 41, 679–682.
Fusswinkel, T., Wagner, T., Wenzel, T., Wälle, M., Lorenz, J., 2014. Red bed and basement sourced fluids recorded in hydrothermal Mn–Fe–As veins, Sailauf (Germany): a LA-ICPMS fluid inclusion study. Chem. Geol. 363, 22–39.
Garven, G., Appold, M.S., Toptygina, V.I., Hazlett, T.J., 1999. Hydrogeologic modeling of the genesis of carbonate-hosted lead-zinc ores. Hydrogeol. J. 7, 108–126.
Geyer, O.F., Gwinner, M.P., 2011. Geologie von Baden -Württemberg. – 5., völlig neu

bearbeitete Auflage. Schweizerbart'sche Verlagsbuchhandlung (Nägele u. Obermiller), Stuttgart. (627pp).
Göb, S., Loges, A., Nolde, N., Bau, M., Jacob, D.E., Markl, G., 2013. Major and trace element compositions (including REE) of mineral, thermal, mine and surface waters in SW Germany and implications for water–rock interaction. Appl. Geochem. 33, 127–152.
Goldstein, R.H., Reynolds, T.J., 1994. Systematics of Fluid Inclusions in Diagenetic Minerals. SEPM Short Course. 31 Society for Sedimentary Geology, Tulsa OK (199 pp).
Grandia, F., Canals, A., Cardellach, E., Banks, D.A., Perona, J., 2003. Origin of ore-forming brines in sediment-hosted Zn–Pb deposits of the Basque-Cantabrian basin, Northern Spain. Econ. Geol. 98, 1387–1411.
Guillong, M., Meier, D.L., Allan, M.M., Heinrich, C.A., Yardley, B.W., 2008. Appendix A6: SILLS: A MATLAB-based Program for the Reduction of Laser Ablation ICP-MS Data of Homogeneous Materials and Inclusions. 40. Mineralogical Association of Canada Short Course, pp. 328–333.
Hann, H.P., Chen, F., Zedler, H., Frisch, W., Loeschke, J., 2003. The rand granite in the southern Schwarzwald and its geodynamic significance in the Variscan belt of SW Germany. Int. J. Earth Sci. 92, 821–842.
Hein, U.F., 1993. Synmetamorphic Variscan siderite mineralisation of the Rhenish Massif, central Europe. Mineral. Mag. 57, 451-451.
Heinrich, C.A., Pettke, T., Halter, W.E., Aigner-Torres, M., Audétat, A., Günther, D., Hattendorf, B., Bleiner, D., Guillong, M., Horn, I., 2003. Quantitative multi-element analysis of minerals, fluid and melt inclusions by laser-ablation inductively-coupled-plasma mass-spectrometry. Geochim. Cosmochim. Acta 67, 3473–3496.
Hoeve, J., Sibbald, T.I., 1978. On the genesis of Rabbit Lake and other unconformity-type uranium deposits in northern Saskatchewan, Canada. Econ. Geol. 73 (8), 1450–1473.
Jenkner, B., 1986. Ein Vorschlag zur Neugliederung des sedimentären Oberrotliegenden in der Baden-Badener Senke und ihrer nordöstlichen Fortsetzung (Nordschwarzwald). Jahrb Geol Landesamtes Baden-Württemberg. 28. pp. 49–159.
Jochum, K.P., Nohl, U., Herwig, K., Lammel, E., Stoll, B., Hofmann, A.W., 2005. GeoReM: a new geochemical database for reference materials and isotopic standards. Geostand. Geoanal. Res. 29 (3), 333–338.
Jochum, K.P., Weis, U., Stoll, B., Kuzmin, D., Yang, Q., Raczek, I., Jacob, D., Stracke, A., Birbaum, K., Frick, D., Günther, D., Enzweiler, J., 2011. Determination of reference values for NIST SRM 610–617 glasses following ISO guidelines. Geostand. Geoanal. Res. 35 (4), 397–429.
Kalt, A., Altherr, R., Hanel, M., 2000. Exkursion A: the Variscan Basement of the Schwarzwald. Suppl. Issues Eur. J. Mineral. 12 (2), 1–44.
Keim, M., Walter, B.F., Neumann, U., Kreissl, S., Bayerl, R., Markl, G., 2018. Polyphase Enrichment and Redistribution Processes in Silver-Rich Mineral Associations of the Hydrothermal Fluorite-Barite-(Ag-Cu) Clara Deposit, SW Germany.
Kessen, K.M., Woodruff, M.S., Grant, N.K., 1981. Gangue mineral $^{87}Sr/^{86}Sr$ ratios and the origin of Mississippi Valley-type mineralization. Econ. Geol. 76 (4), 913–920.
Kolchugin, A.N., Immenhauser, A., Walter, B.F., Morozov, V.P., 2016. Diagenesis of the palaeo-oil-water transition zone in a Lower Pennsylvanian carbonate reservoir: Constraints from cathodoluminescence microscopy, microthermometry, and isotope geochemistry. Mar. Pet. Geol. 72, 45–61.
Kreissl, S., Gerdes, A., Walter, B.F., Neumann, U., Wenzel, T., Markl, G., 2018. Reconstruction of a > 200 Ma multi-stage "five element" Bi-Co-Ni-Fe-As-S system in the Penninic Alps, Switzerland. Ore Geol. Rev. 95, 746–788.
Leach, D.L., Marsh, E., Emsbo, P., Rombach, C.S., Kelley, K.D., Anthony, M., 2004. Nature of hydrothermal fluids at the shale-hosted red dog Zn-Pb-Ag deposits, Brooks Range, Alaska. Econ. Geol. 99 (7), 1449–1480.
Liu, W.H., Zhang, J., Wang, J., 2017. Sulfur isotope analysis of carbonate-hosted Zn–Pb deposits in northwestern Guizhou Province, Southwest China: implications for the source of reduced sulfur. J. Geochem. Explor. 181, 31–44.
Loges, A., Wagner, T., Kirnbauer, T., Göb, S., Bau, M., Berner, Z., Markl, G., 2012. Source and origin of active and fossil thermal spring systems, northern Upper Rhine Graben, Germany. Appl. Geochem. 27, 1153–1169.
Markl, G., Burisch, M., Neumann, U., 2016. Natural fracking and the genesis of five-element veins. Mineral. Deposita 51 (6), 703–712.
Martz, P., Mercadier, J., Cathelineau, M., Boiron, M.C., Quirt, D., Doney, A., Gebeaud, O., De Vally, E., Ledru, P., 2018. Formation of U-rich mineralizing fluids through basinal brine migration within basement-hosted shear zones: a large-scale study of the fluid chemistry around the unconformity-related Cigar Lake U deposit (Saskatchewan, Canada). Chem. Geol. https://doi.org/10.1016/j.chemgeo.2018a.05.042.
Mavrogenes, J.A., Bodnar, R.J., Graney, J.R., McQueen, K.G., Burlinson, K., 1995. Comparison of decrepitation, microthermometric and compositional characteristics of fluid inclusions in barren and auriferous mesothermal quartz veins of the Cowra Creek gold district, New South Wales, Australia. J. Geochem. Explor. 54 (3), 167–175.
McCaffrey, M., Lazar, B., Holland, H., 1987. The evaporation path of seawater and the coprecipitation of Br^- and K^+ with halite. J. Sediment. 57, 928–937.
McCaig, A.M., Tritlla, J., Banks, D.A., 2000. Fluid mixing and recycling during Pyrenean thrusting: evidence from fluid inclusion halogen ratios. Geochim. Cosmochim. Acta 64, 3395–3412.
Mertz, D.F., Lippolt, H.J., Huck, K.H., 1986. K/Ar, Ar-40/Ar-39, and Rb/Sr investigations on the genesis of the Clara vein deposit, Central Black Forest. In: Jahrestagung Dtsch Geophysikalischen Ges. 46. pp. 235.
Metz, R., Richter, M., Schürenberg, H., 1957. Die Blei-Zink-Erzgänge des Schwarzwaldes. Beih Geol Jahrb. 29. pp. 277.
Meyer, M., Brockhamp, O., Clauer, N., Renk, A., Zuther, M., 2000. Further evidence for a Jurassic mineralizing event in central Europe: K-Ar dating of hydrothermal alteration and fluid inclusion systematics in wall rocks of the Käfersteige fluorite vein deposit in the northern Black Forest, Germany. Mineral. Dep. 35, 754–761.
Naden, J., Shepherd, T.J., 1989. Role of methane and carbon dioxide in gold deposition. Nature 342 (6251), 793–795.
Neuser, R., Bruhn, F., Götze, J., Habermann, D., Richter, D.K., 1995. Kathodolumenescenz: Methodik und Anwendung. [Cathodoluminescence: Method and Application.] - Zbl. Geol. Patäont. Teil I, 1995(1/2). pp. 287–306 (Stuttgart).
Nitsch, E., Zedler, H., 2009. Oberkarbon und Perm in Baden-Württemberg. In: LGRB-Information. 22. pp. 7–102.
Pfaff, K., Romer, R.L., Markl, G., 2009. U-Pb ages of ferberite, chalcedony, agate, 'U-mica' and pitchblende: constraints on the mineralization history of the Schwarzwald ore district. Eur. J. Mineral. 21, 817–836.
Pfaff, K., Hildebrandt, L.H., Leach, D.L., Jacob, D.E., Markl, G., 2010. Formation of the Wiesloch Mississippi Valley-type Zn-Pb-Ag deposit in the extensional setting of the Upper Rhinegraben, SW Germany. Mineral. Deposita 45 (7), 647–666.
Pfaff, K., Koenig, A., Wenzel, T., Ridley, I., Hildebrandt, L.H., Leach, D.L., Markl, G., 2011. Trace and minor element variations and sulfur isotopes in crystalline and colloform ZnS: Incorporation mechanisms and implications for their genesis. Chem. Geol. 286, 118–134.
Richard, A., Cathelineau, M., Boiron, M.C., Mercadier, J., Banks, D.A., Cuney, M., 2016. Metal-rich fluid inclusions provide new insights into unconformity-related U deposits (Athabasca Basin and Basement, Canada). Mineral. Deposita 51 (2), 249–270.
Rupf, I., Nitsch, E., 2008. Das geologische Landesmodell von Baden-Württemberg: Datengrundlagen, technische Umsetzung und erste geologische Ergebnisse. Landesamt für Geologie, Rohstoffe und Bergbau Baden-Württemberg.
Seo, J.H., Guillong, M., Aerts, M., Zajacz, Z., Heinrich, C.A., 2011. Microanalysis of S, Cl, and Br in fluid inclusions by LA–ICP-MS. Chem. Geol. 284, 35–44.
Shepherd, T.J., Rankin, A.H., Alderton, D.H., 1985. A Practical Guide to Fluid Inclusion Studies. Blackie Glasgow (239 pp).
Sherlock, R.L., Jowett, E.C., Smith, B.D., Irish, D.E., 1993. Distinguishing barren and auriferous veins in the Sigma Mine, Val-d'Or, Quebec. Can. J. Earth Sci. 30 (3), 413–419.
Shouakar-Stash, O., Alexeev, S.V., Frape, S.K., Alexeeva, L.P., Drimmie, R.J., 2007. Geochemistry and stable isotopic signatures, including chlorine and bromine isotopes, of the deep groundwaters of the Siberian Platform, Russia. Appl. Geochem. 22 (3), 589–605.
Sprengel, H., 2014. Structural Aspects of Vein-Forming Processes: A Case Study From the Hydrothermal Schindlergang in the Teufelsgrund Mine (Bachelor thesis). Eberhard Karls University Tübingen.
Staude, S., Wagner, T., Markl, G., 2007. Mineralogy, mineral compositions and fluid evolution at the Wenzel hydrothermal deposit, Southern Germany: implications for the formation of Kongsberg-type silver deposits. Can. Mineral. 45 (5), 1147–1176.
Staude, S., Bons, P.D., Markl, G., 2009. Hydrothermal vein formation by extension-driven dewatering of the middle crust: an example from SW Germany. Earth Planet. Sci. Lett. 286, 387–395.
Staude, S., Dorn, A., Pfaff, K., Markl, G., 2010a. Assemblages of Ag–Bi sulfosalts and conditions of their formation: the type locality of schapbachite ($Ag_{0.4}Pb_{0.2}Bi_{0.4}S$) and neighboring mines in the Schwarzwald ore district, Southern Germany. Can. Mineral. 48, 441–466.
Staude, S., Mordhorst, T., Neumann, R., Prebeck, W., Markl, G., 2010b. Compositional variation of the tennantite–tetrahedrite solidsolution series in the Schwarzwald ore district (SW Germany): the role of mineralization processes and fluid source. Mineral. Mag. 74, 309–339.
Staude, S., Göb, S., Pfaff, K., Ströbele, F., Premo, W.R., Markl, G., 2011. Deciphering fluid sources of hydrothermal systems: a combined Sr-and S-isotope study on barite (Schwarzwald, SW Germany). Chem. Geol. 286, 1–20.
Staude, S., Mordhorst, T., Nau, S., Pfaff, K., Brügmann, G., Jacob, D.E., Markl, G., 2012a. Hydrothermal carbonates of the Schwarzwald ore district, southwestern Germany: Carbon source and conditions of formation using $\delta^{18}O$, $\delta^{13}C$, $^{87}Sr/^{86}Sr$, and fluid inclusions. Can. Mineral. 50, 1401–1434.
Staude, S., Werner, W., Mordhorst, T., Wemmer, K., Jacob, D.E., Markl, G., 2012b. Multi-stage Ag–Bi–Co–Ni–U and Cu–Bi vein mineralization at Wittichen, Schwarzwald, SW Germany: geological setting, ore mineralogy, and fluid evolution. Mineral. Deposita 47 (3), 251–276.
Steele-MacInnis, M., Bodnar, R.J., Naden, J., 2011. Numerical model to determine the composition of H_2O-NaCl-$CaCl_2$ fluid inclusions based on microthermometric and microanalytical data. Geochim. Cosmochim. Acta 75, 21–40.
Steele-MacInnis, M., Esposito, R., Moore, L.R., Hartley, M.E., 2017. Heterogeneously entrapped, vapor-rich melt inclusions record pre-eruptive magmatic volatile contents. Contrib. Mineral. Petrol. 172 (4), 18.
Stober, I., Bucher, K., 1999. Deep groundwater in the crystalline basement of the Black Forest region. Appl. Geochem. 14, 237–254.
Sun, X., Zheng, Y., Pirajno, F., McCuaig, T.C., Yu, M., Xia, S., Chang, H., 2017. Geology, S–Pb isotopes, and $^{40}Ar/^{39}Ar$ geochronology of the Zhaxikang Sb–Pb–Zn–Ag deposit in Southern Tibet: implications for multiple mineralization events at Zhaxikang. Mineral. Deposita 1–24.
Todt, W., 1976. Zirkon U/Pb-Alter des Malsburg-Granits vom Südschwarzwald. Neues Jahrb. Mineral. Monatshefte 12, 532–544.
Tornos, F., Casquet, C., Locutura, J., Collado, R., 1991. Fluid inclusion and geochemical evidence for fluid mixing in the genesis of Ba-F (Pb-Zn) lodes of the Spanish Central System. Mineral. Mag. 55 (2), 225–234.
Van Alstine, R.E., 1976. Continental rifts and lineaments associated with major fluorspar districts. Econ. Geol. 71 (6), 977–987.
Walter, B.F., Immenhauser, A., Geske, A., Markl, G., 2015. Exploration of hydrothermal carbonate magnesium isotope signatures as tracers for continental fluid aquifers, Schwarzwald mining district, SW Germany. Chem. Geol. 400, 87–105.
Walter, B.F., Burisch, M., Markl, G., 2016. Long-term chemical evolution and modification of continental basement brines–a field study from the Schwarzwald, SW

Germany. Geofluids 16, 604–623.
Walter, B.F., Burisch, M., Marks, M.A.W., Markl, G., 2017a. Major element and trace metal systematics of fluid inclusions in hydrothermal veins: metal provenance and the reconstruction of eroded sedimentary units. Mineral. Deposita. https://doi.org/10.1007/s00126-017-0719-7.
Walter, B.F., Steele-MacInnis, M., Markl, G., 2017b. Sulfate brines in fluid inclusions of hydrothermal veins: Compositional determinations in the system H_2O-Na-Ca-Cl-SO_4. Geochim. Cosmochim. Acta 209, 184–203.
Walter, B.F., Burisch, M., Fusswinkel, T., Marks, M.A.W., Steele-MacInnis, M., Wälle, M., Apukhtina, O., Markl, G., 2018a. Multi-reservoir fluid mixing processes in rift-related hydrothermal veins, Schwarzwald, SW-Germany. J. Geochem. Explor. 186, 158–186.
Walter, B.F., Gerdes, A., Kleinhanns, I.C., Dunkl, I., von Eynatten, H., Kreissl, S., Markl, G., 2018b. The connection between hydrothermal fluids, mineralization, tectonics and magmatism in a continental rift setting: Fluorite Sm-Nd and hematite and carbonates U-Pb geochronology from the Rhinegraben in SW Germany. Geochim. Cosmochim. Acta 240, 11–42.
Walter, B.F., Parsapoor, A., Braunger, S., Marks, M.A.W., Wenzel, T., Martin, M., Markl, G., 2018c. Pyrochlore as a monitor for magmatic and hydrothermal processes in carbonatites from the Kaiserstuhl volcanic complex (SW Germany). Chem. Geol. 498, 1–16.
Walther, H.W., 1982. Zur Bildung von Erz-und Minerallagerstätten in der Trias von Mitteleuropa. Geol. Rundsch. 71, 835–855.
Werner, W., 2011. Mineralische Rohstoffe. In: Hann, P., Zedler, H. (Eds.), Erläuterungen zum Blatt 8113 Todtnau, pp. 98–115 (3 Abb.; Freiburg i. Br. (LGRB, Hrsg.)).
Werner, W., Franzke, H.J., Wirsing, G., Jochum, J., Lüders, V., Wittenbrink, C., 2002. Die Erzlagerstätte Schauinsland bei Freiburg im Breisgau. Bergbau, Geologie, Hydrogeologie, Mineralogie, Geochemie, Tektonik und Lagerstättenentstehung. Berichte der Naturforschenden Gesellschaft Freiburg, Freiburg i. Br., 92:110.
Wernicke, R.S., Lippolt, H.J., 1993. Botryoidal hematite from the Schwarzwald (Germany): heterogeneous uranium distributions and their bearing on the helium dating method. Earth Planet. Sci. Lett. 114 (2–3), 287–300.
Wernicke, R.S., Lippolt, H.J., 1997. (U + Th)–He evidence of Jurassic continuous hydrothermal activity in the Schwarzwald basement, Germany. Chem. Geol. 138 (3), 273–285.
Wilde, A.R., Layer, P., Mernagh, T., Foster, J., 2001. The giant Muruntau gold deposit: geologic, geochronologic, and fluid inclusion constraints on ore genesis. Econ. Geol. 96 (3), 633–644.
Wilkinson, J.J., 2010. A review of fluid inclusion constraints on mineralization in the Irish ore field and implications for the genesis of sediment-hosted Zn-Pb deposits. Econ. Geol. 105 (2), 417–442.
Wilkinson, J.J., Weiss, D.J., Mason, T.F.D., Coles, B.J., 2005. Zinc isotope variation in hydrothermal systems: preliminary evidence from the Irish Midlands ore field. Econ. Geol. 100 (3), 583–590.
Yardley, B.W.D., 2005. Metal concentrations in crustal fluids and their relationship to ore formation. Econ. Geol. 100, 613–632.

Appendix III

Accepted publication

Study 3

Scharrer, M., Reich, R., Fusswinkel, T., Walter, B. F., & Markl, G. (2021). Basement aquifer evolution and the formation of unconformity-related hydrothermal vein deposits: LA-ICP-MS analyses of single fluid inclusions in fluorite from SW Germany. Chemical Geology, 575, 120260.

Chemical Geology 575 (2021) 120260

Contents lists available at ScienceDirect

Chemical Geology

journal homepage: www.elsevier.com/locate/chemgeo

Basement aquifer evolution and the formation of unconformity-related hydrothermal vein deposits: LA-ICP-MS analyses of single fluid inclusions in fluorite from SW Germany

Manuel Scharrer [a,*], Rebekka Reich [a], Tobias Fusswinkel [b], Benjamin F. Walter [c], Gregor Markl [a]

[a] Eberhard Karls University, Schnarrenbergstrasse 94+96, 72074 Tübingen, Germany
[b] RWTH Aachen University, Wüllnerstr. 2, 52062 Aachen, Germany
[c] Karlsruhe Institute of Technology, Adenauerring 20b, 76131 Karlsruhe, Germany

ARTICLE INFO

Editor: Michael E. Boettcher

Keywords:
Fluid mixing
Hydrothermal
Basement fluid reservoir
Fluid reservoir evolution
Fluid inclusion LA-ICP-MS

ABSTRACT

The main ore stage of three similar unconformity-related vein systems in the Schwarzwald, SW Germany spanning a period of activity of ~150 Ma, was investigated to understand the details of fluid penetration from overlying sediments/marine environment into the basement, their evolution as well as the processes involved in vein formation. To investigate temporal and spatial variations of the hydrothermal fluids responsible for mineralization, over 1650 fluid inclusions were analyzed by microthermometry. Of these, a total of 108 fluid inclusions (mainly in fluorite) were successfully analyzed by LA-ICP-MS. The fluid inclusions reveal a binary mixing trend between a $CaCl_2$- and a NaCl-rich endmember. Independent of major element composition, the fluids are metal-bearing (e.g., up to ~100 mg/kg Ba, Pb, Zn, Ni and up to 10 mg/kg Ag), show high As (up to 1000 mg/kg) and low S (below the detection limit in most analyses). Over time, the mixed fluid shows a gradual decrease in $CaCl_2$ and increase in NaCl with slightly decreasing total salinity.

Based on earlier studies and geochemical arguments, the veins formed by anisothermal binary fluid mixing of two fluids, which both were originally derived from seawater and chemically modified through interaction with the basement and sedimentary rocks in different ways. This produced a gradual stratified basement fluid reservoir comprising a modified bittern/halite dissolution brine. The fluids involved in the vein formation are sourced from different depths of this modified bittern/halite dissolution basement brine reservoir: fluid A, a $CaCl_2$-dominated, KCl-poor, deeper seated brine with a salinity of ~25 wt% $CaCl_2$ + NaCl, and fluid B, an NaCl-dominated and KCl-richer brine situated at shallower depths in the crystalline basement with salinities of ~22 wt % NaCl+$CaCl_2$. Based on the Na-Ca-K and Na—K thermometers and on Rb/Cs systematics, fluid A records alteration of the Na-, K- and Ca-bearing feldspars of the host rocks; progressive alteration led to consumption of mainly Ca-rich plagioclase in contact with these basement brines. Accordingly, fluid B that subsequently entered the basement was only in equilibrium with alkali feldspars and clay minerals. This scenario produced a gradual change of fluid composition with depth that was pushed to greater depth over time.

The source temperatures are estimated to ~250 °C while vein formation occurred at 100–170 °C, based on fluid inclusion homogenization temperatures. Thus, significant fluid cooling without abundant fluid mixing (and without major mineralization) must have occurred during fluid ascent (3–7 km, depending on the assumed geothermal gradient). Fluid mixing then resulted in the formation of the major gangue minerals fluorite, quartz, barite and calcite, while the locally confined sulfides must have formed due to an influx of sulfide into the binary mixed fluid. The process of fluid mixing is a rapid and turbulent process. This is recorded by a great diversity of fluid compositions (including ones close to the mixing endmembers) trapped within the same crystal. Compositional variations are even visible within individual fluid inclusion trails.

* Corresponding author.
E-mail address: manuel.scharrer@uni-tuebingen.de (M. Scharrer).

https://doi.org/10.1016/j.chemgeo.2021.120260
Received 20 October 2020; Received in revised form 12 March 2021; Accepted 17 April 2021
Available online 24 April 2021

1. Introduction

The development of unconformity-related hydrothermal systems on a regional scale and their modification in the context of changing geological environments has been and still is the subject of a vast number of publications (e.g., Boiron et al., 2010; Fusswinkel et al., 2013; Gleeson et al., 2001; Grandia et al., 2003; Muchez et al., 2005; Piqué et al., 2008; Walter et al., 2016). However, most previous research was focused on fluid sources or on the fluid evolution between individual stages, which record drastic changes in physiochemical conditions, fluid sources or tectonic setting. The related hydrothermal fluid root zones, feeding systems and their evolution within one stage are not well understood and only seldom directly or indirectly investigated (e.g., Burisch et al., 2016; Everett et al., 1999; Richardson et al., 1987). In this study, the temporal evolution of unconformity-related vein-type fluids within one long-lasting hydrothermal stage and the related gradual evolution of the fluid source reservoirs with respect to both space and time is addressed.

Unconformity-related vein-type deposits typically form in basinal-related settings, where seawater and/or formation fluids may gradually penetrate the basement to great depth and periodically become remobilized during periods of increased tectonic activity (e.g., Bons et al., 2014; Piqué et al., 2008; Walter et al., 2018a; Walter et al., 2018b). Mixing of such fluids typically with sedimentary formation waters during periods of fluid mobilization is commonly believed to be one major process of mineral precipitation in unconformity-related hydrothermal vein type deposits (e.g., Behr and Gerler, 1987; Fusswinkel et al., 2013; Grandia et al., 2003; Wilkinson et al., 2005). The type of mineralization formed is dependent on the fluid compositions and parameters such as (but not limited to) temperature, pressure and redox conditions. However, their compositional characteristics are not only defined by their seawater/formation fluid origin, but also by hydrogeochemical processes such as water-rock interactions at shallow and greater depths that modify their composition. These include, among others, seawater evaporation, salt dissolution, albitization, clay mineral formation (from micas and feldspars) and dolomitization (e.g., Bozau et al., 2015; Davisson and Criss, 1996; Houston et al., 2011; Land and Prezbindowski, 1981; Lowenstein and Timofeeff, 2008; Walter et al., 1990).

Typically, investigations of hydrothermal vein systems do not distinguish between temporal and spatial variations within a vein system. However, hydrothermal veins, especially those formed by fluid mixing, are typically heterogeneous, even within individual stages. This heterogeneity may be recorded by their mineralogy, major, minor or isotope geochemistry or fluid inclusion composition (e.g., Frenzel et al., 2020; Fusswinkel et al., 2013; Schwinn et al., 2006; Staude et al., 2012; Walter et al., 2018a; Walter et al., 2019). Primary fluid inclusions represent the “freezing point” of conditions during formation in time and space and are thus ideal to investigate both temporal and spatial variations within the vein and the source reservoirs. To identify fluid sources and their fluid evolution, chemical tracers such as Cl, Br, K, Mg, Na, Ca, Rb, Cs, Sr are typically used (Burisch et al., 2016; Gleeson et al., 2001).

In this study, the temporal evolution of a highly saline brine penetrating a basement of mostly granitic composition (which includes feldspar- and biotite-bearing gneisses) as well as the process of fluid mixing from aquifers of different basement depth is investigated. Three representative vein systems in the Schwarzwald, SW Germany, have been selected for this purpose. The main hydrothermal stage in these veins lasted a total timespan of ~150 Ma and formed during and subsequent to a marine basinal setting. Through comprehensive fluid inclusion analysis by microthermometry, LA-ICP-MS and Raman spectroscopy, the fluid endmembers involved in the vein formation and their evolution through time are constrained. This is supplemented by further geochemical data, empirical calculations and thermodynamic modeling in order to identify the underlying mechanism of this fluid evolution.

2. Regional geology

The regional geology of SW Germany consists of a Variscan crystalline basement (Fig. 1a) discordantly overlain by a post-Variscan terrestrial to marine sedimentary cover, including clastic, biogenic and evaporitic sequences. Tectonic uplift during the opening of the Upper Rhine Graben (URG) in the Paleogene overprinted the earlier geology by a normal fault-dominated regime. The uplift of the rift flanks with accompanying partial erosion of both the Paleozoic and Mesozoic sedimentary cover sequence and the basement rocks resulted in the present day topography (Geyer et al., 2011 and references therein).

Hydrothermal activity in the region since the Variscan orogeny (Pfaff et al., 2009; Walter et al., 2018b), produced a wide variety of mineralogical and compositionally distinct veins (e.g., Bliedtner and Martin, 1986; Markl, 2017). According to (Walter et al., 2016), the evolution of the vein systems can be summarized by five hydrothermal temporal maxima: (I) Carboniferous greisen mineralization, (II) Permian quartz veins that formed due to cooling of a high temperature and low salinity metamorphic fluid, (III) Triassic-Jurassic quartz-hematite veins that formed from fluids with highly variable salinity, (IV) Jurassic-Cretaceous fluorite-quartz-barite-carbonate veins that formed at ~50–200 °C and salinities of 20–30 wt% NaCl+$CaCl_2$ and (V) post-Eocene quartz-barite-fluorite or carbonate veins that formed from fluids of highly variable salinity related to the URG rifting (e.g. Baatartsogt et al., 2007; Behr et al., 1987; Epp et al., 2018; Pfaff et al., 2011; Pfaff et al., 2009; Schwinn et al., 2006; Staude et al., 2009; Staude et al., 2012; Walter et al., 2016; Walter et al., 2017).

The main precipitation mechanism for vein stages IV and V has been identified to be unconformity-related fluid mixing. For stage IV, a binary mixing model and for stage V, a multi-fluid mixing model has been proposed (Staude et al., 2012; Walter et al., 2018a; Walter et al., 2016; Walter et al., 2017). Most veins in the region are of poly-stage nature and record more than one vein-opening event indicated by banding and various mineral generations. They mostly are situated along pre-existing, commonly Variscan and/or rift- related structures (Fig. 1; Epp et al., 2018; Walter et al., 2016; Werner and Franzke, 2001). The main hydrothermal phase of the veins investigated in this study belongs to stage IV commonly labeled Jurassic-Cretaceous fluorite-quartz-barite-carbonate veins (indirect dating through salinity and temperature by e.g. Walter et al., 2016; direct dating by Walter et al., 2018b). Direct dating revealed that stage IV veins formed over a time period from mid/late Triassic to the early Tertiary (Walter et al., 2018b). The late stage carbonate assemblage in these veins has been dated to be of Oligocene-Miocene age (Burisch et al., 2017; Walter et al., 2018b) and thus belongs to the stage V post-Eocene quartz-barite-fluorite or carbonate vein group.

3. Characteristics of the mineralization

The investigated three vein systems are N-S and/or NE-SW striking, nearly vertically dipping and up to 1, 2 and 5 km in length for Wieden (Zeschke, 1959), Münstertal (Bliedtner, 1978; Schürenberg, 1950) and Urberg (Brill et al., 2018), respectively (Fig. 1). On average, the veins are composed of ~60 vol% fluorite which forms a multi-stage banded structure with quartz and barite (Fig. 2a & b); barite is generally more abundant during the later stages (Brill et al., 2018; Markl, 2017; Metz et al., 1957; Otto, 1964; Steen, 2013; Zeschke, 1959). All investigated localities represent an initial quartz- and breccia-rich ore stage (I) that is characterized by the presence of initial pyrrhotite subsequently replaced by pyrite and marcasite. The volumetrically most abundant stage is the second stage (II), which is characterized by abundant fluorite with variable amounts of quartz, barite and carbonate. There is a general tendency of increasing barite and decreasing fluorite content with time. Carbonate in larger quantities is only present at the Urberg locality

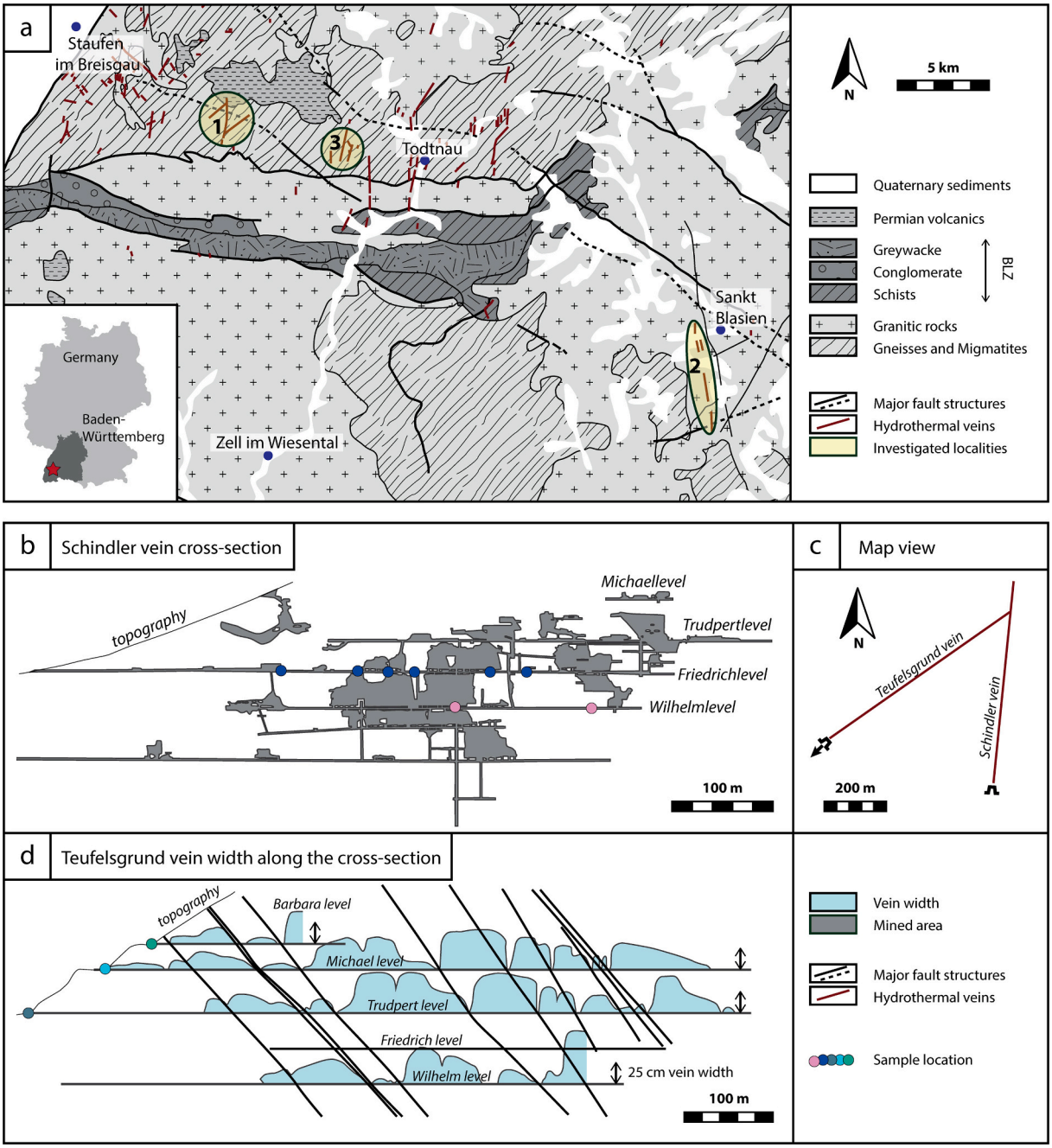

Fig. 1. Geological map and selected vein cross secions.
(a) Geological map and setting of the three investigated vein systems, 1. Teufelsgrund-Schindler-Herrenwald veins in the Münstertal, 2. Ruprecht vein system at the Urberg and 3. Tannenboden and Anton vein at Wieden. (b&c) Cross section and map view (kindly provided by the Landesamt für Geologie, Rohstoffe und Bergbau, Baden-Württemberg) of the partially still accessible mine in the Münstertal and locations of sample selection. (c) Vein width along the vein profile at different depth levels for the Teufelsgrund vein in the Münstertal (modified from Schürenberg, 1950).

(Fig. 2c), where it formed prior to and during the transition to the fluorite-dominated section of the vein. Galena, sphalerite and chalcopyrite (Fig. 2b & c) are the most abundant sulfide minerals within these veins, the last being the least common one (Metz et al., 1957; Steen, 2013). These sulfides are more abundant in brecciated zones (Fig. 2d) where a complete rimming of clasts by sulfides and quartz is common (Fig. 2e). A less abundantly developed partial repetition of this stage with small variations forms the third stage (III) of these veins. Further, minor hydrothermal stages comprise only little fluorite, but late-stage barite, quartz and/or carbonates form together with galena, sphalerite, euhedral pyrite and/or a colloform mixture of pyrite and marcasite.

A peculiarity of these three vein systems, both relative to most hydrothermal veins of the region with similar characteristics and internationally, is the presence of mineralogically rather unusual Ni-Sb-Ag-As ore shoots that texturally belong to the major ore stage (II). They can be classified as “five-element” or “native element-arsenide” associations (Markl et al., 2016; Scharrer et al., 2019). In the Urberg vein system, three distinct temporal ore shoot formation events could be identified. The early ore shoots are associated with purple fluorite and calcite whereas the later are richer in sulfides and are associated with colorless fluorite and sometimes barite.

The width of the veins is highly variable between 1 and 3.5 m and can locally be reduced to only a few centimeters. It is strongly dependent

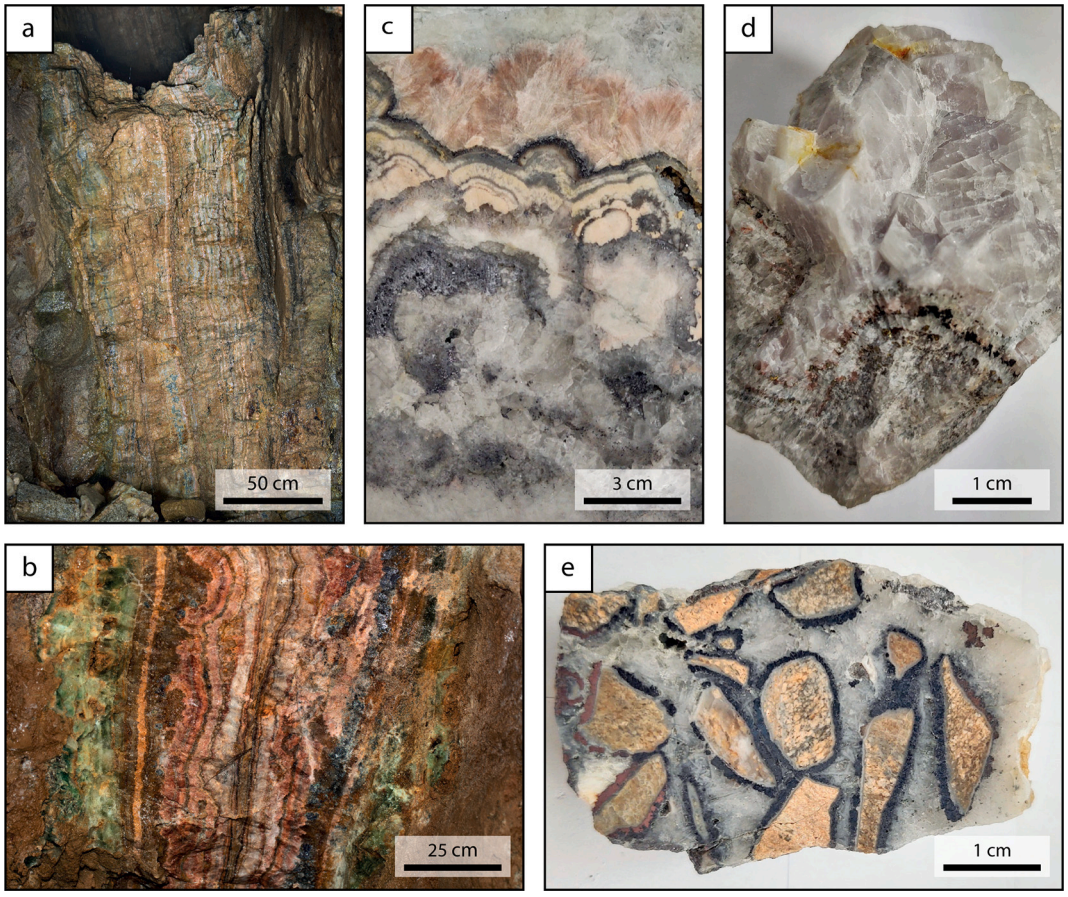

Fig. 2. Hand specimen.
(a) Image of a typically banded fluorite dominated vein and (b) of a banded vein with the transition to the late stage barite dominated vein filling of the main hydrothermal stage. Images (a) and (b) have been kindly provided by Matthias Zizelmann and were taken at Brenden and Hotzenwald respectively. These veins are of the same type as the Urberg Ruprecht vein system but accessible. (c) Hand specimen of a typical single vein band and (d) of the early main stage fluorite-calcite intergrowth only found at the Urberg vein system. (e) Wall rock breccia with host rock bleaching, accumulation of sulfides and indicators for hydraulic brecciation.

on the rheology of the host rock (wider in gneiss than in granite) leading to a vein shape of aligned, elongated lenses (this study; Brill et al., 2018; Metz et al., 1957; Otto, 1964; Otto, 1967). At Wieden and Münstertal, gneisses, which can host significant local enrichments of graphite and/or sulfides, are the most abundant host rocks, but local occurrences of granitic rocks are also common (Bliedtner, 1978; Brill et al., 2018; Geyer et al., 2011; Metz et al., 1957). The geology around Urberg is more complex and is characterized by additional lithologies such as diorites, amphibolites and norites with magmatic Ni-Fe-sulfide lenses (Brill et al., 2018; Otto, 1964). The gneisses are anatectic and hydrothermal bleaching of the host rocks replaced plagioclase by sericite and rarely by calcite (Bliedtner, 1978; Metz et al., 1957; Walter et al., 2019).

4. Sample selection

This study is based on the largest collection of samples available to date which comprises more than thousand hand specimens (many of them with precise information on their underground position) from the private collection of the last author and from the collection of the University of Tübingen. These were carefully compared and inspected; representative samples of ore stage II were selected for further investigations. Furthermore, additional 31 hand specimens were collected from the Teufelsgrund mine in the Münstertal during this study to investigate spatial relations within an individual vein system. The abandoned Teufelsgrund mine (now a mining museum) provides an ideal sampling location as the two veins Teufelsgrund and Schindler of the Teufelsgrund-Schindler-Herrenwald vein system in the Münstertal are both accessible over a depth and length of several hundred meters (Fig. 1b & c). The samples were taken along the whole accessible section of the mine with respect to both length and depth and were taken to best represent the early massive fluorite of the main ore stage (II). In total, 66, 14 and 17 thick sections for fluid inclusion work were prepared for Münstertal, Urberg and Wieden, respectively. To investigate the temporal evolution within a vein, the Urberg vein system was selected and samples with early stage calcite and/or the early stage ore shoots were characterized as early. Furthermore, the dating of the veins by (Walter et al., 2018b) were also considered for the temporal evolution of ore stage II between the three vein systems.

5. Methods

5.1. Fluid inclusion analyses

5.1.1. Microthermometry

Approximately 400 μm thick, double-polished sections of both ore shoot and vein samples were prepared. Individual fluid inclusion assemblages were characterized as primary, clusters and secondary according to the classification of (Goldstein and Reynolds, 1994; Walter et al., 2015) (Fig. 3). The category “clusters” comprises fluid inclusion assemblages interpreted to represent a primary syngenetic growth signature. Contrary to the classical primary fluid inclusion trails, these are not restricted to individual growth zones but form 3D clusters of fluid inclusions. The shape of a particular cluster commonly reflects the growth shape of the crystal (Fig. 3d). Clusters typically occur as fluid

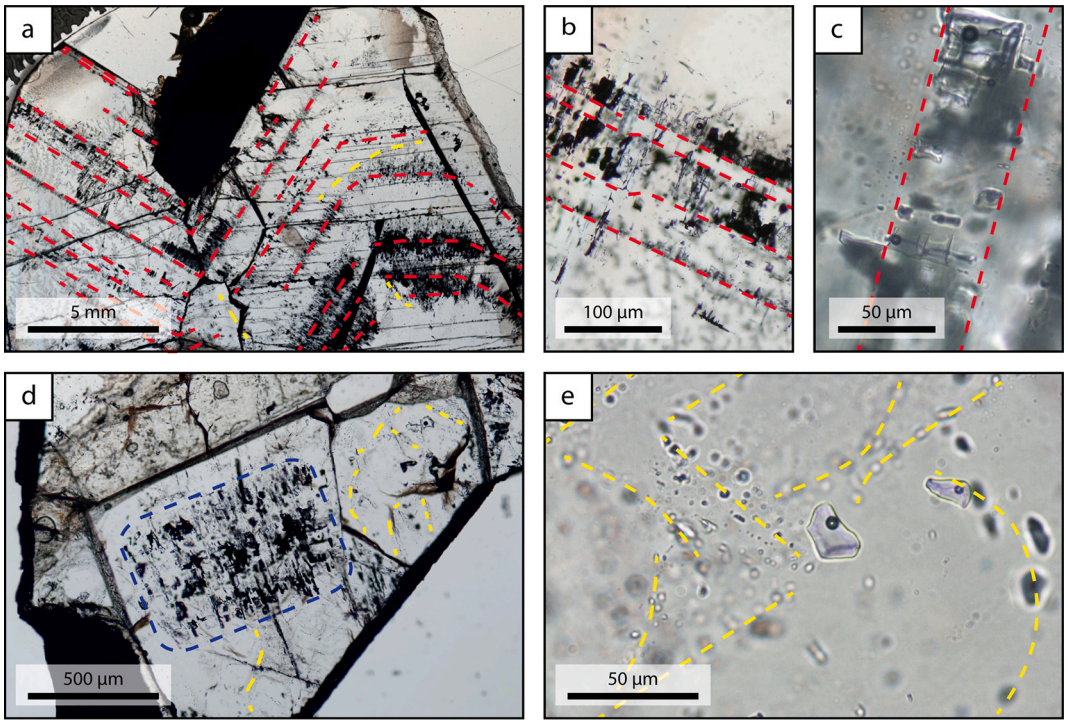

Fig. 3. Fluid inclusion petrography.
Presentation of typical fluid inclusion assemblages in flourite. (a), (b) and (c) demonstrate the typically perpendicular to the growth plane elongated and angular primary inclusion trails, indicated by red dashed lines. (d) fluid inclusions in blue dashed area represent a fluid inclusion cluster that is interpreted to represent original *syn*-crystal formation fluid inclusion signature. Yellow dashed lines are secondary trails. These commonly have the same fluid inclusion shape type as primary fluid inclusions. (e) shows the characteristically rounded secondary fluid inclusion trails. (For interpretation of the references to colour in this figure legend, the reader is referred to the web version of this article.)

inclusion-rich host mineral cores and therefore depict an early stage in crystal growth. To be on the safe side and due to interpretational difficulties arising from pseudo-secondary fluid inclusions, such fluid inclusions are considered secondary in the current contribution. In total, >1400 individual fluid inclusions were analyzed. The analyses were carried out using a Linkam THMS 600 fluid inclusion stage on a Leica DMLP microscope calibrated with synthetic H_2O, H_2O-NaCl and H_2O-CO_2 standards (FlincSys Standard collection) at the University of Tübingen. The $V_{liquid}/(V_{liquid} + V_{vapor})$ ratio was visually estimated and verification was done by rough volume calculations on 20 inclusion.

All fluid inclusions were carefully checked for post-entrapment modifications and potentially metastable lack of discrete phases. All data were processed by using the excel-based calculation sheet of Steele-MacInnis et al. (2012). Due to the fine-grained nature of most quartz samples and/or the general lack of larger fluid inclusions within quartz, only very few quartz-hosted fluid inclusions could be analyzed. Thus, the dominant primary host mineral is fluorite, with some fluid inclusions being hosted in calcite. A high percentage of the fluid inclusions (> 80%) show metastable characteristics concerning the formation of a gas bubble during melting or the formation of hydrohalite during freezing. The latter is significantly less common. Thus, these metastable phases were grown by repetitive re-cooling and re-heating for up to several hours at temperatures between the ternary eutectic and the transition into the three-phase stability field. This being a very time-intensive procedure, individual fluid inclusions could not be reanalyzed for quality control. However, if possible, a large number of fluid inclusions from each assemblage (up to ~30) was analyzed and outliers were disregarded. Furthermore, as a quality test, in three fluid inclusion assemblages showing metastable characteristics, each fluid inclusion was analyzed three times. The variation between the three analyses is on average < 0.03 °C. Fluid inclusions in carbonate could not be completely analyzed by microthermometry as the metastable behavior prevented hydrohalite formation. However, to be able to use this handful of fluid inclusions for LA-ICP-MS, the ice melting temperature was determined and in combination with the total salinity taken from similar fluid inclusions in associated fluorite, the NaCl and $CaCl_2$ content was estimated.

5.1.2. LA-ICP-MS

5.1.2.1. Analytical procedure. Fluid inclusion LA-ICP-MS analyses were performed at RWTH Aachen University using a Coherent GeoLasHD 193 nm laser ablation system coupled to an Agilent 7900 ICP-MS with high sensitivity s-lens ion lens configuration and Pt cone sets. Fluid inclusion wafers were placed inside a small-volume (1 cm^3) fast-washout ablation cell designed at RWTH Aachen University on the basis of a model originally designed at ETH Zurich (See Table 1.). The ICP-MS system was tuned daily to maximize signal-to-background ratios while maintaining optimal ablation, transport and ionization conditions (U/Th = 1.00 ± 0.02) and low oxide (ThO/Th < 0.2%) and doubly charged (Ca^{++}/Ca^{+} < 0.1%) production rates. Interferences to be considered in our highly saline samples are ^{40}Ca—^{35}Cl and ^{40}Ar—^{35}Cl that overlap with ^{75}As. However, these interferences can be excluded to be significance on the basis that there is no correlation between ^{75}As signal and ^{35}Cl signal intensity when considering all analyzed samples, there is no correlation between As and $CaCl_2$/NaCl ratio of the fluid inclusion and many fluid inclusions show no measurable As content (detection limit of As is as low as 0.2 mg/kg). This shows that the formation fractions of Ca-Cl/Cl and Ar-Cl/Cl are several orders of magnitude smaller than the ThO/Th ratio. This is linked to the lower dissociation energy of Ca—Cl and Ar—Cl relative to ThO (Luo, 2007).

Instrumental accuracy and precision were monitored by using NIST 612 as a secondary quality control standard. Refer to table XY for all further instrumental settings. Fluid inclusions were ablated with laser

Table 1
Summary of instrumental parameters used in fluid inclusion LA-ICP-MS analysis.

Laser system	Coherent GeoLasHD 193 nm
Energy density used for fluorite ablation	5 to 15 J/cm^2
Repetition rate	10 Hz
Carrier gas flow rate (Helium 5.6)	1.1 l/min
ICP-MS	Agilent 7900 s
Plasma gas flow rate (Argon 5.0)	15 l/min
Auxiliary gas flow (Argon 5.0)	0.75 l/min
RF Power	1600 W
Isotopes	^{23}Na, ^{29}Si, ^{34}S, ^{35}Cl, ^{39}K, ^{43}Ca, ^{57}Fe, ^{59}Co, ^{62}Ni, ^{65}Cu, ^{66}Zn, ^{75}As, ^{81}Br, ^{85}Rb, ^{88}Sr, ^{107}Ag, ^{121}Sb, ^{127}I, ^{133}Cs, ^{137}Ba, ^{208}Pb, ^{209}Bi, ^{238}U
Dwell times	10 ms: ^{23}Na, ^{29}Si, ^{35}Cl, ^{39}K, ^{43}Ca, ^{65}Cu, ^{66}Zn, ^{85}Rb, ^{88}Sr, ^{107}Ag, ^{121}Sb, ^{133}Cs, ^{137}Ba, ^{208}Pb, ^{209}Bi, ^{238}U 20 ms: ^{34}S, ^{57}Fe, ^{62}Ni, ^{75}As, ^{81}Br, ^{127}I
U/Th	1.00 ± 0.02
ThO/Th	<0.2%
Ca^{2+}/Ca^{+}	<0.1%

fluences of 10 J/cm^2 at 10 Hz repetition rate. In order to avoid depth-dependent fractionation effects (Guillong and Pettke, 2012), the depth-to-diameter ratios of all ablation spots were kept well below 2.

Data reduction, background correction, signal deconvolution and peak evaluation/quality control for each fluid inclusion, with regard to each analyzed element, was performed using the procedures of Pettke et al. (2012) and Fusswinkel et al. (2017) by using the Matlab-based SILLS software package (Guillong et al., 2008). The halogens (Cl and Br) were calibrated by the scapolite reference material Sca 17 (Fusswinkel et al., 2018; Seo et al., 2011) whereas all other elements were calibrated by the reference material NIST SRM 610 (Jochum et al., 2011). Sodium and Ca determined by microthermometry in the $CaCl_2$-NaCl-H_2O system (Steele-MacInnis et al., 2011) were used as internal standards, and Ca content of the host was used as the internal standard for matrix correction.

The statistical uncertainty range provided by SILLS varies between analysis and the percentage uncertainty is independent of absolute elemental content (within the analyzed range). On average, for Cl, K, Rb, Sr and Cs it is <5%, for Zn, Br, Ba, and Pb it is ~25% and for the rest it is ~50%. However, this does not represent the true uncertainty range of the analyzed fluid inclusion. This also includes for example, both methods induced and sample induced problematics. The nature of the short-termed signal of fluid inclusion analysis in combination with a periodical ICP-MS analysis of each element only naturally induces a statistical miss of the peak intensity and thus increases the uncertainty (Fusswinkel et al., 2017). Furthermore, the problematic nature of ablation of fluid inclusions in fluorite also induces a non-quantifiable increase in uncertainty. Heinrich et al. (2003) has shown the analytical precision to be at around 20%, which we assume to be the case for Cl, K, Rb, Sr and Cs. For the rest of the elements we assume an uncertainty of 50%, knowing that the true uncertainty is in fact larger, but not quantifiable.

5.1.2.2. Quality control. Data evaluation was achieved by using Na, Ca, K and Cl as a tracer to identify the fluid inclusion signal interval and by using these with the addition of As, Ba, and Rb as indicators of background quality and leakage. Analyses with signs of significant fluid inclusion leakage were disregarded. Furthermore, the temporal overlap of peak positions between elements during fluid inclusion ablation was used as a quality control and short termed non-systematic element signal peaks of more than 2 orders of magnitude above the directly surrounding matrix and diverging significantly from the fluid inclusion tracer peak position were regarded as spikes. Due to the difficult ablation behavior of fluorite in most samples and due to a clear correlation of analyzed fluorite fragments and signal spikes for most elements, the spike removal tool implemented in SILLS was applied. Some trace elements are strongly influenced by this effect, especially Co, Cu and Pb. There is no correlation between spike occurrence and fluid composition. In addition, Co shows a tendency to produce spikes of up to 4 log units higher than the background during analysis (producing up to several wt % calculated Co). These spikes occur at any point in time during the ablation, are generally more common during fluid inclusion ablation, but rarely match the fluid peak; they are independent of any other element peaks. Thus, these cobalt peaks are either an artifact, possibly due to interference, or indicate solid Co- (non-As- and non-S-bearing) mineral inclusions. Hence, although measured, Co was not quantified for any fluid inclusion. Furthermore, major deviations from similarly composed fluid inclusions with respect to both the major elements and charge balance were disregarded. For each analysis, individual elements were not quantified, when the element peak of the fluid inclusion lies on the shoulder of the initiation peak of fluorite ablation, and the shoulder area (count-time space) in question represents more than ~5% of the fluid inclusion peak area.

After disregarding all non-quantifiable analyses, the rest of the measurements were categorized with respect to the quality of opening of the fluid inclusions (due to the suboptimal ablation behavior of fluorite) into “bad” (very long leakage along fractures with several peaks), “ok” (some leakage with shoulder peaks), “good” (short leakage or minor shoulder peaks present) and “very good” (very short peak time and single peak). For major elements, all of these were considered, whereas for the trace elements, “bad” analyses were disregarded. A lack of a clear relationship between the elemental composition and the different qualities of fluid inclusion openings indicates that precipitation along fractures is insignificant.

5.1.3. Raman micro-spectroscopy

Raman spectra were collected using a 532 nm laser with a 1800 grooves·mm − 1 grating on a Renishaw InVia confocal Raman microspectrometer equipped an Peltier-cooled CCD detector. A laser power of 50% with a 50 × objective with a numerical aperture of 0.75 was selected for analysis. Spectra were collected by a tenfold accumulation from 100 to 4300 cm^{-1} over acquisition times of 50 s each. The laser power remained steady over the course of the measurements. Both corresponding host fluorite and fluid inclusions were analyzed. For qualitative distinction between the fluid and gaseous composition of the fluid inclusions both were analyzed. However, due to the gaseous bubble being mobile within the fluid inclusion during analysis, measurements on the gas bubble where not always successful.

5.2. Thermodynamic modeling

Thermodynamic calculations were preformed using X1t and depicted using P2Plot from the program Geochemist’s Workbench 14 (Bethke, 2007) using the Thermoddem database of 2017 (Blanc, 2017; Blanc et al., 2012). To model a scenario of an originally marine fluid penetrating the basement and evolving over time, the Urberg vein system was used as an example.

For the sake of thermodynamic modeling, the stratigraphy was simplified to only the basement and no overlying sedimentary cover. No distinction between gneiss and granites was made and the basement was assumed to be composed of 35 vol% quartz, 55 vol% feldspar (with 20 vol% Na-, 15 vol% Ca- and 20 vol% K-endmember) and 10 vol% other minerals. Due to convergence issues during thermodynamic modeling, the other 10 vol% minerals, which, among others, include biotite, muscovite, magnetite, graphite and sulfides, were disregarded during modeling. Furthermore, the stability of such clay minerals is strongly dependent on the miscibility between several endmembers and the program Geochemist Workbench is not designed for modeling of solid solutions. Thus, typical Fe- and Mg-bearing hydrous alteration phases, such as illite or other clay minerals, which can be locally abundant in the

basement and would form in the presence of Fe and/or Mg, could not be considered. If they would have been considered, this contribution would have become one almost exclusively dealing with thermodynamic modeling, and this was not intended.

In a basinal setting, a geothermal gradient is typical between 25 and 50 °C/km (e.g., Harper, 1971; Nwankwo and Ekine, 2009; Yuan et al., 2009). During the early onset of basin formation after the Variscan orogeny, the geothermal gradient was most likely relatively high. Thus, a geothermal gradient of 50 °C/km was assumed as the basis of this model. Selecting a temperature of 50 °C at the unconformity, this choice renders a depth of 5 km for a temperature of 300 °C (maximum of the applied database). These 5 km were subdivided into 2000 empirical segments. The time of marine transgression (Geyer et al., 2011) and, thus, the onset of fluid penetration into the basement largely overlaps with the dating of the Urberg vein system (Walter et al., 2018b). Since the basement fluid source aquifer temperature A was calculated to be around 250 °C (see discussion), relating to a depth of 4 km below the unconformity (50 °C/km assumed), the penetration of this fluid must have occurred within the first ~50 Ma (maybe even less). Thus, a fluid flow rate/basement penetration rate of 0.1 mm/yr was chosen, which is sufficient for the originally marine fluid to penetrate to this depth, but slow enough to produce a stratified basement brine reservoir and not to flush the whole basement with the marine brine. The marine brine must have been close to halite saturation and, thus, an NaCl content of 25 wt% and a neutral pH were assumed. Prior to this fluid penetration, the preexisting brine in the basement is likely of residual metamorphic and/or magmatic nature and, thus, it was selected to have a salinity of 5 wt% NaCl eq that is in equilibrium with the host rock at the given temperature. These choices are in accordance with what is known about Schwarzwald basement fluids from the work of Walter et al. (2016) and Walter et al. (2017) and/or in accordance with findings of the current contribution.

6. Results

6.1. Fluid Composition by microthermometry

The fluid inclusions consist of two phases (H2O-rich liquid + vapor), with high degrees of fill, Vliquid/(Vliquid + Vvapor) of 0.85 ± 0.05 at 25 °C. No solid phases entrapped in fluid inclusions were found. As a parameter for quality assurance and to reject possible necking or leakage, individual fluid inclusions that differ by more than 0.5 Vliquid/(Vliquid + Vvapor) from the rest of the assemblage are disregarded. No solid phases were observed at 25 °C. The fluid inclusion freezing temperature varies between −55 °C and − 90 °C and first melting occurs at approximately −50 °C which indicates a ternary eutectic in the NaCl-$CaCl_2$-H_2O system. When frozen, both hydrohalite and ice is observed in all fluid inclusions. Hydrohalite final melting temperatures range from −22 °C to −30 °C and ice melting ranges from −17 °C to −29 °C. During heating, hydrohalite exclusively melts before ice in all analyzed fluid inclusions. The final melting temperatures of hydrohalite and ice show a positive correlation.

The total salinity in wt% (NaCl+$CaCl_2$), calculated using the method by (Steele-MacInnis et al., 2011), varies slightly between the localities and is 21.4–24.2 (22.3 ± 0.5), 20.8–25.8 (23.2 ± 0.9) and 22.2–25.7 (24.5 ± 0.7) for the Münstertal, Urberg and Wieden vein systems, respectively (Fig. 4a). The microthermometric data show a continuous linear correlation between a $CaCl_2$-rich and an NaCl-dominated fluid for each of the three localities (Fig. 4b). The NaCl:$CaCl_2$ ratio of fluid inclusions within each fluid inclusion assemblage varied with an approximate ratio of 1:1. This depicts mixing of two fluid endmembers during the formation of each fluid inclusion assemblage. However, this gradient with respect to all fluid inclusion analyses for each locality is significantly steeper, approximately 1.2:1 to 1.4:1 (Fig. 4c). This shift in ratio considering all relative to individual fluid inclusion assemblages is linked to a temporal factor. For the Urberg locality, a clear trend from a

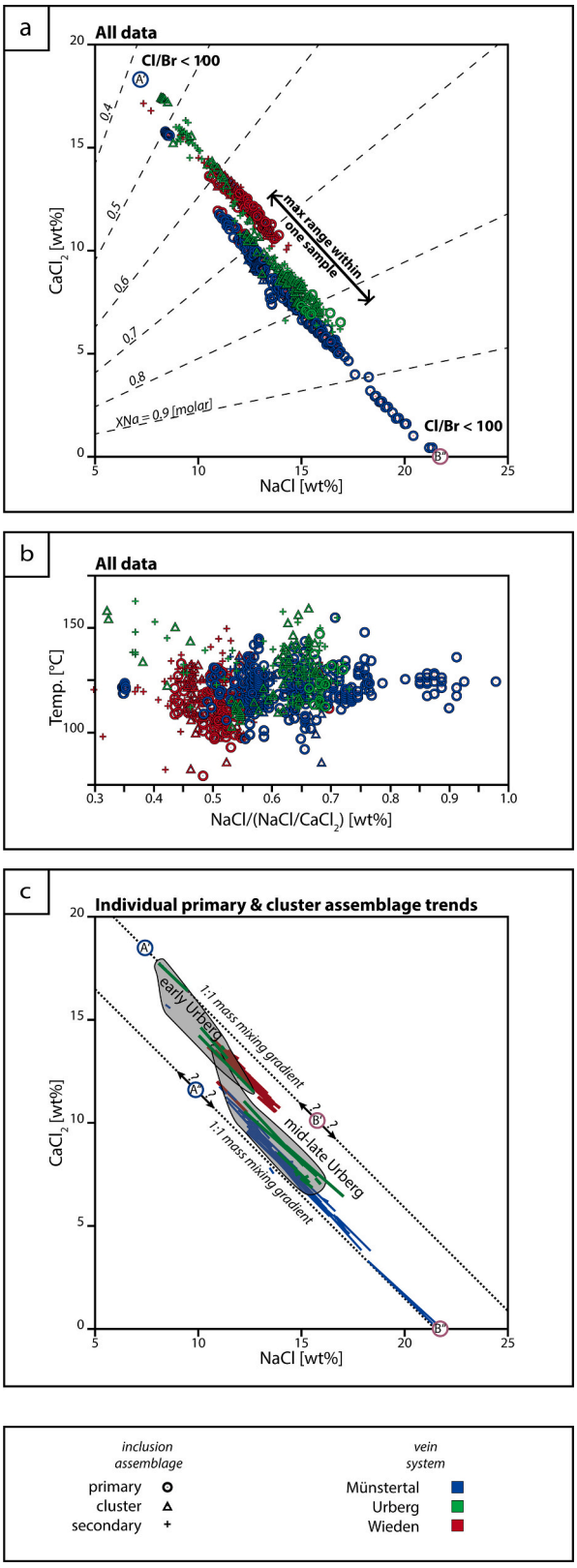

Fig. 4. Microthermometric results.
(a) Microthermometric data from all three investigated vein systems. (b) Within each individual fluid inclusion assemblage, both the melting temperature of hydrohalite and ice varied to some degree. This translates into a variation in both NaCl and $CaCl_2$ while the total salinity is fairly constant. Each colored line represents the line of best fit for a single fluid inclusion assemblage; secondary fluid inclusions are disregarded. Dashed lines represent the average (~1:1) gradient from each fluid inclusion assemblage.

$CaCl_2$-rich early ore stage II to an NaCl-rich mid to late ore stage II is visible when only considering fluid inclusions of the category primary and cluster.

The fluid inclusions exclusively homogenize into the liquid phase. Thus, the fluid at entrapment conditions was of liquid state. The homogenization temperature (in °C) varies between localities and is 90–150 (122 ± 8), 100–170 (131 ± 14) and 80–150 (117 ± 12) for the Münstertal, Urberg and Wieden vein systems, respectively (Fig. 4b). A general correlation between temperature and NaCl/(NaCl+$CaCl_2$) could not be established. No significant differences could be identified between fluid inclusions from the ore shoots and the more standard barren or galena-sphalerite-bearing fluorite veins.

Furthermore, no spatial trend was identified in the Münstertal vein system, where fluid inclusions were analyzed in samples taken over a vein length of ~500 m and a vein depth of ~200 m (Fig. 5). The complete dataset can be found in the electronic supplement (ESM1).

6.2. Fluid composition by LA-ICP-MS

There are slight variations in abundance for some elements between the three localities. However, these variations are relatively subtle, and in part related to the variable NaCl/(NaCl+$CaCl_2$) mass fraction of the fluids. This is presented in Fig. 6, which shows an increase in Rb, Cs, and K and a decrease in Sr and possibly in Br and Ba with increasing NaCl content of the fluid. The transition metals As, Sb and S show no correlation with the NaCl content of the fluid, which may, however, be related to the high degree of uncertainty for these measurements. Although we excluded possible co-analysis of fluid inclusion and accidentally trapped minerals, it is still possible that this remains a factor that produced the spread of the concentrations, especially for the trace elements.

Due to the large number of analyses without detectable element concentrations by LA-ICP-MS for the trace elements, it is also vital to consider the detection limits to fully understand the fluid composition. This has been done and is depicted in Fig. 7. Due to problems accompanying LA-ICP-MS analyses on fluid inclusions in fluorite, we assume the results to be order of magnitude estimations only, especially concerning the trace elements depicted in Fig. 7. The base metals Pb and Zn are in the range of 1–100 mg/kg, Zn commonly being slightly more abundant. Copper is generally less abundant (<<10 mg/kg). Iron is detected to be around 100 mg/kg, Ag in the range of <10 mg/kg. Nickel and As vary significantly between localities, with Ni <5 mg/kg, 1–100 mg/kg and < 10 mg/kg and As <100 mg/kg, <1000 mg/kg and < 50 mg/kg for Münstertal, Urberg and Wieden, respectively. The Sb content is generally quite low (<10 mg/kg) and only reaches slightly higher contents (50 mg/kg) for the Wieden vein system. When discarding outliers from previous LA-ICP-MS studies, which are compiled in (Walter et al., 2020), the compositions of this study are in good agreement with previous studies. The transition metal content of the investigated veins seems to be somewhat lower than in other vein types of the region (Fusswinkel et al., 2013), but also these findings are in agreement with previous data (Walter et al., 2019). The complete dataset can be found in the electronic supplement (ESM2).

6.3. Raman micro-spectroscopy

Most of the 13 fluid inclusions analyzed by RAMAN spectroscopy (for the spectra see Fig. 8 and the EMS3) reveal the presence of H_2(g) within the gaseous phase (Fig. 8). In the cases where H_2(g) was not detected, the H_2O peak size is larger than those in which H_2(g) was detected. This implies a movement of the gaseous phase away from the analyzed area. This can occur due to the mobility of the gas bubble, the fluid inclusion shape and the energy input from the laser.

Both a small N_2(g) and a CO_2(g) peak were present in two and three analyses of the fluid inclusions, respectively. In two fluid inclusions, a CH_4(g) peak is visible: one cogenetic with galena and native arsenic in the Schindler vein at the Münstertal (Fig. 8b), and one with massive galena from the Anton vein at Wieden (EMS3). The presence of sulfate or sulfide species could not be detected as their peak positions overlap with fluorite peaks and no relevant difference in peak height from fluorite to fluid inclusion analyses was visible. There is no systematic difference in Raman-detected species related to variable NaCl/(NaCl+$CaCl_2$) ratios.

O_2(g) in addition to H_2(g) was detectable in three of the 13 analyses (Fig. 8). The presence of O_2(g) together with H_2(g) may be an indicator for chemical disequilibrium (Dubessy et al., 1988). Previous studies have suggested that they can form by radiolysis in the presence of e.g. uranium species (e.g., Dubessy et al., 1988; Dubessy et al., 1989). It could however also be a mixed analysis with the surroundings of the fluid inclusions such as fractures in fluorite or other broken, atmosphere filled, fluid inclusions.

7. Discussion

The focus of this contribution is on the mid/late Triassic to early Paleogene fluorite-quartz-barite ore stage II. According to previous fluid inclusion studies (Walter et al., 2019 and references therein) as well as

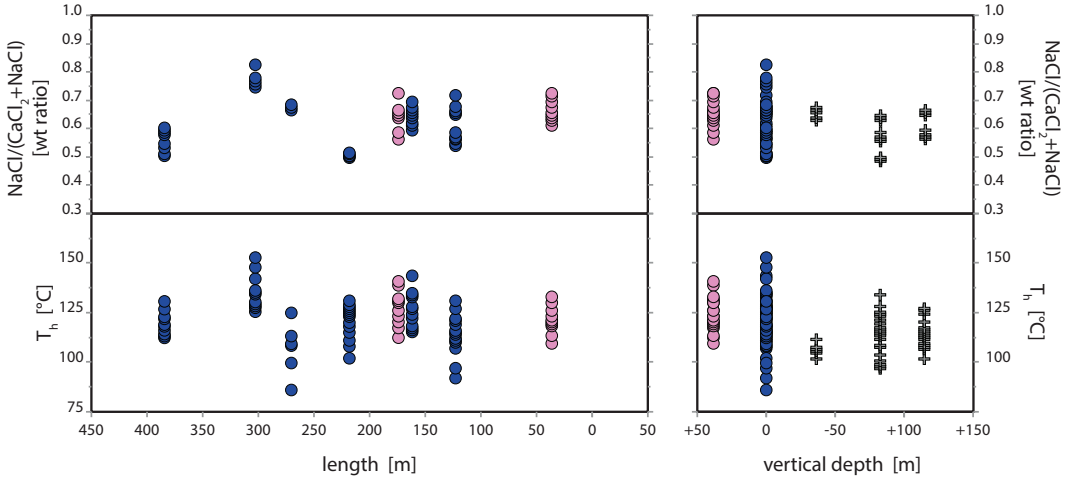

Fig. 5. Spatially depicted microthermometric results.
Microthermometric data for the Teufelsgrund-Schindler section of the Teufelsgrund-Schindler-Herrenwald vein system in the Münstertal. Depicted is the relationship between spatial variations (a) of the fluid parameters (b) within the analyzed fluid inclusions. Samples originating from mine dumps at the mine entrance are symbolized by crosses and indicate an origin of elevation level or higher. Samples taken within the mine are symbolized as filled circles.

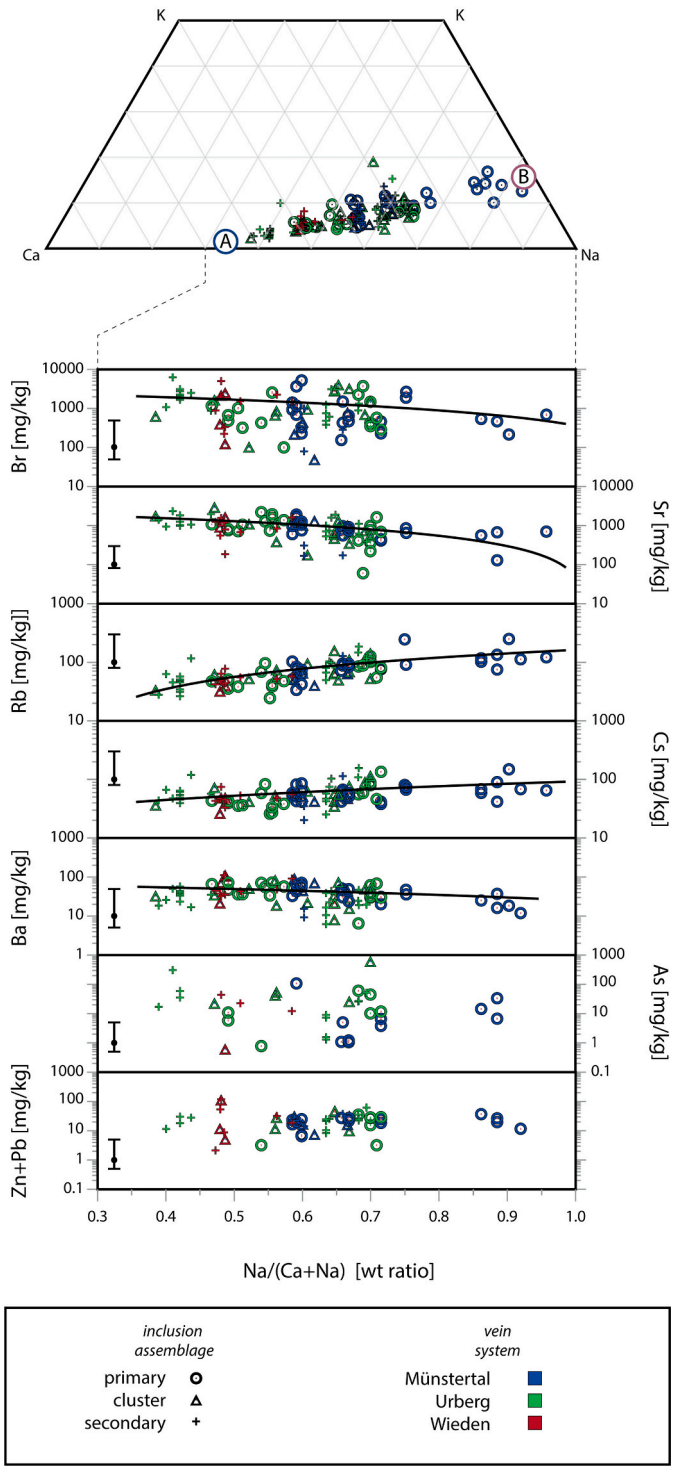

Fig. 6. Fluid inclusion LA-ICP-MS results
Relationship between LA-ICP-MS compositional data for selected elements and microthermometric Na/(Na + Ca) fraction of the fluid inclusion. Linear line of best fit is logarithmically depicted for Br, Sr, Rb, Cs and Ba. The uncertainty regarding the LA-ICP-MS analysis discussed in Chapter 4.1.3 is depicted on the left of each plot.

according to direct dating (Walter et al., 2018b), hydrothermal stage II in these veins is related to the hydrothermal maximum (IV) (see above). These stages/veins have been shown to have formed from a dominantly binary mixing of a metal-rich and an anion-bearing fluid (e.g., Fusswinkel et al., 2013; Staude et al., 2012; Walter et al., 2016). Walter et al. (2019) implies the presence of a third sulfide/reduction agent rich component that is involved in the formation of the sulfides. In the following, we will discuss the framework conditions of the veins, focusing on (1) the seawater/meteoric fluid origin and its penetration into the basement, (2) the temporal evolution of the fluids and their host rocks and (3 + 4) the process of upward fluid flow, constraints on vein formation and the physical process of fluid mixing within a vein (Fig. 9).

7.1. Emplacement of the veins

Today, the hydrothermal veins investigated crop out at the surface. During their time of formation, however, there was basement and sedimentary overburden on top of today's outcrop level. The main stage vein formation occurred between mid-Triassic and Cretaceous times (Walter et al., 2018b): the Urberg vein was dated to approximately the mid Triassic (~251 ± 53 Ma; ~235 ± 63 Ma) while the other two vein systems were dated to be Jurassic-Cretaceous (~75 ± 29 Ma;; ~102 ± 73 Ma ~120 ± 56 Ma; ~136 ± 15 Ma). During this time period, the geologic setting was characterized by a large marine basin. At the time of vein formation, the sedimentary overburden was estimated to be >500 m for Münstertal and Wieden and about >300 m for Urberg (Rupf and Nitsch, 2008). The current day outcrop depth of the veins below the reconstructed unconformity is ~1300 m, ~500 m and ~ 900 m for Münstertal, Urberg and Wieden, respectively (Fig. 10). Assuming geothermal gradients between 25 and 50 °C/km that are typical for basin environments (e.g., Harper, 1971; Nwankwo and Ekine, 2009; Yuan et al., 2009) and an approximate temperature of 25 °C at the unconformity, the emplacement host rock temperatures can be estimated to be between ~50 and 100 °C.

The complete overgrowth of host rock clasts by vein minerals, the common occurrence of partially fractured clasts of various sizes and shapes and the breccia textures indicate that vein opening occurred due to hydraulic fracturing (Jébrak, 1997). Hydraulic fracturing occurs when the trapped fluid pressure exceeds the surrounding lithostatic pressure. The maximum lithostatic pressure is estimated to be ~550, ~250 and ~ 400 bars for the Münstertal, Urberg and Wieden vein systems, respectively. Pressure-corrected formation temperatures (based on Steele-MacInnis et al., 2012 and a pure-H_2O-NaCl system) are 110–170 °C (average of 140 °C) for the Münstertal, 110–180 °C (average of 140 °C) for Urberg and 100–170 °C (average of 140 °C) for Wieden (Fig. 10).

7.2. Formation by mixing

Generally, the most effective way to produce a fluorite-quartz-barite vein is by fluid mixing (e.g., Bouch et al., 2006; Canals and Cardellach, 1993; Schwinn et al., 2006). The microthermometric fluid inclusion data for each investigated vein system clearly show a linear fluid mixing trend between a $CaCl_2$-rich, from now on named fluid A, and an NaCl-rich fluid endmember, from now on named fluid B. It should, however, be noted that all analyzed fluid inclusions only represent already mixed fluids and only trends can provide information on fluid endmember conditions. The mixing of these two fluids has been studied in several previous studies under different aspects (e.g., Fusswinkel et al., 2013; Schwinn et al., 2006; Staude et al., 2012; Walter et al., 2016; Walter et al., 2017). For the sake of completeness, the literature data are compiled here and augmented with the findings of the current contribution.

The vein gangue mineralogy is fluorite, quartz and barite. Fluorite, in general, can form due to reaction with a host rock, fluid cooling, or by fluid mixing (Richardson and Holland, 1979a). Fluorite deposition by fluid-wallrock reaction is typically linked to either an increase in pH or a decrease in Mg/Ca ratio in the fluid (Richardson and Holland, 1979a). Wall rock reaction can be ruled out as a major cause for ore deposition, as the initial fluids are assumed to be in equilibrium with the same type of hostrock (granites and gneisses). Hence, any reaction with these host

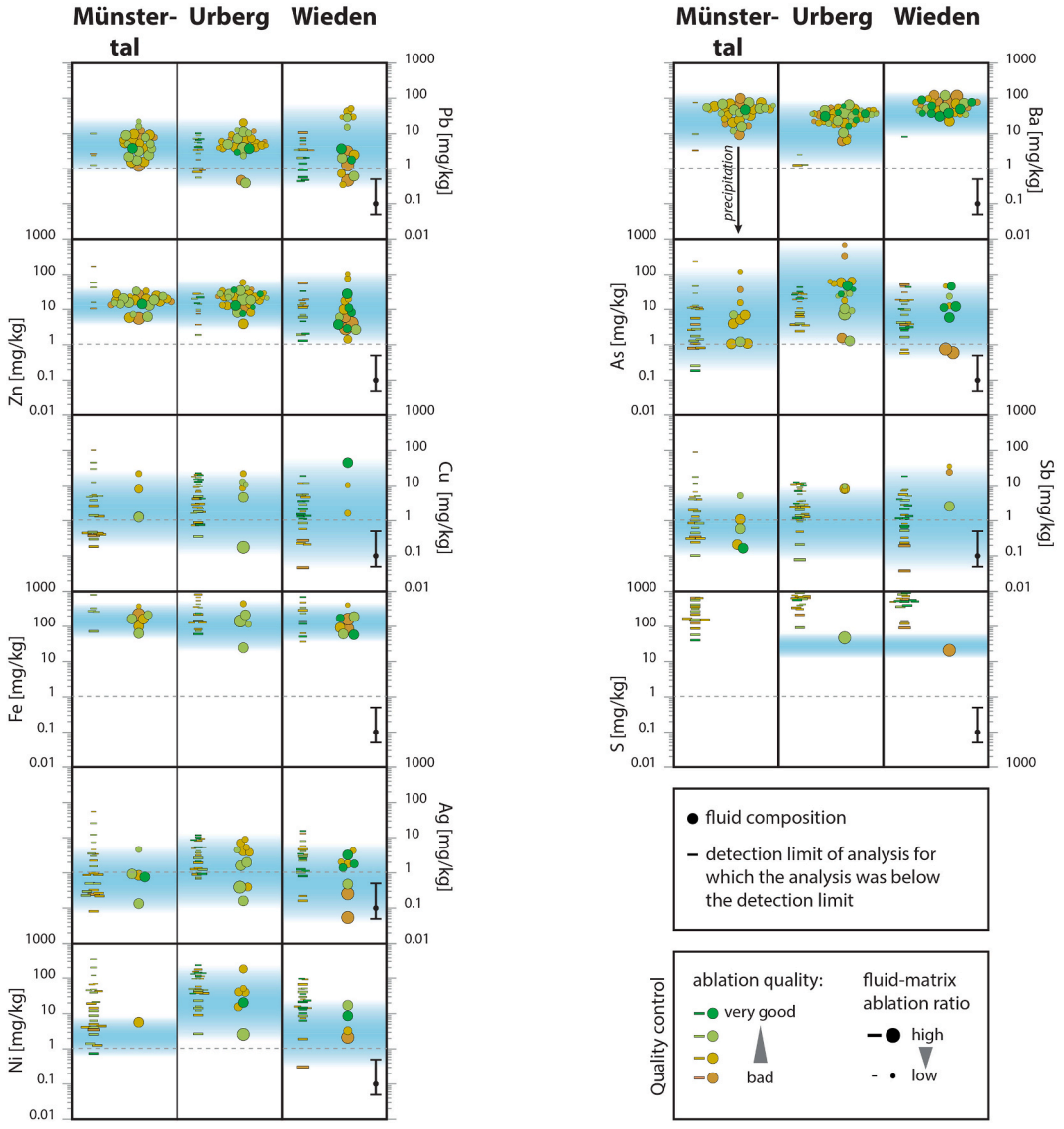

Fig. 7. Fluid inclusion LA-ICP-MS results (Trace elements).
Selected transition metals and As, Sb and S trace element composition of the fluid inclusions, as measured by LA-ICP-MS. Depicted are detected elemental abundance (circle symbols) and the detection limit of those analyses for which quantification was not possible (line symbols). All data have been centered along the x-axis for each locality while making sure all symbols are visible. Blue fields represent range of fluid composition. This ranges from the maximum analyzed elemental content to below the lowest analyzed content or the lowest detection limit. The highest concentrations most likely represent the fluid composition prior to abundant mineral precipitation. (For interpretation of the references to colour in this figure legend, the reader is referred to the web version of this article.)

rocks at the location of vein formation would not significantly shift the pH or the Mg/Ca ratio. Furthermore, in zones of intense fluid-host rock interaction such as brecciated zones of the vein, fluorite is typically less abundant. The proven importance of fluid mixing in the investigated and similar veins in the Schwarzwald (Fig. 4; e.g., Baatartsogt et al., 2007; Schwinn et al., 2006; Walter et al., 2016) makes this effective fluorite precipitation mechanism (Richardson and Holland, 1979a) the most likely cause for fluorite formation. However, fluid cooling may also have aided the precipitation of fluorite. Assuming fluid mixing is responsible for fluorite deposition, either (1) fluid A contained both Ca and F and precipitation occurs due to neutralization or dilution of fluid A during mixing (Brooks and Steele-MacInnis, 2019; Richardson and Holland, 1979a) or, (2) Ca was mainly transported by fluid A (Fig. 4a) and F by fluid B. The latter is more likely since both fluid A and fluid B are assumed to be in equilibrium with a roughly granitic aquifer, a large pH difference between the two fluids is, hence, not expected. This also implies that a higher F-content of fluid B was probably not linked to different host rocks in the fluid source aquifer, but rather a result of F-solubility difference between fluid A and B. Experimental and modeling-based studies have shown the importance of fluid composition on the solubility of F, for example: F is better soluble in NaCl- than in $CaCl_2$-fluids (Richardson and Holland, 1979b; Zhang et al., 2015). This implies that the NaCl-rich fluid B had the potential to transport more F than the $CaCl_2$-rich fluid A. Furthermore, F is also more soluble in the presence of aqueous sulfate (Zhang et al., 2015).

The latter statement fits well with the implication that fluid B was richer in sulfate than fluid A. This implication is based on the fact that the early CaCl2-rich fluid regime is dominated by the precipitation of fluorite whereas the late-stage NaCl-dominated fluid regime more abundantly produced barite. Literature data (Fusswinkel et al., 2013) clearly show that fluid A is the major Ba carrier. Unfortunately, concerning the present contribution, this can only be clearly seen for the Münstertal vein system. If fluid A is the major Ba carrier, then sulfate must be predominantly transported by fluid B. Hence, it is also linked to

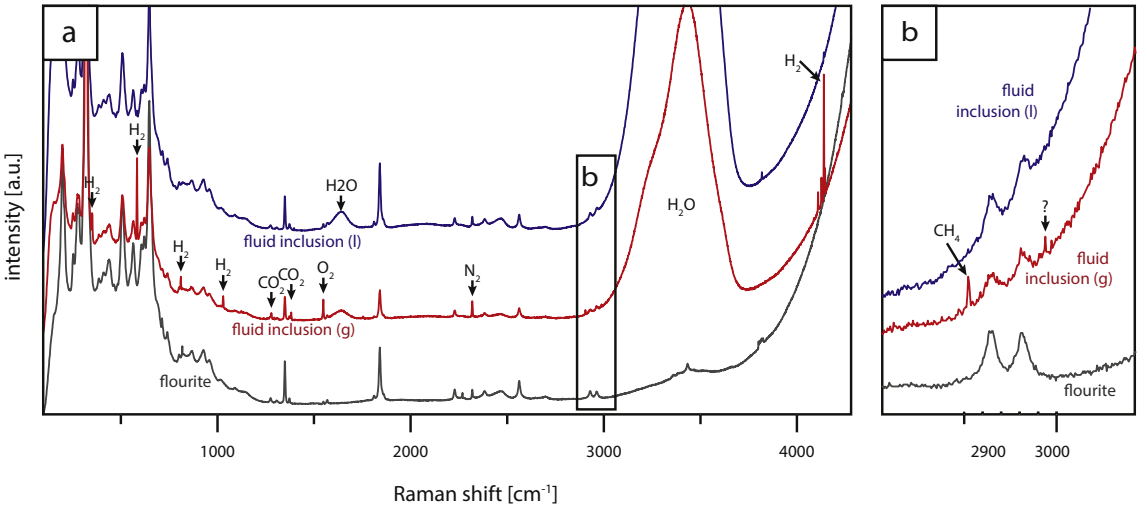

Fig. 8. Selected representative Raman spectra of a fluorite hosted fluid inclusion cogenetic with galena and native arsenic (MT05c_fl_p01_05). Depicted spectra are mean values from 2 fluorite measurements of the host crystal, 3 measurements of the fluid phase in the fluid inclusion and 5 measurements of the gaseous phase in the fluid inclusion. H2(g) is visible in nearly all fluid inclusions analyzed by Raman. N2(g), O2(g), CO2(g) and possibly CH_4(g) are also present in this fluid inclusion.

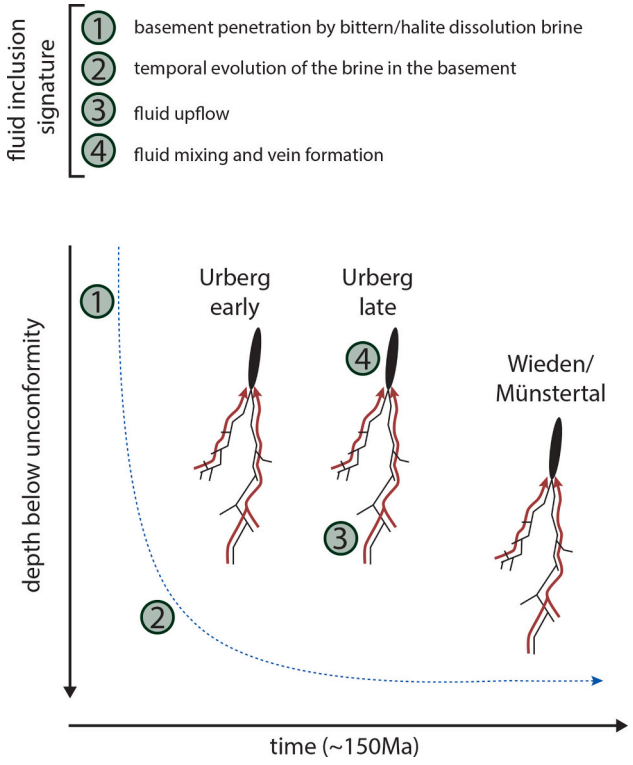

Fig. 9. Fluid flow path and vein formation.
Schematic demonstration of the fluid flow path/fluid evolution until vein formation. Downward fluid flow is illustrated by blue dashed arrow, fluid mobilization from various depth and upward fluid flow by red arrows. Black lines depicts fractures and black ellipse indicates formation of the investigated veins. (For interpretation of the references to colour in this figure legend, the reader is referred to the web version of this article.)

the same process of fluid mixing as fluorite and only represents a shift in fluid mixing ratio and/or in fluid composition. The abundance of both Ca and Ba in the fluid inclusions shows that the anions, F and sulfate must have been the limiting agents for the formation of fluorite and barite.

Quartz is found throughout the whole vein and is probably linked to fluid cooling by mixing or by heat diffusion into the surrounding host rock. Variations in the quartz/fluorite ratio of individual vein bands are most probably linked to variations in pH during fluid mixing or the varying importance of fluid mixing and fluid cooling, respectively.

Thus, the majority of the gangue minerals formed from a binary fluid mixing ± fluid cooling process. However, the hydrothermal veins also locally contain sulfide minerals such as galena and sphalerite. Walter et al. (2019) linked the sulfide formation to either a change in redox state of the fluids or an influx of sulfide. The slow kinetics between sulfate and sulfide (Ohmoto and Lasaga, 1982) as well as the isotopic disequilibrium between coexisting sulfate and sulfide mineral pairs (Schwinn et al., 2006; Staude et al., 2011) strengthen the formation by sulfide influx into the otherwise binary fluid mixing. The formation of the vein sulfides in contrast to native arsenic (which is present in some ore shoots in the investigated hydrothermal veins) is the subject of a different publication.

In a binary fluid mixing scenario, an almost barren (i.e. sulfide-free) hydrothermal vein would form, representing the abundant barren bands within the investigated veins. Completely barren veins in association with mineralized veins are also abundantly present in the Schwarzwald (e.g., Bliedtner and Martin, 1986; Walter et al., 2018a; Walter et al., 2019) and common in many base metal hydrothermal districts worldwide (e.g., Beaudoin et al., 1992; Hein, 1993; Sun et al., 2018). The almost perfect binary trend between fluid A ($CaCl_2$-rich endmember) and fluid B (NaCl-rich endmember) (Fig. 4a) limits the relative volume of sulfide-bearing Fluid C.

7.3. *Penetration of bittern and halite dissolution brines into the basement*

7.3.1. *Geological setting*

To understand the origin and the basement reservoir sources of fluid A and B as well as their evolution with time, the hydrological setting needs to be considered. Both fluid A and fluid B evolved over time from fluid A' and fluid B′ to fluid A" and fluid B″. Thus, in the following we will discuss general characteristics and the temporal evolution will be discussed in the subsequent chapter.

The post-orogenic aqueous regime in the basement during Permian times was dominated by relict metamorphic/magmatic fluids (Epp et al., 2018), with a possible partial dilution by meteoric fluids. The onset of a marine setting and the evaporative environment with halite precipitation during the mid-Triassic (Geyer et al., 2011) enabled the formation of brines. These fluids continuously migrated downwards and

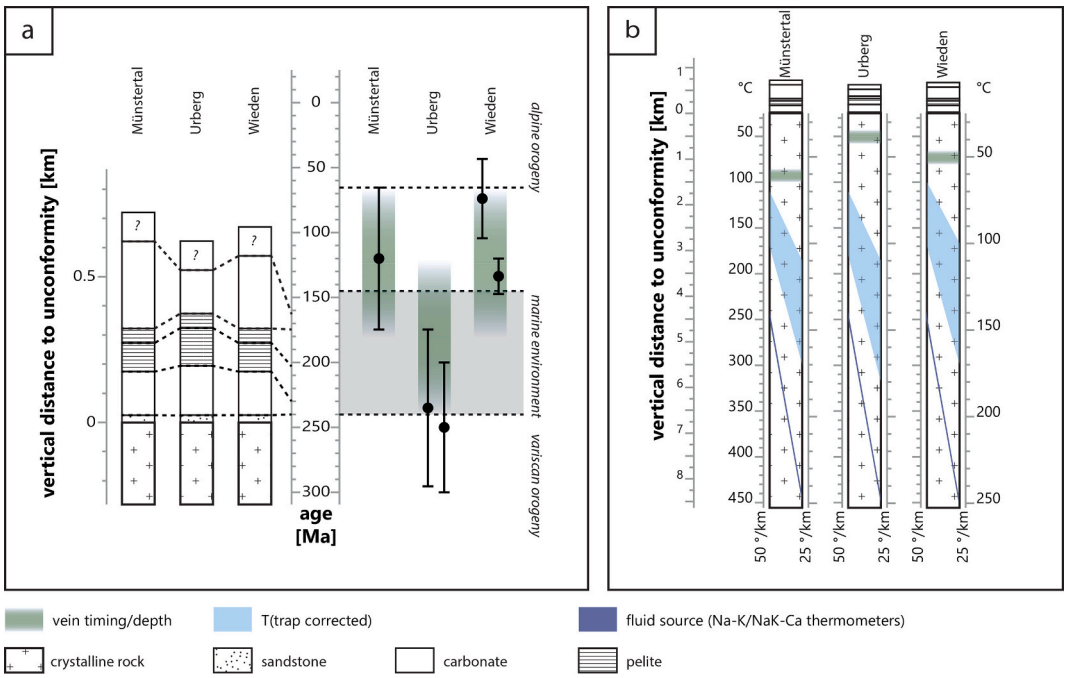

Fig. 10. Spatial and temporal vein formation.
(a) Estimates on the sedimentary overburden (based on data from Rupf and Nitsch, 2008), the absolute time of formation by dating (Walter et al., 2018b) and the estimated time span of vein formation for the main ore stage, which is investigated in this study. (b) Reconstructed relative depth of the vein below the unconformity (based on data from Rupf and Nitsch, 2008) and estimates of basement brine aquifer depth from which the fluids are sourced. These estimates are strongly dependent on the paleo geothermal gradients.

penetrated the "unaltered" Variscan basement rocks, fueled for example by desiccation reactions and thus progressive H_2O consumption during clay mineral formation with depth (Bons et al., 2014; Stober and Bucher, 2004). The hydrothermal mineralogy investigated in this study exclusively formed from the penetrating basement brines and thus we will not discuss the lower salinity preexisting metamorphic/magmatic fluids in the basement at greater depth further.

7.3.2. *Fluid A, characteristics and fluid reservoir*

Fluid A is characterized by a high salinity (20–25 wt% NaCl+$CaCl_2$), its low NaCl/(NaCl+$CaCl_2$) wt. ratio (down to 0.45) and low KCl content (<0.2 wt%). The presence of H_2(g) and rarely CH_4(g) in the fluid inclusions also indicate fairly reducing conditions. Several lines of evidence indicate a marine evaporative environment as the ultimate origin for fluid A: Its high salinity, the for this fluid type in the whole Schwarzwald low Cl/Br mass ratio (typically <80) and the regional geological background (Epp et al., 2018; Schwinn et al., 2006; Walter et al., 2016; Walter et al., 2017; Walter et al., 2018b; Walter et al., 2019). The regionally low Cl/Br ratio indicates an evaporative setting and the occurrence of halite precipitation before penetration into the basement (e.g., Alcalá and Custodio, 2008; Kesler et al., 2003; Richard et al., 2011). Due to the large spread of Cl/Br values in our samples, no clear correlation between Cl/Br and Na/(Na + Ca) mass ratio is visible. However, $CaCl_2$-richest fluid inclusions show a Cl/Br mass ratio between 30 and 110.

The original marine fluid was in or close to halite saturation, and also (based on regional geology), close to or at calcite and gypsum saturation. A fluid at 25 °C at halite saturation contains about 26 wt% of dissolved NaCl (Driesner and Heinrich, 2007) and thermodynamic predictions reveal that such a fluid in equilibrium with calcite and gypsum contains about 0.5 wt% $CaCl_2$. An increase in $CaCl_2$ relative to NaCl within this fluid can occur due to albitization (e.g., Bozau et al., 2015 and references therein). Na + is exchanged by Ca^{2+} in the fluid while Ca-bearing plagioclase is exchanged by Na-rich albite. Furthermore, feldspar alteration to clay minerals may also exchange Ca and Na in the fluid. Both of these processes are abundantly observed in the Variscan basement (e.g., Walter et al., 2019). Proceeding $CaCl_2$-NaCl exchange with time and depth produces stratified basement fluids (Bons et al., 2014). This stratification occurs even if the initial fluid composition is fairly constant through time, but it may be further modified if the initial fluid is variable.

Since the same volume of a 25 wt% $CaCl_2$ fluid contains twice as many Cl ions compared to a 25 wt% NaCl fluid and since there is no significant Cl source in the basement, abundant H_2O consumption is the likely mechanism to increase chlorinity during fluid-host rock interactions. An effective process for this is clay mineral precipitation, which has also been proposed to be the driving force for the downward fluid flow (Bons et al., 2014).

7.3.3. *Fluid B, characteristics and fluid reservoir*

Fluid B is characterized by a high salinity (20–25 wt% NaCl+$CaCl_2$), its high NaCl/(NaCl+$CaCl_2$) wt. ratio (up to 0.95) and high KCl content (up to 2 wt%). The presence of H_2(g) and rarely CH_4(g) in the fluid inclusions also indicate fairly reducing conditions. It has been shown to have highly variable Cl/Br ratios characteristically reaching up to ~9900, which indicates the dissolution of middle Triassic halite (Stober and Bucher, 2000; Walter et al., 2017). This is why the somewhat misleading term "Muschelkalk fluid" is commonly used for this halite dissolution/bittern brine, even though the middle Triassic lithological Muschelkalk unit is not the fluid origin, nor is it the aquifer during vein formation. Furthermore, at regional highs, where no halite precipitation and thus, dissolution occurred in the Triassic, fluid B typically has Cl/Br ratios similar to that of the fluid A (Walter et al., 2017). Its primary fluid origin is most likely meteoric or seawater that dissolved halite and subsequently penetrated the basement. Since the onset of halite precipitation, halite dissolution could also have occurred. The process of halite dissolution must have occurred locally and dependent on parameters such as fluid flow. This in combination with various degrees of evaporation of the most likely sea water surficial fluid produced the large spread in Cl/Br ratios. This spread is not only visible in the late

stage NaCl-richest fluid B endmembers (fluid B″) but also in earlier fluid B endmembers (fluid B′).

The halite dissolution and penetration of fluid B into the basement occurred subsequently to fluid A penetrating the basement, which further produces a stratification of the basement brine reservoir with a deeper-seated fluid A and a shallower seated fluid B. For fluid B, no significant processes of Ca enrichment could occur, as obviously, Ca-rich plagioclase had already been consumed during interaction with fluid A.

7.4. Long term fluid and aquifer evolution

7.4.1. Evolution from a $CaCl_2$- to an NaCl-dominated system

The Urberg locality with its, relative to the other two vein systems, unique mineralogical succession (early calcite) and ore shoots that are used as temporal indicators, enabled the distinction of early and mid to late stage fluorite. This reveals an early $CaCl_2$-dominated fluid regime with a higher total salinity (up to 25 wt%) and a late-stage NaCl-dominated and KCl-richer fluid regime with a slightly lower salinity (down to 21 wt%). We assume this to hold also true for the other two vein systems. This transition could either indicate a transition in relative proportions during mixing or a transition in basement brine reservoir fluid compositions. Individual fluid inclusion assemblages depict a NaCl: $CaCl_2$ mixing gradient of ~1:1, which represents a variation in mixing ratio. However, the shift from early to late stage indicates a gradient of >1:1, which implies a modification of the basement brine, from which the fluids are sourced. Thus, although variations in fluid mixing ratio are naturally still present, the change from and early CaCl2-rich to a late stage NaCl-rich regime is linked to a change in basement brine reservoir composition.

This can be explained by the fact that not only is the fluid altered in the basement, but also the basement host rock is modified with time, as Ca (mainly residing in plagioclase in gneissic and granitic basement rocks) is preferably leached during hydration reaction. Continuous alteration and depletion of Ca leads to a gradual absolute and/or relative enrichment of Na and K in the host rock. The preferred alteration of the anorthite-rich zones in plagioclase by clay minerals and the albitization of plagioclase is a common phenomenon in the Schwarzwald (Brockamp et al., 2003; Bucher and Stober, 2010; Kizler, 2011; Moeller et al., 2005) and albitization has been commonly linked to an increase in Ca in brines all over the world (e.g., Bozau et al., 2015; Davisson and Criss, 1996; Frape and Fritz, 1987; Fritz and Frape, 1982; Yuan et al., 2019). This process has also been shown experimentally (e.g., Hövelmann et al., 2010; O'Neill, 1948). Equilibration of Na, Ca and K with the host rock occurs easily at geologic timescales, as the reservoir fluid must lie somewhere within the temperature range of 150–500 °C and equilibration at these temperatures would take one hundred years to tens of hours, respectively (Henley et al., 1984). Due to the continuous downward fluid flow of fresh NaCl-rich fluids and the depletion of Ca in the host rock over time, the new fluid in equilibrium with the already altered host rock will be NaCl-richer if the availability of Ca is limited. This would also explain the common nature of current day Na-rich and Ca-poor ground waters within the granitic basement (Bucher and Stober, 2016; Göb et al., 2013) as well as the common mixing of NaCl-dominated basement brines with meteoric and/or sedimentary formation waters during the Tertiary (Walter et al., 2018a). The progression of this process produces a scenario, where the Ca-rich fluid is successively pushed to greater depths.

7.4.2. Evolution of the trace elements

The trend of decreasing Ca in the fluid coincides with the trend of decreasing Sr and increasing Rb (Fig. 6) as Sr is preferentially incorporated for Ca in plagioclase and Rb for K in alkali feldspar and mica during their magmatic/metamorphic formation (e.g., Heier, 1962). Less obvious, but still statistically present are these trends for Ba and Cs (Fig. 6). Although both Rb and Cs increase from fluid A to fluid B, Cs increases to a lesser degree, resulting in an increase of Rb/Cs ratio

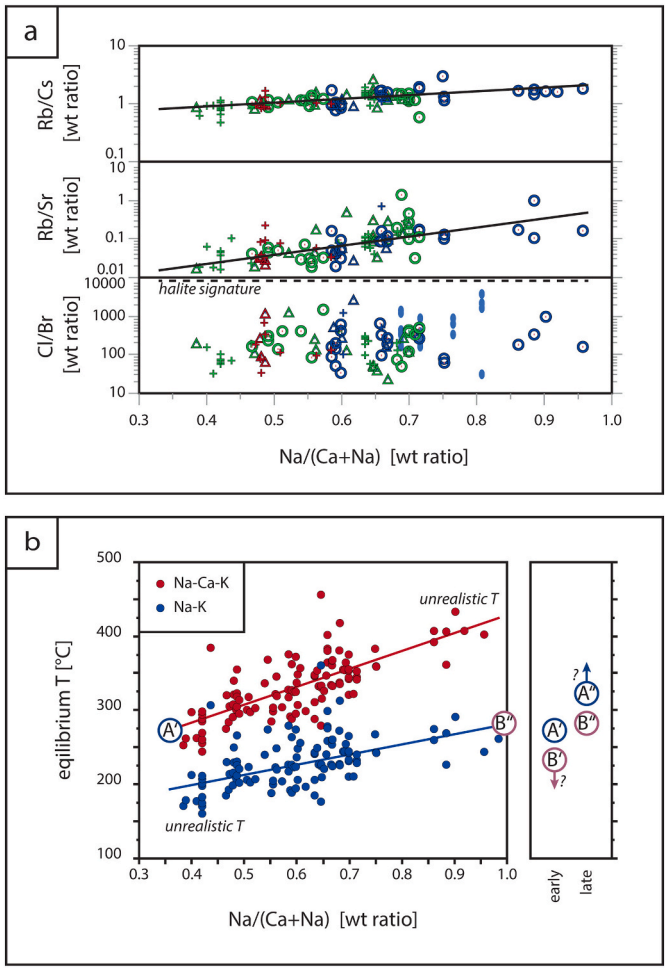

Fig. 11. Geochemical indicators.
(a) LA-ICP-MS analyses trace element ratios with respect to the Na/(Ca + Na) ratio of individual fluid inclusions and (b) equilibration temperatures based on Giggenbach (1988) and Fournier (1979). Lines represent line of best fit. The fluid endmembers A' and B″ are calculated based on K, Ca and Na composition, assuming a K-content of ~0 for fluid A' and a Ca-content of 0 for B″. The fluid endmember composition of A" and B′ are however, unknown, and can thus, not be depicted in this figure. However, fluid B′ must have had a lower basement brine aquifer temperature than fluid A' and fluid A" must have had a higher basement brine aquifer temperature than fluid B″. This shows that fluid A' can be assumed to have been in equilibrium with K-, Na- and Ca-bearing feldspars, whereas fluid B″ was only in equilibrium with K- and Na-bearing feldspars.

(Fig. 11a). It should be noted that not only the presence of K, Na, Ca, Rb, Sr and Cs within the feldspars and/or mica limits their availability to the fluid, but also their possible retention by incorporation in and sorption to the alteration minerals (e.g., Cherian et al., 2018; Deng et al., 2017; Mohamed et al., 2016). This process is essential in understanding the change in Rb/Cs. The Rb/Cs is approximately 2 for the NaCl-rich fluid B, which is a signature for a fluid in equilibrium with clay minerals of the altered granitic rock (Göb et al., 2013). Furthermore, fluid A has a Rb/Cs ratio of <0.8 which has been proposed to be a signature related to the process of host rock alteration and clay mineral formation (Burisch et al., 2016; Göb et al., 2013). This hypothesis is in agreement with the preferred uptake of Cs relative to Rb in alteration minerals such as clays, zeolites and chlorite (Berger et al., 1988). Thus, the Rb/Cs ratios are also in agreement with a general evolution of the basement derived fluids and hence also the expected stratification of the basement fluids, with a Ca- and Sr-rich fluid A at depths with a Rb/Cs < 1 and a more Na- and Rb-rich fluid B with a Rb/Cs ~ 2 at more shallow levels. Renewed fracturing of the host rock (due to brecciation, for example) may,

however, locally decrease the Rb/Cs ratio and thus overprint the basement brine fluid aquifer signature. Such a scenario may be the case in the study of Burisch et al. (2016).

7.4.3. Temporal and spatial evolution of the basement brine aquifer temperature

The model "mixing from below" by Bons et al. (2014) implies that the fluids forming the hydrothermal veins must have originated at greater depth. Based on the host rock temperature estimate, the highest vein formation temperature and assuming no cooling due to heat diffusion prior to mixing, the basement brine aquifers, from which the vein forming fluids are sourced, are situated at least 1.5–3 km or 2.5–5 km below the investigated veins assuming a geothermal gradient of 50 °C/km or 25 °C/km, respectively.

Our interpretation of decreasing availability of Ca-rich feldspar with time and with decreasing depth is further strengthened by the use of empirical Na-K-Ca thermometers (Fournier and Truesdell, 1973; Giggenbach, 1988 and references therein) that are readily applied to show the equilibrium temperatures of a fluid that is hosted by rocks with abundant Na-, K- and Ca-rich feldspars (e.g., Kharaka and Mariner, 1989; Kolesar and Degraff, 1977; Mimi et al., 1998). In our case, these calculated equilibrium temperatures produce realistic results for the Ca-rich fluid endmember A' (Fig. 11b; ~250 °C), for which the Ca-rich feldspar is assumed to still be abundantly present. However, the later Na-rich fluid B endmember produces Na-K-Ca equilibrium temperatures of >400 °C (Fig. 11b), which would have to be sourced from depths of ~8–16 km assuming a geothermal gradient of 50–25 °C/km. These temperatures and depths are not realistic as they would indicate a fluid source from down to below the brittle-ductile transition and would be sourced from below fluid A, which is contrary to the Cl/Br indicator (Walter et al., 2016 and references therein). If, in the absence of available Ca-rich feldspar, the empirical Ca—K thermometer from (Fournier, 1979) is used, which assumes an equilibrium between the fluid, albite and K-feldspar, a reservoir temperature of ~250 °C for fluid B″ is calculated (Fig. 11b). This is significantly lower than the previously described >350 °C basement brine source aquifer temperature, that was based on sulfide-sulfate isotopic equilibrium, which assumed that all sulfur is derived from the same basement source (Schwinn et al., 2006; Walter et al., 2017); this, however, was shown above, not to be the case.. The temperature of 250 °C and a geothermal gradient of 25–50 °C/km results in a depth of 6.5–8.5 km or 3.5–4.5 km, respectively (Fig. 10). This means that, both fluids A and B must have been situated somewhere at this depth.

The Ca—Na exchange in the fluid due to preferred Ca-rich feldspar alteration over the Na-rich counterparts is in accordance to thermodynamic predictions that are based parameters and boundary conditions present for the investigated veins (Fig. 12). It also shows that a fairly sharp boundary forms between the deeper, Ca-rich fluid A and slightly shallower, Na-rich fluid B. This implies only a small temperature difference between these two fluids and would explain the lack of temperature dependence of NaCl/(NaCl+CaCl2) (Fig. 4b). It is however important to note that a basement environment that forms such a stratified aqueous system requires certain boundary conditions. For instance, the flow rate/downward movement of the fluid strongly defines the outcome of the model. Too fast and the basement is flushed by NaCl rich fluids, too slow and the NaCl fluid does not penetrate deep enough into the basement over the required timeframe.

Thus, it is important to understand the temporal evolution of the basement brine source aquifer temperature. Both the earlier fluid A' and the late stage fluid B″ have the same basement brine source aquifer temperature of 250 °C. This implies that fluid B′ must have had a temperature of <250 °C and fluid A" must have had a temperature of >250 °C. Assuming a rather constant geothermal gradient, this implies that, over time, the stratification is pushed to greater depth, so that, late stage fluid B″ is at the same depth as early stage fluid A'. The downward movement of the brines must have been most rapid at the initiation and

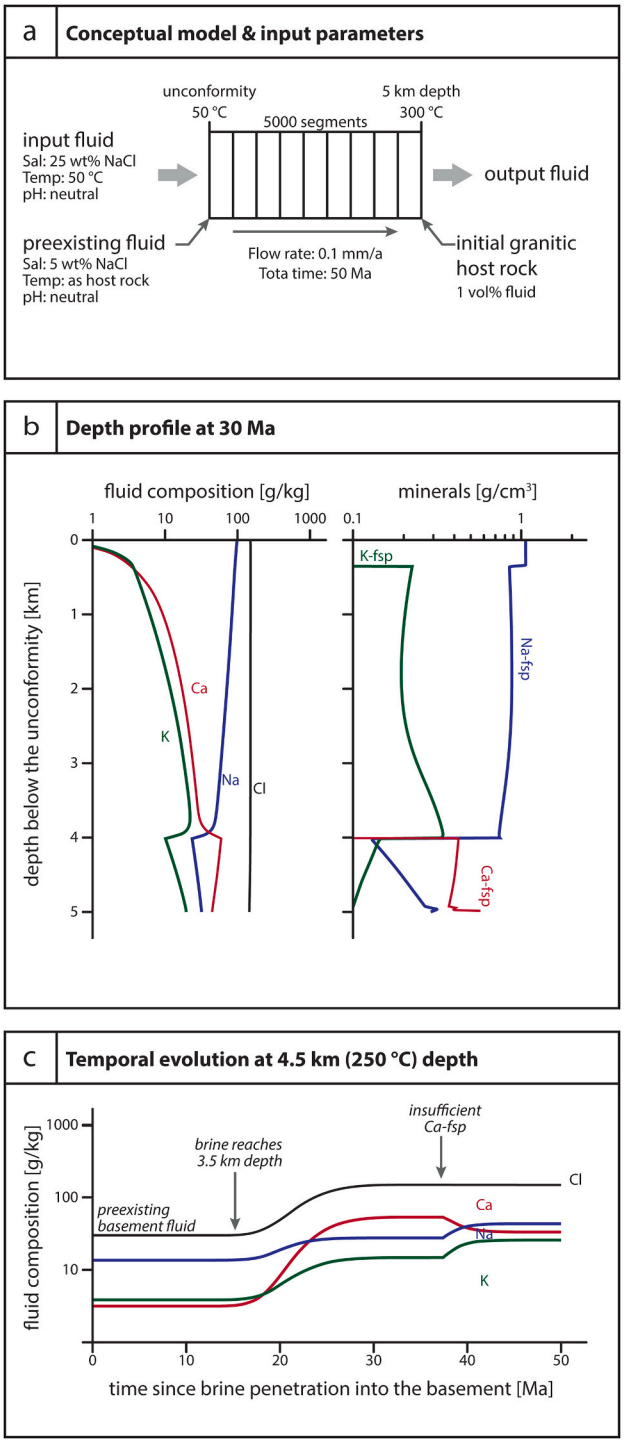

Fig. 12. Thermodynamic model.
(a) Conceptual model of the brine penetration into the basement that is based on all to us available data with (b&c) the corresponding thermodynamic model concerning fluid composition and feldspar abundance. The model shows the spatial and temporal fluid evolution from an NaCl-dominated to a CaCl2-rich fluid by host rock alteration, mainly albitization of Ca-rich plagioclase.

slowed down over time, as the stratification was present for the early Urberg system and the investigated ore stage considering all three veins and uncertainties, has been dated to be active somewhere between 50 and 200 Ma (Walter et al., 2018b). This slowdown of fluid penetration may be explained by the sealing of fluid pathways by mineral (e.g. clay) formation and/or a lack of original marine fluid availability which is

transformed into the basement brine aquifer through basement alteration.

7.4.4. Decrease in salinity over time

Individual fluid inclusion assemblages show an approximately 1:1 mass mixing ratio between the $CaCl_2$-rich fluid A and the NaCl-rich fluid B. However, considering all assemblages for each locality, this ratio increases up to 1.4:1 (Fig. 4c). This in context with the trend from a $CaCl_2$-rich to an NaCl-dominated fluid regime shows a decrease in salinity from fluid A' to A" and fluid B′ to B″ from ~25 wt% to ~22 wt% ($NaCl+CaCl_2$) over time (Fig. 4c). This could be attributed to the marine/sedimentary primary fluid origin being increasingly further away from halite saturation (as a consequence of a marine transgression, for example) the increasing influence of non-saline groundwater and/or the depletion of evaporate layers within the Muschelkalk sequence that can be dissolved. Such changes in the primary marine/meteoric fluid origin will still to some degree be reflected after transition of the surficial fluid into the basement brine reservoir composition. However, the exact reason remains unclear and the current data remains insufficient to further interpret this phenomenon.

7.5. Fluid upflow

Based on the above described comprehensive fluid inclusion study, supplemented by empirical and thermodynamic calculations, the temporal and spatial evolution of the basement aquifer and the modified bittern/halite dissolution basement brine has been deduced. This reservoir represents a single large aquifer with a gradual change in fluid composition and aquifer mineralogy with depth and over time. Thus, the fluids A and B involved in the formation of the hydrothermal vein do not represent two distinct fluid reservoirs but rather two different depths of the same reservoir from which the fluids are sourced. Through the temporal evolution of the reservoir, the fluids A and B change in fluid composition over time.

Both major fluids are sourced from several kilometer depths (Figs. 6 & 7). For this to occur, independent fluid conduits are necessary to transport the two fluids over such distances without mixing. On a regional scale, vein clusters are commonly associated large scale intersections of fault zones (e.g., Staude et al., 2012). It is likely that these regional zones provided the required (hydraulically separated) fluid conduits and enabled fluid mixing.

Considering the sedimentary overburden (Fig. 10) and a resulting approximate temperature estimate of 25 °C at the unconformity for all three vein systems, the host rock temperatures at the timing of the main vein stage can be estimated to be around 60–100 °C for Münstertal, 30–40 °C for Urberg and 50–70 °C for Wieden. Since the basement brine reservoir fluids, from which fluid A and B are sourced, had a temperature of 250 °C and the fluid inclusions show formation temperatures of approximately 130 °C, the fluid must have cooled down significantly prior to fluid mixing at the investigated sites. The silica content of the fluid must have been in equilibrium with the granitic-gneissic host rock at 250 °C and due to the cooling of ~100 °C must have resulted in quartz precipitation at depth. Thus, at depth fluid cooling is expected to be the major vein forming process, and abundant quartz formation is expected, while trapping of the fluids and an increasing importance of fluid mixing occurred at shallower levels, where fluid cooling still continued.

7.6. Spatial and temporal variations within a vein

To understand the spatial variations of banded hydrothermal veins, it is crucial to first discuss the temporal aspect of vein formation. The formation of these veins can be categorized in different spatial and temporal scales (Fig. 13). Each fluid pulse forms at least one growth zone on the mineral-fluid interface within a very short period of time (less than minutes; Walter et al., 2018a). It is normally assumed that a primary growth zone resembles an exposed surface during its formation, and thus, all fluid inclusions on each trail record the same fluid event (Van den Kerkhof and Hein, 2001 and references therein). Thus, the turbulent nature of fluid mixing is best depicted within individual growth zones, where compositional and temperature variations are recorded by contemporary fluid inclusions (e.g., this study; Fusswinkel et al., 2013; Walter et al., 2018a). In our case, the observed variations within individual fluid inclusion assemblages is large enough to be visible in the major elemental composition (microthermometry) (Fig. 4c).

Since a fluid pulse produces at least one growth zone, a batch of

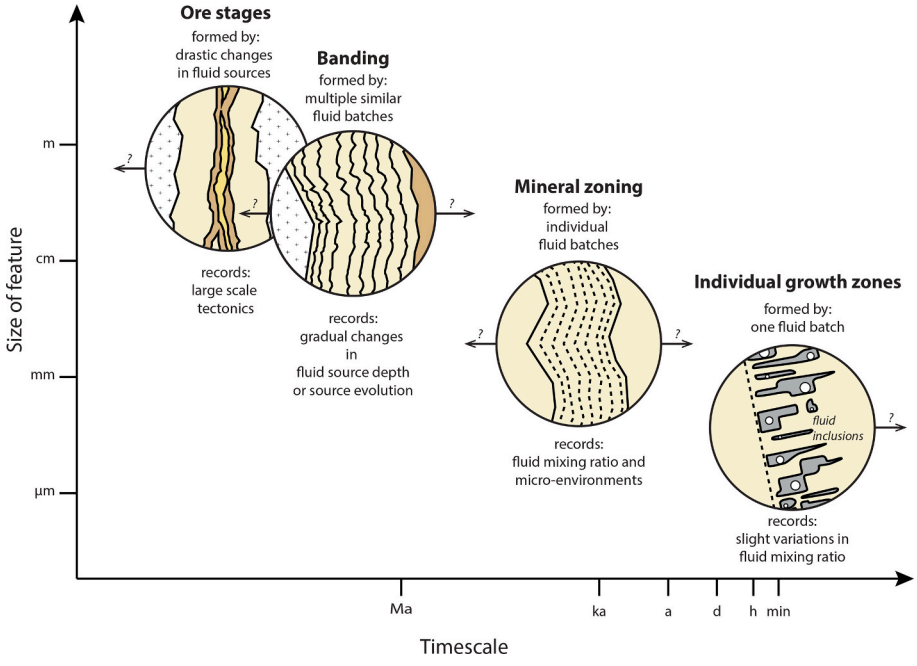

Fig. 13. Variable textures with scale.
Schematic illustration of how temporal and spatial timescales relate with respect to the commonly observed textures in unconformity related veins.

similar pulses produces a mineral zone with many individual fluid inclusion trails on growth zones on the millimeter scale. In our samples, the mass ratio of NaCl/(NaCl+$CaCl_2$) varies up to 0.3 between subsequent growth zones only several hundred micrometers away from each other within the same crystal. This either records fluid mixing ratio variations between fluid pulses or variations of the basement brine reservoir fluid compositions.

A periodic repetition of such fluid pulse batches under slightly different conditions of formation produces a banded structure (millimeter to meter scale) which is a typical feature of unconformity-related veins. Due to the periodic nature of the fluid pulses, it is difficult to determine the time elapsing between pulses. However, this process may last over more than tens of millions of years if the tectonic setting is fairly constant as was the case for the investigated veins (Triassic to Cretaceous). The changes between fluid pulses and batches over such a time period with variations from close to the $CaCl_2$-rich fluid A to close to the NaCl-dominated fluid B endmember almost match the observed changes in mixed fluid composition within the vein on a scale of several hundred meters (Figs. 4 & 5). This is part of the reason why a spatial change in mixed fluid composition within the vein could not be resolved.

7.7. Mixing ratio

The NaCl-$CaCl_2$ mixing line (Fig. 4) reveals analyses close to containing negligible $CaCl_2$ that lie on a linear mixing line. This means that these fluid inclusions represent close to fluid B″ endmember compositions. However, these close to endmember conditions can only be applied to the major element composition since the trace elements are more prone to other factors. Also considering the NaCl-$CaCl_2$-KCl mixing line (Fig. 6), close to fluid A' fluids were also analyzed as they contain very little KCl. This is in accordance to findings of Walter et al. (2015) that have shown that the early stage calcite of the Urberg vein system mainly derives its Mg signature from fluid A, the $CaCl_2$-dominated fluid. Previous studies in the region have determined rough estimations of typical fluid mixing proportions of 75–95% fluid A for the whole vein for similar mid/late Triassic to the early Tertiary veins in the Schwarzwald (Staude et al., 2011). However, their estimations are based on bulk analyses of S- and Sr-isotopes of barite. As we have shown in this current contribution, mixing ratios may vary greatly within only several hundreds of micrometers. Thus, the previously calculated mixing ratios of Staude et al. (2011) may only represent averaged mixing ratios. Furthermore, barite may only be oversaturated at specific mixing ratios, which may not be the case for fluorite (investigated here). This in turn implies that fluid mixing is a chaotic process and that, as long as the host rock minerals are oversaturated, near endmember fluid conditions may actually be trapped during fluid mixing. However, to identify these, a large quantity of samples and analyses are required.

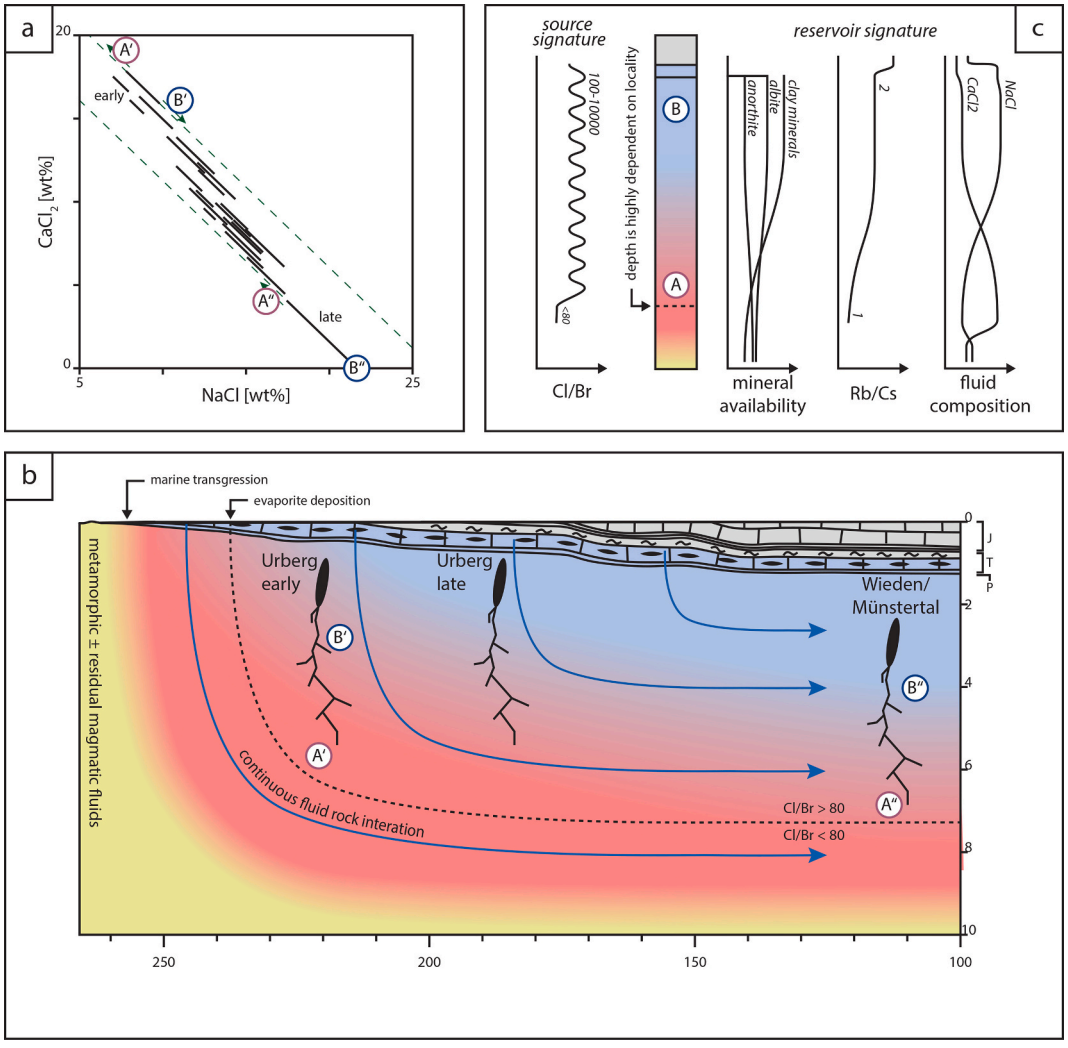

Fig. 14. Concluding figure.
Schematic conclusion of the fluid evolution and the basement brine fluid environment evolution over time. (b) modified from Bons et al. (2014).

8. Conclusions

Fluid reservoirs and aquifers are often viewed as being rather constant over one hydrothermal stage and changes in mineralization to be an effect of either new reservoirs being involved or the conditions of formation changing. We clearly show that an in depth microthermometric study, where spatial and temporal variations within the vein as well as the fluid reservoir and aquifer are considered and distinguished, reveals information to further understand unconformity-related veins. The same also applies to other types of hydrothermal deposits as both the reservoir fluid and the aquifer mineralogy are not necessarily constant, especially on a timescale of tens of millions of years.

The penetration of an originally marine bittern and/or halite dissolution brines into the basement and the associated alteration of the basement minerals (e.g. albitization and clay mineral formation) superimposes a new fluid composition on these brines and changes the composition of the host rock (Fig. 14). Continuous downward fluid flow in combination with the consumption of primary Ca-rich feldspar produces a stratified basement fluid aquifer that gradually changes from Na- and K-rich shallower-seated basement bittern/halite dissolution brine (fluid B) to a Ca-rich deep-seated basement bittern brine (fluid A; Fig. 14) with depth. Over time, this transition is pushed to greater and greater depths which results in a continuous increase in the NaCl/NaCl+$CaCl_2$ fluid fraction recorded within the hydrothermal vein in time.

Prior to anisothermal binary fluid mixing, the fluids must have ascended from their various depth of the bittern/halite dissolution basement brine aquifer environment. Ascension must have occurred over several kilometers without abundant fluid mixing as close to endmember fluid compositions have been analyzed in fluid inclusions. This further proves that fluid mixing in such an environment is a chaotic and inhomogeneous process where, if the host gangue mineral is oversaturated, close to endmember fluids can be trapped. This, however, in combination with a long-term repetition of fluid pulses and batches and a gradually changing basement brine fluid reservoir, makes it difficult to identify spatial gradients in fluid composition over a scale of several hundred meters of the vein.

Declaration of Competing Interest

The authors declare that they have no known competing financial interests or personal relationships that could have appeared to influence the work reported in this paper.

The authors declare the following financial interests/personal relationships which may be considered as potential competing interests.

Acknowledgements

First of all, we thank Dr. Markus Herbener and the whole team at the Teufelsgrund visitors mine in the Schwarzwald, especially Mathias Burgert, for supporting this research by providing access to and/or helping with sample collection. We thank the working group of Lehrstuhl und Institut für Mineralogie und Lagerstättenlehre, RWTH Aachen for the insightful cooperation with this manuscript. We would like to acknowledge the editor and the reviewers for their constructive criticism and feedback, which led to an improved version of this manuscript. We thank Editor in Chief Prof. Dr. Michael E. Böttcher and Editor Dr. Dhilip Kumar. Last but not least, we thank S. Schafflick for fast and reliable sample preparation. This research was funded by the German Research Foundation (DFG), grant no. MA 2135/25-1.

Appendix A. Supplementary data

Supplementary data to this article can be found online at https://doi.org/10.1016/j.chemgeo.2021.120260.

References

Alcalá, F.J., Custodio, E., 2008. Using the Cl/Br ratio as a tracer to identify the origin of salinity in aquifers in Spain and Portugal. J. Hydrol. 359 (1–2), 189–207.
Baatartsogt, B., et al., 2007. Contrasting paleofluid systems in the continental basement: a fluid inclusion and stable isotope study of hydrothermal vein mineralization, Schwarzwald district, Germany. Geofluids 7 (2), 123–147.
Beaudoin, G., Taylor, B., Sangster, D., 1992. Silver-lead-zinc veins and crustal hydrology during Eocene extension, southeastern British Columbia, Canada. Geochim. Cosmochim. Acta 56 (9), 3513–3529.
Behr, H.-J., Gerler, J., 1987. Inclusions of sedimentary brines in post-Variscan mineralizations in the Federal Republic of Germany—a study by neutron activation analysis. Chem. Geol. 61 (1–4), 65–77.
Behr, H.-J., Horn, E., Frentzel-Beyme, K., Reutel, C., 1987. Fluid inclusion characteristics of the Variscan and post-Variscan mineralizing fluids in the Federal Republic of Germany. Chem. Geol. 61 (1–4), 273–285.
Berger, G., Schott, J., Guy, C., 1988. Behavior of Li, Rb and Cs during basalt glass and olivine dissolution and chlorite, smectite and zeolite precipitation from seawater: experimental investigations and modelization between 50 and 300 C. Chem. Geol. 71 (4), 297–312.
Bethke, C.M., 2007. Geochemical and Biogeochemical Reaction Modeling. Cambridge University Press, p. 564.
Blanc, P., 2017. Update for the 2017 version. RP-66811-FR. BRGM. http://thermoddem.brgm.fr/.
Blanc, P., et al., 2012. Thermoddem: a geochemical database focused on low temperature water/rock interactions and waste materials. Appl. Geochem. 27 (10), 2107–2116.
Bliedtner, M., 1978. Blei- und Zink-Prospektion im Gebiet Kaltwasser/Mulden-Untersmünstertal Südschwarzwald. Albert-Ludwigs-Universität Freiburg, Freiburg, p. 131.
Bliedtner, M., Martin, M., 1986. Erz-und Minerallagerstätten des mittleren Schwarzwaldes. Geol. Landesamt Baden-Württemberg.
Boiron, M.C., Cathelineau, M., Richard, A., 2010. Fluid flows and metal deposition near basement/cover unconformity: lessons and analogies from Pb–Zn–F–Ba systems for the understanding of Proterozoic U deposits. Geofluids 10 (1–2), 270–292.
Bons, P.D., et al., 2014. Fluid mixing from below in unconformity-related hydrothermal ore deposits. Geology 42 (12), 1035–1038.
Bouch, J.E., et al., 2006. Direct evidence of fluid mixing in the formation of stratabound Pb–Zn–Ba–F mineralisation in the Alston Block, North Pennine Orefield (England). Mineral. Deposita 41 (8), 821–835.
Bozau, E., Sattler, C.-D., van Berk, W., 2015. Hydrogeochemical classification of deep formation waters. Appl. Geochem. 52, 23–30.
Brill, R.A., Falkenstein, F., Gulich, J., 2018. Die Grube "Gottesehre" bei Urberg im Südschwarzwald. Erzgräber 32 (1), 118.
Brockamp, O., Clauer, N., Zuther, M., 2003. Authigenic sericite record of a fossil geothermal system: the Offenburg trough, Central Black Forest, Germany. Int. J. Earth Sci. 92 (6), 843–851.
Brooks, H.L., Steele-MacInnis, M., 2019. A model for the solubility of minerals in saline aqueous fluids in the crust and upper mantle. Am. J. Sci. 319 (9), 754–787.
Bucher, K., Stober, I., 2010. Fluids in the upper continental crust. Geofluids 10 (1–2), 241–253.
Bucher, K., Stober, I., 2016. Large-scale chemical stratification of fluids in the crust: hydraulic and chemical data from the geothermal research site Urach, Germany. Geofluids 16 (5), 813–825.
Burisch, M., Walter, B.F., Wälle, M., Markl, G., 2016. Tracing fluid migration pathways in the root zone below unconformity-related hydrothermal veins: Insights from trace element systematics of individual fluid inclusions. Chem. Geol. 429, 44–60.
Burisch, M., Walter, B.F., Markl, G., 2017. Silicification of hydrothermal gangue minerals in Pb-Zn-Cu-fluorite-quartz-baryte veins. Can. Mineral. 55 (3), 501–514.
Canals, A., Cardellach, E., 1993. Strontium and sulphur isotope geochemistry of low-temperature barite-fluorite veins of the Catalonian Coastal Ranges (NE Spain): a fluid mixing model and age constraints. Chem. Geol. 104 (1–4), 269–280.
Cherian, C., Kollannur, N.J., Bandipally, S., Arnepalli, D.N., 2018. Calcium adsorption on clays: Effects of mineralogy, pore fluid chemistry and temperature. Appl. Clay Sci. 160, 282–289.
Davisson, M.L., Criss, R.E., 1996. Na Ca Cl relations in basinal fluids. Geochim. Cosmochim. Acta 60 (15), 2743–2752.
Deng, L., et al., 2017. Effects of microstructure of clay minerals, montmorillonite, kaolinite and halloysite, on their benzene adsorption behaviors. Appl. Clay Sci. 143, 184–191.
Driesner, T., Heinrich, C.A., 2007. The system H2O–NaCl. Part I: correlation formulae for phase relations in temperature–pressure–composition space from 0 to 1000 C, 0 to 5000 bar, and 0 to 1 XNaCl. Geochim. Cosmochim. Acta 71 (20), 4880–4901.
Dubessy, J., et al., 1988. Radiolysis evidenced by H2-O2 and H2-bearing fluid inclusions in three uranium deposits. Geochim. Cosmochim. Acta 52 (5), 1155–1167.
Dubessy, J., Poty, B., Ramboz, C., 1989. Advances in COHNS fluid geochemistry based on micro-Raman spectrometric analysis of fluid inclusions. Eur. J. Mineral. 1 (4), 517–534.
Epp, T., et al., 2018. Quartz veins with associated Sb-Pb-Ag±Au mineralization in the Schwarzwald, SW Germany: a record of metamorphic cooling, tectonic rifting, and element remobilization processes in the Variscan belt. Mineral. Deposita 1–26.
Everett, C., Wilkinson, J., Rye, D., 1999. Fracture-controlled fluid flow in the lower Palaeozoic basement rocks of Ireland: implications for the genesis of Irish-type Zn-Pb deposits. Geol. Soc. Lond., Spec. Publ. 155 (1), 247–276.
Fournier, R., Truesdell, A., 1973. An empirical Na K Ca geothermometer for natural waters. Geochim. Cosmochim. Acta 37 (5), 1255–1275.

Fournier, R.O., 1979. A revised equation for the Na/K geothermometer. Trans. Geothermal Resourc. Council 3, 221–224.
Frape, S., Fritz, P., 1987. Geochemical Trends for Groundwaters from the Canadian Shield, Saline Water and Gases in Crystalline Rocks. Geological Association o fCanada, Ottawa, pp. 19–38.
Frenzel, M., et al., 2020. Halogens in hydrothermal sphalerite record origin of ore-forming fluids. Geology. 48 (8), 766–770. https://doi.org/10.1130/G47087.1.
Fritz, P., Frape, S., 1982. Saline groundwaters in the Canadian Shield—a first overview. Chem. Geol. 36 (1–2), 179–190.
Fusswinkel, T., et al., 2013. Fluid mixing forms basement-hosted Pb-Zn deposits: Insight from metal and halogen geochemistry of individual fluid inclusions. Geology 41 (6), 679–682.
Fusswinkel, T., Wagner, T., Sakellaris, G., 2017. Fluid evolution of the Neoarchean Pampalo orogenic gold deposit (E Finland): Constraints from LA-ICPMS fluid inclusion microanalysis. Chem. Geol. 450, 96–121.
Fusswinkel, T., et al., 2018. Combined LA-ICP-MS microanalysis of iodine, bromine and chlorine in fluid inclusions. J. Anal. At. Spectrom. 33 (5), 768–783.
Geyer, O.F., Gwinner, M.P., Geyer, M., Nitsch, E., Simon, T., 2011. Geologie von Baden-Württemberg. Schweizerbart.
Giggenbach, W.F., 1988. Geothermal solute equilibria. Derivation of Na-K-Mg-Ca geoindicators. Geochim. Cosmochim. Acta 52 (12), 2749–2765.
Gleeson, S.A., Wilkinson, J.J., Stuart, F., Banks, D., 2001. The origin and evolution of base metal mineralising brines and hydrothermal fluids, South Cornwall, UK. Geochim. Cosmochim. Acta 65 (13), 2067–2079.
Göb, S., et al., 2013. Major and trace element compositions (including REE) of mineral, thermal, mine and surface waters in SW Germany and implications for water–rock interaction. Appl. Geochem. 33, 127–152.
Goldstein, H., Reynolds, T., 1994. Systematics of fluid inclusions in diagenetic minerals. SEPM Short Course 31, 199.
Grandia, F., Canals, À., Cardellach, E., Banks, D.A., Perona, J., 2003. Origin of ore-forming brines in sediment-hosted Zn-Pb deposits of the Basque-Cantabrian Basin, Northern Spain. Econ. Geol. 98 (7), 1397–1411.
Guillong, M., Meier, D.L., Allan, M.M., Heinrich, C.A., Yardley, B.W., 2008. Appendix A6: SILLS: a MATLAB-based program for the reduction of laser ablation ICP-MS data of homogeneous materials and inclusions. Mineral. Assoc. Can. Short Course 40, 328–333.
Guillong, M., Pettke, T., 2012. Depth dependent element ratios in fluid inclusion analysis by laser ablation ICP-MS. jjj 27 (3), 505–508. https://doi.org/10.1039/C2JA10147E.
Harper, M., 1971. Approximate geothermal gradients in the North Sea Basin. Nature 230 (5291), 235–236.
Heier, K., 1962. Trace elements in feldspars—a review. Nor. Geol. Tidsskr. 42 (2), 415–454.
Hein, U.F., 1993. Synmetamorphic Variscan siderite mineralisation of the Rhenish Massif, Central Europe. Mineral. Mag. 57 (388), 451–467.
Heinrich, C.A., et al., 2003. Quantitative multi-element analysis of minerals, fluid and melt inclusions by laser-ablation inductively-coupled-plasma mass-spectrometry. Geochim. Cosmochim. Acta 67 (18), 3473–3497.
Henley, R.W., Truesdell, A., Barton, P., Whitney, J., 1984. Fluid-Mineral Equilibria in Hydrothermal Systems, 1. Society of Economic Geologists Littleton, CO.
Houston, S., Smalley, C., Laycock, A., Yardley, B.W., 2011. The relative importance of buffering and brine inputs in controlling the abundance of Na and ca in sedimentary formation waters. Mar. Pet. Geol. 28 (6), 1242–1251.
Hövelmann, J., Putnis, A., Geisler, T., Schmidt, B.C., Golla-Schindler, U., 2010. The replacement of plagioclase feldspars by albite: observations from hydrothermal experiments. Contrib. Mineral. Petrol. 159 (1), 43–59.
Jébrak, M., 1997. Hydrothermal breccias in vein-type ore deposits: a review of mechanisms, morphology and size distribution. Ore Geol. Rev. 12 (3), 111–134.
Jochum, K.P., et al., 2011. Determination of reference values for NIST SRM 610–617 glasses following ISO guidelines. Geostand. Geoanal. Res. 35 (4), 397–429.
Kesler, S.E., et al., 2003. Evaluation of the role of sulfidation in deposition of gold, Screamer section of the Betze-Post Carlin-type deposit, Nevada. Econ. Geol. 98 (6), 1137–1157.
Kharaka, Y.K., Mariner, R.H., 1989. Chemical Geothermometers and their Application to Formation Waters from Sedimentary Basins, Thermal History of Sedimentary Basins. Springer, pp. 99–117.
Kizler, C., 2011. Nebengesteinsalteration um hydrothermale Erzlagerstätten im Schwarzwald (Diplom Thesis Thesis). Eberhard Karls Universität Tübingen, Eberhard Karls Universität Tübingen, p. 162.
Kolesar, P.T., Degraff, J.V., 1977. A comparison of the silica and Na-K-Ca geothermometers for thermal springs in Utah. Geothermics 6 (3–4), 221–226.
Land, L.S., Prezbindowski, D.R., 1981. The origin and evolution of saline formation water, lower cretaceous carbonates, south-Central Texas, USA. J. Hydrol. 54 (1–3), 51–74.
Lowenstein, T., Timofeeff, M., 2008. Secular variations in seawater chemistry as a control on the chemistry of basinal brines: test of the hypothesis. Geofluids 8 (2), 77–92.
Luo, Y.-R., 2007. Comprehensive Handbook of Chemical Bond Energies. CRC press.
Markl, G., 2017. Schwarzwald, vol. 4. Südlicher Schwarzwald, Bode Verlag, p. 880.
Markl, G., Burisch, M., Neumann, U., 2016. Natural fracking and the genesis of five-element veins. Mineral. Deposita 51 (6), 703–712.
Metz, R., Richter, M., Schürenberg, 1957. Die Blei-Zink-Erzgänge des Schwarzwaldes. Beihefte zum Geologischen Jahrbuch. Amt für Bodenforschung, Hannover, p. 153.
Mimi, A.L., et al., 1998. Application of chemical geothermometers to thermal springs of the Maghreb, North Africa. Geothermics 27 (2), 211–233.
Moeller, P., et al., 2005. Main and trace elements in KTB-VB fluid: composition and hints to its origin. Geofluids 5 (1), 28–41.
Mohamed, Z., Abdelkarim, A., Ziat, K., Mohamed, S., 2016. Adsorption of Cu (II) onto natural clay: equilibrium and thermodynamic studies. System 10, 11.
Muchez, P., et al., 2005. 7: Extensional tectonics and the timing and formation of basin-hosted deposits in Europe. Ore Geol. Rev. 27 (1–4), 241–267.
Nwankwo, C., Ekine, A., 2009. Geothermal gradients in the Chad Basin, Nigeria, from bottom hole temperature logs. Intern. J. Phys. Sci. 4 (12), 777–783.
Ohmoto, H., Lasaga, A.C., 1982. Kinetics of reactions between aqueous sulfates and sulfides in hydrothermal systems. Geochim. Cosmochim. Acta 46 (10), 1727–1745.
O'Neill, T.F., 1948. The hydrothermal alteration of feldspars at 250 degrees C. to 400 degrees C. Econ. Geol. 43 (3), 167–180.
Otto, J., 1964. Die Fluoritgrube "Gottesehre" (Unpublished Diplom Thesis Thesis). Albert Ludwigs Universität zu, Freiburg, Freiburg.
Otto, J., 1967. Der Fluoritgang der Grube "Gottesehre" bei Urberg Kr. Säckingen (Südschwarzwald). Jh. Geolog, 9. Landesamt Baden-Württemberg, pp. 25–50.
Pettke, T., Oberli, F., Audétat, A., Guillong, M., Simon, A.C., Hanley, J.J., Klemm, L.M., 2012. Recent developments in element concentration and isotope ratio analysis of individual fluid inclusions by laser ablation single and multiple collector ICP-MS. Ore Geol. Rev. 44, 10–38. https://doi.org/10.1016/j.oregeorev.2011.11.001.
Pfaff, K., Romer, R.L., Markl, G., 2009. U-Pb ages of ferberite, chalcedony, agate,'U-mica'and pitchblende: constraints on the mineralization history of the Schwarzwald ore district. Eur. J. Mineral. 21 (4), 817–836.
Pfaff, K., et al., 2011. Trace and minor element variations and sulfur isotopes in crystalline and colloform ZnS: Incorporation mechanisms and implications for their genesis. Chem. Geol. 286 (3–4), 118–134.
Piqué, À., Canals, À., Grandia, F., Banks, D.A., 2008. Mesozoic fluorite veins in NE Spain record regional base metal-rich brine circulation through basin and basement during extensional events. Chem. Geol. 257 (1–2), 139–152.
Richard, A., et al., 2011. An evaporated seawater origin for the ore-forming brines in unconformity-related uranium deposits (Athabasca Basin, Canada): Cl/Br and δ37Cl analysis of fluid inclusions. Geochim. Cosmochim. Acta 75 (10), 2792–2810.
Richardson, C., Cann, J., Richards, H., Cowan, J., 1987. Metal-depleted root zones of the Troodos ore-forming hydrothermal systems, Cyprus. Earth Planet. Sci. Lett. 84 (2–3), 243–253.
Richardson, C.K., Holland, H., 1979a. Fluorite deposition in hydrothermal systems. Geochim. Cosmochim. Acta 43 (8), 1327–1335.
Richardson, C.K., Holland, H., 1979b. The solubility of fluorite in hydrothermal solutions, an experimental study. Geochim. Cosmochim. Acta 43 (8), 1313–1325.
Rupf, I., Nitsch, E., 2008. Das Geologische Landesmodell von Baden-Württemberg: Datengrund lagen, technische Umsetzung und erste geologische Ergebnisse. Landesamt für Geologie, Rohstoffe und Bergbau, Regierungspräsidium Freiburg.
Scharrer, M., Kreissl, S., Markl, G., 2019. The mineralogical variability of hydrothermal native element-arsenide (five-element) mineralizations and the role of aqueous sulfide. Ore Geol. Rev. 113.
Schürenberg, H., 1950. Die Erzgänge Teufelsgrund und Schindler im Untermünstertal und ihr quantitativer Mineralgehalt (Unpublished PhD Thesis Thesis).
Schwinn, G., Wagner, T., Baatartsogt, B., Markl, G., 2006. Quantification of mixing processes in ore-forming hydrothermal systems by combination of stable isotope and fluid inclusion analyses. Geochim. Cosmochim. Acta 70 (4), 965–982.
Seo, J.H., Guillong, M., Aerts, M., Zajacz, Z., Heinrich, C.A., 2011. Microanalysis of S, Cl, and Br in fluid inclusions by LA–ICP-MS. Chem. Geol. 284 (1–2), 35–44.
Staude, S., Bons, P.D., Markl, G., 2009. Hydrothermal vein formation by extension-driven dewatering of the middle crust: an example from SW Germany. Earth Planet. Sci. Lett. 286 (3–4), 387–395.
Staude, S., et al., 2011. Deciphering fluid sources of hydrothermal systems: a combined Sr-and S-isotope study on barite (Schwarzwald, SW Germany). Chem. Geol. 286 (1–2), 1–20.
Staude, S., et al., 2012. Multi-stage Ag–Bi–Co–Ni–U and Cu–Bi vein mineralization at Wittichen, Schwarzwald, SW Germany: geological setting, ore mineralogy, and fluid evolution. Mineral. Deposita 47 (3), 251–276.
Steele-MacInnis, M., Bodnar, R., Naden, J., 2011. Numerical model to determine the composition of H2O–NaCl–CaCl2 fluid inclusions based on microthermometric and microanalytical data. Geochim. Cosmochim. Acta 75 (1), 21–40.
Steele-MacInnis, M., Lecumberri-Sanchez, P., Bodnar, R.J., 2012. Short note: HokieFlincs_H2O-NaCl: a Microsoft Excel spreadsheet for interpreting microthermometric data from fluid inclusions based on the PVTX properties of H2O-NaCl. Comput. Geosci. 49, 334–337.
Steen, H., 2013. Bergbau auf Lagerstätten des Südlichen Schwarzwalds. Ein Beitrag zur Bergbauge-schichte und Lagerstättenkunde zwischen Dreisamtal und Hochrhein. Books on Demand, Nor-derstedt.
Stober, I., Bucher, K., 2000. Herkunft der Salinität in Tiefenwässern des Grundgebirges–unter besonderer Berücksichtigung der Kristallinwässer des Schwarzwaldes. Grundwasser 5 (3), 125–140.
Stober, I., Bucher, K., 2004. Fluid sinks within the earth's crust. Geofluids 4 (2), 143–151.
Sun, X., et al., 2018. Geology, S–Pb isotopes, and 40 Ar/39 Ar geochronology of the Zhaxikang Sb–Pb–Zn–Ag deposit in Southern Tibet: implications for multiple mineralization events at Zhaxikang. Mineral. Deposita 53 (3), 435–458.
Van den Kerkhof, A.M., Hein, U.F., 2001. Fluid inclusion petrography. Lithos 55 (1–4), 27–47.
Walter, B.F., Immenhauser, A., Geske, A., Markl, G., 2015. Exploration of hydrothermal carbonate magnesium isotope signatures as tracers for continental fluid aquifers, Schwarzwald mining district, SW Germany. Chem. Geol. 400, 87–105.

Walter, B.F., Burisch, M., Markl, G., 2016. Long-term chemical evolution and modification of continental basement brines–a field study from the Schwarzwald, SW Germany. Geofluids 16 (3), 604–623.
Walter, B.F., Burisch, M., Marks, M.A., Markl, G., 2017. Major element compositions of fluid inclusions from hydrothermal vein-type deposits record eroded sedimentary units in the Schwarzwald district, SW Germany. Mineral. Deposita 52 (8), 1191–1204.
Walter, B.F., et al., 2018a. Multi-reservoir fluid mixing processes in rift-related hydrothermal veins, Schwarzwald, SW-Germany. J. Geochem. Explor. 186, 158–186.
Walter, B.F., et al., 2018b. The connection between hydrothermal fluids, mineralization, tectonics and magmatism in a continental rift setting: Fluorite Sm-Nd and hematite and carbonates U-Pb geochronology from the Rhinegraben in SW Germany. Geochim. Cosmochim. Acta 240, 11–42.
Walter, B.F., et al., 2019. Chemical evolution of ore-forming brines–Basement leaching, metal provenance, and the redox link between barren and ore-bearing hydrothermal veins. A case study from the Schwarzwald mining district in SW-Germany. Chem. Geol. 506, 126–148.
Walter, B.F., et al., 2020. Formation of hydrothermal fluorite-hematite veins by mixing of continental basement brine and redbed-derived fluid: Schwarzwald mining district, SW-Germany. J. Geochem. Explor. 212, 106512.
Walter, L.M., Stueber, A.M., Huston, T.J., 1990. Br-Cl-Na systematics in Illinois basin fluids: Constraints on fluid origin and evolution. Geology 18 (4), 315–318.
Werner, W., Franzke, H.J., 2001. Postvariszische bis neogene Bruchtektonik und Mineralisation im südlichen Zentralschwarzwald. Z. Dtsch. Geol. Ges. 405–437.
Wilkinson, J.J., Eyre, S.L., Boyce, A.J., 2005. Ore-forming processes in Irish-type carbonate-hosted Zn-Pb deposits: evidence from mineralogy, chemistry, and isotopic composition of sulfides at the Lisheen Mine. Econ. Geol. 100 (1), 63–86.
Yuan, G., et al., 2019. A review of feldspar alteration and its geological significance in sedimentary basins: from shallow aquifers to deep hydrocarbon reservoirs. Earth Sci. Rev. 191, 114–140.
Yuan, Y., et al., 2009. "Uniform geothermal gradient" and heat flow in the Qiongdongnan and Pearl River Mouth Basins of the South China Sea. Mar. Pet. Geol. 26 (7), 1152–1162.
Zeschke, G., 1959. Die Flusspatvorkommen der Gewerkschaft Finstergrund. Rhöndorf a. R, Germany.
Zhang, W., et al., 2015. Modeling geochemical factors controlling fluoride concentration in groundwater. Arab. J. Geosci. 8 (11), 9133–9147.

Appendix IV

Accepted publication

Study 4

Walter, B. F., Scharrer, M., Burisch, M., Apukthina, O., & Markl, G. (2020). Limited availability of sulfur promotes copper-rich mineralization in hydrothermal Pb-Zn veins: A case study from the Black Forest, SW Germany. Chemical Geology, 532, 119358.

Chemical Geology 532 (2020) 119358

Contents lists available at ScienceDirect

Chemical Geology

journal homepage: www.elsevier.com/locate/chemgeo

Limited availability of sulfur promotes copper-rich mineralization in hydrothermal Pb-Zn veins: A case study from the Schwarzwald, SW Germany

Benjamin F. Walter[a,b,*], Manuel Scharrer[b], Mathias Burisch[c], Olga Apukthina[d], Gregor Markl[b]

[a] Institute of Applied Geosciences, Karlsruhe Institute of Technology (KIT), Adenauerring 20b 76131 Karlsruhe, Germany
[b] Department of Geoscience, University of Tübingen, Wilhelmstr. 56, 72074 Tübingen, Germany
[c] Professur für Lagerstättenlehre und Petrologie, Technische Universität Bergakademie Freiberg, Brennhausgasse 14, 09599 Freiberg, Germany
[d] School of Earth Sciences, University of Melbourne, Melbourne, Victoria 3010, Australia

ARTICLE INFO

Editor: Michael E. Boettcher

Keywords:
Ore deposit
Mineralization
Variscan deposit
Rifting
Sulfides
Fluid mixing
Basement brine

ABSTRACT

Mixing of compositionally contrasting fluids is widely accepted as the major ore-forming process in unconformity-related hydrothermal Pb-Zn-fluorite-barite veins. Although the general process is relatively well understood, the temporal evolution of such fluid systems which may result in distinct mineralogical changes of the ore and gangue minerals precipitating are insufficiently constrained. One specific example is the occurrence of late-stage siderite-chalcopyrite-gersdorffite mineralization in 28 hydrothermal veins of the Schwarzwald, SW Germany post-dating the major fluorite-barite-galena-sphalerite phase which is very common in the whole area. To investigate the underlying process for this late-stage Cu-Ni-stage, published fluid inclusion data have been complemented by detailed confocal Raman micro-spectroscopy of fluid inclusions, petrographic observations and electron microprobe analyses.

Petrography as well as mineral compositions of sphalerite, gersdorffite, pyrite, arsenopyrite, fahlore and galena record a gradual, but significant influx of Cu and Ni into a prevailing Pb-Zn hydrothermal system. This influx caused a distinct shift towards lower fO_2 and Pb + Zn + Sb + Ag (+ S) in the hydrothermal system at the transition from the Pb-Zn to the Cu-Ni mineralization stage. This transition in mineralogy and the related gradual change of the hydrothermal fluid can be explained by changes in the relative proportion of involved fluid components. However, the transition to the Cu-Ni mineralization stage by fluid influx is significantly different compared to the common rapid fluid mixing from below (which is thought to be responsible for the typical Pb-Zn veins) and probably records the gradual transition from long-term stable deep fluid reservoirs with constant chemical compositions towards more shallow and perturbed fluid reservoirs during rifting and exhumation.

1. Introduction

Hydrothermal fluorite-barite-Pb-Zn veins are widespread in Europe (Bauer et al., 2019; Muchez et al., 2005; Boiron et al., 2010; Lüders and Möller, 1992; Walter et al., 2016; Sośnicka and Lüders, 2019) and are an important resource for fluorite, barite and to lesser degree Pb, Zn, Cu and Ag. Besides the economic interest, such veins represent archives that conserve valuable information on ancient upper crustal fluid systems associated with rift zones (Carignan et al., 1997; Muchez et al., 2005; Piqué et al., 2008; Walter et al., 2018a). They may be basement-hosted or sediment-hosted and occur in relative proximity to unconformities below sedimentary basins. The fundamental ore-forming process is mixing of two (or more) chemically contrasting fluids (e.g. Duane and de Wit, 1988; Wilkinson, 2001; Fusswinkel et al., 2013). These fluids usually include a hot, deep-seated brine and a shallower, colder fluid of sedimentary origin. Highly saline basement brines have typically low concentrations of reduced sulfur (also often low total sulfur; Frape et al., 1984; Stober and Bucher, 2004; Fusswinkel et al., 2013, 2014), and have consequently a high capacity to transport base metals (e.g. Yardley, 2005; Walter et al., 2019; Burisch et al., 2016a). Leaching of large rock volumes at the source of the basement fluids enriches them in base metals (Burisch et al., 2016a; Burisch et al., 2016b) and fluorine (e.g. de Graaf et al., 2019). Fluids of sedimentary origin are very variable in their fluid composition (Stober and Bucher, 1999, 2004; Burisch et al., 2018; Walter et al., 2017a, b) and more than one sedimentary fluid may be involved in the mixing process (Walter

* Corresponding author at: Institute of Applied Geosciences, Karlsruhe Institute of Technology (KIT), Adenauerring 20b 76131 Karlsruhe, Germany.
E-mail address: b.walter@kit.edu (B.F. Walter).

https://doi.org/10.1016/j.chemgeo.2019.119358
Received 13 May 2019; Received in revised form 8 October 2019; Accepted 31 October 2019
Available online 01 November 2019
0009-2541/

et al., 2017b; Burisch et al., 2017). Precipitation related to fluid mixing may be initiated by a change in T, pH, log fO_2 and/or the inflow of aqueous species by one of the involved fluids (e.g. $H_2SO_4^{2-}$, HS^-). Although all parameters change concomitantly upon mixing, the key parameter for the precipitation of base metal sulfides and barite is the inflow of sulfur species by the sedimentary fluid(s) (Burisch et al., 2017).

Numerous districts with hydrothermal vein type mineralization worldwide contain a Pb-Zn dominated mineralization stage (e.g. Zhou et al., 2017; Cugerone et al., 2018 and references therein). Previous studies showed that Pb-Zn-fluorite-barite veins form due to mixing of two chemically contrasting fluids, namely a deep-seated basement brine and a sediment-derived fluid (Fußwinkel et al. 2013, Walter et al., 2017a, b, 2018a, and Burisch et al., 2016b). For precipitation, either the second fluid endmember has to contain reduced sulfur or a third fluid containing the reducing agent participates in the fluid mixing process (e.g. Markl et al., 2016; Burisch et al., 2017; Walter et al., 2019 and references therein). The precipitation mechanism of a paragenetically late Cu-rich mineralization stage, however, is not adequately understood.

The exceptionally well-studied Schwarzwald mining district offers the opportunity to investigate the transition from the Pb-Zn to the Cu-Ni-rich mineralization stage (Staude et al., 2009; Walter et al., 2019 and references therein). Hydrothermal veins of the Schwarzwald are polystadial and distinct temporal changes of the mineralogy of the vein can be recognized (Walter et al., 2016; Burisch et al., 2018; Staude et al., 2012a, b), which are most probably related to the geodynamic evolution of the province. Besides these systematic temporal changes between the observed mineralization stages (Walter et al., 2016; Burisch et al., 2018), distinct mineralogical changes within each stage may be related to compositional differences in the sedimentary cover sequence (Walter et al., 2016) or to different proportions of fluids involved in mixing (Walter et al., 2017a).

Conspicuous chalcopyrite-siderite mineralization occurs at numerous localities (e.g. Gabler vein, Riggenbach, Felsenkeller, Böschlisgrund, Immisberg) within the southwestern part of the Schwarzwald district. Chalcopyrite and siderite occur as late stage vein infill in Pb-Zn-fluorite-barite veins. This sub-economic, but nonetheless interesting Cu mineralization has not yet been investigated in detail.

Detailed microscopy and electron microprobe analyses in combination with confocal Microraman measurements of fluid inclusions have been carried out to understand the process responsible for the district-scale occurrence of late-stage Cu-Ni mineralization in Pb-Zn veins. This in turn can be used to include this as of yet poorly understood mineralization stage into existing hydrochemical models. Furthermore, this provides new insight into the behavior of Cu, Ni, Pb and Zn in low-temperature hydrothermal environments in general.

1.1. Geological setting

The Schwarzwald is composed of Variscan paragneisses, migmatites and granites covered by Permian to Upper Jurassic terrestrial and marine sediments (Fig. 1). Within the paragneiss and migmatite units, small bodies of orthogneisses, granulites and amphibolites may occur. Syn- and post-tectonic S-type granites intruded the Variscan metamorphic units between 335 and 315 Ma (Altherr et al., 2000; Hann et al., 2003; Kalt et al., 2000; Todt, 1976). During the Permian, the Variscan rocks were eroded, resulting in local, small-scale sediment basins filled by proximal clastic sediments, i.e. red bed arkoses and conglomerates (Geyer and Gwinner, 2011; Jenkner, 1986; Nitsch and Zedler, 2009). Subsequently, Lower Triassic sandstones were deposited on top of the Permian or directly on the Variscan basement units (as in the case for the study area). A marine transgression resulted in the deposition of limestones (Muschelkalk) and evaporites (Walter et al., 2017a). In the Upper Triassic (Keuper), evaporitic units and clastic sediments reached a maximum thickness of about 300 m (Geyer and Gwinner, 2011), which were followed by thick (up to 1000 m) Jurassic limestones. After the Jurassic subsidence, uplift prevailed and inhibited the deposition of Cretaceous sediments in the Schwarzwald area (Geyer and Gwinner, 2011). Since the initial opening of the Upper Rhinegraben rift in the Paleogene, up to 4000 m of clastic sediments and evaporites were deposited on top of the Mesozoic sediments (Geyer and Gwinner, 2011; Rupf and Nitsch, 2008). Simultaneous with the subsidence and rifting in the center of the graben, the rift shoulders were uplifted by up to three kilometers (Geyer and Gwinner, 2011). Due to an asymmetric exhumation of the area, the basement-cover unconformity is still preserved in the middle and northern Schwarzwald, while the southern Schwarzwald is exhumed to a total depth of about 3.5–4 km below the Upper Jurassic surface (Rupf and Nitsch, 2008; Walter et al., 2017a). During the rifting alkaline magmatism was common (Lustrino and Wilson, 2007; Braunger et al., 2018; Walter et al., 2018c; Giebel et al., 2019)

1.2. Hydrothermal veins in SW Germany

About 1000 hydrothermal veins are known in the Schwarzwald mining district (Metz et al., 1957; Behr et al., 1987; Keim et al., 2018; Epp et al., 2018). Five distinct stages related to maxima of hydrothermal activity in the Schwarzwald mining district can be recognized: (i) Carboniferous (ii) Permian, (iii) Triassic-Early Jurassic, (iv) Middle Jurassic-Cretaceous and (v) post-Cretaceous. The Carboniferous veins (i) are mostly barren quartz-tourmaline veins with very minor amounts of scheelite, wolframite and cassiterite (Marks et al., 2013; Walter et al., 2016). These veins are related to Variscan magmatic activity (Marks et al., 2013) and their fluid chemistry and temperatures (< 550 °C) indicate a cooling of a magmatic fluid as major precipitation process (Marks et al., 2013; Walter et al., 2016). The Permian group (ii) comprises mainly very weakly mineralized Sb ± Ag ± Au-bearing quartz veins. Precipitation happened by cooling of a low salinity, high temperature late-Variscan metamorphic basement fluid (Staude et al., 2009 and references therein; Wagner and Cook, 2000). Veins from the Triassic-Jurassic boundary (iii) are barren quartz-chalcedony-hematite veins (Brander, 2000). Cooling of metamorphic low to high salinity fluids is probably the major precipitation process (Walter et al., 2016). The Jurassic-Cretaceous group (iv) contain variable modal amounts of fluorite, barite, quartz and carbonates with Ag-Bi-Co-Ni-U, Fe-Mn or Pb-Zn-Cu ores (e.g., Staude et al., 2009; Walter et al., 2019). Their formation is triggered by fluid mixing of a deep seated highly saline brine (20–28 wt% salinity), which mixed with also highly saline colder formation waters in extensional basin-related fault systems under presence of a redox agent (Staude et al., 2009; Fusswinkel et al., 2013, Walter et al., 2019). Since late-stage Cu mineralization is invariably associated with post-Cretaceous veins (v), we only focus on a detailed description of this mineralization stage (see Walter et al. (2016) for more details on mineralization stages i to iv).

During the Tertiary breakup of the Upper Rhinegraben rift and the associated strike-slip tectonics, numerous Upper Rhinegraben-parallel NE-SW to NNE-SSW-striking fault systems were reactivated or newly established. The hydrothermal veins of group (v) are related to these fault zones (Pfaff et al., 2009 and references therein; Staude et al. 2012b; and references therein) and were cyclically reactivated during active rifting. Commonly, the veins are characterized by large amounts of barite and quartz (Metz et al., 1957; Staude et al., 2009; Walter et al., 2018a, b). Only a minority of the veins contains also fluorite and various carbonates with Pb-Zn mineralization and, rarely in the sense of numbers of veins, As, U, Cu, Co, Bi and Ni mineralization (Staude et al., 2009; Walter et al., 2017a). The fluid chemistry of the rift related veins is highly variable (salinity 1–30 wt% NaCl + $CaCl_2$) and heterogeneous due to multi-component, multi-aquifer fluid mixing processes caused by a juxtaposition of different aquifers during Neogene rift tectonics (e.g. Walter et al., 2015, 2018a). In many veins, mineralogy changes with time (Metz et al., 1957), but the physico-chemical reasons for these

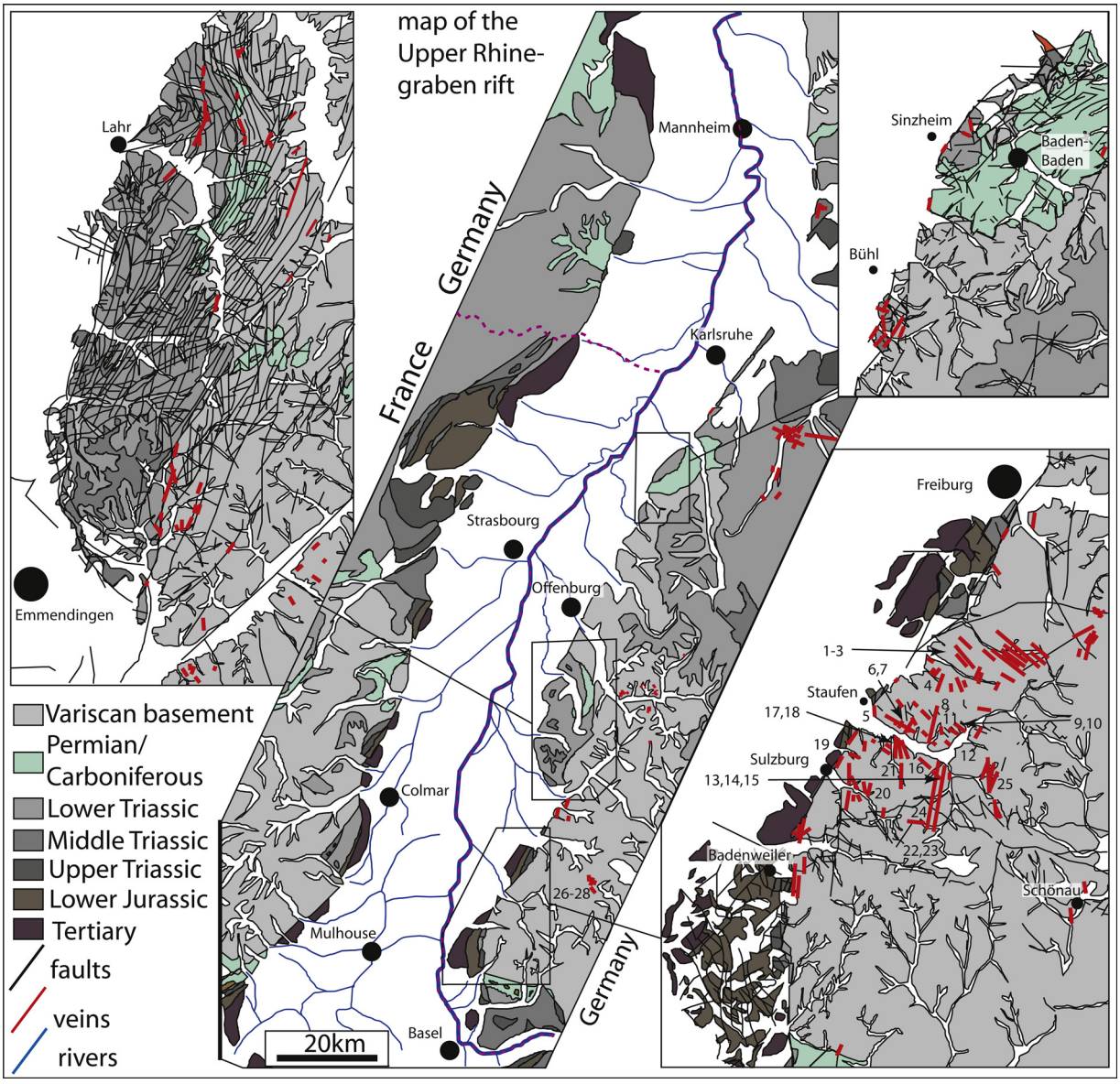

Fig. 1. Geological map of the Upper Rhinegraben modified after Walter et al. (2019); and references therein).

changes have never been investigated (Table 1).

Typically, the sequence starts with a silification of the host rock followed by a quartz-barite stage with galena and sphalerite ± fahlore. This stage may repeatedly crystallize several times. Subsequently, at many localities distinctively different mineral assemblages include native As ± NiAs mineralization, U-Bi-Co-Ni-Ag or Cu + Ni mineralization. In many cases, this stage is followed by a remobilization stage. The last mineralization stages (post-mineralization stages) are again more or less homogeneous and are characterized by barren sulfate-carbonate assemblages that document the transition from a deep to a shallow geothermal system which is still active today (Burisch et al., 2018). These barren sulfate-carbonate assemblages also post-date the chalcopyrite + gersdorffite + siderite mineralization stage of this contribution on several of the studied veins (Metz et al., 1957; Burisch et al., 2018; Walter et al., 2018a). In the following chapter, petrographic observations are presented in detail. Absolute ages of the veins (on siderite of the Cu-Ni mineralization stage) scatter between 4 and 20 Ma (with a few ages going back to 68 Ma) and hence indicate precipitation in Cenozoic times (Walter et al., 2018c).

2. Sample material and petrography

For this study, 54 samples from 28 hydrothermal veins were studied petrographically to obtain a paragenetic sequence (for details on the individual veins and the samples please see Table 2). It is important to note that the complete paragenetic sequence is only present in the larger veins like Riggenbach, Böschlisgrund, Süßenbrunn, Gabler vein and Knappengrund, while smaller veins exhibit an incomplete paragenetic sequence. Furthermore, in the veins Böschlisgrund and Riggenbach, the age-dated siderite texturally post-dates the typical Mesozoic Pb-Zn mineralization, but pre-dates the late-stage carbonate-sulfate assemblages investigated and age-dated by Burisch et al (2018).

All veins show an early silification of the host rock (mainly paragneisses, Fig. 2A, B), often associated with brecciation. Rock fragments are cemented by a second generation of quartz (chalcedony and hematite flakes) followed by crustiform chalcedony with anhedral pyrite (< 100 µm), arsenopyrite (Fig. 2B) and rare barite (Brt I).

Mineralization stage I starts with euhedral grains of pyrite II, arsenopyrite II, sphalerite I and galena I (all < 200 µm; Figs. 3–6B, C). Mineralization stage II begins with the precipitation of arsenopyrite II which only occurs associated with pyrite II (Fig. 6D, E, F) as small nests

Table 1
Types of veins and fluid signatures of the Schwarzwald ore district modified after Walter et al. (2016, 2017, 2018a, b, 2019) and Epp et al. (2019) and references therein.

group	age	mineralogy	mineralisation	structural position	age constraints	fluid type	salinity in wt% (NaCl + $CaCl_2$)	T_h in °C	Cl/Br mass ratio
i	Carboniferous	quartz-tourmaline	W-Sn	Spatially associated and genetically related to specific granites	U-Pb age of host granite	H_2O-NaCl ± (CO_2 ± CH_4)	0-4	100-400 °C	48-146
ii	Permian	quartz	Sb ± Ag ± Au	Only in basement rocks (granite and gneiss)	High fluid temperatures > 250 °C never reached again after Permian times by the SW German basement at shallow depths; comparison with very similar veins from the Taunus	H_2O-NaCl-KCl	< 5	100-320 °C	94
iii	Triassic-Jurassic	quartz-hematite	Fe	Only in basement rocks (granite and gneiss)	(U-Th)/He age UPbSSI ages, Sm-Nd ages	H_2O-NaCl-KCl & H_2O-NaCl-$CaCl_2$	0.7-3.3 & 23.3-25.8	120-230 °C	60-112
iv	Jurassic-Cretaceous	fluorite- quartz-barite barite-quartz	Pb-Zn-Cu-Ag & U-Bi-Co-Ni-Ag & Fe-Mn	From > 2000 m below the basement/ cover unconformity up to the boundary between Lower and Middle Triassic sediments	Rb-Sr and U-Pb age-dating, UPbSSI ages, Sm-Nd ages	H_2O-NaCl-$CaCl_2$	20-28	50-190 °C	49-824
v	post-Cretaceous	quartz-barite-fluorite, carbonate	Pb-Zn-Cu-Ag & Cu-Ni-Bi-Ag	Spatially closely associated with Upper Rhinegraben faults or tributary fault systems	Structural position on Rhinegraben-related faults, UPbSSI ages, Sm-Nd ages	H_2O-NaCl-$CaCl_2$ ± (SO_4 ± CO_2 ± HCO_3)	0-25	50-320 °C	2-144

(< 5 mm). Sphalerite I and galena I can be observed as anhedral to euhedral nests (< 1 cm) in quartz II with crystal sizes up to several cm. Rarely, chalcopyrite I (< 500 µm) overgrows galena I, sphalerite I and oscillatory zoned fahlore I (with sizes below 1 mm; Figs. 4C, 6 A). At Gabler Vein, Süßenbrunn, Rammelsbacher Eck and Schlossberg W and E, minor amounts of euhedral fluorite I occur (< 800 µm), but are often replaced by quartz II.

Mineralization stage III is dominated by sphalerite II, galena II and minor amounts of chalcopyrite II and fahlore II. Chalcopyrite III is very rare and only occurs at Wogenbrunn. The sequence is overgrown by massive and tabular barite II and very minor amounts of siderite III (only present at Felsenkeller). At Mooswaldsattel and Wogenbrunn, tiny hematite II flakes can be observed on the rims of euhedral siderite II and III crystals. Hence, this stage can also be summarized as a Pb-Zn mineralization stage.

An intense silification and replacement (Figs. 3A-H, 5 A, B) of the previous precipitates initiates mineralization stage IV (quartz II). Minor amounts of sphalerite III, galena III and fahlore III crystals can be observed at Finkerstal, Amalie near Grunern, Gabler Vein, Schlossberg E and W, Süßenbrunn and Riggenbach (Fig. 4A, B, D, E, F, H). However, at most locations, a massive chalcopyrite generation (< 30 cm thickness; Figs. 2C, D; 3 D, 4 A, B, D, F) directly overgrows euhedral pyrite III and gersdorffite crystals on top of quartz II (Fig. 6G, H). If present, sphalerite III, galena III and fahlore III crystals are also overgrown by pyrite III, gersdorffite and chalcopyrite (Fig. 6G, H). At Süßenbrunn, a second brecciation produces clasts of the older material (Figs. 2C, 3 G). Only at Süßenbrunn and Finkerstal, rare euhedral barite III and galena IV crystals were observed. Large quantities of pure siderite IV occur at the end of mineralization stage III and cements clasts of host rock and previous mineralization stages (Fig. 3E).

In mineralization stages V and VI, galena and sphalerite form tiny crystals in vugs (< 1 mm), but the modal amount of this Pb-Zn mineralization stages are negligible compared to stages I and II (Fig. 5E–H). At Süßenbrunn, a third brecciation event occurred between mineralization stage IV and V. The post-mineralization stage is only present in vugs of the older precipitates and is dominated by various generations of carbonates and sulfates, a fluorite generation and collomorph FeOOH aggregates. All these textural observations are summarized in the paragenetic sequence diagram of Fig. 7.

3. Methods

3.1. Electron microprobe

Electron microprobe analyses were performed on polished thin sections. After an optical texture analysis, the samples were carefully selected for their representative character. A JEOL SUPERPROBE JXA-8900RL at the Institute for Geosciences at the Eberhard Karls University Tübingen was used for wavelength dispersive analyses. Acceleration voltage was 25 kV and the beam current was set to 20 nA for sulfides and carbonates. The sulfides were analyzed with a focused beam. For major elements, the counting time was set to 16 s and 8 s on the peak and background, respectively, for minor elements to 30 s and 15 s. Natural and synthetic standards were used for calibration (ASTIMEX SCIENTIFIC LIMITED, Toronto, Canada; Micro-Analysis Consultants Limited, St. Ives, UK). The detection limits and standard deviations, given in the electronic supplement, were estimated as average based on all measurements. The Kβ line was used for Cu quantification on a LIF crystal, thus making it unnecessary to change the analyzing crystal during the measurements and hence to reduce measurement time. All routines were carefully checked for peak overlaps. No peak overlap corrections were necessary for the analyses performed. Details on the individual routines are presented in the electronic supplement. Data reduction was done for all routines using the internal ZAF matrix correction software of JEOL (Bence and Albee, 1968; Armstrong, 1991).

Table 2
Summary on the studied locations in SW Germany.

map	location	coordinates	Ore stage I	Ore stage II	Ore stage III	Ore stage IV	Ore stage V	Age in Ma	Th	salinity	LA-ICPMS on single FI	Microscopy (n = samples)	Mineral chemistry (this study)
1	Kirchengrund	47.881461 7.792658	X	X	XXX							1	x
2	Aschbächlekamm	47.884789 7.798478	X		XX							1	
3	Erzgründlekamm	47.888142 7.796139	X		XX							1	
4	Finkerstal	47.899134 7.771334	X	X	X			9.8 ± 0.56				1	
5	Felsenkeller	47°52'35.60 7°44'6.01	X		XX							3	x
6	Dietzelbach E	47.862638 7.767815	X	X	XX		X					1	x
7	Dietzelbach W	47.863674 7.767579	X	X	X				117-210	17.86-30.1		1	x
8	Riggenbach	47°51'52.6 7°46'54.03	X	X	XXX	X	X	8.7 ± 1.8	90-200	9.6-24.6	X	4	x
9	Hirzenbühl	47.870944 7.790496	X		X							1	
10	Mooswaldsattel	47.864769 7.788951	X		X							1	
11	Laisacker	47.858952 7.784402	X		X							1	
12	Breitmatt	47.859269 7.779960	X		X							1	
13	Süßenbrunn	47.839873 7.774253	X	X	XXX	X	X		102-153	26.8-30.7		3	x
14	Wogenbrunn	47.849178 7.772002	X		X							1	
15	Köpfle auf der Viehwiese	47.849911 7.781466	X		X							1	
16	Wildsbach S	47.851023 7.765435	X		X							2	
17	Karl Ausgust vein II	47.863079 7.752314	X	X	X	X	X					3	x
18	Karl Ausgust vein III	47.863079 7.752314	X		X							1	x
19	Amalie near Grunern	47.860654 7.717445	X	X	XX	X						2	x
20	Böschlisgrund	47°49'42.03 7°44'14.31	X		XXX			4 ± 5.7 68.4 ± 2.4	101-158	23.6-27.9	X	4	x
21	Kapuzinergrund/ Ludwig Heinrich near Kropbach	47.854567 7.743093	X		X							2	x
22	Schlossberg E	47.821571 7.774778	X		XXX							2	
23	Schlossberg W	47.821758 7.773689	X		XX				148-153	2.3-23.1		2	
24	Große Gabel	47.833960 7.778343	X		XXX							3	x
25	Knappengrund	47.841729 7.824541	X		X				138-230	10.7-18.2		2	x
26	Silbereck	47°53'39.97 7°57'21.05	X		X			14 ± 11 20 ± 8.3 28 ± 16	147-338	1.6-4.1		3	x
27	Fuchsdobel	47°53'43.43 7°57'15.19	X		X			21.9 ± 4.9 32.3 ± 2 34 ± 4.7	111-354	1.6-22.7		3	
28	Katzensteig	47.888405 7.957728	X		X				93-146	19.9-20.3		3	

3.2. Confocal microraman spectroscopy

Raman micro spectroscopy measurements were done on single aqueous two-phase fluid inclusions of representative fluid inclusion assemblages in the selected veins with a confocal Raman spectrometer Renishaw InVia Reflex at the Eberhard Karls University of Tübingen to identify invisible volatile phases, solid phases, and dissolved polyatomic ions (e.g. carbonate, sulfate). Fluid inclusion textures, assemblages and analyses of the samples were previously published in Walter et al. (2017b, 2018, 2019) and are therefore not repeated here. A laser wavelength of 532 nm (green) was used with a laser output energy of 10–50 % for all analyses. The use of a 50x objective causes a numerical aperture of 0.55 with an opening angle of 66.7°. The correction and regulation of the slit diaphragm was done automatically. The focus diameter was approximately 3–5 μm, the measurement time was 50 s with six accumulations. For matrix Raman band identification, analyses of the host mineral were done under identical crystal orientations and conditions. For larger inclusions (> 50 μm), liquid and vapor analyses were done separately to identify species in the liquid and vapor phase. The Raman database for fluid inclusions of Frezzotti et al. (2012) was

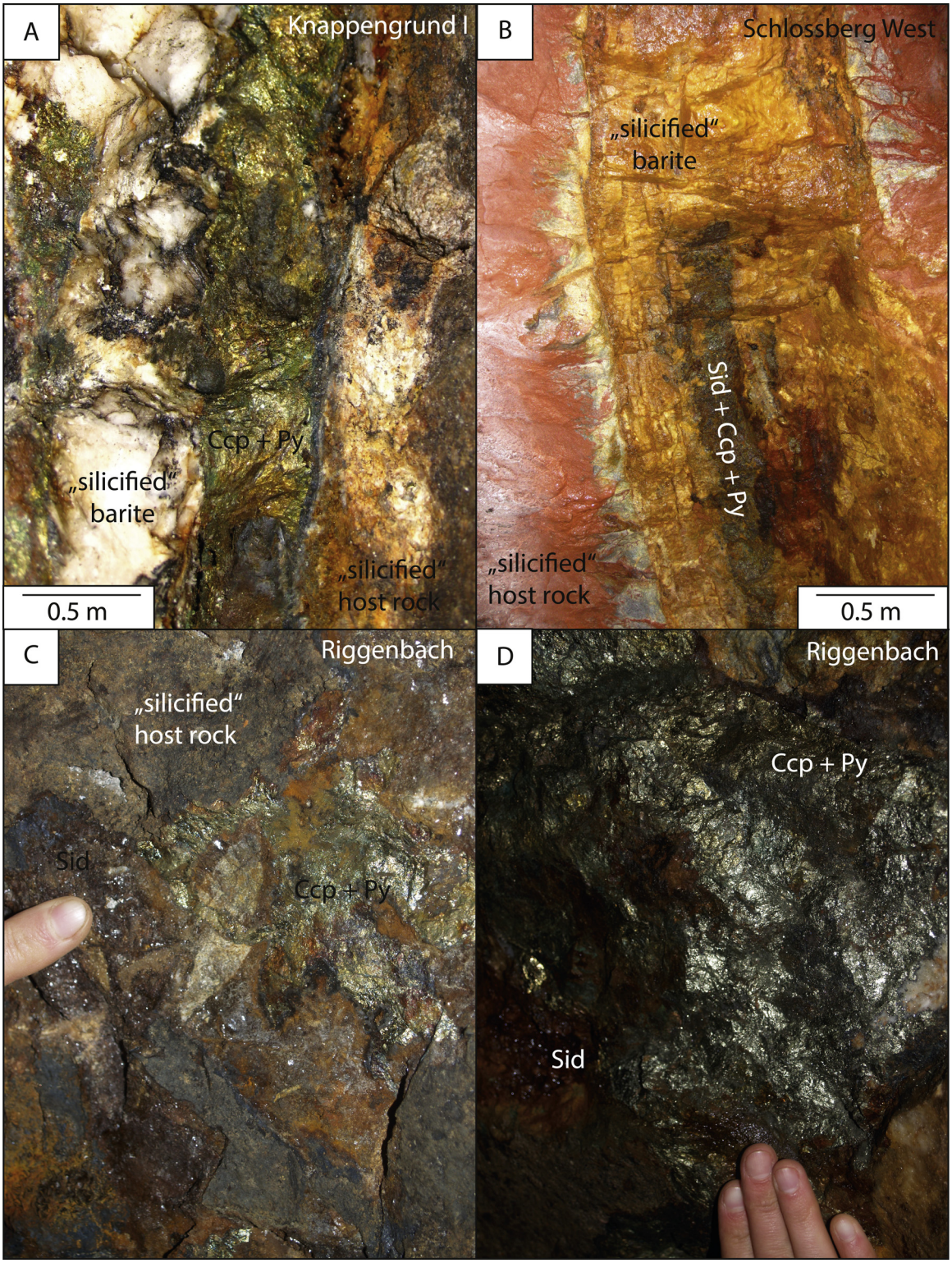

Fig. 2. A–D) Outcrop pictures from the Knappengrund I vein (photo by S. Staude), the Schlossberg West mine (photo by S. Staude) and the Riggenbach mine.

used for qualitative phase discrimination.

3.3. Cathodoluminescence microscopy

Cathodoluminescence microscopy (CL) of the gangue and associated sulfide minerals was done to assist the optical petrography and to obtain detailed textural information on the petrographic relationship and relative timing of the investigated phases (e.g. Kolchugin et al., 2016; Walter et al., 2018a, 2018b; Kreissl et al., 2018). For imaging, a 'hot cathode' CL microscope (type HC1-LM) at the University of Tübingen was used with an average acceleration voltage of ~14 kV and a beam current density of approximately 9 μA mm-2.

3.4. Thermodynamic calculations

Thermodynamic modeling was done using The Geochemist's

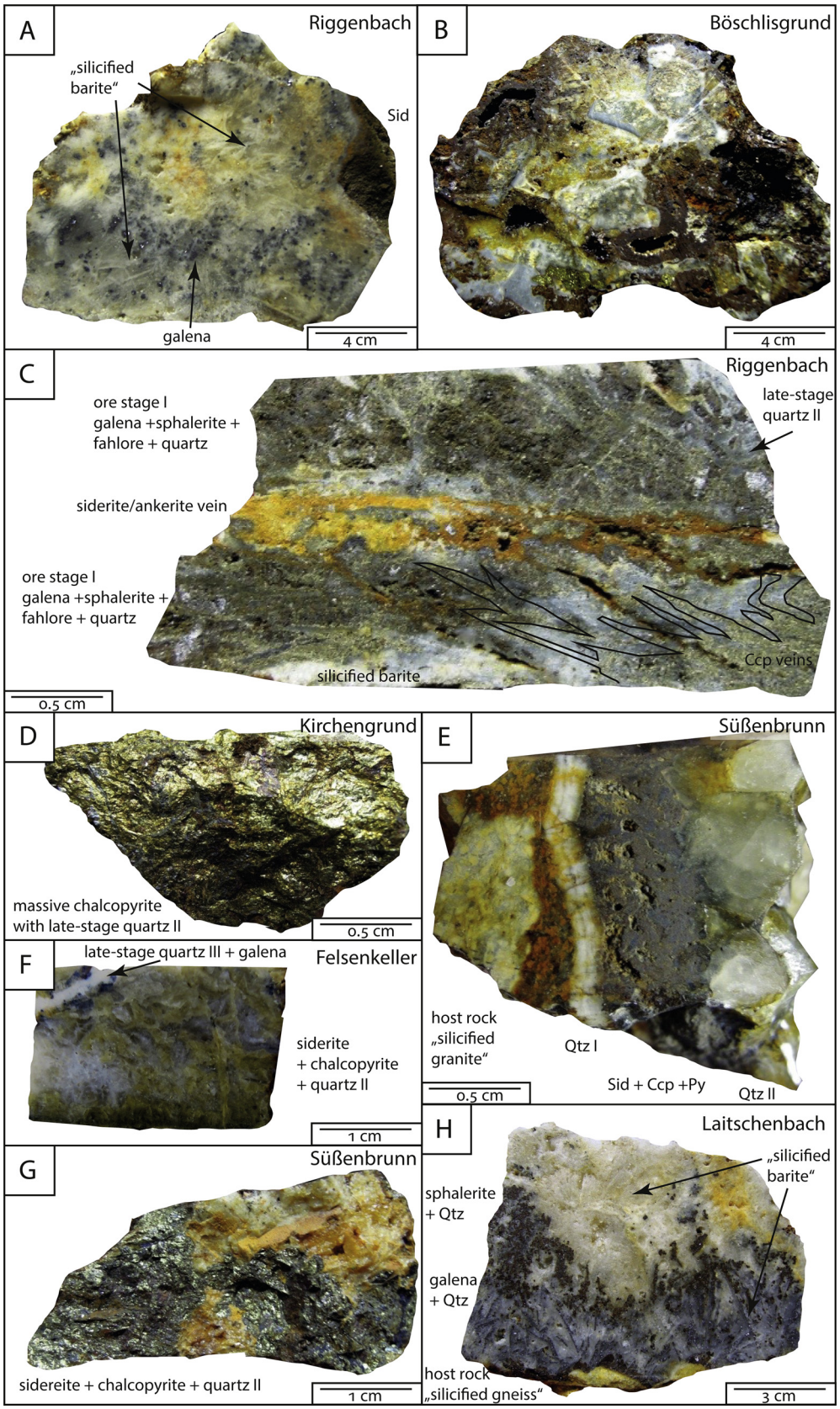

Fig. 3. A) Sample from Riggenbach mine containing silificated barite, galena and sphalerite of mineralization stage I. B). Sample from Böschlisgrund contains chalcopyrite and quartz of mineralization stage III, which is overgrown by siderite (partly altered to FeOOH-phases). C) Sample from Riggenbach shows the mineralization stage I assemblage which is penetrated by mineralization stage III veins. D) Sample from Riggenbach contains massive pyrite-chalcopyrite aggregates. E) At the Süßenbrunn vein, a late stage euhedral quartz generation overgrows mineralization stage III siderite. F) A mineralization stage IV vein crosscuts the mineralization stage III assemblages in the Felsenkeller vein. G) At Süßenbrunn, massive chalcopyrite crosscut silificated barite and is overgrown by late stage quartz. H) The Laitschenbach vein shows a massive silification of barite. Note pseudomorphic replacement of quartz by galena.

Workbench 12® (Bethke, 2007) software package including the pre-implemented thermos.tdat thermodynamic database. The application Phase2 and P2plot were used to produce solubility diagrams (which depict the mineral stability in contrast to the more common approach of mineral predominance), due to the significantly different topology between the stability boundary and the predominance boundary. It was the aim to discuss stability regions of minerals during fluid mixing. If not noted otherwise, all calculations were done at a temperature of

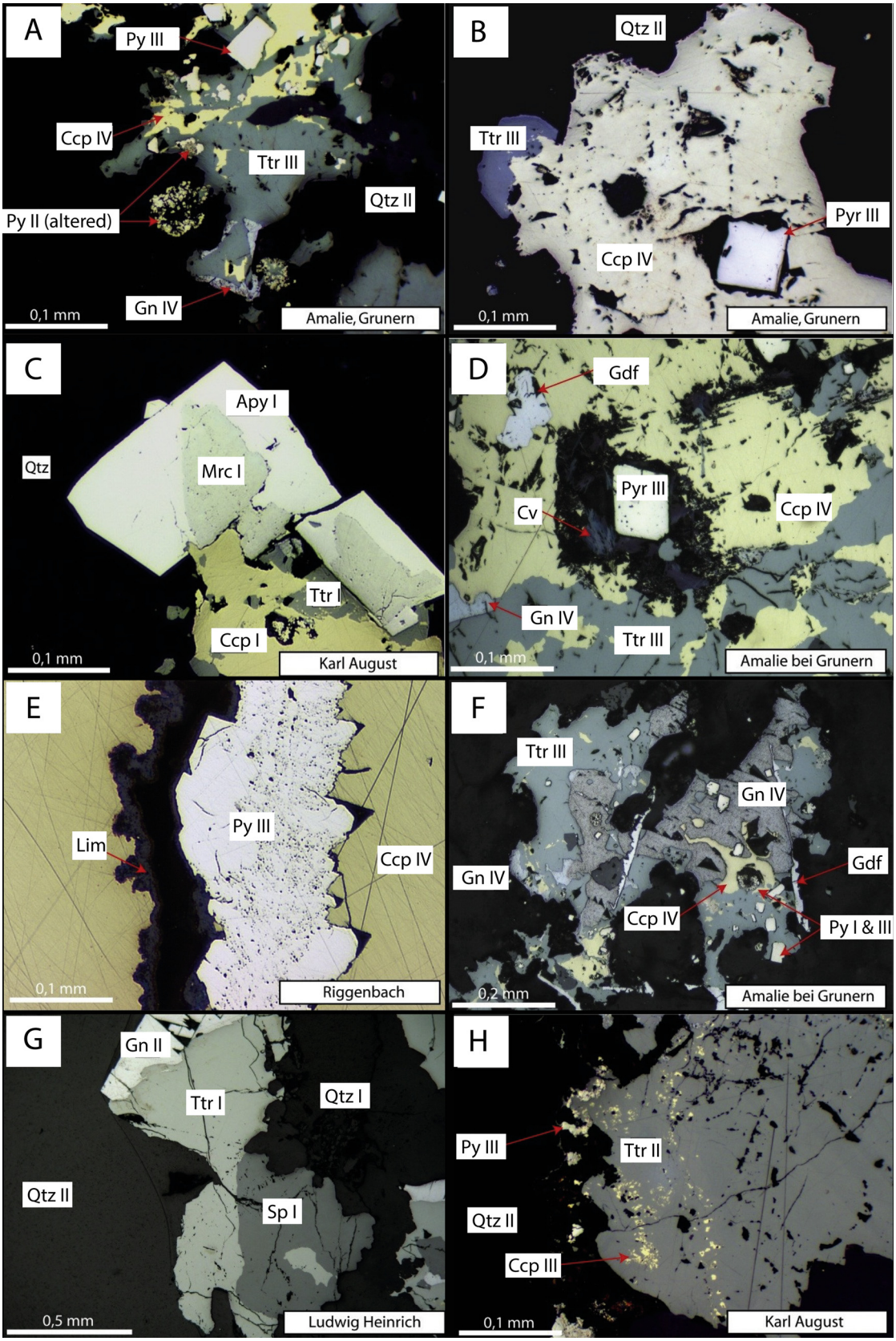

Fig. 4. A) Anhedral pyrite II is partly dissolved. Euhedral pyrite III is overgrown by fahlore III and chalcopyrite IV. B) Euhedral pyrite III is overgrown by zoned fahlore III and quartz II. C) Chalcopyrite I and fahlore I is overgrown by marcasite and arsenopyrite. D) Pyrite III shows overgrows of chalcopyrite IV, fahlore III and galena IV. E) Massive zoned pyrite aggregates show overgrows by large aggregates of unzoned chalcopyrite IV. F) Pyrite I and III is overgrown by chalcopyrite IV, galena IV and fahlore III. G) Quartz I is overgrown by sphalerite I which is followed by fahlore I and galena II. Quartz II overgrows all previous assemblages. H) Fahlore II occasionally show chalcopyrite disease.

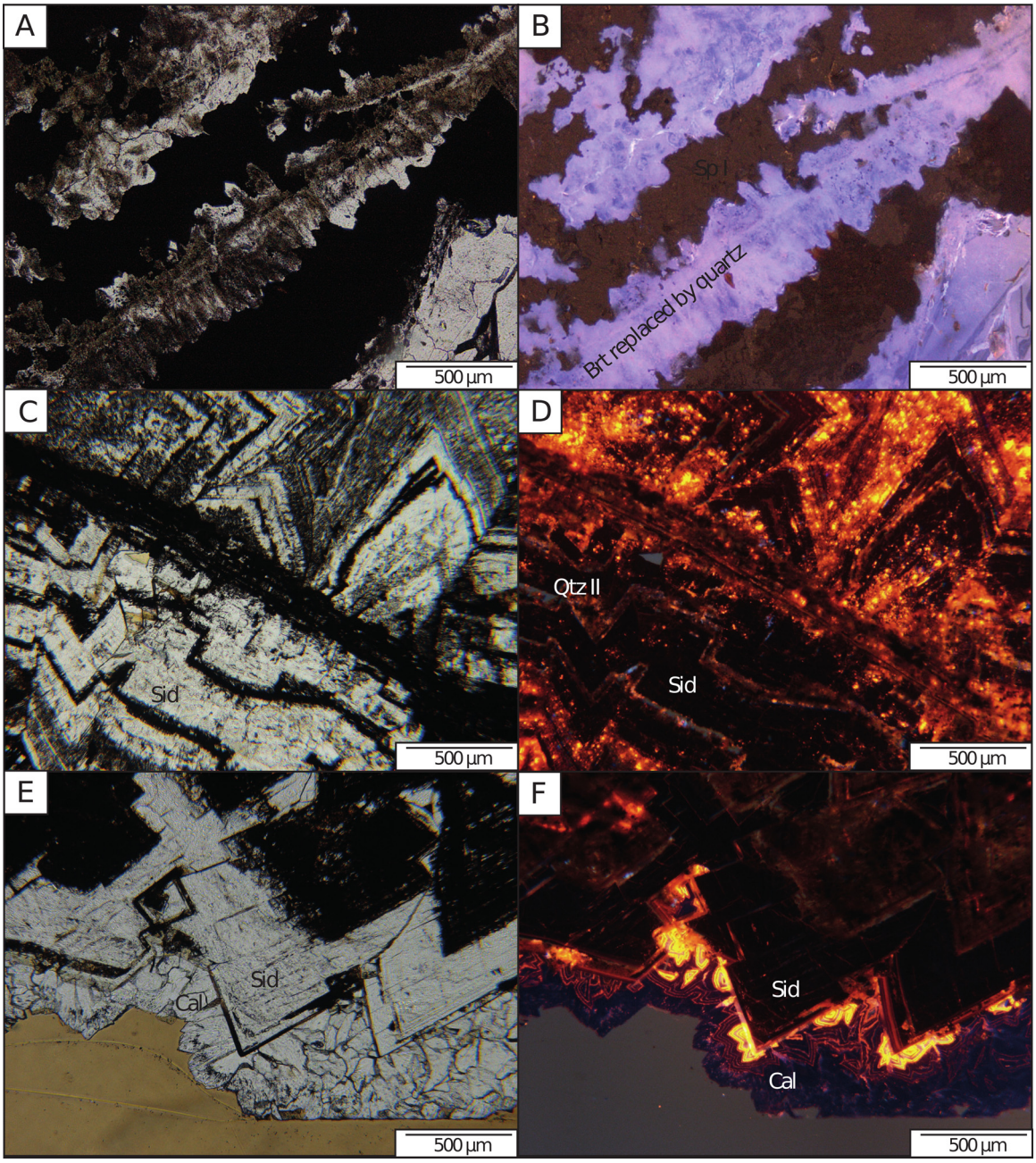

Fig. 5. A and B) Optical microscopy and CL image is illustrating barite plates replaced by quartz and a perimorphic overgrowth of sphalerite in mineralization stage I. C and D) Optical microscopy and CL image illustrating complex zoning in some of late siderite assemblages. E and F) Optical microscopy and CL image showing overgrowth of the siderite by late-stage carbonates.

150 °C and a salinity of 20eq wt.% (NaCl + $CaCl_2$) with a molar ratio of 1:1, which is in good agreement with fluid compositions reported in Walter et al. (2018a; 2018b). The ore formation model, among others, consists of a sulfide influx into a metal-bearing solution. Due to the vast difference in solubility of the involved transition metals between a sulfur free and a sulfur bearing solution, this variation has been considered in our calculations. For quantification of the sulfur-free system, the charge balance was obtained by Na^+ to maintain constant Cl activities, since they would affect calculated base metal sulfide solubilities. Elemental concentrations (presented for each model in the top left corner of the diagram) were selected to best represent the fluids according to literature data and fluid inclusion data from Walter et al (2018a) and thermodynamic constraints stated in the discussion. Minerals considered in the thermodynamic calculations are: bornite, chalcocite, chalcopyrite, cuprite, hematite, magnetite, native Cu, pyrite, tenorite and wüstite. It should be noted that the thermodynamic models are only a rough order of magnitude estimation, as the ionic strengths exceed the boundaries of the Expanded Debye Hückel coefficients implemented in GWB.

4. Results

4.1. Mineral chemistry

In the following sections, mineral compositions are presented in alphabetical order. The individual analyses are presented in the electronic supplement (ES).

4.1.1. Arsenopyrite

Arsenopyrite of mineralization stage I was analyzed on 21 spots in 3

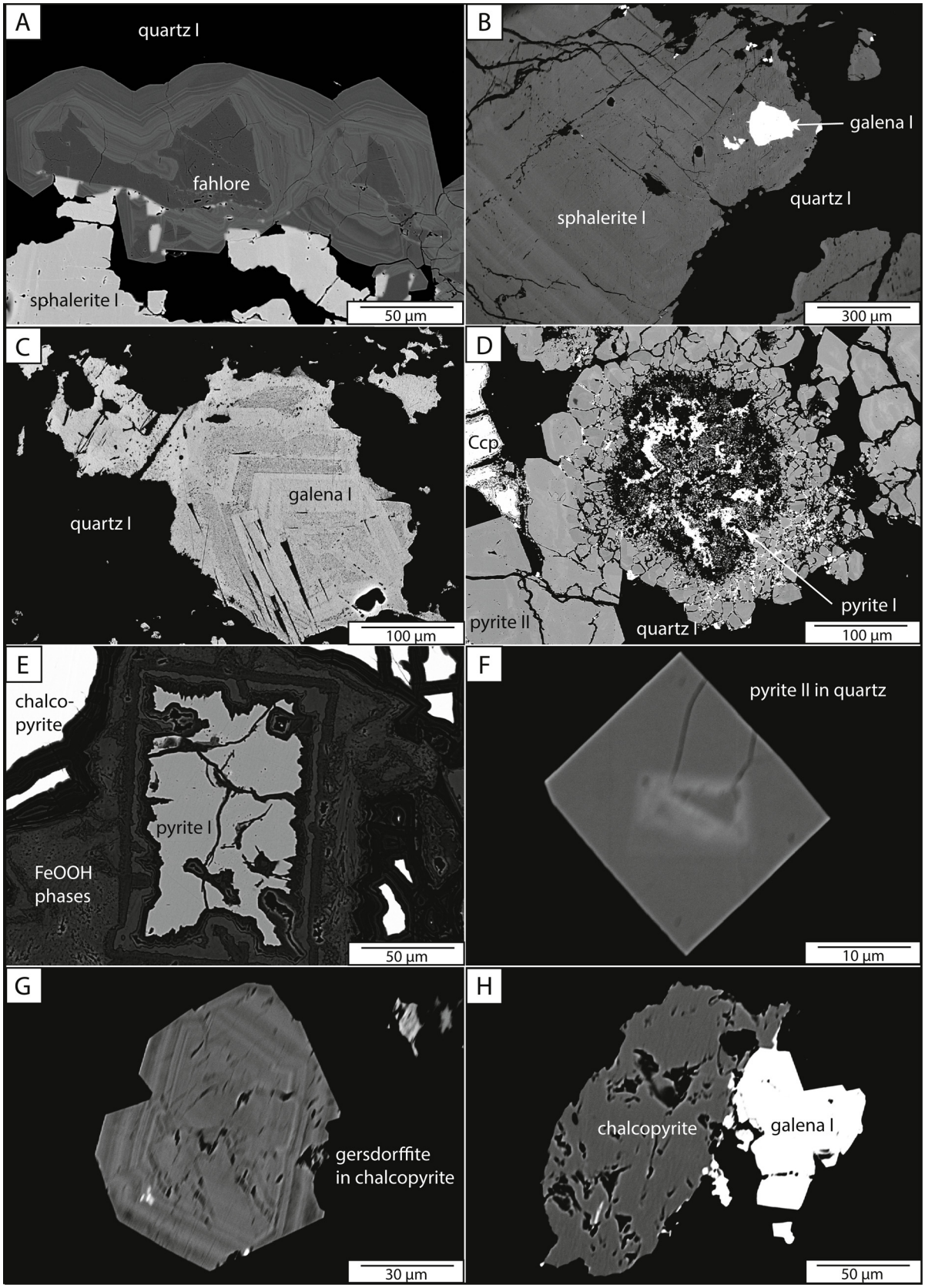

Fig. 6. BSE images (COMPO mode) for A) Sphalerite I, fahlore I and quartz I. B) Galena I which is overgrown by sphalerite I. C) Complex zoned galena I which is overgrown by quartz I. D) Pyrite I is partly resorbed and overgrown by pyrite III. Massive chalcopyrite IV overgrows pyrite III. E) Often pyrite I is altered to FeOOH phases along cracks. F) Rare euhedral pyrite II in quartz typically contain zoning. G) Gersdorffite typically shows an oscillatory zoning. H) Galena I is overgrown by aggregates of chalcopyrite II.

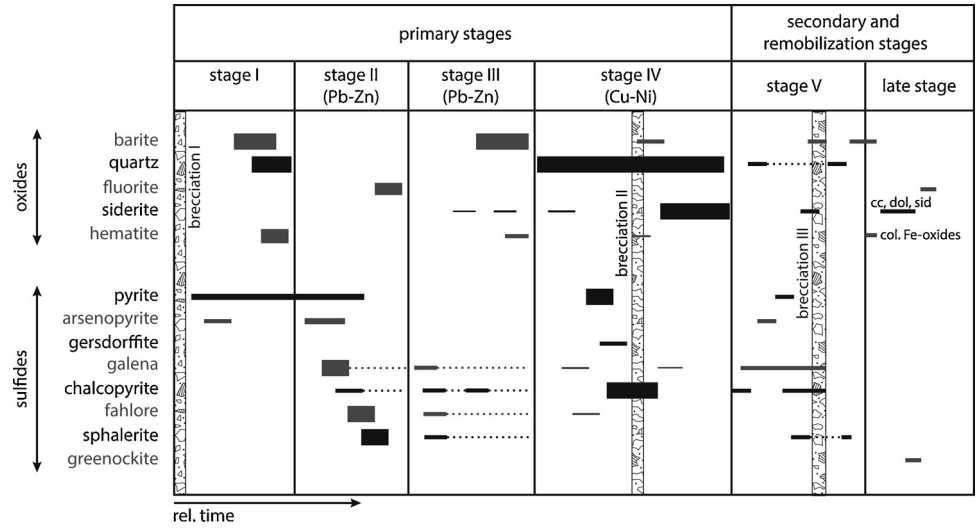

Fig. 7. The paragenetic sequence summarizes all textural observations.

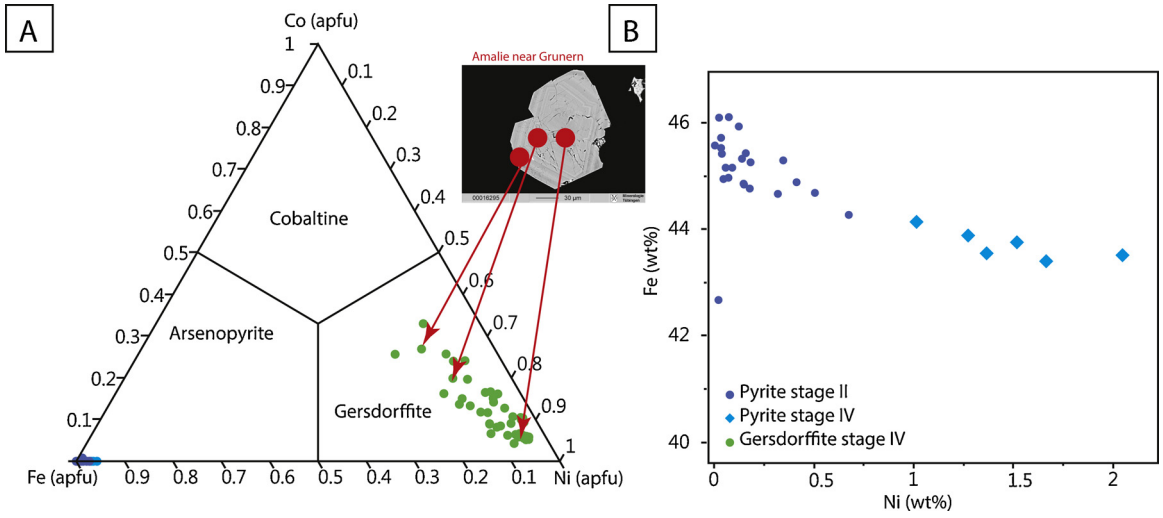

Fig. 8. A) Figure is illustrating the chemical evolution of the gersdorffites which are exclusively present in mineralization stage III. B) Figure is illustrating the mineral chemical evolution of pyrite between stage II and IV.

samples (BO66b, BO76, BO59A). On average a formula of $(Fe_{1.01}As_{0.92}Sb_{0.02})S_{1.05}$ can be calculated (Fig. 8). Moreover, trace element concentrations of Bi (up to 900 mg/kg), Hg (up to 880 mg/kg), Zn (up to 1100 mg/kg), Cu (up to 2350 mg/kg), Ni (up to 500 mg/kg) und Au (up to 560 mg/kg) were recognized. Ag is always below detection limit. All analyses show significant Sb and Se incorporation up to 5 wt% and 2060 mg/kg, respectively.

4.1.2. Fahlore

The mineral chemistry of fahlore was investigated with 100 analyses in 14 samples from 11 veins (Fig. 9). The analyzed compositions resulted in an average formula of $(Cu_{5.06}Ag_{0.85})Cu_4(Fe_{0.70}Zn_{1.33})[(Sb_{2.47}As_{1.58})S_{13}]$. Almost all analyses bear Se-contents up to 1200 mg/kg. Exceptional analyses contain Co up to 190 mg/kg and Au below 820 mg/kg. Furthermore, some analyses show Hg-concentrations up to 1300 mg/kg whereas Bi is variable between b.d.l. (below detection limit) and 1780 mg/kg. Ag and Sb are enriched in mineralization stage I fahlores. In contrast, mineralization stage III fahlores show a higher As-, Au- and Se-concentration. All analyses form a solid solution series between the tennantite and tetraedrite endmember compositions, but mineralization stage III fahlores form a significant wider compositional range and mineralization stage I fahlores (Fig. 9A, B). Cu is enriched in fahlores of mineralization stage III (Fig. 9B).

4.1.3. Galena

Galena was studied in 14 samples from 12 veins with 172 analyses (Fig. 10). The average formula is $Pb_{0.99}S_{0.99}$. With a few exceptions, Fe was above detection limit with concentrations up to 840 mg/kg. Commonly, Ag and Sb are also above detection limit with concentrations up to 1.5 wt.% and 1.7 wt%, respectively. Rarely, Hg (< 1740 mg/kg) and Tl (< 4890 mg/kg) were detected. Only in one sample each, As (BO66) and Bi (BO43) were significantly above detection limit (< 1230 mg/kg; < 1.04 wt%). The most significant difference between mineralization stage I (core) and mineralization stage I (rim)/core stage III galena is an enrichment of Ag and Sb and a depletion in Hg in mineralization stage I (core areas).

4.1.4. Gersdorffite

Gersdorffite (only present in mineralization stage III) was analyzed in 4 samples comprising 43 analyses (Fig. 8A). All analyses plot in the gersdorffite field of Fig. 8A with a chemical evolution towards higher Co and Fe concentrations. The average formula is $(Ni_{0.80}Co_{0.13}Fe_{0.08})As_{0.96}S_{1.02}$. In all analyses, Se was above detection limit with up 2420 mg/kg. With the exception of two measurements, Sb

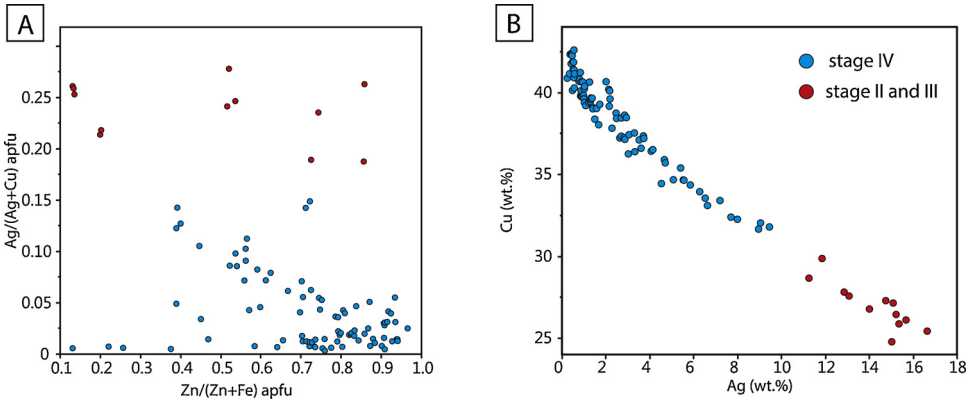

Fig. 9. A) Image is showing a trend towards Zn and Fe enrichment in mineralization stage IV. D) Fahlores in mineralization stage IV show a clear enrichment in Cu compared to those of mineralization stage II.

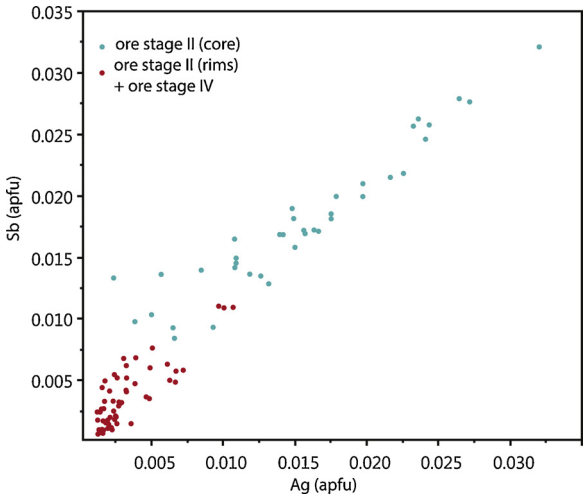

Fig. 10. Figure shows a clear depletion in mineralization stage IV in Sb and Ag.

was detected with concentrations up 8500 mg/kg. Furthermore, in about half of the data, a significant amount of Bi (< 1.76 wt%) was recognized. However, only in a few analyses Au (< 600 mg/kg), Ag (< 1260 mg/kg), Hg (< 850 mg/kg), Zn (< 700 mg/kg) und Cu (< 8850 mg/kg) were detected.

4.1.5. Pyrite

Pyrite was analyzed in 15 samples from 9 veins comprising crystals of mineralization stages I and III (Fig. 8B). The average formula is $(Fe_{0.98}As_{0.01}Cu_{0.01})S_2$ for both mineralization stages, the pyrite compositions show only minor variability. The major difference is the Ni-content with < 1 wt.% in mineralization stage I pyrites and between 1 and 2.05 wt% in mineralization stage III (Fig. 8B). One third of the analyses in both mineralization stages contain Cu and Sb-concentrations up to 1.33 wt.% and 1.21 wt.%, respectively. In about two thirds of the measurements, variable As-contents up to 4.11 wt.% were detected. However, only in a few analyses Bi (< 1300 mg/kg), Ag (< 8300 mg/kg), Se (< 510 mg/kg), Hg (< 970 mg/kg) and Zn (< 1500 mg/kg) were above detection limit. Au was invariably below detection limit.

4.1.6. Sphalerite

Sphalerite of mineralization stages I and III was analyzed 145 times in 12 samples from 10 veins (Fig. 11). The average formula is $(Zn_{0.93}Fe_{0.06})S_{1.00}$. Rarely Mn (< 230 mg/kg), Cl (< 690 mg/kg), As (< 4210 mg/kg), Ag (< 3210 mg/kg), Sb (< 1.02 wt.-%) and Cu (< 2.02 wt.-%) were above the detection limit. More common, Cd was

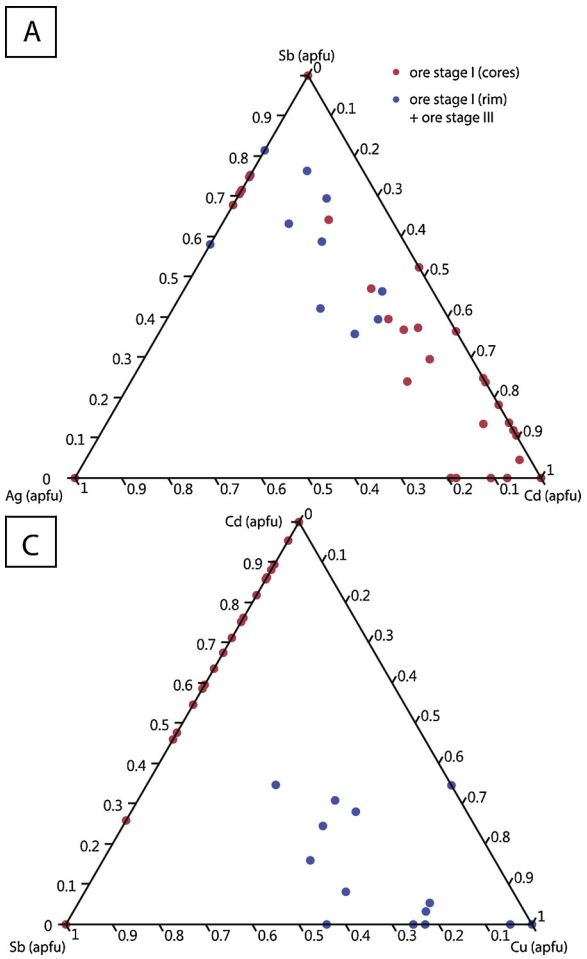

Fig. 11. A) No significant variation between Sb, Ag and Cd is visible whereas in B) a clear enrichment of Cu in mineralization stage IV sphalerite can be seen in sphalerite of stage II are depleted in Cu but enriched in As and Ag.

detected with concentrations up to 1.7 wt.%. Mineralization stage I sphalerite shows a higher Fe-content whereas Ag and Sb are enriched in mineralization stage III sphalerites (Fig. 11A, B). The zoning of the sphalerite in BSE images is mainly related to variable Fe-concentrations. Fig. 11B shows a relative enrichment of Cu in mineralization stage III sphalerites.

4.1.7. Chalcopyrite

Chalcopyrite was analyzed 54 times in 11 samples. However, no

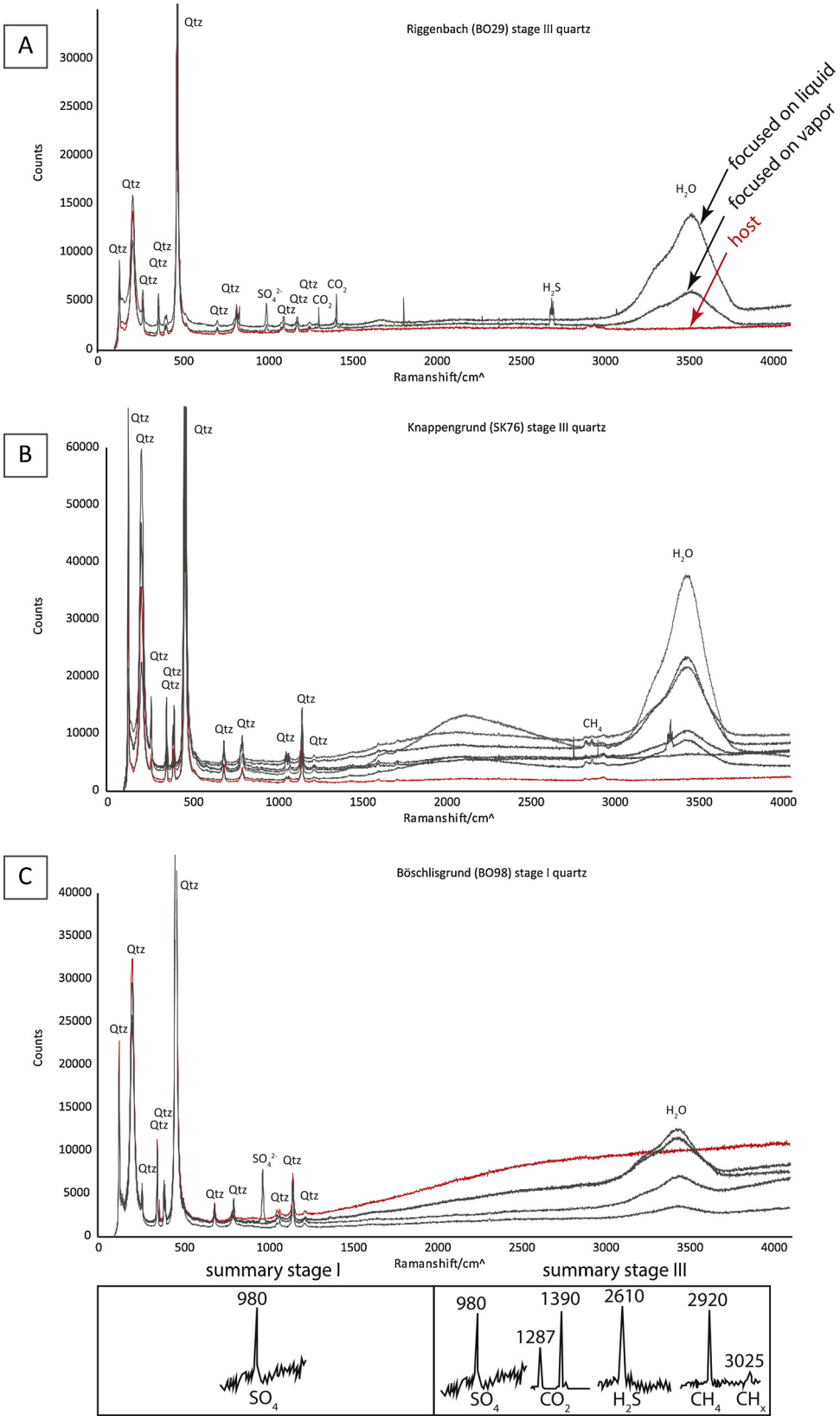

Fig. 12. A) Raman spectra of a Riggenbach sample shows SO_4^{2-}, CO_2 and H_2S bands in the fluid inclusions. B) In fluid inclusions of the Knappengrund I mine, CH_4 was detected whereas at Böschlisgrund C) SO_4^{2-} without CO_2 and H_2S bands was detected.

variation on the mineral chemistry was observed. Only in three analyses As and Zn was above detection limit.

4.2. Confocal microraman spectroscopy

Primary and secondary fluid inclusions from quartz crystals of the (Pb + Zn) mineralization stages (from Riggenbach, Böschlisgrund, Süßenbrunn, Karl August mine, Knappengrund and Gabler vein) contain only H_2O and rarely CH_4. According to Raman results, FI of all FIAs in siderite host no volatiles other than H_2O. However, primary and secondary quartz hosted fluid inclusions of the Cu-Ni stage commonly contain SO_4^{2-} at 980 cm^{-1} and H_2S at 2611 cm^{-1} (Fig. 12A–C), in addition to characteristic Raman bands of quartz (e.g. Frezzotti et al., 2012). In some rare cases, bands at 1387 cm^{-1} and 1284 cm^{-1} record CO_2 in the vapor phase (Fig. 12A; Frezzotti et al., 2012).

5. Discussion

5.1. Interpretation of mineral chemistry and mineralogy

Post-Cretaceous base metal mineralization comprises three stages with base metal sulfides (II, III and IV). Although all stages contain the same sulfide minerals, they show distinct differences in their modal abundance within each stage. Since the overall systematic of each stage is recurring, it is most likely that each stage reflects one distinct fluid mixing event (Burisch et al., 2016a, 2018). A successive decrease of the amount of galena and sphalerite from stage II to IV indicates a gradual temporal evolution (e.g. systematic variations in fluid mixing ratios), but on the other hand, the sudden occurrence of large quantities of chalcopyrite at the beginning of stage IV marks an abrupt change in this evolutionary trend. The high amount of chalcopyrite indicates an increase in Cu + activity, which is further supported by an increase of Cu content in fahlore, sphalerite and pyrite from stage II to IV. Small amounts of gersdorffite may indicate an increase in the Ni activity, but also changes in fO_2 could cause gersdorffite precipitation (Markl et al., 2016). Higher Ni contents in pyrite related to stage IV compared to pyrite of stage II, however, are an argument for an increase in the absolute Ni concentration of the fluid in stage IV. Gersdorffite composition shows a systematic trend from Ni-rich cores towards Co-richer rims. This trend from Ni to Co is known from many Ni-Co-Fe-arsenide occurrences (Markl et al., 2016; Burisch et al., 2017; Kreissl et al., 2018), although the underlying reason remains unconstrained.

Silver and Sb become successively depleted in fahlore and galena from stage II to IV. Previous studies from the Schwarzwald area show, that these elements are enriched in the basement fluid, while they are depleted (or even absent) in the sedimentary fluids of that region (Pfaff et al., 2009, Staude et al., 2012a). Consequently, their absence in stage IV minerals may indicate a lower proportion of basement fluid involved in the mixing process.

5.2. Formation conditions of the chalcopyrite-siderite stage

Fluid inclusions help to constrain fluid compositions and thereby the aquifers involved in mixing. Walter et al. (2018) reported variably high salinities (10–25 wt.% NaCl + $CaCl_2$) and variable homogenization temperatures between 50 and 230 °C of the fluids, which is within the range of all overserved post-Cretaceous veins of the district (Walter et al., 2016). Low Cl/Br ratios and high concentrations of Pb and Zn in primary fluid inclusions related to the Cu-stage indicates the involvement of basement brines (data taken from Walter et al., 2018a). However, Burisch et al (2018) could demonstrate that such basement brines were no longer involved in late stage carbonate-sulfate assemblages, which follow the Cu-stage (Fig. 13A, B, C). The general absence of sulfur in these fluid inclusions (only 5% of all analyses show S above the detection limit, which is interpreted as an artefact by contamination, Fig. 13B) in combination with the absence of barite and a low Cl/Br mass ratio is interpreted to show the lack of involvement of a sulfate-rich fluid reservoir (such as the evaporitic Middle Triassic Muschelkalk). This observation probably indicates that the Muschelkalk strata were already eroded at the time of mineralization. The massive occurrence of chalcopyrite in stage IV and high Cu in associated fluid inclusions (Walter et al., 2018b) indicates a drastic change in the metal budget of the ore fluid composition. However, the successive increasing Cu and Ni enrichment in stage IV indicates no sudden change, but rather a continuous transition of the involved fluid systems.

5.3. Genesis of chalcopyrite-siderite stage at low sulfur activities

Besides mineralogical and mineral chemical arguments, the presence of up to 1000 mg/kg Cu (∅ 140 mg/kg) in fluid inclusions related to Cu-rich stage IV (Walter et al., 2018a) indicates a significant change in fluid composition. The analyzed fluid inclusions capture fluids after the mixing process and therefore reflect mixtures of at least two fluid components. Copper and Ni concentration in fluids related to stage III are significantly higher than those in the Pb-Zn-Ag-rich basement fluid, which has been captured in fluid inclusions related to stage II and III (Walter et al., 2018a, 2019). This indicates that substantial Cu and Ni are mainly introduced by the sedimentary fluid. Still, the ore fluid of stage IV contains a significant basement component, and thus, Pb, Zn and Ba are also present in significant quantities. If this sedimentary fluid would have also contained significant amounts of sulfur – such as the sedimentary fluid involved in stage I-III – galena, sphalerite and barite should precipitate along with the chalcopyrite. This is, however, not the case. For the given metal concentrations, chalcopyrite has a significantly lower solubility at low sulfur concentrations compared to galena and sphalerite (see Fig. 14/Blanc et al., 2012). Consequently, mixing of a basement fluid with a fluid with anomalously low sulfur (and high Cu) concentrations could initiate chalcopyrite precipitation, while other base metals remain in solution. Sulfur concentrations below detection limit in stage IV fluid inclusions and the absence of barite during chalcopyrite precipitation further support that assumption.

Besides S and Cu, Fe is another important factor that must be considered, since thermodynamic computations reveal, that the observed paragenetic sequence (pyrite - pyrite + chalcopyrite – chalcopyrite) requires a systematic increase of the Cu/Fe ratio of the fluid. Fluid inclusions reported by Walter et al. (2018a) show very high Cu and Fe concentrations (1–1000 and 100–5000 mg/kg, respectively). Such high amounts of Fe and Cu in the fluid require slightly acidic and relatively reduced conditions, as the solubility of hematite and native copper would limit metal mobilities under reducing conditions. Furthermore, magnetite would prohibit high Fe concentrations in the fluid at more neutral and basic pH (Fig. 14A); the pH of natural aquifers of SW Germany are in the range of 5–8 (Fig. 14A; Sanjuan et al., 2016; Stober and Bucher, 2004; Pauwels et al., 1993; Göb et al., 2013) and therefore, moderate pH conditions seem reasonable. The presence of CH_4 in some fluid inclusions (Fig. 14A) supports the reducing character of the ore fluid. This in combination with the neutral pH being at ca. 6.8 at 150 °C and the pH-fO_2 constraints by Cu and Fe in solution allows us to assume a realistic initial pH of ca. 5 and an initial logfO_2 of ca. -50, before sulfide influx.

A fluid with abundant Cu and Fe (as indicated by fluid inclusion analyses) in a reduced environment with sufficient sulfide does not form the typically observed pyrite to chalcopyrite sequence, but a bornite- and chalcocite-dominated mineralogy (Fig. 14B). This sequence is largely independent of the initial pH of the fluid as a decrease in initial pH from 5 to 3 only increases the required amount of sulfur but does not affect the overall paragenetic sequence. To reproduce the observed mineralogy in a geochemical model, a successive titration of a Cu-rich into an Fe-dominated fluid (Fe/Cu > ca. 1000) is necessary (see Fig. 14B). Based on this consideration, Fe and Cu have to be introduced by different fluids. This assumption includes that linear

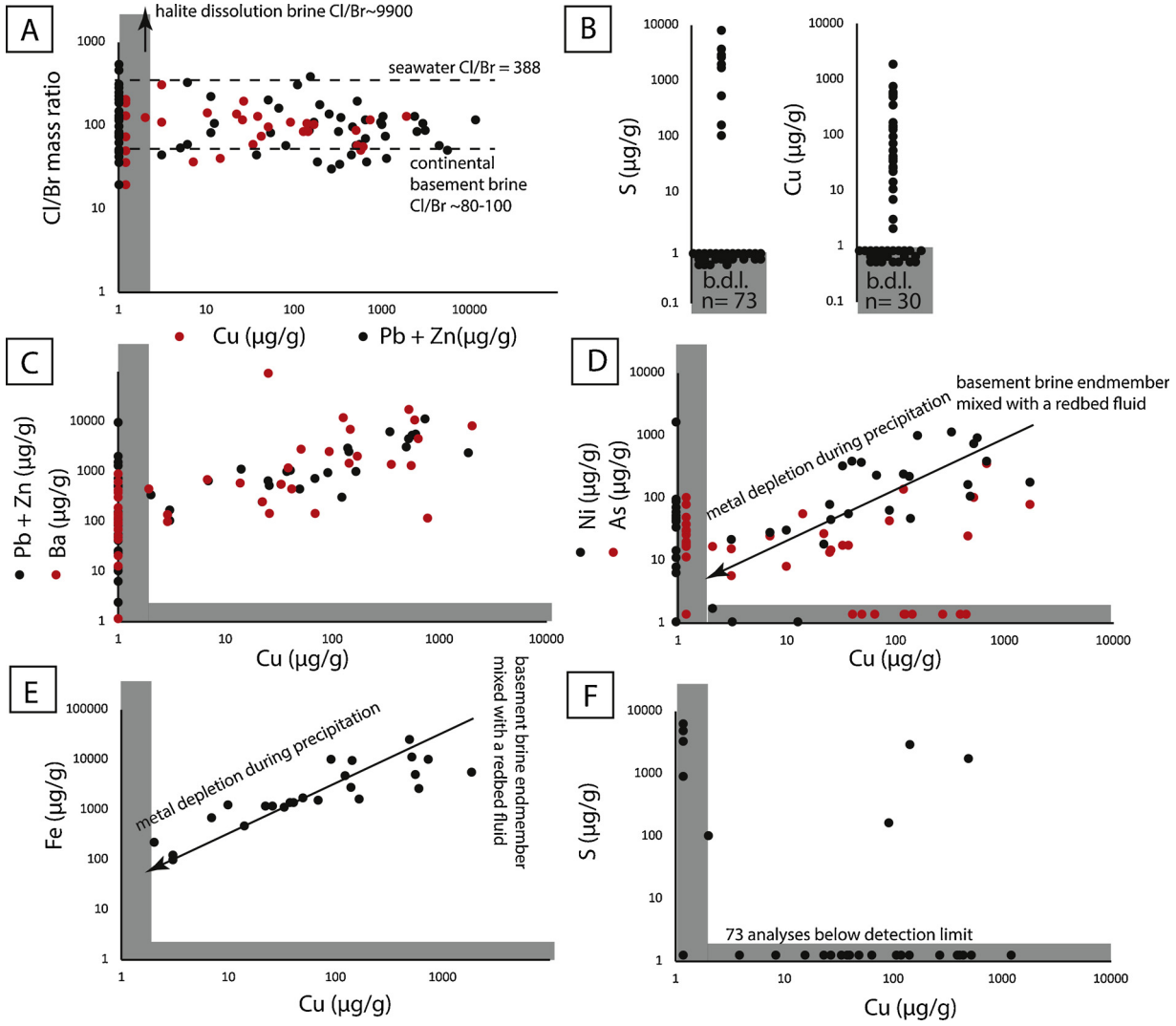

Fig. 13. Fluid inclusion data taken from Walter et al. (2018a). A) Cl/Br versus Cu and Ni + Zn content of the fluid showing a scatter in the same interval. B) Content of S and Cu. Note the majority of the analyses are below detection limit for S. The analyses above detection limit are interpreted as contaminated because of a slight shift between the Na, Cl and S signals. C) Pb + Zn and Ba content versus Cu indicate a common source of Ba and Pb + Zn. D) Ni and As versus Cu plot illustrates metal depletion during precipitation. E) Same argumentation fits for Fe. F) Less than 5% of the analyses show S-contents above detection limit.

correlations between the elemental compositions of Pb, Zn, Fe, Ni, As and Cu, which are recognized in the fluid inclusions, do not record mixing lines, but rather reflect precipitation vectors that follow the main mixing event (Fig. 13D, E).

The absence of sulfur (Fig. 13B, F) in combination with the occurrence of the observed minerals as massive shoots indicates, however, a continuous precipitation and therefore excludes simple cooling as a key parameter in the S-poor fluid mixture. Furthermore, to explain the observed textures, an influx of sulfur is needed to precipitate the sulfides as the mixed fluid is depleted in sulfur. However, the kinetically hindered redox reactions among the sulfur species (sulfate-sulfide) at temperatures below 200 °C (Ohmoto and Lasaga, 1982) suggest that the formation of the massive pyrite-chalcopyrite aggregates requires an influx of sulfide. There are several possible sources of aqueous sulfide such as: oil field brines from the graben (for CH_4), formation fluids from Jurassic shales or reduced fluids in the crystalline gneisses that dissolved (for H_2S) primary sulfides (Stober and Bucher, 1999; Degueldre et al., 2003; Göb et al., 2013; Walter et al., 2018a). The source of the observed redox agents CH_4 and H_2S is not clear (see discussion in Walter et al., 2018a).

Siderite precipitation as typically observed after brecciation event 2 and after chalcopyrite mineralization is probably related to an incomplete consumption of Fe during chalcopyrite precipitation. The remaining Fe-content of the fluid probably reacts with the H_2CO_3 content of the sediment-derived fluid which lead to siderite mineralization under reduced conditions. Late-stage barites probably reflect the influence of SO_4-rich sediment-derived fluids which mix under oxidized conditions with a Ba-carrier fluid, i. e. with the continental basement brine.

5.4. Fluid sources

Recent work by Fusswinkel et al. (2013); Bons et al. (2014) and Walter et al. (2016, 2017a, b, 2018a, 2019) suggested that the modified bittern brine supplies Pb, Zn and Ba, but can also transport significant Fe. As these elements are abundantly present in the fluid inclusions and as the Cl/Br fluid inclusion mass ratios of ca. 80 correlate with literature values for a continental basement brine (Yardley, 2005; Walter et al., 2016, 2017a; Fig. 13A), the Fe-bearing fluid needed for the chalcopyrite mineralization stage is still the modified bittern brine.

The low sulfur content is a strong argument against the Lower Triassic Buntsandstein reservoir (Göb et al., 2013) which is deposited below the Muschelkalk and which was probably not completely eroded at the time of mineralization. As modern Buntsandstein-derived fluids

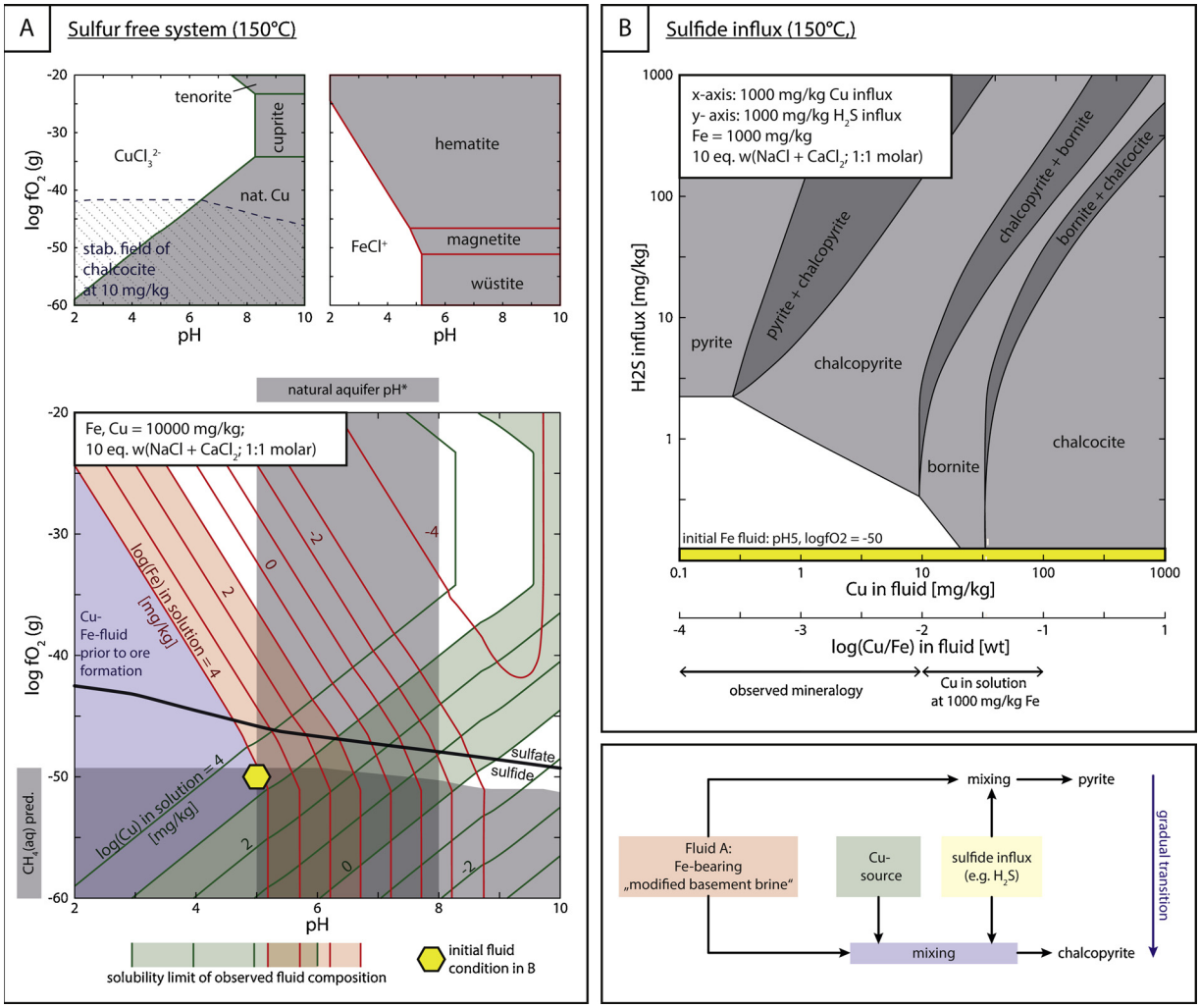

Fig. 14. Thermodynamic model based on literature, analytical and theoretical constrains. Considering a realistic formation environment, the stability field relations are to some degree independent temperature. A) The solubility of Fe and Cu are determined by the stability fields of the native Cu and the respective oxides, where a high solubility is reached at basic conditions. Natural aquifer pH* represents modern aquifer fluids from Baden-Württemberg, Germany (e.g., Stober and Bucher, 2004; Pauwels et al., 1993; Göb et al., 2013) B) The initial fluid pH and $logfO_2$ is constrained in Fig. 14A which, with respect to various Cu content is reacted with variable amounts of H_2S for sulfide precipitation. Variable initial f_{O2} and/or pH does not alter the general stability sequence with respect to H_2S and Cu abundance. C) schematic scheme for the formation of the pyrite-chalcopyrite sequence observed in the mineralization.

are typically enriched in Cu and Ni (Göb et al., 2013), mineralization stage IV therefore suggest that Buntsandstein fluid participated in a significant proportion. The correlation of Cu + Ni (which is typically not enriched in basement brines but in redbed-derived fluids; e.g. Göb et al., 2013) with the metals typically being carried by the basement brine (Pb, Zn, Sb, As) is best explained by trapping of the already mixed fluids in a “post-mixing” quartz (Fig. 13).

5.5. Mineralogy as a function of uplift and formation depth in continental rift systems

A key for interpretation of the observed mineralogical, mineral chemical and fluid inclusion results is the concept of a fluid stratified upper crust, where fluids of different reservoirs are stored even if the source lithology is eroded (Stober and Bucher, 2004; Bons et al., 2014; Walter et al., 2016, 2017; Burisch et al., 2018). The work of Bons et al. (2014) and Walter et al (2016) discussed the evolution of the fluid stratification whereas modern deep-drillings prove their existence (Pauwels et al., 1993; Stober and Bucher, 2004). Based on these observations, the continental basement brine is overlain by redbed-derived fluids (Buntsandstein and Permian redbeds, if present). These fluid strata are equivalent to lithological strata (in the southern Schwarzwald, Rotliegend and Zechstein is missing), however fluids may be decoupled from their original aquifers without changing their chemical properties for relatively long geological time spans (Bons et al., 2014; Walter et al., 2016; Burisch et al., 2018).

In the context of shoulder-uplift and erosion of the sedimentary cover, it seems plausible that the transition of the fluid regimes (Pb-Zn stage towards Cu-Ni stage) is related to a continuous downwards migration of the root zones (Burisch et al., 2016b) of the veins within the fluid stratification. This interpretation fits nicely to the observation of a continuous transition (indicated by Cu-enrichment of the minerals, see above) and to the discussed fluid data, which also indicates a downwards shift from the shallower Muschelkalk reservoir towards the deeper Buntsandstein reservoir (see also Bons et al., 2014; Walter et al., 2016). Moreover, the typically occurring brecciations indicate hydraulic fracturing which fit well to the interpretation of a fluid aquifer getting overpressured and dewatered by exhumation. Hence, the mineralogical and mineral chemical variations observed in the veins of this contribution probably reflect a successive exhumation of the study site in an active rift.

Additionally, the interpretation presented above fits very well to the intensively studied late stage carbonate-sulphate assemblages which form the late stage precipitates of the veins. After successive uplift of

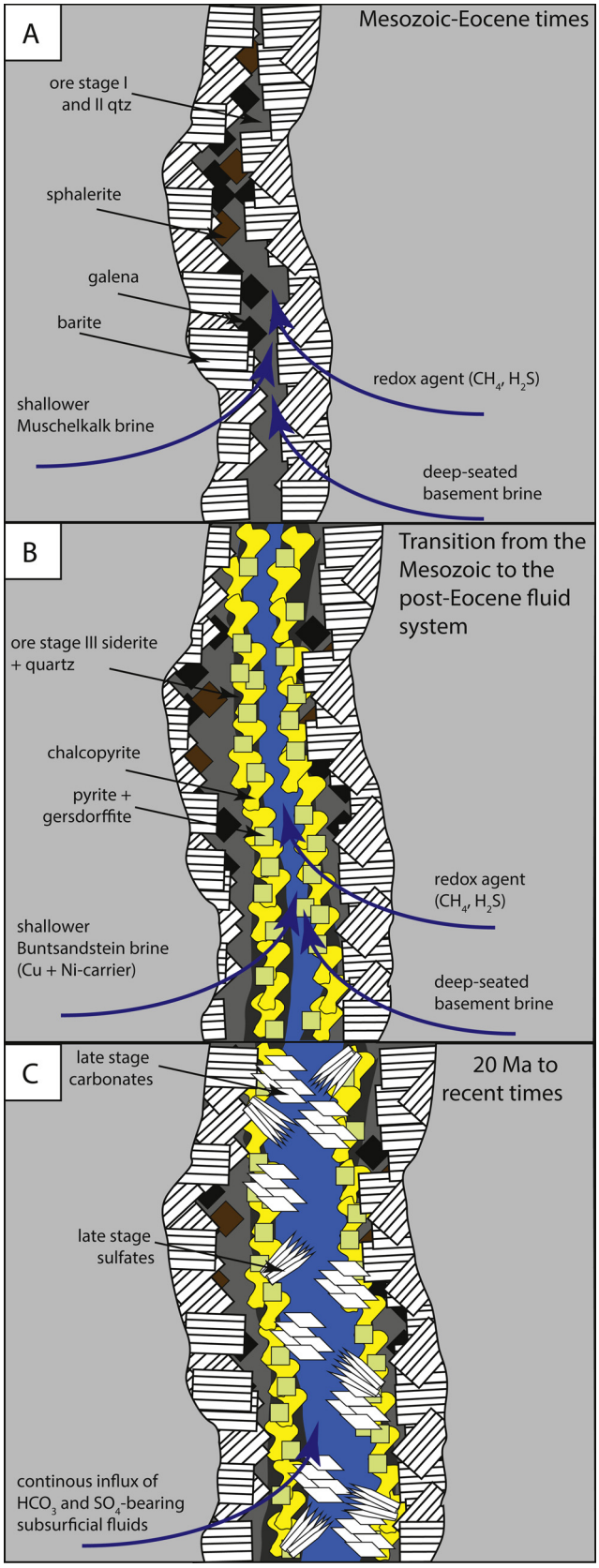

Fig. 15. Schematic model illustrating the three stages of vein formation: A) Generation of the Pb and Zn mineralization during Mesozoic times. B) Precipitation of the Cu + Ni mineralization of the Cenozoic. Note: Continuous open fractures and high fluid flow lead to a modification of the long-term stable reservoirs. C) Precipitation of the late-stage carbonate-sulfate assemblage which depict the transition from the mineralized deep geothermal towards the shallow, barren geothermal system.

the area, the final transition from the deep to the shallow (and still active) system took place within the last 20 Ma (Burisch et al., 2018); during this time, physicochemical conditions (hydraulic properties, temperature, mixing ratio) changed significantly. The shallow, modern geothermal system is therefore mainly characterized by continuous fluid flow upwards to surficial wells and precipitation of sulphates and carbonates as sinters (e.g. spas in Baden-Baden with 66 °C or Wiesbaden with 65–70 °C hot hydrothermal water; Loges et al., 2012; Göb et al., 2013).

In summary, the Cu-Ni-rich mineralization stage in the Pb-Zn veins records the first step from an episodically active deep hydrothermal system (Fig. 15A) towards a shallow, barren, continuously active geothermal system (Fig. 15B, C). Moreover, the influx of a Cu-rich fluid indicates a significant change of the involved sedimentary aquifers (from a Muschelkalk fluid towards a redbed-derived Buntsandstein fluid) and a change in the mixing ratio between basement brine and sedimentary aquifer. The last stage of this transition can be observed still today in the numerous thermal wells and spas along the Rhinegraben.

6. Conclusions

This study provides evidence that a changing mineralogy in a hydrothermal vein is related to chemically contrasting fluid endmembers which successively replaced the fluids generating a common Pb-Zn mineralization in a hydrothermal vein. This change of fluid composition between the different mineralization stages are also manifested in the composition of sphalerite, fahlore, pyrite, gersdorffite and galena. In the case of the Schwarzwald, exhumation and fracturing of the different reservoirs leads to a transition from a deep mineralized geothermal system to a shallow barren one and, hence, vein mineralogy appears to be a function of erosion and uplift. This study provides an interpretation of the missing link between short living mixing events of the Jurassic-Cretaceous time and the still active geothermal system.

Declaration of Competing Interest

The authors declare that they have no known competing financial interests or personal relationships that could have appeared to influence the work reported in this paper.

Acknowledgements

We thank S. Schafflick and Per Jeiseke for sample preparation. Thomas Wenzel is thankfully acknowledged for fruitful discussions and help during microprobe work. Moreover, we want to thank two anonymous reviewer for their critical comments and Michael E. Boettcher for his editorial guidance. This study was supported by the German Science Foundation (DFG), grant MA 2135/20-1, which is gratefully acknowledged.

Appendix A. Supplementary data

Supplementary material related to this article can be found, in the online version, at doi:https://doi.org/10.1016/j.chemgeo.2019.119358.

References

Altherr, R., Holl, A., Hegner, E., Langer, C., Kreuzer, H., 2000. High-potassium, calc-alkaline I-type plutonism in the European Variscides: northern Vosges (France) and northern Schwarzwald (Germany). Lithos 50, 51–73.
Armstrong, J.T., 1991. Quantitative elemental analysis of individual microparticles with electron beam instruments. Electron Probe Quantitation. Springer US, pp. 261–315.
Bauer, M., Burisch, M., Ostendorf, J., Krause, J., Frenzel, M., Seifert, T., Gutzmer, J., 2019. Trace element geochemistry of sphalerite in contrasting hydrothermal fluid systems of the Freiberg district, Germany: insights from LA-ICP-MS analysis, near-

infrared light microthermometry of sphalerite-hosted fluid inclusions and sulfur isotope geochemistry. Miner. Depos. 54, 237–262. https://doi.org/10.1007/s00126-018-0850-0.
Brander, T., 2000. U/He-chronologische Fallstudien an Eisen-und Manganerzen (Doctoral dissertation). Heidelberg. pp. 273.
Braunger, S., Marks, M.A.W., Walter, B.F., Neubauer, R., Reich, R., Wenzel, T., Parsapoor, A., Markl, G., 2018. The petrology of the kaiserstuhl volcanic complex, SW Germany: the importance of metasomatized and oxidized lithospheric mantle for carbonatite generation. J. Petrol. 59 (9), 1731–1762.
Behr, H.J., Horn, E.E., Frentzel-Beyme, K., Reutel, C., 1987. Fluid inclusion characteristics of the Variscan and post-Variscan mineralizing fluids in the Federal Republic of Germany. Chem. Geol. 61 (1–4), 273–285.
Bence, A.E., Albee, A.L., 1968. Empirical correction factors for the electron microanalysis of silicates and oxides. J. Geol. 76 (4), 382–403.
Bethke, C.M., 2007. Geochemical and Biogeochemical Reaction Modeling. Cambridge University Press, pp. 536.
Blanc, P., Lassin, A., Piantone, P., Azaroual, M., Jacquemet, N., Fabbri, A., Gaucher, E.C., 2012. Thermoddem: a geochemical database focused on low temperature water/rock interactions and waste materials. Appl. Geochem. 27 (10), 2107–2116.
Bons, P.D., Fusswinkel, T., Gomez-Rivas, E., Markl, G., Wagner, T., Walter, B., 2014. Fluid mixing from below in unconformity-related hydrothermal ore deposits. Geology 42 (12), 1035–1038.
Boiron, M.C., Cathelineau, M., Richard, A., 2010. Fluid flows and metal deposition near basement/cover unconformity: lessons and analogies from Pb–Zn–F–Ba systems for the understanding of Proterozoic U deposits. Geofluids 10, 270–292.
Burisch, M., Marks, M.A., Nowak, M., Markl, G., 2016a. The effect of temperature and cataclastic deformation on the composition of upper crustal fluids — An experimental approach. Chem. Geol. 433, 24–35.
Burisch, M., Walter, B.F., Wälle, M., Markl, G., 2016b. Tracing fluid migration pathways in the root zone below unconformity-related hydrothermal veins: insights from trace element systematics of individual fluid inclusions. Chem. Geol. 429, 44–50.
Burisch, M., Gerdes, A., Walter, B.F., Neumann, U., Fettel, M., Markl, G., 2017. Methane and the origin of five-element veins: mineralogy, age, fluid inclusion chemistry and ore forming processes in the Odenwald, SW Germany. Ore Geol. Rev. 81, 42–61.
Burisch, M., Walter, B.F., Gerdes, A., Lanz, M., Markl, G., 2018. Hydrothermal anhydrite-gypsum-siderite-dolomite-calcite assemblages record the transition from a deep to a shallow hydrothermal system in the Schwarzwald mining district, SW Germany. Geochim. Cosmochim. Acta 223, 259–278.
Carignan, J., Gariépy, C., Hillaire-Marcel, C., 1997. Hydrothermal fluids during Mesozoic reactivation of the St. Lawrence rift system, Canada: C, O, Sr and Pb isotopic characterization. Chem. Geol. 137, 1–21.
Cugerone, A., Cenki-Tok, B., Chauvet, A., Le Goff, E., Bailly, L., Alard, O., Allard, M., 2018. Relationships between the occurrence of accessory Ge-minerals and sphalerite in Variscan Pb-Zn deposits of the Bossost anticlinorium, French Pyrenean Axial Zone: chemistry, microstructures and ore-deposit setting. Ore Geol. Rev. 95, 1–19.
de Graaf, S., Lüders, V., Banks, D.A., Sośnicka, M., Reijmer, J.J., Kaden, H., Vonhof, H.B., 2019. Fluid evolution and ore deposition in the Harz Mountains revisited: isotope and crush-leach analyses of fluid inclusions. Miner. Depos. 1–16. https://doi.org/10.1007/s00126-019-00880-w.
Degueldre, C., Scholtis, A., Laube, A., Turrero, M.J., Thomas, B., 2003. Study of the pore water chemistry through an argillaceous formation: a paleohydrochemical approach. Appl. Geochem. 18 (1), 55–73.
Duane, M.J., De Wit, M.J., 1988. Pb-Zn ore deposits of the northern Caledonides: products of continental-scale fluid mixing and tectonic expulsion during continental collision. Geology 16 (11), 999–1002.
Epp, T., Walter, B.F., Scharrer, M., Lehmann, G., Henze, K., Heimgärtner, C., Bach, W., Markl, G., 2018. Quartz veins with associated Sb-Pb-Ag ± Au mineralization in the Schwarzwald, SW Germany: a record of metamorphic cooling, tectonic rifting, and element remobilization processes in the Variscan belt. Miner. Depos. 1–26.
Fusswinkel, T., Wagner, T., Wälle, M., Wenzel, T., Heinrich, C.A., Markl, G., 2013. Fluid mixing forms basement-hosted Pb-Zn deposits: insight from metal and halogen geochemistry of individual fluid inclusions. Geology 41 (6), 679–682.
Fusswinkel, T., Wagner, T., Wenzel, T., Wälle, M., Lorenz, J., 2014. Red bed and basement sourced fluids recorded in hydrothermal Mn–Fe–As veins, Sailauf (Germany): a LA-ICPMS fluid inclusion study. Chem. Geol. 363, 22–39.
Frape, S.K., Fritz, P., McNutt, R.T., 1984. Water-rock interaction and chemistry of groundwaters from the Canadian Shield. Geochim. Cosmochim. Acta 48, 1617–1627.
Frezzotti, M.L., Tecce, F., Casagli, A., 2012. Raman spectroscopy for fluid inclusion analysis. J. Geochem. Explor. 112, 1–20.
Geyer, O.F., Gwinner, M.P., 2011. Geologie von Baden -Württemberg. – 5, völlig neu bearbeitete Auflage. Schweizerbart`sche Verlagsbuchhandlung (Nägele u. Obermiller), Stuttgart, pp. 627.
Giebel, R.J., Parsapoor, A., Walter, B.F., Braunger, S., Marks, M.A.W., Wenzel, T., Markl, G., 2019. Evidence for magma – wall rock interaction in carbonatites from the Kaiserstuhl Volcanic Complex (Southwest Germany). J. Petrol. 60 (6), 1163–1194.
Göb, S., Loges, A., Nolde, N., Bau, M., Jacob, D.E., Markl, G., 2013. Major and trace element compositions (including REE) of mineral, thermal, mine and surface waters in SW Germany and implications for water–rock interaction. Appl. Geochem. 33, 127–152.
Hann, H.P., Chen, F., Zedler, H., Frisch, W., Loeschke, J., 2003. The rand granite in the southern Schwarzwald and its geodynamic significance in the Variscan belt of SW Germany. Int. J. Earth Sci. 92, 821–842.
Jenkner, B., 1986. Ein Vorschlag zur Neugliederung des sedimentären Oberrotliegenden in der Baden-Badener Senke und ihrer nordöstlichen Fortsetzung (Nordschwarzwald). Jahrb Geol Landesamtes Baden-Württemberg 28, 49–159.
Kalt, A., Altherr, R., Hanel, M., 2000. Exkursion a:-the Variscan basement of the Schwarzwald. Suppl. Issues Euro J. Miner. 12 (2), 1–44.
Keim, M., Walter, B.F., Neumann, U., Kreissl, S., Bayerl, R., Markl, G., 2018. Polyphase enrichment and redistribution processes in silver-rich mineral associations of the hydrothermal fluorite-barite-(Ag-Cu) Clara deposit, SW Germany. Miner. Depos. 54 (2), 155–174.
Kolchugin, A.N., Immenhauser, A., Walter, B.F., Morozov, V.P., 2016. Diagenesis of the palaeo-oil-water transition zone in a Lower Pennsylvanian carbonate reservoir: constraints from cathodoluminescence microscopy, microthermometry, and isotope geochemistry. Mar. Petrol. Geol. 72, 45–61.
Kreissl, S., Gerdes, A., Walter, B.F., Neumann, U., Wenzel, T., Markl, G., 2018. Reconstruction of a &200 Ma multi-stage “five element” Bi-Co-Ni-Fe-As-S system in the Penninic Alps, Switzerland. Ore Geol. Rev. 95, 746–788.
Loges, A., Wagner, T., Kirnbauer, T., Göb, S., Bau, M., Berner, Z., Markl, G., 2012. Source and origin of active and fossil thermal spring systems, northern Upper Rhine Graben, Germany. Appl. Geochem. 27, 1153–1169.
Lüders, V., Möller, P., 1992. Fluid evolution and ore deposition in the Harz Mountains (Germany). Eur. J. Miner. 4, 1053–1068.
Lustrino, M., Wilson, M., 2007. The circum-Mediterranean anorogenic Cenozoic igneous province. Sci. Rev. 81 (1), 1–65.
Markl, G., Burisch, M., Neumann, U., 2016. Natural fracking and the genesis of five-element veins. Miner. Depos. 51 (6), 703–712.
Marks, M.A., Marschall, H.R., Schühle, P., Guth, A., Wenzel, T., Jacob, D.E., Barth, M., Markl, G., 2013. Trace element systematics of tourmaline in pegmatitic and hydrothermal systems from the Variscan Schwarzwald (Germany): the importance of major element composition, sector zoning, and fluid or melt composition. Chem. Geol. 344, 73–90.
Metz, R., Richter, M., Schürenberg, H., 1957. Die blei-zink-Erzgänge des schwarzwaldes. Beih Geol Jahrb 29, 277.
Muchez, P., Heijlen, W., Banks, D., Blundell, D., Boni, M., Grandia, F., 2005. 7: extensional tectonics and the timing and formation of basin-hosted deposits in Europe. Ore Geol. Rev. 27 (1–4), 241–267.
Nitsch, E., Zedler, H., 2009. Oberkarbon und Perm in Baden-Württemberg. LGRB-Inf. 22, 7–102.
Ohmoto, H., Lasaga, A.C., 1982. Kinetics of reactions between aqueous sulfates and sulfides in hydrothermal systems. Geochim. Cosmochim. Act 46 (10), 1727–1745. https://doi.org/10.1016/0016-7037(82)90113-2.
Pauwels, H., Fouillac, C., Fouillac, A.M., 1993. Chemistry and isotopes of deep geothermal saline fluids in the Upper Rhine Graben: origin of compounds and water-rock interactions. Geochim. Cosmochim. Acta 57 (12), 2737–2749.
Pfaff, K., Romer, R.L., Markl, G., 2009. U-Pb ages of ferberite, chalcedony, agate,'U-mica'and pitchblende: constraints on the mineralization history of the Schwarzwald ore district. Euro J. Miner. 21, 817–836.
Piqué, À., Canals, À., Grandia, F., Banks, D.A., 2008. Mesozoic fluorite veins in NE Spain record regional base metal-rich brine circulation through basin and basement during extensional events. Chem. Geol. 257 (1–2), 139–152.
Rupf, I., Nitsch, E., 2008. Das geologische Landesmodell von Baden-Württemberg: Datengrundlagen, technische Umsetzung und erste geologische Ergebnisse. Landesamt für Geologie, Rohstoffe und Bergbau Baden-Württemberg. Freiburg im Breisgau. pp. 153.
Sanjuan, B., Millot, R., Innocent, C., Dezayes, C., Scheiber, J., Brach, M., 2016. Major geochemical characteristics of geothermal brines from the Upper Rhine Graben granitic basement with constraints on temperature and circulation. Chem. Geol. 428, 27–47.
Sośnicka, M., Lüders, V., 2019. Super-deep, TSR-controlled Phanerozoic MVT type Zn-Pb deposits hosted by Zechstein-2 gas reservoir carbonate (Ca2), Lower Saxony Basin, Germany. Chem. Geol. 508, 62–77.
Staude, S., Bons, P.D., Markl, G., 2009. Hydrothermal vein formation by extension-driven dewatering of the middle crust: an example from SW Germany. Earth Planet. Sci. Lett. 286, 387–395.
Staude, S., Mordhorst, T., Nau, S., Pfaff, K., Brügmann, G., Jacob, D.E., Markl, G., 2012a. Hydrothermal carbonates of the Schwarzwald ore district, southwestern Germany: Carbon source and conditions of formation using δ18O, δ13C, 87Sr/86Sr, and fluid inclusions. Can. Miner. 50, 1401–1434.
Staude, S., Werner, W., Mordhorst, T., Wemmer, K., Jacob, D.E., Markl, G., 2012b. Multi-stage Ag–Bi–Co–Ni–U and Cu–Bi vein mineralization at Wittichen, Schwarzwald, SW Germany: geological setting, ore mineralogy, and fluid evolution. Miner. Depos. 47 (3), 251–276.
Stober, I., Bucher, K., 1999. Deep groundwater in the crystalline basement of the Black Forest region. Appl. Geochem. 14, 237–254.
Stober, I., Bucher, K., 2004. Fluid sinks within the earth's crust. Geofluids 4 (2), 143–151.
Todt, W., 1976. Zirkon U/Pb-Alter des Malsburg-Granits vom Südschwarzwald. Neues Jahrb Mineral/ Monatsh 12. pp. 532–544.
Wagner, T., Cook, N.J., 2000. Late-Variscan antimony mineralisation in the Rheinisches Schiefergebirge, NW Germany: evidence for stibnite precipitation by drastic cooling of high-temperature fluid systems. Miner Depos 35 (2–3), 206–222.
Walter, B.F., Immenhauser, A., Geske, A., Markl, G., 2015. Exploration of hydrothermal carbonate magnesium isotope signatures as tracers for continental fluid aquifers, Schwarzwald mining district, SW Germany. Chem. Geol. 400, 87–105.
Walter, B.F., Burisch, M., Markl, G., 2016. Long-term chemical evolution and modification of continental basement brines–a field study from the Schwarzwald, SW Germany. Geofluids 16, 604–623.
Walter, B.F., Burisch, M., Marks, M.A.W., Markl, G., 2017a. Major element and trace metal systematics of fluid inclusions in hydrothermal veins: metal provenance and the reconstruction of eroded sedimentary units. Miner. Depos. 52 (8), 1191. https://doi.org/10.1007/s00126-017-0719-7.
Walter, B.F., Steele-MacInnis, M., Markl, G., 2017b. Sulfate brines in fluid inclusions of

hydrothermal veins: compositional determinations in the system H_2O-Na-Ca-Cl-SO_4. Geochim. Cosmochim. Acta 209, 184–203.
Walter, B.F., Burisch, M., Fusswinkel, T., Marks, M.A.W., Steele-MacInnis, M., Wälle, M., Apukhtina, O., Markl, G., 2018a. Multi-reservoir fluid mixing processes in rift-related hydrothermal veins, Schwarzwald, SW-Germany. J. Geochem. Explor. 186, 158–186.
Walter, B.F., Gerdes, A., Kleinhanns, I.C., Dunkl, I., von Eynatten, H., Kreissl, S., Markl, G., 2018b. The connection between hydrothermal fluids, mineralization, tectonics and magmatism in a continental rift setting: fluorite Sm-Nd and hematite and carbonates U-Pb geochronology from the Rhinegraben in SW Germany. Geochim. Cosmochim. Acta 240, 11–42.
Walter, B.F., Parsapoor, A., Braunger, S., Marks, M.A.W., Wenzel, T., Martin, M., Markl, G., 2018c. Pyrochlore as a monitor for magmatic and hydrothermal processes in carbonatites from the Kaiserstuhl volcanic complex (SW Germany). Chem. Geol. 498, 1–16.
Walter, B.F., Kortenbruck, P., Scharrer, M., Zeitvogel, C., Wälle, M., Mertz-Kraus, M.G., 2019. Chemical evolution of ore-forming brines-Basement leaching, metal provenance, and the redox link between barren and ore-bearing hydrothermal veins. A case study from the Schwarzwald mining district in SW-Germany. Chem. Geol. 506, 126–148. https://doi.org/10.1016/j.chemgeo.2018.12.038.
Wilkinson, J.J., 2001. Fluid inclusions in hydrothermal ore deposits. Lithos 55 (1–4), 229–272.
Yardley, B.W.D., 2005. Metal concentrations in crustal fluids and their relationship to ore formation. Econ. Geol. 100, 613–632.
Zhou, Z., Wen, H., Qin, C., Liu, L., 2017. Geochemical and isotopic evidence for a magmatic-hydrothermal origin of the polymetallic vein-type Zn-Pb deposits in the northwest margin of Jiangnan Orogen, South China. Ore Geol. Rev. 86, 673–691.

Appendix V

Accepted manuscript

Study 5

Scharrer, M., Epp, T., Walter, B. F., Pfaff, K., Vennemann, T., & Markl, G. (accepted). The formation of (Ni-Co-Sb)-Ag-As ore shoots in hydrothermal galena-sphalerite-fluorite veins

The formation of (Ni-Co-Sb)-Ag-As ore shoots in hydrothermal galena-sphalerite-fluorite veins

Manuel Scharrer[1], Tatjana Epp[1], Benjamin Walter[2], Katharina Pfaff[3], Torsten Vennemann[4], Gregor Markl[1]

[1] Eberhard Karls University, Schnarrenbergstraße 94–96, 72076 Tübingen, Germany

[2] Karlsruhe Institute of Technology, Adenauerring 20b, 76131 Karlsruhe, Germany

[3] Center for Mineral Resources Science, Colorado School of Mines, 1516 Illinois Street, Golden, Colorado

[4] University of Lausanne, Quartier Mouline, 1015 Lausanne, Switzerland

Corresponding author:

Manuel Scharrer

manuel.scharrer@uni-tuebingen.de

https://orcid.org/0000-0001-8632-1291

Declaration:

Funding: This research was funded by a combination of the German Research Foundation (DFG), grant no. MA 2135/25-1 and by the German-American Fulbright Commission.

Conflict of interest/competing interests: There are no conflicts of interest present.

Availability of data and material: All new data provided in this manuscript, EPMA data and sulfur isotope data, is provided in the electronic supplement

Key words:

- Five-element association
- Native arsenic
- Hydrothermal ore shoot
- Reduction
- Native silver

Abstract

Unusual hydrothermal native As-sulfide ± native Ag ± arsenide ± antimonide ± sulfosalt ore shoots and their cogenetic sulfide-fluorite-barite-quartz host veins, which are common in the region and in whole Central Europe, were investigated at three localities in the Schwarzwald, SW Germany, to understand the physico-chemical processes governing the change from a normal (= common) hydrothermal to an exceptional ore-shoot regime.

Based on fluid inclusions, the formation of the gangue minerals is the result of binary mixing between a NaCl- and a $CaCl_2$-rich brine (both ~20 wt% NaCl eq). This mixing correlation, major and minor fluid composition, formation temperature (~150 °C), and $\delta^{34}S$ signature are identical (within error) in ore shoots and host veins. Thermodynamic modeling indicates that ore shoot formation must have resulted from a change in redox conditions by a local influx of a volumetrically minor reducing agent, probably hydrocarbons. The elemental content and the mineralogy of each ore shoot locality (Ag-As-rich: Münstertal; Ag-Ni-As-rich: Urberg; Ag-Ni-As-Sb-rich: Wieden) reflect the metal content of the binary mixed fluid, while mineral textures, successions, and assemblages are thermodynamically and, regarding sulfur, kinetically controlled. The formation of vein and ore shoot sulfides requires an addition of sulfide, most probably from the sulfide-bearing host rocks, because thermodynamic and kinetic reasons suggest that the two major vein-forming and metal-bearing fluids are not the source of the sulfur. The final ore shoot textures are influenced by later hydrothermal remobilization processes of As and Ag. This results in a number of sulfosalts, mostly proustite-pyrargyrite. Interestingly, the greater thermodynamic stability of Sb-endmember sulfosalts enables them to form even in As-dominated fluid systems.

Introduction

In many hydrothermal deposits, the ratio of gangue to ore minerals varies significantly within a specific deposit (e.g., Lindgren 1913; Guilbert and Park 2007). Those parts which are or have been economically mineable are commonly referred to as ore shoot or - in the case of economically extremely valuable ore shoots - as bonanzas (e.g., Lindgren 1913; Guilbert and Park 2007; Squire et al. 2008).

The formation of ore shoots, in general, is closely linked to the origin of each deposit and the spatial variability of chemical and physical conditions during deposition (Hise 1900; Penrose 1910). Thus, reasons for the formation of local ore concentrates are numerous, including:

- Physical segregation and accumulation (e.g., Penrose 1910; Ewers and Hudson 1972; Tomkins 2010);
- Structure and intersection of fissures as well as the physical character of the wall rock that may provide preferred pathways, offer advantageous space, or trap the metal-bearing solution/magma into favorable positions (e.g., Hulin 1929; Gough 1965; Stone and Archibald 2004; Páez et al. 2016);
- Local mixing or influx of a further gaseous or liquid fluid into or phase separation of the ore-bearing solution/magma (e.g., Penrose 1910; Hulin 1929; Shepherd et al. 1991; Markl et al. 2016);
- Chemical character of the wall rock (e.g., Hulin 1929; Shepherd et al. 1991; Squire et al. 2008; Kreissl et al. 2018);
- Post-depositional remobilization by alteration and/or weathering (e.g., Tomkins et al. 2004; Collins et al. 2012; Fougerouse et al. 2016; Páez et al. 2016).

Most ore shoots are structurally controlled, for example directly or indirectly by preferred fluid pathways, but structure alone does not promote ore formation (Penrose 1910). Thus, not only one, but a combination of the above-named and further factors leads to the formation of ore shoots.

In this study, three ore shoot-bearing unconformity-related hydrothermal fluorite-quartz-barite vein systems in the Schwarzwald, SW Germany, are investigated to understand the formation of such ore shoots and the

transition from normal barite-fluorite-sulfide veins to these native element- and arsenide-dominated ore shoots. In the following, we chose to label the fluorite-barite-carbonate vein type with galena, sphalerite and chalcopyrite, which is very common in the Schwarzwald region and over the whole of Europe, as "normal", knowing, that there are many other vein types which could be equally designated like this. The ore shoots investigated here differ from many other ore shoots worldwide in that they not only show an enrichment in ore minerals but also a significant change in ore mineralogy relative to the larger, hosting, hydrothermal vein system. Specifically, ore mineralogy changes from a common galena-sphalerite-chalcopyrite assemblage to an unusual native element + arsenide + sulfarsenide association, while the gangue minerals vary only in relative mineral abundance (Otto 1967; Brill et al. 2018; Steen 2020).

Such strongly contrasting mineral assemblages in hydrothermal veins are easily interpreted either to represent two different mineralization stages operating at different times or to represent a change in fluid composition and/or source in combination with a change in parameters such as pH, f_{O2} or temperature. As in some cases, most of the economic value of a specific vein lies in bonanza-style ore shoots (Lindgren 1913; Guilbert and Park 2007; Gloyn-Jones and Kisters 2019), it is vital to understand the formation of these features in relation to the larger hydrothermal vein system.

Hydrothermal veins generally form by either a change in pressure, a change in temperature (mostly cooling), fluid-host rock reaction, fluid mixing, effervescence, boiling or a combination of those (Barnes 1997). For the ore shoot-bearing main hydrothermal stage in the localities investigated in this study, Scharrer et al. (2021) concluded the veins to have formed by fluid mixing which agrees with many precursor studies on similar veins in the region (e.g., Baatartsogt et al. 2007; Fusswinkel et al. 2013; Walter et al. 2016).

The ore shoot assemblage studied strongly resembles typical features of hydrothermal native element-arsenide assemblages (Kissin 1992). These consist of dendritic native Ag and/or native Bi, zoned Ni-, Co- and Fe-arsenides and sulfarsenides and late-stage native As (Bastin 1939; Kissin 1988; Kissin 1992; Markl et al. 2016; Scharrer et al. 2019; Guilcher et al. submitted). The importance of the redox state during the formation of native element-arsenide associations has been assumed before (Robinson and Ohmoto 1973;

Kissin 1993; Ondrus et al. 2003a), but Markl et al. (2016) first proposed an integrated model explaining all textural, mineralogical and geochemical features of five-element associations. Since then, several studies showed their formation to be directly linked to the process of reduction (Naumov et al. 1971a; Markl et al. 2016; Burisch et al. 2017a; Kreissl et al. 2018; Scharrer et al. 2019). Scharrer et al. (2019) proposed (but could not prove unequivocally) that the sole process of reduction suffices to account for the formation of native element-arsenide associations and that the rest of the fluid chemistry could remain unchanged. This hypothesis was based on the fact, that parameters such as elemental abundance in the ore, formation temperature, salinity and host rock can greatly vary between all native element-arsenide associations worldwide, while their conspicuous dendritic textures are ubiquitous and the typical mineralogical sequence of native Ag ± native Bi → Ni-arsenides → Co-arsenides → Fe-arsenides → native As is the same at almost all localities. Furthermore, this mineral sequence can be thermodynamically modelled by simple reduction (Scharrer et al. 2019).

All these studies, however, could not show that the ore shoots formed from exactly the same fluid (or mixed fluid) as the rest of the vein. In this respect, we are lucky, because the main difference between our ore shoots and many other worldwide occurrences of native element-arsenide assemblages is that the latter typically form as an individual ore stage that is succeeded by a sulfide-bearing stage, while in our study area, the normal sulfide-bearing assemblage forms prior to, during, and subsequent to the native element-arsenide-bearing ore shoots. This fact renders them ideal candidates to investigate the difference in physico-chemical conditions between the normal and the native element-arsenide assemblages and the geological and/or geochemical process behind the change from one to the other.

Regional geology

The three hydrothermal veins investigated in the present study include the former Teufelsgrund-Schindler-Herrenwald vein system in the Münstertal with Ag-As ore shoots, the former Gottesehre mine with associated parallel veins near Urberg with Ag-Ni-As ore shoots and the Anton and Tannenboden veins near Wieden with Ag-Ni-As-Sb ore shoots. These three localities are the only ones in the Schwarzwald which

show ore shoots rich in native arsenic and native silver and are described in detail in the subsequent chapter. The investigated vein systems are situated in the southern Schwarzwald, a Variscan basement area in SW Germany (Fig. 1a). The basement consists of mostly granitic and gneissic Variscan crystalline rocks which are discordantly overlain by a Mesozoic terrigenous to marine sedimentary cover (Geyer et al. 2011). This setting was disturbed during the opening of the Upper Rhine Graben with its normal fault-dominated regime (Geyer et al. 2011). Uplift of the rift flanks led to partial erosion of the sedimentary cover as well as part of the basement and resulted in the present-day topography: a mountain range with an elevation between 300 and 1500 meters above sea level. Today's outcropping surface in the southern Schwarzwald was originally situated about 2-3 km below the former basement-cover unconformity (Rupf and Nitsch 2008).

The preexisting geological, mineralogical and geochemical literature on the Schwarzwald is vast and includes its geology (Geyer et al. 2011), stable and radiogenic isotope studies (e.g., Staude et al. 2011; Walter et al. 2015), mineralogical studies (e.g., Metz et al. 1957; Staude et al. 2007; Staude et al. 2010; Staude et al. 2012; Markl 2017a), geochronological studies (e.g., Pfaff et al. 2009; Walter et al. 2018b), fluid inclusion studies (e.g., Schwinn et al. 2006; Baatartsogt et al. 2007; Walter et al. 2016; Burisch et al. 2017b) and weathering studies (e.g., Keim et al. 2018). This solid geoscientific background helps in constraining the boundary conditions for the present study.

The region has a long lasting history of hydrothermal activity which ranges from the Variscan Orogeny to recent times (Walter et al. 2018b). This hydrothermal activity produced more than 1000 unconformity-related, hydrothermal veins showing a large variability of mineral associations, of which some have been mined since pre-Roman times (Markl 2015; Markl 2016; Markl 2017a; Markl 2017b). Walter et al. (2016) characterized five temporal maxima of hydrothermal mineralization based on the mineralogy, fluid characteristics and age dating. Direct dating of individual minerals of the investigated vein systems by Walter et al. (2018b) showed that the ore shoot-bearing major hydrothermal stage lasted from the Triassic until the early Cretaceous. This in combination with the fluid composition and vein mineralogy lets Scharrer et al. (2021) conclude that the investigated ore shoots and the associated main ore stage of these veins formed during the fourth of the five hydrothermal maxima in the Schwarzwald (see Walter et al. 2016, for

the detailed terminology). Thus, this stage belongs to the Triassic-Cretaceous vein group (Walter et al. 2018b), commonly labeled Jurassic-Cretaceous fluorite-quartz-barite-carbonate vein group, which generally formed at temperatures between ~50 and 200 °C and salinities of 20-30 wt% NaCl+$CaCl_2$ (Walter et al. 2016; Walter et al. 2017). Reactivation of these veins during the Upper Rhine Graben rifting produced other subsequent metal occurrences and deposits.

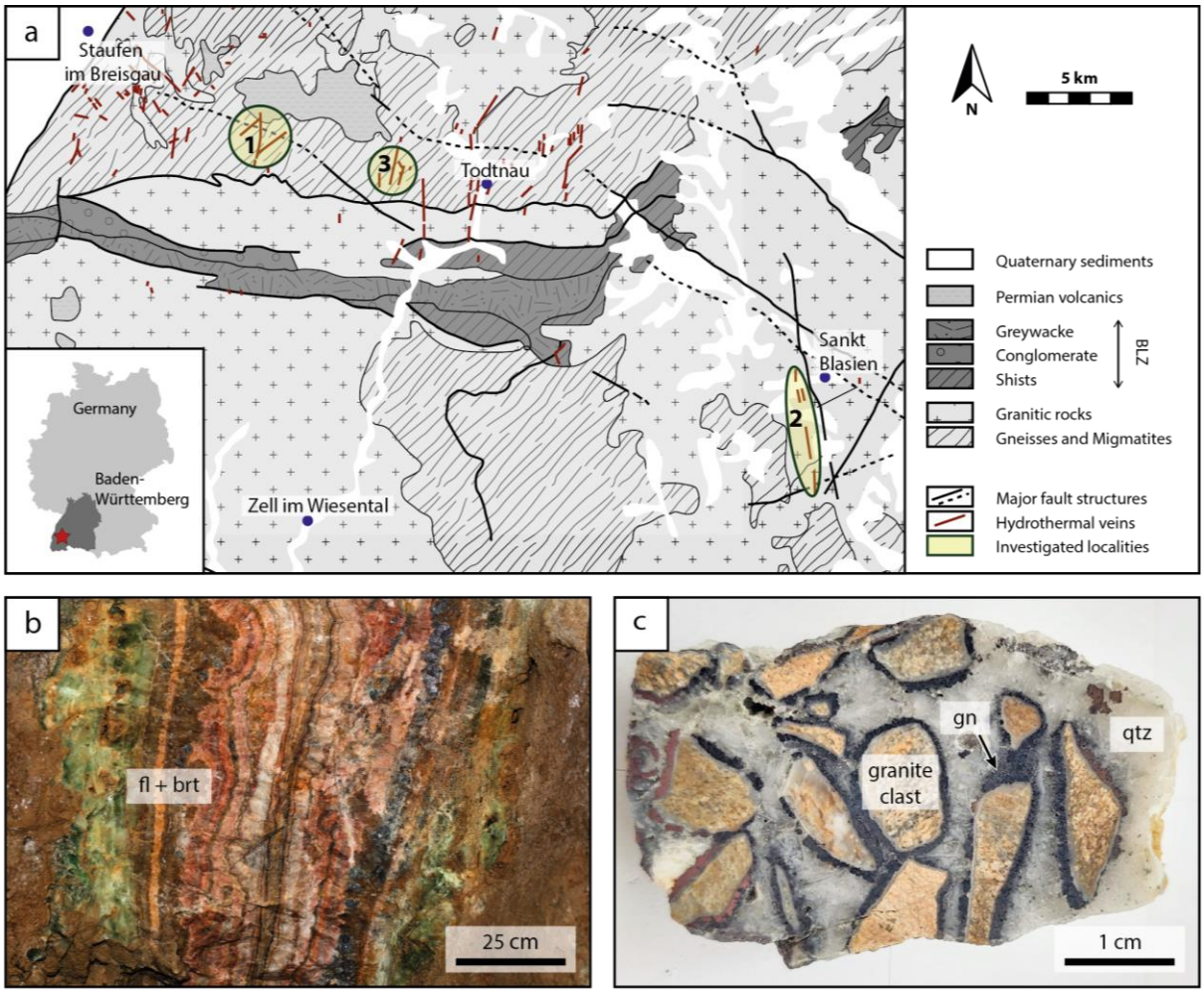

Fig. 1 (a) Geological map of the Southern Schwarzwald in SW Germany with the investigated localities highlighted (modified from Scharrer et al. 2021; original geological map from LRGB GÜK300). 1: Teufelsgrund and Giftgrube mine, Münstertal; 2: Gottesehre mine, Urberg; 3: Anton and Tannenboden mine near Wieden. BLZ stands for Badenweiler-Lenzkirch-Zone, which represents an east-west striking Variscan suture zone filled with low-grade metamorphic clastic sediments. (b) Image of a typical banded vein by Matthias Zizelmann and (c) image of a granitic wall rock breccia which are typically cemented by sulfides and quartz. Both (b) and (c) are modified from Scharrer et al. (2021)

Location of study

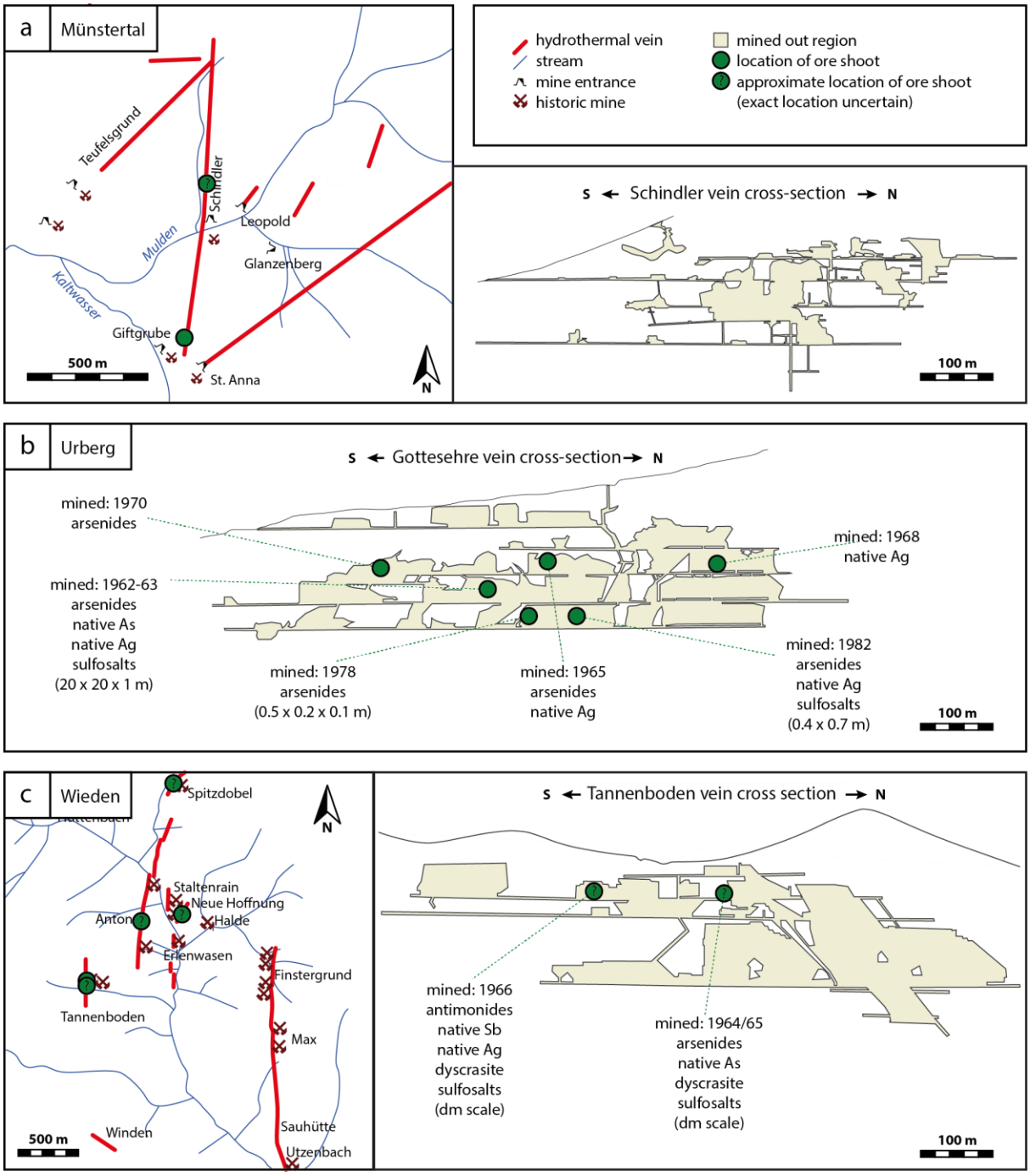

Fig. 2 Maps and cross sections of the three investigated localities showing the ore shoot distribution. Ore shoot description shows mining date, characteristic mineralogy and size. Depicted ore shoot information and location has been inferred from literature (Grundmann 1971; Bliedtner 1978; Markl 2017a; Brill et al. 2018). Maps and ore shoot cross sections are modified from Brill et al. (2018) and Markl (2017a) and references therein

Each investigated vein system comprises several veins which are N-S and/or NE-SW striking and nearly vertically dipping. Individual veins are under 1 km, up to 2 km and up to 5 km in length for Wieden (Zeschke 1959; Werner et al. 2020), Münstertal (Schürenberg 1950; Bliedtner 1978) and Urberg (Otto 1967; Brill et al. 2018), respectively. The veins consist of elongated, up to 100 m long lenses and vein sections with a highly variable width between 1 and 3.5 m (e.g., this study; Schürenberg 1950). The width is strongly dependent on the host rock, it is wider in gneiss than in granite, and can locally decrease to only a few centimeters (this study; Metz et al. 1957; Otto 1964; Otto 1967; Brill et al. 2018). On average, the veins consist of ~60 vol% fluorite, which together with mainly quartz and barite forms a banded structure (Fig. 1b; Metz et al. 1957; Zeschke 1959; Otto 1964; Steen 2013; Markl 2017a; Brill et al. 2018). Sulfides occur as either local aggregates within the banded structure, or more commonly, are bound to host rock breccias (Fig. 1c). Each of the three vein systems hosted several ore shoots in the mined portions of the veins, at least three in the Münstertal, five at Wieden and at least six at Urberg (Fig. 2). While the gangue mineralogy and mineral successions are fairly similar for the three vein systems (Metz et al. 1957), the ore shoots show an interesting variation from Ag-poor in the Münstertal to Sb-rich and Ni-bearing in Wieden and to Ag- and Ni-rich in Urberg. These ore shoots and/or vein sulfide accumulations are commonly spatially related to wider vein sections, brecciated zones and/or bound to the vein-host rock boundary (Fig. 1c; Metz et al. 1957; Zeschke 1959; Grundmann 1971; Widemann 1988; Markl 2017a; Brill et al. 2018). Impregnations of the ore shoot mineralogy into the host rocks are very rare or absent (Zeschke 1959; Brill et al. 2018). The local host rocks of the veins at the three localities are mostly made up of gneisses with local enrichments of graphite and/or sulfides (Metz et al. 1957; Bliedtner 1978; Brill et al. 2018). Locally dikes of granitic rocks occur (Geyer et al. 2011). In addition to gneisses and granites, the region around Urberg also comprises local occurrences of diorites, amphibolites and norites with associated magmatic Ni-Fe-sulfide lenses (Otto 1964; Brill et al. 2018).

The veins in question were subject to various mining efforts dating back to medieval silver extraction and ending with fluorite extraction during the second half of the 20th century (Markl 2004). In the 20th century

200 the fluorite concentrate production totaled ~0.5 Mt and ~0.15 Mt for the Wieden and Urberg veins over a
201 period of ~40 and ~30 years, respectively (Markl 2017a). The calculated remaining reserves for Wieden
202 were another 0.4 Mt at the time of mine closures at 1965 (Hauck 2020). Although fluorite concentrate was
203 the main product, small amounts of barite concentrate and mixed sulfide concentrate were also recovered
204 at Wieden in the 20th century (Markl 2017a). The mixed sulfide concentrate was used to extract both silver
205 and lead as minor byproducts, but the amounts were quite low (Markl 2017a). As an example, rough
206 estimates indicate that the mined vein material without the ore shoots contained a total of ~20 t Ag at
207 Urberg, while the ore shoots therein contained up to twice as much Ag.
208 All ore shoots have been mined out between 1960 and 1982 and are inaccessible today. Hence, the structural
209 relations between vein and ore shoot can only be inferred from the literature (Schürenberg 1950; Otto 1967;
210 Grundmann 1971; Bliedtner 1978; Brill et al. 2018; Steen 2020; Werner et al. 2020). Their mineralogical
211 composition is based on collection material from the senior author and from the University of Tübingen,
212 while additional microscopic images of samples from the Wieden vein system were provided by Günter
213 Grundmann who had previously worked on the Wieden ore shoots (Grundmann 1971). The hand specimens
214 were carefully compared and inspected; representative samples of ore shoots and associated veins meters
215 to tens of meters away from the ore shoots were selected for further investigations. In total, 38, 33 and 29
216 thick sections for microscopy and microprobe analytical work were prepared from Münstertal, Urberg and
217 Wieden, respectively.
218
219 **Petrography of the mineralization**
220 The paragenetic sequence of both the veins and the ore shoots is presented in Fig. 3 and augmented by
221 literature data in Table 1.
222

		Teufelsgrund	Urberg	Wieden	
sphalerite	**sph**	**+**	**o**	**+**	sulfides
galena	**gn**	**++**	**++**	**++**	
pyrite/ marcasite		**o**	**o**	**o**	
chalcopyrite	**cp**	**-**	**-**	**-**	
acanthite	**act**	**o**	**o**	**o**	
argentite	**arg**			**o**	
native Ag (primary)	**Ag**		**++**	**o**	native elements
native As	**As**	**++**	**-**	**++**	
native Sb	Sb			o	
native Ag (wire)	**Ag**	**o**	**+**	**o**	
niccolite	**nic**		**++**	**o**	arsenides & antimonides
gersdorffite	**gdf**	**-**	**+**	**o**	
rammelsbergite -safflorite ss	**ram**	**-**	**++**	**+**	
skutterudite	**skut**		**++**	**o**	
breithauptite	**brth**			**+**	
ullmannite				**o**	
dyscrasite	dys			**o**	
proustite-pyrargyrite ss	**prou**	**o**	**+**	**++**	Ag-sulfosalts
xantocon-pyrostilpnite ss		-	**o**	**o**	
stephanite		-		**o**	
tennantite-tetrahedrite ss		-	o	**o**	
polybasite			-	**o**	
sternbergite/ argentopyrite	agpy	-		**+**	
miargyrite				o	
matildite			o		
freieslebenite		**-**			
diaphorite		**o**	**o**		
bismuthinite			-		other sulfosalts
ferberite		-		o	
cinnabar			-	-	
boulangerite		**-**			
seligmannite-bournonite ss		**o**	**o**		

Table 1:

Header: Ore shoot associated hydrothermal minerals

Table footnote: Relative abundance is depicted by - (rare), + (common) and ++ (abundant). No information on abundance is depicted by (o). Minerals present in the investigated samples are shown in bold and literature additions in regular font. Literature additions are taken from Otto (1967), Grundmann (1971), Markl (2017a), Brill et al. (2018) and Steen (2020). Abbreviations correspond to the rest of the manuscript

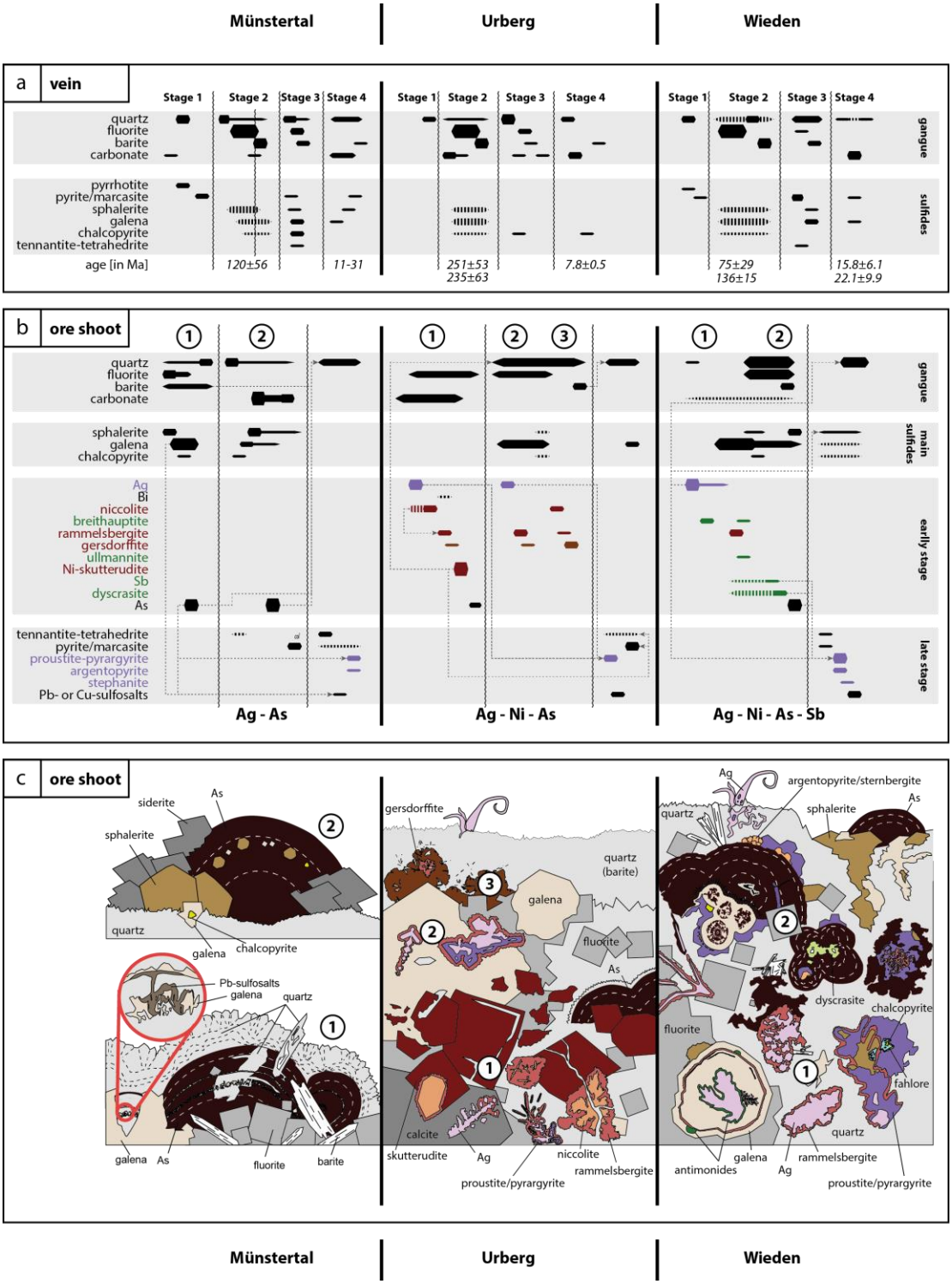

225

226 **Fig. 3** Paragenetic sequence of the hydrothermal vein (a) and of the ore shoot mineralogy (b) with the corresponding
227 schematic textural sketch provided in (c). (a & b) Relative mineral abundance is indicated by line thickness, for which
228 ore and gangue minerals are considered separately. Numbers in (b) and (c) represent the ore shoot sequences. The
229 ages presented in (a) are taken from (Walter et al. 2018b). Dotted arrows in (b) represent typical replacement reactions
230 observed in many samples

The hydrothermal veins

The schematic paragenetic sequence for each vein (Fig. 3a) was taken from Metz et al. (1957) and supplemented/revised according to own observations and to other authors, where reasonable (Schürenberg 1950; Zeschke 1959; Otto 1964; Otto 1967; Bliedtner 1978; Steen 2013; Markl 2017a; Brill et al. 2018; Werner et al. 2020). The mineralization was initiated by a quartz-dominated stage (I) rich in Fe-sulfides and breccias. It shows initial pyrrhotite (not found at Urberg) which was subsequently replaced by pyrite and marcasite (Fig. 3a). The volumetrically most abundant stage is the fluorite-dominated second stage (II), which also contains variable amounts of quartz, barite and carbonate. Barite content increases with time (Fig. 3a). Coarse-grained, massive carbonate is generally rare in stage II and only occurs in larger quantities in Urberg, where it formed prior to and during the transition to the subsequent fluorite-dominated substage of stage II. The fluorite-barite-quartz mixture forms a banded structure with variable proportions of the three minerals. The most abundant sulfide minerals within stage II of these veins are galena, sphalerite and chalcopyrite, the last being the least common of the three (Metz et al. 1957; Steen 2013). The relative proportion of galena and sphalerite within individual thin sections ranges from solely galena to solely sphalerite and no typical sequence regarding the relative time of formation is visible, nor is there a systematic change from early to late within stage II. Tetrahedrite occurs only rarely and locally. Brecciated zones show an increasing abundance of sulfides and quartz – both minerals grow around clasts (this study; Metz et al. 1957; Zeschke 1959; Widemann 1988; Markl 2017a; Brill et al. 2018; Scharrer et al. 2021). There is no textural evidence for sulfide dissolution in the host rock during vein formation. This stage started > 200 Ma ago and lasted until about 75 Ma for the three localities studied here (Walter et al. 2018b). A less abundant, partial repetition of this stage with small variations forms stage III. The last stage IV is temporally and tectonically linked to the opening of the Upper Rhine Graben between ~22 and 8 Ma (Walter et al. 2018b). This stage is dominated by carbonates and forms discontinuously within the vein, mostly within vugs or small veinlets. In the later, generally fluorite-poorer, volumetrically minor hydrothermal stages III and IV, late-stage barite, quartz and/or carbonates form together with rare galena, sphalerite, euhedral pyrite and/or a colloform mixture of pyrite and marcasite.

As-(Ag)-ore shoots in the Münstertal

The Teufelsgrund-Schindler-Herrenwald vein system in the Münstertal comprises two ore shoot sequences which are distinctly different with respect to their gangue, but very similar concerning their ore minerals (Fig. 3b). The initial ore shoot (1) is characterized by the presence of abundant native As on (Fig. 4a) or within fluorite, commonly overgrown by fine-grained micro-crystalline quartz which successively increases in size and sometimes forms euhedral crystals in open spaces (Fig. 4a). The native As is also commonly associated with co-genetic galena (Fig. 4b & c). Less common is the association with sphalerite, which generally forms prior to native As. Fluorite co-precipitated with barite, quartz, galena and native As (Fig. 4d & e), the sub- to euhedral barite was subsequently partially replaced by quartz (Fig. 4e). This texture is a common feature in many Schwarzwald veins (Burisch et al. 2017b). Rarely and locally confined sulfosalts such as minerals of the proustite-pyrargyrite series (Ag_3AsS_3-Ag_3SbS_3), freieslebenite ($AgPbSbS_3$), argentopyrite ($AgFe_2S_3$), sternbergite ($AgFe_2S_3$) and boulangerite ($Pb_5Sb_4S_{11}$) are present (Fig. 4c). These minerals generally form as reaction products from native As or galena either rimming galena in replaced native As aggregates (Fig. 4c) or as independent crystals on top of native As bands.

The later ore shoot sequence (2) was identified in the Giftgrube mine ~1 km south of the Teufelsgrund mine (Fig. 2; Bliedtner 1978) and in the Trudpert adit of the Teufelsgrund mine. It is characterized by the abundance of siderite. The common mineral sequence observed in these samples is early quartz with some fluorite overgrown by chalcopyrite, galena and sphalerite, with the latter being most abundant. The base metal sulfides are in turn overgrown by siderite. During siderite formation, sphalerite, and less commonly galena, continued to form to a lesser extent. Co-genetic with these minerals, colloform native As (Fig. 4f & g) is abundantly present and can reach up to 60 vol% in some hand specimens (see also Bliedtner 1978). Later carbonates such as calcite and dolomite are not uncommon. Several repetitions of this mineral sequence have been observed even on a small scale.

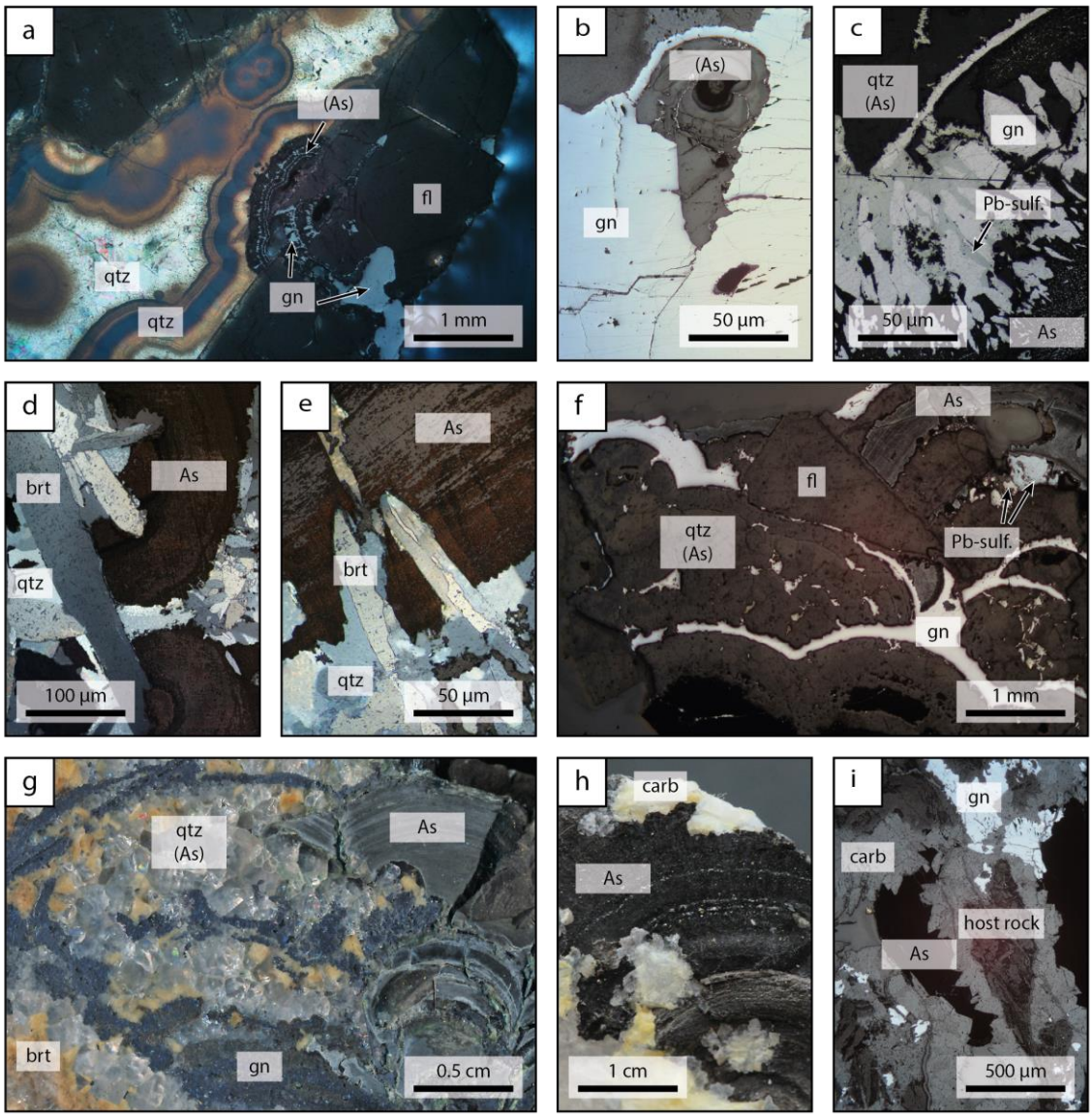

Fig. 4 Textural images of ore shoot sequence 1 (a-g) and ore shoot sequence 2 (h & i). Reflected light images (a-f & i) and macro images (g & h). (a) Early cogenetic intergrowth of fluorite and galena with subsequent intergrowth of galena, native As and fluorite. Late-stage quartz typically shows a coarsening from microcrystalline colloform quartz to palisade quartz. (b) Co-genetic intergrowth of galena and native As in which the latter has been dissolved during alteration. (c) Co-genetic intergrowths of commonly lath-shaped galena and native As in individual bands of the colloform native As. These textures occasionally show a replacement by Pb-sulfosalts such as boulangerite and freieslebenite. (d) Barite rich samples show a co-genetic intergrowth between barite and native As, in which (e) barite is partially replaced by quartz during subsequent alteration. (f & g) Replacement of native As by quartz and rare barite. (h & i) Overgrowth and co-genetic growth of native As on carbonates and sulfides

As-Ag-Ni-Co-ore shoots at Urberg

The Gottesehre vein system near Urberg differs from the other two vein systems with respect to ore shoot abundance and the presence of an early pinkish calcite as one of the gangue minerals. Six different ore shoot pockets have been reported in the literature (Fig. 2; Brill et al. 2018). The largest discovered ore shoot with dimensions of ~20 m x 20 m x 1 m, was mined in 1962–1963 (Otto 1967). Five further (and smaller) ore shoots were discovered and mined in 1965, 1968, 1970, 1978 and 1982, respectively (Brill et al. 2018). The complete mineralogical ore shoot sequence (1-3; Fig. 3b) can only be found in samples of the first and largest ore shoot (this study; Otto 1967), all later ones only show parts of the whole sequence. Individual samples commonly show a high variability in mineral abundance (this study; Brill et al. 2018). As an example, the 1968 ore shoot was mainly composed of native Ag, whereas the 1970 and 1978 ore shoots lacked native Ag and contained abundant arsenides (Brill et al. 2018). Furthermore, the 1970 and 1982 ore shoots showed signs of U enrichment recorded by the presence of secondary U-bearing minerals (Brill et al. 2018). The presence of U is also indicated by the characteristic dark purple color of fluorite of the 1982 ore shoot (Markl 2017a) which was in addition especially rich in niccolite. Although differences in modal amount and presence of minerals exist between ore shoots and samples, the overall mineral sequence (Fig. 3b) is identical in all of them.

The investigation of samples from all ore shoots shows three distinct mineral sequences. The earliest ore shoot sequence was initiated by dendritic aggregates of native Ag up to 10 cm in size and various textural forms of niccolite, ranging from sub- or euhedral individual crystals to dendritic shapes. Interestingly, native Ag and niccolite are not intergrown, even in samples where they occur in close vicinity (< 1 mm). However, since native Ag is commonly isolated within the gangue minerals (Fig. 5a) and only sometimes overgrown by rammelsbergite (Fig. 5b), while niccolite is always overgrown by rammelsbergite (Fig. 5c), a slightly earlier formation of native Ag relative to niccolite may be inferred. The rammelsbergite is then overgrown by abundant skutterudite (Fig. 5d); at the transition, rammelsbergite and skutterudite zones alternate repetitively. Native Bi was only found as small flakes of less than 10 µm size included within arsenides of the first shoot sequence. These ore minerals are found in both colorless and dark purple fluorite

and abundantly in fine- to medium-grained quartz. In these cases, the dark purple fluorite is almost exclusively associated with early-stage pinkish calcite. Skutterudite is rarely overgrown by native As (Fig. 5e), that can also incorporate relics of native Ag. Galena may be present at any point within this sequence but is generally more abundant during the second sequence (Fig. 5f) in which skutterudite is absent and fluorite is always colorless. Hydraulic brecciation (Jébrak 1997) of the first mineral sequence and cementation by subsequent minerals are typical.

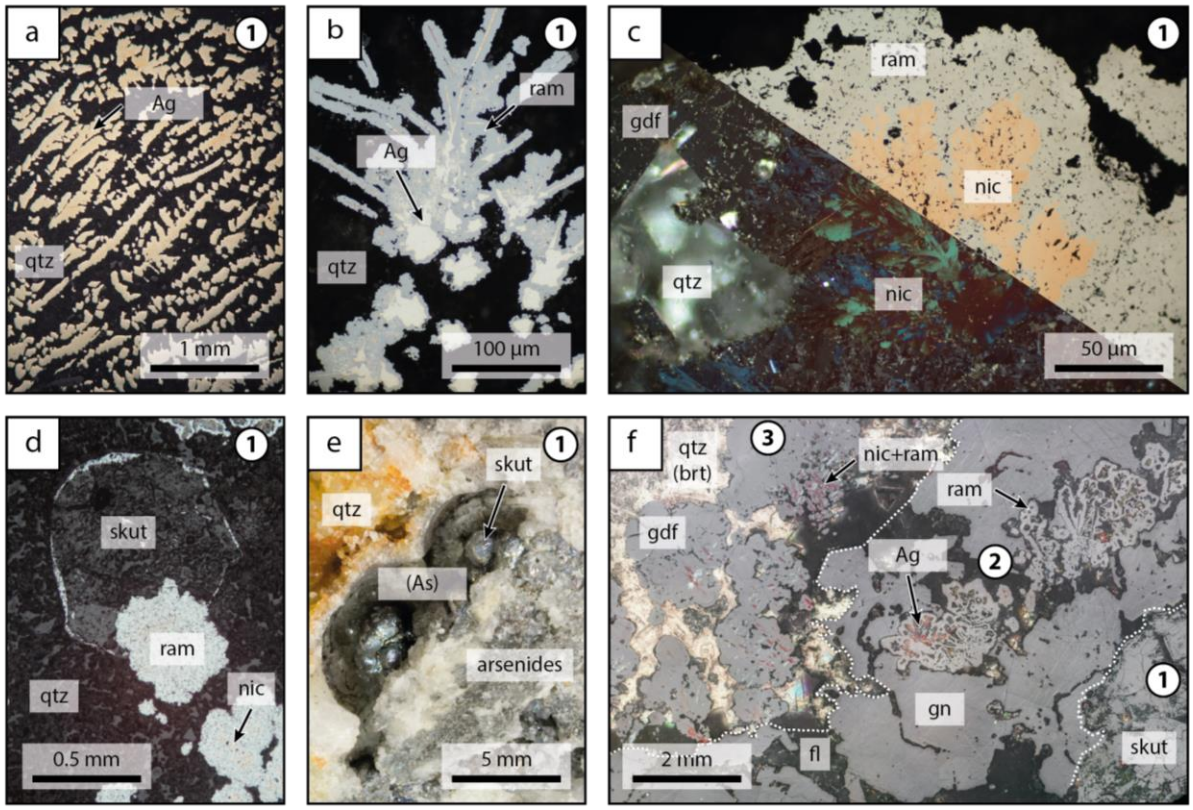

Fig. 5 Reflected light images (a-d & f) and macro image (e) of the Urberg locality. Native Ag is commonly found in dendritic form, either enclosed in the gangue mineral (a) or overgrown by arsenides (b). (c & d) The arsenide sequence is generally niccolite → rammelsbergite → skutterudite. (d) Skutterudite is commonly partially replaced by quartz. (e) The arsenides are in turn rarely overgrown by native As. Both native As and skutterudite are prone to remobilization (d & e). (f) Overgrowth of ore shoot 1 by ore shoot 2 and ore shoot 3, showing the change in mineralogy with time

In the second sequence, native Ag is overgrown by rammelsbergite with abundant galena (Fig. 5f). In the third sequence, dendritic niccolite is overgrown by rammelsbergite and then by colloidal gersdorffite (Fig.

5f). These aggregates are occasionally overgrown by galena or colloform pyrite. Contemporaneous with and subsequent to the gersdorffite, barite could form, which in turn was commonly replaced by later quartz (Fig. 5f).

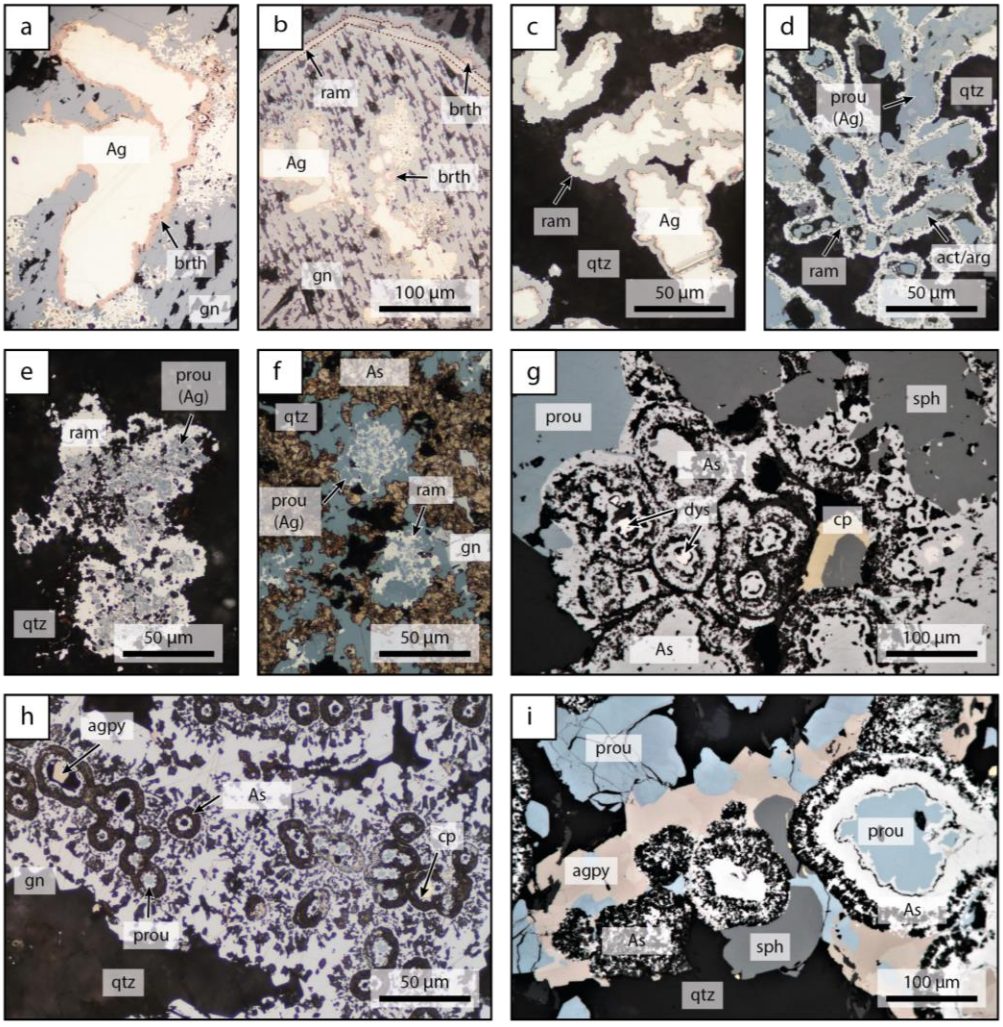

Fig. 6 Reflected light images (a-f) of the Wieden locality. (a & b) Native Ag is intergrown with and overgrown by breithauptite and galena, partial oscillatory repetition of these minerals with the addition of later rammelsbergite. (c & d) Common texture of dendritic native As being directly overgrown by rammelsbergite. (e & f) More intergrown dendritic native Ag with rammelsbergite, overgrown by native As. (g-i) Typical layered intergrowth between galena and native As with discrete sphalerite grains and seldom preserved cores of dyscrasite. Most cores and some native As rich layers (h & i) as well as native Ag (d-f) are replaced by sulfosalts such as argentopyrite, minerals of the proustite-pyrargyrite series and sometimes sphalerite or galena. These minerals are otherwise found as overgrowth on the primary ore shoot minerals (g & i). Images (g) and (i) have been kindly made available by Dr. Günter Grundmann on www.mindat.org (Photo ID: 1038791 and 881932)

As-Ag-(Ni)-Sb-ore shoots at Wieden

A previous descriptive study (Grundmann 1971) reported the occurrence of two spatially separated ore shoots with two types of mineral assemblages in the Tannenboden vein near Wieden: an Sb-Ag-rich one mined in 1964/65 and an As-Ag-rich one mined in 1966 (see Fig. 2c). Similar ore shoots were also found in the Anton, Spitzdobel and Neue Hoffnung veins of the Wieden vein system (Steen 2020). Although the mineralogy varies between ore shoots and samples, the overall mineralogical sequence does not. Thus, for Wieden, each sample represents only a portion of the whole ore shoot mineralogical sequence. The samples investigated in this study, in combination with a revisited textural analysis of the original samples from the Grundmann (1971) study, let us conclude that the two ore shoot assemblages reported by Grundmann (1971) represent an earlier and a later stage within a continuous mineral sequence (see type 1 and 2 in Fig. 3b & c). It is important to note that many of the smaller ore shoots lacked the presence of arsenides, antimonides and native antimony (Markl 2017a).

The Wieden vein system ore shoots are characterized by an abundance of native Ag, native As and Ag-Sb-sulfosalts. The latter formed during the replacement of the primary ore shoot minerals. The initial and locally dominant ore mineral native Ag (Fig. 6a & b) occurs in a variety of dendritic shapes. Rarely it is overgrown by breithauptite (Fig. 6a & b), while rammelsbergite (Fig. 6c & d) is more common. The antimonide formed prior to the arsenide, but this sequence could be repeated several times (Fig. 6b). Intertwined intergrowth between native Ag and rammelsbergite occurs occasionally (Fig. 6e & f), especially in close spatial association with native As. Skutterudite was identified at this locality, but due to its rarity and due to the lack of suitable textures, its relative time of formation could not be ascertained. The replacement of native Ag by minerals of the pyrargyrite-proustite series and to a lesser extent also by other sulfosalts (see table 1) is ubiquitous in all samples, only the degree of replacement varies (Fig. 6d & f). Native As encloses intergrowths between rammelsbergite and minerals of the pyrargyrite-proustite series (originally native Ag ± native As) which implies a later formation of native As relative to rammelsbergite and native Ag (Fig. 6e & f). The native As is commonly intergrown with galena, showing a colloform banded structure (Fig. 6g & h). Galena commonly forms elongated needles oriented perpendicular to the

growth direction or monomineralic bands within the colloform structure. Sphalerite does not show these textures, but more commonly forms euhedral crystals. Individual sub- to euhedral crystals of native As are only visible in rare instances on the outermost zones of the native As aggregates. Not only quartz, but also native Sb rimmed by dyscrasite (As_3Sb; Fig. 6g) can be found as primary cores within the native As aggregates. As in the Münstertal, native As and barite coexist without a reaction boundary. The native As is overgrown by a large variety of different sulfides and sulfosalts, which include the base metal sulfides, tetrahedrite, minerals of the pyrargyrite-proustite series, xanthoconite, argentopyrite, sternbergite and late-stage stephanite and polybasite. However, these sulfosalts more typically form as crystal aggregates together with quartz pseudomorphic after native Ag. They also replace individual layers or the cores of native As. The latter are interpreted as replacement textures of dyscrasite cores by sulfosalts (Fig. 6h & i).

Supergene remobilization

A typical supergene alteration phenomenon in all of these ore shoots is the gradual dissolution of the native As along compositionally and texturally defined zones. Furthermore, the Ag-bearing sulfosalts are successively replaced by Ag-richer sulfides and finally by plates or wires of native Ag. The latter are also found in vugs on carbonates or quartz as well as in negative imprints of native As, produced by dissolution. These reactions are typically accompanied by the formation of other secondary minerals such as oxides, arsenates and carbonates. They are not considered here further.

Methods

Mineral Analyses

Scanning Electron Microscope (SEM) and Electron Microprobe (EMP)

The Hitachi TM3030 SEM Plus Tabletop Microscope in combination with reflected light microscopy at the University of Tübingen was used as a qualitative mineral identification and textural visualization tool. For quantitative mineral analysis in 31 thin-sections, the JEOL SUPERPROBE JXA - 8900RL at the University of Tübingen was used. To avoid the tarnishing of arsenic, the thin sections were re-polished, cleaned with

ethanol and dried at room temperature in a dry-box for half a day before being sputtered with carbon. Analytical condition details and reference materials are described in ESM 1.

Special notice was given to the Lα line used for the analysis of As. Using the ZAF or φ(ρz) correction method yields vastly different results (up to ~10 wt% difference in As content). The latter provides acceptable results for As contents > 70 wt%, while the ZAF correction yields acceptable results for As contents < 55 wt%. For comparability, mono-, di- and sulfarsenides were corrected using the ZAF correction method, while the triarsenides and native As were corrected using the φ(ρz) correction method. To forego this problem in general, we suggest using the Kα line instead.

Sulfur Isotopes

Sulfur isotope samples were carefully handpicked and separated into monomineralic, preferably cogenetic samples of sphalerite, galena, chalcopyrite, pyrite, gersdorffite, proustite and barite. The S isotope compositions were measured with He carrier gas and a Carlo Erba (CE 1100) elemental analyzer linked to a Thermo Fischer Delta V mass spectrometer at Lausanne University, Switzerland. Samples were reacted at 1050 ºC in a stream of He-carrier gas spiked with oxygen gas. External reproducibility of standards was better than 0.15 ‰ and samples were calibrated against IAEA standards S1 and S3 (Ag_2S) and NBS-127 ($BaSO_4$) with accepted values of –0.3, –32.1 and 20.3 ‰ $\delta^{34}S$ (V-CDT), respectively.

Thermodynamic modelling

Thermodynamic modelling was done using the Geochemist's Workbench 14 software bundle (Bethke 2007). Reaction path modelling was performed using the application react and predominance, stability diagrams were produced using the application phase2. The Thermoddem thermodynamic database version June 2017 (Blanc et al. 2012) was used and our mineral additions to it are presented in Table 2. Minerals for which $\Delta_f H^0$, S^0 and $c_p(T)$ are known or estimated, were implemented by the Thermoddem team to keep internal consistency as high as possible. Mineral additions include trechmannite, proustite, mirargyrite, pyrargyrite, rammelsbergite, dyscrasite, allargentum and gersdorffite. In addition to minerals, the database

was also extended to include Ni-chloride complexes and more aqueous Sb species. $NiCl^+$, $NiCl_2$ (aq) and $NiCl_3^-$ from Liu et al. (2012) were implemented using the Ryzhenko parameters and the Thermoddem database temperature-dependent dissociation of H_2O to further increase internal consistency. The added aqueous Sb species were taken from Obolensky et al. (2007) and augmented by the compilation of Bessinger and Apps (2003).

Table 2:

Header: Thermodynamic data for mineral additions to the Thermoddem database

								C_p			
		$\Delta_f H^0$			S^0			a	$b*10^3$	$c*10^{-5}$	
Mineral	Formula	(kJ/mol)			(J/mol.K)			(J/mol.K)	($J/mol.K^2$)	(J/mol/K)	
trechmannite	$AgAsS_2$	-75.69	±1.6	[2]	151	±5	[2]	80.25*	46.9*	1.265*	[1]
proustite	Ag_3AsS_3	-121.4	±2.8	[2]	283	±10	[2]	145.65*	82.88*	1.265*	[1]
mirargyrite	$AgSbS_2$	-135.1	±0.19	[3]	182.21	±0.11	[3]	141.36*	2.65*	7.565*	[1]
pyrargyrite	Ag_3SbS_3	-202.3	±0.48	[3]	301.99	±0.25	[3]	206.76*	38.63*	7.565*	[1]
rammelsbergite	$NiAs_2$	-90.10	±8	[4]	110	±10	[4]	95.40	-5.91	5.33	[4]
breithauptite	NiSb	-74.48	±13	[1]	75.73	±4	[1]	23.31	61.66	9.88	[1]
dyscrasite	Ag_3Sb	-0.190	±0.20	[6]	195.410	±0.30	[5]	only $\Delta_f G(T)$ available [6]			
allargentum	Ag_6Sb	2.576	±0.07	[6]	335.912	±0.10	[5]	only $\Delta_f G(T)$ available [6]			
gersdorffite	NiAsS	only log K(T) available [4]									

Table footnote: Temperature-dependent cp function, given as $c_p(T) = a + b*T + c*T^{-2}$, was estimated according to the Neumann-Kopp rule, assuming $\Delta_r c_p = 0$, for the following reactions: $3Ag_2S + X_2S_3 = 2Ag_3XS_3$, $Ag_2S + X_2S_3 = 2AgXS_3$, NiAs + Sb = As + NiSb, in which X is As or Sb. For NiSb, $\Delta_f H^0$ and S^0 are averaged from the compiled values by Naumov et al. (1971b) and Barin (1995) and the standard deviation represents one sigma. References: [1] this study, [2] Gasanova et al. (2014), [3] Aspiala et al. (2016), [4] Scharrer et al. (2019), [5] Aspiala et al. (2015)

Results

Mineral Analysis

Scanning Electron Microscope (SEM) and Electron Microprobe (EMPA)

Representative analyses can be found in Table 3, the entire dataset is presented in ESM 2. In the following, selected compositional features of each mineral will be discussed.

	sulfosalts								native elements				arsenides - antimonides									
mineral	tet	prou	pyra	brn	dia	frl	agp	Ag	Ag	As	As	Bi	skut	skut	ram	gdf	ulm	nic	brh	asp	
locality	W	U	W	M	M	M	W	U	W	M	M	U	U	U	U	U	W	U	W	M	
sample	WA15	UG02	WA07	MT02	MT16	MT16	WT08	UG03	WT13	KG02	MT02	UG05	UG03	UG05	UG03	UG01	WT10	SUB3	WT10	MT16	
timing	late	late	late	late	late	late	late	2	late	2	1	2	1	2	2	3	1	2	1	1	
Ag	29.97	59.61	67.15	0.07	23.03	19.56	33.81	98.24	99.59	0.46	3.46							0.04			
Cu	15.83			14.07	0.14												0.14				
Zn	6.30	0.01								0.01											
Pb				43.31	31.33	39.64					4.05						1.27				
Fe	0.64			0.02	0.01	0.01	35.52				0.02	0.03	1.60	1.70	1.32	1.22		0.03		34.72	
Co		0.02					0.04					0.03	0.96	3.43	1.00	0.39	0.03	0.27		0.05	
Ni		0.02						0.04				2.21	18.64	15.96	27.68	30.46	27.08	42.47	35.90		
Bi		0.10						0.10				97.21		0.14	0.11	1.74		1.82			
Sb	24.43	20.45	0.44	15.30	25.68	21.95		0.36		1.01	2.33		0.09	0.04	0.06	0.07	55.75	0.09	47.66	0.57	
As	0.63	1.36	13.79	6.10	0.35	0.35	0.17	0.33	0.05	97.92	86.42	0.28	76.21	75.45	65.56	52.34	0.03	52.51	14.14	40.60	
S	21.13	17.70	18.90	20.76	19.03	18.35	30.48	0.11	0.04	0.32	2.65		1.11	1.77	3.06	11.65	14.87	0.55	1.42	21.05	
Se			0.04			0.03				0.32	0.30	0.07	0.38	0.41	0.40	0.25	0.06	0.30	0.11	0.13	
Hg								0.85					0.07				0.07		0.08	0.06	
Total	98.93	99.27	100.32	99.63	99.57	99.89	100.02	100.03	99.68	100.04	99.23	99.83	99.06	99.90	99.19	98.12	99.30	98.08	99.31	97.18	
	$Ag_{5.4}Cu_{4.81}Zn_{1.86}Fe_{0.22}Sb_{3.87}As_{0.16}S_{12.71}$	$Ag_{3.00}Sb_{0.91}As_{0.10}S_{2.99}$	$Ag_{3.10}Sb_{0.02}As_{0.92}S_{2.95}$	$Cu_{1.03}Pb_{0.98}Sb_{0.59}As_{0.38}S_{3.02}$	$Ag_{2.90}Cu_{0.03}Pb_{2.06}Sb_{2.87}As_{0.06}S_{8.07}$	$Ag_{1.00}Pb_{1.02}Sb_{0.96}As_{0.02}S_{3.04}$	$Ag_{1.00}Fe_{2.01}As_{0.01}S_{3.00}$						$Fe_{0.08}Co_{0.05}Ni_{0.89}As_{2.87}S_{0.10}$	$Fe_{0.09}Co_{0.16}Ni_{0.76}As_{2.82}S_{0.15}$	$Fe_{0.05}Co_{0.03}Ni_{0.95}As_{1.76}S_{0.19}$	$Fe_{0.04}Co_{0.01}Ni_{0.96}As_{1.29}S_{0.67}$	$Pb_{0.01}Ni_{0.99}Sb_{0.99}S_{1.00}$	$Co_{0.01}Ni_{0.96}As_{0.96}S_{0.02}$	$Ni_{0.99}Sb_{0.63}As_{0.30}S_{0.07}$	$Fe_{1.02}Sb_{0.01}As_{0.89}S_{1.08}$	

Table 3:

Header: Chemical composition of selected ore minerals (EMPA)

Footnote: Compositional values presented as wt%. Timing represents the shoot sequence described in Fig. 3b. "late" represents remobilization processes. Mineral abbreviations: tet=tetrahedrite, prou=proustite, pyra=pyrargyrite, brn=bournonite, dia=diaphorite, frl=freieslebenite, agp=argentopyrite, Ag=native Ag, As=native As, Bi=native bismuth, skut=skutterudite, ram=rammelsbergite, gdf=gersdorffite, ulm=ullmannite, nic=niccolite, brh=breithauptite, asp=arsenopyrite. Locality abbreviations: M=Münstertal, U=Urberg, W=Wieden

Native As has a variable composition, which can differ distinctly between localities, samples and individual bands within colloform arsenic aggregates (ESM 3). These differences mainly concern the elements Ag, Pb, Sb, S and Se which reach contents of up to 7.27, 7.49, 7.89, 3.04 and 0.56 wt% with an average of 1.32, 1.14, 1.87, 0.98 and 0.35 wt%, respectively. There is a negative correlation between As and these elements, generated by a typical gradual trend of decreasing elemental content within individual bands from the center to the outer margin of colloform arsenic aggregates (ESM 3). In some bands, inhomogeneities on the µm scale are visible. These could represent cogenetic or exsolved micrograins of Ag-S-rich minerals (ESM 3). Based on the Ag-S ratio (ESM 3), the presence of Sb and the absence of other elements, the microinclusions seem to represent either $Ag_3Sb_4S_6$ (aramayoit) or $Ag_3(As,Sb)S_3$ (e.g. proustite-pyrargyrite). However, these are only present in some individual bands, commonly linked to lower Sb contents in the surrounding native As, and it is not suggested that microinclusions are the reason for the high contents of minor elements in native arsenic in the continuously banded regions (ESM3). Rather, these elements appear to represent real minor elements substituted into the crystal structure of native arsenic. Similar contents have been reported from other localities by George et al. (2015).

Native Ag shows a clear compositional distinction between primary dendritic silver formed cogenetically with the ore shoot minerals and remobilized platy or wire silver. The latter has significantly lower trace element contents, commonly below the detection limit of the electron microprobe. Average trace element contents of the primary silver are 0.25 wt% Sb, 0.36 wt% As, 0.10 wt% S and 1.25 wt% Hg (ESM 3). In rare patchy zonations of native Ag of the first ore shoot sequence at Urberg, Hg may locally reach up to 14 wt% (ESM 3).

Due to the small size of native Bi, mixed analyses with the surrounding rammelsbergite cannot be excluded (Table 3). However, the analyzed compositional variation among the six analyses is fairly low and the molar Ni/As ratio is about 8 and not 0.5 as in rammelsbergite. The Ni and As contents in native Bi are 1.7 ± 0.3 wt% and 0.27 ± 0.04 wt%, respectively.

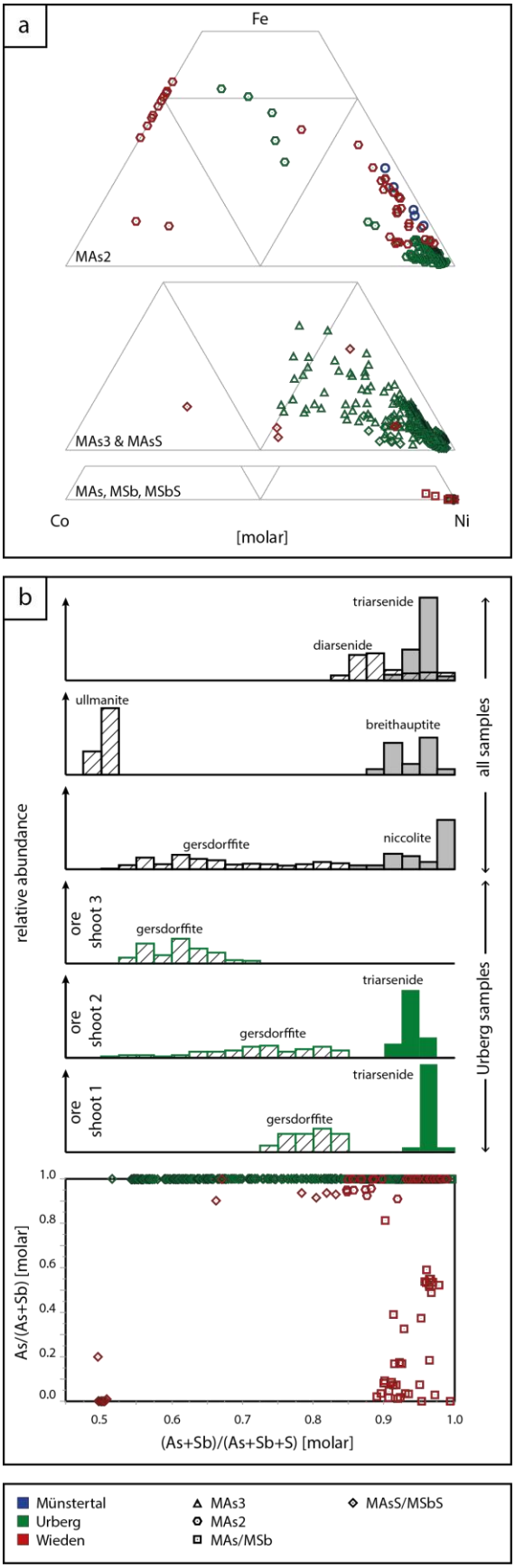

Fig. 7 Compositional variations of the arsenides and antimonides. (a) Most arsenides and antimonides are Ni-dominated, with the monoarsenides and monoantimonides showing the least spread with respect to Ni, Co and Fe. (b) Compositional distribution with respect to sulfur content and As/(As+Sb) ratio within all samples and between different ore shoot sequences of Urberg. The distribution between the As- and Sb-endmembers shows the sole presence of arsenides for Urberg and the presence of both with a partial solid solution for Wieden. Arsenopyrite is excluded in this figure

477

The arsenides, sulfarsenides, antimonides and sulfantimonides are mostly Ni-dominated with average molar Ni/(Ni+Co+Fe) ratios of 0.79 for skutterudite, 0.80 for diarsenides, 0.995 for niccolite, 0.92 for gersdorffite, 0.993 for breithauptite and 0.997 for ullmannite (Fig. 7a). Thus, the diarsenides are almost exclusively of rammelsbergite composition. This excludes one outlier sample from Wieden that contains diarsenides of the safflorite-loellingite series. These are associated only with quartz and therefore cannot be texturally correlated with the other minerals. The arsenides and antimonides incorporate sulfur to various degrees (Fig. 7b). This is especially visible for gersdorffite, which ranges from 0.31 to 0.95 atoms per formula unit sulfur. Furthermore, the degree of As-S exchange varies with time at the Urberg locality and thus, an increase in sulfur relative to arsenic is visible with progressing ore shoot sequences (Fig. 7b). Bismuth was detected in niccolite and shows an average content of ~1.4 wt%. Selenium is present in all arsenides and antimonides and reaches up to ~0.4 wt%. The arsenides and sulfarsenides typically show some degree of Sb-As exchange. For example, arsenides of the Wieden locality, which is also host to cogenetic antimonides, show the highest contents of antimony, reaching up to ~10 wt% (Fig. 7b).

Galena is the most common base metal sulfide, contains up to 2 wt% of silver and has an average formula of $Pb_{0.99}Ag_{0.01}Sb_{0.01}S_{0.99}$. Sphalerite is more variable in composition and the molar Fe/(Fe+Zn) ratio ranges from ~0.001 to 0.13. It is manganese-poor and the cadmium content is below 1 wt% with an average of ~0.3 wt%. Analyzed pyrite reveals a high arsenic content of on average 4.5 wt% and a trace elemental composition of on average ~0.5 wt% Ag, 0.3 wt% Sb and 0.06 wt% Co. The colloform pyrite variety also contains up to 2.5 wt% Pb, which may be related to microinclusions of galena that could not be resolved.

Although the primary mineralogy of the ore shoots is dominated by arsenic-rich endmembers, most sulfosalts that form during remobilizing processes are in fact Sb-dominated (ESM 4). This includes diaphorite, freieslebenite, tetrahedrite and bournonite with molar As/(As+Sb) ratios of less than 0.4. Minerals of the proustite-pyrargyrite solid solution series show the presence of both As- and Sb-rich minerals, ranging from the pure As-endmember to a molar As/(As+Sb) ratio of ~0.1. The Sb-rich pyrargyrite forms independent of texture, even if it directly replaces native As and no primary Sb-minerals

503 are present. The only As-dominated sulfosalt besides proustite is argentopyrite with an average formula of

504 $Ag_{0.94}Fe_{2.02}As_{0.01}S_{3.02}$ and an average molar As/(As+Sb) ratio of 0.997.

505

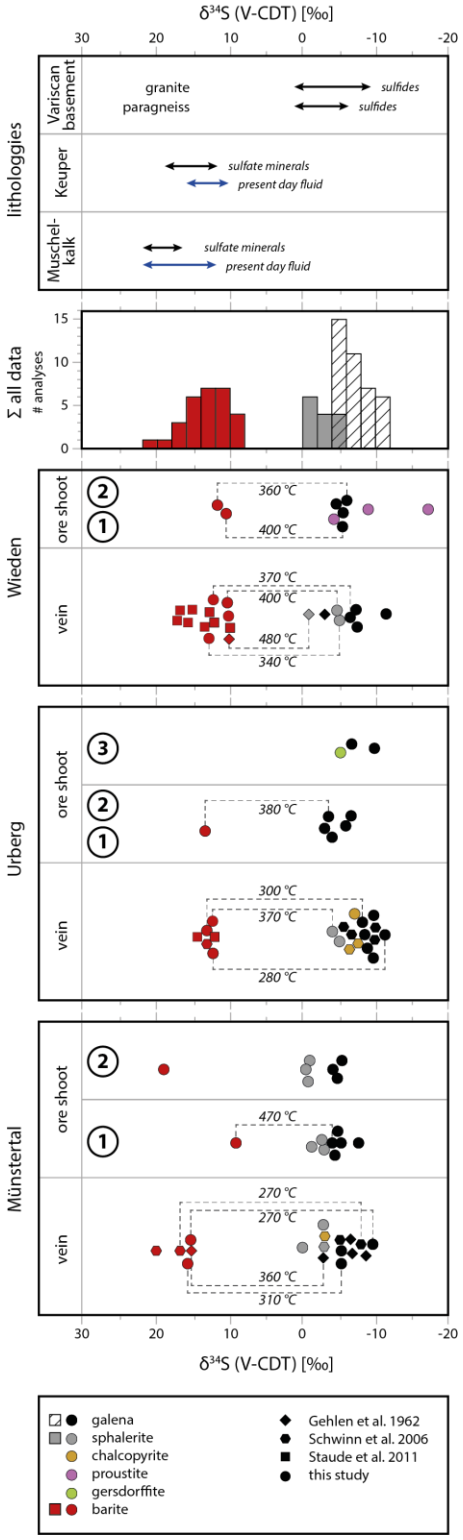

Fig. 8 Isotopic signature of vein and ore shoot sulfates, sulfides and sulfosalts. Texturally classified co-genetic sulfate-sulfide pairs are linked by a dashed line and the respective calculated equilibrium temperatures are given in °C. Possible regional sulfate and sulfide source, with the present-day aquifer isotopic range depicted by blue arrows and sulfate-/sulfide-mineral isotopic ranges depicted by black arrows. Literature data from Müller et al. (1966), Siewers (1977), and Rick (1990) of possible sulfate and sulfide sources reveal the large overlap between the sedimentary sulfate for sulfate and the basement sulfides for the sulfides

506

507 Sulfur Isotopes

508 The minerals selected for sulfur isotope compositional analyses were chosen to cover (I) all localities, (II)
509 all ore shoot mineral assemblages, (III) cogenetic barite and sulfides or sulfarsenides at each locality and
510 (IV) sulfides and barite from the hydrothermal veins far away from the ore shoots. All analyzed samples
511 and respective values are presented in ESM 5 and, together with calculated equilibrium temperatures for
512 cogenetic sulfide-barite pairs, in Fig. 8.

513 The $\delta^{34}S$ (V-CDT) of barite ranges from ~10 to 20 ‰, whereas the sulfides show more negative values,
514 below 0 ‰ $\delta^{34}S$ (V-CDT). Only the late-stage colloform pyrite commonly associated with barite from
515 Münstertal and Wieden reaches strongly depleted $\delta^{34}S$ values of –27.8 to –36.2 ‰ (ESM 5), while the other
516 sulfides are in the range from 0 to –10 ‰ $\delta^{34}S$ (V-CDT). The weighted $\delta^{34}S$ (V-CDT) average including all
517 localities is –6.8 ‰ for galena, –3.6 ‰ for sphalerite and –5.3‰ for chalcopyrite. Proustite and gersdorffite
518 lie in the range of these sulfides.

519 Considering variations between the samples, there is no recognizable difference between the ore shoots and
520 the rest of the hydrothermal system (Fig. 8): S isotope values of sulfides in the ore shoots and in the veins,
521 and of barite in the ore shoots and in the veins are very similar to each other. The only exception is one
522 barite analysis of the first ore shoot sequence of the Münstertal, which is more than 5 ‰ lower than barite
523 from the vein.

524 In samples with co-genetic sulfide and sulfate, sulfate-sulfide equilibrium temperatures were calculated.
525 These are presented in Fig. 8 and result in temperatures between 270 and 480 °C (excluding pyrite) for all
526 three localities and independent of ore shoot or vein. In view of the fluid inclusion constraints (see below),
527 these temperatures are considered unrealistic and the S-bearing phases were obviously not in isotopic
528 equilibrium. This will be discussed below. The late-stage colloform pyrite, which generally occurs as layers
529 within or on top of barite, indicates an equilibrium temperature of 110 °C.

530

531 **Fluid constraints**

532 **Fluid composition and temperature**

Extensive fluid inclusion investigations of more than 1600 individual fluid inclusions from both the ore shoots and the veins of all three localities are presented by Scharrer et al. (2021). The most important aspects of this work will be repeated here with a specific focus on the variations between the ore shoots and the vein and the range of trace element composition. The fluid composition was determined by microthermometry (Fig. 9) and LA-ICP-MS (Fig. 10) on individual fluid inclusions in fluorite, quartz and carbonate. Fluid inclusion assemblages were characterized as primary, clusters and secondary according to the classification of (Goldstein and Reynolds 1994; Walter et al. 2015). In addition, fluid inclusion assemblages were grouped into those co-genetic with the primary minerals of the ore shoots and those co-genetic with the common vein association. The dataset by Scharrer et al. (2021) includes ~1650 fluid inclusions analyzed by microthermometry that were chosen based on both spatial and temporal coverage of the main hydrothermal stage of the investigated veins. Furthermore, if available, fluid inclusion assemblages in fluorite that formed contemporaneously with minerals, in which fluid inclusions could not be measured, were preferentially analyzed (Scharrer et al. 2021). This includes early calcite for the Urberg samples and sulfides, arsenides and native elements for all samples.

Both major (Fig. 9) and some minor elements (Scharrer et al. 2021) in fluid inclusions show a linear correlation in samples from all three localities, suggesting a mixing process between two endmember fluids. These endmember fluids both showed a high salinity (20-25 wt% NaCl eq.); fluid A was rich in $CaCl_2$, whereas fluid B was NaCl-dominated and richer in KCl (Table 4). The approximate position of endmember A' in the NaCl-$CaCl_2$-space presented in Fig. 9 is estimated by extrapolation of the KCl content to near 0. There is no statistical difference between fluids A and B regarding homogenization temperature and most trace elements such as As, Bi, Sb, S and the transition metals. The homogenization temperature (in °C) varies between localities and is 90-150 (average: 122 ± 8), 100-170 (average: 131 ± 14) and 80-150 (average: 117 ± 12) for the Münstertal, Urberg and Wieden vein systems, respectively (Fig. 9). Pressure-corrected, this results in formation temperatures (in °C) of 110-170 (average: 140), 110-180 (average: 140) and 100-170 (average: 140) respectively. These values perfectly agree with many earlier values in similar veins from the region reported in e.g., Baatartsogt et al. (2007) and Walter et al. (2017).

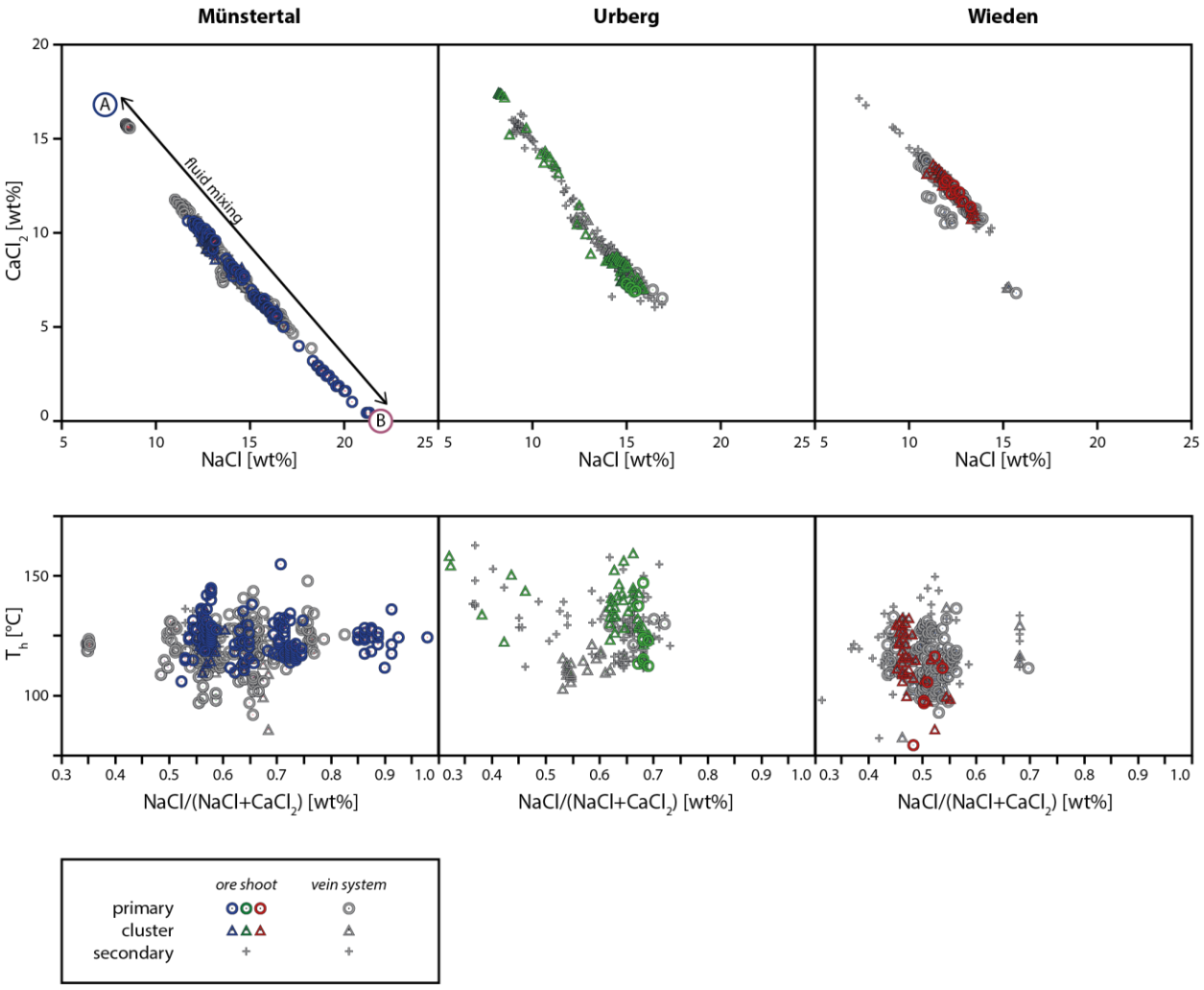

559

560 **Fig. 9** The binary fluid mixing of fluid A and fluid B is visible for both the ore shoot (colored) and the vein-hosted
561 fluid inclusions (grey) for each of the three investigated localities. Furthermore, no change in homogenization
562 temperature is visible between vein and ore shoot assemblage. Data from Scharrer et al. (2021)

563

564 The trace elemental abundance typically shows a large spread of commonly one or more orders of
565 magnitude (Fig. 10). This can be attributed to either inhomogeneities in the primary fluid composition, or
566 more likely, evidence for prior mineral precipitation (Scharrer et al. 2021). Due to the high detection limit
567 and uncertainties of LA-ICP-MS fluid inclusion analyses in fluorite (Scharrer et al. 2021), it is vital to
568 consider both the analyzed content as well as the detection limit for those analyses below the detection limit
569 (Fig. 10).

570

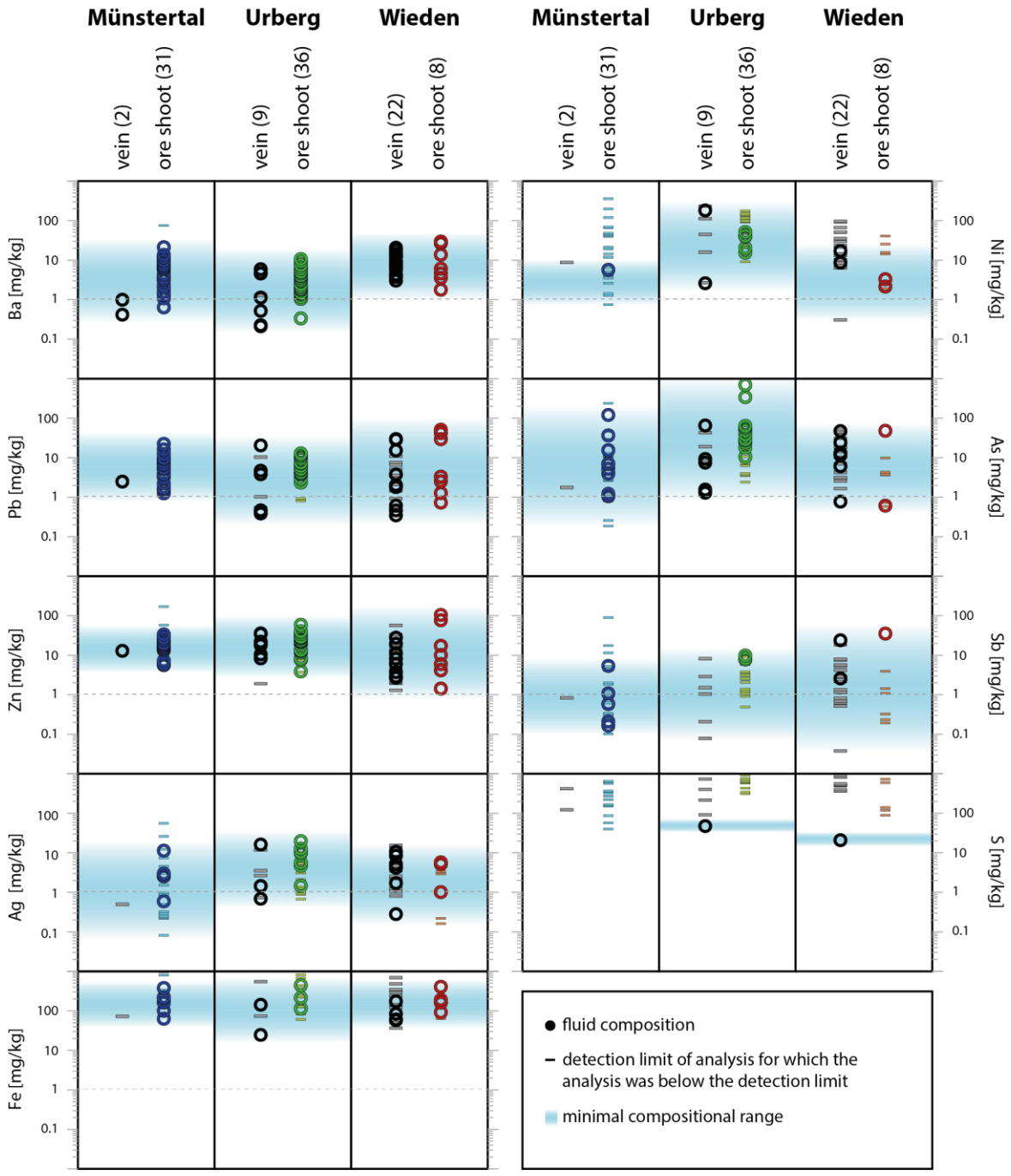

Fig. 10 Selected transition metals and As, Sb and S trace element composition of fluid inclusions of both the vein and the ore shoots, as measured by LA-ICP-MS. Blue fields are estimated realistic ranges of the fluid composition. These estimations are based on detected elemental abundance (circle symbols), detection limit of those analyses for which the analysis was below the detection limit and thus quantification was not possible (line symbols). Number of analyses (in brackets) does not always reflect number of symbols, as some elements could not be quantified for some analyses. Data from Scharrer et al. (2021). No significant difference between vein and ore shoot could be identified

For subsequent thermodynamic modelling, rounded maximum analyzed concentrations from LA-ICP-MS analyses were used. The Pb content was rounded up to 100 mg/kg to represent both Pb (up to 40 mg/kg) and Zn (up to 80 mg/kg). Such a simplification is possible due to the similar behavior of the two elements (e.g., Barrett and Anderson 1988). To reduce an obscuring complexity in the modeled diagrams, the number of components was reduced during modeling. To better depict the differences in mineralogy, Ni was assumed to be 0 for the Münstertal and Sb to be 0 for the Münstertal and Urberg localities. The summary of the analyzed fluid compositions and the fluid composition used for thermodynamic modeling is given in Table 4.

Table 4: Fluid compositions

		Münstertal			Urberg			Wieden		
		fluid A	fluid B	model	fluid A	fluid B	model	fluid A	fluid B	model
T	[°C]	110-170		150	110-180		150	100-170		150
NaCl	[wt%]	<8	22	20	<8	>17	20	<7	>15	20
CaCl2	[wt%]	>16	0		>18	<7		>17	<10	
K	[wt%]	<0.4	1.5		0.2	>1		<0.4	>1	
Ba	[mg/kg]	20-100		100	20-70		100	30-100		100
Pb	[mg/kg]	2-20		100	0.4-20		100	0.3-40		100
Zn	[mg/kg]	6-30			<2-60			5-80		
Ag	[mg/kg]	<0.09-5		10	0.2-9		10	<0.1-4		10
Fe	[mg/kg]	60-400			20-400			60-400		
Ni	[mg/kg]	<0.9-6*		0	3-200		100	<0.3-20		10
U	[mg/kg]	n.a.			<0.03-30			n.a.		
As	[mg/kg]	0.02-100		1000	2-700		1000	0.6-50		50
Bi	[mg/kg]	n.a.			<0.02-4			n.a.		
Sb	[mg/kg]	<0.1-5		0	<0.09-10		0	<0.04-40		
S6+	[mg/kg]	<40			50*			20*		
S2-	[mg/kg]	n.a.		10	n.a.		10	n.a.		10

Table Footnote: Model represents the values used for thermodynamic modeling. ”n.a.” represents not analyzed elements. Fluid compositional range is rounded to one significant figure

Aqueous species

The implementation of all essential and available aqueous thermodynamic species is a vital step for thermodynamic modeling. The aqueous species calculated for the established fluid composition (see section above and Table 4) at the temperature of vein formation (ca. 150 °C based on fluid inclusion data of Scharrer et al. 2021) are depicted in ESM 6. Although the Cl-content of the fluid is high, the non-metal Cl-complexes for arsenic and antimony are mostly confined to an acidic pH. Therefore, the most prominent species are hydroxide complexes. For As and for Sb, the H_3AsO_3 and the H_3SbO_3 complexes are the most prominent under hydrothermal, moderately reduced conditions and a roughly neutral pH, which reflect a crustal environment. This is in accordance with Marini and Accornero (2007) for As. At more oxidizing conditions, arsenite complexes become more prominent. Unfortunately, the necessary thermodynamic data for some antimonite-complexes are still lacking. The metal species show the importance of Cl-complexes that are stable under a wide pH range, up to a pH of ~8-9.

Discussion

Gangue mineral formation (simple binary fluid mixing)

To understand the formation of the ore shoots themselves, it is crucial to first understand the formation of the normal hydrothermal veins that host them. Their petrogenesis in the Schwarzwald region was the subject of several previous contributions (e.g., Schwinn et al. 2006; Baatartsogt et al. 2007; Staude et al. 2011; Bons et al. 2014; Walter et al. 2016; Walter et al. 2018b; Walter et al. 2019). Furthermore, a recent study (Scharrer et al. 2021) focused specifically on the three vein systems of the current contribution. The previous studies showed that the vein stage hosting the ore shoots under consideration here belongs to a large group of so-called Jurassic-Cretaceous fluorite-quartz-barite-carbonate veins that formed from the late Triassic to the early Tertiary (Walter et al. 2016; Walter et al. 2018b; Scharrer et al. 2021). Gangue mineral precipitation occurred due to mixing of fluid A, a $CaCl_2$-dominated, KCl-poor, deeper seated modified bittern brine with a salinity of ~25 wt% $CaCl_2$ + NaCl, and fluid B, a NaCl-dominated and KCl-richer bittern or halite dissolution brine situated at shallower depths in the crystalline basement with

salinities of ~22 wt% NaCl + $CaCl_2$ (Scharrer et al. 2021). Simple binary fluid mixing, likely in combination with various degrees of fluid cooling, has resulted in the precipitation of gangue minerals (e.g., Schwinn et al. 2006; Baatartsogt et al. 2007; Walter et al. 2017; Scharrer et al. 2021). The sulfides in this normal vein type consist mainly of galena, sphalerite and chalcopyrite. Their formation will be discussed in more below, together with the formation of sulfides in the arsenide-dominated ore shoots.

Formation of the main ore shoot mineralogy without the sulfides by reduction

The native As-bearing ore shoot mineral assemblage is quite different from the mineral association in the normal hydrothermal veins. The ore shoots can be regarded as different entities within the same vein structure that formed contemporaneously, but locally and temporally confined within the vein.

Formation mechanism

In general, the stabilities of hydrothermal mineral assemblages are defined by parameters such as pressure, temperature, fluid composition, redox and pH at the time of formation. Hence, a change in one of these parameters should govern the change from the normal vein assemblage to an ore shoot assemblage.

As veins and ore shoots formed contemporaneously, a pressure change can be ruled out. Furthermore, our comprehensive fluid inclusion study showed no involvement of fluid boiling either in the veins or in the ore shoots (Scharrer et al. 2021). In addition, fluid inclusion homogenization temperatures of both the ore shoots and the rest of the vein cover the same range (Fig. 9) and, hence, also exclude changes in temperature to be responsible for the change from vein to ore shoot precipitation. The fluid inclusion work by Scharrer et al. (2021) also shows no systematic difference between the fluid mixture that formed the normal vein and that, which formed the ore shoots with respect to their major (Fig. 9) or minor (Fig. 10) element composition. Furthermore, Figure 9 provides clear evidence that both fluid A and fluid B, whose mixing formed the normal vein assemblage, were present not only during vein, but also during ore shoot formation. A change in fluid composition or the involvement of a volumetrically major and compositionally different third fluid involved in the formation of the ore shoots can, thus, be excluded.

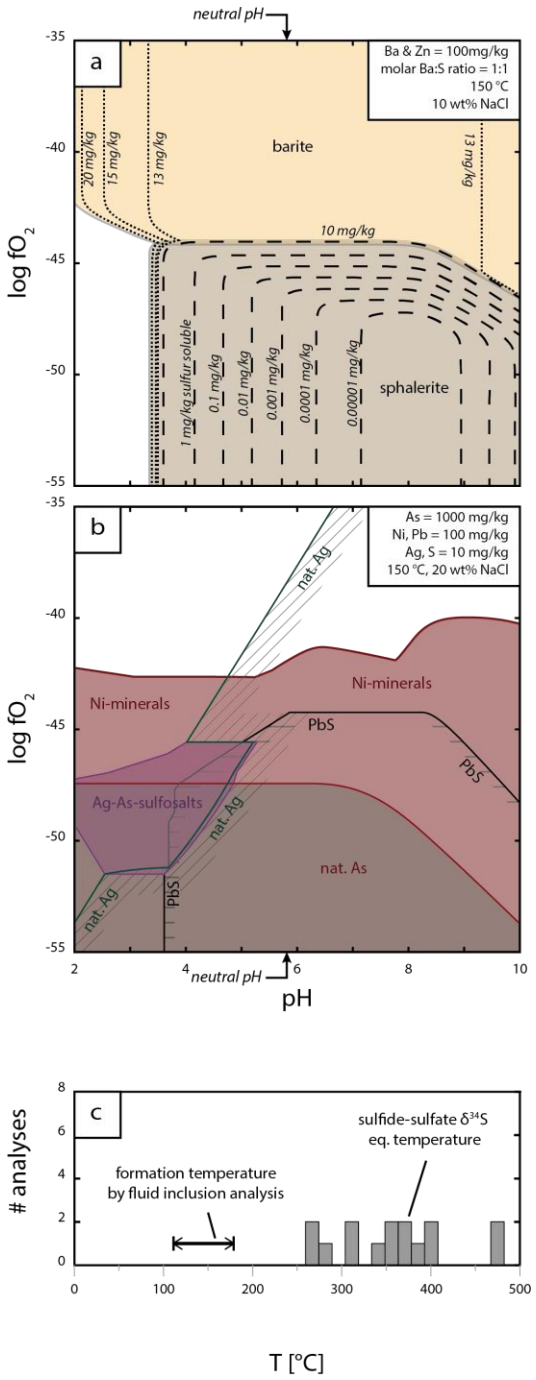

643

644 **Fig. 11** Thermodynamic model of the redox-pH relationship of various minerals. For the sake of clarity, the stability
645 region of native Ag is not completely filled. Its shaded area is only depicted as a rim. (a) The solubility of sulfur is
646 depicted in an equilibrium system considering the rounded typical Ba- and Pb-content of the vein fluids. (b) Simplified
647 mineral relations in the Ni-Ag-Pb-As-S system considering the typical fluid composition of Urberg as an example.
648 Both native Ag and Ni-minerals (such as Ni-arsenides, Ni-sulfarsenide, Ni-sulfides and native Ni) form at more
649 oxidizing environments than galena

650

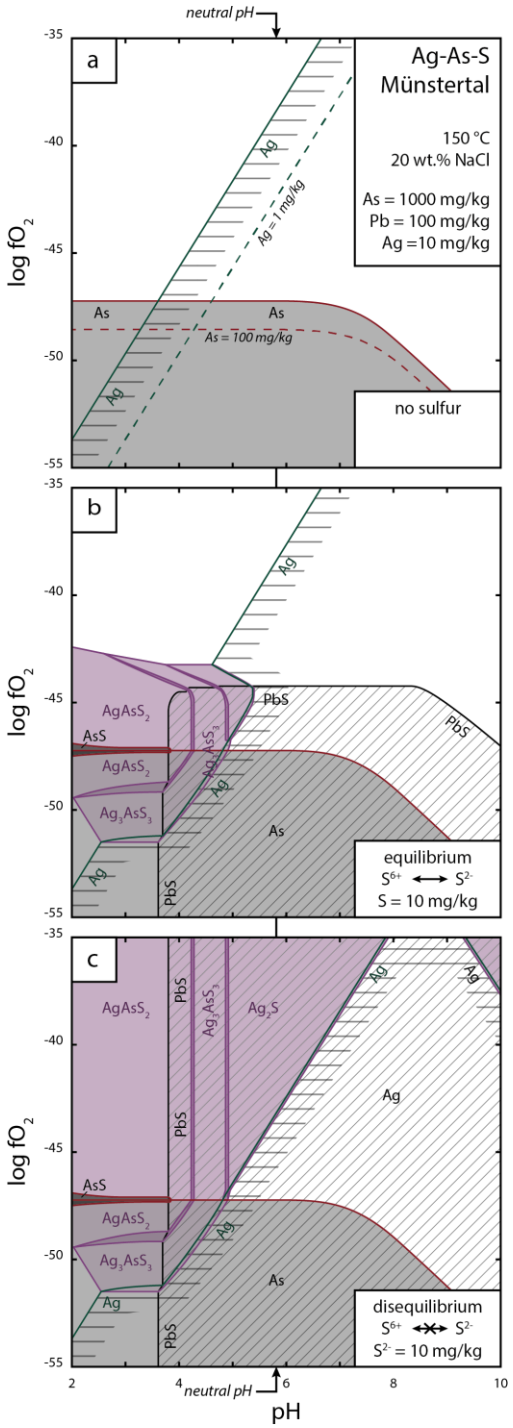

Fig. 12 Thermodynamic modeling of (Ag)-As ore shoots of the Münstertal locality. For the sake of clarity, the stability region of native Ag is not completely filled. Their shaded area, by diagonal and horizontal lines respective, is only depicted as a rim. Fluid composition is taken from Table 4 and (a) represents a sulfur-free system, (b) represents a sulfur poor system with a sulfate-sulfide equilibrium and (c) represents a sulfur-poor system with a sulfate-sulfide disequilibrium as is the case at hand

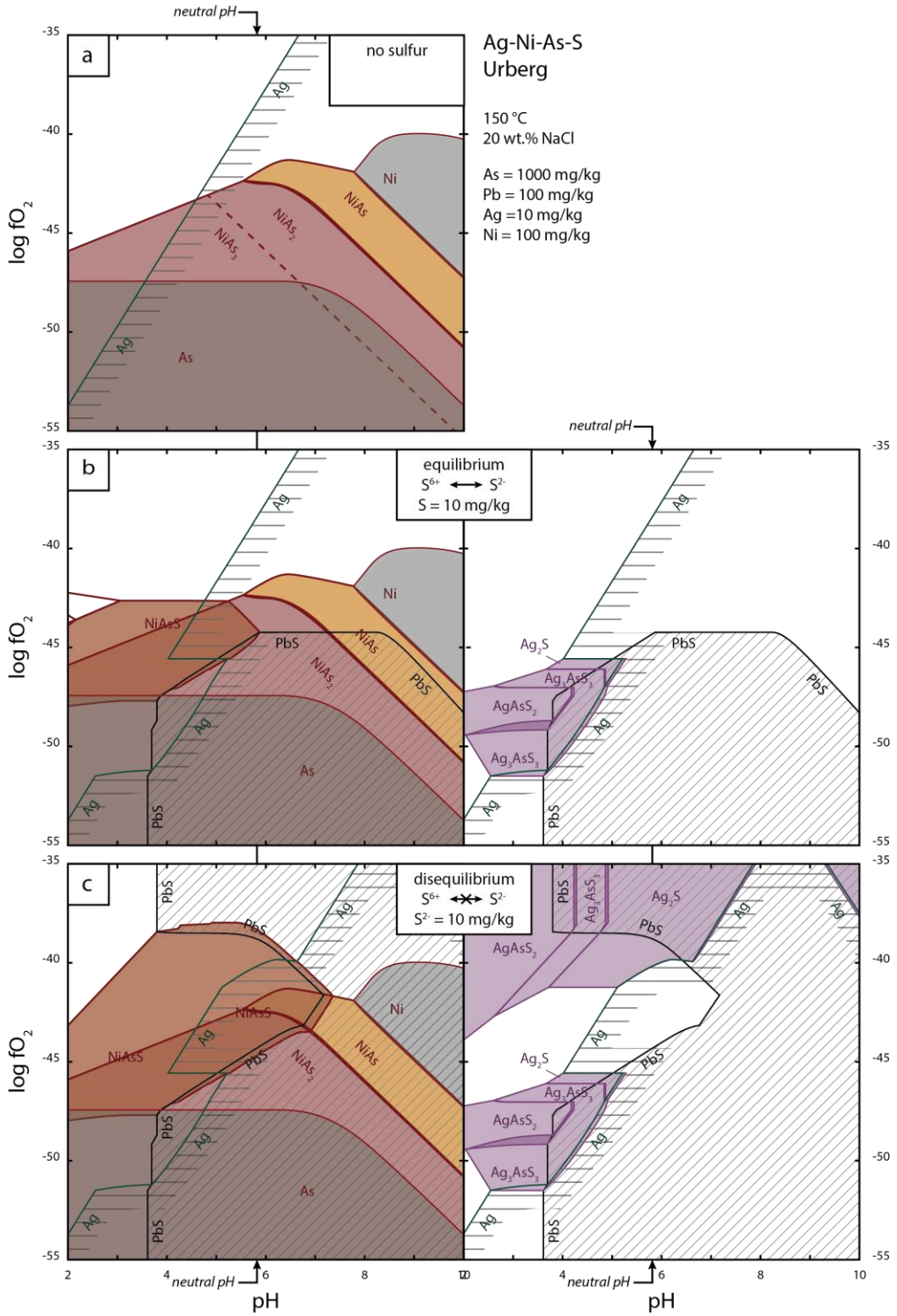

Fig. 13 Thermodynamic modeling of Ag-Ni-As ore shoots of the Urberg locality. For the sake of clarity, the stability region of native Ag is not completely filled. Their shaded area, by diagonal and horizontal lines respective, is only depicted as a rim. Fluid composition is taken from Table 4 and (a) represents a sulfur-free system, (b) represents a sulfur poor system with a sulfate-sulfide equilibrium and (c) represents a sulfur-poor system with a sulfate-sulfide disequilibrium as is the case at hand

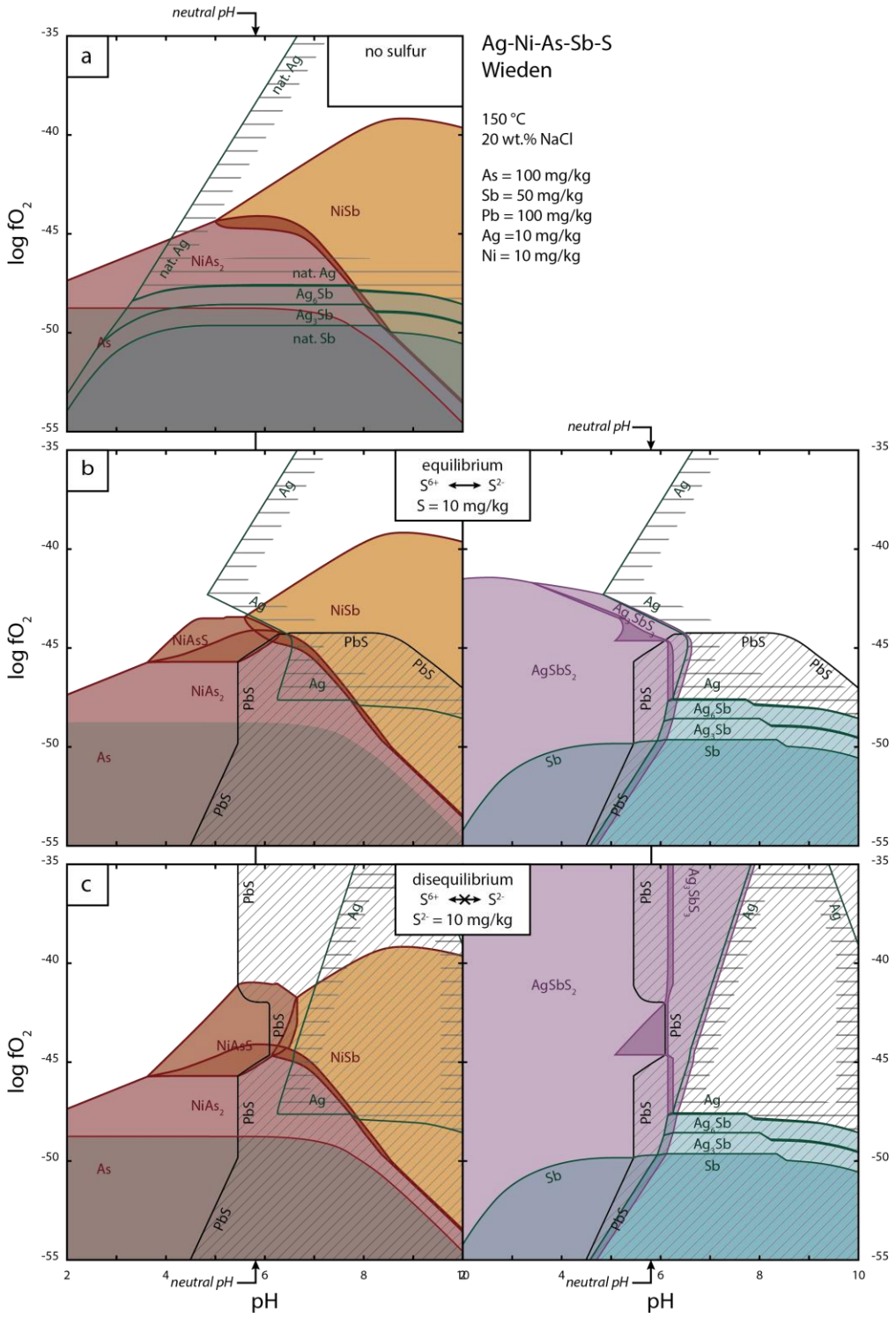

Fig. 14 Thermodynamic modeling of Ag-Ni-Sb-As ore shoots of the Wieden locality. For the sake of clarity, the stability region of native Ag is not completely filled. Their shaded area, by diagonal and horizontal lines respective, is only depicted as a rim. Fluid composition is taken from Table 4 and (a) represents a sulfur-free system, (b) represents a sulfur poor system with a sulfate-sulfide equilibrium and (c) represents a sulfur-poor system with a sulfate-sulfide disequilibrium as is the case at hand

Based on the line of arguments above, the process of fluid mixing was still present during ore shoot formation. The fact, that the normal vein assemblage is also present in the ore shoots, corroborates this statement. On the other hand, native elements and/or arsenides exclusively formed in the ore shoots which calls for a change in redox and or pH. Although pH is crucial in defining which aqueous and mineral species are stable, a change in pH does not suffice to explain the formation of these ore shoots (Fig. 11). For example, an increase or decrease in pH from roughly neutral starting conditions does not result in the formation of native As, in the consecutive formation of niccolite and rammelsbergite, or of native Ag followed by native As (see Fig. 12, 13 & 14) which are so strikingly present in our samples (Fig. 3, Fig. 4, Fig. 5 and Fig. 6). Based on these arguments, we conclude that normal vein mineralization and ore shoots formed from the same mixing process of the same two fluids, but that an additional reducing agent must have taken part in ore shoot formation. This is in agreement with earlier work of e.g., Markl et al. (2016), Burisch et al. (2017a), Kreissl et al. (2018) and Scharrer et al. (2019), but it is a significant and important step forward, as for the first time, it is shown that identical fluids can produce normal veins and five-element ore shoots, just by adding a reducing agent.

Type and source of the reducing agent

In the following, possible reducing agents for the investigated ore shoot assemblages will be discussed. Solid reducing agents such as Fe^{2+}-bearing minerals or graphite have been proposed as reducing agents for native element-arsenide associations (Robinson and Ohmoto 1973; Kissin 1993; Ondrus et al. 2003a; Kreissl et al. 2018). However, they are unlikely to have been involved here, because neither relics of such phases nor reaction textures involving such phases were observed in our samples. Instead, both graphite and Fe^{2+}-minerals like biotite are present in the host rocks and there is no spatial correlation between them and the ore shoots. Furthermore, they are distributed throughout most of the host rocks (graphite only in the gneiss) which would not explain the very localized occurrence of the ore shoots.

This leaves as possible agents mobile species such as gases, liquids or aqueous compounds, and specifically mobile hydrocarbons or possibly H_2. Scharrer et al. (2021) did indeed find H_2 and rarely minor amounts of hydrocarbons in the gaseous phase of the fluid inclusions by Raman spectroscopy at room temperature. The small amounts of such gases are not surprising, because as long as the reducing agent is the limiting factor, it will be completely consumed, while the oxidant, e.g., arsenite or arsenate, would only be partially consumed. Thus, it is very rare to find mobile reducing agents as they typically completely react as long as oxidized aqueous arsenic species are present. Kerrich et al. (1986), Essarraj et al. (2005), Levresse et al. (2016) and Burisch et al. (2017a) report such findings, which proves that hydrocarbons are viable reducing agents to produce native element-arsenide assemblages.

The source of such hydrocarbons, however, remains somewhat enigmatic. One potential source of hydrocarbons are rocks of the paleo subduction zone of the Badenweiler–Lenzkirch suture (BLZ), which today outcrops ~5 km south of the Münstertal and Wieden localities and which dips towards the north (Huth and Zedler 2019). The rocks of this suture zone comprise, among others, greywackes and marine clay stones metamorphosed only at very low grades (Huth and Zedler 2019) which contain small coal occurrences (Geyer et al. 2011) and, hence, potentially also hydrocarbons. On the other hand, the Urberg vein system is south of the BLZ and, hence, cannot be related to it.

Other hydrocarbon-bearing lithologies in the region are, for example, organic-rich shales in the (partially eroded) sedimentary cover. If the sedimentary cover units acted as a hydrocarbon source, these buoyant substances must have migrated into the underlying basement to depths of several kilometers. Burisch et al. (2017) described a reasonable scenario based on the model of Bons et al. (2014), how sedimentary brines are sucked into the crust (Stober and Bucher 2004) and thus can transport hydrocarbons dissolved in aqueous fluids to greater depths. This process could explain the presence of hydrocarbons at all three localities.

The overlying sedimentary cover being the origin of the reducing agent requires the hydrocarbons to be present in an aqueous solution; gaseous or liquid hydrocarbons would be too buoyant. A mass balance

720 calculation shows that in order to precipitate all of the 100-1000 mg/kg aqueous As as native As according
721 to
722 $As(OH)_3$ (aq) + 0.375 CH_4 (aq) ↔ As (s) + 2.25 H_2O + 0.375 CO_2 (aq) (Eq. 1),
723 a total amount of only 0.5-5.0 mmol CH_4 (aq) per kg fluid would be required. This amount is in agreement
724 with the influx of ~1.5-1.9 mmol/l CH_4 (aq) determined for the ore shoots of the Wittichen locality in the
725 central Schwarzwald by Markl et al. (2016). An aqueous fluid at 150 °C at a lithostatic formation pressure
726 of 250-550 bar (Scharrer et al. 2021) can transport up to ~60-100 mmol/kg CH_4 (aq) (Duan and Mao 2006).
727 The near linear mixing between fluids A and B during ore shoot formation (Fig. 9) limits the relative amount
728 of the reducing agent-bearing aqueous fluid which could take part in the mixing process without disturbing
729 the linear binary mixing trend. If the reducing fluid was less than 5 % of (fluid A + fluid B), a maximum of
730 3-5 mmol of CH_4 (aq) would have been available for reduction of 1 kg (fluid A + fluid B), which is in good
731 agreement with what is required.
732
733 Mineralogical variability and fluid composition
734 The mineralogical differences between the three investigated localities are attributed to a difference in the
735 respective fluid's metal content. This hypothesis is supported by LA-ICP-MS fluid inclusion analyses which
736 show variations between the localities (Fig. 10; Scharrer et al. 2021). The different ore shoot mineral
737 assemblages at Münstertal (Fig. 12), Urberg (Fig. 13) and Wieden (Fig. 14) can be nicely modelled using
738 these different metal contents (Table 4).
739 Before discussing the calculated diagrams, it is important to note that these thermodynamic models also
740 show the importance of pH in defining the mineralogy. Hence, pH and other minor, local fluid variations
741 are sufficient to explain the differences in mineralogy between various ore shoots at one specific locality.
742 In the simple Ag-As fluid system, as is present at the Münstertal, the only two minerals stable at moderate
743 to reduced epithermal conditions are native Ag and native As. Under all but lower than slightly acidic pH
744 conditions, two pH units below the neutral pH, they form at different redox states (Fig. 12a). During a fluid
745 reduction of a neutral fluid, native Ag would precipitate first and would therefore form inclusions in native

As (Fig. 12a). This is in accordance with our observations and with many observations worldwide: dendritic native Ag occurs within typically collomorphic native As (e.g., Hösel 2003; Ondrus et al. 2003b; Hiller and Schuppan 2008; Pekov et al. 2010).

In the case of Urberg, the availability of Ni in addition to an As and Ag stabilizes Ni-arsenides. Due to the abundance of As relative to Ni, the reduction sequence at neutral pH is native Ag → niccolite → rammelsbergite → skutterudite → native As (Fig. 13a). This finding is congruent with that of Scharrer et al. (2019). Due to the lack of thermodynamic data, the stability field of $NiAs_3$ could not be empirically modeled. However, a predicted $NiAs_2$-$NiAs_3$ stability boundary field is shown in Fig. 13a. The exact position of this and, thus, the formation of either $NiAs_2$ or $NiAs_3$ are strongly dependent on the As/Ni ratio of the fluid, the pH and the redox conditions. At higher As/Ni ratios, lower pH and more reducing conditions, the triarsenide is more stable than the diarsenide. One of these factors is most likely the reason for the abundance of triarsenides in ore shoot sequence 1 and the increased abundance of diarsenide in ore shoot sequence 2 at Urberg. The abundance of Ni in the Urberg fluids can be explained by the spatially close occurrence of mafic rocks and magmatic Ni-sulfide deposits in the region around Urberg (Otto 1964; Geyer et al. 2011; Markl 2017a; Brill et al. 2018); these rocks are very likely the source of the Ni in the Urberg fluids.

The Wieden ore shoots show Sb-bearing phases in addition to As phases. Based on both textural and thermodynamic evidence, the Sb-equivalent of niccolite, breithauptite, becomes thermodynamically stable over niccolite in the presence of additional aqueous Sb (Fig. 14a). This even occurs at fluid compositions, in which As is more abundant than Sb (see Wieden fluid composition; Fig. 10). In addition, allargentum, dyscrasite, and native Sb form over a large pH range at a redox state similar to that of native As (Fig. 14a). Their stability is strongly dependent on both the availability of Sb and Ag. During reduction of a fluid with a composition of, for example, the Ag-Ni-As-Sb ore shoot at Wieden (Table 4), allargentum and dyscrasite form after breithauptite and rammelsbergite, but prior to native As during fluid reduction. This is in accordance with the paragenetic sequence.

Formation of sulfides in normal vein and ore shoot assemblages

As shown above, gangue minerals form by simple binary fluid mixing, the typical native element-arsenide assemblage of the ore shoots by the same fluid mixing process accompanied by reduction. However, the presence of clustered and disseminated base metal sulfides (mainly galena and sphalerite) in the vein as well as the presence of sulfides in some and the absence of sulfides in other ore shoots has not been discussed and explained yet. Based on the lack of statistically significant differences between their sulfur isotope signatures (Fig. 8), sulfides in the ore shoots and sulfides in the normal veins are believed to have the same source and the same formation mechanism. We propose that the sulfide was added to the fluid discontinuously and locally during the mixing process, most likely by interaction with the surrounding host rock. The line of arguments is as follows:

(1) Textures: The sulfides are not evenly distributed throughout the veins, but they occur as local accumulations such as bands or directly overgrowing host rock clasts in breccias (e.g., Fig. 1c; Metz et al. 1957; Markl 2017a). The brecciated clasts are typically overgrown by sulfide- and quartz-rich material which implies a formation process different from (or at least: additional to) the other normal vein minerals.

(2) Fluid thermodynamics: Fluids A and B contain some metals such as Ba, Pb and Zn (Fusswinkel et al. 2013; Scharrer et al. 2021) and thus cannot transport significant amounts of sulfur at the temperature range in question (e.g., Allison et al. 1991; Ball and Nordstrom 1991). Depending on redox conditions, thermodynamic modelling predicts that a maximum of 10 mg/kg of sulfate or a maximum of 0.05 mg/kg of sulfide can be transported at a neutral pH (Fig. 11a) for the fluid compositions of the three localities (Table 4). LA-ICP-MS measurements of Scharrer et al. (2021) showed detectable sulfur only in two fluid inclusions, namely 20 ± 10 mg/kg and 50 ± 25 mg/kg, which are in the same order of magnitude as values of thermodynamically possible dissolved sulfate. This implies that the sulfur in the fluid A or B (or both) was likely present as sulfate species.

(3) Mineral thermodynamics: Based on the disagreement between thermodynamic phase stability fields and the observed mineralogy, a thermodynamic disequilibrium between a few minerals must be

assumed both in the veins and in the ore shoots. The most striking example is the apparently stable assemblage of oxidized and reduced minerals such as barite and native As. Under equilibrium conditions, this assemblage would not form, as the sulfate in barite would be reduced to sulfide under the redox state of native As stability. Furthermore, fluids containing Ni, As, Pb and Zn, as the ones investigated here (Fig. 10) cannot precipitate the base metal sulfides galena and sphalerite without the contemporaneous formation of Ni-sulfides and/or arsenides under equilibrium conditions (Fig. 11b). This is not only at odds with the observations from the three veins investigated here, but with thousands of hydrothermal veins in the Schwarzwald (Markl 2015; Markl 2016; Markl 2017a; Markl 2017b), in Central Europe and world-wide (e.g., Baumann et al. 2000; Sangster 2009), where Ni-minerals are rather rare.

(4) Kinetics: Experimentally determined kinetic rates of sulfate-sulfide equilibration (Ohmoto and Lasaga (1982) are insufficiently slow to allow sulfate reduction during short-lived mixing processes in hydrothermal systems below 200 °C. The formation of individual growth zones during such mixing processes takes less than minutes (Walter et al. 2018a), while the minimum time required for the attainment of a 90 % equilibrium between aqueous sulfide and sulfate requires ~4000 years at 150 °C at roughly neutral conditions (Ohmoto and Lasaga 1982).

All these arguments imply that sulfide was not transported in fluid A or fluid B in sufficient quantities, but that it had to be added from outside. Also sulfate reduction can be ruled out for kinetic reasons.

Sulfate-sulfide disequilibrium based on $\delta^{34}S$

The kinetic disequilibrium between sulfate and sulfide discussed in the preceding chapter is corroborated by the $\delta^{34}S$-signature of both sulfates and sulfides from ore shoots and normal vein assemblages (Fig. 8). The calculated equilibrium temperatures between sulfides and cogenetic sulfates from the three investigated localities seem to record temperatures of formation between 270 and 470 °C (Fig. 12c), while the pressure-corrected fluid inclusions record temperatures of about 150 °C (Scharrer et al. 2021) which are in agreement with many other fluid inclusion studies in the region (see above). Hence, the apparently cogenetic sulfate-

sulfide textures do not prove sulfate-sulfide isotope equilibrium; rather, sulfides and sulfates are in textural equilibrium, but in sulfur isotope disequilibrium. This agrees with a sulfur isotope study from the whole Schwarzwald showing unrealistic equilibrium temperatures ranging from ~200 to ~500 °C (Schwinn et al. 2006). There is no evidence for a post-formational isotopic equilibration of barite or the sulfides with each other or a further sulfur source. This is because there is no correlation between the barite, galena and sphalerite δ^{34}S-value and the sampled crystal size or mineral paragenesis. Furthermore, the sulfides and barite from this Jurassic-Cretaceous hydrothermal stage from all over the Schwarzwald show a similar disequilibrium isotopic range (Gehlen et al. 1962; Schwinn et al. 2006; Staude et al. 2011). A full equilibration of all sulfides or sulfates with a subsequent fluid is disregarded since these are systems governed by localized fluid pathways.

In summary, we interpret the sulfur isotope values of barite and sulfides to reflect a sulfate-sulfide isotopic disequilibrium during vein formation. Therefore, sulfate and sulfide must have originated from different sources and for sulfide, this source was not fluid A or B. This finding is in sharp contrast to the results and interpretations of previous studies (Walter et al. 2016; Walter et al. 2018a; Walter et al. 2020).

Sulfide source

This chapter discusses the potential sources of the externally derived sulfide. The regional geology permits the sulfide to either be sourced from the surrounding host rock or from the (at the time of ore formation) overlying sedimentary lithologies. The latter would require sulfide from the organic-rich and/or sulfide-rich layers in the sedimentary cover penetrating the basement during downward fluid flow as was e.g. suggested by Bons et al. (2014). However, sedimentary, mostly organically- or diagenetically-sourced sulfide generally shows strongly negative δ^{34}S values, most between –5 and –50 (Marowsky 1969; Maynard 1980; Gautier 1987) as does the most likely sedimentary sulfide source candidate in the region, the lower Jurassic Posidonian shale (Geyer et al. 2011), namely δ^{34}S values between –15 and –40 (Brumsack 1991; Raiswell et al. 1993). This is significantly lighter than our analyzed sulfides (Fig. 8). Thus, a major organic sulfide source component can, in all probability, be excluded.

850 The most likely sulfide source is, hence, the surrounding basement rock sulfides. Remobilization of this
851 sulfide during hydraulic fracturing is a viable mechanism of sulfide addition to the mixing hydrothermal
852 fluids. It is well known that the Schwarzwald basement rocks, specifically the gneisses, bear high amounts
853 of sulfides, including pyrite, pyrrhotite and arsenopyrite (e.g., Wager 1935; Otto 1964; Hofmann 1989;
854 Geyer et al. 2011; Staude et al. 2011; Drüppel et al. 2020). We also observed them in our host rock samples.
855 The importance of the host rock characteristics on the occurrence of sulfides in Schwarzwald hydrothermal
856 veins has also been described by Walter et al. (2019) who found that gneiss-hosted veins contain a higher
857 modal abundance of sulfides compared to granite-hosted veins. Furthermore, galena and sphalerite are most
858 abundant in hydraulic breccia zones (this study; Metz et al. 1957; Widemann 1988; Markl 2017a), where
859 interactions between the hydrothermal fluid and the fresh, non-leached host rock are strongest. As the new
860 fractures typically occur in the center of a vein or at the marginal selvages, which are covered and thereby
861 sealed by clay minerals (Metz et al. 1957; Burisch et al. 2016; Walter et al. 2016), repetitive opening of the
862 same fractures nicely explains the typical banded gangue textures (e.g., Keim et al. 2019) and the general
863 rarity of sulfides. The latter are distributed unevenly reflecting the rare addition of sulfide to the
864 hydrothermal fluid. This is related to the preexisting vein being a structurally inherited weak zone (Virgo
865 et al. 2014) which is a typical feature in many hydrothermal systems (e.g., Cathelineau et al. 2017). The
866 sulfide isotope signature of both ore shoots and vein sulfides ($\delta^{34}S$ ~ 0 to –12) overlaps with the range of
867 the basement sulfides ($\delta^{34}S$ ~ +2 to –9 ‰; Siewers 1977) which corroborates our inference that sulfide was
868 derived from the gneissic host rocks.
869 This concludes the sulfide, which is the prerequisite for sulfide formation, and the reducing agent, which is
870 required for the ore shoot formation, having two separate origins. Which of these fluids, a sulfide-bearing
871 or a reducing agent-bearing fluid, is tapped, results in the formation of the normal vein sulfides or an ore
872 shoot assemblage, respectively.
873
874 The mineralogical consequences of sulfide addition and sulfate-sulfide disequilibrium on the ore shoot
875 assemblage

The ore shoots show a highly variable sulfide content, from absent to abundant, which implies that the availability of sulfide and reducing agent may have been variable between ore shoots. Thus, it is vital to consider the effect sulfide has on the ore shoot mineralogy. In the following, the consequences of sulfide addition under equilibrium (Fig. 12b, Fig. 13b and Fig. 14b) and under sulfate-sulfide disequilibrium conditions (Fig. 12c, Fig. 13c and Fig. 14c) on the ore shoot mineralogy will be discussed.

In a simplified As-S system and under equilibrium conditions, realgar and orpiment would form at acidic to neutral conditions. Their stability field is increased to more oxidized environments under sulfate-sulfide disequilibrium conditions. Only when the available sulfide is used up, native arsenic would form. However, realgar and orpiment were not found in any of the investigated samples. This is attributed to their stability strongly depending on the availability of reduced sulfur, which in turn is also dependent on the stability of other sulfides and, thus, on the availability of, for example, Pb and Zn in the fluid (Scharrer et al. 2020). As Pb and Zn are very abundant in the mixture of fluid A with fluid B, nearly all LA-ICP-MS analyses show them in a similar range of 1 to 100 ppm, and as galena and sphalerite have very low solubilities, their formation uses up the reduced aqueous sulfide which is the ultimate reason for the stability of native As over realgar and orpiment.

During reduction of a sulfide-bearing Ag-As-Pb fluid under equilibrium conditions and at neutral pH, galena precipitation is succeeded by native As formation (Fig. 12b). In our samples, although galena does also form prior and subsequent to native As, it also forms simultaneously to native As (e.g., Fig. 4b). As an example, in an equilibrium system with the fluid condition at Münstertal (Table 4), the amount of galena that can precipitate simultaneously with native As during reduction is several orders of magnitude less than native As. A co-precipitation is however possible, when sulfide influx occurs contemporaneous with the reduction, as is the case at hand. Thus, the simultaneous precipitation of these two minerals at a neutral pH reflects the sulfide influx during reduction under sulfate-sulfide disequilibrium conditions. At these conditions, the stability and formation of galena is independent of the redox state of the fluid (Fig. 12c) and whether galena or native As forms depends on the relative abundance of sulfide and reducing agent. Temporal variations in redox state and/or sulfide influx nicely explain the commonly observed banded

onion-layer texture between native As and galena and the lath-shaped oriented galena crystals in native As (Fig. 6e).

In the presence of dissolved Ni, the thermodynamic modeling predicts the formation of gersdorffite under slightly basic to strongly acidic conditions (Fig. 13b). Under sulfate-sulfide disequilibrium conditions, the stability of gersdorffite increases, based on the availability of sulfide, to more oxidizing and more basic conditions (Fig. 13c). Due to the As-S exchange in the arsenides and sulfarsenides (Fig. 7b), we assume that S-rich rammelsbergite forms at low sulfide, As-rich gersdorffite at moderate sulfide and stoichiometric gersdorffite at high sulfide availability. This would explain the mineralogical differences in the three ore shoot sequences at Urberg, in which a steady increase in sulfur content in the $Ni(As, S)_2$ and $NiAs_3$ minerals can be witnessed from ore shoot sequence 1 to 3 (Fig. 7b). It is important to note that under moderately reduced conditions, only a few mg/kg of sulfide are needed to increase the stability of even stoichiometric gersdorffite to form over a large pH range. The non-stoichiometric gersdorffite would form at even lower sulfide contents. The availability of sulfide is, however, not only constrained by the absolute sulfide content, but (as already described above) also by the content of other elements such as Pb or Zn that contest for the sulfide due to the low solubility of their respective sulfides (Scharrer et al. 2020). The fact, that both Pb and Zn were detected in most fluid inclusions (i.e. in the mixed fluids after mineral precipitation) indicates a high metal/sulfide ratio.

The presence of Sb in addition to Ni, As, Pb and sulfide in the fluid stabilizes some Sb-minerals at the expense of their respective As-counterparts, even if the fluid is richer in As than in Sb (Fig. 14b). This explains the formation of breithauptite (Fig. 14b) and possibly ullmannite in As-dominated ore shoots, although the stability of the latter could not be modeled due to the lack of suitable thermodynamic data.

The mineralogical consequences of sulfate-sulfide disequilibrium on the normal vein assemblage

Although the sulfate-sulfide disequilibrium does influence the mineralogy of the ore shoots (Fig 12c, Fig. 13c and Fig. 14c), with minor changes in mineral abundance and mineral succession, similar ore shoots could also form under sulfate-sulfide equilibrium conditions (Fig 12b, Fig. 13b and Fig. 14b). However,

928 the normal sulfide assemblage of the vein observed here could not have formed under equilibrium
929 conditions. The sulfate-sulfide disequilibrium does not only stabilize mineral assemblages that would not
930 form otherwise, but it also prevents the formation of some equilibrium assemblages or textural successions
931 which would usually be expected to form. For example, under equilibrium conditions (Fig. 12b, 13b &
932 14b), the base metal sulfides should always form after native Ag (Fig. 12c), arsenides (Fig. 13c) or
933 antimonides (Fig. 14c), but the typical vein sulfide assemblage completely lacks native Ag, arsenides and
934 antimonides. This is identical in almost all other hydrothermal veins of the same hydrothermal stage in the
935 Schwarzwald (Markl 2015; Markl 2016; Markl 2017a; Markl 2017b) and can be explained by the
936 disequilibrium conditions, which (1) prevent sulfide from acting as a reducing agent for e.g. Ag^+, aqueous
937 arsenite or aqueous antimonite and (2) increase the stability of sulfide-bearing minerals such as base metal
938 sulfides to oxidizing conditions.
939 Finally, under sulfate-sulfide disequilibrium conditions, an influx of sulfide into a fluid of variable redox
940 state invariably either co-precipitates galena and Ag-sulfides/Ag-sulfosalts (Fig. 12c, Fig. 13c and 14c) or
941 Ag is incorporated into galena via coupled substitution. The latter could not be modelled due to the lack of
942 thermodynamic miscibility data. However, extrapolation from higher temperature experiments to below
943 200 °C of the coupled substitution of $Ag(As, Sb, Bi)S_2$ into galena reveals that up to ~ 3 mol% of ∑(Ag,
944 As, Sb, Bi) can be incorporated into galena (Chutas et al. 2008; Renock and Becker 2011). Thus, the
945 observed elevated contents of Ag, As, Sb and Bi in galena which are both present in the ore shoots and the
946 vein sulfide assemblages could only form due to the sulfate-sulfide disequilibrium, which prohibits native
947 Ag to form. Hence, the main medieval Ag-source, argentiferous galena, is a direct result of the sulfate-
948 sulfide disequilibrium during the formation of these veins (Markl 2017a).
949
950 **Alternative formation mechanisms for ore shoot and vein sulfides**
951 The model presented here suggests that the vein formed by mixing of fluid A and fluid B, the vein sulfides
952 precipitated due to an influx of host rock-sourced sulfide and the ore shoot assemblages formed by a local
953 influx of a mobile reducing agent, most likely hydrocarbons. Although we have provided abundant textural,

mineralogical, geochemical, fluid inclusion and modeling data to support the hypothesis of such a three fluid ± host rock interaction model, possible alternatives should also be mentioned. Alternative models to explain the presence of both vein sulfides and ore shoots are, for example, that the change from vein sulfides to ore shoots may be governed by (a) a different magnitude of external (rock) vs. internal (fluid) buffering and (b) differences in the magnitude of the net fluid flux.

We do not consider both alternatives as viable, because, concerning (a), the internal buffering of fluids A+B forms only the gangue minerals, while the external (rock) buffering is, in principle, the mechanism that we suggest forming the vein sulfides. A stronger interaction with the surrounding host rocks produces a higher sulfide ore content in the vein, but not an arsenide-bearing ore shoot. This statement is even texturally supported by the increased sulfide concentrations at places where host rock breccias are present in the banded vein (see vein sulfide formation chapter). Alternative (b) proposes that a different degree of reaction progress of the overall fluid system is responsible for the shift between the normal vein sulfide and the ore shoot assemblage. However, our modeling clearly shows that variations in magnitude of net fluid flux of fluids A+B or the sulfide- and reducing agent-bearing fluid do not suffice to explain the mineralogical difference between the vein sulfides and the ore shoots. A single fluid with a given sulfide/reducing agent ratio cannot thermodynamically result in the formation of sulfide-free ore shoots, sulfide-bearing ore shoots and normal vein sulfides.

Hydrothermal overprint, sulfosalt assemblage and worldwide comparison to other occurrences

The previous models nicely explained the formation of the native element-arsenide-sulfarsenide assemblages, with or without the base-metal sulfides, but they did not discuss the silver sulfides and sulfosalts, mainly proustite-pyrargyrite solid solutions, which are abundant. These minerals formed in a later process by hydrothermal remobilization of the primary ore assemblages. Similar processes have been described for other Ag-rich hydrothermal systems in the region (Keim et al. 2019). To understand their formation is of vital importance since remobilization processes can increase or decrease the economic value

of many types of deposit dramatically (e.g., Hobbs 1987; Marshall et al. 2000; van Dongen et al. 2010; Hastie et al. 2020).

In the deposits investigated in the present contribution, the most common consequence of hydrothermal overprint of the primary ore shoot assemblages is the formation of minerals of the proustite (Ag_3AsS_3) - pyrargyrite (Ag_3SbS_3) solid solution series at the cost of mainly native Ag and sometimes native As. Depending on sample and locality, they form in association with other sulfosalts and sulfides (Table 1). As is the case in our samples, these Ag-sulfosalts generally form during a later stage or at the end of an ore stage in many Ag-rich hydrothermal associations worldwide (Ryall 1979; Ruvalcaba-Ruiz and Thompson 1988; Mladenova et al. 2004; Camprubí et al. 2006; Staude et al. 2007; Fanlo et al. 2010; Kallstrom 2012; Yesares et al. 2017; Epp et al. 2018). The formation of sulfosalts has been linked both to a primary hydrothermal fluid (Foley 1984), but more commonly to exsolution and/or remobilization processes (e.g., Boni and Koeppel 1985; Loucks and Petersen 1988; Mladenova et al. 2004; Takahashi et al. 2006; Epp et al. 2018).

The formation of proustite-pyrargyrite series minerals must have started after the ore shoot formation, but during the same hydrothermal stage II (Fig. 3a) since euhedral sulfosalts are found imbedded in gangue minerals of this stage. As the sulfosalts do not just replace, but also overgrow the primary minerals, an elemental flux at constant volume during remobilization cannot be calculated. However, the observation that native arsenic and native silver are replaced by proustite clearly shows, that an influx of sulfide is a necessary pre-requisite for their formation. It is suggested that the replacement processes involved batches of either fluid A or fluid B, both of which are not in equilibrium with and more oxidized than the ore shoot, plus sulfide.

The sulfide isotope signature of proustite ranges from the same as that of the primary ore shoot and main stage vein sulfides to significantly lower. The same isotopic signature as the rest of the vein sulfides suggests that the sulfide originated from the same sulfide fluid source or remobilization of sulfides within the vein. The significantly lower isotopic signature can be explained by a subsequent fluid, or sulfate

1004 reduction being involved. Such reaction processes are not temporally confined to a short process such as
1005 fluid mixing. Thus, sulfate reduction may play a role for these remobilization processes.
1006 For the investigated samples at hand, the large variety of sulfosalts forming during the replacement process
1007 can be traced back to local, small scale variations in preexisting mineralogy and, possibly, fluid
1008 composition. Although minerals of the proustite-pyrargyrite series ($Ag_3(As,Sb)S_3$) are abundantly present,
1009 minerals of the smithite-miargyrite series ($Ag(As,Sb)S_2$) are rare or absent. This is a common feature at
1010 many Ag-sulfosalt-bearing localities worldwide (e.g., Gillerman and Whitebread 1953; Gemmell et al.
1011 1989; Chutas and Sack 2004; Camprubí et al. 2006). The formation of either of these minerals is defined
1012 by the elemental abundance (Chutas and Sack 2004), specifically of Ag, Sb, As and S, and by prevailing
1013 formation conditions, specifically pH. The proustite-pyrargyrite series preferably forms at more neutral to
1014 slightly basic conditions and at higher Ag and S activities relative to miargyrite (Fig. 14c). A high Ag
1015 activity was provided by the dissolution of native Ag. The favorable neutral to basic pH was given if the
1016 involved initial fluid was at roughly neutral pH, moderately reduced to moderately oxidized and As-bearing.
1017 Local variations in fluid composition and primary ore shoot mineralogy then determined, which sulfosalt
1018 formed during this hydrothermal overprint (see also Keim et al. 2019).
1019 These required initial fluid conditions are met by fluids A and B. At initially roughly neutral pH and under
1020 moderately reduced to moderately oxidized conditions, both arsenite and arsenate are present in the fluid
1021 (ESM 6). During dissolution of native Ag or native As, arsenate is progressively reduced to arsenite
1022 (Scharrer et al. 2019), which in turn increases the fluids pH (Eq. 2 and 3)

1023 $As\ (s) + 1.5\ H^+ + 1.5\ H_2O + 1.5\ H_2AsO_4^- \leftrightarrow 2.5\ As(OH)_3\ (aq)$ (Eq. 2)

1024 $Ag\ (s) + 1.5\ H^+ + 0.5\ H_2AsO_4^- + 2Cl^- \leftrightarrow 0.5\ H_2O + 0.5\ As(OH)_3\ (aq) + AgCl_2^-$ (Eq. 3)

1025 Hence, the sulfosalts form in the presence of a sulfide influx during ore shoot remobilization and the
1026 sulfosalt mineralogy is defined by the elemental availability and formation conditions. Interestingly, if
1027 fluids A and B react with the ore shoots in the absence of sulfide, the primary mineralogy is only dissolved
1028 and replaced by gangue minerals, without the formation of secondary ore minerals. This has also been

observed in several samples, in which preferably native As and native Ag were dissolved, while their colloform and dendritic shapes are still preserved in the replacing gangue minerals (Fig. 4f & g).

In some samples from Wieden, minerals of the proustite-pyrargyrite series are occasionally replaced by acanthite (Ag_2S) and in turn by native Ag. This formation of secondary native Ag by the dissolution of acanthite is a typical reaction which has been described from many localities worldwide (e.g., Fanlo et al. 2010; Arribas et al. 2020). The secondary native Ag commonly forms wires in open vugs. This process shows a progressive enrichment of Ag relative to As, Sb and S. While the primary native Ag contains significant amounts of Sb, Hg and As, the process of remobilization, first to proustite and then to secondary native silver, preferably removes Sb, Hg and As and, hence, purifies the native silver. The whole process is most likely related to weathering fluids of different composition than fluid A or B.

Conclusions

Although drastic mineralogical changes in a hydrothermal vein are commonly interpreted to indicate a new hydrothermal stage with the influx of a new fluid of different composition, this study shows that such changes can simply reflect a spatially and temporally restricted change in redox conditions. In this case, a local influx of a reducing agent can result in the formation of Ag- and As-rich ore shoots. The mineralogy of these ore shoots is strongly dependent on the presence of the metals in the fluid, as the mineralogy reflects the maximum elemental fluid composition analyzed by LA-ICP-MS in single fluid inclusions. This in turn implies that the elemental composition of the ore, at least to some degree, reflects the source fluid and, thus, the source rock.

The mineralogy of the ore shoots is further influenced by the redox state, the pH, the availability of sulfide and the already precipitated mineralogy. The presence of sulfide during reduction results in the formation of sulfide-bearing minerals such as base metal sulfides, sulfarsenides and sulfantimonides. The influx of sulfide and lack of reduction of sulfate is due to a thermodynamic disequilibrium between sulfate and sulfide, which stem from two different sources and which could not equilibrate due to slow reaction kinetics (Ohmoto and Lasaga 1982). In the presence of a sulfide influx without a reducing agent, only normal base

metal sulfides such as galena, sphalerite or chalcopyrite form. This sulfide influx also promotes the incorporation of Ag, Sb, As and Bi into galena. The most likely sulfide source is the sulfide-bearing gneisses (= host rocks), while the reducing agent was most probably represented by hydrocarbons from the sedimentary cover.

The final ore shoot textures found in the samples are strongly influenced by post-depositional remobilization processes. These include the typical hydrothermal dissolution of native Ag and native As and reprecipitation as sulfosalts as well as later reaction processes that re-remobilize the Ag-bearing sulfosalts and form secondary native Ag. Thermodynamic calculations show that the larger stability of Ag-Sb-sulfosalts such as pyrargyrite compared to their respective Ag-As-endmembers (in this case: proustite) enables their formation even in As-dominated hydrothermal systems.

Acknowledgements

First, we thank the Thermoddem team of the BRGM for the very friendly cooperation and the implementation of new species into the thermodynamic database. Furthermore, we thank Dr. Günter Grundmann for providing microscope images of his private samples of the Wieden ore shoots. We would like to acknowledge the Chief and Associate Editor and the reviewers for their constructive criticism and feedback, which led to an improved version of this manuscript. Last but not least, we thank S. Schafflick for fast and reliable sample preparation. This research was funded by a combination of the German Research Foundation (DFG), grant no. MA 2135/25-1 and by the German-American Fulbright Commission.

References

Allison JD, Brown DS, Novo-Gradac KJ (1991) MINTEQA2/PRODEFA2, a geochemical assessment model for environmental systems: version 3.0 user's manual. Environmental Research Laboratory, Office of Research and Development, US Environmental Protection Agency.

Arribas A, Mathur R, Megaw P, Arribas I (2020) The Isotopic Composition of Silver in Ore Minerals. Geochemistry, Geophysics, Geosystems 21. https://doi.org10.1029/2020GC009097.

Aspiala M, Tesfaye F, Taskinen P (2015) Electrochemical study on the Ag–Sb system by advanced experimental method. Electrochim Acta 173:649-655. https://doi.org10.1016/j.electacta.2015.05.065.

Aspiala M, Tesfaye F, Taskinen P (2016) Thermodynamic study in the Ag–Sb–S system by the EMF method. The Journal of Chemical Thermodynamics 98:361-366. https://doi.org10.1016/j.jct.2016.03.009.

Baatartsogt B, Schwinn G, Wagner T, Taubald H, Beitter T, Markl G (2007) Contrasting paleofluid systems in the continental basement: a fluid inclusion and stable isotope study of hydrothermal vein mineralization, Schwarzwald district, Germany. Geofluids 7:123-147. https://doi.org10.1111/j.1468-8123.2007.00169.x.

Ball JW, Nordstrom DK (1991) WATEQ4F--User's manual with revised thermodynamic data base and test cases for calculating speciation of major, trace and redox elements in natural waters. Survey USG. Open-File Report 91-183.

Barin I (1995) Thermochemical data of pure substances. Wiley-VCH, New York.

Barnes HL (1997) Geochemistry of hydrothermal ore deposits. John Wiley & Sons.

Barrett TJ, Anderson GM (1988) The solubility of sphalerite and galena in 1–5 m NaCl solutions to 300 C. Geochim Cosmochim Ac 52:813-820. https://doi.org10.1016/0016-7037(88)90353-5.

Bastin ES (1939) The nickel-cobalt-native silver ore type. Econ Geol 34:40-79. https://doi.org10.2113/gsecongeo.34.1.1.

Baumann L, Kuschka E, Seifert T (2000) Lagerstätten des Erzgebirges. Enke, Stuttgart.

Bessinger B, Apps JA (2003) The hydrothermal chemistry of gold, arsenic, antimony, mercury and silver. U.S. Department of Energy. pp 52.

Bethke CM (2007) Geochemical and biogeochemical reaction modeling. Cambridge University Press.

Blanc P, Lassin A, Piantone P, Azaroual M, Jacquemet N, Fabbri A, Gaucher EC (2012) Thermoddem: A geochemical database focused on low temperature water/rock interactions and waste materials. Appl Geochem 27:2107-2116. https://doi.org10.1016/j.apgeochem.2012.06.002.

Bliedtner M (1978) Blei- und Zink-Prospektion im Gebiet Kaltwasser/Mulden-Untersmünstertal Südschwarzwald. Albert-Ludwigs-Universität Freiburg

Boni M, Koeppel V (1985) Ore-lead isotope pattern from the Iglesiente-Sulcis area (SW Sardinia) and the problem of remobilization of metals. Miner Deposita 20:185-193. https://doi.org10.1007/BF00204563.

Bons PD, Fusswinkel T, Gomez-Rivas E, Markl G, Wagner T, Walter B (2014) Fluid mixing from below in unconformity-related hydrothermal ore deposits. Geology 42:1035-1038. https://doi.org10.1130/G35708.1.

Brill RA, Falkenstein F, Gulich J (2018) Die Grube "Gottesehre" bei Urberg im Südschwarzwald. Erzgräber 32:118.

Brumsack H-J (1991) Inorganic geochemistry of the German 'Posidonia Shale': palaeoenvironmental consequences. Geol Soc Lon, Spec Publ 58:353-362. https://doi.org10.1144/GSL.SP.1991.058.01.22.

Burisch M, Walter BF, Wälle M, Markl G (2016) Tracing fluid migration pathways in the root zone below unconformity-related hydrothermal veins: Insights from trace element systematics of individual fluid inclusions. Chem Geol 429:44-60. https://doi.org10.1016/j.chemgeo.2016.03.004.

Burisch M, Gerdes A, Walter BF, Neumann U, Fettel M, Markl G (2017a) Methane and the origin of five-element veins: Mineralogy, age, fluid inclusion chemistry and ore forming processes in the Odenwald, SW Germany. Ore Geol Rev 81:42-60. https://doi.org10.1016/j.oregeorev.2016.10.033.

Burisch M, Walter BF, Markl G (2017b) Silicification of Hydrothermal Gangue Minerals in Pb-Zn-Cu-fluorite-quartz-baryte Veins. Can Mineral 55:501-514. https://doi.org10.3749/canmin.1700005.

Camprubí A, González-Partida E, Iriondo A, Levresse G (2006) Mineralogy, fluid characteristics, and depositional environment of the paleocene epithermal Au-Ag deposits of the El Barqueno District, Jalisco, Mexico. Econ Geol 101:235-247. https://doi.org10.2113/gsecongeo.101.1.235.

Cathelineau M, Myagkiy A, Quesnel B, Boiron M-C, Gautier P, Boulvais P, Ulrich M, Truche L, Golfier F, Drouillet M (2017) Multistage crack seal vein and hydrothermal Ni enrichment in serpentinized ultramafic rocks (Koniambo massif, New Caledonia). Miner Deposita 52:945-960. https://doi.org10.1007/s00126-016-0695-3.

Chutas NI, Sack RO (2004) Ore genesis at La Colorada Ag-Zn-Pb deposit in Zacatecas, Mexico. Mineral Mag 68:923-937. https://doi.org10.1180/0026461046860231.

Chutas NI, Kress VC, Ghiorso MS, Sack RO (2008) A solution model for high-temperature PbS-AgSbS2-AgBiS2 galena. Am Mineral 93:1630-1640. https://doi.org10.2138/am.2008.2695.

Collins JE, Barnes SJ, Hagemann SG, McCuaig TC, Frost K (2012) Postmagmatic variability in ore composition and mineralogy in the T4 and T5 ore shoots at the high-grade Flying Fox Ni-Cu-PGE deposit, Yilgarn craton, Western Australia. Econ Geol 107:859-879. https://doi.org10.2113/econgeo.107.5.859.

Drüppel K, Stober I, Grimmer JC, Mertz-Kraus R (2020) Experimental alteration of granitic rocks: Implications for the evolution of geothermal brines in the Upper Rhine Graben, Germany. Geothermics 88:101903. https://doi.org10.1016/j.geothermics.2020.101903.

Duan Z, Mao S (2006) A thermodynamic model for calculating methane solubility, density and gas phase composition of methane-bearing aqueous fluids from 273 to 523 K and from 1 to 2000 bar. Geochim Cosmochim Ac 70:3369-3386. https://doi.org10.1016/j.gca.2006.03.018.

Epp T, Walter B, Scharrer M, Lehmann G, Henze K, Heimgärtner C, Bach W, Markl G (2018) Quartz veins with associated Sb-Pb-Ag±Au mineralization in the Schwarzwald, SW Germany: a record of metamorphic cooling, tectonic rifting, and element remobilization processes in the Variscan belt. Miner Deposita 52:1-26. https://doi.org10.1007/s00126-018-0855-8.

Essarraj S, Boiron M-C, Cathelineau M, Banks DA, Benharref M (2005) Penetration of surface-evaporated brines into the Proterozoic basement and deposition of Co and Ag at Bou Azzer (Morocco): Evidence from fluid inclusions. J African Earth Sci 41:25-39. https://doi.org10.1016/j.jafrearsci.2005.03.001.

Ewers W, Hudson D (1972) An interpretive study of a nickel-iron sulfide ore intersection, Lunnon Shoot, Kambalda, Western Australia. Econ Geol 67:1075-1092. https://doi.org10.2113/gsecongeo.67.8.1075.

Fanlo I, Subías I, Mateo E (2010) Supergene enrichment of primary Cu-Ag assemblages in Ag at the Padros deposit, Iberian range, Spain. Can Mineral 48:415-430. https://doi.org10.3749/canmin.48.2.415.

Foley NK (1984) Characteristics of some silver-, and base metal-bearing, epithermal deposits of Mexico and Peru. US Geological Survey.

Fougerouse D, Micklethwaite S, Tomkins AG, Mei Y, Kilburn M, Guagliardo P, Fisher LA, Halfpenny A, Gee M, Paterson D (2016) Gold remobilisation and formation of high grade ore shoots driven by dissolution-reprecipitation replacement and Ni substitution into auriferous arsenopyrite. Geochim Cosmochim Ac 178:143-159. https://doi.org10.1016/j.gca.2016.01.040.

Fusswinkel T, Wagner T, Wälle M, Wenzel T, Heinrich CA, Markl G (2013) Fluid mixing forms basement-hosted Pb-Zn deposits: Insight from metal and halogen geochemistry of individual fluid inclusions. Geology 41:679-682. https://doi.org10.1130/G34092.1.

Gasanova Z, Mashadieva L, Zlomanov V, Babanly M (2014) Thermodynamic study of the Ag2S-As2S3-S system by EMF measurements with Ag4RbI5 as a solid electrolyte. Inorg Mater 50:6-9. https://doi.org10.1134/S0020168514010075.

Gautier DL (1987) Isotopic composition of pyrite: relationship to organic matter type and iron availability in some North American Cretaceous shales. Chem Geol: Iso Geo Sec 65:293-303. https://doi.org10.1016/0168-9622(87)90009-1.

Gehlen Kv, Nielsen H, Ricke W (1962) S-Isotopen-Verhältnisse in Baryt und Sulfiden aus hydrothermalen Gängen im Schwarzwald und Jängeren Barytgängen in Süddeutschland und ihre genetische Bedeutung. Geochim Cosmochim Ac 26:1189-1207. https://doi.org10.1016/0016-7037(62)90051-0.

Gemmell JB, Zantop H, Birnie RW (1989) Silver sulfosalts of the Santo Nino vein, Fresnillo District, Zacatecas, Mexico. Canadian Mineralogist 27:401-418.

George L, Cook NJ, Ciobanu CL, Wade BP (2015) Trace and minor elements in galena: A reconnaissance LA-ICP-MS study. Am Mineral 100:548-569. https://doi.org10.2138/am-2015-4862.

Geyer OF, Gwinner MP, Geyer M, Nitsch E, Simon T (2011) Geologie von Baden-Württemberg. Schweizerbart.

Gillerman E, Whitebread DH (1953) The Uranium-bearing nickel-cobalt-native silver deposits in the Black Hawk district, Grant County, New Mexico. US Geological Survey. Bulletin pp 313.

Gloyn-Jones J, Kisters A (2019) Ore-shoot formation in the Main Reef Complex of the Fairview Mine—multiphase gold mineralization during regional folding, Barberton Greenstone Belt, South Africa. Miner Deposita 54:1157-1178. https://doi.org10.1007/s00126-019-00865-9.

Goldstein H, Reynolds T (1994) Systematics of fluid inclusions in diagenetic minerals. SEPM short course 31:199.

Gough D (1965) Structural analysis of ore shoots at Greenside lead mine, Cumberland, England. Econ Geol 60:1459-1477. https://doi.org10.2113/gsecongeo.60.7.1459.

Grundmann G (1971) Neues über Silbererze vom Tannenbodengang bei Wieden (Sdschwarzwald). Aufschluss 22:195-200.

Guilbert JM, Park CFJ (2007) The geology of ore deposits. Waveland Press.

Guilcher M, Gerdes A, Albert R, Gutzmer J, Burisch M (submitted) Timing of native metal-arsenide (Bi-Co-Ni-As-Ag±U) veins in continental rift zones – New insights from LA-ICP-MS U-Pb geochronology of carbonates from the Erzgebirge/ Krušné Hory province (Germany and the Czech Republic).

Hastie EC, Kontak DJ, Lafrance B (2020) Gold Remobilization: Insights from Gold Deposits in the Archean Swayze Greenstone Belt, Abitibi Subprovince, Canada. Econ Geol 115:241-277. https://doi.org10.5382/econgeo.4709.

Hauck M (2020) Bergbau- und Fördertechnik auf Wiedener Gruben, in Lagerstätten und Bergbau bei Wieden im Südschwarzwald. Unter besonderer Berücksichtigung der Grube Finstergrund. Erzgräber 35:117-136.

Hiller A, Schuppan W (2008) Geologie und Uranbergbau im Revier Schlema-Alberoda. Landesamt für Umwelt, Landwirtschaft und Geologie. Bergbau in Sachsen pp 200.

Hise CV (1900) Some principles controlling the deposition of ores. The Journal of Geology 8:730-770.

Hobbs BE (1987) Principles involved in mobilization and remobilization. Ore Geol Rev 2:37-45. https://doi.org10.1016/0169-1368(87)90022-9.

Hofmann B (1989) Genese, Alteration und rezentes Fliess-System der Uranlagerstätte Krunkelbach (Menzenschwand, Südschwarzwald). Dissertation, Universität Bern

Hösel G (2003) Die polymetallische Skarnlagerstätte Pöhla-Globenstein. Landesamt für Umwelt, Landwirtschaft und Geologie. Bergbau in Sachsen pp 147.

Hulin CD (1929) Structural control of ore deposition. Econ Geol 24:15-49. https://doi.org10.2113/gsecongeo.24.1.15.

Huth T, Zedler H (2019) Entlang der kontinentalen Schweißnaht im Südschwarzwald–die Badenweiler–Lenzkirch-Zone (BLZ). Schriftenreihe der Deutschen Gesellschaft für Geowissenschaften:166-192.
Jébrak M (1997) Hydrothermal breccias in vein-type ore deposits: a review of mechanisms, morphology and size distribution. Ore Geol Rev 12:111-134. https://doi.org10.1016/S0169-1368(97)00009-7.
Kallstrom MJ (2012) Fluid and metal sourcing for the native silver deposits in the Batopilas Mining District, Chihuahua, Mexico. Unpublished MSc Thesis, University of Texas at Austin
Keim MF, Staude S, Marquardt K, Bachmann K, Opitz J, Markl G (2018) Weathering of Bi-bearing tennantite. Chem Geol 499:1-25. https://doi.org10.1016/j.chemgeo.2018.07.032.
Keim MF, Walter BF, Neumann U, Kreissl S, Bayerl R, Markl G (2019) Polyphase enrichment and redistribution processes in silver-rich mineral associations of the hydrothermal fluorite-barite-(Ag-Cu) Clara deposit, SW Germany. Miner Deposita 54:155-174. https://doi.org10.1007/s00126-018-0799-z.
Kerrich R, Strong D, Andrews A, Owsiacki L (1986) The silver deposits at Cobalt and Gowganda, Ontario. III: Hydrothermal regimes and source reservoirs-evidence from H, O, C, and Sr isotopes and fluid inclusions. Can J Earth Sci 23:1519-1550. https://doi.org10.1139/e86-145.
Kissin SA (1988) Nickel-cobalt-native silver (five-element) veins: A riftrelated ore type. In: Kisvarsany G, Grant S (eds) North American Conference on Tectonic Control of Ore Deposits and the Vertical and Horizontal Extent of Ore Systems. Univ. Missouri - Rolla, Rolla, pp 268-279.
Kissin SA (1992) Five-element (Ni-Co-As-Ag-Bi) veins. Geoscience Canada 19:113-124.
Kissin SA (1993) The geochemistry of transport and deposition in the formation of five-element (Ag-Ni-Co-As-Bi) veins. Eight Quadrennial International Association on the Genesis of Ore Deposits Symposium. Schweizerbart'sche Verlagsbuchhandlung, pp 14.
Kreissl S, Gerdes A, Walter B, Neumann U, Wenzel T, Markl G (2018) Reconstruction of a >200 Ma multi-stage “five element” Bi-Co-Ni-Fe-As-S system in the Penninic Alps, Switzerland. Ore Geol Rev 95:746-788. https://doi.org10.1016/j.oregeorev.2018.02.008.
Levresse G, Bouabdellah M, Cheilletz A, Gasquet D, Maacha L, Tritlla J, Banks D, Rachid ASM (2016) Degassing as the main ore-forming process at the Giant Imiter Ag–Hg vein deposit in the Anti-Atlas Mountains, Morocco Mineral Deposits of North Africa. Springer, pp 22.
Lindgren W (1913) Mineral deposits. McGraw-Hill Book Company, Incorporated.
Liu W, Migdisov A, Williams-Jones A (2012) The stability of aqueous nickel (II) chloride complexes in hydrothermal solutions: Results of UV–Visible spectroscopic experiments. Geochim Cosmochim Ac 94:276-290. https://doi.org10.1016/j.gca.2012.04.055.
Loucks RR, Petersen U (1988) Polymetallic epithermal fissure vein mineralization, Topia, Durango, Mexico; Part II, Silver mineral chemistry and high resolution patterns of chemical zoning in veins. Econ Geol 83:1529-1558. https://doi.org10.2113/gsecongeo.83.8.1529.
Marini L, Accornero M (2007) Prediction of the thermodynamic properties of metal–arsenate and metal–arsenite aqueous complexes to high temperatures and pressures and some geological consequences. Environ Geol 52:1343-1363. https://doi.org10.1007/s00254-006-0578-5.
Markl G (2004) Silber Kupfer Kobalt, Bergbau im Schwarzwald. Markstein Verlag für Kultur- und Wissenschaftsgeschichte, Filderstadt.
Markl G (2015) Schwarzwald, Vol. 1, Nordschwarzwald and Grube Clara. Bode Verlag, Lauenstein.
Markl G (2016) Schwarzwald, Vol. 2, Mittlerer Schwarzwald Teil 1. Bode Verlag, Lauenstein.
Markl G, Burisch M, Neumann U (2016) Natural fracking and the genesis of five-element veins. Miner Deposita 51:703-712. https://doi.org10.1007/s00126-016-0662-z.
Markl G (2017a) Schwarzwald, Vol. 4, Südlicher Schwarzwald. Bode Verlag, Lauenstein.
Markl G (2017b) Schwarzwald, Vol. 3, Mittlerer Schwarzwald Teil 2. Bode Verlag, Lauenstein.
Marowsky G (1969) Schwefel-, Kohlenstoff-und Sauerstoff-Isotopenuntersuchungen am Kupferschiefer als Beitrag zur genetischen Deutung. Contrib Mineral Petr 22:290-334. https://doi.org10.1007/BF00400127.
Marshall B, Vokes F, Larocque A (2000) Regional metamorphic remobilization: upgrading and formation of ore deposits. Rev Econ Geol 11:19-38. https://doi.org10.5382/Rev.11.02.
Maynard JB (1980) Sulfur isotopes of iron sulfides in Devonian-Mississippian shales of the Appalachian Basin: control by rate of sedimentation. Am J Sci;(United States) 280. https://doi.org10.2475/ajs.280.8.772.
Metz R, Richter M, Schürenberg (1957) Die Blei-Zink-Erzgänge des Schwarzwaldes. Amt für Bodenforschung, Hannover.
Mladenova V, Kerestedjian T, Dimitrova D (2004) The Balkan mountains Paleozoic gold deposits. Bull Geol Soc Greece 36:424-433. https://doi.org10.12681/bgsg.16729.
Müller G, Nielsen H, Ricke W (1966) Schwefel-isotopen-verhältnisse in formationswässern und evaporiten nord-und süddeutschlands. Chem Geol 1:211-220. https://doi.org10.1016/0009-2541(66)90017-9.
Naumov GB, Motorina ZM, Naumov VB (1971a) Conditions of formation of carbonates in veins of the lead-cobalt-nickel-silver-uranium type (translation from Geokhimiya, No 8, pp. 938-948, 1971). Geochem Int+ 8:590-598.
Naumov GB, Ryzhenko BN, Khodakovsky IL (1971b) Handbook of thermodynamic data (in Russian). Moscow Atomizdat., Moscow

Obolensky A, Gushchina L, Borisenko A, Borovikov A, Pavlova G (2007) Antimony in hydrothermal processes: solubility, conditions of transfer, and metal-bearing capacity of solutions. Russ Geol Geophys 48:992-1001. https://doi.org10.1016/j.rgg.2007.11.006.

Ohmoto H, Lasaga AC (1982) Kinetics of reactions between aqueous sulfates and sulfides in hydrothermal systems. Geochim Cosmochim Ac 46:1727-1745. https://doi.org10.1016/0016-7037(82)90113-2.

Ondrus P, Veselovsky F, Gabasova A, Drabek M, Dobes P, Maly K, Hlousek J, Sejkora J (2003a) Ore-forming processes and mineral parageneses of the Jáchymov ore district. J GeoSci-Czech 48:157-192.

Ondrus P, Veselovsky F, Gabasova A, Hlousek J, Srein V, Vavrin I, Skala R, Sejkora J, Drabek M (2003b) Primary minerals of the Jáchymov ore district. J GeoSci-Czech 48:19-146.

Otto J (1964) Die Fluoritgrube "Gottesehre". Unpublished Diplom Thesis, Albert Ludwigs Universität zu Freiburg

Otto J (1967) Der Fluoritgang der Grube "Gottesehre" bei Urberg Kr. Säckingen (Südschwarzwald). Jh geolog Landesamt Baden-Württemberg 9:25-50.

Páez GN, Ruiz R, Guido DM, Ríos FJ, Subias I, Recio C, Schalamuk I (2016) High-grade ore shoots at the Martha epithermal vein system, Deseado Massif, Argentina: The interplay of tectonic, hydrothermal and supergene processes in ore genesis. Ore Geol Rev 72:546-561. https://doi.org10.1016/j.oregeorev.2015.07.026.

Pekov IV, Levitskiy VV, Krivovichev VG (2010) Mineralogy of the Belorechenskoye deposit (Northern Caucasus, Russia). Mineral Almanac 15:1-96.

Penrose RAF (1910) Some causes of ore shoots. Econ Geol 5:97-133. https://doi.org10.2113/gsecongeo.5.2.97.

Pfaff K, Romer RL, Markl G (2009) U-Pb ages of ferberite, chalcedony, agate,'U-mica'and pitchblende: constraints on the mineralization history of the Schwarzwald ore district. Eur J Mineral 21:817-836. https://doi.org10.1127/0935-1221/2009/0021-1944.

Raiswell R, Bottrell SH, Al-Biatty HJ, Tan MM (1993) The influence of bottom water oxygenation and reactive content on sulfur incorporation into bitumen from jurassic marine shales. Am J Sci 293:569-596. https://doi.org10.2475/ajs.293.6.569

Renock D, Becker U (2011) A first principles study of coupled substitution in galena. Ore Geol Rev 42:71-83. https://doi.org10.1016/j.oregeorev.2011.04.001.

Rick B (1990) Sulphur and oxygen isotopic composition of Swiss Gipskeuper (Upper Triassic). Chem Geol: Iso Geo Sec 80:243-250. https://doi.org10.1016/0168-9622(90)90031-7.

Robinson B, Ohmoto H (1973) Mineralogy, fluid inclusions, and stable isotopes of the Echo Bay U-Ni-Ag-Cu deposits, Northwest Territories, Canada. Econ Geol 68:635-656. https://doi.org10.2113/gsecongeo.68.5.635.

Rupf I, Nitsch E (2008) Das Geologische Landesmodell von Baden-Württemberg: Datengrund lagen, technische Umsetzung und erste geologische Ergebnisse. Regierungspräsidium Freiburg: Landesamt für Geologie RuB. Regierungspräsidium Freiburg: Landesamt für Geologie, Rohstoffe und Bergbau. LGRB-Informationen 21: pp 82.

Ruvalcaba-Ruiz DC, Thompson TB (1988) Ore deposits at the Fresnillo mine, Zacatecas, Mexico. Econ Geol 83:1583-1597. https://doi.org10.2113/gsecongeo.83.8.1583.

Ryall W (1979) Mercury in the Broken Hill (NSW, Australia) lead-zinc-silver lodes. J Geochem Explor 11:175-194. https://doi.org10.1016/0375-6742(79)90022-0.

Sangster D (2009) Geology of base metal deposits. Eolss Publishers Co. Ltd., Singapore.

Scharrer M, Kreissl S, Markl G (2019) The mineralogical variability of hydrothermal native element-arsenide (five-element) mineralizations and the role of aqueous sulfide. Ore Geol Rev 113. https://doi.org10.1016/j.oregeorev.2019.103025.

Scharrer M, Sandritter K, Walter BF, Neumann U, Markl G (2020) Formation of native arsenic in hydrothermal base metal deposits and related supergene U6+ enrichment: The Michael vein near Lahr, SW Germany. Am Mineral 105:727-744. https://doi.org10.2138/am-2020-7062.

Scharrer M, Reich R, Fusswinkel T, Walter B, Markl G (2021) Physical and chemical aspects of the formation of unconformity-related hydrothermal vein type deposits in a continental basement setting (Schwarzwald, Germany) based on LA-ICP-MS analyses of single fluid inclusions in fluorite Chem Geol 575:120260. https://doi.org10.1016/j.chemgeo.2021.120260.

Schürenberg H (1950) Die Erzgänge Teufelsgrund und Schindler im Untermünstertal und ihr quantitativer Mineralgehalt. Dissertation, Albert-Ludwigs-Universität Freiburg

Schwinn G, Wagner T, Baatartsogt B, Markl G (2006) Quantification of mixing processes in ore-forming hydrothermal systems by combination of stable isotope and fluid inclusion analyses. Geochim Cosmochim Ac 70:965-982. https://doi.org10.1016/j.gca.2005.10.022.

Shepherd T, Bottrell S, Miller M (1991) Fluid inclusion volatiles as an exploration guide to black shale-hosted gold deposits, Dolgellau gold belt, North Wales, UK. J Geochem Explor 42:5-24. https://doi.org10.1016/0375-6742(91)90058-3.

Siewers U (1977) Beitrag zur Häufigkeit und Isotopenzusammensetzung des Schwefels in magmatischen und metamorphen Gesteinen. PhD Thesis, University of Göttingen

Squire RJ, Robinson JA, Rawling TJ, Wilson CJ (2008) Controls on Ore Shoot Locations and Geometries at the Stawell Gold Mine, Southeastern Australia: Contributions of the Volcanosedimentary, Alteration, and Structural Architecture. Econ Geol 103:1029-1041. https://doi.org10.2113/gsecongeo.103.5.1029.

Staude S, Wagner T, Markl G (2007) Mineralogy, mineral compositions and fluid evolution at the Wenzel hydrothermal deposit, Southern Germany: Implications for the formation of Kongsberg-type silver deposits. Can Mineral 45:1147-1176. https://doi.org10.2113/gscanmin.45.5.1147.

Staude S, Mordhorst T, Neumann R, Prebeck W, Markl G (2010) Compositional variation of the tennantite–tetrahedrite solid-solution series in the Schwarzwald ore district (SW Germany): the role of mineralization processes and fluid source. Mineral Mag 74:309-339. https://doi.org 10.1180/minmag.2010.074.2.309.

Staude S, Göb S, Pfaff K, Ströbele F, Premo WR, Markl G (2011) Deciphering fluid sources of hydrothermal systems: a combined Sr-and S-isotope study on barite (Schwarzwald, SW Germany). Chem Geol 286:1-20. https://doi.org10.1016/j.chemgeo.2011.04.009.

Staude S, Werner W, Mordhorst T, Wemmer K, Jacob DE, Markl G (2012) Multi-stage Ag–Bi–Co–Ni–U and Cu–Bi vein mineralization at Wittichen, Schwarzwald, SW Germany: geological setting, ore mineralogy, and fluid evolution. Miner Deposita 47:251-276. https://doi.org10.1007/s00126-011-0365-4.

Steen H (2013) Bergbau auf Lagerstätten des Südlichen Schwarzwalds. Ein Beitrag zur Bergbauge-schichte und Lagerstättenkunde zwischen Dreisamtal und Hochrhein. Books on Demand, Norderstedt.

Steen H (2020) Mineralien, in Lagerstätten und Bergbau bei Wieden im Südschwarzwald. Unter besonderer Berücksichtigung der Grube Finstergrund. Erzgräber 35:59-96.

Stober I, Bucher K (2004) Fluid sinks within the earth's crust. Geofluids 4:143-151. https://doi.org10.1111/j.1468-8115.2004.00078.x.

Stone W, Archibald N (2004) Structural controls on nickel sulphide ore shoots in Archaean komatiite, Kambalda, WA: the volcanic trough controversy revisited. J Struct Geol 26:1173-1194. https://doi.org10.1016/j.jsg.2003.11.014.

Takahashi R, Matsueda H, Okrugin VM, Ono S (2006) Polymetallic and Au-Ag Mineralizations at the Mutnovskoe Deposit in South Kamchatka, Russia. Resour Geol 56:141-156. https://doi.org10.1111/j.1751-3928.2006.tb00275.x.

Tomkins AG, Pattison DR, Zaleski E (2004) The Hemlo gold deposit, Ontario: An example of melting and mobilization of a precious metal-sulfosalt assemblage during amphibolite facies metamorphism and deformation. Econ Geol 99:1063-1084. https://doi.org10.2113/gsecongeo.99.6.1063.

Tomkins AG (2010) Wetting facilitates late-stage segregation of precious metal–enriched sulfosalt melt in magmatic sulfide systems. Geology 38:951-954. https://doi.org10.1130/G31263.1.

van Dongen M, Weinberg RF, Tomkins AG (2010) REE-Y, Ti, and P remobilization in magmatic rocks by hydrothermal alteration during Cu-Au deposit formation. Econ Geol 105:763-776. https://doi.org10.2113/gsecongeo.105.4.763.

Virgo S, Abe S, Urai JL (2014) The evolution of crack seal vein and fracture networks in an evolving stress field: Insights from Discrete Element Models of fracture sealing. J Geophys Res-Sol Ea 119:8708-8727. https://doi.org10.1002/2014JB011520.

Wager R (1935) Die Schwarzwälder Gneise. Geol Rundsch 26:161-185. https://doi.org10.1007/BF01807727.

Walter BF, Immenhauser A, Geske A, Markl G (2015) Exploration of hydrothermal carbonate magnesium isotope signatures as tracers for continental fluid aquifers, Schwarzwald mining district, SW Germany. Chem Geol 400:87-105. https://doi.org10.1016/j.chemgeo.2015.02.009.

Walter BF, Burisch M, Markl G (2016) Long-term chemical evolution and modification of continental basement brines–a field study from the Schwarzwald, SW Germany. Geofluids 16:604-623. https://doi.org10.1111/gfl.12167.

Walter BF, Burisch M, Marks MA, Markl G (2017) Major element compositions of fluid inclusions from hydrothermal vein-type deposits record eroded sedimentary units in the Schwarzwald district, SW Germany. Miner Deposita 52:1191-1204. https://doi.org10.1007/s00126-017-0719-7.

Walter BF, Burisch M, Fusswinkel T, Marks MA, Steele-MacInnis M, Wälle M, Apukhtina OB, Markl G (2018a) Multi-reservoir fluid mixing processes in rift-related hydrothermal veins, Schwarzwald, SW-Germany. J Geochem Explor 186:158-186. https://doi.org10.1016/j.gexplo.2017.12.004.

Walter BF, Gerdes A, Kleinhanns IC, Dunkl I, von Eynatten H, Kreissl S, Markl G (2018b) The connection between hydrothermal fluids, mineralization, tectonics and magmatism in a continental rift setting: Fluorite Sm-Nd and hematite and carbonates U-Pb geochronology from the Rhinegraben in SW Germany. Geochim Cosmochim Ac 240:11-42. https://doi.org10.1016/j.gca.2018.08.012.

Walter BF, Kortenbruck P, Scharrer M, Zeitvogel C, Wälle M, Mertz-Kraus R, Markl G (2019) Chemical evolution of ore-forming brines–Basement leaching, metal provenance, and the redox link between barren and ore-bearing hydrothermal veins. A case study from the Schwarzwald mining district in SW-Germany. Chem Geol 506:126-148. https://doi.org10.1016/j.chemgeo.2018.12.038.

Walter BF, Jensen JL, Coutinho P, Laurent O, Markl G, Steele-MacInnis M (2020) Formation of hydrothermal fluorite-hematite veins by mixing of continental basement brine and redbed-derived fluid: Schwarzwald mining district, SW-Germany. J Geochem Explor:Article nr. 106512. https://doi.org10.1016/j.gexplo.2020.106512.

Werner W, Markl G, Steen H (2020) Lagerstätteninhalt und Entstehung der Gänge bei Wieden, in Lagerstätten und Bergbau bei Wieden im Südschwarzwald. Unter besonderer Berücksichtigung der Grube Finstergrund. Erzgräber 35:28-45.

Widemann N (1988) Die neuen Gang- und Nebengesteinsaufschlüsse im Bereich der Grube 'Gottesehre' bei Urberg im Südschwarzwald mit Aufnahme der Gangmineralisation bei den 'Erzlöchern'. Diplomarbeit, Univ. Freiburg

Yesares L, Sáez R, De Almodóvar GR, Nieto JM, Gómez C, Ovejero G (2017) Mineralogical evolution of the Las Cruces gossan cap (Iberian Pyrite Belt): from subaerial to underground conditions. Ore Geol Rev 80:377-405. https://doi.org10.1016/j.oregeorev.2016.05.018.

Zeschke G (1959) Die Flusspatvorkommen der Gewerkschaft Finstergrund. pp 44.

Appendix VI

Accepted publication

Study 6

Scharrer, M., Sandritter, K., Walter, B. F., Neumann, U., & Markl, G. (2020). Formation of native arsenic in hydrothermal base metal deposits and related supergene U^{6+} enrichment: The Michael vein near Lahr, SW Germany. American Mineralogist: Journal of Earth and Planetary Materials, 105(5), 727-744.

American Mineralogist, Volume 105, pages 727–744, 2020

Formation of native arsenic in hydrothermal base metal deposits and related supergene U^{6+} enrichment: The Michael vein near Lahr, SW Germany

Manuel Scharrer[1,*], Katharina Sandritter[1], Benjamin F. Walter[1,†], Udo Neumann[1], and Gregor Markl[1]

[1]Department of Geoscience, University of Tuebingen, Wilhelmstr. 56, D-72074 Tübingen, Germany

Abstract

Native arsenic is an occasional ore mineral in some hydrothermal base metal deposits. Its rarity (compared to pyrite, arsenopyrite, galena, sphalerite, or chalcopyrite, for example) is surprising, as arsenic is a common constituent of upper crustal fluids. Hence, the conditions of formation must be quite special to precipitate native arsenic. An ideal location to investigate the formation of native As and to explore the parameters constraining its crystallization is the Michael vein near Lahr, Schwarzwald, southwest (SW) Germany. Here, galena, sphalerite, and native arsenic are the most abundant ore minerals. The two important ore stages comprise (1) galena-barite and (2) sphalerite-native arsenic-quartz, the latter with a general mineral succession of pyrite → sphalerite ± jordanite-gratonite solid solution → galena → native As. The native arsenic-bearing mineralization formed by cooling of an at least 130 °C hot saline fluid accompanied by a reduction due to the admixing of a sulfide-bearing fluid.

Thermodynamic calculations reveal that for the formation of native arsenic, reduced conditions in combination with very low concentrations of the transition metals Fe, Co, and Ni, as well as low sulfide concentrations, are essential. "Typical" hydrothermal fluids do not fulfill these criteria, as they typically can contain significant amounts of Fe and sulfide. This results in the formation of arsenides, sulfarsenides, or As-bearing sulfides instead of native arsenic. Very minor amounts of pyrite, sulfarsenides, and arsenides record the very low concentrations of Fe, Co, and Ni present in the ore-forming fluid. High concentrations of aqueous Zn and Pb lead to early saturation of sphalerite and galena that promoted native arsenic precipitation by decreasing the availability of sulfide and hence suppressing realgar formation.

Interestingly, native arsenic in the Michael vein acted as a trap for uranium during supergene weathering processes. Infiltrating oxidizing, U^{+VI}-bearing fluids from the host lithologies reacted under ambient conditions with galena and native arsenic, forming a variety of U^{+VI} (±Pb)-bearing arsenates such as hügelite, hallimondite, zeunerite, heinrichite, or novacekite together with U-free minerals like mimetite or anglesite. Some parts of the vein were enriched to U concentrations of up to 1 wt% by this supergene process. Reduced (hypogene) uranium phases like uraninite were never observed.

Keywords: Native arsenic, jordanite-gratonite, hydrothermal, base metal, uranylarsenates, hallimondite

Introduction

Although arsenic is not a rare element in soils and upper crustal waters (e.g., Dudas 1987; Nordstrom 2002; Peters et al. 2006; Drahota and Filippi 2009), native arsenic is a relatively rare mineral (<400 localities worldwide reported in https://www.mindat.org in March 2019). However, in some types of ore deposits, it occurs in large quantities and samples up to dozens of kilograms have been recovered (e.g., Hösel 2003; Ondrus et al. 2003; Hiller and Schuppan 2008). Arsenic is a toxic metalloid, and some of its compounds are harmful to the environment and human health (e.g., Bowell et al. 2014; Mitchell 2014). Therefore, numerous recent publications have studied the abundance, sorption behavior, biotic and abiotic mobility, and redistribution of arsenic at ambient conditions (e.g., Pierce and Moore 1982; Nordstrom and Young 2000; Mandal and Suzuki 2002; Nordstrom 2002; Drahota and Filippi 2009; Amend et al. 2014; Bowell et al. 2014; Bowell and Craw 2014; Mitchell 2014; Wu et al. 2017). However, at higher temperature, the behavior of arsenic is considerably less investigated and understood, although arsenic is a common element in various hydrothermal systems (e.g., Ballantyne and Moore 1988; Horton et al. 2001; Price and Pichler 2005).

Arsenic naturally occurs in six oxidation states (As^{-II}, As^{-I}, As^{0}, As^{+II}, As^{+III}, and As^{+V}), and forms various gaseous, aqueous, and solid species of different toxicity (e.g., Boitsov and Kaikova 1965; Sergeyeva and Khodakovskiy 1969; Pokrovski et al. 2013; Keller et al. 2014; Nordstrom et al. 2014). Thus, redox state and redox reactions play a crucial role in processes involving arsenic. Dissolved arsenic is present as As^{+V} under oxidized and/or basic conditions, and as As^{+III} under more

* E-mail: scharrer.ma@gmail.com. Orcid 0000-0001-8632-1291.
† Present address: Institute for Applied Geoscience, Karlsruhe Institute of Technology (KIT), Adenauerring 20b, D-76313 Karlsruhe, Germany.

0003-004X/20/0005–727$05.00/DOI: https://doi.org/10.2138/am-2020-7062

reducing and/or neutral to acidic conditions, occurring as ions or complexes. Under geothermal conditions, As^{+III}, in the form of $As(OH)_3$, is the most common species of dissolved As (e.g., Sergeyeva and Khodakovskiy 1969; Ballantyne and Moore 1988; Criaud and Fouillac 1989; Zheng et al. 2015). The formation of oxide and hydroxide complexes (mainly arsenate and arsenite) leads to a high solubility of arsenic (e.g., Glaskova et al. 1999). This solubility is, however, greatly decreased due to enhanced mineral precipitation in the presence of transition metals such as Ni, Co, Fe, and/or under reduced conditions (e.g., Glaskova et al. 1999; Markl et al. 2016; Kreissl 2018). In turn, this implies that the presence and redox state of arsenic are essential in defining the mobility of other elements, and thus the formation of specific minerals both in hydrothermal and near-surface processes. The source of arsenic in a specific enrichment zone (i.e., deposit, placer, weathering crust) can be highly variable, since groundwater, metamorphic fluids, magmatic fluids, as well as brines have been proposed to form arsenic-rich mineralizations (e.g., Robinson and Ohmoto 1973; Migdisov and Bychkov 1998; Essarraj et al. 2005; Su et al. 2009; Epp et al. 2018). The aim of the present study is to investigate the fate of arsenic in hydrothermal base-metal vein-type deposits, the relative importance of dissolved species, and the stable As-phases formed during mineral precipitation rather than the origin of the As-bearing fluid.

Specifically, the present contribution will focus on the natural occurrence of native arsenic (native As). Where present, it generally forms as an abundant hypogene mineral under hydrothermal conditions (e.g., Vokes 1963; Nokleberg 2005; Voudouris et al. 2008; Radosavljević et al. 2014; Zheng et al. 2015; Burisch et al. 2017a) or as a minor mineral during the breakdown of As-bearing minerals/solid solutions (Cook 1996). It is common in five-element associations (Reuss 1863; Hiller and Schuppan 2008; Pekov et al. 2010; Staude et al. 2012; Burisch et al. 2017a), much less common, though, in "normal" base-metal-rich veins with galena, sphalerite, and/or chalcopyrite. Mineralization types with native As are assembled in Table 1.

A mineralogically particularly interesting example of a native arsenic-bearing base-metal vein is the Michael mine near Lahr, Schwarzwald, southwest (SW) Germany, since it operated on a hydrothermal vein comprised of a simple base metal mineralogy (galena, barite), followed by a hydrothermal phase of quartz with native arsenic and base-metal sulfides (galena, sphalerite) and a supergene enrichment of uranium by the formation of uranyl arsenates. Based on numerous studies on the geology, mineralogy, geochemistry, and conditions of formation of Schwarzwald hydrothermal veins (e.g., Burisch et al. 2016; Walter et al. 2017, 2018), this occurrence provides an ideal case to study the fate of arsenic in a Pb-Zn-base metal hydrothermal environment. A specific focus will be put on the conditions of formation of native As, in comparison to the more common arsenic-bearing hydrothermal minerals such as sulfarsenides and As-bearing sulfosalts/sulfides.

Regional geology and geochemical background

The Michael mine is situated in the central Schwarzwald near Lahr and on the eastern flank of the Upper-Rhine-Graben (Fig. 1). Its radioactivity led to a detailed investigation in the 1950s, during the search for uranium in Western Europe. During this time, samples were taken underground and mineralogically investigated by Walenta and Wimmenauer (1961) and Kirchheimer (1957), without finding an economic uranium mineralization. The local geology consists of a Variscan crystalline basement discordantly overlain by a terrestrial to marine sedimentary cover, which are both tectonically uplifted and overprinted by a normal fault-dominated regime due to the opening of the Upper Rhine Graben (URG) during the Paleogene. An inclined uplift of the rift flanks led to partial erosion of the Paleozoic and Mesozoic sedimentary cover sequence resulting in the present-day topography (Geyer et al. 2011 and references therein).

The Michael vein is at least 1.3 km long and up to 2 m wide (average of 80 cm; Bliedtner and Martin 1986). It is hosted by a crystalline basement consisting of late Variscan post-collisional granites and cordierite- and graphite-bearing metasedimentary gneisses and metatexites (Kirchheimer 1957; Metz and Richter 1957; Walenta and Wimmenauer 1961; Kaiser 1983). It occurs on a rift-parallel normal fault that juxtaposes Rotliegend rhyolitic volcanics and clastic sediments with Buntsandstein and crystalline basement (Fig. 1; Geyer et al. 2011). The sedimentary units overlaying the Buntsandstein are abundant to the east, at the far side of the rift flank, and inside the graben structure, but due to long-lasting erosion and rift flank uplift, they are no longer present in the area of investigation (Geyer et al. 2011). Paleogene sediments of up to 4000 m thickness occur in the URG, including Oligocene halite-bearing evaporites (Geyer et al. 2011).

The URG rifting, as well as previous large-scale tectonic events, have resulted in five hydrothermal maxima (Pfaff et al. 2009; Staude et al. 2012; Walter et al. 2016) producing more than 1000 mineralized hydrothermal veins in the Schwarzwald mining district between Karlsruhe and Basel. These veins consist dominantly of barite, fluorite, quartz, and carbonates besides base and precious metal oxides, sulfides, and arsenides (Metz and Richter 1957; Bliedtner and Martin 1986; Staude et al. 2009). The last hydrothermal maximum (post-Cretaceous) was related to the URG rifting; juxtaposition of different rock units in conjunction with abundant small- to large-scale fracturing led to the connection of different fluid aquifers that were separated prior to this tectonic activity (Walter et al. 2018). This favored a multi-fluid mixing scenario that resulted in the formation of mineralogically diverse hydrothermal veins (Walter et al. 2018).

Sample location

Samples analyzed in this study were taken from the dumps of the Michael vein, from the mineralogical collection of the University of Tübingen and the Geological Survey of Baden-Württemberg (among them samples from the most comprehensive study of this vein by Kirchheimer 1957), and from the private collection of the last author. The samples cover the whole mineralogical diversity of the vein and originate from both mine dumps and (the Kirchheimer samples) from underground. The Michael vein was worked from two historic adits; the Michael mine at the southern end of the vein and the Silbereckle mine close to its northern end (Fig. 1). Samples from both mines and from dumps in between were investigated.

TABLE 1. Compilation of mineralizations that are native As-bearing

Mineralization type	Examples	Major ore minerals	Major arsenic mineral (with sequence)	Nat. As abundance	Formation mechanism of the mineralization	Temp [°C]	sal [NaCl eq. wt.%]	Fluid composition of As paragenesis	
Sediment hosted replacement (Carlin-type) gold deposits	Guizhou, China Betze, USA Vorontsovskoe, Russia	Asp, Py	Asp, (Nat. As) → Rg, Orp (after py formation)	–	Sulfidation of the host rock (and reduction of the fluid)	150–220		ca. 50–350 mg/kg As, Fe is b.d.l.	Kesler et al. 2003, Su et al. 2009, Woitsekhowskaya and Peters 2015, Murzin et al. 2017
Vein-type Orogenic/ magmatic gold deposits	Baia Mare, Romania Baogutu, China	Asp, Py, Sbn	Asp → Nat. As (after Py formation)	–	Fluid cooling	150–300	0–5		Bailly et al. 1998, Grancea et al. 2002, Zheng et al. 2015
Nat. Element-arsenide ("five-element")	Erzgebirge, Germany Schwarzwald, Germany Odenwald, Germany	Arsenides, Nat. Ag, Nat. Bi	arsenides → Nat. As	++	Reduction	100–500	0–50		Markl et al 2016, Scharrer et al. 2019, Burisch et al 2017
Epithermal ore shoots in base metal veins	Schwarzwald, Germany	Gn, Sph	Nat. As, arsenides	0					Schürenberg 1950, Metz et al. 1957
Polymetallic veins	Rujevac, Serbia Schwarzwald, Germany	Gn, Sph, Py, Pb-sulfosalts	Asp/Py → Nat. As → Rg, Orp	0		100–230			Radosavljević et al. 2014, this study
Stratabound As mineralizations in fractured Karbonates	Saualpe, Austria Binntal, Switzerland	Rg, Nat. As	Rg, Orp → Nat. As	+					Göd and Zemann 2000, Hofmann and Knill 1996
Fracture controlled As-mineralization in rhyolitic rocks	Sailauf, Germany	Nat. As	Nat. As	+					Fusswinkel et al. 2014
Disseminated ore in pegmatites	Bernic lake, Canada	Nat. Bi, Gn, Stibarsen, Nat. As	Nat. As, stibarsen	–		<300			Cerny and Harris 1978, Pieczka 2010
Active geothermal fields (hotsprings)	Uzon, Russia	Sbn, Rg, Orp	Nat. As → Rg → Orp, (alacranite, uzonite)	0	Boiling, cooling and mixing	75–85		pH 3–6, ca 130 mg/l S, 0.2–9 mg/l As	Migdisov and Bychkov 1998; Cleverley et al. 2003
Metamorphosed Au deposit	Hemlo Au-deposit, Canada		Nat. As, Rg, Orp	–	Exolution from metamorpic solid solution	<600			Tomkins et al 2014, Muir 1997, Powell and Pattison 1997
Coal combustion	Kladno, Czech Republic St. Etiene, France		Nat. As, Rg, Orp	+					Majzlan et al 2014

Note: Mineral abbreviations: Asp = arsenopyrite, Gn = galena, Nat. As = native arsenic, Nat. Bi = native bismuth, Orp = orpiment, Py = pyrite, Rg = realgar, Sbn = stibnite, Sph = sphalerite.

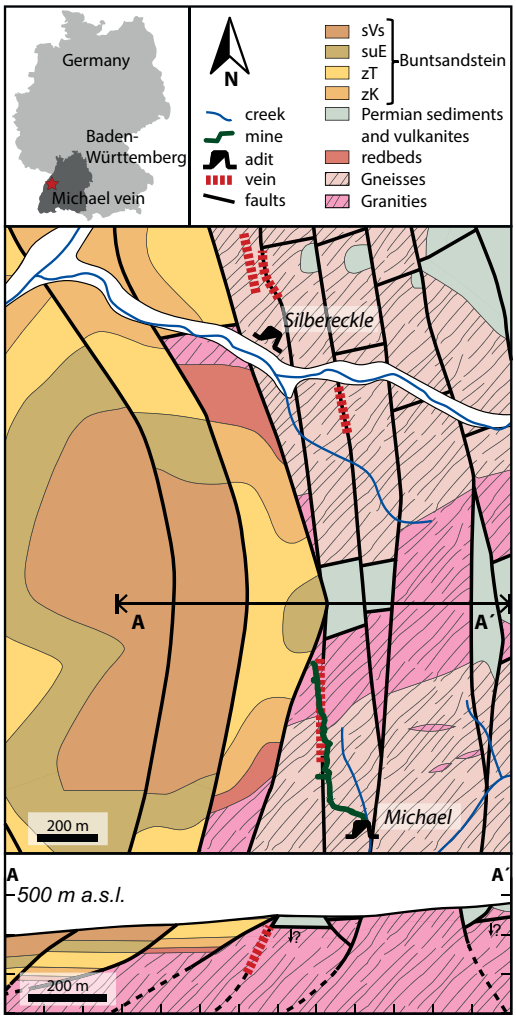

FIGURE 1. Geological map (after the 1:50000 LGRB map of Baden-Wuerttemberg) and cross-section presenting the horst-graben type structural control of the mineralization of the Michael vein. (Color online.)

PETROGRAPHY OF THE MINERALIZATION

Based on detailed ore microscopy and macroscopic observations in addition to observations from the literature, the mineralization consists of three hydrothermal stages, with more than 95 vol% of the mineralization formed during the first two stages (Fig. 2). An initial, barite- and galena-dominated stage (Fig. 3a) was followed by the formation of a quartz-sphalerite-native arsenic assemblage (Figs. 3b–d), which in turn was overgrown by small amounts of carbonates (calcite, dolomite). Supergene processes resulted in the formation of typical secondary Pb and Zn phases and, interestingly, in the formation of uranium minerals, although primary (= hypogene) uranium phases are missing.

The vein itself is characterized by intense tectonic brecciation, partial dissolution of earlier and subsequent cementation by successive minerals. Thus, the relative ages of individual minerals have been interpreted not based on individual, but on the sum of all available textures. Interestingly, there is a gradual transition in the manifestation of the second ore stage from north to south, with a more colloform and skeletal appearance in the north (Fig. 3c) and well-crystallized minerals in the south (Fig. 3d). The mineralogical differences between these textural variations of stage 2 mineralization are shown in Figure 2b.

I. Barite stage: Quartz is the initial mineral of stage I and forms as a rim on host rock fragments. It is directly overgrown by abundant barite forming white to slightly yellow fans of slender needle crystals occasionally arranged in an unusual cauliflower-like texture (Fig. 3a). The inter-crystal porosity of the barite crystals is commonly filled by quartz that intermediately forms during barite crystallization (Walenta and Wimmenauer 1961; Krahé 2012). The only ore of this barite stage consists of up to several centimeters large euhedral galena crystals embedded in barite (Fig. 3a).

II. Quartz stage: Intense brecciation of ore stage I is followed by precipitation of the three prevalent minerals of ore stage II, quartz, sphalerite, and native As (Fig. 3b). These minerals cement the clasts of ore stage I, of pyrite (brecciated relictic pyrite inclusions in sphalerite indicate a formation prior to the other stage IIa ore minerals but after ore stage I; Fig. 4a) and of euhedral, but

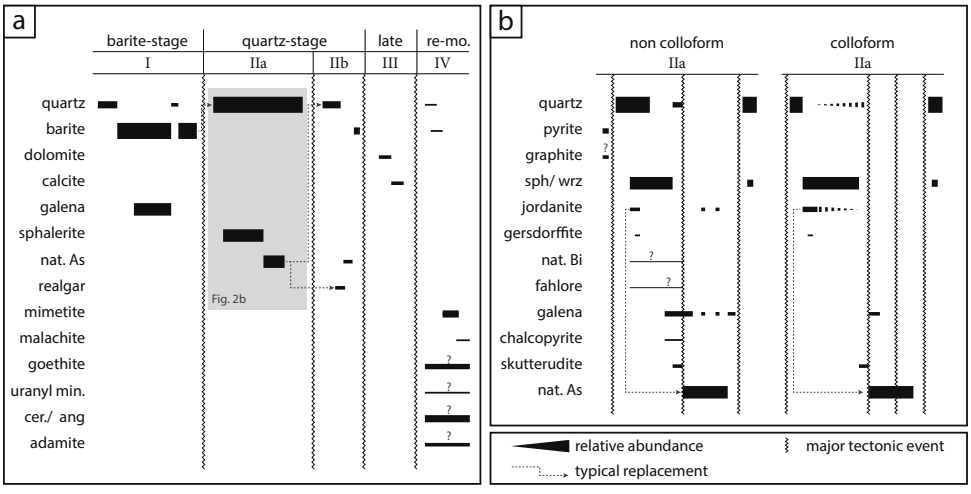

FIGURE 2. (**a**) Generalized paragenetic sequence of important ore, gangue, and supergene minerals. (**b**) Detailed mineralogical sequence of ore stage IIa with respect to the two texturally occurring types.

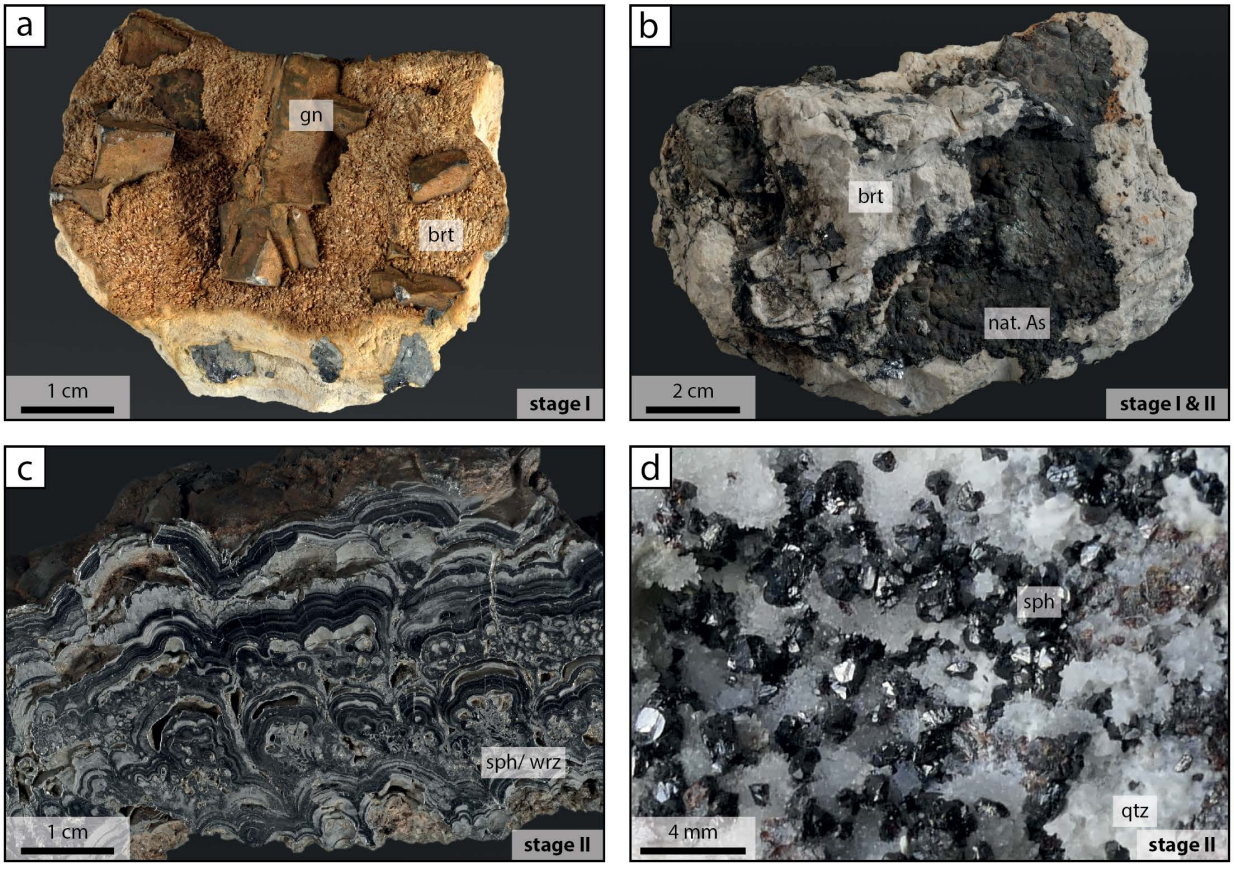

Figure 3. Images of hand specimen that depict the typical occurrence of stage I (**a**) and stage II (**b**–**d**). (**b**) Characteristic brecciation of the vein and subsequent cementing by stage II minerals, in this case arsenic. The Zn-sulfides occur as either colloform textured aggregates of sphalerite and wurzite (**c**) or as aggregates of sub- to euhedral crystals of sphalerite (**d**). (Color online.)

deformed graphite (from graphite-bearing host rocks; Fig. 4b). Partial quartz pseudomorphs after barite are abundant.

The Zn sulfides of ore stage II show two textural and mineralogical manifestations: one is characterized by medium- to coarse-grained, non-colloform Zn-sulfides (mostly sphalerite; e.g., Fig. 3d) and the other consists of colloform Zn-sulifdes (a mixture of both sphalerite and wurtzite, confirmed by XRD; Fig. 3c). The former is more common in the southern, the latter in the northern part of the vein. In the following, they are designated as colloform and non-colloform, but due to their abundant similarities and irrelevance for the understanding of the behavior of arsenic, most of the discussion lumps both types of Zn-sulfides together as sphalerite (sph). Both types show a typical generalized sequence of quartz → jordanite/gratonite + gersdorffite + sphalerite/wurtzite → sphalerite/wurtzite → galena → native arsenic → quartz (Figs. 4c–h). The non-colloform variety shows a more complex mineralogy (small flakes of chalcopyrite, fahlore, and native bismuth are only present in the non-colloform assemblage; see Fig. 2b), but skeletal jordanite/gratonite (Fig. 4c) is more abundant and formed over a longer precipitation interval in the colloform compared to the non-colloform type (Fig. 4e). Furthermore, galena is more common in the non-colloform ore samples (Figs. 4e and 4f). Small subhedral to euhedral inclusions of Ni-sulfarsenide (<20 μm; gersdorffite) formed during the initiation of sphalerite crystallization, while round aggregates of Ni-rich triarsenide (<20 μm; skutterudite) formed subsequently to sphalerite, but before the precipitation of native As (Fig. 3g).

Native As exclusively occurs in a colloform texture (irrespective of the Zn sulfide textures in the same samples), overgrows all other stage II minerals (Figs. 4e and 4f) and in some cases embeds brecciated clasts of these or fills cavities, e.g., in sphalerite-wurtzite clasts (Fig. 3h). Some native arsenic aggregates (e.g., Fig. 4i) resemble the characteristic elongated shapes of Pb-sulfosalts (jordanite; Fig. 4d) in sphalerite/wurtzite. This texture is interpreted as native arsenic pseudomorphs after Pb-sulfosalts; the same generation of native As overgrows sphalerite (Fig. 4i). These native As-quartz-sphalerite associations are in some cases overgrown by another generation of sphalerite that is in turn overgrown by quartz. Later breccias of all earlier mineral stages are cemented by various barren quartz stages (Fig. 5a). During the final part of the quartz stage, native arsenic is dissolved (Fig. 5b) and/or replaced by realgar; realgar also forms euhedral crystals in cavities (Figs. 5c and 5d). Rarely, the realgar crystals in cavities are in turn overgrown by small needles of a still later second generation of native As (Fig. 5d). An extensive search for hydrothermal uranium-bearing minerals like uraninite or coffinite in radioactive hand specimens (as measured by a Geiger counter) produced no results, as did

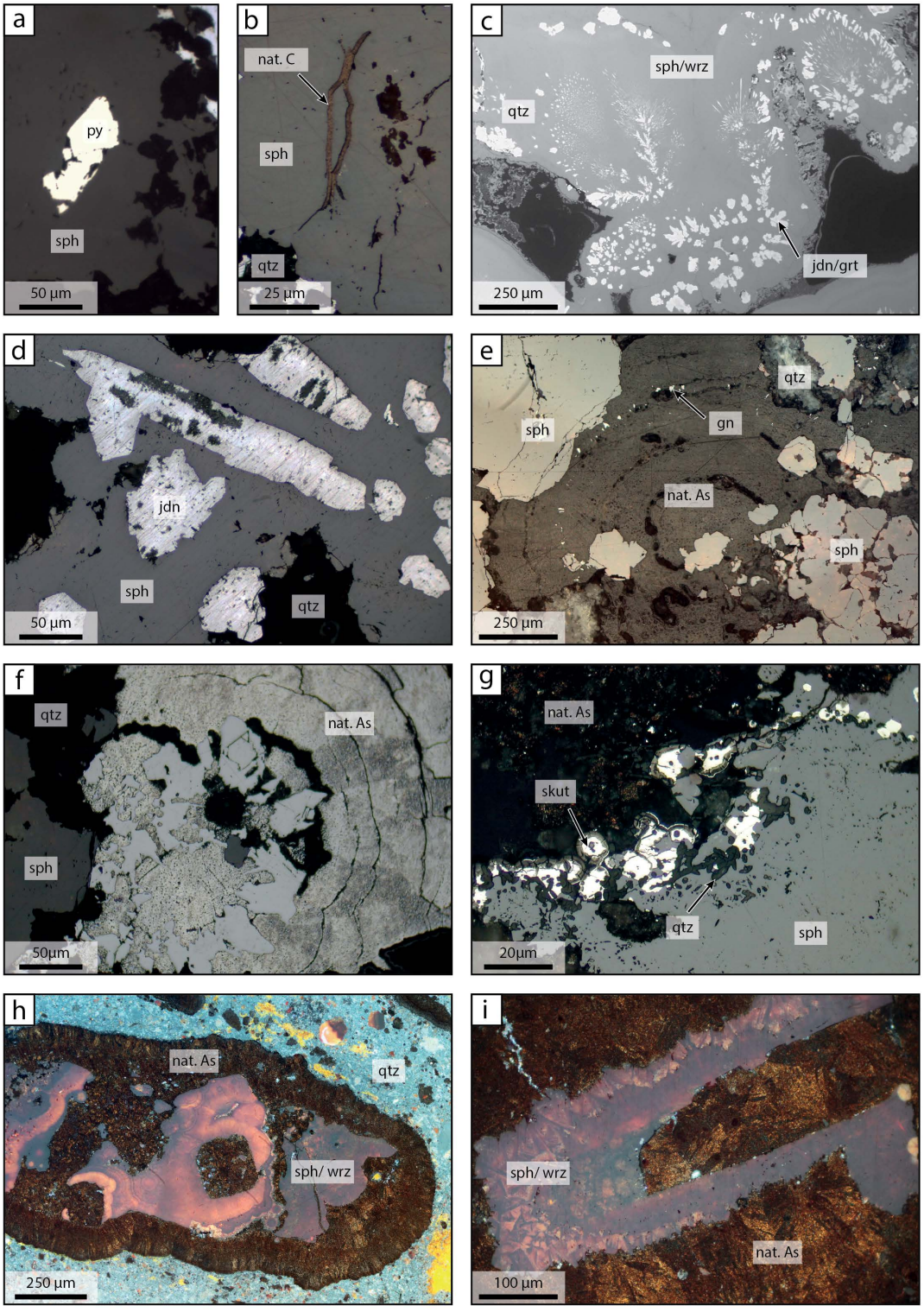

Figure 4. Pyrite (**a**) and graphite (**b**) are enclosed in sphalerite. Jordanite-gratonite solid solution minerals formed prior to/during sphalerite precipitation (**c** and **d**). Galena can also be found as small grains in individual native As bands (**e**), but typically forms before/during the initiation of native As, and is thus found as inclusions in native As (**f**). The triarsenide, skutterudide, is rare and mostly occurs at the transition between sphalerite and native As formation (**g**). Mineral aggregates are characteristically brecciated and cemented by subsequent minerals, where jordanite crystals are commonly pseudomorphed by native As (**h** and **i**). (**c**, **g, h**, and **i**) represent colloform samples and (**a**, **b**, **d**, **e**, and **f**) represent non-colloform samples. Image types: (**c**) BSE image, (**a**, **b**, **d**–**h**) reflected light and (**h** and **i**) slightly adjusted but crossed polarized reflected light. (Color online.)

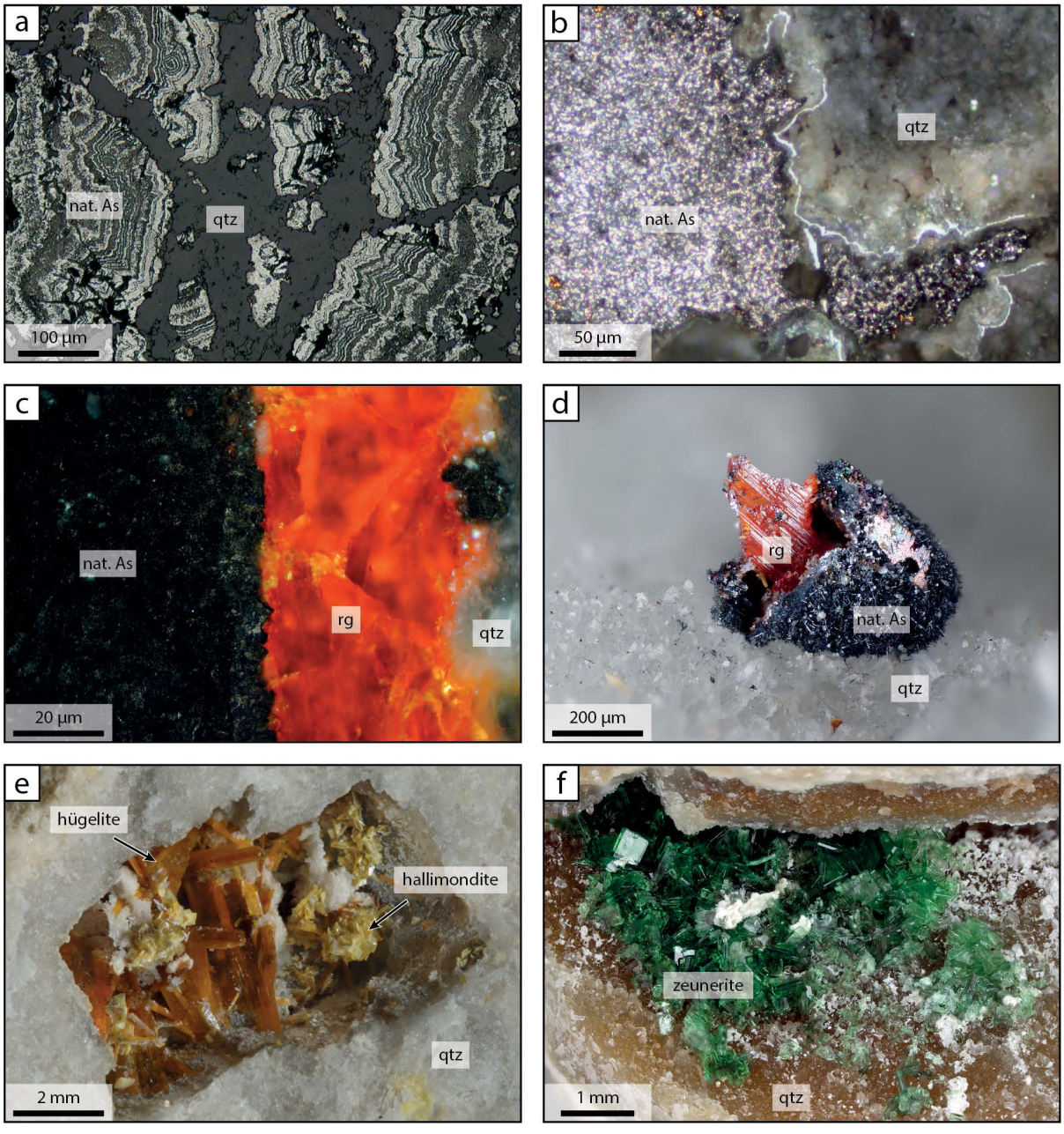

Figure 5. Ore stage IIa minerals are commonly brecciated and cemented by fine-grained quartz (**a**), partially dissolved (**b**), or replaced (**c**). (**d**) A rare second generation of native As can form remarkable overgrowths on realgar crystals. (**e** and **f**) Supergene druse fillings sometimes incorporate uranyl arsenates. Image types: (**a**) reflected light, (**b** and **c**) crossed polarized reflected light, and (**d**, **e**, and **f**) hand specimen images. (Color online.)

similar attempts by Walenta and Wimmenauer (1961). Based on the large number of fresh samples investigated by Walenta and Wimmenauer (1961) and by us (including microscopy, XRD, and radiology techniques), we can exclude the presence of primary (= hydrothermal) uranium-bearing minerals in the Michael vein.

III. Carbonate stage: The occurrence of late, well-crystallized carbonates is a typical feature in many hydrothermal veins in the Schwarzwald district and records erosional uplift of the vein and near-surface conditions of formation at low temperatures (Burisch et al. 2017b). They are particularly common close to the URG (see e.g., Markl 2017). In the Michael vein, dolomite is generally overgrown by calcite, and both fill small fractures and/or voids as euhedral crystals. No ore minerals are associated.

Supergene processes (uranium enrichment): During supergene weathering, first- and second-stage ore minerals release mainly Pb, Zn, and As and, hence, secondary minerals mainly comprise arsenates, carbonates, and sulfates of Pb and Zn, and, to a lesser extent, also of Cu (Markl 2017). The most common

supergene phases are mimetite, anglesite, and cerussite, rarer, but still common phases include adamite and minerals of the beudantite-segnitite-hidalogoite series. Furthermore, an interesting suite of supergene uranium-bearing minerals exclusively occurs on fine-grained quartz III and IV (chert) samples. These include hallimondite (microcrystalline, yellow crusts), heinrichite (yellow plates), novacekite (yellow plates), hügelite (orange needles), widenmannite (yellow tabular crystals), and zeunerite (green tabular crystals) (Figs. 5e and 5f; Markl 2017). Although these minerals are relatively rare in the investigated samples, an increased radioactivity in the mine and in hand specimens from the dumps has already been detected by Kirchheimer (1957), who determined whole-rock U contents up to almost 1 wt% in some underground samples. The supergene enrichment of U is also recorded by the occasional incorporation of U in the abundant supergene mineral mimetite (Walenta and Wimmenauer 1961). Primary U-bearing minerals are, as mentioned above, not present in the Michael vein and, hence, the uranium must have been introduced by the supergene, meteoric weathering fluids.

Analytical methods

Scanning electron microscope (SEM) and electron microprobe analyses (EMPA)

For qualitative mineral analyses and texture documentation, a Hitachi TM3030 REM Plus Tabletop Microscope at the University of Tübingen was used. The quantitative analysis of the minerals was carried out on 24 thin sections using a JEOL SUPERPROBE JXA-8900RL at the University of Tübingen. To avoid tarnishing of arsenic, the thin sections were re-polished, cleaned with ethanol, and dried for half a day before being spattered with carbon. Details of the analytical conditions and choice of reference materials used are described in Electronic Supplemental Materials[1] (ESM) 1.

X-ray diffraction (XRD)

Minerals were identified based on XRD analyses using a Bruker AXS D8-Discover Co-Source diffractometer, equipped with a HOPG-monochromator and a VANTEC500 detector, at the University of Tübingen. Measurements with 50 and 300 μm diameter were performed between 5.7° to 69–100° with 0.05° steps and a collection time of 120 s per step at room temperature (25 °C) with a Co$K\alpha$ beam at 30 kV and 30 mA. Data evaluation was done using the DIFFRACPLUSEVA software package.

Sulfur isotopes

A handpicked sample of cogenetic sphalerite and galena was powdered and the S-isotopic composition was then measured with a Finnigan Delta Plus XL mass spectrometer. The resulting S-isotopic compositions are calibrated to $\delta^{34}S$ values of several in-house standards: NBS-123 (ZnS, $\delta^{34}S$ = 17.1‰, relative to V-CDT), NBS-127 ($BaSO_4$, $\delta^{34}S$ = 20.31‰, relative to V-CDT), IAEA-S1 ($\delta^{34}S$ = –0.30‰, relative to the CDT), and IAEA-S-3 ($\delta^{34}S$ = 21.70‰, relative to the CDT). The long-term reproducibility of the $\delta^{34}S$ measurements are ±0.3‰ (2σ) and of the sulfur content are 5%.

Fluid inclusion analyses

For fluid inclusion analyses, several 250 μm thick, double-polished sections of quartz and sphalerite crystals were prepared. Individual fluid inclusion assemblages after Goldstein and Reynolds (1994) were characterized. No primary fluid inclusions could be detected in quartz. The only primary fluid inclusions found in any sample occur in sub- to euhedral sphalerite. They are very small (seldom larger than 10 μm) and rare. The microthermometric analyses were carried out at the University of Tübingen using a Linkam THMS 600 fluid inclusion stage on a Leica DMLP microscope calibrated with synthetic H_2O, H_2O-NaCl, and H_2O-CO_2 standards. For statistical purposes, each inclusion was analyzed at least 3 times. For the homogenization temperature, a variation of less than 0.5 °C, and for melting temperatures, a variation of no more than 0.1 °C was accepted between runs. A pressure correction was not applied since the salinity is unknown and a very shallow depth of formation under hydrostatic pressure can be assumed (e.g., Burisch et al. 2017b).

Thermodynamic modeling

Thermodynamic modeling was done using the software package Geochemist's Workbench 12 (GWB; Bethke 2007). For stability diagrams, the phase 2 and P2plot GWB application and for solubility calculations during fluid cooling, the react GWB application was used. Detailed information on the thermodynamic modeling approach as well as the process of thermodynamic data selection for zeunerite and data estimation for jordanite and hallimondite is given in the ESM[1] 2 and the results presented in Table 2.

Results

Mineral identification and composition

All ore minerals of ore stage II and some supergene minerals have been analyzed by electron microprobe (crystalline sphalerite = 66 analyses, colloform sphalerite = 143, skutterudite = 7, pyrite = 11, native As = 12, jordanite-gratonite solid-solution = 47, gersdorffite = 11, galena = 32, fahlore = 30, chalcopyrite = 2, realgar/pararealgar = 4, pyromorphite group minerals = 39) and their respective end-member formula are given in Table 3. The analyzed mineral compositions are presented in the ESM[1] 3 and only some major aspects are discussed here. Selected representative analysis are given in Table 4.

The close to ideal stoichiometric pyrite and chalcopyrite are nearly free of trace elements—only Ni, Co, and As have been detected in some grains. Ni and Co are, where at all detected,

Table 3. Compilation of minerals discussed in this manuscript

Mineral	Formula
Sulfosalts, sulfarsenides, and arsenides	
Chalcopyrite	$CuFeS_2$
Galena	PbS
Gersdorffite	NiAsS
Gratonite	$Pb_9As_4S_{15}$
Jordanite-geocronite	$Pb_{14}(As,Sb)_6S_{23}$
Orpiment	As_2S_3
Pyrite	FeS_2
Realgar	As_4S_4
Skutterudite	$(Ni,Co,Fe)As_3$
Sphalerite/wurzite	ZnS
Tennantite	$Cu_6[Cu_4(Fe,Zn)_2]As_4S_{13}$
Native elements	
Graphite	C
Native arsenic	As
Supergene minerals	
Adamite	Zn_2AsO_4OH
Anglesite	$PbSO_4$
Cerussite	$PbCO_3$
Goethite	FeO(OH)
Hallimondite	$Pb_2(UO_2)(AsO_4)_2{\cdot}2H_2O$
Heinrichite	$Ba(UO_2)_2(AsO_4)_2{\cdot}8–10H_2O$
Hügelit	$Pb_2(UO_2)_3(AsO_4)_2O_2{\cdot}5H_2O$
Malachite	$Cu_2CO_3(OH)_2$
Meta-zeunerite	$Cu(UO_2)_2(AsO_4)_2{\cdot}8H_2O$
Mimetite	$Pb_5(AsO_4)_3Cl$
Parsonsite	$Pb_2(UO_2)(PO_4)_2{\cdot}2H_2O$

Table 2. Thermodynamic data (Δ_fG in kJ/mol) estimated or selected and incorporated into the preexisting thermodynamic databases used in this study

	0 °C	25 °C	60 °C	100 °C	150 °C	200 °C	250 °C	300 °C	Source
$Pb_{14}As_6S_{23}$	–1670	–1679	–1693	–1710	–1736	–1765	–1798	–1834	Estimated
$Pb_2UO_2(AsO_4)_2{\cdot}2H_2O$	–3012±15								Estimated
$Cu(UO_2)_2(AsO_4)_2{\cdot}8H_2O$	–5315								[1]

Note: [1] represents Vochten and Goeminne (1984).

TABLE 4. Representative EPMA analyses

Mineral	Pyrite	Sphalerite coll.	Sphalerite non-coll.	Sphalerite non-coll.	Jordanite	Jordanite	Galena	Fahlore	Chalcopyrite	Skutterudite	Nat. arsenic	Parealgar		Mimetite	Mimetite
Sample	LK11	BW95	KS8	LK11	1376	LK2	KS5a	Fhl	L4	L4	BW100	BW102		KS1	KS3
EPMA analysis [wt%]															
Mn		b.d.l.	b.d.l.	b.d.l.									PbO	78.831	74.931
Fe	46.390	0.047	0.247	0.034	0.909	0.011	0.044	0.043	1.340	30.127	5.195	b.d.l.	0.009	b.d.l.	CaO	b.d.l.	b.d.l.
Co	b.d.l.					b.d.l.	b.d.l.	b.d.l.	b.d.l.	b.d.l.	3.444	b.d.l.	b.d.l.	b.d.l.	BaO	b.d.l.	b.d.l.
Ni	b.d.l.					b.d.l.	b.d.l.	b.d.l.	b.d.l.	b.d.l.	12.618	b.d.l.	b.d.l.	b.d.l.	ZnO	b.d.l.	b.d.l.
Cu	b.d.l.	b.d.l.	b.d.l.	b.d.l.	b.d.l.	b.d.l.	b.d.l.	42.807	33.102	b.d.l.	b.d.l.	b.d.l.	b.d.l.	b.d.l.	CuO	b.d.l.	b.d.l.
Ag	b.d.l.	b.d.l.	b.d.l.	b.d.l.	b.d.l.	b.d.l.	0.035	b.d.l.	b.d.l.	b.d.l.	b.d.l.	b.d.l.	b.d.l.	b.d.l.	FeO	b.d.l.	b.d.l.
Cd		0.401	b.d.l.	b.d.l.											SiO_2	b.d.l.	b.d.l.
Zn	b.d.l.	65.781	64.905	66.693	66.127	0.140	0.253	0.019	6.859	b.d.l.	b.d.l.	b.d.l.	0.167	0.017	SO_2	b.d.l.	b.d.l.
Pb	b.d.l.	0.299	1.311	0.041	b.d.l.	67.596	69.355	86.274	b.d.l.	b.d.l.	b.d.l.	b.d.l.	0.132	b.d.l.	P_2O_5	6.439	b.d.l.
Se	b.d.l.					0.018	0.031	b.d.l.	b.d.l.	b.d.l.	0.578	b.d.l.	0.597	0.180	As_2O_5	14.173	23.499
Hg	b.d.l.					0.083	b.d.l.	b.d.l.	b.d.l.	b.d.l.	b.d.l.	b.d.l.	b.d.l.	b.d.l.	V_2O_3	b.d.l.	b.d.l.
S	53.779	32.696	32.397	33.193	32.768	17.103	17.933	13.561	28.710	35.002	5.520	0.341	0.446	29.036	UO_2	b.d.l.	0.812
Bi	b.d.l.					b.d.l.	b.d.l.	b.d.l.	b.d.l.	b.d.l.	b.d.l.	b.d.l.	b.d.l.	b.d.l.	Cl	2.37	2.02
As	0.137	0.128	0.205	0.035	0.066	5.223	8.226	0.074	19.534	0.173	73.529	98.134	98.691	70.655	F	b.d.l.	b.d.l.
Sb	b.d.l.	0.187	0.424	b.d.l.	b.d.l.	8.144	4.154	b.d.l.	0.830	b.d.l.	b.d.l.	0.354	0.253	0.266			
Σ	100.31	99.61	99.58	100.01	99.87	98.32	100.00	100.01	100.08	98.40	100.31	99.41	100.30	100.15			
Empirical formula																	
	$Fe_{0.99}S_{2.00}$	$Zn_{1.00}S_{1.00}$	$Zn_{0.99}Pb_{0.01}$ $S_{1.00}$	$Zn_{0.99}S_{1.01}$	$Zn_{1.00}S_{1.00}$	$Fe_{0.01}Zn_{0.09}$ $Pb_{14.14}Se_{0.01}$ $Hg_{0.01}S_{22.95}$ $As_{3.00}Sb_{2.88}$	$Fe_{0.03}Zn_{0.16}$ $Pb_{13.80}Se_{0.02}$ $S_{23.06}As_{4.53}$ $Sb_{1.41}$	$Pb_{1.00}S_{1.00}$	$Cu_{0.94}Fe_{0.35}$ $Zn_{1.55}S_{13.21}$ $As_{3.85}Sb_{0.10}$	$Cu_{0.97}Fe_{1.00}$ $S_{2.03}$	$Ni_{0.57}Co_{0.15}$ $Fe_{0.24}As_{2.58}$ $S_{0.45}$	$As_{1.02}S_{0.98}$			$Pb_{5.01}$ $P_{1.29}As_{1.75}$ $O_{12}Cl_{0.95}$	$Pb_{5.01}U_{0.05}$ $P_{1.28}As_{1.75}$ $O_{12}Cl_{0.95}$

FIGURE 6. Compositional analyses of Zn-sulfides, classified according to their textural occurrence, plotted to visualize potential micro-intergrowth with other minerals. Mineral abbreviations: chalcopyrite (cp), fahlore (fhl), galena (gn), gersdorffite (gdf), jordanite-gratonite solid-solution (jdn-gtn), and skutterudite (skut). (Color online.)

very close to the detection limit, but As incorporation can reach up to 0.1 wt%.

As explained above, Zn-sulfides have been categorized into two texturally distinct groups, the colloform and non-colloform type. By X-ray diffraction, the colloform Zn-sulfide was identified to be a mixture of both needle-shaped sphalerite and wurtzite. The analytical totals of all Zn-sulfide measurements range from 95 to 101 with an average of 100 wt% for the non-colloform and with an average of 98.5 wt% for the colloform samples. No correlation between analysis total and stoichiometry of the calculated formula exists, and the variations in totals reflect variations in porosity. However, for interpretation, only analyses with a total between 98 and 101 wt% have been considered. Elevated Pb and As concentrations in both types of sphalerites (Table 4) indicate the presence of jordanite-gratonite solid-solution microinclusions in sphalerite; they are more common in the colloform textures (Fig. 6). This compositional argument is supported by the close association of visible jordanite-gratonite solid-solution bands within the colloform sphalerite. Sub-microscopic inclusions of other sulfides in sphalerite have been previously reported from other localities (e.g., Taylor and Radtke 1969; Kelley et al. 2004; Pfaff et al. 2011). Besides Pb and As, the sphalerite of both textural types is generally poor in trace elements and only Cd can be present up to 3.5 wt% in a handful of analyses. Sphalerite contains generally <<1 wt% Fe and shows the transparent reddish to brownish color typical of Fe-poor varieties. The analyzed galena has a stoichiometric formula and lacks trace elements.

X-ray diffraction and compositional analyses revealed the presence of both jordanite [ideally $Pb_{14}(As,Sb)_6S_{23}$] and gratonite (ideally $Pb_9As_4S_{15}$). Both minerals are commonly intergrown and embedded within the colloform sphalerite. The only significant trace element is Zn, which can reach values of up to several wt% (but this may be due to microinclusions again, see above). Due to their small grain size, no gersdorffite and almost no skutterudite grains could be analyzed without contamination by galena and/or

sphalerite. However, such mixed analyses still indicate their ternary nature with respect to Fe, Co, and Ni (0.2:0.15:1 and 0.54:0.3:1 for skutterudite and gersdorffite, respectively). Furthermore, gersdorffite is enriched in Se (ca. 0.2 wt%). The fahlore is a near end-member Cu-Zn-tennantite with an average mineral formula of $Cu_{10.02}Fe_{0.33}Zn_{1.52}As_{3.88}Sb_{0.09}S_{13.15}$. Native As incorporates up to 0.2 wt% Zn, 0.4 wt% Pb, and 0.6 wt% Se and Sb each. In all these As-bearing minerals, other trace elements are close to or below the detection limit.

Realgar/pararealgar shows a similar trace element budget as native As and is enriched in Sb and Se. The pyromorphite group minerals of the Michael vein are commonly close to end-member mimetites. Occasionally, however, phosphate substitution in individual crystals is high enough to reach pyromorphite composition. The Ca content rarely reaches 0.2 wt%. Uranium is generally absent, but individual analyses can reach up to 1 wt% UO_2 (Table 4).

Temperature of formation

To constrain the temperature of formation of the stage II mineralization, two independent thermometers were applied: sulfide isotope equilibrium and fluid inclusion homogenization. For the isotope analyses, the cogenetic minerals (colloform sphalerite/wurtzite mixture and galena (KS13)) were carefully isolated and hand-picked. The sphalerite has a $\delta^{34}S$-value (V-CDT, ‰) of –3.68(0.3) and the galena of –8.58(0.3). Applying the isotope fractionation factors of Seal (2006 and references therein), and assuming the literature isotope fractionation factor for ZnS applies to both wurtzite and sphalerite, the resulting calculated equilibrium temperature is ~110(20) °C (Gauss uncertainty propagation). The eight primary fluid inclusions analyzed in non-colloform sphalerite (100, 102, 104, 109, 110, 119, 123, 128 °C) nicely support this result: they indicate a homogenization temperature range of 100–128 °C with an average of ~110(10) °C (1σ).

Due to the formation of metastable phases at low temperatures in the fluid inclusions, the salinity of the primary fluid inclusions in sphalerite could not be quantitatively determined—but it could still be qualitatively constrained to some degree. The approximate temperature of first melting is around –50 °C. In combination with the presence of abundant hydrohalite, this constrains the fluid to be of high salinity with an at least ternary composition ($NaCl-CaCl_2-H_2O$). The presence of hydrohalite and the absence of Ca-chlorides suggest a possible NaCl dominance over $CaCl_2$.

Thermodynamic modeling and fluid constraints

The highly saline and most probably NaCl-dominated fluid is in good agreement with typical fluid inclusion analyses from veins related to Upper-Rhine-Graben tectonics (5–25 wt% $NaCl+CaCl_2$ Walter et al. 2018). For thermodynamic modeling, we used an intermediate salinity of 10 wt% NaCl. Based on the above temperature estimations, and because sphalerite precipitation is commonly preceded by some quartz crystallization in ore stage II, it is estimated that mineral precipitation occurred between 150 and 50 °C, with most of the ore minerals probably precipitating between 130 and 90 °C.

The elemental fluid composition for the thermodynamic modeling is based on qualitative constraints, empirical calculations, and a literature compilation/comparison. The precipitation mechanism for quartz is assumed to be fluid cooling and for the sulfides to be reduction related to the influx of a sulfide-rich fluid. At close to neutral pH (neutral ±2), 1 kg of H_2O fluid cooled from 150 to 50 °C can precipitate ca. 150 mg SiO_2. Based on the estimated abundance of the major minerals in ore stage II (quartz 90 vol%, sphalerite 7 vol%, and native As 3 vol%), the amounts of sphalerite and native As that have to precipitate from 1 kg of fluid can be calculated (ca. 20 and 10 mg/kg, respectively). This implies that the fluid must have contained at least 10 mg/kg Zn and As, respectively. Furthermore, for the whole mineral sequence to form, Zn has to be successively depleted relative to sulfide. Thus, the calculated 10 mg/kg of Zn is not a minimum but a rough absolute estimate. Assuming the relative abundance of Zn, Pb, and Ni in the mineralization, we estimate the fluid composition to be roughly 10 mg/kg of Zn and As, 1 mg/kg of Pb, and 0.1 mg/kg of Ni. This composition is in very good agreement with naturally occurring Upper-Rhine-Graben brines that are related to the Buntsandstein aquifer: such brines contain up to 10 mg/kg Zn and As each, up to 1 mg/kg Pb and up to 0.1 mg/kg Ni (Sanjuan et al. 2010).

Discussion

Precipitation mechanism

The first mineralization stage with barite and galena is a very common type of mineralization in the vicinity of the URG (e.g., Metz and Richter 1957; Markl 2015, 2017) and formed by a three component fluid mixing process involving a metal-bearing basement-derived, a sulfate-bearing sedimentary cover-derived and a sulfide-bearing fluid (e.g., Walter et al. 2018).

In contrast, the subsequent native As-sphalerite-quartz stage II is a regionally unique and worldwide rare type of mineralization. Hence, it needed very special conditions of formation, which are, obviously, only rarely fulfilled in nature. The large quantities of fine-grained crystalline quartz indicate that cooling was the dominant precipitation mechanism. This is supported by textures, i.e., the typical pseudomorphs of quartz after barite (Burisch et al. 2017c) and native As after jordanite/gratonite. Fluid cooling does not, however, explain the amount of sphalerite present relative to quartz, as the decrease of sphalerite solubility with temperature is minimal in the investigated temperature range of 150–50 °C (e.g., Hayashi et al. 1990; Hanor 1996). Native arsenic precipitation has been proposed to be facilitated by a decrease in temperature, pressure, and most importantly f_{O_2} (e.g., Su et al. 2009; Zheng et al. 2015; Markl et al. 2016; Burisch et al. 2017a; Scharrer et al. 2019). Thus, even though fluid cooling promotes some precipitation of sphalerite and native As, an influx of a redox agent is needed to precipitate the whole sequence of minerals in the observed quantities. The presence of abundant native As (As^0) and some arsenides (As^{-II}) in combination with the absence of graphite dissolution textures in the samples (Fig. 4b) demonstrates a strongly reduced environment during the formation of the ores. Due to the presence of abundant sulfides and the slow kinetics of sulfate to sulfide reduction in the observed temperature range (Sakai 1968; Malinin and Khitarov 1969; Rye and Ohmoto 1974; Ohmoto and Lasaga 1982), it is most likely that an influx of sulfide was essential. An abiotic in situ reduction of sulfate to sulfide can be excluded since the most abundant source of sulfate present is the partially dissolved barite, which at ~100 °C is in strong isotopic disequilibrium with the sphalerite (Schwinn et al. 2006; Seal 2006). It has been proposed that colloform sphalerite

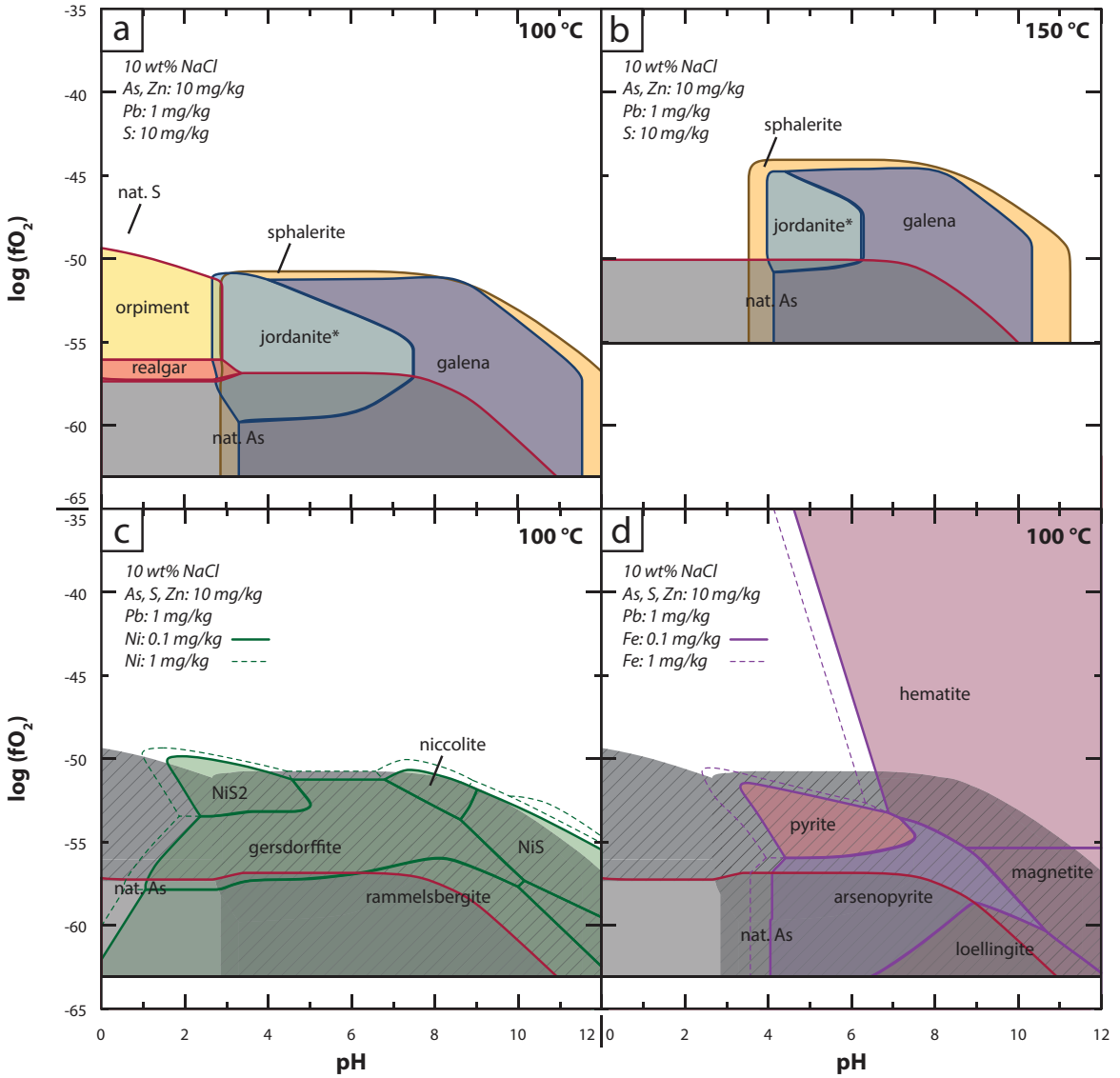

FIGURE 7. pH-logf_{O_2} diagrams depicting mineral stabilities. Note stabilities may overlap, e.g., at the stability conditions of galena, sphalerite is also stable. Diagrams (**a** and **b**) show the thermodynamic stability of the Michael vein mineralogy at roughly neutral conditions. (**c** and **d**) Striped-shaded region represents the stability fields of As-sulfides, sphalerite, galena, and jordanite and is identical to **a**. The bottom diagrams (**c** and **d**) show the impact of even slight amounts of Ni or Fe on the stability of Ni- and Fe-minerals. (Color online.)

can form by mixing of a fluid containing bacteriogenic sulfur and a metal-bearing hydrothermal fluid (Wilkinson et al. 2005; Barrie et al. 2009; Pfaff et al. 2011). Bacteriogenic sulfate reduction has been proven to prevail to temperatures up to 110 °C with an optimal range of 30–40 °C (e.g., Jørgensen et al. 1992; Seal 2006). Thus, groundwater sulfate reduction is a possible sulfide source for the mineralization in question. Other possible sources of sulfide are magmatic or metamorphic sulfides from the host rocks, diagenetic/sedimentary sulfides, or URG oil field brines. In summary, a combination of fluid cooling and the influx of a sulfide and redox agents was responsible for the formation of the sphalerite-native As-quartz stage II assemblage. This, however, does not explain the uniqueness of the abundance of native arsenic in this mineralization, as the combination of reducing conditions in the presence of aqueous arsenic is probably not very rare; most As-rich associations are sulfide, sulfarsenide or arsenide dominated and completely lack of or very poor in native As (e.g., most five element deposits, Scharrer et al. 2019).

Conditions of formation

Thermodynamic calculations show that at roughly neutral pH, the paragenetic sequence of ZnS + galena + Pb-As-sulfosalts → native As, the precipitation of the Ni sulfarsenide (gersdorffite) during sphalerite formation and the arsenide formation at the transition to the native As formation can be nicely reproduced using the element concentrations discussed above (Fig. 7). However, this only explains that it is thermodynamically possible to form this mineralization by a fluid mixing/reduction/sulfide

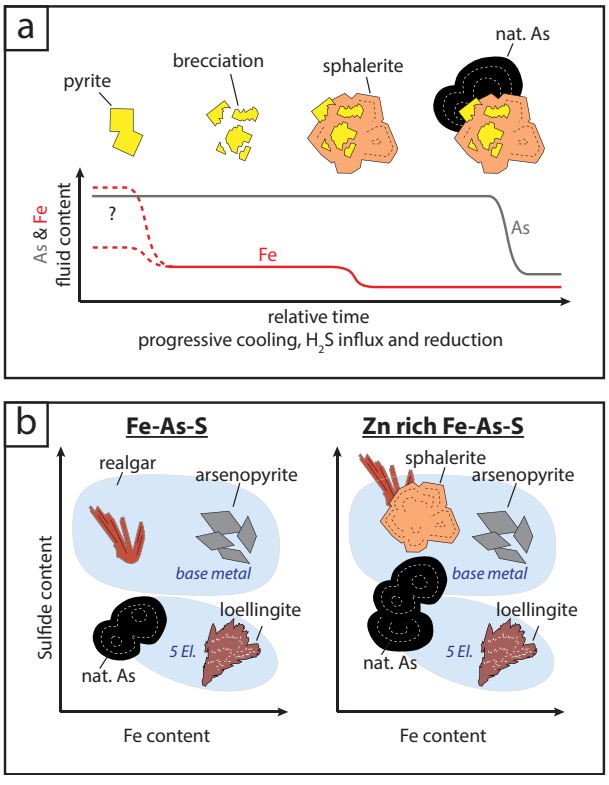

FIGURE 8. (**a**) Qualitative formation model of the Michael vein native As-base metal mineralization. (**b**) Qualitative diagrams depicting the impact of abundant Zn in stabilizing native As at higher sulfidation states. (Color online.)

influx scenario. It does, however, not explain the scarcity of native arsenic in base-metal mineralizations in general. Normally, arsenic is almost exclusively stored in other, significantly more common minerals such as arsenopyrite, As-rich pyrite, sulfosalts, and arsenides.

The important parameters constraining a native As-bearing base-metal mineralization to form are summarized here (Fig. 8) and further discussed in the following subsections. Obviously, it is essential for the mineralizing fluid to contain sufficient Zn, Pb, S, and As. However, for native arsenic to form, it is crucial that the transition elements Ni, Co, and Fe have very low concentrations, as otherwise sulfarsenides and/or arsenides would form instead of native As (see below). A lower temperature favors native As stability, but it also favors the formation of realgar and orpiment. The stability of these As-sulfides is, however, suppressed at roughly neutral conditions by the abundance of dissolved metals such as Zn and Pb that limit the availability of sulfide.

Low concentrations of Fe, Co, and Ni. In hydrothermal systems, such as base metal mineralizations, arsenic most commonly precipitates as arsenopyrite or gersdorffite, while native arsenic is comparatively rare (~10 000 vs. 400 occurrences worldwide, Mindat.org). To promote the formation of native As instead of arsenopyrite, either sulfide or iron has to be limited. Since native As also occurs in sulfide/sulfosalt-rich mineralizations (e.g., Bailly et al. 1998; An and Zhu 2009; Su et al. 2009; Radosavljević et al. 2014), and as this is also in the present situation, sulfide is most likely not the defining factor. The assumption of low concentrations of Fe, Co, and Ni in the mineralizing fluid during native As crystallization is in accordance with many textural observations, as native arsenic typically precipitates after the precipitation of theses transition metals (Noble 1950; McKinstry 1963; Bailly et al. 1998; Su et al. 2009; Zheng et al. 2015; Scharrer et al. 2019). Thus, it is likely that these metals were depleted by the time the reducing conditions allowed native As to precipitate.

Thermodynamic calculations show, in general, that for native As to form the fluid has to be either extremely acidic or deprived of Fe, Co, and Ni relative to As, since, otherwise, the sulfarsenides or arsenides would form (Fig. 9). Strongly acidic conditions can be excluded based on the presence of sphalerite and galena (stable at pH > ~3; 100 °C) and the lack of dissolution textures of these phases during native As precipitation. The absence of the transition elements Fe, Co, and Ni in the Michael vein is also recorded by the observed mineralogy (Fig. 2). Co- and Ni-bearing minerals are very rare, their crystals are tiny and the only relevant Fe-bearing minerals in the mineralization are scarce pyrite grains and the abundant, but conspicuously Fe-poor sphalerite (commonly significantly less than 1 mol% Fe). The Fe-Zn substitution in sphalerite means that from a fluid precipitating 10 mg/kg of Zn in the form of sphalerite, less than 0.1 mg/kg of Fe is co-precipitated. Hence, the fluid was iron-poor already prior to sphalerite formation.

In contrast to Ni and Co, Fe is omnipresent in all lithological units in the region and, hence, every hydrothermal fluid should contain abundant Fe (dependent on redox and pH state, however). This is recorded by the common presence of pyrite, arsenopyrite and/or chalcopyrite in most hydrothermal veins of the region (e.g., Metz and Richter 1957; Bliedtner and Martin 1986), by the presence of iron in thermal spring fluids (0.01–10 mg/kg; Göb et al. 2013) and by hydrothermal fluid inclusions of the region (up to ~10 000 mg/kg; Walter et al. 2018). Thus, for the case at hand, either the transport of Fe is retarded by, for example, the stability of hematite and/or Fe-oxyhydroxides at neutral to basic pH or the initially present Fe had been precipitated prior to the formation of the Fe-poor mineralization of stage IIa. The latter would explain the presence of brecciated clasts of pyrite occasionally embedded in sphalerite, which could be more abundant at depth. Furthermore, the lack of trace elements (nearly all below the detection limit) indicates a low-temperature formation of pyrite and not a remobilization of host rock pyrite, and the lack of these clasts within stage I minerals indicates a formation after stage I but before stage IIa. However, at present we cannot distinguish whether the fluid was primarily Fe-poor or if significant pyrite precipitation occurred at greater depth that depleted the fluid in iron. It is, however, clear that if sulfarsenides are absent, very low Fe concentrations are essential for this native As-rich base metal mineralization to form.

Temperature, sulfur abundance and the stability of native As. The solubility of all minerals in question decreases with decreasing temperature (Fig. 10) and, hence, the formation of mineral assemblage IIa is favored by and related to fluid cooling. Furthermore, native As is only stable at < ~300 °C (at low pressure) and becomes increasingly stable at lower temperatures. The even more significant temperature dependence

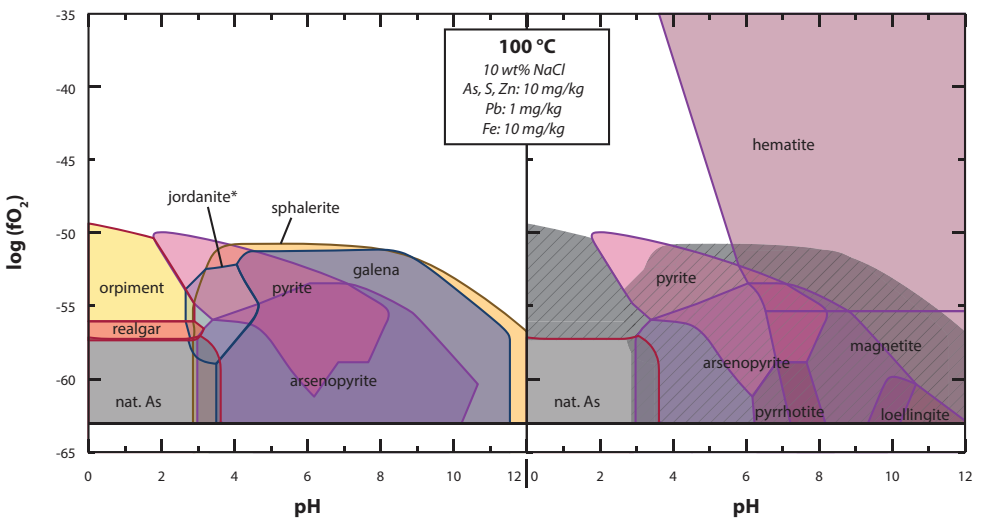

►**FIGURE 9.** pH-logf_{O_2} diagrams depicting mineral stabilities at higher Fe concentrations. Note stabilities may overlap, e.g., at the stability conditions of galena, sphalerite is also stable. The stability of arsenopyrite suppresses the stability of native As and thus prevents it from forming at a neutral pH, even at reduced conditions. (Color online.)

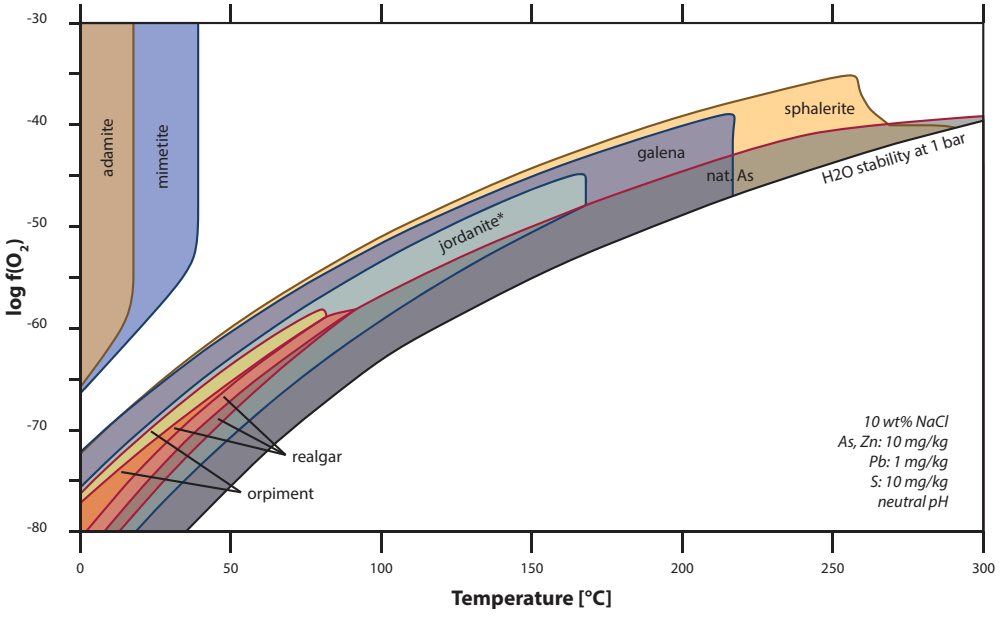

►**FIGURE 10.** *T*-logf_{O_2} diagram at neutral conditions showing the impact of temperature on the stabilities of the minerals from the Michael vein. Fluid conditions are identical to Figure 7a. (Color online.)

of the realgar and orpiment stability field relative to native As (Fig. 10) explains the late-stage overprint of native As by realgar, which is also typical of native As occurrences worldwide (e.g., Bailly et al. 1998; Cleverley et al. 2003). The increased stability of As-minerals at lower temperatures explains the generally described correlation between arsenic content and temperature in hydrothermal fluids and springs (e.g., Ballantyne and Moore 1988; Aiuppa et al. 2003).

Although lower temperatures favor the formation of native As, they also favor the formation of realgar and orpiment in the presence of sulfide. This explains the more common presence of realgar over native As in cooler and/or high sulfidation mineralizations (e.g., Arehart et al. 1993; Migdisov and Bychkov 1998; Cleverley et al. 2003; Su et al. 2009; Zhu et al. 2011). It is essential to understand the stability of realgar and orpiment, since these are absent during the precipitation of the main ore phases of stage II, and their lack of stability promotes the formation of native As. The stability of realgar/orpiment is confined to low temperatures, an acidic to neutral pH, and by the availability of both As and sulfide (e.g., Sergeyeva and Khodakovskiy 1969; Ballantyne and Moore 1988, Figs. 10 and 11). The availability of sulfide is, however, not only defined by the absolute abundance of S or kinetic disequilibrium between sulfate and sulfide (Scharrer et al. 2019) in the fluid, but also by the abundance of metals. The presence of transition metals such as Pb and Zn limits the availability of sulfur at reducing conditions by the precipitation of sulfides (Fig. 11). This interdependence, variable affinity of different elements to sulfur (Shcherbina 1978), enables the precipitation of native As in the presence of sulfide; e.g., in roughly neutral fluids at 100 °C containing ~10 mg/kg or 100 mg/kg of Zn or Pb at least 5–15 mg/kg (depending on As content) or 50 mg/kg of sulfur is needed, respectively, for realgar/orpiment

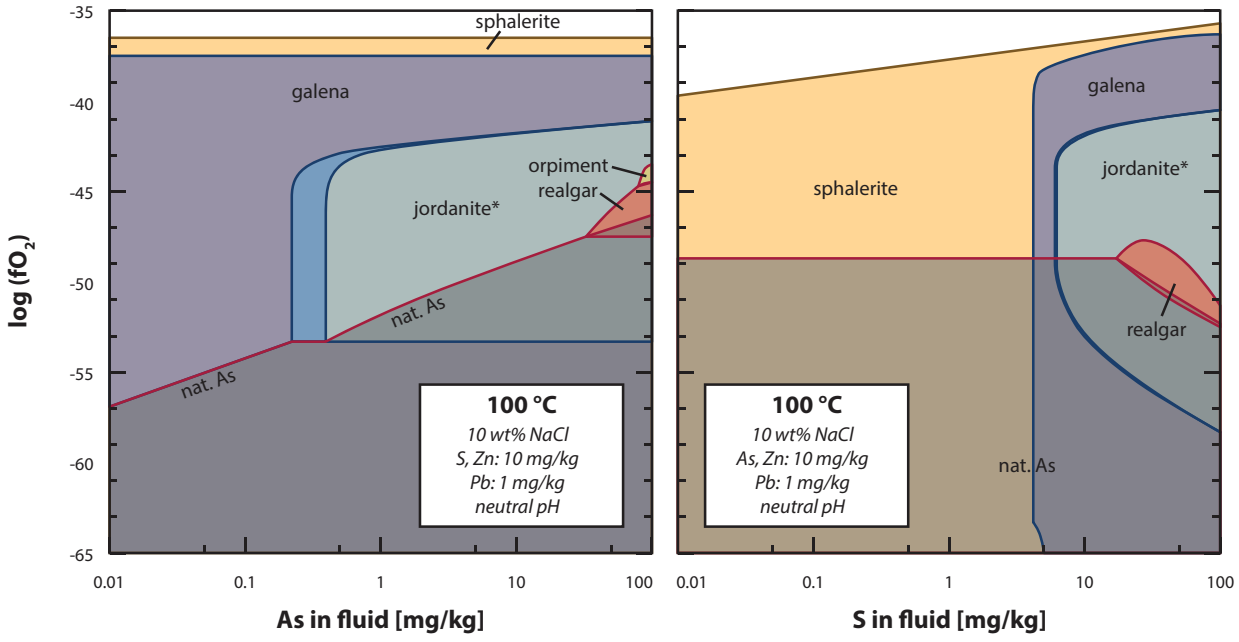

FIGURE 11. As- and S-logf_{O_2} diagrams depicting the impact of variable As and S content on the stability of the minerals from the Michael vein at neutral conditions. Both As and S increase the stability of the As-sulfides. Thus, to form natural As from a fluid with abundant As, sulfide must be absent. (Color online.)

to form instead of native As (e.g., Fig. 11). A fluid containing >1000 mg/kg of these base metals would need an unrealistically high amount of sulfur (>>1000 mg/kg) to form realgar, even at high arsenic contents (>1000 mg/kg). Thus, the availability of abundant Zn or Pb in a sulfide-rich environment, as is the case for the Michael vein, decreases the stability of the As-sulfides and thus promotes native As formation.

Native arsenic as a trap for uranium during supergene processes

Generally, low-temperature uranium deposits/enrichments form either by reduction of dissolved U^{+VI} to U^{+IV} or by sorption at strongly acidic pH, where U^{+VI} may also be subsequently reduced (Langmuir 1978; Dahlkamp 2009; Dahlkamp 2013). Typical reducing agents are for example organic material, sulfide, or pyrite (Andreev and Chumachenko 1964; Sharp et al. 2011; Dahlkamp 2013). During supergene overprinting of such primary uranium bearing associations, U^{+IV} is re-oxidized, during which uranyl-bearing minerals form (e.g., Finch and Ewing 1991; Gorman-Lewis et al. 2008). This is however not the case for the Michael vein. The Michael vein is quite unique as it contains a wealth of supergene uranium-bearing minerals (including rare Pb- bearing uranylarsenates), while primary uranium minerals such as uraninite are missing entirely (this study, Walenta and Wimmenauer 1961). Thus, uranium is present exclusively as U^{+VI} both in Ba-, Pb-, Cu-, and Mg-uranyl arsenates and as a minor constituent in mimetite. In some places along the vein, the accumulations of supergene uranium-bearing minerals result in significant whole-rock uranium contents up to 1 wt% (Kirchheimer 1957).

Due to the lack of primary U^{+IV}-bearing minerals, the supergene uranyl minerals must have directly precipitated from a U^{+VI}-bearing fluid where the mineralized vein acted as the uranium trap (Fig. 12a). The most likely source of uranium is the granitic host rock, which is slightly enriched in uranium (Martin 2009; Dahlkamp 2013). The release of uranium from such rocks to the fluid by weathering is indicated by the presence of uranium in granitic formation waters from southwest Germany (occasionally up to 30 µg/kg; Käß and Käß 2008; Göb et al. 2013) and the lower uranium concentration in altered granite compared to fresh granite in the Schwarzwald (e.g., Hofmann 1989). Although native As has a strong reduction potential, it did not directly act as a uranium immobilization agent by U^{+VI} reduction. However, during weathering and oxidation of the vein system, the arsenic in the native As is oxidized, which can then react with the uranyl bearing fluid to form the uranylarsenates. The uranylarsenates also needed metal ions (e.g., Cu, Pb, Ba) that are provided by weathering and dissolution of minerals such as galena, chalcopyrite, and barite. It has been argued that U^{+VI} sorption can limit the solubility of uranium even though the stabilities of uranyl arsenates are not reached (Langmuir 1978) and that sorption may be a precursor step to the local enrichment of uranium/formation of uranyl minerals (Barton 1956). This, however, seems not to be the case in the Michael vein, since the uranyl-bearing minerals form exclusively in quartz vugs and on fractures independent of typical adsorbents such as ferric oxides, hydroxides or organic material. Thus, we assume a direct precipitation from the fluid due to oversaturation of the respective uranyl arsenates by small-scale fluid mixing of compositionally contrasting fluids that reacted with variable amounts of the host rock and gangue minerals, etc. (Fig. 12a).

The dominance of uranyl arsenates over phosphates or silicates can be explained by the relatively high solubility of

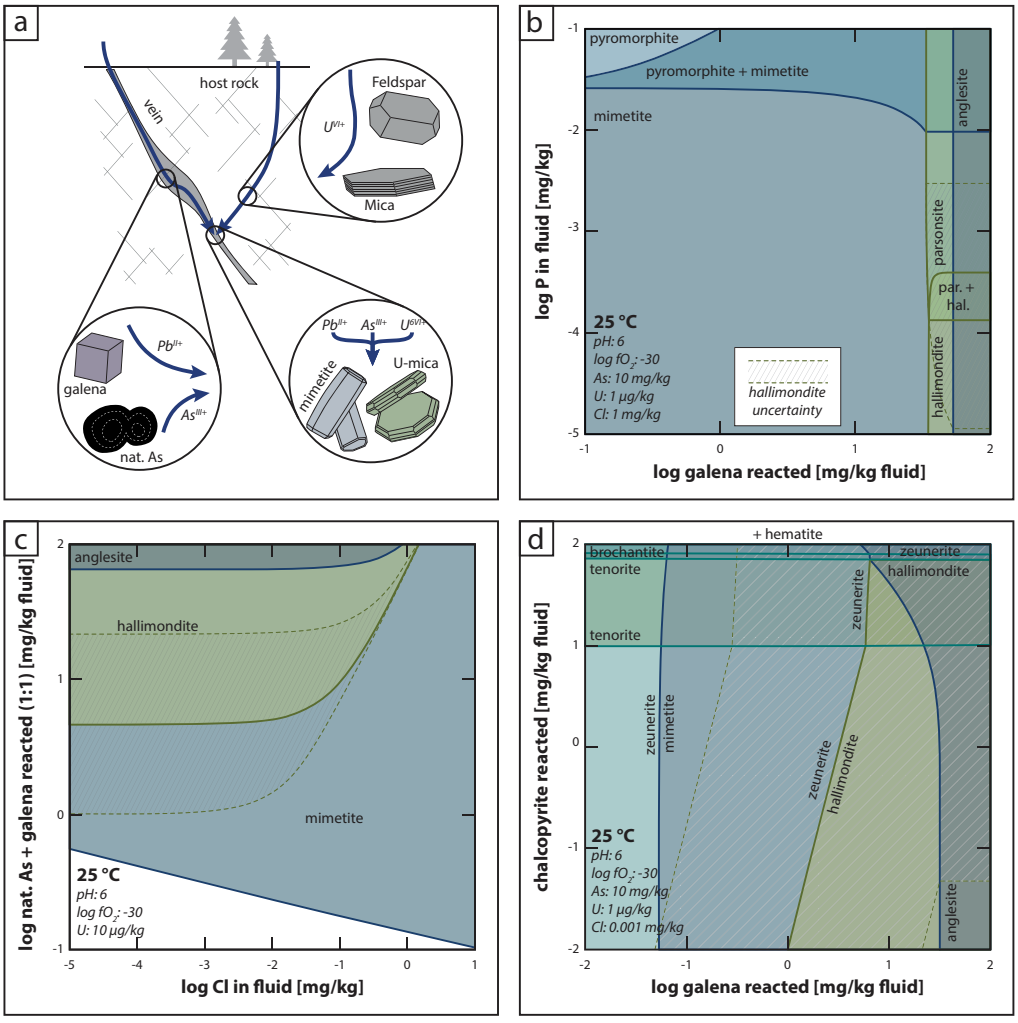

FIGURE 12. (**a**) Qualitative formation model for the uranyl arsenates presented by the example of the Pb-uranyl arsenates hügelite and hallimondite. Fluid-mineral reaction stability diagrams for (**b**) an arsenic-bearing fluid reacting with galena in the presence of various amounts of phosphor, (**c**) the stability of Pb-arsenate, uranylarsenate, and sulfate in the presence of various amount of chlorine, and (**d**) an arsenic-bearing fluid reacting with galena in the presence of various amounts of chalcopyrite. The uncertainty introduced by the solubility estimation of hallimondite is given by the striped area and dashed lines. The diagrams show that even at low U content of the fluid, uranyl arsenates can form. Furthermore, the Cu-uranyl arsenates are significantly more stable than the predicted Pb-uranyl arsenates. (Color online.)

the latter two (Langmuir 1978). Still, the formation of such an abundance of uranyl arsenates is an abnormal scenario, as dissolved phosphate and silicate are naturally much more common than arsenate under supergene conditions in "common" surface waters (e.g., Johnson 1971; Göb et al. 2013). In the present case, though, arsenates are stabilized by the high arsenate concentrations released during supergene weathering of native arsenic from which several orders of magnitude more is needed than phosphor to produce arsenates instead of phosphate (Fig. 12). The formation of the uranyl minerals is further promoted by other parameters, such as pH and temperature. The typical weathering fluids and mine drainage fluids in the Schwarzwald have an ideal pH (average of pH 6; Göb et al. 2013) for uranyl mineral formation as it coincides with the pH of lowest uranyl solubility and the stability of most important uranyl minerals (pH range from 5 to 8.5, Langmuir 1978). This pH range is also roughly the stability boundary for both zeunerite and hallimondite at the given conditions.

Although uranyl arsenates are generally less common than, for example, uranyl phosphates or silicates, their general occurrence is nothing unusual. Extremely rare, however, is the formation of Pb-bearing uranyl arsenates such as hallimondite and hügelite. Both have less than 10 occurrences worldwide (https://www.mindat.org) and their type locality is the Michael vein. Their stability is normally limited by the highly insoluble Pb-arsenate mimetite that is an extremely common mineral with thousands of occurrences worldwide. The stability of mimetite, however, is strongly dependent on the Cl content of the fluid (Fig. 12c). Accordingly, the Pb-uranyl arsenates form due to the presence of sufficient Pb and As (supplied by the weathered hypogene minerals galena and native As) combined with the depletion of Cl. The initial Cl content of mine waters is com-

monly in the range of 0.5–50 mg/kg (Göb et al. 2013). Due to the abundance of native As and galena in the vein, mimetite is the most abundant supergene mineral of the Michael vein. The precipitation of mimetite successively depletes the fluid in Cl, which enables the formation of Pb-uranyl arsenates (Fig. 12c). Finally, the quite common occurrence of the Cu uranyl arsenate zeunerite in the almost Cu-free Michael vein needs some explanation. Primary Cu-bearing minerals such as chalcopyrite are not absent, but very rare in the Michael vein, and hence, zeunerite was not expected to form in such an environment. However, due to the significantly lower solubility of zeunerite relative to Pb-uranyl arsenates (clearly visible, even when considering the large solubility uncertainty of hallimondite), zeunerite forms at a very low Cu content, if the arsenate content of a fluid is high (Fig. 12d).

Implications

The native As-bearing mineralization stage of the Michael vein is a prime example to study the mobility and precipitation mechanism of arsenic not only in hydrothermal base metal veins but many other types of hydrothermal environments. The requirements for native As formation can be summarized as follows:

- the availability of abundant aqueous arsenic;
- reduced conditions;
- very low concentrations of the transition metals Fe, Co, and Ni;
- very low sulfide concentrations (which can be reached by a lack of sulfide or presence of significant amounts of transition elements such as Pb and Zn).

If these requirements are met (which rarely occurs in nature), native As can form in large masses and can become a substantial part of a mineralization. These conditions not only provide insight on the formation of native As but also on the absence of native As and presence of other As-bearing minerals, which is important to understand the fate of (toxic) arsenic in natural environments. If for example condition 3 is not fulfilled, the resulting mineralization is arsenide-dominated, which is typical of the native element-arsenide (five element) type of deposit (Bastin 1939; Kissin 1992; Markl et al. 2016; Scharrer et al. 2019). If condition 4 is not achieved, the result is a realgar-orpiment mineralization, such as the geothermal fields of Uzon, Russia (Migdisov and Bychkov 1998; Cleverley et al. 2003) or the As-mineralization at Saualp, Austria (Göd and Zemann 2000). If both Fe and sulfide are abundantly present, the resulting dominant As-mineral is arsenopyrite, which is common in most other As-bearing hydrothermal mineralizations.

The initial lack of native As stability during ore formation by a predominating stability of other As-bearing minerals does not exclude the late-stage formation of native As. A relative abundance of dissolved arsenic over dissolved Fe, Co, Ni, and S and their depletion during ore precipitation can lead to a saturation of native As. This explains the general late-stage occurrence of native As (e.g., Su et al. 2009; Zheng et al. 2015; Scharrer et al. 2019). This late-stage native As formation is further facilitated by lower temperatures.

If condition two (reduced environment) is not given, the mineralization is dominated by highly insoluble arsenate minerals. Such an environment is, for example, produced by weathering of native As-bearing mineralizations. The presence of native As and its highly reactive nature under oxidized conditions can act as a natural barrier for uranium (U^{+VI}) dissolved in groundwater where native arsenic becomes oxidized to arsenate and forms various different uranyl arsenates, depending on the availability of metals such as Pb, Cu, or Ba. The insoluble nature of these uranyl arsenates enables them to form at even low uranium concentrations (~1 μg/kg) as are typical of the granitic aquifers of the region (Käß and Käß 2008; Göb et al. 2013). This shows that native As-rich mineralizations can act as a natural trap for U from groundwater.

Acknowledgments and Funding

We thankfully acknowledge Manfred Martin and the Landesamt für Geologie, Rohstoffe und Bergbau (LRGB) for providing unique and historic samples from the Geological Survey of Baden-Württemberg. Furthermore, we thank Tatjana Epp and Thomas Wenzel for beneficial feedback on textural and genetic interpretations. An anonymous reviewer and associate editor Thomas Mueller are thanked for constructive feedback. Moreover, we thank Simone Schafflick and Per Jeiseke for sample preparation. A significant part of this research was achieved due to the DFG grant MA 2135/25-1.

References cited

Aiuppa, A., D'Alessandro, W., Federico, C., Palumbo, B., and Valenza, M. (2003) The aquatic geochemistry of arsenic in volcanic groundwaters from southern Italy. Applied Geochemistry, 18(9), 1283–1296.

Amend, J.P., Saltikov, C., Lu, G.-S., and Hernandez, J. (2014) Microbial arsenic metabolism and reaction energetics. Reviews in Mineralogy and Geochemistry, 79(1), 391–433.

An, F., and Zhu, Y. (2009) Significance of native arsenic in the Baogutu gold deposit, western Junggar, Xinjiang, NW China. Chinese Science Bulletin, 54(10), 1744.

Andreev, P., and Chumachenko, A. (1964) Reduction of uranium by natural organic substances. Geochemistry International, 1, 3–7.

Arehart, G.B., Chryssoulis, S.L., and Kesler, S.E. (1993) Gold and arsenic in iron sulfides from sediment-hosted disseminated gold deposits; implications for depositional processes. Economic Geology, 88(1), 171–185.

Bailly, L., Milesi, J.-P., Leroyb, J., and Marcouxa, E. (1998) The Au-Cu-Zn-Sb epithermal mineralisations of the Baia Mare district (North Romania): new mineralogical and microthermometric results. Comptes Rendus de l'Académie des Sciences-Series IIA-Earth and Planetary Science, 327(6), 385–390.

Ballantyne, J.M., and Moore, J.N. (1988) Arsenic geochemistry in geothermal systems. Geochimica et Cosmochimica Acta, 52(2), 475–483.

Barrie, C.D., Boyce, A.J., Boyle, A.P., Williams, P.J., Blake, K., Wilkinson, J.J., Lowther, M., McDermott, P., and Prior, D.J. (2009) On the growth of colloform textures: a case study of sphalerite from the Galmoy ore body, Ireland. Journal of the Geological Society, 166(3), 563–582.

Barton, P.B. (1956) Fixation of uranium in the oxidized base metal ores of the Goodsprings district, Clark County, Nevada. Economic Geology, 51(2), 178–191.

Bastin, E.S. (1939) The nickel-cobalt-native silver ore type. Economic Geology, 34(1), 40–79.

Bethke, C.M. (2007) Geochemical and Biogeochemical Reaction Modelling, 564 p. Cambridge University Press.

Bliedtner, M., and Martin, M. (1986) Erz-und Minerallagerstätten des mittleren Schwarzwaldes. Geol. Landesamt Baden-Württemberg.

Boitsov, V., and Kaikova, T. (1965) Uranium and arsenic in the hydrothermal process. Soviet Atomic Energy, 18(4), 473–479.

Bowell, R.J., and Craw, D. (2014) The management of arsenic in the mining industry. Reviews in Mineralogy and Geochemistry, 79(1), 507–532.

Bowell, R.J., Alpers, C.N., Jamieson, H.E., Nordstrom, D.K., and Majzlan, J. (2014) The environmental geochemistry of arsenic: an overview. Reviews in Mineralogy and Geochemistry, 79(1), 1–16.

Burisch, M., Walter, B.F., Wälle, M., and Markl, G. (2016) Tracing fluid migration pathways in the root zone below unconformity-related hydrothermal veins: Insights from trace element systematics of individual fluid inclusions. Chemical Geology, 429, 44–60.

Burisch, M., Gerdes, A., Walter, B.F., Neumann, U., Fettel, M., and Markl, G. (2017a) Methane and the origin of five-element veins: Mineralogy, age, fluid inclusion chemistry and ore forming processes in the Odenwald, SW Germany. Ore Geology Reviews, 81, 42–60.

Burisch, M., Walter, B.F., Gerdes, A., Lanz, M., and Markl, G. (2017b) Late-stage anhydrite-gypsum-siderite-dolomite-calcite assemblages record the transition from a deep to a shallow hydrothermal system in the Schwarzwald mining district, SW Germany. Geochimica et Cosmochimica Acta, 223, 259–278.

Burisch, M., Walter, B.F., and Markl, G. (2017c) Silicification of hydrothermal

gangue minerals in Pb-Zn-Cu-fluorite-quartz-baryte veins. Canadian Mineralogist, 55(3), 501–514.
Cerny, P., and Harris, D. (1978) The Tanco pegmatite at Bernic Lake, Manitoba; XI, Native elements, alloys, sulfides and sulfosalts. Canadian Mineralogist, 16(4), 625–640.
Cleverley, J.S., Benning, L.G., and Mountain, B.W. (2003) Reaction path modelling in the As–S system: a case study for geothermal As transport. Applied Geochemistry, 18(9), 1325–1345.
Cook, N.J. (1996) Mineralogy of the sulphide deposits at Sulitjelma, northern Norway. Ore Geology Reviews, 11(5), 303–338.
Criaud, A., and Fouillac, C. (1989) The distribution of arsenic (III) and arsenic (V) in geothermal waters: Examples from the Massif Central of France, the Island of Dominica in the Leeward Islands of the Caribbean, the Valles Caldera of New Mexico, USA, and southwest Bulgaria. Chemical Geology, 76(3-4), 259–269.
Dahlkamp, F.J. (2009) Uranium deposits of the world. Springer Science & Business Media.
——— (2013) Uranium Ore Deposits, 460 p. Springer.
Drahota, P., and Filippi, M. (2009) Secondary arsenic minerals in the environment: a review. Environment International, 35(8), 1243–1255.
Dudas, M. (1987) Accumulation of native arsenic in acid sulphate soils in Alberta. Canadian Journal of Soil Science, 67(2), 317–331.
Epp, T., Walter, B., Scharrer, M., Lehmann, G., Henze, K., Heimgärtner, C., Bach, W., and Markl, G. (2018) Quartz veins with associated Sb-Pb-Ag±Au mineralization in the Schwarzwald, SW Germany: a record of metamorphic cooling, tectonic rifting, and element remobilization processes in the Variscan belt. Mineralium Deposita, 1–26.
Essarraj, S., Boiron, M.-C., Cathelineau, M., Banks, D.A., and Benharref, M. (2005) Penetration of surface-evaporated brines into the Proterozoic basement and deposition of Co and Ag at Bou Azzer (Morocco): Evidence from fluid inclusions. Journal of African Earth Sciences, 41(1), 25–39.
Finch, R., and Ewing, R. (1991) Alteration of natural UO_2 under oxidizing conditions from Shinkolobwe, Katanga, Zaire: A natural analogue for the corrosion of spent fuel. Radiochimica Acta, 52(2), 395–402.
Fusswinkel, T., Wagner, T., Wenzel, T., Wälle, M., and Lorenz, J. (2014) Red bed and basement sourced fluids recorded in hydrothermal Mn–Fe–As veins, Sailauf (Germany): A LA-ICPMS fluid inclusion study. Chemical Geology, 363, 22–39.
Geyer, O.F., Gwinner, M.P., Geyer, M., Nitsch, E., and Simon, T. (2011) Geologie von Baden-Württemberg. Schweizerbart.
Glaskova, O., Azaroual, M., and Piantone, P. (1999) Arsenic behaviour in subsurface hydrogeochemical systems (a critical review of thermodynamic data for minerals and aqueous species of arsenic). BRGM report number R 40629; 43 pages.
Göb, S., Loges, A., Nolde, N., Bau, M., Jacob, D.E., and Markl, G. (2013) Major and trace element compositions (including REE) of mineral, thermal, mine and surface waters in SW Germany and implications for water–rock interaction. Applied Geochemistry, 33, 127–152.
Göd, R., and Zemann, J. (2000) Native arsenic–realgar mineralization in marbles from Saualpe, Carinthia, Austria. Mineralogy and Petrology, 70(1-2), 37–53.
Goldstein, H., and Reynolds, T. (1994) Systematics of fluid inclusions in diagenetic minerals. SEPM short course, 31, 199.
Gorman-Lewis, D., Burns, P.C., and Fein, J.B. (2008) Review of uranyl mineral solubility measurements. The Journal of Chemical Thermodynamics, 40(3), 335–352.
Grancea, L., Bailly, L., Leroy, J., Banks, D., Marcoux, E., Milési, J., Cuney, M., André, A., Istvan, D., and Fabre, C. (2002) Fluid evolution in the Baia Mare epithermal gold/polymetallic district, Inner Carpathians, Romania. Mineralium Deposita, 37(6-7), 630–647.
Hanor, J.S. (1996) Controls on the solubilization of lead and zinc in basinal brines. Carbonate-hosted Lead–Zinc Deposits, SEG Special Publication, 4, 483–500.
Hayashi, K., Sugaki, A., and Kitakaze, A. (1990) Solubility of sphalerite in aqueous sulfide solutions at temperatures between 25 and 240 °C. Geochimica et Cosmochimica Acta, 54(3), 715–725.
Hiller, A., and Schuppan, W. (2008) Geologie und Uranbergbau im Revier Schlema-Alberoda. Bergbau in Sachsen, 14, 200. Landesamt für Umwelt, Landwirtschaft und Geologie.
Hofmann, B. (1989) Genese, Alteration und rezentes Fliess-System der Uranlagerstätte Krunkelbach (Menzenschwand, Südschwarzwald), Ph.D. thesis, 195. Universität Bern.
Hofmann, B., and Knill, M. (1996) Geochemistry and genesis of the Lengenbach Pb-Zn-As-Tl-Ba-mineralisation, Binn Valley, Switzerland. Mineralium Deposita, 31(4), 319–339.
Horton, T.W., Becker, J., Craw, D., Koons, P., and Chamberlain, C.P. (2001) Hydrothermal arsenic enrichment in an active mountain belt: Southern Alps, New Zealand. Chemical Geology, 177(3-4), 323–339.
Hösel, G. (2003) Die polymetallische Skarnlagerstätte Pöhla-Globenstein. Bergbau in Sachsen, 8, 147. Landesamt für Umwelt, Landwirtschaft und Geologie.
Johnson, D.L. (1971) Simultaneous determination of arsenate and phosphate in natural waters. Environmental Science & Technology, 5(5), 411–414.
Jørgensen, B.B., Isaksen, M.F., and Jannasch, H.W. (1992) Bacterial sulfate reduction above 100 C in deep-sea hydrothermal vent sediments. Science, 258, 1756–1757.
Kaiser, H. (1983) Die Mineralien der Grube Michael, Weiler bei Lahr, Schwarzwald. Lapis, 8(12).
Käß, W., and Käß, H. (2008) Deutsches Bäderbuch [Manual of spa therapy and german spas]. Schweizerbart.
Keller, N.S., Stefánsson, A., and Sigfússon, B. (2014) Arsenic speciation in natural sulfidic geothermal waters. Geochimica et Cosmochimica Acta, 142, 15–26.
Kelley, K., Leach, D., Johnson, C., Clark, J., Fayek, M., Slack, J., Anderson, V., Ayuso, R., and Ridley, W. (2004) Textural, compositional, and sulfur isotope variations of sulfide minerals in the Red Dog Zn-Pb-Ag deposits, Brooks Range, Alaska: Implications for ore formation. Economic Geology, 99(7), 1509–1532.
Kesler, S.E., Fortuna, J., Ye, Z., Alt, J.C., Core, D.P., Zohar, P., Borhauer, J., and Chryssoulis, S.L. (2003) Evaluation of the role of sulfidation in deposition of gold, Screamer section of the Betze-Post Carlin-type deposit, Nevada. Economic Geology, 98(6), 1137–1157.
Kirchheimer, F. (1957) Bericht über das Vorkommen von Uran in Baden-Württemberg. Kommissionsverlag von Herder.
Kissin, S.A. (1992) Five-element (Ni-Co-As-Ag-Bi) veins. Geoscience Canada, 19(3), 113–124.
Krahé, L. (2012) Geochemische und mineralogische Untersuchungen am Erzgang Michaelgang bei Lahr. Thesis. Albert-Ludwigs-Universität Freiburg.
Kreissl, S. (2018) Alpine five element veins: reconstruction of a 225 Ma multi-stage Bi-Co-Ni-Fe-As-S system in the Penninic Alps, Switzerland—unraveling compositional, mineralogical and genetic features of five element veins. Petrology and Mineral Resources, Thesis. Eberhard Karls University, Tübingen, Germany.
Langmuir, D. (1978) Uranium solution-mineral equilibria at low temperatures with applications to sedimentary ore deposits. Geochimica et Cosmochimica Acta, 42(6), 547–569.
Majzlan, J., Drahota, P., and Filippi, M. (2014) Parageneses and crystal chemistry of arsenic minerals. Reviews in Mineralogy and Geochemistry, 79(1), 17–184.
Malinin, S., and Khitarov, N. (1969) Reduction of sulfate sulfur by hydrogen under hydrothermal conditions. Geochemistry International Ussr, 6(6), 1022–1027.
Mandal, B.K., and Suzuki, K.T. (2002) Arsenic round the world: a review. Talanta, 58(1), 201–235.
Markl, G. (2015) Schwarzwald, Vol. 1, Nordschwarzwald and Grube Clara, 672 p. Bode Verlag.
—— (2017) Schwarzwald, Vol. 3, Mittlerer Schwarzwald Teil 2. 640 p.
Markl, G., Burisch, M., and Neumann, U. (2016) Natural fracking and the genesis of five-element veins. Mineralium Deposita, 51(6), 703–712.
Martin, M. (2009) Geogene Grundgehalte (Hintergrundwerte) in den petrogeochemischen Einheiten von Baden-Württemberg. Informationen, 98. Landesamt für Geologie, Rohstoffe und Bergbau, Freiburg.
McKinstry, H. (1963) Mineral assemblages in sulfide ores; the system Cu-Fe-As-S. Economic Geology, 58(4), 483–505.
Metz, R., and Richter, M. (1957) Die Blei-Zink-Erzgänge des Schwarzwaldes. 153 p. Amt für Bodenforschung, Hannover.
Migdisov, A.A., and Bychkov, A.Y. (1998) The behaviour of metals and sulphur during the formation of hydrothermal mercury–antimony–arsenic mineralization, Uzon caldera, Kamchatka, Russia. Journal of Volcanology and Geothermal Research, 84(1-2), 153–171.
Mitchell, V.L. (2014) Health risks associated with chronic exposures to arsenic in the environment. Reviews in Mineralogy and Geochemistry, 79(1), 435–449.
Muir, T. (1997) Hemlo Gold Deposit Area. Ontario Geological Survey Report, 289, 219.
Murzin, V., Naumov, E., Azovskova, O., Varlamov, D., Rovnushkin, M.Y., and Pirajno, F. (2017) The Vorontsovskoe Au-Hg-As ore deposit (Northern Urals, Russia): Geological setting, ore mineralogy, geochemistry, geochronology and genetic model. Ore Geology Reviews, 85, 271–298.
Noble, J.A. (1950) Ore mineralization in the Homestake gold mine, Lead, South Dakota. Geological Society of America Bulletin, 61(3), 221–252.
Nokleberg, W.J. (2005) Metallogenesis and tectonics of the Russian far east, Alaska, and the Canadian cordillera. U.S. Geological Survey Professional Paper 1697, 429.
Nordstrom, D.K. (2002) Worldwide occurrences of arsenic in ground water. Science, 296, 2143–2145.
Nordstrom, D.K., and Young, C. (2000) Thermodynamic properties of environmental arsenic species: Limitations and needs. Minor Elements, 325–331.
Nordstrom, D.K., Majzlan, J., and Königsberger, E. (2014) Thermodynamic properties for arsenic minerals and aqueous species. Reviews in Mineralogy and Geochemistry, 79(1), 217–255.
Ohmoto, H., and Lasaga, A.C. (1982) Kinetics of reactions between aqueous sulfates and sulfides in hydrothermal systems. Geochimica et Cosmochimica Acta, 46(10), 1727–1745.
Ondrus, P., Veselovsky, F., Gabasova, A., Hlousek, J., Srein, V., Vavrin, I., Skala, R., Sejkora, J., and Drabek, M. (2003) Primary minerals of the Jáchymov ore district. Journal of GEOsciences, 48(3-4), 19–146.
Pekov, I.V., Levitskiy, V.V., and Krivovichev, V.G. (2010) Mineralogy of the Belorechenskoye deposit (Northern Caucasus, Russia). Mineralogical Almanac, 15(2), 1–96.

Peters, S.C., Blum, J.D., Karagas, M.R., Chamberlain, C.P., and Sjostrom, D.J. (2006) Sources and exposure of the New Hampshire population to arsenic in public and private drinking water supplies. Chemical Geology, 228(1-3), 72–84.
Pfaff, K., Koenig, A., Wenzel, T., Ridley, I., Hildebrandt, L.H., Leach, D.L., and Markl, G. (2011) Trace and minor element variations and sulfur isotopes in crystalline and colloform ZnS: Incorporation mechanisms and implications for their genesis. Chemical Geology, 286(3-4), 118–134.
Pfaff, K., Romer, R.L., and Markl, G. (2009) U-Pb ages of ferberite, chalcedony, agate,'U-mica'and pitchblende: constraints on the mineralization history of the Schwarzwald ore district. European Journal of Mineralogy, 21(4), 817–836.
Pieczka, A. (2010) Primary Nb-Ta minerals in the Szklary pegmatite, Poland: New insights into controls of crystal chemistry and crystallization sequences. American Mineralogist, 95, 1478–1492.
Pierce, M.L., and Moore, C.B. (1982) Adsorption of arsenite and arsenate on amorphous iron hydroxide. Water Research, 16(7), 1247–1253.
Pokrovski, G.S., Borisova, A.Y., and Bychkov, A.Y. (2013) Speciation and transport of metals and metalloids in geological vapors. Reviews in Mineralogy and Geochemistry, 76(1), 165–218.
Powell, W.G., and Pattison, D.R. (1997) An exsolution origin for low-temperature sulfides at the Hemlo gold deposit, Ontario, Canada. Economic Geology, 92(5), 569–577.
Price, R.E., and Pichler, T. (2005) Distribution, speciation and bioavailability of arsenic in a shallow-water submarine hydrothermal system, Tutum Bay, Ambitle Island, PNG. Chemical Geology, 224(1-3), 122–135.
Radosavljević, S.A., Stojanović, J.N., Radosavljević-Mihajlović, A.S., and Vuković, N.S. (2014) Rujevac Sb-Pb-Zn-As polymetallic deposit, Boranja orefield, Western Serbia: native arsenic and arsenic mineralization. Mineralogy and Petrology, 108(1), 111–122.
Reuss, E. (1863) Über die Paragenese der auf den Erzgängen von Příbram einbrechenden Mineralien. Neues Jahrbuch für Mineralogie(65), 13–103.
Robinson, B., and Ohmoto, H. (1973) Mineralogy, fluid inclusions, and stable isotopes of the Echo Bay U-Ni-Ag-Cu deposits, Northwest Territories, Canada. Economic Geology, 68(5), 635–656.
Rye, R.O., and Ohmoto, H. (1974) Sulfur and carbon isotopes and ore genesis: a review. Economic Geology, 69(6), 826–842.
Sakai, H. (1968) Isotopic properties of sulfur compounds in hydrothermal processes. Geochemical Journal, 2(1), 29–49.
Sanjuan, B., Millot, R., Dezayes, C., and Brach, M. (2010) Main characteristics of the deep geothermal brine (5 km) at Soultz-sous-Forêts (France) determined using geochemical and tracer test data. Comptes Rendus Geoscience, 342(7-8), 546–559.
Scharrer, M., Kreissl, S., and Markl, G. (2019) The mineralogical variability of hydrothermal native element-arsenide (five-element) associations and the role of physicochemical and kinetic factors concerning sulfur and arsenic. Ore Geology Reviews, 113, 103025.
Schürenberg, H. (1950) Die Erzgänge Teufelsgrund und Schindler im Untermünstertal und ihr quantitativer Mineralgehalt. Neues Jahrbuch für Mineralogie-Abhandlungen, 81, 123–182.
Schwinn, G., Wagner, T., Baatartsogt, B., and Markl, G. (2006) Quantification of mixing processes in ore-forming hydrothermal systems by combination of stable isotope and fluid inclusion analyses. Geochimica et Cosmochimica Acta, 70(4), 965–982.
Seal, R.R. (2006) Sulfur isotope geochemistry of sulfide minerals. Reviews in Mineralogy and Geochemistry, 61(1), 633–677.
Sergeyeva, E., and Khodakovskiy, I. (1969) Physicochemical conditions of formation of native arsenic in hydrothermal deposits. Geokhimiya, 7, 846–859.
Sharp, J.O., Lezama-Pacheco, J.S., Schofield, E.J., Junier, P., Ulrich, K.-U., Chinni, S., Veeramani, H., Margot-Roquier, C., Webb, S.M., and Tebo, B.M. (2011) Uranium speciation and stability after reductive immobilization in aquifer sediments. Geochimica et Cosmochimica Acta, 75(21), 6497–6510.
Shcherbina, V.V. (1978) Chemical reactions in natural sulfide systems. Geokhimiya, 9, 1283–1291.
Staude, S., Bons, P.D., and Markl, G. (2009) Hydrothermal vein formation by extension-driven dewatering of the middle crust: An example from SW Germany. Earth and Planetary Science Letters, 286(3-4), 387–395.
Staude, S., Werner, W., Mordhorst, T., Wemmer, K., Jacob, D.E., and Markl, G. (2012) Multi-stage Ag–Bi–Co–Ni–U and Cu–Bi vein mineralization at Wittichen, Schwarzwald, SW Germany: geological setting, ore mineralogy, and fluid evolution. Mineralium Deposita, 47(3), 251–276.
Su, W., Heinrich, C.A., Pettke, T., Zhang, X., Hu, R., and Xia, B. (2009) Sediment-hosted gold deposits in Guizhou, China: products of wall-rock sulfidation by deep crustal fluids. Economic Geology, 104(1), 73–93.
Taylor, C.M., and Radtke, A.S. (1969) Micromineralogy of silver-bearing sphalerite from Flat river, Missouri. Economic Geology, 64(3), 306–318.
Tomkins, A.G., Pattison, D.R., and Zaleski, E. (2004) The Hemlo gold deposit, Ontario: An example of melting and mobilization of a precious metal-sulfosalt assemblage during amphibolite facies metamorphism and deformation. Economic Geology, 99(6), 1063–1084.
Vochten, R., and Goeminne, A. (1984) Synthesis, crystallographic data, solubility and electrokinetic properties of meta-zeunerite, meta-kirchheimerite and nickel-uranylarsenate. Physics and Chemistry of Minerals, 11(2), 95–100.
Vokes, F.M. (1963) Geological studies on the Caledonian pyritic zinc-lead orebody at Bleikvassli, Norland, Norway. Universitetsforlaget.
Voudouris, P., Melfos, V., Spry, P., Bonsall, T., Tarkian, M., and Economou-Eliopoulos, M. (2008) Mineralogical and fluid inclusion constraints on the evolution of the Plaka intrusion-related ore system, Lavrion, Greece. Mineralogy and Petrology, 93(1-2), 79–110.
Walenta, K., and Wimmenauer, W. (1961) Der Mineralbestand des Michaelganges im Weiler bei Lahr (Schwarzwald). Jahreshefte des Geologischen Landesamts in Baden-Wuerttemberg, 4, 7–37.
Walter, B.F., Burisch, M., and Markl, G. (2016) Long-term chemical evolution and modification of continental basement brines–a field study from the Schwarzwald, SW Germany. Geofluids, 16(3), 604–623.
Walter, B.F., Burisch, M., Marks, M.A., and Markl, G. (2017) Major element compositions of fluid inclusions from hydrothermal vein-type deposits record eroded sedimentary units in the Schwarzwald district, SW Germany. Mineralium Deposita, 52(8), 1191–1204.
Walter, B.F., Burisch, M., Fusswinkel, T., Marks, M.A., Steele-MacInnis, M., Wälle, M., Apukhtina, O.B., and Markl, G. (2018) Multi-reservoir fluid mixing processes in rift-related hydrothermal veins, Schwarzwald, SW-Germany. Journal of Geochemical Exploration, 186, 158–186.
Wilkinson, J.J., Eyre, S.L., and Boyce, A.J. (2005) Ore-forming processes in Irish-type carbonate-hosted Zn-Pb deposits: Evidence from mineralogy, chemistry, and isotopic composition of sulfides at the Lisheen Mine. Economic Geology, 100(1), 63–86.
Woitsekhowskaya, M., and Peters, S. (1998) Geochemical modeling of alteration and gold deposition in the Betze deposit, Eureka County, Nevada. Contributions to the gold metallogeny of northern Nevada. US Geological Survey Open-File Report 98, 211–222.
Wu, Y., Zhou, X.-y., Lei, M., Yang, J., Ma, J., Qiao, P.-w., and Chen, T.-b. (2017) Migration and transformation of arsenic: contamination control and remediation in realgar mining areas. Applied Geochemistry, 77, 44–51.
Zheng, B., Zhu, Y., An, F., Huang, Q.-y., and Qiu, T. (2015) As–Sb–Bi–Au mineralization in the Baogutu gold deposit, Xinjiang, NW China. Ore Geology Reviews, 69, 17–32.
Zhu, Y., An, F., and Tan, J. (2011) Geochemistry of hydrothermal gold deposits: a review. Geoscience Frontiers, 2(3), 367–374.

Manuscript received March 21, 2019
Manuscript accepted November 24, 2019
Manuscript handled by Thomas Mueller

Endnote:

[1]Deposit item AM-20-57062, Supplemental Material. Deposit items are free to all readers and found on the MSA website, via the specific issue's Table of Contents (go to http://www.minsocam.org/MSA/AmMin/TOC/2020/May2020_data/May2020_data.html).

Appendix VII

Accepted publication

Study 7

Scharrer, M., Kreissl, S., & Markl, G. (2019). The mineralogical variability of hydrothermal native element-arsenide (five-element) associations and the role of physicochemical and kinetic factors concerning sulfur and arsenic. Ore Geology Reviews, 113, 103025.

Ore Geology Reviews 113 (2019) 103025

Contents lists available at ScienceDirect

Ore Geology Reviews

journal homepage: www.elsevier.com/locate/oregeorev

The mineralogical variability of hydrothermal native element-arsenide (five-element) associations and the role of physicochemical and kinetic factors concerning sulfur and arsenic

Manuel Scharrer[a,*], Stefan Kreissl[b,*], Gregor Markl[a]

[a] Eberhard Karls University, Faculty of Science, Department of Geosciences, Petrology and Mineral Resources, Wilhelmstraße 56, 72074 Tübingen, Germany
[b] Aalen University of Applied Sciences, Beethovenstraße 1, 73430 Aalen, Germany

ARTICLE INFO

Keywords:
Arsenides
Stability diagrams
Five-element mineralization
Reduction
Sulfate-sulfide kinetics
Dendritic/skeletal growth

ABSTRACT

The hydrothermal native element-arsenide mineralization comprises Ni-, Co-, and Fe-arsenides and -sulfarsenides, which typically form characteristic overgrowth textures on skeletal native silver and/or bismuth aggregates. Native arsenic, native antimony, antimony-arsenic-silver alloys, and uraninite are present in some of these deposits. Famous deposits of this type include Cobalt, Ontario; Bou Azzer, Morocco; Kongsberg, Norway; Jáchymov, Czech Republic; and Schneeberg, Germany. As the physico-chemical conditions of formation (e.g., p, T, fluid composition) and the host rocks are variable, the only unifying feature for their crystallization is a geologically fast reduction process of a Ni-, Co-, Fe-, As bearing fluid e.g., by methane, graphite or Fe^{2+}-bearing minerals. The present contribution combines a comprehensive literature review with novel calculated stability relations of native elements (Ag, Bi, As), Ni-, Co- and Fe-mono-, di- and sulfarsenides, and sulfides/sulfosalts to understand the details of this formation mechanism and to explain the mineralogical and textural diversity observed in five-element assemblages.

The characteristic sequence of Ni- → Co- → Fe-diarsenides is ubiquitous and can be explained by continuous reduction of an arsenic- and metal-bearing aqueous solution. This unique succession is largely independent of the metal ratios in the fluid, as three orders of magnitude differences between Fe, Co, and Ni concentrations are needed to change this sequence at neutral pH. At more basic conditions, the diarsenide sequence changes to Co → Ni → Fe, which has been observed at only two localities (Valais and Pirineos). Also, the prevalence of mono- vs. diarsenides is mainly pH-dependent. Furthermore, differences in reduction agent, initial pH, fluid/rock ratio, and the crystallization in contained microenvironments all produce visible differences in mineralogy and/or textures that record the details of the formation processes. The stability of dissolved sulfide plays a crucial role in five-element mineralogy, as Co- and Fe-arsenides would not form in the presence of appreciable amounts of sulfide. The absence of large quantities of sulfide in the arsenide stage can be attributed to a lack of sulfur or a thermodynamic disequilibrium between sulfate and sulfide; both cases occur in nature. While the fluid prior to reduction must have been oxidized, slow reaction kinetics for the sulfate-sulfide compared to the arsenite/arsenate-arsenide conversion favor the formation of arsenides and native metals. Their formation is, hence, kinetically controlled, which is supported by the commonly skeletal textures. Sulfarsenides and/or sulfides of Co, Ni, Fe, Pb, and Cu appear only late in the five-element assemblages, when sulfide reduction progresses, and the system re-attains thermodynamic equilibrium or sufficient influx of sulfide has occurred.

1. Introduction

Hydrothermal ore deposits dominated by Ni-Co-arsenides ± native elements have been called “five-element vein type”, “five element association”, “nickel-cobalt-native silver ore type”, “Bi-Co-Ni-As-U-Ag-Formation”, and “Ag-Co-Ni-As-Bi type” (e.g., Müller, 1860, Bastin, 1939, Kissin, 1988, 1992, Baumann et al., 2000, Markl et al., 2016). The name “five-element veins” was originally proposed by Halls and Stumpfl (1972), who mainly focused on the occurrence of Ni, Co, As, Ag, and Bi and who, for the first time, compiled the various hypotheses on the genesis of this type of deposit, which were then modified or augmented later on. This mineralization type is of hydrothermal origin,

* Corresponding authors.
E-mail addresses: manuel.scharrer@uni-tuebingen.de (M. Scharrer), stefan.kreissl@uni-tuebingen.de (S. Kreissl), markl@uni-tuebingen.de (G. Markl).

https://doi.org/10.1016/j.oregeorev.2019.103025
Received 22 November 2018; Received in revised form 13 June 2019; Accepted 18 July 2019
Available online 20 July 2019

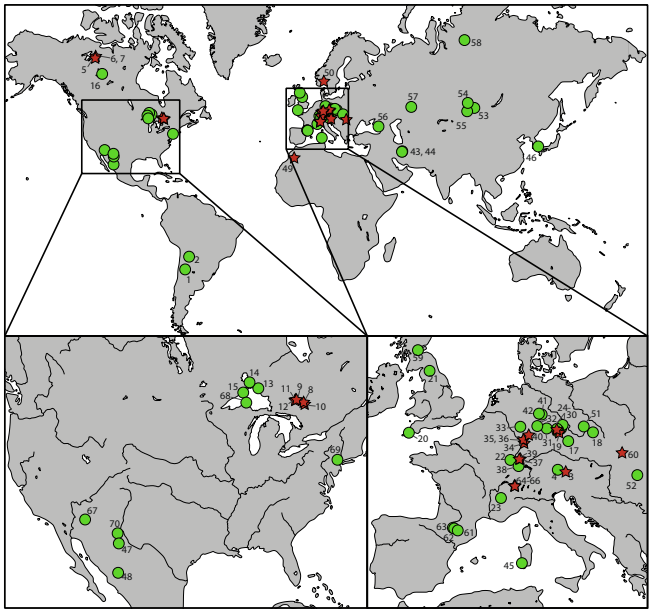

Fig. 1. Native element-arsenide (five-element) assemblage occurrences. World map with magnification of North America and Europe, due to the abundance of arsenide occurrences there. The numbers correlate the occurrences listed in Table 1. All listed localities are used to produce the compilation presented in Fig. 2, whereas the stars indicate those, that are presented in Fig. 3a–c. The map is a modified version of the OpenStreetMap generalized dataset.

generally occur as veins but can also be stratabound and/or replace the host rock, and ore-rich sections generally occur in the form of ore shoots. Their characteristic textural association and mineralogical succession with variable elemental content can be found in ore deposits scattered all over the world and found in various types of geological settings and host rocks (Fig. 1, Table 1 and references therein). The mineralogy and mineralogical sequence seems not to correlate with the host rock or geological setting. Furthermore, these deposits have been and in parts still are of economic importance (Table 2), which varies between deposits and has been strongly variable over time for individual deposits (Bastin, 1939). The abundant occurrences in the Erzgebirge, for example, were rich silver deposits since medieval times, were exploited for Co in the 16th to 18th century, but were exclusively mined for uranium after 1950, even though thousands of tonnes of Co, Ni, and Ag could have been extracted (Runge and Wolf, 2010).

Although the name “five-element veins” implies a certain restriction on the number of elements involved, that is not actually the case, and this type of ore should better be termed “Ni-Co-Fe-arsenide type” or “native element-arsenide mineralization”, as it invariably contains hydrothermal Ni-, Co-, and Fe-arsenides and/or sulfarsenides together with variable quantities of native elements such as silver, bismuth, arsenic, antimony, metal alloys (such as dyscrasite, allargentum, or allemontite), and in rare cases gold as well as uraninite and Cu arsenides (Table 1 and references therein). In addition, antimonides occur in a few of the deposits, such as St. Andreasberg/central Germany or the Wenzel mine in SW Germany (Schnorrer-Köhler, 1983, Staude et al., 2007). The relative abundance and occurrence of the native elements, uranium- and Cu-arsenides, as well as the arsenide/sulfarsenide ratio varies strongly between localities and one can distinguish Ag-, Bi-, Sb-, As-, S-, and/or Cu-dominated subtypes (see Table 1).

This native element-arsenide mineralization represents an intermediate stage within a hydrothermal polymetallic multistage sequence, where the native element-arsenide stage succeeds earlier oxide (e.g., uraninite) and/or minor sulfide-bearing quartz stages and is succeeded by a later sulfide-rich and commonly carbonate-dominated stage (e.g., Kissin, 1992). The native element-arsenide mineralization stage is characterized by dendritic native elements, alloys and/or niccolite overgrown by a succession of arsenides and sulfarsenides (e.g., Kissin, 1992, Markl et al., 2016). For some localities, a general arsenide succession from Ni → Co → Fe, a transition from mono- → di- → triarsenide, and a transition from arsenides to sulfarsenides has been observed (e.g., Ondrus et al., 2003a, Markl et al., 2016, Burisch et al., 2017). This general arsenide to sulfarsenide transition in combination with the unambiguous presence of a subsequent sulfide dominated ore stage (e.g. Markl et al., 2016) indicates a gradual importance of sulfide during the successive development of this mineralization, which has not yet been investigated in detail.

1.1. Metal provenance and formation mechanism

Due to the long-lasting and intensive research of native element-arsenide assemblages worldwide, several theories about their formation have been proposed. The fluid origin and metal provenance has been speculated to be:

(i) introduction of juvenile solutions from the crust-mantle boundary (Halls and Stumpfl, 1972);
(ii) hydrothermal exolution from magmatic intrusions (e.g. Bastin, 1939, Sampson and Hriskevich, 1957, Jambor, 1971a);
(iii) connate brine circulation in continental rifts (Kissin, 1988);
(iv) leaching (reaction) of the basement by sedimentary halite-saturated brines (e.g. Boyle and Dass, 1971, Kerrich et al., 1986, Smyk and Watkinson, 1990, Essarraj et al., 2005, Kreissl et al., 2018);

while ore and gangue precipitation was attributed to:

(i) dilution and cooling through mixing of hyper-saline brines with meteoric water (Kissin, 1993, Marshall et al., 1993, Marshall and Watkinson, 2000, Essarraj et al., 2005);
(ii) a single process of successive increase in CO_2 partial pressure in combination with host rock leaching which produces the carbonates during reducing and sulfide free conditions that favor arsenide precipitation, which are possibly produced by reducing agents such as hydrocarbons, graphite, hydrogen or sulfide (Naumov et al., 1971a);
(iii) fluid reduction by oxidation of Fe^{2+}-bearing minerals to precipitate precious metals and changes in pressure and temperature with subsequent back-oxidation (e.g., by Fe^{3+} or $UO_2{}^{2+}$ influx) to produce the Ni-Co-Fe-arsenide sequence (Ondrus et al., 2003a);
(iv) simple and continuous fluid reduction by reaction with ferrous (Fe^{2+}) minerals to precipitate the precious metals and Ni-Co-Fe-arsenide sequence (Robinson and Ohmoto, 1973, Kreissl et al., 2018);
(v) progressive fluid reduction by sulfides and/or organic carbon to precipitate the succession of the uraninite-, arsenide-native element- and the sulfide assemblage (Kissin, 1993).
(vi) Markl et al. (2016) quantified the process of reduction and exclusively relate these types of ores and their specific textures to reduction, and the sequence of the Ni-Co-Fe-arsenides to subsequent host rock pH re-equilibration,
(vii) and Burisch et al. (2017) developed this process further and proposes that the native element-arsenide mineralization forms by influx of hydrocarbons (e.g. methane) into a simple fluid mixing scenario that would otherwise form base-metal sulfide veins.

The formation temperature of the arsenide stage varies greatly between localities (50–400 °C; e.g. Bouabdellah et al., 2016, Markl et al., 2016; and references in both), which indicates a principally temperature-independent mechanism of formation. This temperature range is based on fluid inclusion evidence, and not on the problematic applications of phase stabilities in dry, experimental sulfarsenide systems, as the latter results in unrealistically high temperatures (e.g., Misra and

Table 1
Localities of five-element assemblages with references.

	Country	Disrtrict	Sublocality	M-AsS/As/Sb	M-As_x	M-Sb_x	Other	Native el.	T °C	sal. wt%	Dominant Host Rock	Selected Literature
1	Argentinia	Cerro Negro		As	Ni, Co		Te	Ag, Au			shale	Schalamuk and Logan (1994)
2	Argentinia	Purísima-Rumicruz		As, AsS	Ni, Co		U				sandstone	López and Echeveste (2012)
3	Austria	Schladming, Eastern Alps	Zinkwand-Vötternbaue	As > AsS	Ni, Co, Fe			Bi			gneisses, sulfidic/graphitic phyllites, amphibolites	Paar and Chen (1979)
4	Austria	Leogang, Eastern Alps	Nöckelberg, Schwarzleo, Vogelhalt	As, AsS	Ni, Co			Ag-Hg			dolomites,schists	Buchrucker (1891), Haditsch and Mostler (1970)
5	Canada	Great Bear Lake	Camsell River	As > AsS	Ni, Co, Fe		U	Ag	120–480	18–33	intermediate- felsic volcanic rocks	Changkakoti et al. (1986), Robinson and Ohmoto (1973), Badham (1975)
6	Canada		Echo Bay									
7	Canada		Eldorado Mine									
8	Canada	Cobalt-Gowganda	Cobalt	As > AsS > Sb	Co > Ni, Fe			Ag, Bi	290–350	48	diabase sills, metasediments, volcanics, tholeiitic basalt, granite, lamprophyr,	Bastin (1949, 1950), Petruk (1968, 1971a,b), Sergiades (1968), Marshall et al. (1993),
9	Canada		Gowganda									
10	Canada		So. Lorraine									
11	Canada		Tyrrel-Knight area									
12	Canada		Shiningtree									
13	Canada	Thunder Bay district	Port Arthur-Fort William	As, AsS	Ni, Co, Fe > Cu			Ag-Hg	100–450	2–30	gabbro, sedimentary rocks,	Moore (1934), Sergiades (1968), Franklin et al. (1986), Kissin and Jennings (1987)
14	Canada		Silver Islet									
15	Canada		Thunder Bay									
16	Canada	Great Slave lake		As, AsS	Ni > Co > Fe		Mo	Ag, Bi			diorite, trachytic rocks	Badham (1978), Badham and Muda (1980)
17	Czech Republic	Příbram, Březové Hory	Černojamské	Sb, As	Ni, Co, Fe	Ni	U	Sb-Ag, As			sedimentary, volcanosedimentary and granitoid rocks	Reuss (1863), Kribek et al. (1999), Tvrdý and Vary (2003), Sejkora and Litochleb (2003)
18	Czech Republic	Zálesí		As, AsS	Ni, Co, Fe		U	Ag, Bi	80–130	0–27	gneiss and schist with locally marl, quarzites, amphibolites	Dolníček et al. (2009)
19	Czech Republic	Krušné hory	Jáchymov	As > AsS	Ni, Co, Fe		U	Ag, Bi	100–145	22–24	granites, shists, gneisses	Ondrus et al (2003a–c)
20	England	Cornwall	St Austell Consols	AsS	Ni, Co		U				granitic rocks	Merry and Weiß (2017)
21	England	Garrgill	Tynebottom Mine	As > AsS	Ni, Co, Fe			Ag			limestone	Ixer and Stanley (1987)
22	France	Vosges	Ste Marie-aux-Mines	As, AsS	Ni, Co,Fe			Ag			metasediments	Meyer and Hohl (1994)
23	France	Allemont, Western Alps	Chalanches	As, AsS	Ni, Co, Fe	Ni		Ag-Hg, Bi, Sb			basic volcanics, gabbro, gneiss	Clavel (1963), Ypma (1963,1972)

(*continued on next page*)

Table 1 (*continued*)

	Country	Disrtrict	Sublocality	M-AsS/As/Sb	M-As_x	M-Sb_x	Other	Native el.	T °C	sal. wt%	Dominant Host Rock	Selected Literature
24	Germany	Ore Mountains	Pöhla		Ni, Co		U	Ag, As				Hösel (2003)
25	Germany		Schlema-Alberoda	As	Ni, Co, Fe		U	Ag, Bi, As	90–160		diabase, schists, granite, carbonates	Hiller and Schuppan 2008
26	Germany		Annaberg	As, AsS	Ni, Co > Fe		U	Ag, Bi, As			graphite and pyrite rich paragneiss	Lahl (1992), Hofmann (1992), Baumann et al. (2000)
27	Germany		Freiberg	As, AsS	Ni, Co, Fe		U	Ag, Bi, As				Hofmann (1986)
28	Germany		Johanngeorgenstadt	As, AsS	Ni, Co, Fe			Bi				Bastin (1939)
29	Germany		Marienberg	As, AsS	Ni, Co > Fe		U	Ag, Bi, As				Seifert and Baumann (1994), Baumann et al. (2000)
30	Germany		Schneeberg	As > AsS	Ni, Co, Fe		U	Ag, Bi	90–150		schist, metabasite, granitic rocks	Lipp and Flach (2003) and ref. therein
31	Germany	Thuringian Forest	Kamsdorf	As	Ni, Co, Fe			Bi, As				Bastin (1939)
32	Germany		Schweina	As	Ni, Co, Fe							
33	Germany	Rhenish Massif	Nanzenbach	As, AsS	Ni, Co, Fe			Bi				
34	Germany	Odenwald	Mackenheim	As	Ni, Co, Fe			Bi	290	27	gneiss, amphibolite	Heimig (2015), Burisch et al. (2017)
35	Germany		Nieder-Beerbach					Ag, As			gabbro	
36	Germany		Nieder-Ramstadt					Ag			gabbro	
37	Germany	Schwarzwald	Wittichen	As > AsS	Ni, Co, Fe		U	Ag, Bi	50–150	25	granite	Staude et al. (2012), Markl (2016)
38	Germany		Urberg	As, AsS	Ni, Co		U	Ag, As			granite, gneiss	Otto (1964), Markl (2017)
39	Germany		Wenzel	Sb > As	Ni, Co, Fe	Sb		Ag-Sb	120–150	25–30	gneiss, amphibolites	Staude et al. (2007)
40	Germany	Spessart	Bieber	As > AsS	Ni, Co, Fe			Bi			silt-sandstone, dolomite, gneiss	Wagner and Lorenz (2002)
41	Germany	Harz	Mansfeld	As	Ni, Co, Fe							Bastin (1939)
42	Germany		St. Andreasberg		Ni, Co, Fe	Ni	Se	Ag, Sb, As			Metasediments, lamprophyre	Schnorrer-Köhler (1983)
43	Iran	Anārak	Talmessi, Gowd-e-Morad	As	Cu > Ni, Co		U		90–240	1–15	basaltic-trachyandesite, ultrapotassic rocks	Tarkian et al. (1983), Bagheri et al. (2007), Kuhanestani et al. (2014)
44	Iran		Meskani									
45	Italy	Sardinia	Rin Planu Is Castangias	As > Sb > AsS	Ni, Co, Fe	Ni		Bi				Naitza et al. (2013, 2015)
46	South Korea	Ulsan Mine		As, AsS	Fe > Ni, Co		Te	Bi			granitic rocks and ultramafic bodies	Choi and Imai (1985)
47	Mexico	Sabinal			Ni, Co			Ag, Au			granite	Krieger (1935)

(*continued on next page*)

Table 1 (*continued*)

	Country	Disrtrict	Sublocality	M-AsS/As/Sb	M-As_x	M-Sb_x	Other	Native el.	T °C	sal. wt%	Dominant Host Rock	Selected Literature
48	Mexico	Batopilas			Ni > Co			Ag	140–260	8–13	dacite, granodiorite, serpentinized basalts	Wilkerson et al. (1988); Kallstrom (2012)
49	Morocco	Bou Azzer		As, AsS	Co, Ni, Fe			Au-Ag	200–400	36–51	serpentinites, granitic-dioritic rocks	Dolansky (2007) and re erences therein; Ahmed et al. (2009), Gervilla et al. (2012), Bouabdellah et al. (2016), Essarraj et al. (2016)
50	Norway	Kongsberg-Modum		AsS > As	Ni, Co, Fe			Ag-Hg	250–300	21	gneiss, amphibolite, fahlbands (py + po rich gneisses)	Segalstad (2008), Kotková et al. (2017)
51	Poland	Kowary		As	Ni, Co, Fe		U	As, Ag			carbonate	Hoehne (1936)
52	Romania	Bihor	Avram Iancu	As, AsS	Ni, Co		U, Mo	Bi			marl, metavolvanic shist	Zajzon et al. (2015)
53	Russia	Altai-Sayan province	Khovu-Aksy ore cluster		Co > Ni, Fe		U	Ag, Bi			various	Tretiakova et al. (2010)
54	Russia		Abakan ore cluster									
55	Russia		Yustid ore cluster			Ni						
56	Russia	Belorechenskoe deposit		As > AsS > Sb	Ni	Ni	U	Ag, As			granitoids	Pekov et al. (2010)
57	Russia	Ishkinino Co-Cu deposit		AsS > As	Ni > Co, Fe		Te	Au			serpentine with massive sulfide deposits	Zaikov and Melekestseva (2006)
58	Russia	Noril'sk Ore Field		As,Sb > AsS	Ni > Co > Fe	Ni	U	As, Ag-Hg	130–220	7–13	Mafic-ultramafic magmatic Cu-Ni sulfide deposit	Spiridonov et al. (2007), Gritsenko and Spiridonov (2008)
59	Scotland	Clackmannshire	Alva		Co > Ni			Ag-Hg			andesitic volcanics	Moreton et al. (1998)
60	Slovakia	Dobšiná		As, AsS	Ni, Fe > Co			Bi	180		amphibolites, gneisses	Kiefer et al. (2017)
61	Spain	Pirineos	Solita Mine	AsS	Ni, Co, Fe						conglomerates and sandstones, red beds, black shales	Manuel et al. (2018)
62	Spain		Crescencia	As, AsS	Ni		U				ankeritic black shales, carbonates	Fanlo et al. (2006), Manuel et al. (2018)
63	Spain		San Juan de Plan	As, AsS	Ni, Co							Fanlo et al. (2004), Manuel et al. (2018)
64	Switzerland	Valais	Pipji									
65	Switzerland		Grand-Praz	As > AsS	Fe > Co, Ni			Bi	210–330	20–35	amphibolites, gneisses, schishts	Kreissl et al. (2018)
66	Switzerland		Kaltenberg									
67	USA	Wickenburg	Monte Cristo	As	Ni > Co, Fe			Ag			gneiss with diabase dikes	Bastin (1922)
68	USA	Mohawk		As	Cu, Ni > Co			Cu-As			basalts	Moore (1971)

(*continued on next page*)

Table 1 (*continued*)

	Country	Distrtict	Sublocality	M-AsS/As/Sb	M-As_x	M-Sb_x	Other	Native el.	T °C	sal. wt%	Dominant Host Rock	Selected Literature
69	USA	Franklin mining district	Trotter shaft	As > Sb	Ni, Fe > Co	Ni						Palache (1937), Oen et al. (1984), Verbeek and Sutphin (1990)
70	USA	Black Hawk district		As, AsS	Ni > Co		U	Ag	160–390	< 6	gneiss with numerous pegmatite, diabase, and aplite dikes	Gillerman and Whitebread (1953), von Bargen (1993)

Information on the mineralogy and formation parameters represent only the native element-arsenide stage. Where information on the relative abundance of elements is known, it is indicated by a greater than symbol (>).

Fleet, 1975, Kiefer et al., 2017), which are however, still being applied. Not only the absolute temperature is variable, but also the temperature change during mineralization: While at most localities, the temperature decreases systematically from the arsenide to the later sulfide stage (e.g., Bouabdellah et al., 2016 and references therein), other localities such as those at the Great Bear Lake show a temperature increase from the arsenide to the later sulfide stage (Robinson and Ohmoto, 1973). Furthermore, due to a lack of systematic temperature study within the arsenide stage and due to a complex ore forming history for many of the localities, including possible interruptions in depositions between the arsenide and sulfide stage, no generalized temperature trend from the arsenide to the sulfide stage for this assemblage type can be specified.

Fluid inclusion data from gangue minerals co-genetic with the arsenide stage record salinities up to 50 wt% NaCl equivalent containing dominantly NaCl and $CaCl_2$ (e.g., Bouabdellah et al., 2016, Markl et al., 2016; and references in both). The source of the salinity and the origin of the highly saline ore-forming fluids is under debate for most localities (e.g., Cobalt-Gowganda, Petruk, 1968; Echo-Bay, Robinson and Ohmoto, 1973; Bou Azzer Bouabdellah et al., 2016). Generally, it is proposed that the saline brines developed from sedimentary brines, which migrated through the basement rocks and further evolved by desiccation and fluid-mineral reactions. A magmatic origin has been excluded (e.g., Robinson and Ohmoto, 1973, Markl et al., 2016, Kreissl, 2018), although, due to the close spatial relation to magmatic bodies at some localities, at least a partially magmatic origin has been discussed in the past (granitic and mafic; e.g. Bastin, 1939, Petruk, 1968). The temporal hiatus between magmatism and ore formation for several occurrences (e.g. Odenwald: Burisch et al., 2017, Valais: Kreissl, 2018), however, excludes this interpretation.

Since the arsenides, sulfarsenides, and native elements are stable under reduced conditions relative to to the dissolved species typically present in such hydrothermal, highly saline brines (arsenic: $As^{0,I-,II-}$ vs. $[As^{V+}O_4]^{3-}$, $As^{III+}(OH)_3$; sulfur: S^{II-} vs. $[S^{VI+}O_4]^{2-}$; silver: Ag^0 vs. $[Ag^{I+}Cl_2]^-$; bismuth: Bi^0 vs. $[Bi^{III+}Cl_4]^-$), Markl et al. (2016) related the formation of native element-arsenide assemblages to a process of strong and rapid reduction. Furthermore, the redox potential successively decreases from As^{V+} [H_3AsO_4] to As^{III+} [$As(OH)_3$] to As^0 [native As] to As^{III-} [AsH_3] (Haynes, 2016), where the more reduced aqueous As species (As^{III-}) is present only at significantly more reducing conditions than the solid arsenic species. The spatial association of ore suites with reducing agents such as siderite, sulfide, and/or graphite-rich host rocks and organic-rich shales (e.g., Kissin, 1993 and references therein, Cheilletz et al., 2002, Lipp and Flach, 2003, Kreissl, 2018) and the identification of hydrocarbons in fluid inclusions from the Odenwald (Burisch et al., 2017), Cobalt-Gowganda (Kerrich et al., 1986), Bou Azzer (e.g., Essarraj et al., 2005, Essarraj et al., 2016) and Imiter (Levresse et al., 2016) support this argument.

1.2. Objectives

The aim of this study is to compile available literature data on worldwide occurrences of this mineralization type to identify typical characteristics, to produce a generalized mineral sequence and to test by thermodynamic modelling, if the formation hypothesis of reduction, which is abundantly suggested in the literature and discussed above, can explain the development of these textural characteristics. During the compilation, extra attention was given to:

- parameters such as host rock, formation temperature and relative mineral abundance
- the commonly described Ni → Co → Fe diarsenide sequence
- whether a characteristic di-, tri- and sulfarsenide sequence is present with respect to Ni-Co-Fe
- the proposed mono- → di- → triarsenide and the arsenide → sulfarsenide sequence

Table 2
Past and present economic significance of native element-arsenide assemblage examples.

	locality	produced [t]			total ore [kt]	grade [wt %]				source
		Ag	Co	U-salt		Ag	Co	Ni	U	
5	Camsell River	404			28	0.1				Silke (2009); Gov. of NWT (2016)
6	Echo Bay	793								
7	Eldorado mine	379	250	750						
8	Cobalt	12,546	11,346		5331	0.3	0.1			Sergiades (1968); Rogers (1996)
9	Gowganda	1659	614		1276	0.1	0.05			
10	South Lorrain	662	1583		322	0.2	0.3			
15	Thunder Bay	113								
49	Bou Azzer				5700		1.5			Slack et al. (2017)
65	Grand Praz				0.28		8	14		Schmidt (1920); Meisser (2003)
66	Kaltenberg				0.05		8	2		

In the thermodynamic modelling part, we focused on:

- The influence of variable fluid composition and physiochemical conditions (pH, T, P, redox conditions (logfO_2), metal contents, arsenic/sulfur activities)
- the process of reduction and whether it suffices to explain the observed mineralogical sequences
- the effect of variable reducing agents
- the effect of sulfur and the transition from the arsenide to the sulfide stage

2. Compositional and mineralogical data compilation

To investigate these open questions, it is of vital importance to form a fundamental understanding of the mineralogical and compositional variability as well as the mineral succession, based on a large quantity of localities. The following section presents a general review style description of these native element-arsenide assemblages, where all localities considered are reported in Table 1. A compilation of all literature compositional data of the arsenides and sulfarsenides is given in Appendix A, electronic supplement.

2.1. Typical succession of stages

The defining native element-arsenide assemblage commonly occurs as an intermediate stage within a polymetallic mineralization, preceded by quartz-rich oxide bearing stages and succeeded by base-metal sulfide- and sulfosalt-bearing mineralization stages (Fig. 2a-d). At some occurrences, a base metal-bearing quartz assemblage is present before or instead of the quartz-rich oxide stage. In detail, the typical succession is as follows:

(i) The quartz-rich oxide-bearing stage can comprise botryoidal uraninite as the dominant ore mineral at individual occurrences (Fig. 2b), but uraninite may be completely lacking at others. The sulfides, arsenides, and sulfarsenides present in these assemblages are found along fractures and replacement textures and thus belong to the later stages (e.g., Ondrus et al., 2003a; Bailey, 2017).
(ii) The transition towards the subsequent native element-arsenide stage is characterized by fracturing of the earlier assemblages and the initial formation of native elements (commonly bismuth and silver) as well as niccolite (Fig. 2e–g). All of them follow dendritic growth patterns and act as crystallization nuclei for consecutive di-, tri-, and sulfarsenide formation (Fig. 2c, f). At localities where a prior uraninite-bearing stage is present, thin bands of uraninite that most likely formed due to remobilization, are sometimes present around these cores (Fig. 2c). In most cases, the arsenide minerals occur in a gangue of carbonates (typically calcite, dolomite, ankerite or more rarely siderite; Markl et al., 2016), where fluorite, barite, and quartz may be present, but are much rarer (Bastin, 1939).
(iii) The characteristic transition towards the succeeding sulfide stage is gradual, where both replacement and overgrowth textures (Fig. 2c and f) as well as the formation of new veins (Fig. 2d and h) is common. Indicative minerals of this stage are Ag-, Sb-, As-bearing sulfosalts together with native arsenic and base-metal sulfides. Although native silver and bismuth from the arsenide stage are commonly replaced by sulfosalts, sulfides, and gangue minerals (Fig. 2d and f), in some cases new generations of these native elements form. Furthermore, the minerals in this stage are heavily intergrown and reaction textures are typical, producing a complex mineral succession (Fig. 2d).

This typical succession of stages implies similar, long-lived, multi-stage hydrothermal systems. The similarity of this mineralization type between different localities is even more pronounced when the observed mineralogy and textures are compared. A similar paragenetic sequence that commonly contains crystalline arsenide crusts and rosettes successively overgrowing skeletal aggregates of native bismuth and silver. The abundance of carbonates during and after the arsenide stage, indicates an influx or relative enrichment of carbonate of the ore-forming fluids.

2.2. The arsenide stage

To supplement the general understanding of the arsenide stage, a thorough review is compiled, for which all literature stated in Table 1 was considered, but specific focus was given to 15 localities that were chosen based on their historic or present economic importance, the availability of sufficient published mineral composition data, and the quality of available textural observations (Fig. 3a–c). We specifically compiled data on the paragenetic sequence and arsenide/sulfarsenide composition and compositional evolution. Some compositional data was augmented by EDX analyses (arsenides and sulfarsenides from Schneeberg, Germany and Schladming, Austria; sulfarsenides from the Odenwald; see Appendix A). In some cases, where no or only limited information on paragenetic sequences is available (e.g., Jáchymov), the sequences shown in Fig. 3 were constructed carefully from literature descriptions of mineral intergrowths, textural images, and figures of incomplete paragenetic sequences. Note that some localities involve various mines, veins, or small deposits, which may show small differences on the local scale. This was neglected in the effort to produce a general mineralization sequence for each investigated district. We did, however, make sure that no published or investigated individual sample

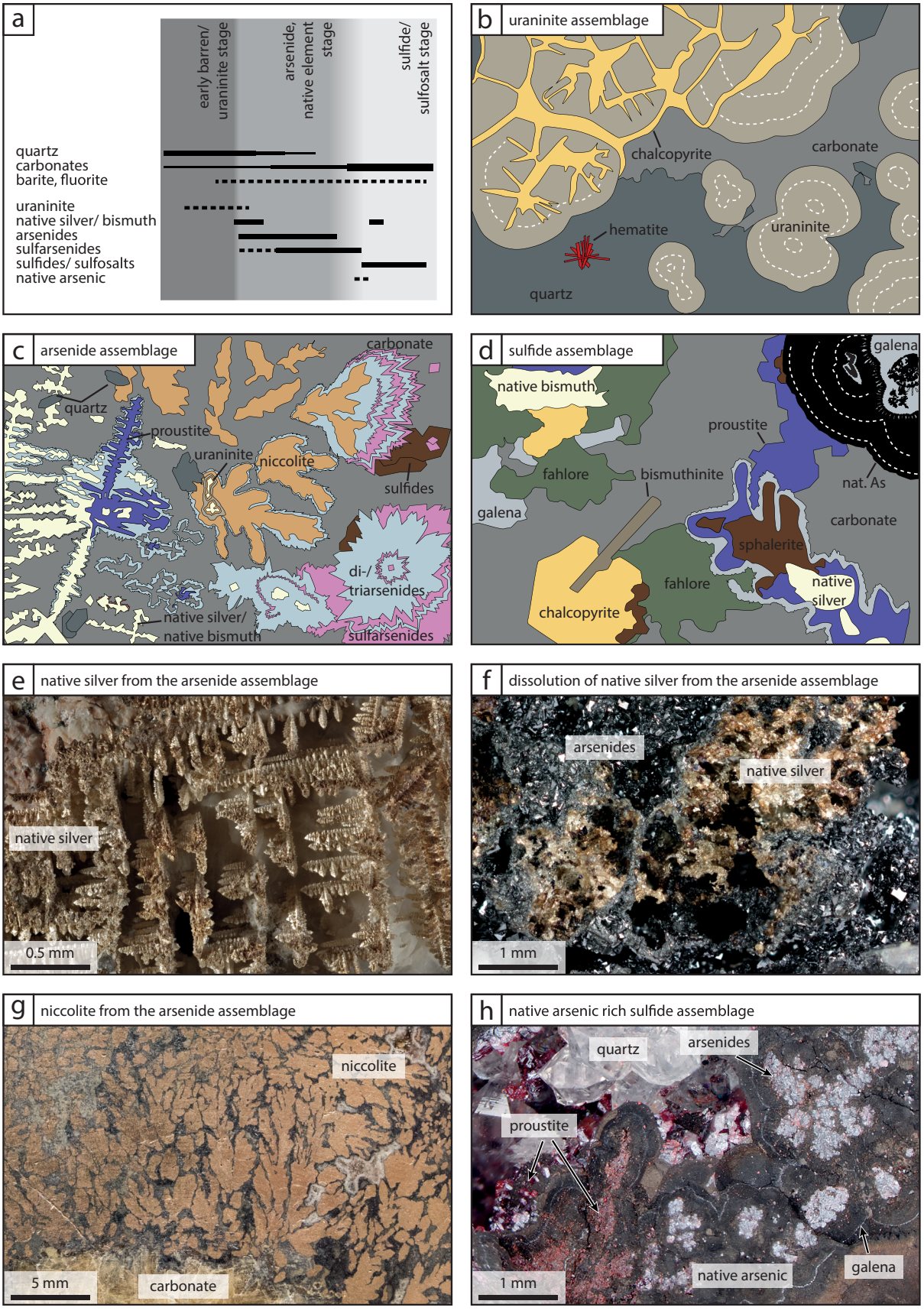

Fig. 2. Representative ore textures with respect to ore stages. (a) Generalized and simplified mineral sequence with respect to the stages commonly present for five-element assemblages. (b–d) Schematic sketches of typical textures of assemblages (compiled from the abundant literature stated in Table 1) that are found within the stages shown in (a). (e–h) Images of hand specimen from the private Schwarzwald collection of Gregor Markl (e, f, h) and from the Mining Museum Příbram (g) that show some of the textures present in (b–d).

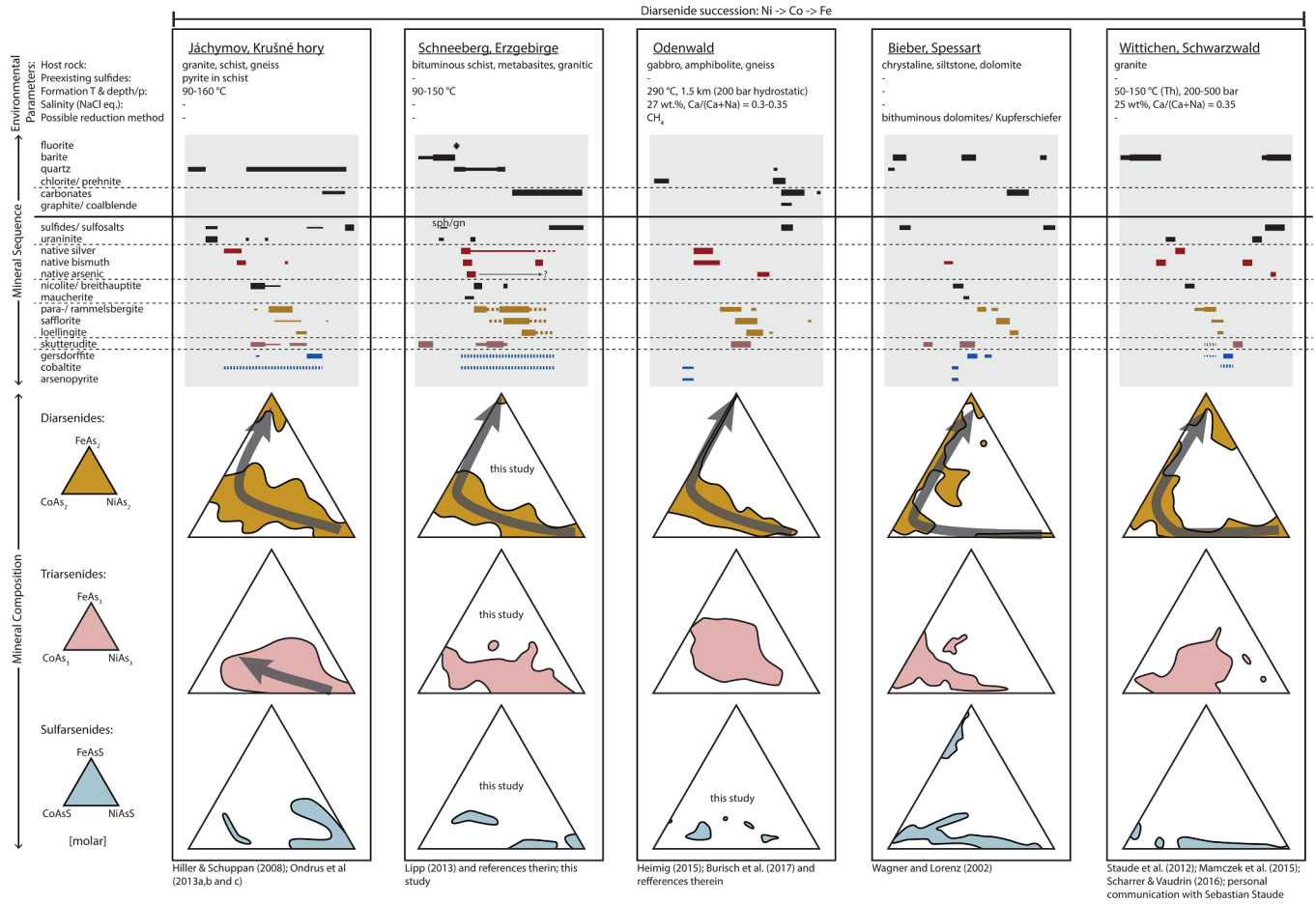

Fig. 3. Detailed presentation of selected native element-arsenide assemblages. (a–c) Environmental parameters, mineral sequences, and di-, tri-, and sulfarsenide composition for selected localities compiled from literature data. The environmental conditions represent only the native metal – arsenide – sulfarsenide stages within these multistage systems. Mineral sequences are compiled from literature and are supplemented by own interpretation from available textures. Composition is presented as molar composition. Additionally, qualitative analyses were carried out by EDX, where insufficient compositional data was available. Note that skutterudite represents all triarsenides and cobaltite all Co-sulfarsenides. References are given at the bottom of each locality. (See above-mentioned references for further information.).

or sub-locality (e.g. vein or mine) contradicts this general paragenetic sequence for each locality. In cases where the paragenetic sequences implied a crystallization sequence among Ni, Co, and Fe or a general trend was described in the respective literature, the general trend is shown as grey arrows in the ternary diagrams of Fig. 3. The relative quantity and the textural occurrence of the arsenides, sulfarsenides, and native metals may vary between individual samples in a specific deposit, and thus, a complete paragenetic sequence can only be deduced from a large sample set. Furthermore, the relative abundance of Ni-mono- vs. -diarsenides, native metals vs. arsenides, and Ni- vs. Co- vs. Fe-diarsenides can vary greatly between different localities or in different samples of a single deposit (Fig. 1 and Table 1 and references therein). As a textural summary of the arsenide stage ore minerals, the schematic sketches, images and wave length dispersive maps of Fig. 4 were produced to reflect the general trend in the paragenetic sequence.

2.2.1. *Initial ore minerals: native silver, native bismuth, and niccolite*

Typically, mineral aggregates can be subdivided into a core aggregate, which governs the habit of the overall texture, and subsequent overgrowths or perimorphs of later-formed sub- to euhedral aggregates of Ni-, Co- and Fe-arsenides and/or sulfarsenides. The core crystal aggregates are typically either niccolite, native silver, or native bismuth. Niccolite shows a fern-like, broccoli-amoeboid shape (Fig. 4) or rarely euhedral crystals, and the native metals show skeletal, dendritic, grid-like or wire-shaped growth (Fig. 4). Besides these zoned textures, the arsenides may also form individual euhedral crystals and disseminated or massive ores (Fig. 4).

An interesting phenomenon is the extreme rarity of intergrowths between native silver and native bismuth (as far as we know, only observed in a few samples from Wittichen, south-west Germany). Furthermore, in some districts where both native metals were observed, native silver is associated with Ni-rich and native bismuth with Co- and Fe-rich arsenide assemblages (e.g., Keil, 1933, Ondrus et al., 2003a, Heimig, 2015). In the Erzgebirge, on the other hand, aggregates of native silver and native bismuth are confined to different ore shoots which sometimes are correlated with different host rocks (Keil, 1933). However, other occurrences show silver with an assemblage of both Ni- and Co-arsenides (Cobalt Gowganda, Petruk et al., 1971). The primary native silver of the arsenide stage may be enriched in Hg up to 30 wt% (e.g., Burisch et al., 2017, Kotková et al., 2017).

2.2.2. *Mono-, di-, and triarsenide sequence*

In the native element-arsenide mineralization type, niccolite is the only monoarsenide, where mono-, di-, and triarsenides generally occur, and niccolite only forms during the initial phase of the arsenide sequence. In some occurrences, a general trend of increasing As/(Ni + Co + Fe) ratio within the arsenide sequence produces a succession of monoarsenide → diarsenide → triarsenide (e.g., Ondrus et al., 2003a; Dolníček et al., 2009). However, although this can be the case for some localities, in general the temporal appearance of the

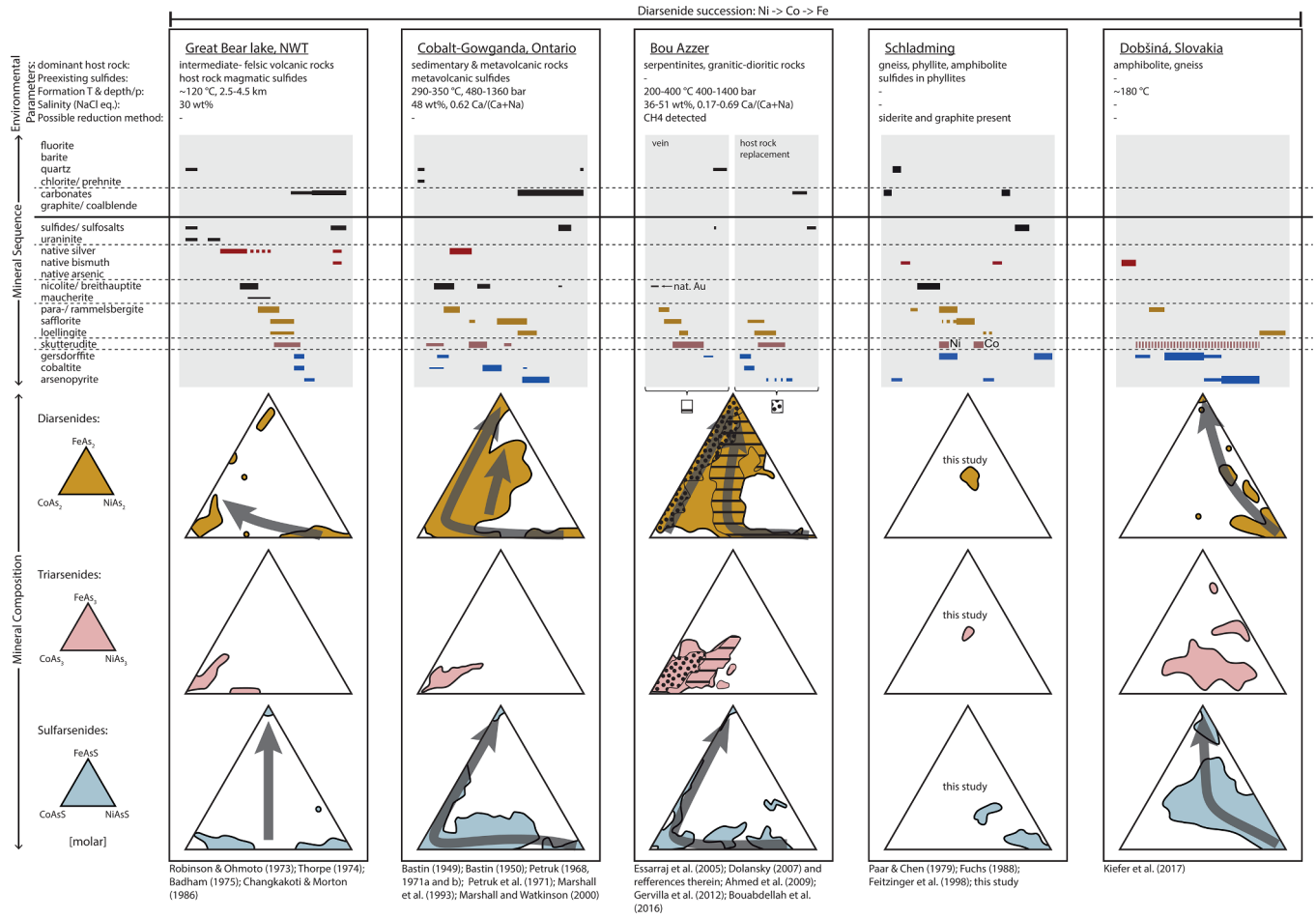

Fig. 3. (*continued*)

triarsenides in the mineralization sequence is variable and can coincide with the whole crystallization interval of the other arsenides (Fig. 3 and references therein). Several generations of skutterudite are common, and a coprecipitation of skutterudite with native bismuth and/or Ni-, Co- and Fe-diarsenides is characteristic (Fig. 3; e.g., Petruk, 1968, Heimig, 2015), which involves individual growth zones spanning over the tri-diarsenide boundary. A lack of information in most of the available literature on the exact correlation between temporal position within the arsenide stage and composition, renders it hard to identify a general compositional evolution within the triarsenides. In general, most triarsenides are Co-dominated with a ternary composition, and some are Ni-dominated with a complete solid solution between Co and Ni. Iron-dominated triarsenides are rare, and near-Fe-endmember triarsenides are absent.

2.2.3. Diarsenides

At most localities, all three diarsenides (Ni-, Co- and Fe-dominated) are present and only their relative abundance varies. The diarsenides occur as rosettes of zoned aggregates around the core aggregate, and commonly show the trend Ni → Co → Fe which has been described for most localities with the exception of the Pirineos and Valais which show a trend from Co → Ni (Fig. 3 and references therein). It has to be noted that this general trend is not always present in individual samples, where more complex sequence repetitions are typical. Furthermore, some stages of the sequence may be locally lacking or the degree of development of these trends is variable (Fig. 4e). The most detailed information on mineral successions in single aggregates, which reflect the complete chemical evolution of a distinct hydrothermal pulse, were documented for the Bieber deposit, Spessart (Wagner and Lorenz, 2002) and the Nieder-Beerbach deposit, Odenwald (Heimig, 2015) and were thus used as templates for Fig. 4. The transition between different diarsenides (e.g., between rammelsbergite and safflorite or between safflorite and loellingite) is in part gradual, but a compositional gap in individual textures as well as an oscillatory transition is common. The combination of all compositional data of diarsenides shows a complete ternary solid solution between Ni, Co, and Fe (dataset in the electronic supplement). Based on a comparison of this data set with the respective formation temperatures estimated by fluid inclusion studies, a small immiscibility gap between loellingite ($FeAs_2$) and the Ni-Co diarsenide solid solution appears to be present only in veins that formed at temperatures below ca. 200 °C. Thus, the diarsenides are much more miscible in hydrothermal ores than predicted by experimental data from Roseboom (1963). It should however be noted that other factors such as presence of mixtures due to nano-scaled intergrowths or re-equilibration cannot be excluded.

2.2.4. Sulfarsenides

With the exception of a few sulfarsenide-dominated occurrences, the Co- and Ni- sulfarsenides are typically less abundant than the di- and triarsenides. The temporal position of the sulfarsenides within the paragenetic sequence varies, and they may form prior to, during, or after diarsenide precipitation (Fig. 3a, b, and c). They form as reaction products around preexisting sulfides and thus as inclusions in the cores of zoned aggregates (e.g., Petruk et al., 1971; Fanlo et al., 2004; Fanlo et al., 2006; Heimig, 2015), as individual oscillatory layers within diarsenides (e.g., Petruk, 1971b; Petruk et al., 1971; Heimig, 2015), as replacements of niccolite (Fanlo et al., 2004; Fanlo et al., 2006), or as individual, commonly euhedral grains (e.g., Petruk, 1971b). Ni- and Co-

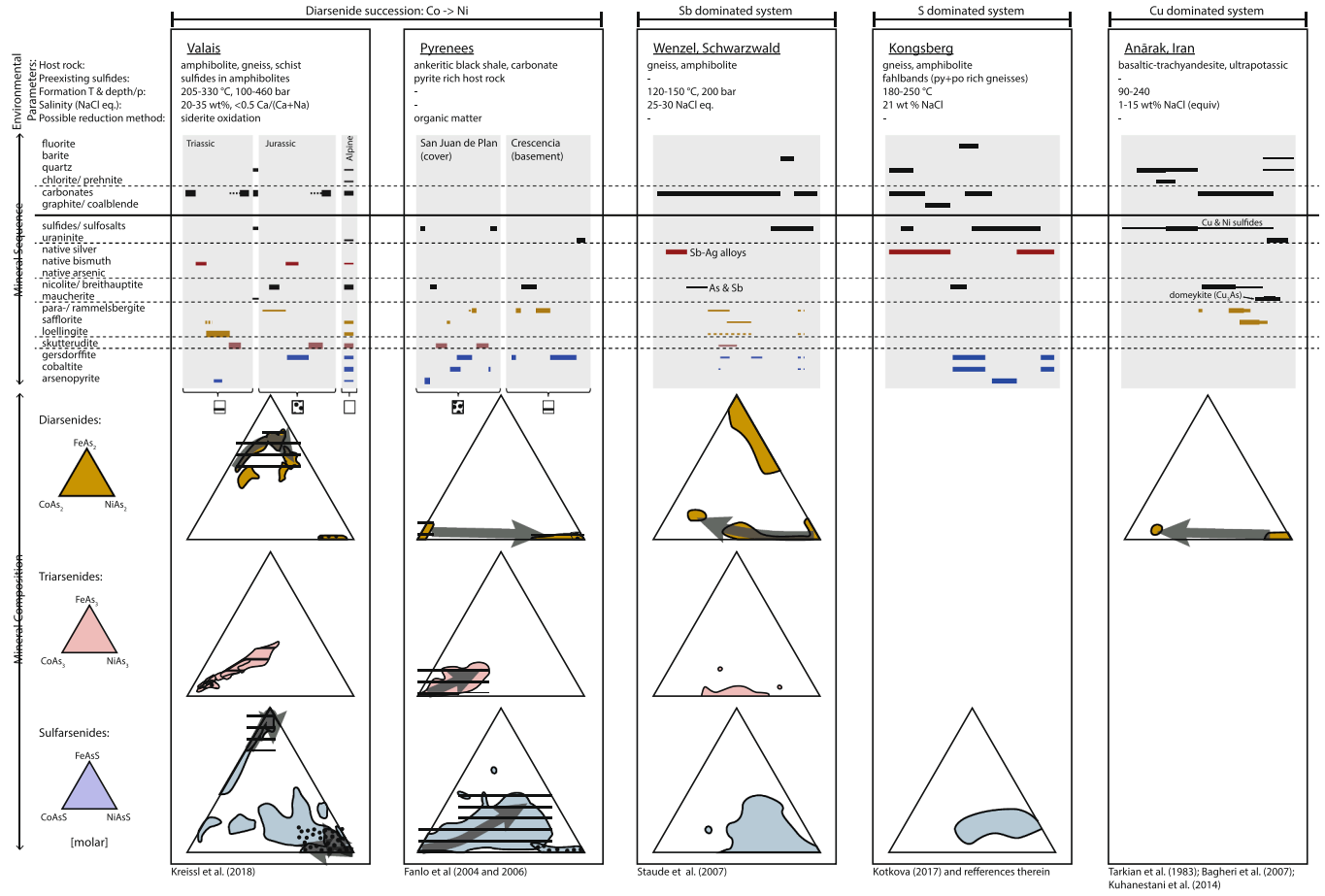

Fig. 3. (*continued*)

sulfarsenides such as gersdorffite and cobaltite show a complete solid solution which can also incorporate large quantities of Fe (up to a molar Fe/(Ni + Co) ratio of 2:1). The Fe-sulfarsenide (arsenopyrite) seems to be more compositionally limited with respect to substitution of Ni and Co. It is typically only found during later stages of arsenide mineralization (e.g., Kissin, 1993) or in Fe-dominated localities such as Valais, where arsenopyrite is intergrown with loellingite (Kreissl et al., 2018). In the less abundant latter case, it is predominantly the initial phase that is overgrown by loellingite rosettes (Fig. 5 and references therein).

2.2.5. *Native arsenic*

Native arsenic is relatively common at some localities (e.g., Schneeberg; Lipp, 2013 and Odenwald; Heimig, 2015), but can be completely lacking at others (e.g., Bou Azzer). It forms as colloidal masses during the transition from the arsenide to the sulfide stage. Common inclusions in native arsenic are galena and/or dendritic native silver (most likely a second silver generation), and this native arsenic is overgrown by Ag-bearing sulfosalts and base-metal sulfides (Fig. 4 and Fig. 3 and references therein), or in rare occurrences by loellingite (Burisch et al., 2017).

2.2.6. *Complexity of the assemblages*

A few of these arsenide assemblages contain not only Ni-, Co-, and Fe-arsenides, but also Cu-arsenides, e. g. in Anārak, Iran (Fig. 3c; e.g., Tarkian et al., 1983; Bagheri et al., 2007) and the Mlakva polymetallic deposit in Serbia (Fig. 3c; e.g., Radosavljević et al., 2015, Radosavljević-Mihajlović et al., 2017). These occurrences contain domeykite (Cu_3As) and/or koutekite (Cu_5As_2), that precipitated subsequently to the other arsenides (e.g., Bagheri et al., 2007; Radosavljević-Mihajlović et al., 2017). Interestingly, Cu-sulfides form simultaneously with the Ni- and Co-arsenides (Bagheri et al., 2007), which may indicate that Cu-sulfides are more stable than Cu-sulfarsenides.

The arsenide stages of most localities shown in Table 1 contain antimony to a variable degree, but there are assemblages such as Wenzel, Příbram and Allemont that contain large quantities of Sb minerals such as breithauptite, ullmannite, native antimony, allemontite, dyscrasite and allargentum (Fig. 3c; e.g., Ypma, 1963; Staude et al., 2007; Hiller and Schuppan, 2008). Breithauptite commonly occurs together with niccolite, and ullmannite with gersdorffite (Fig. 3c and references therein). Due to the lack thermodynamic data for the Cu-arsenides and for the antimonides, these interesting ores, unfortunately, cannot be addressed further here.

3. Application of thermodynamic modelling

The work of Markl et al. (2016) reported thermodynamic calculations only on some Co phases, native silver, and rough estimations on native bismuth. Hence, the detailed evolution of the fluid and the textural variation of the arsenide-bearing assemblages could not be constrained in sufficient detail to understand the variability observed in nature. By compiling and estimating thermodynamic data, a new, comprehensive (albeit rough) thermodynamic database of Co, Ni, and Fe-bearing phases relevant for the understanding of native element-bearing arsenide-assemblages is presented and discussed in the present contribution. This enables us to model the observed mineralogical variability of the dominant minerals in native element-arsenide occurrences and to compare it to carefully compiled mineralogical, mineral compositional, and fluid data from all well-documented native element-arsenide type occurrences worldwide.

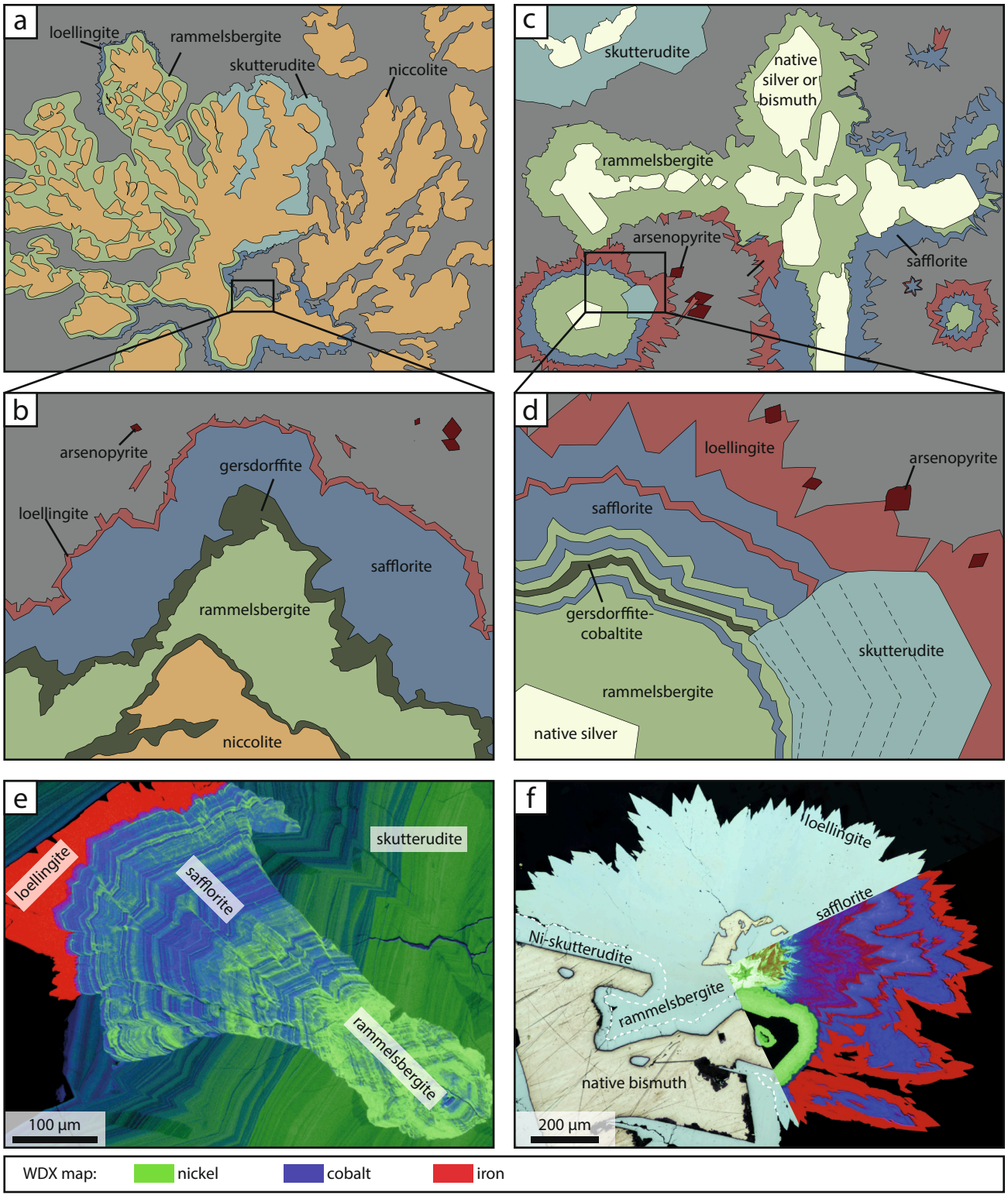

Fig. 4. Representative ore textures with respect to the arsenide ore stage. (a–d) Schematically illustrated typical textures of native metal – arsenide – sulfarsenide ores of the five-element type that have been compiled from all publications given in Table 1 and from samples of the mineralogical collection at the University of Tübingen. The textures show niccolite (NiAs; nic) and/or native metals (native silver and native bismuth) overgrown by a general sequence of rammelsbergite ($NiAs_2$; ram, par), safflorite ($CoAs_2$; saf) and loellingite ($FeAs_2$; loe). Sulfarsenides such as cobaltite (CoAsS; cob) or gersdorffite (NiAsS; gdf) commonly occur as intermediate zones within arsenide rosettes and skutterudite ($(Ni,Co,Fe)As_3$; skut) precipitates contemporaneously together with the diarsenides. (e, f) Note, that these sequences are only partially present in most samples and seldom show the whole evolution of such a system and/or the trend is oscillatory and complex. WDX maps of two samples from the Odenwald where generated with the JOEL Superprobe JXA-8900RL at the Eberhard Karls Universität, Tübingen, and the monochrome qualitative elemental peak intensity maps where colored, overlain and edited for best representation of the arsenide sequence.

Table 3
Compiled and estimated thermodynamic properties of arsenides, native bismuth, and sulfosalts at 298.15 K and 1 bar.

Formula	ΔH_f^0 kJ/mol			S^0 J/mol K			c_p J/mol K				
							a	b	c	d	
NiAs	−70.820		[1]	50.76		[1]	36.60	41.70	1.57		[1]
$NiAs_2$	−90.10	± 8	[3]	110.00	± 10	[2]	95.40	−5.91	5.33		[2]
CoAs	−53.97		[2]	61.92		[2]	21.13	68.40	13.25		[2]
$CoAs_2$	−87.65		[2]	96.65		[2]	69.87	25.00	−0.38		[2]
FeAs	−43.512		[1]	62.50		[1]	27.95	46.50	7.60		[1]
$FeAs_2$	−85.776		[1]	80.10		[1]	76.69	3.10	−6.03		[1]
FeAsS	−144.370		[1]	68.50		[1]	75.51	4.78	−7.54		[1]
Bi				56.74		[4]	26.85	17.289		4.1802	[5]
Bi_2S_3	−135.19		[6]	200.40		[6]	119.60	15.280	9.464		[6]
Ag_3AsS_3	−121.4	± 2.8	[7]	283	± 10	[7]	145.65	82.88	1.265		[2]
$AgAsS_2$	−75.69	± 1.6	[7]	151	± 5	[7]	80.25	46.90	1.265		[2]

Note: Δ_fH^0 and S^0 for CoAs are not recommended for use. Specific heat capacity is given in the form of: $cp(T) = a + b*10^{-3}*T + c*10^5*T^{-2} + d*10^{-5}*T^2$.
References: [1] Thermoddem database and references therein; [2] estimated in this study; [3] Gamsjäger et al. (2005); [4] Barin (1995); [5] Robie and Hemingway (1995); [6] Tooth et al. (2013); [7] Gasanova et al. (2014).

Table 4
Compiled and estimated thermodynamic properties of sulfarsenides. logK corresponds to the reaction $As_s + S_s + M_s = MAsS_s$.

	logK of As(s) + S(alpha) + M(s) = MAsS(s)								
	0 °C	25 °C	60 °C	100 °C	150 °C	200 °C	250 °C	300 °C	
NiAsS	23.94	21.93	19.64	17.56	15.53	13.94	12.66	11.61	[1]
CoAsS	25.33	23.17	20.68	18.41	16.17	14.41	12.99	11.82	[1]
FeAsS	26.2190	23.9050	21.2466	18.8167	16.4223	14.5313	12.9993	11.7328	[2]

[1] Estimated solubility, logK values, of stoichiometric Ni- and Co sulfarsenide and [2] literature solubility values for arsenopyrite from the Thermoddem database.

In order to calculate mineral stabilities, thermodynamic data of relevant minerals and aqueous species in the system Ag-Bi-Fe-Co-Ni-As-S-Na-Ca-Cl have been compiled (Section 3.1) and, where lacking, integrated into the existing Thermoddem database of 2017 (Blanc et al., 2012) while keeping the internal consistency of the database intact (Section 3.1). As demonstrated by Kinniburgh and Cooper (2004), multicomponent systems need a consideration of the complete fluid composition and all resulting aqueous species. For this purpose and to prevent misleading interpretation based on simplistic models, the fluid composition is constrained (Section 3.2) and an adequate thermodynamic modelling tool chosen and applied (Sections 3.3–3.5).

3.1. Thermodynamic data estimation and integration

As the fundamental thermodynamic database, the internally consistent Thermoddem version of 2017 was used, which already includes, among others, $FeAs_2$, FeAs, FeAsS, NiAs, native arsenic, native silver, FeS_2, CoS_2, and NiS_2 and is applicable up to 300 °C (Blanc et al., 2012). It is comprised of well evaluated and revised thermodynamic data for the species of interest (Blanc, 2008, Blanc and Gaboreau, 2013, Blanc and Lassin, 2013) that is updated regularly (Blanc, 2017). Further thermodynamic data for Co- and Ni-arsenides are sparse and possibly imprecisely determined, which is why we cannot differentiate between isochemical minerals (for example, rammelsbergite and para-rammelsbergite). Even though a large compositional variability is present in natural arsenide samples, all minerals are only referred to by their respective endmember formula and solid solutions are thermodynamically neglected. It is true that this is a significant simplification. However, after careful consideration, this has been done, as available and estimated thermodynamic data are not precise, thermodynamic solid solution parameters are lacking, and as only the general mineral successions are investigated for which an endmember scenario suffices. If in future publications, small scale processes of individual samples or aggregates are investigated in more detail, a consideration of solid solutions may be crucial and a thermodynamic solid solution model would be adequate. However, before this can be done, the thermodynamic data for all arsenides involved has to be determined experimentally, by techniques yielding internally consistent data.

In the following section, the thermodynamic data for these additional solid phases are critically discussed and selected. Due to the experimental complexity of producing thermodynamic arsenide data and due to the compositional variability of natural samples, we are compelled to use the sparse literature values and supplement these by estimation methods. Minerals incorporated into the thermoddem database and their respective selected thermodynamic properties, are presented in Tables 3 and 4, and were implemented by Philippe Blanc, the creator of the data base (Blanc et al., 2012) in order to maintain internal consistency.

The compilations of Naumov et al. (1971b) and Kubaschewski and Alcock (1979) both contain enthalpy of formation (ΔH_f^0) and standard state entropy (S^0) values for CoAs and $CoAs_2$. The average of these values is used, which lies within the uncertainty of the individual measurements and resulted in a general trend Ni → Co → Fe for both ΔH_f^0 and S^0 for diarsenides and monoarsenides (Fig. 5a). This trend coincides, for example, with the crystallographic structure of the diarsenides, which has a continuous decrease in M-As-M angle and M-M distance and a continuous As-As distance increase from Ni to Fe (Yang et al., 2008). A general Ni-Co-Fe trend is also in accordance with ΔH_f^0 and S^0 as well as the Gibbs energy of formation (ΔG_f^0) of many aqueous and mineral phases among these elements (Fig. 5a). A nearly linear relationship between Ni, Co and Fe is visible in several fundamental parameters such as electronegativity (Haynes, 2016), the ligand field stabilizing energy of Fe, Co, and Ni, (Kissin, 1993), and the inverse ionic radius (Fig. 5a; Haynes, 2016) of these transition metals in their divalent octahedral state (present for the $MeAs_2$ minerals; Tossell et al., 1981). The temperature-dependent specific heat capacity (c_p) was estimated by assuming $\Delta c_p^{reaction} = 0$, according to the Neumann-Kopp rule, for the following reaction:

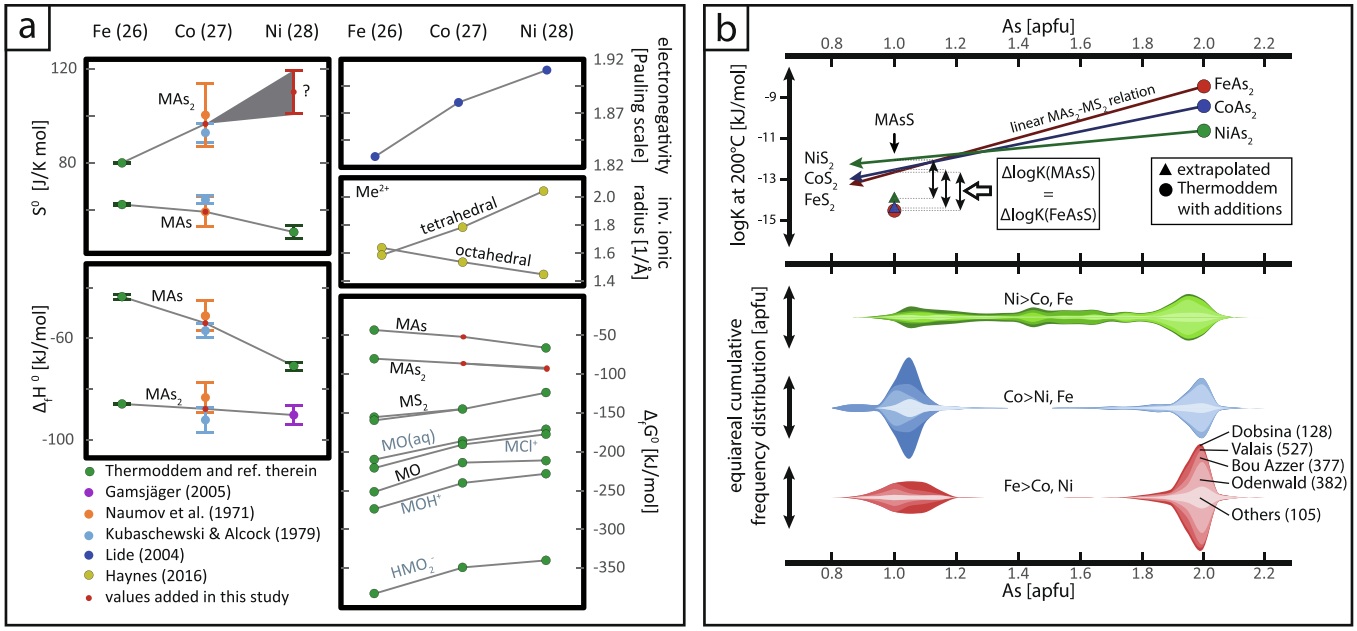

Fig. 5. Thermodynamic compilation. (a) Compilation of thermodynamic properties, enthalpy of formation (Δ_fH^0), standard state entropy (S^0), and Gibbs energy of formation (Δ_fG^0), of solid and some aqueous species of the elements Fe, Co, and Ni relevant for this study at standard state conditions, where a general trend between Fe, Co, and Ni is present. The entropy of formation for $NiAs_2$ is extrapolated to lie within the red oval (between 110 and 115 J/K mol). (b) Due to the lack of thermodynamic data of Co- and Ni-sulfarsenides, their Gibbs energy of formation was estimated by the assumption that the difference between the actual Gibbs energy of formation from the elements and that of a stoichiometric linear estimation between the disulfides and the diarsenides is equal to that of the Fe system. Lower half of the diagram shows an equiareal cumulative frequency distribution of the di- and sulfarsenides, of literature compositional data (Petruk et al., 1971, Misra and Fleet, 1975, Watkinson et al., 1975, Paar and Chen, 1979, Tarkian et al., 1983, Choi and Imai, 1985, Changkakoti and Morton, 1986, Borisenko et al., 1999, Hem et al., 2001, Wagner and Lorenz, 2002, Ondrus et al., 2003c, Fanlo et al., 2004, Fanlo et al., 2006, Dolansky, 2007, Staude et al., 2007, Ahmed et al., 2009, Gervilla et al., 2012, Staude et al., 2012, Heimig, 2015, Maacha et al., 2015, Radosavljević et al., 2015, Zajzon et al., 2015, Scharrer and Vaudrin, 2016, Kiefer et al., 2017, Radosavljević-Mihajlović et al., 2017, Kreissl et al., 2018), with respect to As per formula unit. The Ni-sulfarsenide is commonly of non-stoichiometric nature and can incorporate large quantities of As (complete solubility between NiAsS and $NiAs_2$). (For interpretation of the references to colour in this figure legend, the reader is referred to the web version of this article.)

$$FeS_2 + MAs_x = FeAs_x + MS_2 \quad (1)$$

where M is either Ni or Co and x is 1 or 2 and the literature values from the Thermoddem database were used (Table 3).

The thorough thermodynamic compilation of Ni phases by Gamsjäger et al. (2005) states that there is only one ΔH_f^0 for $NiAs_2$ available in the literature (Stolyrova, 1982) where a second one (Skeaff et al., 1985), although experimental thermodynamic equilibrium was not achieved, suggests a similar value. Thus, the recommended value and uncertainty of 90,1 ± 8 kJ/mol by Gamsjäger et al. (2005) is used in this study. Traditionally, the missing value of S^0_{NiAs2} would be estimated by [1] linear correlation to volume, [2] the ionic additive method, or [3] difference rules (Glasser, 2013) or by other correlations [4]. [1] The method by molar volume (Jenkins and Glasser, 2003), produces a significantly lower entropy for $NiAs_2$ than other estimates (81 J/K mol compared to up to 110 J/K mol). Considering that this volume-based estimate is less than that of $CoAs_2$, even though there is a steady increase in individual molar volume between $FeAs_2$, $CoAs_2$ and $NiAs_2$ from 27,44 cm^3/mol, 27.92 cm^3/mol to 28,79 cm^3/mol, respectively (Robie and Bethke, 1962), and as there is a common linear relation between molar volume and entropy (Jenkins and Glasser, 2003), this computed entropy seems to underestimate the true value. This underestimation can be attributed to the uncertainty margin since, when considering all sulfide- and arsenide-bearing minerals from the Thermoddem database, their true S^0 value commonly varies up to 50% from estimations made by this method. Thus, we only consider minerals of a similar structure type to that of rammelsbergite ($NiAs_2$ with marcasite structure) to calculate a linear correlation between molar volume and entropy. Minerals fulfilling these requirements are marcasite [FeS_2], arsenopyrite [FeAsS], safflorite [$CoAs_2$] and loellingite [$FeAs_2$] and the molar volume is taken from Tossell et al. (1981) and the entropy from the Thermoddem database. The resulting entropy for $NiAs_2$ (rammelsbergite) is 108 J/K mol (rough linear correlation with only 4 values; $R^2 = 0.92$). [2] The use of the additive single-ion method (e.g., Glasser, 2013) has also been considered. However, there is no literature available for arsenide ions. In addition, the single ion entropy values of Fe^{2+}, Co^{2+} and Ni^{2+} are strongly dependent on which minerals were used during their computation, as some mineral types such as MAs_2 and MS_2 have a negative entropy correlation between Ni, Co and Fe whereas others such as MAs, MS, MF_2 and MCl_2 have a positive one with respect to S^0. Considering that the diarsenides, disulfides and arsenopyrite are similar, this enables us to calculate single ion entropies specific for this mineral group (equivalent to the method used by Glasser and Jenkins 2009) with which we can estimate the entropy of formation of $NiAs_2$. Computing the single ion entropies, a specific ion is commonly fixed on a literature value. Depending on the selected transition metal, single-ion the entropy is fixed based on the values provided by Glasser (2013), the resulting estimated entropy of formation of $NiAs_2$ results in the range of 100–110 J/K mol. [3] Furthermore, S^0_{NiAs2} can be estimated to be equal to the sum of the elements (101 J/K mol) or by $\Delta S_{reaction}$ being zero for the exchange reaction of $CoAs_2$ and NiS_2 (Reaction (1); 102 J/K mol). [4] Since an approximately linear relationship between Ni, Co and Fe is visible in several fundamental parameters, the transition metals (Ni, Co and Fe) of the diarsenides are all octahedrally coordinated and divalent in mineral structures that are very similar (Tossell et al., 1981), S^0_{NiAs2} can be estimated by extrapolation from S^0_{FeAs2} and S^0_{CoAs2} with respect to the atomic number of the transition elements, resulting in a value of 113 J/K mol. Summarizing all the estimation methods described above we selected an S^0_{NiAs2} value of 110 ± 10 J/K mol for our thermodynamic modelling (Fig. 5a). This results in a stability diagram where both NiAs and $NiAs_2$ are present at

approximately neutral pH, which is expected from the common natural assemblage of both minerals.

The implementation of CoAs using the mean S^0_{CoAs} of both available literature values (Naumov et al., 1971b, Kubaschewski and Alcock, 1979) into the database resulted in stability diagrams in which the extremely rare mineral CoAs (langisite) is stable over a wide pH range from strongly basic to nearly neutral conditions. Reducing the stability field by applying the lower S^0_{CoAs} from Naumov et al. (1971b) does not sufficiently diminish it. As CoAs (langisite) is extremely rare in nature (only six localities worldwide; www.mindat.org) and has been described from just one native element-arsenide assemblage (Cobalt-Gowganda; Petruk et al., 1969), we suppressed CoAs in further calculations. The discrepancy between model results and natural occurrence could be due to either kinetic inhibition of its precipitation or due to erroneous data of Naumov et al. (1971b) and Kubaschewski and Alcock (1979).

Data from natural native element-arsenide assemblages shows that cobaltite (CoAsS) and arsenopyrite (FeAsS) are close to stoichiometric (As/S ratios of $\pm < 1.2$ a.p.f.u; Fig. 5b and references therein), indicating a lack of stability of these sulfarsenides at higher As contents. At some localities, the Fe-dominant sulfarsenide shows a slightly lower As/S ratio than the Co counterpart. The Ni-sulfarsenide gersdorffite, however, can incorporate such large quantities of As that a distinction between the sulfarsenide and the diarsenide based on microprobe analyses alone is not always possible (Fig. 5b; e.g., Ondrus et al., 2003c). Thus, the structural formula for gersdorffite should accurately be stated as $Ni(As,S)_2$, but will from now on be labeled as NiAsS. The ΔG_f^0 of stoichiometric sulfarsenides can be roughly estimated by a two-step process. Firstly, linear estimate of $\Delta G_{f,\ MAsS}{}^0$ is calculated by the sum of polyhedral contributions (MS_2 and MAs_2)/linear mixing. Secondly, it is assumed that the difference in ΔG_f^0 between the stoichiometric linear mixing of MAs_2 and MS_2 and the true sulfarsenide is equal for the Fe, Co, and Ni system ($\Delta_{linear\text{-}true}G_{f,\ FeAsS}{}^0 = \Delta_{linear\text{-}true}G_{f,\ MAsS}{}^0$; Fig. 5b) where $\Delta_{linear\text{-}true}G_{f,\ FeAsS}{}^0$ is known and M is either Ni or Co. In principle, this is a variant of the general method provided by Craig and Barton (1973), which has been modified to better represent the sulfarsenides. The resulting rough estimate log K values are presented in Table 4. If the aqueous Fe-, Co-, and Ni-complexes such as oxo-, hydroxo-, or chloride-complexes are considered, the stability field sequence with decreasing fO_2 is NiAsS → CoAsS → FeAsS. Considering that the environment is rich in As relative to S and the nonstoichiometric nature of the Ni-sulfarsenide with higher arsenic content, the stability field of the Ni-sulfarsenide would be even larger.

Due to the common occurrence of native bismuth, we implemented native bismuth according to the $S^0_{native\ bismuth}$ data from Barin (1995) and data for the c_p polynomial terms from Robie and Hemingway (1995). Since the fluids of interest are of highly saline nature, $BiCl_{3(aq)}$, $BiCl_{4(aq)}^-$, $BiCl_{5(aq)}^{2-}$, and $BiCl_{6(aq)}^{3-}$ from Etschmann et al. (2016) are also incorporated into our database. It must be noted, however, that these Bi-Cl complexes are based on experimental ΔG_f^0 estimates that are not internally consistent with the rest of the database.

Since the thermodynamic input parameters of the estimated species are afflicted with a high uncertainty, the results shown here semi-quantitatively predict the phase stabilities and resulting textural features of the native element-arsenide assemblages, but one cannot predict the exact pH, fO_2, and elemental composition needed for a specific situation. It should, however, be noted that the stability field trend, Ni- → Co- → Fe-arsenides is not only a result of the ΔG_f^0 of these minerals, but also of the aqueous complexes, for which this trend is even more pronounced (Fig. 5a). Thus, the interpretations made here based on our thermodynamic model are robust.

3.2. Constraining the input parameters

Unfortunately, only limited data constrain the elemental composition (As, Fe, Co, Ni) of natural fluids related to native element-arsenide assemblages. These few studies are from the Odenwald (Burisch et al., 2017), Bou Azzer (Maacha et al., 2015), and Wittichen (Markl et al., 2016). The concentrations of the transition metals are 50–100 mg/kg, slightly below 1000 mg/kg, and 100 mg/kg in the respective studies, while the arsenic content is reported as about 5000 mg/kg, up to 100 mg/kg, and 300 mg/kg, respectively. It has to be noted that crush leach analyses were used in the Wittichen and Odenwald studies, which may be prone to produce excessively high metal contents, and that a Ni content of nearly 0.1 wt% at Bou Azzer appears unrealistically high.

However, the fluid can be qualitatively constrained to some degree by theoretical restrictions. If a two- or multiple-component fluid mixing between a metal-bearing brine and a reducing fluid (hydrous or non-hydrous such as gaseous methane; e.g. Markl et al., 2016, Burisch et al., 2017) is considered, the arsenic content of the fluid must be significantly higher than the content of (Fe + Co + Ni). If this were not the case, As would be depleted for example during the Ni-arsenide precipitation and no Co- or Fe-arsenides would form after the Ni-arsenides. The lack of sufficient arsenic would also increase the stability fields of the monoarsenides, so that CoAs and FeAs could become stable at basic to slightly acidic conditions instead of the respective diarsenides. For example, a composition of 250 mg/kg As and 50 mg/kg of each Ni, Co, and Fe produces a stability diagram in which $FeAs_2$ is not stable and is substituted by FeAs. Furthermore, native arsenic only precipitates from a Ni-, Co-, and Fe-bearing fluid at a realistic pH and after the Fe-, Co-, and Ni-arsenides, if arsenic is present in excess. Thus, the arsenic content is mineralogically limited to at least one order of magnitude larger than that of the individual transition metals. Furthermore, native element-arsenide assemblages typically encompass large quantities of ore minerals that formed at a rapid pace, as can be seen by dendritic crystallization (Markl et al., 2016). Thus, either an immense amount of ore forming fluid is needed, or the elemental concentrations of the ore forming fluids are high; probably no less than in the range of mg/kg. This, however, does not exclude small scale assemblages of the native element-arsenide assemblage, such as ore shoots in base metal deposits (e.g., Otto, 1964), to have formed from fluids with lower concentrations. An upper boundary for a realistic concentration ranges can be somewhat constraint by also considering hydrothermal fluids from other ore deposit types. The highest concentration measured in hydrothermal solutions are approximately 10^4 mg/kg for S and As, 10^2 mg/kg for Ni and Co and 10^5 mg/kg for Fe (e.g., Karpov, 1991, Ulrich et al., 2002, Yardley, 2005, Fusswinkel et al., 2014, Goryachev et al., 2014, Walter et al., 2018).

Thus, by combining these theoretical arguments with the consideration that some of the measured literature values may be partially erroneous, the elemental fluid content is assumed to be somewhere in the order of 50 mg/kg for each transition metals and 1000 mg/kg for arsenic, which is in accordance with other types of sulfarsenide-bearing assemblages studied by LA-ICP-MS (Goryachev et al., 2014). Concentrations of Ag and Bi were assumed to be about 10 mg/kg, which is in rough accordance with literature data from basement-hosted hydrothermal systems (e.g., Bortnikov et al., 2007, Fusswinkel et al., 2013, Markl et al., 2016). This only represents a rough estimation for these elements as they may strongly vary for/between localities, probably in the range of plus/minus one order of magnitude. Thus, in the generic model section, the effect of elemental availability on arsenide and native element formation are considered.

The salinity of fluid inclusions from native element-arsenide assemblages may reach exceptionally high values varying between a few and 50 wt% (Table 1). Typical values range from 20 to 50 wt% with Ca/(Ca + Na) ratios from 0 to 0.7 (Table 1 and references therein). Unfortunately, no activity model exists for such high ionic strengths, and insufficient data are available for calculating activity coefficients for all species at elevated temperatures. Thus, we are forced to use the extended Debye-Hückel activity model implemented in the Thermoddem database and the GWB software, which is only valid up to 1 molal ionic strength (ca. 3 wt% NaCl). However, for a model created to explore only

the general behavior and evolution of a fluid system and not to predict exact conditions/concentrations, an extrapolation to higher ionic strengths appears justified (Bethke, 2007). In reality, for high ionic strengths, the activity coefficients decrease and then increase, while in the extended Debye-Hückel model they decreases towards higher ionic strength and then nearly stagnate. Thus, by using a concentration of 10 wt% NaCl and 10 wt% $CaCl_2$ in our calculations, we essentially use activity coefficients corresponding to a lower salinity with the heighten activity of Na, Ca, and Cl, which is important for complexes to form. The underestimated activity coefficients imply that the stability fields of all minerals are slightly larger than represented in the figures. However, the difference in activity coefficients between Ni, Co, and Fe species are minimal and often not even considered (Geochemist's Workbench 12), demonstrating that the relative mineral sequence will not be affected by this uncertainty.

Due to the general temperature independence of this mineralization type, and given the fact that, although the temperature range varies between localities, the formation temperature commonly ranges from up to 400 °C down to 200 °C or from as low as 100 °C up to 200 °C, a temperature of 200 °C is chosen as our model parameter. Note that different localities, for example Wittichen and Odenwald, which formed at 150 and 240 °C, respectively, show nearly identical textural features as well as mineralogical and chemical successions (cf. Fig. 3a). The pressure of formation is generally low, both lithostatic and hydrostatic pressures can prevail (e.g., Kissin, 1992), and a pressure-dependence of the mineral stability is within the uncertainty of the thermodynamic data, which is why the pressure along the water–vapor saturation curve at 200 °C is applied.

3.3. Phase diagrams: assemblage vs. predominance

There are several ways how stability fields of minerals are calculated and presented in activity-activity diagrams. Popular are simple predominance stability diagrams, which only consider one predominant species of each element being present on each side of every stability boundary. The drawback of these predominance stability diagrams is that the calculations prohibit an assemblage of several solids and commonly also aqueous species of the same element at the same conditions. Furthermore, a predominance stability diagram is calculated for one specific element (diagram species) in the presence of other speciated elements. This simplification can be problematic, especially in complex multicomponent fluid systems as is the case for native element- arsenide assemblages. For example, in the case at hand, completely different diagrams result depending on whether a transition metal or arsenic is chosen as the diagram species. Specifically, the boundary between the monoarsenide and the diarsenide field has a positive gradient for As and a negative one for Ni as the main species (Fig. 6a). Nevertheless, there are numerous recent papers (including also authors of the present contribution) that interpret ore and gangue mineralogy with respect to parameters such as T, pH, fO_2, fS_2, or element activities based on such predominance stability diagrams.

A more complex approach is that of assemblage stability diagrams, where at each situation in the activity-activity diagram, the abundance of all species of all involved elements is considered in the calculation of the stability fields, and the stability fields of minerals commonly represent the saturation surface instead of the predominance boundary. This diagram type eliminates some of the major drawbacks of predominance stability diagrams. In an assemblage stability diagram, the following points are considered:

(i) Which elements are in excess or in short supply?
(ii) Which and how many aqueous species are present at each pH and fO_2?
(iii) What are the absolute and relative individual species activities?

Consequently, assemblage stability diagrams can deviate significantly from the predominance stability diagrams (Fig. 6a). Since recent literature on native element-arsenide assemblages (Staude et al., 2012, Markl et al., 2016, Kreissl et al., 2018) applied predominance stability diagrams based on the transition metals as the diagram species and the assemblage stability diagram is calculated for a fluid with abundant As compared to Ni, this difference is even more significant. Moreover, since the mineral precipitation starts prior to the fluid path hitting the predominance boundary, the saturation surface in the assemblage stability diagrams is larger than that of the predominance stability field (Fig. 6a).

3.4. Phase diagrams: modelling procedure

For the calculation of assemblage stability diagrams, the Phase2 application of the software package Geochemist's Workbench 12® (Bethke, 2007) is used with a linear stepsize of 0.001 and back-react enabled. The species Cl^- was selected as for charge balancing, generally resulting in Cl content shift of less than 0.2 wt% (pH 1–9) and a maximum shift of 2 wt% of the total initial Cl content which is only present at very high and low pH. Thus, no mass balancing was done, as, over the range of the modelled diagrams, the variations in total mass of the system is negligible. The reaction paths and fluid evolutionary paths have been calculated using the React application of the software package Geochemist's Workbench 12® (Bethke, 2007) and overlain on the assemblage stability fields calculated using Phase 2 for the same conditions. The React application was used with a linear stepsize of 0.0001, back-react enabled and flush disabled to represent a closed system.

3.5. Solid and aqueous species

Due to the high salinity of the fluid, the transition metals Ni, Co, Fe and Ag are transported mainly as chloride complexes, and only under more basic conditions, O and OH complexes become more relevant. Furthermore, under modelled conditions, Ni and Co predominantly occur in their divalent aqueous state whereas both divalent and trivalent Fe can be predominant. The trivalent state becomes more significant under more oxidized and basic conditions, where Fe-OH complexes are stable.

The two most important elements, with respect to oxidation state, to consider for understanding the formation of native element-arsenide assemblages (and also of other hydrothermal systems), are sulfur and arsenic, which have aqueous species of different oxidation and pH state (Fig. 6b). The thermodynamic fO_2 and pH buffer capacity of such aqueous species at their transition reactions depends on the abundance of the respective element and the specific reaction equation. Due to the slow reaction kinetics of sulfur in low-temperature hydrothermal fluids (Ohmoto and Lasaga, 1982), it is only of importance in high temperature native element-arsenide assemblages or where longer retention times of the reducing agent are present. In other words, for the formation of native element-arsenide assemblages, the arsenate-arsenite reaction plays a crucial role in buffering the reduction path to more basic conditions (Fig. 6b). This buffer capacity of arsenate-arsenite is especially of importance when considering the fluid evolution with respect to fO_2-pH reaction path modelling such as reduction.

It should be noted that at the sulfate-sulfide transition, several intermediately reduced dissolved sulfur species such as thiosulfates and sulfites may be present. These intermediate species have been investigated in great detail for low temperature environments (e.g., Jørgensen and Bak, 1991, Habicht et al., 1998). Thermodynamic data for these intermediate species is discussed in Shock et al. (1997), Blanc et al. (2006) and Chivot (2004) are implemented in the Thermoddem database. They predict that these intermediate species are not the predominant sulfur species at the conditions of interest. However, their presence has been considered during thermodynamic calculations. Furthermore, dissolved arsenic-sulfur species (Bessinger and Apps,

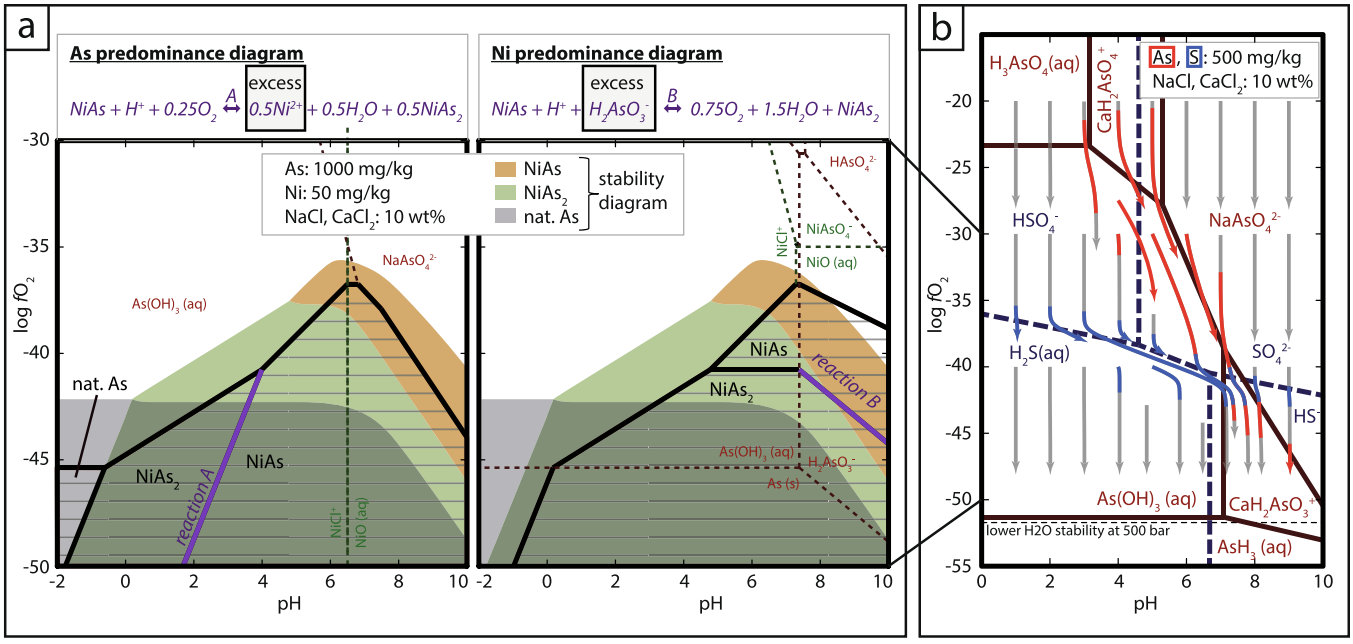

Fig. 6. Stability and predominance diagrams for the Ni-, Co-, and Fe arsenides calculated at 200 °C along the vapour-saturated water pressure curve. (a) log fO_2-pH predominance diagrams, where As (left) and Ni (right) were chosen as the main species for the predominance diagrams. Activities are calculated using GSS. In contrast, the calculation of the stability fields simultaneously considers all aqueous species/complexes and solids that are present at each given fO_2 and pH condition. (b) During fO_2 decrease, the effect of aqueous-aqueous buffers plays a major role in altering the pH of the fluid, shown by this reduction diagram where all mineral species have been suppressed. The arrow magnitude is of no significance but the degree of pH buffering is dependent on the quantity of the specific element being present in the fluid. Red arrows indicate that the fluid path is mainly affected by As-species conversion and blue arrows by S-species conversion. Lines represent predominance boundaries between aqueous species of sulfur (solid and blue) and arsenic (dashed and red). (For interpretation of the references to colour in this figure legend, the reader is referred to the web version of this article.)

2003), which form at reduced conditions in the presence of both sulfide and arsenide, are also considered but are not the predominant dissolved sulfur or arsenic species throughout the whole investigated fO_2-pH range. Their abundance is limited by the formation of sulfide-bearing minerals and the general absence of dissolved sulfide in hydrothermal solutions that form native element-arsenide assemblages.

Marini and Accornero (2007) showed that in typical fluid compositions, metal arsenate complexes may play a major role. According to their thermodynamic parameter estimates of M-AsO_3 and M-AsO_4 complexes in highly saline, oxidized, and neutral-to-basic fluids containing both $CaCl_2$ and NaCl, the Ca and Na arsenate complexes become the dominant arsenic species. Therefore, these species, which were already present in the Thermoddem database, are considered in our thermodynamic modelling. In more reduced and/or more acidic environments, undissociated arsenious acid ($As(OH)_3$) is by far the prevailing dissolved species of arsenic (Marini and Accornero, 2007). Only at significantly more oxidized and/or basic conditions, arsenate species are predominant (Fig. 6b). The stability of the arsenide minerals is not limited to the dissolved arsenide stability. Thus, Ni-, Co- and Fe arsenides form by reduction of an arsenite/arsenate bearing solution.

Since the aim of this study is to produce a generalized formation model of the native element-arsenide mineralization, we cannot incorporate the vast mineralogical complexity into our thermodynamic models. Thus our focus is on the most important mineral occurrences and those that constrain their stabilities. Only the following solid phases are present in our models: $NiAs_2$ (rammelsbergite or para-rammelsbergite), $CoAs_2$ (safflorite), $FeAs_2$ (loellingite), NiAs (niccolite), FeAs (westerveldite), NiAsS (gersdorffite), CoAsS (cobaltite), FeAsS (arsenopyrite), NiS_2 (vaesite), CoS_2 (cattierite), FeS_2 (pyrite and marcasite), NiS (millerite), CoS (jaipurite), FeS (troilite), Bi (native bismuth), Ag (native silver), As (native arsenic), PbS (galena), Bi_2S_3 (bismuthinite), Ag_3AsS_3 (proustite), Ag_2S (acanthite), $AgAsS_2$ (trechmannite or smithite). It should however be noted that other phases, which are not incorporated in the models and not depicted in the figures, such as arsenates and oxides, especially magnetite and hematite, have, to some degree, been considered during the development and interpretation of the models.

The stability fields of the solid sulfides are largely constrained by the stability of aqueous sulfide species, whereas those of the solid arsenides overlie that of the aqueous arsenites. Thus, the Ni-, Co- and Fe-arsenides are stable at much more oxidizing conditions relative to the aqueous arsenide species. Consequently, at roughly equal concentrations of sulfur and arsenic in the fluid, the Ni-arsenides are more stable than the respective sulfides at higher fO_2 values. The thermodynamic modelling reveals that all arsenide, sulfarsenide or sulfide species are only stable under more reduced conditions, relative to the respective aqueous species which are predominant under more oxidizing conditions. This in turn strengthens the process of reduction being essential for the formation of these ores.

4. Genetic model

The following section represents the discussion and implementation of the fundamental formation process of reduction that has been proposed by previous publications (e.g. Markl et al., 2016, Burisch et al., 2017) into a reformed and novel thermodynamic model that is based on all available mineralogical (Section 2) and thermodynamic data (Section 3.1) in combination with empirically and theoretically constrained controlling factors (Sections 3.2–3.4). During the development of the thermodynamic model, specific focus was attributed to the involvement of sulfur during the precipitation of native element-arsenide assemblages Due to major revisions and additions applied, the enhanced and reworked model presented here is only congruent with the previous first order thermodynamic approach by Markl et al. (2016) with respect to the importance of pH and the reduction precipitation sequence of native elements and subsequent arsenides.

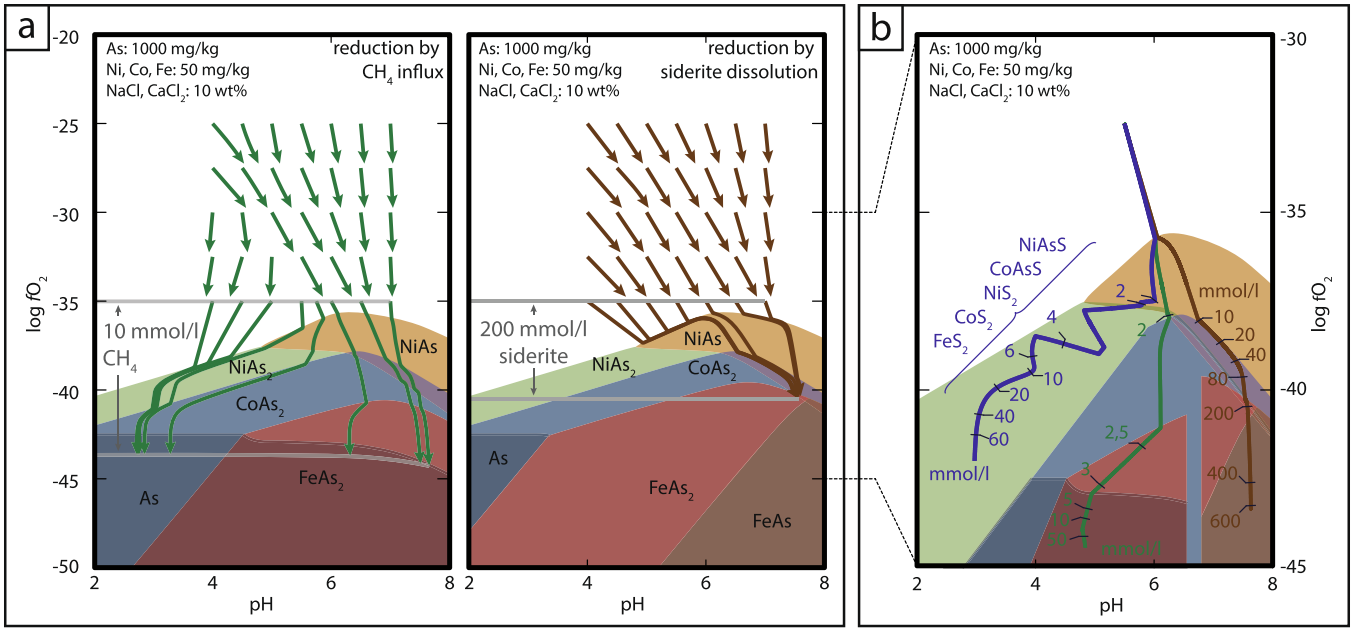

Fig. 7. Reduction mechanisms. Fluid path calculations at 200 °C along the vapour-saturated water pressure curve. Arsenide, but no native metal, precipitation has been considered in these diagrams. Shaded and colored stability fields represent those of Fig. 9a ($NiAs_2$, green; $CoAs_2$, blue; $FeAs_2$ red; NiAs, orange). (a) In red, fluid paths calculated for various initial pH and fO_2 during CH_4 influx and for siderite dissolution. Higher initial fO_2 and pH lead to more basic precipitation conditions due to aqueous species conversion. (b) Comparison of the amount of reducing agent needed between H_2S (blue), CH_4 (green), and siderite (red), and which minerals precipitate. Initial conditions are log fO_2 = -30 and neutral pH. (For interpretation of the references to colour in this figure legend, the reader is referred to the web version of this article.)

4.1. Initial conditions and reduction method

Thermodynamic modelling shows that variable ore textures can be produced at different pH conditions during reduction. The initial pH and redox state of a fluid is generally defined by equilibration with the host rock. During ore formation and subsequent fluid flow, this initial fO_2-pH state changes due to contact with other host rocks (fluid-rock interaction), dissolution of earlier formed minerals, precipitation of new minerals, or by mixing with another fluid. Due to the presence of aqueous buffers such as arsenate-arsenite, both initial pH and initial fO_2 constrain the fluid evolution path. Considering these aqueous buffers, initially more oxidized fluids generally reach a higher pH during reduction (Fig. 6b). Due to the highly variable and unknown degree of involvement of other factors influencing pH and redox conditions during reduction, such as host rock re-equilibration, which could not be incorporated into our models, the fluid evolutionary paths presented here (Fig. 6b and 7) should be considered with care when applied to natural systems. They do however show that the specifics of the fO_2-pH paths also depend on the reduction method, since different reduction agents influence pH differently congruent with the fO_2 decrease (Fig. 7). Several mechanisms have been proposed to be responsible for fluid reduction (Naumov et al., 1971a, Robinson and Ohmoto, 1973, Kissin, 1993, Ondrus et al., 2003a, Markl et al., 2016, Kreissl et al., 2018):

(i) The influx of hydrocarbons or dissolution of graphite;
(ii) Dissolution of Fe^{2+}-bearing minerals such as siderite or Fe^{2+}-bearing silicates;
(iii) The influx of H_2S or the dissolution of sulfides.

4.1.1. Reduction by hydrocarbons or graphite vs. Fe^{2+}-mineral dissolution

As shown by Markl et al. (2016) and Kreissl et al. (2018), the influx of hydrocarbons and the dissolution of graphite or siderite would explain the typical occurrence of carbonates at the end of the arsenide stage by a steady increase of carbon in the fluid. This is in accordance to the findings of Naumov et al. (1971a) who measured an increase in CO_2 partial pressure with successive precipitation. The effect of either rising acidity (methane, graphite) or basicity (siderite) of the fluid is shown by reactions (2)–(5):

$$CH_4 + 2O_2(aq) = H_2O + HCO_3^- + H^+ \quad (2a)$$

$$CH_4 + 2O_2(aq) = 2H_2O + CO_2(aq) \quad (2b)$$

$$C + O_2(aq) + H_2O = HCO_3^- = H^+ \quad (3a)$$

$$C + O_2(aq) = CO_2(aq) \quad (3b)$$

$$4FeCO_3 + 8H^+ + O_2(aq) = 4Fe^{3+} + 4HCO_3^- + 2H_2O \quad (4a)$$

$$4FeCO_3 + 12H^+ + O_2(aq) = 4Fe^{3+} + 6H_2O + 4CO_2(aq) \quad (4b)$$

Since these reactions occur under reduced conditions where $H_2(aq)$ is more abundant than $O_2(aq)$, it should be noted that in the reactions above, $O_2(aq)$ is tied to $H_2(aq)$ by:

$$2H_2O = 2H_2(aq) + O_2(aq) \quad (5)$$

However, no direct spatial correlation between arsenides and the dissolution of pre-existing graphite could be found in individual samples, indicating that graphite is probably not the immediate reducing agent, but acts (if at all) through an intermediate volatile hydrocarbon species produced during fluid-rock interaction distant from the site of reduction. Furthermore, the fluid path of graphite dissolution is very similar to that of CH_4. The defining factor controlling the reduction path, is how much H^+ is consumed or produced relative to O_2 being depleted. The results show that the reduction paths of siderite dissolution and CH_4 influx differ greatly, especially at neutral to acidic pH. The pH-dependence of the mineralization is further amplified by the fact that, at slightly basic conditions, a precipitation of the complete mineralization sequence requires the least quantity of reducing agent.

The process of reduction by Fe^{2+} to Fe^{3+} oxidation is only shown for the example of siderite dissolution (reactions (4a) and (4b)). However, the involvement of Fe^{2+}-silicates is also possible and reactions involving these are for example Fe^{2+}-bearing biotite, amphibole, or pyroxene to Fe^{3+}-bearing epidote, serpentine, or chlorite. These

reactions are typical host rock alteration phenomena for at least some native element-arsenide assemblages (e.g., Jambor, 1971b; Kreissl et al., 2018).

4.1.2. Reduction by sulfide oxidation

A further reduction method is the dissolution of sulfides (Kissin, 1993) or the direct influx of H_2S:

$$H_2S(aq) + 2O_2(aq) = 2H^+ + SO_4^{2-} \quad (6a)$$

$$H_2S(aq) + 2O_2(aq) = H^+ + HSO_4^- \quad (6b)$$

It should be noted that intermediately reduced sulfur species may form as an intermediate step between sulfate and sulfide, but these are not predominantly present in our cases (see Section 3.5). These reactions result in the most acidic fluid evolution (reaction (6a) and (6b); Fig. 7b). However, a reduction due to a sole influx of H_2S seems unlikely, since the predicted precipitation sequence would produce large quantities of sulfides instead of the respective diarsenides (Fig. 7b), which is in contrast to most textural observations. This evolution would not precipitate $CoAs_2$ and $FeAs_2$, which are indicative of most occurrences of this ore type.

An exception may be Kongsberg, which represents a relatively S-rich assemblage where H_2S might be an important reducing agent. This is indicated by the native silver mineralization almost exclusively occurring at the intersections of the calcite veins and the sulfide-enriched fahlbands, the abundance of sulfarsenides and sulfides, and the lack of diarsenides (Kotková et al., 2017 and references therein). In such a case, where H_2S is the reducing agent, base-metal sulfides, sulfosalts and/or Cu-sulfides may be present cogenetic to sulfarsenides. This can also be seen at Kongsberg, where pyrargyrite forms simultaneously with cobaltite and gersdorffite (Kotková et al., 2017). In Ni-, Co-, and Fe-rich hydrothermal systems with an even higher S/As ratio, Ni-, Co-, and/or Fe-sulfides occur together with sulfarsenides (e.g., Zimmerlake area, Northern Saskatchewan; Watkinson et al., 1975). Such Ni-, Co-, and/or Fe-sulfides are, however, even though still rare, more common as minor occurrences in the subsequent sulfide stage due to remobilization (Petruk, 1968).

4.2. Native elements

4.2.1. Native silver and bismuth

Whether the native element part of an assemblage is dominated by native bismuth or native silver, and which of the elements precipitates first in the textural sequence, is not only defined by the metal activity in the fluid, but also by the pH of the solution (Fig. 8). However, considering a roughly neutral pH, as is common for hydrothermal fluid systems, whether a locality is arsenide- or native-metal-dominated is primarily defined by the composition of the fluid (i.e. Ag and Bi vs. Ni, Co, Fe, and As concentration). In highly saline solutions, bismuth forms according to the experimental thermodynamic data (Etschmann et al., 2016) hydroxo- and oxy-complexes at neutral to basic conditions and Cl-complexes at more acidic conditions, whereas silver only forms Cl-complexes within the relevant pH range (< 10). This leads to a differentiation of the stability fields relative to pH; native silver precipitates initially at more basic, native bismuth at more neutral to acidic conditions.

This pH dependence is probably a reason why native bismuth and native silver are rarely intergrown or occur in separate vein systems, which are often characterized by different host rock lithologies (e.g., Keil, 1933, Lipp and Flach, 2003, Ondrus et al., 2003c, Heimig, 2015). It seems unlikely that the intergrowth between Ag and Bi is more common than previously described by various authors. Since both native elements are overgrown by a complete subsequent arsenide sequence (Ni-, Co-, and Fe-arsenides) where the Ni-rich arsenides are more abundant around native silver, while Co-rich arsenides are more abundant around native bismuth (e.g., Keil, 1933, Heimig, 2015); this phenomenon cannot be explained by a reduction of a single homogeneous metal-bearing fluid. Due to this and the fact that the two types of native element occurrences are commonly found in separate veins or ore shoots, within different host rocks (e.g., Keil, 1933, Lipp and Flach, 2003, Heimig, 2015), we propose this to be an effect of locally variable composition of the fluid, where the fluid batch rich in Ag is also more enriched in Ni and the batch rich in Bi is also more enriched in Co. A compositional variability of less than one order of magnitude between Co and Ni suffices to explain the variable abundance between the arsenides, and such a difference can easily be related to variable source rocks or water-rock interaction during ascent. The presence of compositionally variable fluids is however not the case for all localities, as, for example, at Wittichen, intergrowths of both silver and bismuth are present.

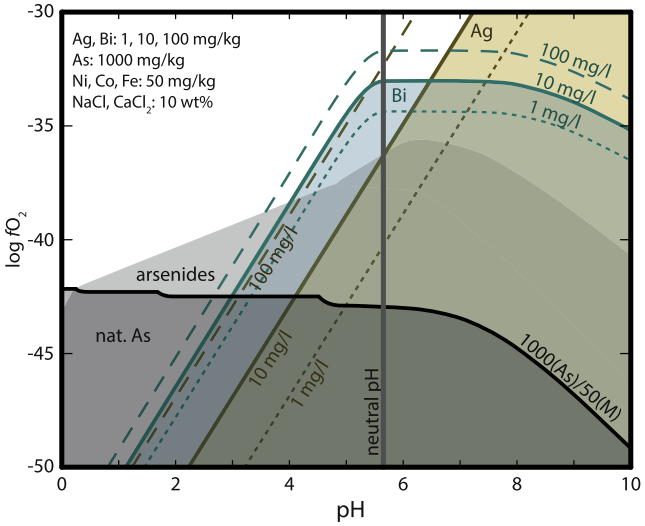

Fig. 8. Stability diagram of the native metals. Calculations are done with respect to variable concentrations in the fluid, at 200 °C along the vapour-saturated water pressure curve. "M" represents the transition metals Ni, Co, and Fe. Shaded area represents arsenide stability of Fig. 9a.

4.2.2. Native arsenic

Native arsenic does not form as the initial phase from a realistic fluid containing Ni, Co, or Fe. According to the model in Fig. 8, only unrealistically acidic fluids (pH < 4.5, < 1.8, and < 0 at 50 mg/kg Fe, Co, and Ni, respectively) are able to precipitate native arsenic prior to the diarsenides upon reduction. The pH-dependence of native arsenic has previously been shown in an FeAsS saturated environment, where native arsenic formed at highly acidic conditions and $FeAs_2$ at more alkaline conditions (Vilor et al., 2014). In accordance with the observations from nature, native arsenic typically forms after/during the late stages of the arsenide mineralization (Fig. 8). Native arsenic is a typical mineral in the post-arsenide, sulfide stage (e.g., Ondrus et al., 2003c; Staude et al., 2012; Heimig, 2015). In special cases, such as in the Odenwald, native arsenic is overgrown by loellingite and thus forms during the final arsenide sequence (Heimig, 2015; Burisch et al., 2017). This implies that either (i) native arsenic precipitated from an initially transition metal-poor fluid; (ii) kinetics permitted native arsenic to form while suppressing arsenide precipitation; or (iii) the native arsenic formed after safflorite and before loellingite by an acidic fluid (Fig. 9). We interpret the reported data as suggesting the latter.

4.3. Arsenides & sulfarsenides

4.3.1. Arsenides: mono- vs. di- vs triarsenides

The only monoarsenide commonly occurring in native element-arsenide assemblages is the Ni-monoarsenide, niccolite. At neutral to

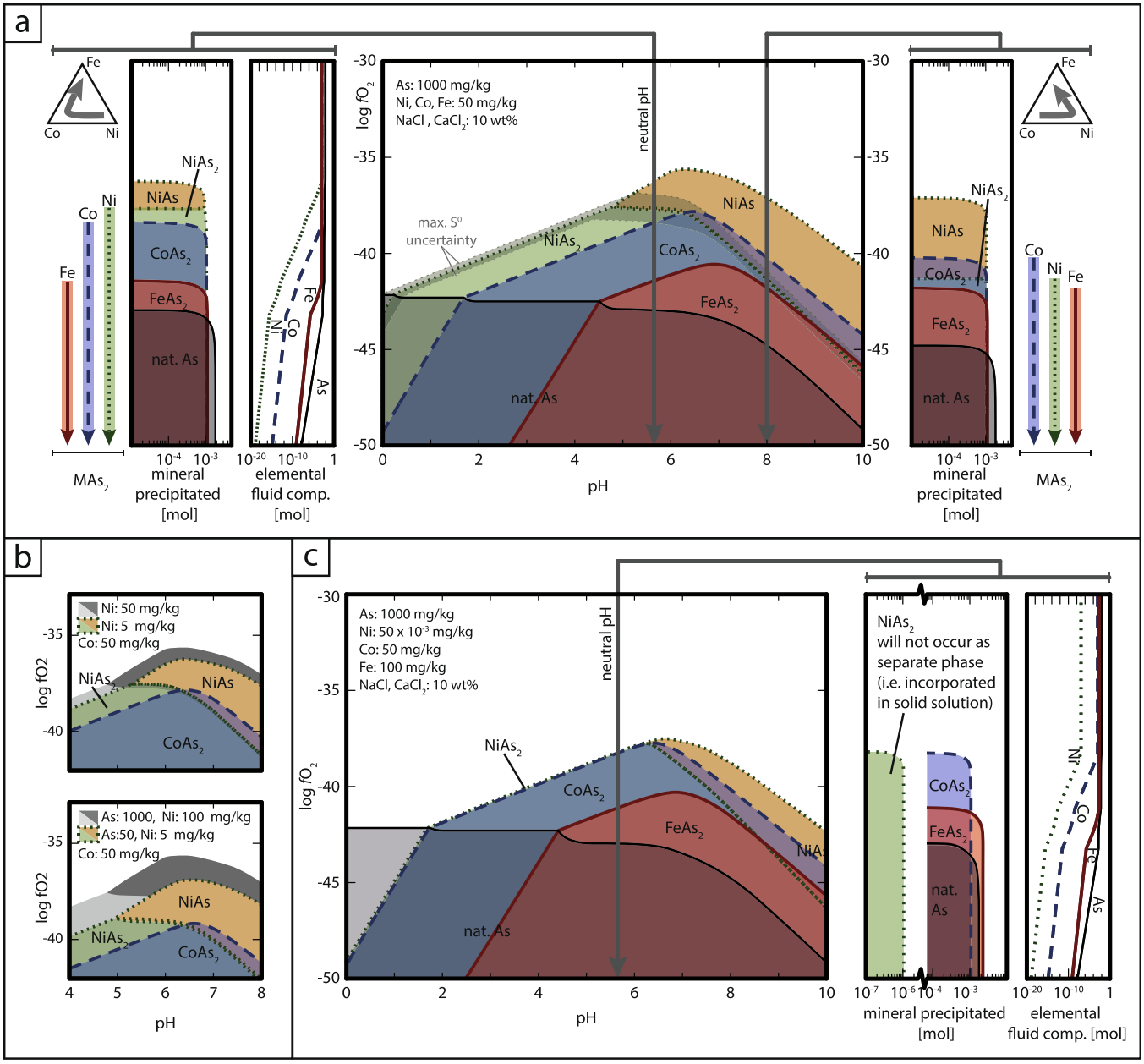

Fig. 9. The stability of the arsenide. Stability diagrams for the Ni-, Co-, and Fe arsenides calculated at 200 °C along the vapour-saturated water pressure curve. (a) log fO_2-pH stability diagram at equal Ni, Co, and Fe content with two cross sections (one at neutral pH and one at pH 8) show the pH dependent diarsenide sequence. The monoarsenide is favored over the diarsenide at higher pH and fO_2. (b) The effects of the fluid composition on the arsenide stability fields by the example of the nickel system. A lower As and Ni content alters the overall stability boundary to lower fO_2 values where the location of the stability boundary between the mono- and diarsenide is only dependent on the As content. (c) log fO_2-pH stability diagram for a fluid strongly depleted in Ni and slightly enriched in Fe relative to the concentrations of Fig. 5a. The results show that Ni has to be depleted so strongly relative to Co to alter the transition metal sequence, so that no independent $NiAs_2$ would form.

basic conditions, NiAs is the earliest arsenide, whereas at more acidic and more reducing conditions, $NiAs_2$ (rammelsbergite or para-rammelsbergite) forms (Fig. 9a). The position of the boundary between the mono- and diarsenide stability fields relative to fO_2 and pH is defined by the As content of the fluid, whereas the Ni content only affects the overall stability of the Ni-arsenides (Fig. 9b). This can be used to understand the stability relations of the triarsenides (e.g., skutterudite), for which thermodynamic data are lacking. Its stability field must lie at more reducing and more acidic conditions than that of the diarsenide, and the position of the di- and triarsenide boundary is defined by the equilibrium constant as well as the arsenic activity of the fluid. The reaction that defines this boundary is:

$$4\,NiAs_3 + 6\,H_2O + 3\,O_2(aq) = 4\,NiAs_2 + 4\,As(OH)_3(aq) \quad (7)$$

which is contrary to the suggestions made by Markl et al. (2016) and Kreissl et al. (2018). This is due to the discrepancy as to whether arsenic or the transition metals are the limiting agents within the fluids (Fig. 6a).

4.3.2. Diarsenides: the Ni-Co-Fe sequence

The overall precipitation sequence of arsenides in most occurrences is Ni → Co → Fe. This general trend has been described for the arsenides and/or sulfarsenides at most occurrences and has been explained by a genetic model where the geochemical trend reflects the temporal evolution of a hydrothermal system that is depleted in specific elements in

the hydrothermal fluid due to precipitation (e.g., Bouabdellah et al., 2016). Markl et al. (2016) proposed that this chemical trend could be achieved by re-equilibration of the pH due to host rock buffering. Our model, however, shows that a simple reduction is sufficient to produce this sequence. At mildly basic to acidic conditions, the sequence is $NiAs_2 \rightarrow CoAs_2 \rightarrow FeAs_2$, whereas at strongly basic conditions the sequence changes to $CoAs_2 \rightarrow NiAs_2 \rightarrow FeAs_2$ (Fig. 9a). This change depends on the fact that the stability boundaries between $NiAs_2$-NiAs and $CoAs_2$-CoO(aq) have different fO_2-pH gradients, and CoO(aq) is the most relevant Co species at pH > 6.5. As long as the fluid contains Ni, the transitional pH is primarily dependent on the As and Co content of the fluid. A $CoAs_2 \rightarrow NiAs_2 \rightarrow FeAs_2$ trend at neutral to acidic pH is not possible since it would require Co:Ni ratios in the fluid to be > 1000, which considering the presence of solid solutions, would result in precipitation of nearly pure Co-arsenides and no Ni-arsenides (Fig. 9b, c). Thus, explaining why the first sequence is the most common (e.g., Erzgebirge, Odenwald, Bou Azzer, and Ontario) and the second one only rarely occurs in nature (e.g., Pirineos and Valais). The necessary basic environment for the latter at the Valais locality is related to siderite dissolution (Kreissl et al., 2018), and in the Pirineos might be attributed to the presence of abundant carbonates in the host rock. Other diarsenide sequences deviating from the common evolution, such as those from Dôbsína (mostly NiAs2 → FeAs2; Kiefer et al., 2017) compensate the lack of intermediate $CoAs_2$ by the abundant precipitation of Co-dominated triarsenides and/or sulfarsenides or the relative lack of either Ni, Co, or Fe in the primary hydrothermal fluid.

The model implies that the main precipitation stage of each diarsenide is a narrow region at slightly lower fO_2 than the stability field boundary (see the log fO_2 profiles in Fig. 9). This, however, reflects the lack of thermodynamic data for the solid solutions and does not represent the actual ore formation process. The natural occurrences show a gradual chemical transition among the end members. If all three elements (Ni, Co, and Fe) are not present in approximately the same order of magnitude, the arsenides of those elements with the least abundance will be incorporated into a solid solution of the other arsenides and not form individual minerals. These solid solutions, however, still represent the overall geochemical trends as has been shown for Valais and for individual samples of the Odenwald (Heimig, 2015; Kreissl, 2018).

Due to the stability of hematite and magnetite at neutral to basic conditions, Fe would be relatively insoluble and only minor amounts of Fe-arsenides would form from such solutions. Magnetite is, however, only present at very few occurrences within the arsenide stage, and hematite is only present in small quantities (e.g., Oen et al., 1984; von Bargen, 1993; Staude et al., 2012; Kreissl, 2018). Thus, due to the large quantities of loellingite present in some veins and due to the rapid formation of these ores (Markl et al., 2016), the typical native element-arsenide assemblage fluid must carry large quantities of Fe. This could be explained by the presence of abundant carbon and the stability of aqueous Fe-CO_3 complexes instead of the Fe-oxides at neutral to basic pH, as is predicted by the thermodynamic data from (Chivot, 2004). Fe-arsenate complexes further promote the mobility of Fe (Marini and Accornero, 2007; Chai et al., 2017). Furthermore, a deviation and significantly higher solubility of Fe than is predicted by Fe-oxide and Fe hydroxide stability was also experimentally present in Fe-As solutions (Pokrovski et al., 2002).

4.3.3. Diarsenides: microenvironments

The complete arsenide-sequence Ni → Co → Fe is not always visible in individual samples and aggregates, especially on a scale of several tens to hundreds of μm, where partial repetitions or more complex trends are common (Fig. 4d–f). An ideal example of such small-scale compositional variations in contrast to the overall trend is given by the assemblages in the Cobalt-Gowganda region (Fig. 10): The paragenetic sequence of the ore minerals (Fig. 3b) and the spatial and temporal transition of distinct ore zones within the veins (Ni-As → Ni-Co-As → Co-As → Co-Fe-As → Fe-As; Fig. 10) demonstrates the evolution from Ni to Co to Fe, which is not represented in all small-scale profiles of individual aggregates (Fig. 10b).

This apparent discrepancy may be explained by considering the hydrothermal arsenide system not as a homogenous fluid batch, but as a sum of individual small-scale fluid systems that have locally slightly variable conditions. These variabilities in elemental composition, pH, and/or redox state can be caused for example by mineral precipitation linked to the local influx of a reducing agent. The kinetically controlled skeletal textures and the typical occurrence of ore shoots rather than of homogeneously distributed ores in a vein system (Markl et al., 2016) provide evidence of local changes in reduction potential.

4.3.4. Sulfarsenides

Some occurrences (e.g., Dobšiná, Kiefer et al., 2017, Kongsberg, Kotková et al., 2017, , Valais, Kreissl et al., 2018; Fig. 3c) are characterized by the predominance of sulfarsenides over arsenides. The estimated thermodynamic data of the sulfarsenides indicate that the formation sequence of the sulfarsenides with progressive reduction is NiAsS → CoAsS → FeAsS (Fig. 11a). The exact sulfarsenide composition is determined by the stage during which the sulfide influx occurs (and thus, which of the metals have been depleted and which are still present), as well as by the mineral that is being replaced. Furthermore, secondary sulfarsenides typically show replacement textures (e.g., Fanlo et al., 2006; Kiefer et al., 2017; Kreissl et al., 2018), which probably correspond to circulating fluids of the post-native element-arsenide assemblage, sulfide, or the late arsenide stage. Gersdorffite occurs at more reducing conditions than niccolite and thus forms subsequent to it, which is in agreement with textural observations from sulfarsenide-dominated deposits such as Pirineos, Kongsberg and Valais (Fanlo et al., 2004; Kotková et al., 2017; Kreissl, 2018, respectively).

The solubility of the arsenides is several orders of magnitudes higher than that of the sulfarsenide, as was experimentally shown for the Fe system by Perfetti et al. (2008). Thus, even if small quantities of sulfide are present (e.g., 1 mg/kg), the sulfarsenide stability fields cover those of the arsenides, and NiAsS, CoAsS, or FeAsS crystalize with the diarsenides (Fig. 11a). At higher sulfide content, the sulfarsenides form instead of the respective diarsenides. Since the arsenides dominate over the sulfarsenides at most localities, the ore-forming solution must be generally poor in reduced sulfur (Kissin, 1992). Due to the common occurrence of sulfarsenides as layers within zoned aggregates, it is likely that these textures represent a local and short-lived increase of the sulfide activity in an otherwise sulfide-deficient solution. An increase in aqueous sulfide that results in the formation of sulfarsenides and/or sulfides may be due to remobilization of sulfide from the host rock (sulfide-rich fahlbands are a common feature at several localities (e.g., Petruk, 1968; Kotková et al., 2017; Kreissl et al., 2018), due to an influx of a sulfide-rich fluid into the system, or due to dissolution of earlier (pre-native element-arsenide mineralization) sulfides in the vein.

An example of such an increase in sulfide activity by minor dissolution of earlier pyrite in the vein (Fig. 11b) has been documented from the Odenwald deposit (Heimig, 2015). By the incorporation of large quantities of As into the Ni-sulfarsenide, it becomes stable at much lower sulfide content than the Co-sulfarsenide, which can be seen by the example of Fig. 11b where the Co-diarsenide forms instead of the Co-sulfarsenide after the Ni-sulfarsenide, during a continuous sulfur increase. Thus, the variation in the As content of gersdorffite can provide qualitative information about the sulfide content in the fluid; a higher As content in gersdorffite correlates with a lower sulfide content in the fluid.

4.4. The sulfide enigma

The common presence of arsenides, sulfarsenides, sulfides and sulfosalts in combination with a gradual transition from an arsenide to

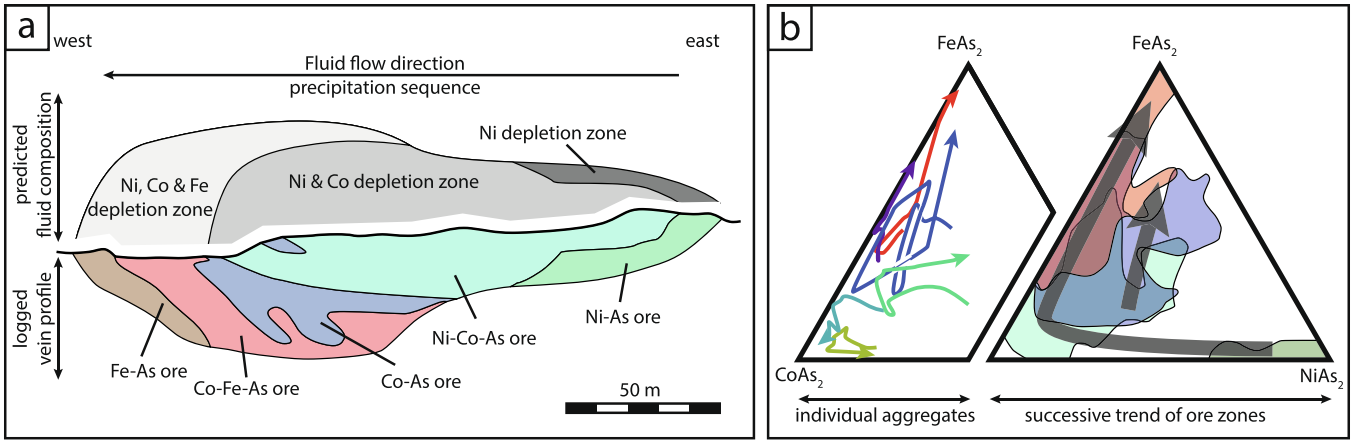

Fig. 10. Small scale complexities revealed. (a) Sketch of a vein profile of the Silverfields deposit in Ontario, modified after Petruk (1968). The resulting Ni → Co → Fe trend is in accordance with the paragenetic sequence, indicating a general progressive precipitation from East to West (Fig. 3b). (b) This general trend from Ni → Co → Fe is not always present in small-scale trends of individual aggregates of samples from the Cobalt-Gowganda region as shown by Petruk et al. (1971).

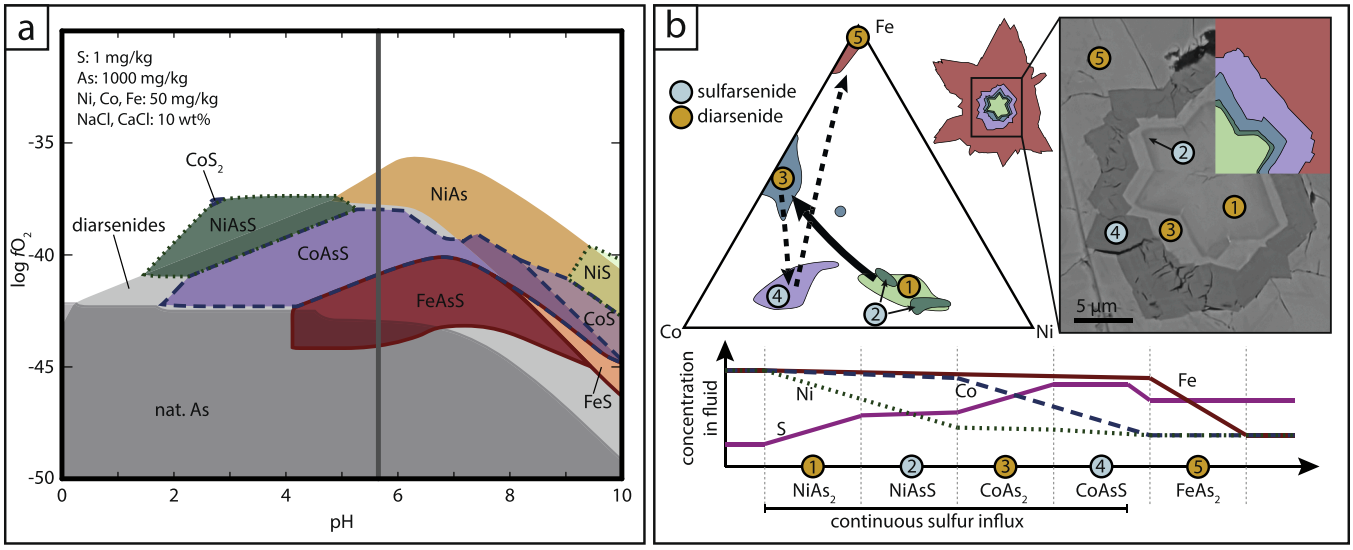

Fig. 11. Local influx of sulfur. (a) Calculated stability fields of sulfur-bearing species at 200 °C along the vapour-saturated water pressure curve. Shaded area represents the diarsenide stability. (b) Shown is an example of a small-scale sulfide influx into the otherwise arsenide-dominated and sulfide-barren system from a sample of Heimig (2015) with additional EDX analysis.

sulfide dominated assemblage provides a key process in understanding the formation of hydrothermal native element-arsenide assemblages. This temporal skew between arsenide and sulfide is explained by the novel approach, combining thermodynamic and kinetic effects.

To understand the gradual transition of the arsenide-native element stage to the subsequent sulfide stage, one has to keep in mind that the stability of sulfides depends on the stability of aqueous sulfide in solution. However, the aqueous sulfate-sulfide transition is at more reduced conditions than the typical formation conditions of the Ni-arsenides. As shown in Fig. 12, the stability fields of the representative sulfides (e.g. galena, bismuthinite, and proustite) overlie those of the arsenides and sulfarsenides. This also holds true for native arsenic and realgar or orpiment (Vilor et al., 2014). This shows that a complete arsenide sequence (Ni → Co → Fe) with native metals and without sulfides cannot form under equilibrium conditions if sulfur is present, since only sulfarsenides and base-metal sulfides as well as Ag-, Ni-, Co-bearing sulfides would form instead of the Co- and Fe-arsenides and native elements (Fig. 12). It has been proposed that a short-termed introduction of hydrocarbons into an normal mixing scenario between a metal bearing fluid and a sulfide bearing fluid, which would otherwise form a base metal assemblage, produces the five element assemblages with a subsequent re-equilibration to the base metal assemblage (Burisch et al., 2017). This would however, thermodynamically, result in an absence of Co- and Fe arsenides and instead a presence of sulfarsenides and sulfides. Thus, the sulfide activity is limited during the arsenide stage and has to increase towards the sulfide stage.

In some native element-arsenide systems, such as Wittichen and Schneeberg, the fluid must have been rich in sulfur, specifically in sulfate, due to the occurrence of large quantities of barite together with and overgrowing the arsenides (Lipp and Flach, 2003; Staude et al., 2012). This can only be explained by the kinetically controlled process of sulfate to sulfide reduction, which occurs at a relatively low rate in low-temperature hydrothermal systems (< 200 °C; Ohmoto and Lasaga, 1982) as is the case for these localities. Due to the fast process of precipitation by reduction, indicated by the typical dendritic growth textures (Markl et al., 2016), the kinetics of sulfate reduction are important up to temperatures well above 200 °C. This is in agreement with the sulfur isotope study of Robinson and Ohmoto (1973) on native element-arsenide occurrences near the Great Bear Lake, which concluded that sulfur was present in the initial fluid and was successively reduced during the arsenide and sulfide stage.

We propose that the kinetics of arsenite or arsenate to arsenide

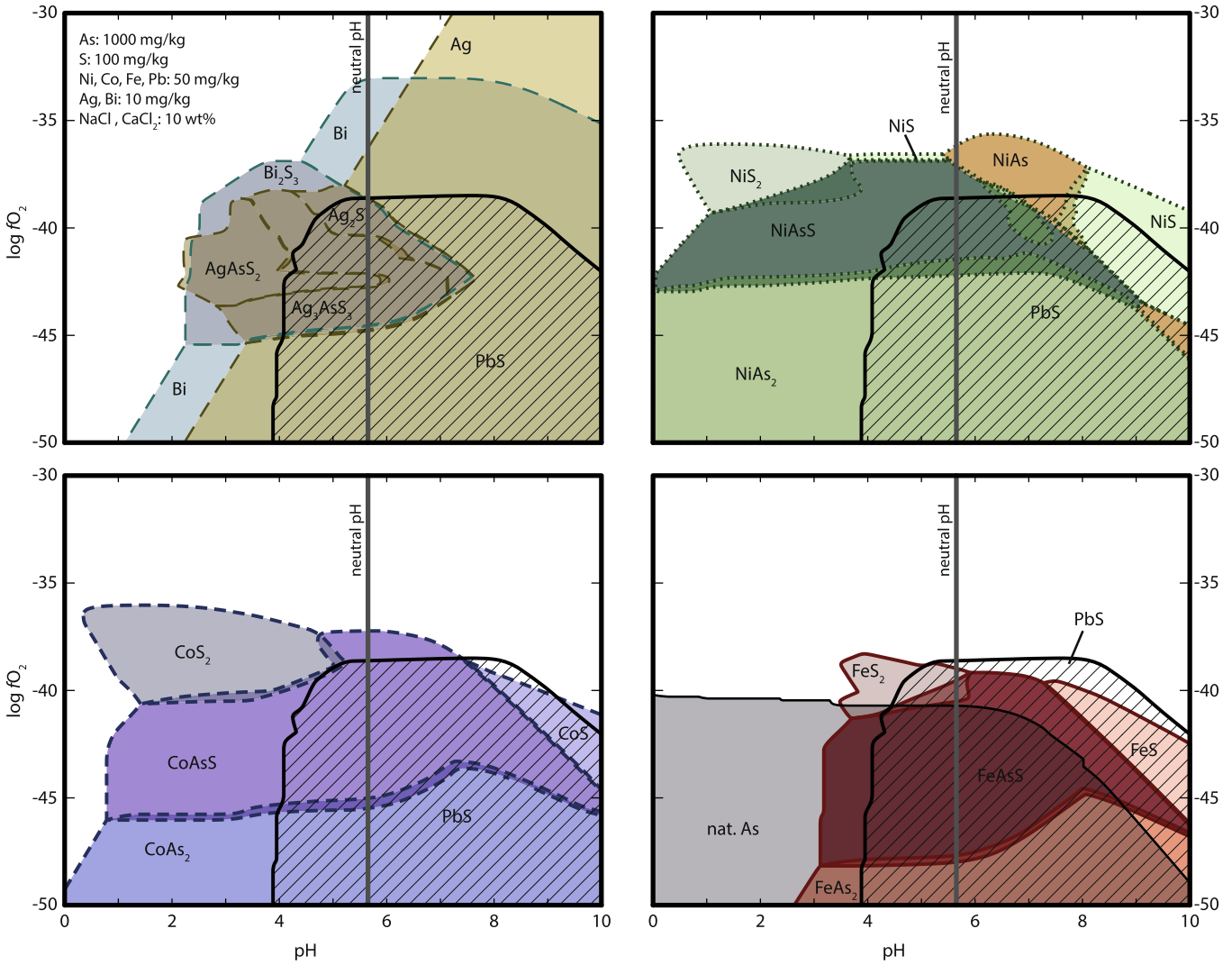

Fig. 12. The effect of sulfide. Stability diagram for the Ag-Bi-Fe-Co-Ni-As-S-Pb-Na-Ca-Cl system calculated at 200 °C along the vapour-saturated water pressure curve. The diagram has been subdivided into 4 subplots for a clearer representation. However, the 4 subplots are to be overlain to understand the complex system since the mineral stability fields overlap. Galena (PbS; hatched field) is presented as a representative mineral stability field for other base-metal sulfides.

reduction is much faster than the sulfate to sulfide reduction, and that the typical native element-arsenide mineralogy is stabilized by a combination of kinetic and thermodynamic effects. The slower reduction kinetics for oxidized sulfur species relative to oxidized arsenic species may be attributed to the significantly more stable intermediately reduced species for arsenic, arsenite, than for sulfur, e.g. sulfite and thiosulfate, and the resulting predominance of arsenite at intermediately reduced conditions (Fig. 6b). Thus, the reduction of arsenic occurs with an intermediate step and the difference in oxidation state is less. Native element-arsenide assemblages formed at higher temperatures (e.g., 400 °C), may, however, require a primarily sulfur-free fluid.

Even at low temperatures, sulfate will be reduced to sulfide in time, and, hence, sulfarsenides commonly appear in larger quantities at the final phase of the arsenide stage and in the succeeding sulfide stage. Increasing sulfide activities in the fluid also stabilize Ag- and Bi-sulfides and -sulfosalts relative to native silver and Bi, which is why these elements are commonly dissolved (see Fig. 2f) and reprecipitated as sulfosalts and sulfides in the late stages of the native element-arsenide evolution (see Fig. 2d). Also, the stability field of millerite (NiS) increases with increasing sulfide activity, and this phase occurs in sulfide-rich, basic localities such as the Valais (Kreissl et al., 2018). For most other localities, Ni- and Co-sulfides are commonly lacking since these elements have been depleted by arsenide precipitation before sufficient sulfide is present. Finally, elements that do not or rarely form arsenides in nature, such as Cu, Pb and Zn (Markl et al., 2016), precipitate as sulfides, only after sufficient sulfur is reduced or after sulfide influx occurred.

5. Conclusions

A comprehensive review of textural and mineral chemical observations from dozens of hydrothermal native element-arsenide (i.e. five-element) assemblages worldwide, combined with revised and novel thermodynamic calculations, allowed us to identify the key aspects of the formation and textural evolution of these hydrothermal Ni-Co-Fe arsenide bearing deposits. The mineralization sequences present in all localities form by simple reduction of fluids quite variable in salinity, metal content, initial pH/fO_2, and reducing agents. Other processes besides reduction, such as dilution of salinity of the metal-bearing fluid by mixing, cooling, boiling, or fluid-rock interaction, are not essential for the formation of these ores. A key factor to suppress the precipitation of sulfides or sulfarsenides, however, appears to be the more sluggish reaction kinetics of the sulfate to sulfide reduction compared to the arsenate/arsenite to arsenide reduction. Hence, the formation of native element-arsenide assemblages depends on both kinetic and thermodynamic effects, where the arsenide and native element

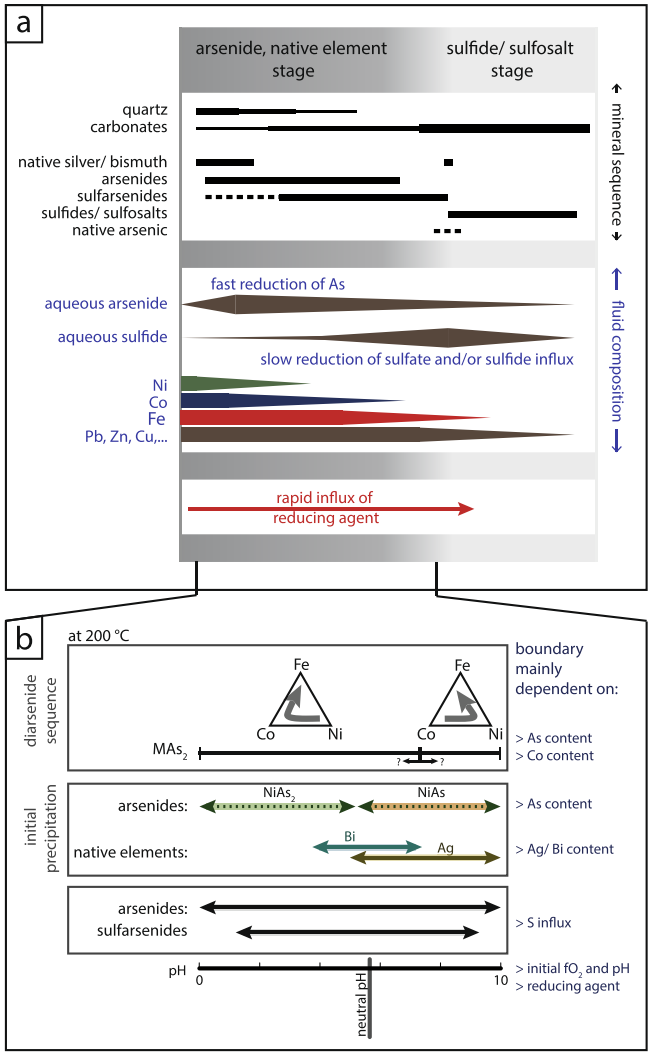

Fig. 13. Simplified qualitative conclusion model. (a) The evolution of the fluid composition with respect to a generalized paragenetic sequence of both the arsenide and the transition to the sulfide stage. (b) Presentation of the parameters, controlling the individual characteristics of ore shoots, samples, and aggregates of the arsenide stage.

sequence is defined by the thermodynamics, and the absence of sulfides and transition towards the sulfide stage by kinetics. The textural evolution in a sulfide-deficient system can, however, be thermodynamically modelled since we can partially restrict the availability of sulfide, which is the kinetically controlled factor (Fig. 13a).

The mineral sequence of a native element-arsenide assemblage depends primarily on the pH during reduction (Fig. 13b), which is defined by

- the initial pH and fO_2 of the fluid, and
- the type of reducing agent,

while the variable abundance of different arsenides, sulfarsenides, and native elements depends on:

- the relative and absolute elemental abundances in the ore forming fluids.

When considering the reduction paths, not only aqueous-solid buffers but also aqueous-aqueous buffers have to be considered. Therefore, an arsenic-rich, initially oxidized fluid is forced towards more basic conditions during reduction.

The compositional sequence of the diarsenides is generally Ni → Co → Fe; only under strongly basic conditions is the sequence Co → Ni → Fe observed. Small-scale variations of these sequences as well as oscillatory mineralogical repetitions are attributed to microenvironments and the spatially restricted influx of the reducing agents. The initial formation of either NiAs or $NiAs_2$ is determined by pH and the arsenic activity of the fluid. Furthermore, the pH also defines the precipitation sequence of native bismuth and native silver relative to that of the arsenides. If the fluid contains large enough quantities of Bi and Ag, native silver initially precipitates under more basic, native bismuth under neutral to acidic conditions. The preferred association of native silver with Ni-arsenides and of native bismuth with Co-arsenides observed at some localities is attributed to variable initial fluid compositions, probably imposed by variable host or source rocks.

Sulfarsenides are stable over most of the relevant pH range, and their presence generally indicates an increase of the sulfide activity in the metal-bearing solution. The composition of the sulfarsenides is a result of the relative timing of this sulfide activity increase, as this determines which elements have already been depleted and which are still present in the fluid. The stability field sequence Ni → Co → Fe observed for the diarsenides during reduction is also valid for the sulfarsenides. The Ni-sulfarsenide gersdorffite can incorporate large quantities of As and forms a continuous solid solution towards the Ni-diarsenides, whereas the other sulfarsenides are close to stoichiometric (As/S = 1).

The general predominance of arsenides relative to sulfarsenides and the lack of sulfides in the arsenide stage of native element-arsenide assemblages, in conjunction with the thermodynamic argument that sulfarsenides and sulfides form together and/or instead of arsenides if sulfide is present, indicates the general absence of aqueous sulfide in the fluid, thus implying that sulfur is either absent or only present in an oxidized state during the arsenide stage. The evolution from the arsenide stage towards the subsequent sulfosalt stage is related to either an influx of sulfide, or the gradual reduction of sulfate to sulfide during the precipitation of the arsenides. Due to the increase in sulfide activity, base-metal sulfides such as sphalerite and galena can form, and arsenides as well as native metals are partially dissolved and redistributed into sulfarsenides and sulfosalts. This, in turn, implies that the native element-arsenide mineralization stage did not evolve from a fluid that previously formed base-metal sulfide-bearing veins, but rather formed from a Ni-, Co-, Fe-, and As-rich oxidized fluid batch.

Acknowledgements

A special thanks is given to Philippe Blanc for implementing the discussed thermodynamic properties of the investigated minerals into the Thermoddem database. Furthermore, Samuel Scharrer is specifically acknowledged and thanked for developing a computer program to simplify the process of producing stability diagrams from rastered constant pH paths from GWB for a previous version of the manuscript. We thank Wolfgang Bach for the insightful hints on kinetics and thermodynamic calculations. Thomas Wenzel, Sebastian Staude, Udo Neumann and Samuel Scharrer are thanked for reviews and literature additions. Furthermore, Sebastian Staude is thanked for supplying information and discussions about the Schwarzwald five-element veins. We acknowledge the PhD Thesis of Virgle Roland Goodgame for being an inspiration on estimating thermodynamic data of the arsenides and sulfarsenides. Furthermore, we thank the editor in chief Franco Pirajno and associate editor Thomas Blenkinsop as well as two annonymous reviewers for constructive critisism on the manuscript. Lastly we acknowledge Thomas Seifert and an annonymous reviewer for feedback on a previous version of the Manuscript. Part of this research was achieved by the Deutsche Forschungsgemeinschaf, Germany, MA 2135/25-1 grant.

Appendix A

A.1. Mineral analyses

The present contribution mostly relies on the compilation of literature data on all five-element-type occurrences where chemical compositions are available (Table 1). In some cases, where no compositional data are available, but the paragenetic sequence was well documented, and thin sections existed at Tübingen University (arsenides and sulfarsenides from Schneeberg/Germany and Schladming/Austria; sulfarsenides from the Odenwald). About 250 mineral analyses were performed using the EDX system of a HITACHI TM3030 Plus SEM at the Fachbereich Geowissenschaften, University Tübingen. Analyses are in wt% and normalized to 100%. For the ternary diagrams, the composition was calculated on total atoms per formula unit (2 for monoarsenides, 3 for di- and sulfarsenides and 4 for triarsenides).

Appendix B. Supplementary data

Supplementary data to this article can be found online at https://doi.org/10.1016/j.oregeorev.2019.103025.

References

Ahmed, A.H., Arai, S., Ikenne, M., 2009. Mineralogy and paragenesis of the Co-Ni arsenide ores of Bou Azzer, Anti-Atlas, Morocco. Econ. Geol. 104, 249–266. https://doi.org/10.2113/gsecongeo.104.2.249.

Badham, J., 1975. Mineralogy, paragenesis and origin of the Ag-Ni, Co arsenide mineralisation, Camsell River, NWT Canada. Miner Deposita 10, 153–175. https://doi.org/10.1007/BF00206530.

Badham, J., 1978. Magnetite-apatite-amphibole-uranium and silver-arsenide mineralizations in lower Proterozoic igneous rocks, East Arm, Great Slave Lake, Canada. Econ. Geol. 73, 1474–1491. https://doi.org/10.2113/gsecongeo.73.8.1474.

Badham, J., Muda, M., 1980. Mineralogy and paragenesis of hydrothermal mineralisations in the East Arm of Great Slave Lake. Econ. Geol. 75, 1220–1226. https://doi.org/10.2113/gsecongeo.75.8.1220.

Bagheri, H., Moore, F., Alderton, D., 2007. Cu–Ni–Co–As (U) mineralization in the Anarak area of central Iran. J. Asian Earth Sci. 29, 651–665. https://doi.org/10.1016/j.jseaes.2006.03.011.

Bailey, M., 2017. Ore Mineralogy and Uraninite Trace Element Chemistry of Hydrothermal Polymetallic U-Ag-(Co-Ni-As-Bi-Sb-Cu) Vein Deposits, Eldorado Mine, Port Radium, NWT. Unpublished MSc Thesis. Saint Mary's University, Halifax, Nova Scotia, pp. 54.

Barin, I., 1995. Thermochemical Data of Pure Substances, third ed. Wiley-VCH, New York.

Bastin, E.S., 1922. Primary native-silver ores near Wickenburg, Arizona and their bearing on the genesis of the silver ores of Cobalt, Ontario. U.S. Geol. Surv. Bull. 735, 25.

Bastin, E.S., 1939. The nickel-cobalt-native silver ore type. Econ. Geol. 34, 40–79. https://doi.org/10.2113/gsecongeo.34.1.1.

Bastin, E.S., 1949. Deposition and resolution of native silver at Gowganda, Ontario. Econ. Geol. 44, 437–444. https://doi.org/10.2113/gsecongeo.44.5.437.

Bastin, E.S., 1950. Significant replacement textures at Cobalt and South Lorraine, Ontario, Canada. Econ. Geol. 45, 808–817. https://doi.org/10.2113/gsecongeo.45.8.808.

Baumann, L., Kuschka, E., Seifert, T., 2000. Lagerstätten des Erzgebirges. Enke, Stuttgart, pp. 303.

Bessinger, B., Apps, J.A., 2003. The Hydrothermal Chemistry of Gold, Arsenic, Antimony, Mercury and Silver. U.S. Department of Energy, LBNL-57395, pp. 52.

Bethke, C.M., 2007. Geochemical and Biogeochemical Reaction Modeling, second ed. Cambridge University Press, pp. 564.

Blanc, P., 2008. Sélection de Propriétés Thermodynamiques Pour les Principales Espèces Aqueuses et Minérales Porteuses de fer. Thermoddem Report, RP-56587-FR,. BRGM, pp. 70.

Blanc, P., 2017. Update for the 2017 Version. BRGM, pp. 20 Thermoddem Report RP-66811-FR.

Blanc, P., Gaboreau, S., 2013. Sélection de Propriétés Thermodynamiques pour les Principales Espèces Aqueuses et Minérales Porteuses de Nickel. BRGM, pp. 35 Thermoddem Report RP-61871-FR.

Blanc, P., Lassin, A., 2013. Sélection de Propriétés Thermodynamiques pour les Principales Espèces Aqueuses et Minérales Porteuses d'arsenic. BRGM, pp. 29 Thermoddem Report RP-62585-FR.

Blanc, P., Lassin, A., Piantone, P., Azaroual, M., Jacquemet, N., Fabbri, A., et al., 2012. Thermoddem: a geochemical database focused on low temperature water/rock interactions and waste materials. Appl. Geochem. 27, 2107–2116. https://doi.org/10.1016/j.apgeochem.2012.06.002.

Blanc, P., Piantone, P., Lassin, A., Burnol, A., 2006. Selection de Constantes Thermodynamiques Pour les Elements Majeurs, le Plomb et le Cadmium. BRGM, pp. 151 54902-FR.

Borisenko, A., Pavlova, G., Borovikov, A., Obolenskiy, A., 1999. Ag-Sb deposits of the Yustid depression, eastern Russia and northwest Mongolia. Int. Geol. Rev. 41, 639–664. https://doi.org/10.1080/00206819909465163.

Bortnikov, N., Gamyanin, G., Vikent'Eva, O., Prokof'ev, V.Y., Alpatov, V., Bakharev, A., 2007. Fluid composition and origin in the hydrothermal system of the Nezhdaninsky gold deposit, Sakha (Yakutia), Russia. Geol Ore Deposit. 49, 87–128. https://doi.org/10.1134/S1075701507020018.

Bouabdellah, M., Maacha, L., Levresse, G., Saddiqi, O., 2016. The Bou Azzer Co–Ni–Fe–As (± Au ± Ag) district of Central Anti-Atlas (Morocco): A long-lived late Hercynian to Triassic magmatic-hydrothermal to low-sulphidation epithermal system. In: Bouabdellah, M., Slack, J.F. (Eds.), Mineral Deposits of North Africa. Springer, Cham, Switzerland, pp. 229–247.

Boyle, R., Dass, A., 1971. The origin of the native silver veins at Cobalt, Ontario. In: Berry, L.G. (Ed.), The Silver-Arsenide Deposits of the Cobalt-Gowganda Region, Ontario. Mineralogical Association of Canada, Quebec, pp. 414–429.

Buchrucker, L., 1891. Die mineralien der erzlagerstätten von leogang in salzburg. Z. Krist.-Cryst. Mater. 19, 113–166. https://doi.org/10.1524/zkri.1891.19.1.113.

Burisch, M., Gerdes, A., Walter, B.F., Neumann, U., Fettel, M., Markl, G., 2017. Methane and the origin of five-element veins: mineralogy, age, fluid inclusion chemistry and ore forming processes in the Odenwald, SW Germany. Ore Geol. Rev. 81, 42–60. https://doi.org/10.1016/j.oregeorev.2016.10.033.

Chai, L., Yang, J., Zhang, N., Wu, P.-J., Li, Q., Wang, Q., et al., 2017. Structure and spectroscopic study of aqueous Fe (III)-As (V) complexes using UV–Vis, XAS and DFT-TDDFT. Chemosphere 182, 595–604. https://doi.org/10.1016/j.chemosphere.2017.05.018.

Changkakoti, A., Morton, R., 1986. Electron microprobe analyses of native silver and associated arsenides from the Great Bear Lake silver deposits, Northwest Territories, Canada. Can. J. Earth Sci. 23, 1470–1479. https://doi.org/10.1139/e86-142.

Changkakoti, A., Morton, R., Gray, J., Yonge, C., 1986. Oxygen, hydrogen, and carbon isotopic studies of the Great Bear Lake silver deposits, Northwest Territories. Can. J. Earth Sci. 23, 1463–1469. https://doi.org/10.1139/e86-141.

Cheilletz, A., Levresse, G., Gasquet, D., Azizi-Samir, M., Zyadi, R., Archibald, D.A., et al., 2002. The giant Imiter silver deposit: Neoproterozoic epithermal mineralization in the Anti-Atlas, Morocco. Miner Deposita 37, 772–781. https://doi.org/10.1007/s00126-002-0317-0.

Chivot, J., 2004. Thermodynamique des Produits de Corrosion. Fonctionc Thermodynamiques Diagrammes de Solubilité Diagrammes E-pH des Systèmes Fe-HO FeCO-HO Cr-HO et Ni-HO en Fonction de la Température. Agence Nationale pour la gestion des Déchets Radioactifs, Châtenay-Malabry, France, pp. 142.

Choi, S.-G., Imai, N., 1985. Ni-Fe-Co arsenides and sulpharsenides from the Ulsan Mine, Republic of Korea. Min. Geol. 35, 1–16. https://doi.org/10.11456/shigenchishitsu1951.35.1.

Clavel, M., 1963. Contribution à l'étude Métallogénique de la Région d'Allemont (Massif de Belledonne-Isère)-Alpes françaises. Unpublished PhD Thesis. Université de Nancy, pp. 187.

Craig, J.R., Barton, P.B., 1973. Thermochemical approximations for sulfosalts. Econ. Geol. 68, 493–506. https://doi.org/10.2113/gsecongeo.68.4.493.

Dolansky, L.M., 2007. Controls on the Genesis of Hydrothermal Cobalt Mineralization: Insights from the Mineralogy and Geochemistry of the Bou Azzer Deposits, Morocco. Unpublished MSc Thesis. McGill University, Montreal, QC, Canada, pp. 192.

Dolníček, Z., Fojt, B., Prochaska, W., Kučera, J., Sulovský, P., 2009. Origin of the Zálesí U-Ni–Co–As–Ag/Bi deposit, Bohemian Massif, Czech Republic: fluid inclusion and stable isotope constraints. Miner. Deposita 44, 81–97. https://doi.org/10.1007/s00126-008-0202-6.

Essarraj, S., Boiron, M.-C., Cathelineau, M., Banks, D.A., Benharref, M., 2005. Penetration of surface-evaporated brines into the Proterozoic basement and deposition of Co and Ag at Bou Azzer (Morocco): evidence from fluid inclusions. J. African Earth Sci. 41, 25–39. https://doi.org/10.1016/j.jafrearsci.2005.03.001.

Essarraj, S., Boiron, M.-C., Cathelineau, M., Tarantola, A., Leisen, M., Boulvais, P., et al., 2016. Basinal brines at the origin of the Imiter Ag-Hg deposit (Anti-Atlas, Morocco): evidence from LA-ICP-MS data on fluid inclusions, halogen signatures, and stable isotopes (H, C, O). Econ. Geol. 111, 1753–1781. https://doi.org/10.2113/econgeo.111.7.1753.

Etschmann, B.E., Liu, W., Pring, A., Grundler, P.V., Tooth, B., Borg, S., et al., 2016. The role of Te (IV) and Bi (III) chloride complexes in hydrothermal mass transfer: An X-ray absorption spectroscopic study. Chem. Geol. 425, 37–51. https://doi.org/10.1016/j.chemgeo.2016.01.015.

Fanlo, I., Subías, I., Gervilla, F., Manuel, J., 2006. Textures and compositional variability in gersdorffite from the Crescencia Ni–(Co–U) showing, Central Pyrenees, Spain: primary deposition or re-equilibration? Can. Mineral. 44, 1513–1528. https://doi.org/10.2113/gscanmin.44.6.1513.

Fanlo, I., Subías, I., Gervilla, F., Paniagua, A., García, B., 2004. The composition of Co–Ni–Fe sulfarsenides, diarsenides and triarsenides from the San Juan de Plan deposit, Central Pyrenees, Spain. Can. Mineral. 42, 1221–1240. https://doi.org/10.2113/gscanmin.42.4.1221.

Feitzinger, G., Günther, W., Brunner, A., 1998. Bergbau-und Hüttenaltstandorte im Bundesland Salzburg. Land Salzburg, pp. 234.

Franklin, J., Kissin, S., Smyk, M., Scott, S., 1986. Silver deposits associated with the Proterozoic rocks of the Thunder Bay district, Ontario. Can. J. Earth Sci. 23, 1576–1591. https://doi.org/10.1139/e86-148.

Fuchs, H.W., 1988. Erzmikroskopische und mineralchemische Untersuchungen der Erzvorkommen Zinkwand-Voettern in den Niederen Tauern bei Schladming. Archiv für Lagerstättenforschung der Geologischen Bundesanstalt, 9, pp. 33–45.

Fusswinkel, T., Wagner, T., Wälle, M., Wenzel, T., Heinrich, C.A., Markl, G., 2013. Fluid mixing forms basement-hosted Pb-Zn deposits: insight from metal and halogen geochemistry of individual fluid inclusions. Geology 41, 679–682. https://doi.org/10.1130/G34092.1.

Fusswinkel, T., Wagner, T., Wenzel, T., Wälle, M., Lorenz, J., 2014. Red bed and basement sourced fluids recorded in hydrothermal Mn–Fe–As veins, Sailauf (Germany): a LA-ICPMS fluid inclusion study. Chem. Geol. 363, 22–39. https://doi.org/10.1016/j.chemgeo.2013.10.026.
Gamsjäger, H., Bugajski, J., Gajda, T., Lemire, R.J., Preis, W., 2005. Chemical Thermodynamics of Nickel. Elsevier Science, pp. 648.
Gasanova, Z., Mashadieva, L., Zlomanov, V., Babanly, M., 2014. Thermodynamic study of the Ag2S-As2S3-S system by EMF measurements with Ag4RbI5 as a solid electrolyte. Inorg. Mater. 50, 6–9. https://doi.org/10.1134/S0020168514010075.
Gervilla, F., Fanlo, I., Colás, V., Subías, I., 2012. Mineral compositions and phase relations of Ni–Co–Fe arsenide ores from the Aghbar mine, Bou Azzer, Morocco. Can. Mineral. 50, 447–470. https://doi.org/10.3749/canmin.50.2.447.
Gillerman, E., Whitebread, D.H., 1953. The Uranium-Bearing Nickel-cobalt-Native Silver Deposits in the Black Hawk District, Grant County, New Mexico. 1009-K. US Geological Survey, Bulletin, pp. 313.
Glasser, L., 2013. Thermodynamic estimation: ionic materials. J. Solid State Chem. 206, 139–144. https://doi.org/10.1016/j.jssc.2013.08.008.
Goryachev, N., Gamyanin, G., Prokof'ev, V.Y., Savva, N., Velivetskaya, T., Ignat'ev, A., 2014. Silver-cobalt mineralization in the Upper Seymchan ore cluster, Northeastern Russia. Geol. Ore Deposit. 56, 322–345. https://doi.org/10.1134/S1075701514050055.
Gov. of NWT, 2016. A guide to the mineral deposits of the Northwest Territories. https://www.iti.gov.nt.ca/en/newsroom/guide-mineral-deposits-northwest-territories (accessed 1. Jan. 2018), Government of Northwest Territories, Mineral Resources Division, pp. 187.
Gritsenko, Y.D., Spiridonov, E., 2008. Maucherite from metamorphic-hydrothermal assemblages of the Noril'sk ore field. Geol. Ore Deposit. 50, 590–598. https://doi.org/10.1134/S1075701508070106.
Habicht, K.S., Canfield, D.E., Jo, Rethmeier, 1998. Sulfur isotope fractionation during bacterial reduction and disproportionation of thiosulfate and sulfite. Geochim. Cosmochim. Acta 62, 2585–2595. https://doi.org/10.1016/S0016-7037(98)00167-7.
Haditsch, J.G., Mostler, H., 1970. Die Kupfer-Nickel-Kobalt-Vererzung im Bereich Leogang (Inschlagalm, Schwarzleo, Nöckelberg). Institut für Mineralogie und Gesteinskunde, Archiv für Lagerstättenforschung in den Ostalpen, pp. 161–209 11.
Halls, C., Stumpfl, E., 1972. The five-element (Ag-Bi-Co-Ni-As) vein deposit – A critical appraisal of the geological environments in which it occurs and of the theories affecting its origin, Proceedings Volume: 24th International Geological Congress. Campbell.
Haynes, W.M., 2016. CRC Handbook of Chemistry and Physics, 96th ed. CRC Press, pp. 1838.
Heimig, C., 2015. Ni-Co-As-Ag-Bi-Mineralisationen aus dem Odenwald. Unpublished MSc Thesis. Eberhard Karls University, Tübingen, Germany, pp. 119.
Hem, S.R., Makovicky, E., Gervilla, F., 2001. Compositional trends in Fe, Co and Ni sulfarsenides and their crystal-chemical implications: results from the Arroyo De La Cueva deposits, Ronda peridotite, Southern Spain. Can. Mineral. 39, 831–853. https://doi.org/10.2113/gscanmin.39.3.831.
Hiller, A., Schuppan, W., 2008. Geologie und Uranbergbau im Revier Schlema-Alberoda. Landesamt für Umwelt, Landwirtschaft und Geologie, Bergbau in Sachsen, pp. 200 14.
Hoehne, K., 1936. Über einige Arsen, Nickel, Kobalt, Silber, Wismut und Uranerzführende Kalkspatgänge der Grube Bergfreiheit zu Oberschmiedeberg im Riesengebirge. Chem Erde. 10, 432–474.
Hofmann, F., 1986. Die Freiberger Mineralien. Lapis 11, 13–60.
Hofmann, F., 1992. Die Minerale des Annaberger Reviers im Sächsischen Erzgebirge. Lapis 24–32.
Hösel, G., 2003. Die polymetallische Skarnlagerstätte Pöhla-Globenstein. Landesamt für Umwelt, Landwirtschaft und Geologie, Bergbau in Sachsen, pp. 147 8.
Ixer, R., Stanley, C., 1987. A silver-nickel-cobalt mineral association at Tynebottom Mine, Garrigill, near Alston, Cumbria. Proc. Yorkshire Geol. Soc. 46, 133–139. https://doi.org/10.1144/pygs.46.2.133.
Jambor, J., 1971a. Origin of the silver veins of the Cobalt-Gowganda region. In: Berry, L.G. (Ed.), The Silver-Arsenide Deposits of the Cobalt-Gowganda Region, Ontario. The Canadian Mineralogist, pp. 12.
Jambor, J., 1971b. Wall rock alteration. In: Berry, L.G. (Ed.), The Silver-Arsenide Deposits of the Cobalt-Gowganda Region, Ontario. Mineralogical Association of Canada, Quebec, pp. 272–304.
Jenkins, H.D.B., Glasser, L., 2003. Entropy, standard absolute S0 298, values from volume or density. Inorg. Chem. 42, 8702–8706. https://doi.org/10.1021/ic030219p.
Jørgensen, B.B., Bak, F., 1991. Pathways and microbiology of thiosulfate transformations and sulfate reduction in a marine sediment (Kattegat, Denmark). Appl. Environ. Microbiol. 57, 847–856.
Kallstrom, M.J., 2012. Fluid and Metal Sourcing for the Native Silver Deposits in the Batopilas Mining District, Chihuahua, Mexico. Unpublished MSc Thesis. University of Texas at Austin, pp. 271.
Karpov, G., 1991. Complex mercury-antimony-arsenic mineralization of the Uzon-Waiotapu type in modern hydrothermal systems. Int. Geol. Rev. 33, 599–611. https://doi.org/10.1080/00206819109465714.
Keil, K., 1933. Über die Ursachen der charakteristischen Paragenesenbildung von gediegen Silber und gediegen Wismut mit den Kobalt-Nickel-Eisen-Arseniden auf den Gängen der Kobalt-Nickel-Wismut-Silber-Erzformation im sächsisch-böhmischen Erzgebirge und dem Cobalt-District. Neues Jb Geol P. 66, 407–424.
Kerrich, R., Strong, D., Andrews, A., Owsiacki, L., 1986. The silver deposits at Cobalt and Gowganda, Ontario. III: Hydrothermal regimes and source reservoirs-evidence from H, O, C, and Sr isotopes and fluid inclusions. Can. J. Earth Sci. 23, 1519–1550. https://doi.org/10.1139/e86-145.
Kiefer, S., Majzlan, J., Chovan, M., Števko, M., 2017. Mineral compositions and phase relations of the complex sulfarsenides and arsenides from Dobšiná (Western Carpathians, Slovakia). Ore Geol. Rev. 89, 894–908. https://doi.org/10.1016/j.oregeorev.2017.07.026.
Kinniburgh, D.G., Cooper, D.M., 2004. Predominance and mineral stability diagrams revisited. Environ. Sci. Technol. 38, 3641–3647. https://doi.org/10.1021/es034927l.
Kissin, S.A., 1988. Nickel-cobalt-native silver (five-element) veins: A riftrelated ore type. In: Kisvarsany, G., Grant, S. (Eds.), Proceedings Volume: North American Conference on Tectonic Control of Ore Deposits and the Vertical and Horizontal Extent of Ore Systems. Univ. Missouri, Rolla, pp. 268–279.
Kissin, S.A., 1992. Five-element (Ni-Co-As-Ag-Bi) veins. Geosci. Can. 19, 113–124.
Kissin, S.A., 1993. The geochemistry of transport and deposition in the formation of five-element (Ag-Ni-Co-As-Bi) veins, Proceedings Volume: Eight Quadrennial International Association on the Genesis of Ore Deposits Symposium. Schweizerbart'sche Verlagsbuchhandlung, pp. 14.
Kissin, S.A., Jennings, E.A., 1987. The genesis of silver vein deposits in the Thunder Bay area, northwestern Ontario, Grant 300. Ontario Geological Survey, Geoscience Research Grant Program, pp. 230–241.
Kotková, J., Kullerud, K., Šrein, V., Drábek, M., Škoda, R., 2017. The Kongsberg silver deposits, Norway: Ag-Hg-Sb mineralization and constraints for the formation of the deposits. Miner. Deposita 1–15. https://doi.org/10.1007/s00126-017-0757-1.
Kreissl, S., 2018. Alpine Five Element Veins: Reconstruction of a 225 Ma Multi-stage Bi-Co-Ni-Fe-As-S System in the Penninic Alps, Switzerland – Unraveling Compositional, Mineralogical and Genetic Features of Five Element Veins. Unpublished PhD Thesis. Eberhard Karls University, Tübingen, Germany, pp. 141.
Kreissl, S., Gerdes, A., Walter, B., Neumann, U., Wenzel, T., Markl, G., 2018. Reconstruction of a > 200 Ma multi-stage "five element" Bi-Co-Ni-Fe-As-S system in the Penninic Alps, Switzerland. Ore Geol. Rev. 95, 746–788. https://doi.org/10.1016/j.oregeorev.2018.02.008.
Kribek, B., Zak, K., Spangenberg, J.E., Jehlicka, J., Prokes, S., Kominek, J., 1999. Bitumens in the late Variscan hydrothermal vein-type uranium deposit of Příbram, Czech Republic; sources, radiation-induced alteration, and relation to mineralization. Econ. Geol. 94, 1093–1114. https://doi.org/10.2113/gsecongeo.94.7.1093.
Krieger, P., 1935. Primary silver mineralization at Sabinal, Chihuahua, Mexico. Econ. Geol. 30, 242–259. https://doi.org/10.2113/gsecongeo.30.3.242.
Kubaschewski, O., Alcock, C., 1979. Metallurgical Thermochemistry, fifth ed. Pergamon Press, pp. 462.
Kuhanestani, N.M., Mohammadi, B.M., Alderton, D., Tabatabaei, S., Bagheri, H., 2014. Mineralogical and geochemical studies on the Gowd-e-Morad (Ni Co, As–Cu) mineral deposit, Anarak (Central Iran). Arab J. Geosci. 7, 4779–4791. https://doi.org/10.1007/s12517-013-1033-z.
Lahl, B., 1992. Die Geologie des Annaberger Bergbaugebiets. Lapis 1–40.
Levresse, G., Bouabdellah, M., Cheilletz, A., Gasquet, D., Maacha, L., Tritlla, J., et al., 2016. Degassing as the Main Ore-forming Process at the Giant Imiter Ag–Hg Vein Deposit in the Anti-Atlas Mountains, Morocco. Mineral Deposits of North Africa, Springer., pp. 22.
Lipp, U., Flach, S., 2003. Wismut-, Kobalt-, Nickel-und Silbererze im Nordteil des Schneeberger Lagerstättenbezirkes. Landesamt für Umwelt, Landwirtschaft und Geologie, Bergbau in Sachsen, pp. 215 10.
López, L., Echeveste, H., 2012. Paragénesis Mineral del Depósito Tipo Five Element Purísima-Rumicruz, Jujuy. Revista de la Asociación Geológica Argentina, pp. 7 69.
Maacha, L., Lebedev, V., Saddiqi, O., Borisenko, A., Pavlova, G., Yarmolyuk, V., 2015. Arsenide deposits of the Bou-Azzer ore district (Anti-Atlas metallogenic province) and their economic outlook. TuvIENR SB RAS, http://ipc-publisher.ru/monographs.aspx?id_mn=15. pp. 66.
Manuel, J., Subías, I., Fanlo, I., Arranz, E., Gervilla, F., 2018. Multi-isotope survey on the metallogenesis of the hydrothermal Co-Ni deposits in the Alpine Central Pyrenees of Spain. Ore Geol. Rev. 94, 225–238. https://doi.org/10.1016/j.oregeorev.2018.01.030.
Marini, L., Accornero, M., 2007. Prediction of the thermodynamic properties of metal–arsenate and metal–arsenite aqueous complexes to high temperatures and pressures and some geological consequences. Environ. Geol. 52, 1343–1363. https://doi.org/10.1007/s00254-006-0578-5.
Markl, G., 2016. Schwarzwald, Vol. 2, Mittlerer Schwarzwald Teil 1. Bode Verlag, pp. 648.
Markl, G., 2017. Schwarzwald Vol. 4 Südlicher Schwarzwald. Bode Verlag, pp. 880.
Markl, G., Burisch, M., Neumann, U., 2016. Natural fracking and the genesis of five-element veins. Miner. Deposita 51, 703–712. https://doi.org/10.1007/s00126-016-0662-z.
Marshall, D., Watkinson, D., 2000. The Cobalt mining district: Silver sources, transport and deposition. Explor. Min. Geol. 9, 81–90. https://doi.org/10.2113/0090081.
Marshall, D.D., Diamond, L.W., Skippen, G.B., 1993. Silver transport and deposition at Cobalt, Ontario, Canada; fluid inclusion evidence. Econ. Geol. 88, 837–854. https://doi.org/10.2113/gsecongeo.88.4.837.
Meisser, N., 2003. Le district cobalto-nickélifère d'Anniviers - Tourtemagne (Valais, Suisse). Minaria Helv. 23b, 57–64.
Merry, M., Weiß, S., 2017. Nickel- und Kobaltmineralien aus der St. Austell Consols Mine, Cornwall (GB). Lapis 42, 24–29.
Meyer, J., Hohl, J.-L., 1994. Minéraux et Mines du Massif Vosgien. Editions du Rhin, Mulhouse, pp. 271.
Misra, K., Fleet, M., 1975. Textural and compositional variations in a Ni-Co-As assemblage. Can. Mineral. 13, 8–14.
Moore, E.S., 1934. Genetic relations of silver deposits and Keweenawan diabases in Ontario. Econ. Geol. 29, 725–756. https://doi.org/10.2113/gsecongeo.29.8.725.
Moore, P., 1971. Copper-nickel arsenides of Mohawk no. 2 Mine, Mohawk, Keweenaw co, Michigan. Am. Mineral. 56, 1319–1331.

Moreton, S., Aspen, P., Green, D.I., Ingram, S.M., 1998. The silver and cobalt mineralization near Alva, Central Region, Scotland. J. Russel Soc. 7, 23–30.
Müller, H., 1860. Der Erzdistrict von Schneeberg im Erzgebirge. Cotta's Gangstud. 3, pp. 1–223.
Naitza, S., Garbarino, C., Secchi, F., Tocco, S., 2013. The Ni-Co hydrothermal ore deposits of the Arburese Variscan district (SW Sardinia, Italy), Poster: Geoitalia 2013.
Naitza, S., Secchi, F., Oggiano, G., Cuccuru, S., 2015. New observations on the Ni-Co ores of the southern Arburese Variscan district (SW Sardinia, Italy), Proceedings Volume: EGU General Assembly Conference. pp. 1.
Naumov, G.B., Motorina, Z.M., Naumov, V.B., 1971a. Conditions of formation of carbonates in veins of the lead-cobalt-nickel-silver-uranium type (translation from Geokhimiya, No 8, pp. 938-948, 1971). Geochem. Int. 8, 590–598.
Naumov, G.B., Ryzhenko, B.N., Khodakovsky, I.L., 1971b. Handbook of Thermodynamic Data (in Russian). Moscow Atomizdat., Moscow, pp. 239.
Oen, I., Dunn, P.J., Kieft, C., 1984. The nickel-arsenide assemblage from Franklin, New Jersey; description and interpretation. Neues Jb. Miner. Abh. 150, 259–272.
Ohmoto, H., Lasaga, A.C., 1982. Kinetics of reactions between aqueous sulfates and sulfides in hydrothermal systems. Geochim. Cosmochim. Acta 46, 1727–1745. https://doi.org/10.1016/0016-7037(82)90113-2.
Ondrus, P., Veselovsky, F., Gabasova, A., Drabek, M., Dobes, P., Maly, K., et al., 2003a. Ore-forming processes and mineral parageneses of the Jáchymov ore district. J. GeSci.-Czech. 48, 157–192.
Ondrus, P., Veselovsky, F., Gabasova, A., Hlousek, J., Srein, V., 2003b. Geology and hydrothermal vein system of the Jáchymov (Joachimsthal) ore district. J. GeSci.-Czech. 48, 16.
Ondrus, P., Veselovsky, F., Gabasova, A., Hlousek, J., Srein, V., Vavrin, I., et al., 2003c. Primary minerals of the Jáchymov ore district. J. GeSci.-Czech. 48, 19–146.
Otto, J., 1964. Die Fluoritgrube “Gottesehre”. Unpublished Diplom Thesis. Albert Ludwigs Universität zu Freiburg, Freiburg, pp. 84.
Paar, W., Chen, T., 1979. Gersdorffit (in zwei Strukturvarietäten) und Sb-hältiger Parkerit, Ni3 (Bi, Sb) 2 S2, von der Zinkwand, Schladminger Tauern, Österreich. Tscher Miner. Petrog. 26, 59–67. https://doi.org/10.1007/BF01081291.
Palache, C., 1937. The minerals of Franklin and Sterling Hill, Sussex County, New Jersey. U.S. Geol. Surv. Bull. 180, 161.
Pekov, I.V., Levitskiy, V.V., Krivovichev, V.G., 2010. Mineralogy of the Belorechenskoye deposit (Northern Caucasus, Russia). Mineral. Almanac. 15, 1–96.
Perfetti, E., Pokrovski, G.S., Ballerat-Busserolles, K., Majer, V., Gibert, F., 2008. Densities and heat capacities of aqueous arsenious and arsenic acid solutions to 350° C and 300 bar, and revised thermodynamic properties of As(OH)3∘(aq), AsO(OH)3∘(aq) and iron sulfarsenide minerals. Geochim. Cosmochim. Acta 72, 713–731. https://doi.org/10.1016/j.gca.2007.11.017.
Petruk, W., 1968. Mineralogy and origin of the Silverfields silver deposit in the Cobalt area, Ontario. Econ. Geol. 63, 512–531. https://doi.org/10.2113/gsecongeo.63.5.512.
Petruk, W., 1971a. Geochemistry of the ores. In: Berry, L.G. (Ed.), The Silver-Arsenide Deposits of the Cobalt-Gowganda Region, Ontario. Mineralogical Association of Canada, Quebec, pp. 140–149.
Petruk, W., 1971b. Mineralogical characteristics of the deposits and textures of the ore minerals. In: Berry, L.G. (Ed.), The Silver-Arsenide Deposits of the Cobalt-Gowganda Region, Ontario. Mineralogical Association of Canada, Quebec, pp. 108–139.
Petruk, W., Harris, D., Stewart, J., 1969. Langisite, a new mineral, and the rare minerals cobalt pentlandite, siegenite, parkerite and bravoite from the Langis Mine, Cobalt-Gowganda area, Ontario. Can. Mineral. 9, 597–616.
Petruk, W., Harris, D.C., Stewart, J.M., 1971. Characteristics of the arsenides, sulfarsenides, and antimonides. In: Berry, L.G. (Ed.), The Silver-Arsenide Deposits of the Cobalt-Gowganda Region, Ontario. Mineralogical Association of Canada, Quebec, pp. 150–186.
Pokrovski, G.S., Kara, S., Roux, J., 2002. Stability and solubility of arsenopyrite, FeAsS, in crustal fluids. Geochim. Cosmochim. Acta 66, 2361–2378. https://doi.org/10.1016/S0016-7037(02)00836-0.
Radosavljević-Mihajlović, A.S., Stojanović, J.N., Radosavljević, S.A., Pačevski, A.M., Vuković, N.S., Tošović, R.D., 2017. Mineralogy and genetic features of the Cu-As-Ni-Sb-Pb mineralization from the Mlakva polymetallic deposit (Serbia)—new occurrence of (Ni-Sb)-bearing Cu-arsenides. Ore Geol. Rev. 80, 1245–1258. https://doi.org/10.1016/j.oregeorev.2016.08.036.
Radosavljević, S.A., Stojanović, J.N., Vuković, N.S., Radosavljević-Mihajlović, A.S., Kašić, V.D., 2015. Low-temperature Ni-As-Sb-S mineralization of the Pb (Ag)-Zn deposits within the Rogozna ore field, Serbo-Macedonian Metallogenic Province: ore mineralogy, crystal chemistry and paragenetic relationships. Ore Geol. Rev. 65, 213–227. https://doi.org/10.1016/j.oregeorev.2014.09.029.
Reuss, E., 1863. Über die Paragenese der auf den Erzgängen von Příbram einbrechenden Mineralien. Neues Jb. Miner. 13–103.
Robie, R.A., Bethke, P.M., 1962. Molar Volumes and Densities of Minerals. TEI-822. US Geological Survey, Bulletin, pp. 37.
Robie, R.A., Hemingway, B.S., 1995. Thermodynamic Properties of Minerals and Related Substances at 298.15 K and 1 bar (10^5 Pascals) Pressure and at Higher Temperatures. 2131. US Geological Survey, Bulletin, pp. 470.
Robinson, B., Ohmoto, H., 1973. Mineralogy, fluid inclusions, and stable isotopes of the Echo Bay U-Ni-Ag-Cu deposits, Northwest Territories, Canada. Econ. Geol. 68, 635–656. https://doi.org/10.2113/gsecongeo.68.5.635.
Rogers, M.C., 1996. Grade-tonnage Deposit Models of Selected Ontario Mineral Deposit Types. Ontario Geological Survey, Open File Report, 5945, pp. 128.
Roseboom, E., 1963. Co-Ni-Fe diarsenides-composition and cell dimensions. Am. Mineral. 48, 271–299.
Runge, W., Wolf, F., 2010. Chronik der WISMUT CD-ROM. Wismut GmbH, Chemnitz., pp. 3134.
Sampson, E., Hriskevich, M.E., 1957. Cobalt-arsenic minerals associated with aplites, at Cobalt, Ontario. Econ. Geol. 52, 60–75. https://doi.org/10.2113/gsecongeo.52.1.60.
Schalamuk, I., Logan, M., 1994. Polymetallic Ag-Te-bearing paragenesis of the Cerro Negro district, Famatina Range, La Rioja, Argentina. Can. Mineral. 32, 667–679.
Scharrer, M., Vaudrin, R., 2016. Regional Spatial Variation of the Cu-Bi Mineralization around Wittichen, SW Germany: A Structural, Mineralogical and Geochemical Study. Unpublished MSc Thesis. Eberhard Karls University, Tübingen, Germany, pp. 192.
Schnorrer-Köhler, G., 1983. Das Silbererzrevier St. Andreasberg im Harz. Aufschluss. 34, pp. 153–333.
Segalstad, T.V., 2008. Thermochemical modelling of the Kongsberg silver ore deposit, Norway, Proceedings Volume: 33rd International Geological Congress. pp. 1.
Seifert, T., Baumann, L., 1994. On the metalllogeny of the central Erzgebirge anticlinal area (Marienberg district), Saxony, Germany. In: von Gehlen, K., Klemm, D.D. (Eds.), Mineral Deposits of the Erzgebirge/Krusné Hory (Germany/Czech Republik). Gebrüder Borntraeger Berlin, Stuttgart, pp. 169–190.
Sejkora, J., Litochleb, J., 2003. Die primären mineralien der příbramer erzzone. Lapis 28, 32–59.
Sergiades, A.O., 1968. Silver Cobalt Calcite Vein Deposits of Ontario. Ontario Department of Mines, Mineral Resources Circular No. 10, pp. 498.
Shock, E.L., Sassani, D.C., Willis, M., Sverjensky, D.A., 1997. Inorganic species in geologic fluids: correlations among standard molal thermodynamic properties of aqueous ions and hydroxide complexes. Geochim. Cosmochim. Acta 61, 907–950. https://doi.org/10.1016/S0016-7037(96)00339-0.
Silke, R., 2009. The Operational History of Mines in the Northwest Territories, Canada – An Historical Research Project, pp. 513.
Skeaff, J.M., Mainwaring, P.R., Speelman, J.L., 1985. Thermochemical arsenide-oxide equilibria in the system Ni-As-O determined electrochemically between 438 and 866°C. Can. Metall. Q. 24, 349–382.
Slack, J., Kimball, B.E., Shedd, K.B., 2017. Cobalt, Chapter F, Critical Mineral Resources of the United States – Economic and Environmental Geology and Prospects for Future Supply. US Geological Survey, Professional Paper 1802–F, pp. 52.
Schmidt, C., 1920. Texte explicatif de la carte des gisements des matières premières minérales de la Suisse 1: 500,000. En commission chez A. Francke.
Smyk, M.C., Watkinson, D.H., 1990. Sulphide remobilization in Archean volcano-sedimentary rocks and its significance in Proterozoic silver vein genesis, Cobalt, Ontario. Can. J. Earth Sci. 27, 1170–1181. https://doi.org/10.1139/e90-124.
Spiridonov, E., Gritsenko, Y.D., Kulikova, I., 2007. Ferroskutterudite (Fe, Co) As 3: A new mineral species from the dolomite-calcite veins of the Noril'sk ore field. Doklady Earth Sci. 417, 1278–1280 Proceedings Volume.
Staude, S., Wagner, T., Markl, G., 2007. Mineralogy, mineral compositions and fluid evolution at the Wenzel hydrothermal deposit, Southern Germany: Implications for the formation of Kongsberg-type silver deposits. Can. Mineral. 45, 1147–1176. https://doi.org/10.2113/gscanmin.45.5.1147.
Staude, S., Werner, W., Mordhorst, T., Wemmer, K., Jacob, D.E., Markl, G., 2012. Multi-stage Ag–Bi–Co–Ni–U and Cu–Bi vein mineralization at Wittichen, Schwarzwald, SW Germany: geological setting, ore mineralogy, and fluid evolution. Miner. Deposita 47, 251–276. https://doi.org/10.1007/s00126-011-0365-4.
Stolyrova, T.A., 1982. Enthalpy of formation of CoAs2 and NiAs2. Geokhimiya 8, 1211–1212.
Tarkian, M., Bock, W., Neumann, M., 1983. Geology and mineralogy of the Cu − Ni − Co − U ore deposits at Talmessi and Meeskani, central Iran. Tscher Miner. Petrog. 32, 111–132. https://doi.org/10.1007/BF01081105.
Tooth, B., Etschmann, B., Pokrovski, G.S., Testemale, D., Hazemann, J.-L., Grundler, P.V., et al., 2013. Bismuth speciation in hydrothermal fluids: an X-ray absorption spectroscopy and solubility study. Geochim. Cosmochim. Acta 101, 156–172. https://doi.org/10.1016/j.gca.2012.10.020.
Tossell, J., Vaughan, D., Burdett, J., 1981. Pyrite, marcasite, and arsenopyrite type minerals: crystal chemical and structural principles. Phys. Chem. Miner. 7, 177–184.
Tretiakova, I., Borisenko, A., Lebedev, V., Pavlova, G., Goverdovsky, V., Travin, A., 2010. Cobalt mineralization in the Altai-Sayan orogen: age and correlation with magmatism. Russ. Geol. Geophys. 51, 1078–1090. https://doi.org/10.1016/j.rgg.2010.08.012.
Tvrdý, J., Vary, K., 2003. Geologie und Erzgänge des Reviers Příbram. Lapis 28, 23–31.
Ulrich, T., Günther, D., Heinrich, C.A., 2002. The evolution of a porphyry Cu-Au deposit, based on LA-ICP-MS analysis of fluid inclusions: Bajo de la Alumbrera, Argentina. Econ. Geol. 97, 1889–1920. https://doi.org/10.2113/gsecongeo.97.8.1889.
Verbeek, E.R., Sutphin, H.B., 1990. Breithauptite from the Nickel-Arsenide Assemblage at Franklin, New Jersey. The Picking Table, pp. 2–5 31.
Vilor, N., Kaz'min, L., Pavlova, L., 2014. Aresenopyrite-pyrite paragenesis in gold deposits (thermodynamic modeling). Russ. Geol. Geophys. 55, 824–841. https://doi.org/10.1016/j.rgg.2014.06.003.
von Bargen, D., 1993. Minerals of the Black Hawk district New Mexico. Rocks Miner. 68, 96–133. https://doi.org/10.1080/00357529.1993.9926536.
Wagner, T., Lorenz, J., 2002. Mineralogy of complex Co-Ni-Bi vein mineralization, Bieber deposit, Spessart, Germany. Mineral. Mag. 66, 385–407. https://doi.org/10.1180/0026461026630036.
Walter, B.F., Burisch, M., Fusswinkel, T., Marks, M.A., Steele-MacInnis, M., Wälle, M., et al., 2018. Multi-reservoir fluid mixing processes in rift-related hydrothermal veins, Schwarzwald, SW-Germany. J. Geochem. Explor. 186, 158–186. https://doi.org/10.1016/j.gexplo.2017.12.004.
Watkinson, D.H., Heslop, J.B., Ewert, W.D., 1975. Nickel sulphide-arsenide assemblages associated with uranium mineralization, Zimmer Lake area, Northern Saskatchewan. Can. Mineral. 13, 198–210.
Wilkerson, G., Deng, Q., Llavona, R., Goodell, P.C., 1988. Batopilas mining district, Chihuahua. Econ. Geol. 83, 1721–1736. https://doi.org/10.2113/gsecongeo.83.8.1721.

Yang, H., Downs, R.T., Eichler, C., 2008. Safflorite, (Co, Ni, Fe) As2, isomorphous with marcasite. Acta Crystallogr. Sect. E: Struct. Rep. Online 64, 62–68. https://doi.org/10.1107/S1600536808026688.

Yardley, B.W., 2005. 100th Anniversary Special Paper: metal concentrations in crustal fluids and their relationship to ore formation. Econ. Geol. 100, 613–632. https://doi.org/10.2113/gsecongeo.100.4.613.

Ypma, P.J.M., 1963. Rejuvenation of Ore Deposits as Exemplified by the Belledonne Metalliferous Province. Unpublished PhD Thesis. University of California, pp. 212.

Ypma, P.J.M. 1972. The multistage emplacement of the Chalances (France) Ni-Co-Bi-As-Sb-Ag deposits and the nature of the mineralization solutions (abstract). In: Campbell, F.A., Wilson, H.D.B. (Eds.), Proceedings Volume: International Geological Congress (24). Campbell, pp. 525.

Zaikov, V., Melekestseva, I.Y., 2006. The Ishkinino Co-Cu massive sulfide deposit hosted in ultramafic rocks of the Main Ural Fault Zone, the southern Urals. Geol. Ore Deposit. 48, 151–174. https://doi.org/10.1134/S1075701506030019.

Zajzon, N., Szentpéteri, K., Szakáll, S., Kristály, F., 2015. The origin of the Avram Iancu U-Ni–Co–Bi–As mineralization, Băiţa (Bihor) metallogenic district, Bihor, Mts Romania. Int. J. Earth Sci. 104, 1865–1887. https://doi.org/10.1007/s00531-015-1175-1.

Appendix VIII

Manuscript in preparation

Study 8

Staude, S., Simon, I., Scharrer, M., Blanc, P., Pfaff, K., & Markl, G., (in preparation). Vein-type pentlandite, $(Ni,Fe)_9S_8$: formation conditions and its implication for orogenic gold deposits

Vein-type pentlandite, $(Ni,Fe)_9S_8$: formation conditions and its implication for orogenic gold deposits

Sebastian Staude[1], Isaac Simon[2], Manuel Scharrer[1], Philippe Blanc[3], Katharina Pfaff[2], Thomas Monecke[2], Gregor Markl[1]

[1]Department of Geosciences, University of Tübingen, Schnarrenbergstrasse 94-96, D-72076 Tübingen, Germany

[2] Center for Mineral Resources Science, Department of Geology and Geological Engineering, Colorado School of Mines, 1516 Illinois Street, Golden, Colorado 80401, USA

[3]Brgm - Service Géologique National Headquarters, 3 Avenue Claude Guillemin, 45100 Orléans, France

Abstract

Pentandite, $(Ni_xFe_y)_9S_8$ that formed from a hydrothermal fluid as opposed to magmatic processes is rare. In Kambalda (Western Australia), hydrothermal pentlandite has been identified occurring in three different assemblages: (1) pentlandite-rich veins with biotite, quartz, and an albite alteration halo in the host rock, (2) pentlandite-bearing quartz-carbonate-scheelite veins and biotite-epidote host-rock alteration, and (3) pentlandite-poor carbonate veins with arsenides, base metal sulfides, and gold and magnetite replacement of magmatic sulfides. All pentlandite at Kambalda is associated with pyrrhotite. Hydrothermal pentlandite can only be found in close proximity (less than 10 m) to magmatic Ni sulphides, while distal portions of the same structures are barren of pentlandite. Similarly, a literature review shows that hydrothermal pentlandite is found mostly near older magmatic sulfides or ultramafic rocks.

Hydrothermal pentlandite has higher Fe- and lower Co-contents compared to neighbouring magmatic pentlandite. Sulfarsenides also show bimodal characteristics in their chemistry. While magmatic sulfarsenides are rich in Co, hydrothermal sulfarsenides are dominated by Ni. Intermediate compositions are found where hydrothermal sulfarsenides directly overgrow magmatic sulfides.

Thermodynamic calculations show that hydrothermal pentlandite can form from very reduced fluids, relative to the hematite/magnetite fluid buffer, at near neutral pH by an increase in pH and/or by decrease in temperatures. Associated silicates such as biotite, feldspars and quartz were precipitated due to concomitant fluid-rock interaction at the site of deposition. High temperatures (>450-500 °C) favour pentlandite formation due to an increase in Ni solubility. The pentlandite-pyrrhotite-biotite assemblage has a narrow stability field coinciding with a field of higher Au solubility leading to the absence of gold in association with this mineral assemblage. The pentlandite-arsenide assemblage shows a larger stability field which overlaps with stability fields that allow for potential Au precipitation. Arsenic and subordinately pentlandite is often associated with orogenic gold deposits and hence, an assemblage of pentlandite with arsenides can be used as pathfinder minerals for orogenic gold deposits.

1. Introduction

Table 1

Summary of pentlandite occurrences formed by aqueous fluids.

Country/ocean	Location	Geology	Mineralogy	Fluid conditions	Reference
Atlantic Ocean	Rainbow, Logatchev, and Ashadze hydrothermal fields	Active hydrothermal vents on (partly) serpentinized ocean floor. Ni is mobilized during serpentinization of gabbroic intrusion.	Trace Co-bearing pentlandite Magnetite, pyrite, pyrrhotite, chalcopyrite, sphalerite	365°C pH=2.8 reduced	Marques et al., 2006; Borodaev et al., 2007
Australia	New South Wales, Coolac	Serpentinization of ultramafic intrusions leached and mobilized Ni. Sulfide precipitation occurred on contacts to younger granite.	Minor pentlandite Cu and Fe-bearing sulfides (pyrite, pyrrhotite, chalcopyrite, bornite and cubanite), magnetite and awaruite with minor Ni (-Co-Fe) sulfides (heazlewoodite, millerite, mackinawite), arsenides and sulfarsenides (nickeline, maucherite, arsenopyrite, tetradymite, tetrahedrite), Pb and Bi minerals (galena, bismuth, bismuthinite), breithauptite, sphalerite	unknown	Ashley, 1973
	South Australia, Challenger	Gold deposition by metamorphic fluids in pelitic garnet-cordierite-orthopyroxene gneiss´. Gold-rich polymetallic melt formed during peak-metamorphism	Gold, minor pentlandite Löllingite, arsenopyrite, pyrrhotite, minor chalcopyrite, bismuth, maldonite, molybdenite, sphalerite	800°C	Tomkins and Mavrogenes, 2001; 2002
	Tasmania, Avebury	Serpentinized dunite contact metamorphically overprinted by the Heemskirk granite, granite derived fluids leached Ni from serpentinite and mineralized the contact area. 300 m wide Ni arsenide aureole around mineralization.	High proportion of pentlandite minor pyrrhotite, millerite, mackinawite, nickeline, gersdorffite, maucherite, magnetite	unknown	Keays and Jowitt, 2013; Kamenetsky et al., 2016
	Western Australia, Boddington	Low sulfide Au-Mo-Cu porphyry in andesites	Trace pentlandite, gold Actinolite-biotite veins with scheelite and pyrrhotite dominated sulfides	unknown	Symons et al., 1990
	Western Australia, Griffin's Find	Mafic granulite hosted gold deposit. Orogenic gold deposit metamorphosed and formation of gold-rich polymetallic melt.	Gold, minor pentlandite Arsenopyrite, löllingite, pyrrhotite, chalcopyrite, quartz, calcite	unknown	Tomkins and Grundy, 2009
	Western Australia, Kambalda, Long North Ni deposit	Komatiite-hosted Ni sulfide deposit. Metamorphic fluids mobilize Ni and precipitates it in surrounding trondhjemite	High proportion of pentlandite – no gold Pyrrhotite, pyrite, chalcopyrite, sphalerite, melonite, tetradymite, biotite, quartz, calcite, plagioclase	±500°C, 2.5 kbar, strongly reduced	This study
	Western Australia, Kambalda, McLeay Ni deposit	Komatiite-hosted Ni sulfide deposit. Metamorphic fluids mobilize Ni and precipitates it in surrounding basalt and komatiite	moderate pentlandite – no gold pyrrhotite, chalcopyrite, quartz, carbonate, scheelite, epidote, biotite	±500°C, 2.5 kbar, strongly reduced	This study
	Western Australia, Kambalda, Moran Ni deposit	Komatiite-hosted Ni sulfide deposit. Metamorphic fluids mobilize Ni and precipitates it in older massive sulfides and basalt	Minor pentlandite - gold Carbonate, talc, tremolite, pyrrhotite, pyrite, magnetite, maucherite, nickeline, gersdorffite,	±500°C, 2.5 kbar, medium f_{O2}	This study

			arsenopyrite, greenockite, silver, bismuth, argentopentlandite, galena, bornite, mackinawite		
	Western Australia, Kambalda, East Repulse gold deposit	Pentlandite formation in reduced assemblage in the hanging wall of the orogenic gold deposit.	Minor pentlandite, gold Pyrite, millerite, cobaltite, siegenite, bismuthinite, galena, biotite, clinozoisite	480±60°C	Bath et al., 2013
	Western Australia, Kambalda, Wattle Dam	Komatiite-hosted orogenic gold deposit, 300m wide arsenide halo around mineralization	Gold, minor Pentlandite Pyrrhotite, chalcopyrite, cobaltite, biotite-chlorite-actinolite alteration, carbonate and minor quartz, dissolution of magnetite	Alkaline and oxidized fluid	Bath et al., 2020
	Western Australia, Miitel	Hydrothermal fluids mobilized Ni from komatiite-hosted sulfide deposit and mineralized the adjacent komatiite	Minor pentlandite, gold Gersdorffite, nickeline, chalcopyrite, pyrrhotite, millerite, amphibole, chlorite, biotite, quartz, carbonate	unknown	Le Vaillant et al., 2015
	Western Australia, Southern Cross, Fraser mine	Mafic granulite hosted gold deposit. Syntectonic and synmetamorphic mineralization	Minor pentlandite, gold Pyrrhotite, chalcopyrite, galena, diopside, calcite	500-550°C, 3-5 kbar	Barnicoat et al., 1991
	Western Australia, Spotted quoll	Komatiite hosted magmatic sulfides were tectonically displaced and overprinted by orogenic gold hydrothermal fluids. The authors describe euhedral magmatic gersdorffite and anhedral hydrothermal gersdorffite around nickeline.	Pentlandite, gold Nickeline, pyrrhotite, chalcopyrite, irarsite, sudburyite, carbonate	unknown	Prichard et al., 2013
	Western Australia, Sarah's Find	Komatiite hosted magmatic sulfides were tectonically displaced and overprinted by orogenic gold hydrothermal fluids. The authors describe gersdorffite in tectonically mobilized and hydrothermal overprinted sulfides.	Pentlandite Pyrrhotite, sulfarsenides, chalcopyrite, galena, sphalerite	unknown	Le Vaillant et al., 2016
Brazil	Carajás Province, Jatobá	Transition from magmatic to deep hydrothermal system related to an IOCG deposit. Ni leaching from mafic-ultramafic rocks in the vicinity.	Co-pentlandite Magnetite, apatite, actinolite, Ni-pyrrhotite, Ni-pyrite, Co-chalcopyrite	>600°C	Veloso et al., 2020
	Carajás Province, GT-34 deposit	Sulfide-rich breccia within hornblende-chlorapatite±plagioclase alteration related to an IOCG deposit hosted in orthogneiss.	Pentlandite, gold Pyrrhotite, apatite, chalcopyrite, melonite, pyrite, Fe-oxides, monazite Alteration: scapolite, orthopyroxene, hornblende, plagioclase, phlogopite, talc, magnetite	>700°C, 5-7 kbar, highly saline	Garcia et al., 2020
	Minas Gerais, Fortaleza de Minas	Komatiite-hosted Ni deposit hydrothermally remobilized into discordant veins	Pentlandite Pyrrhotite, chalcopyrite, magnetite, carbonates, amphibole, minor sulfarsenides	CO_2-bearing, neutral to alkaline, reduced	De Almeida et al., 2007
Canada	Athabasca basin	Unconformity sandstone-hosted U deposits	Minor pentlandite, gold Uraninite, galena, pyrite, arsenopyrite, chalcopyrite	Oxidized, kaolinite-illite buffer: pH 4.5 at 200°C Saline brine, 140-250°C	Jefferson et al., 2007

China	Guangxi Province, Longhua	Disseminated and vein-type Ni mineralization in carbonaceous sandstone and siltstone formed from circulating meteoric water	Minor pentlandite Nickeline, gersdorffite, maucherite, cobaltite, skutterudite, parkerite, chalcopyrite, pyrite, arsenopyrite	118-219°C, 1.2-8.8 wt.% NaCl equivalent	Huang et al., 2020
Cyprus	Limassol Forest, Pevkos	Hydrothermal mineralization formed during serpentinization of ultramafic host rock	Pentlandite, gold troilite, valleriite, maucherite, chalcopyrite, chromite, cubanite, magnetite, mackinawite, molybdenite, sphalerite, oregonite, gersdorffite, Ni-cobaltite, westerveldite, bornite, neodigenite, covellite	400-500°C	Thalhammer et al., 1986
Czech Republic	Kamenec and Hromnice	Metal-rich black shales hosted, always closely associated with mafic volcanic rocks. Sulfide deposition by bacterial reduction.	Minor pentlandite Pyrite, quartz, carbonate	seawater	Pašava et al., 1996
Finland	Kuhmo greenstone belt	Orogenic gold deposits	Pentlandite, gold Pyrrhotite, arsenopyrite, pyrite, chalcopyrite, magnetite, quartz, feldspar	450-550°C, reduced	Novoselov et al., 2013
	Outokumpu	Metamorphosed sedimentary exhalative sulfides in ultramafic rocks	Minor pentlandite, minor gold pyrite, pyrrhotite, chalcopyrite, sphalerite, cubanite, Co-As-rich pyrite, magnetite, stannite, mackinawite	unknown	Peltonen et al., 2008.
	Talvivaara	Black shale hosted pentlandite, Ni-sulfide precipitation from seawater	Minor pentlandite sphalerite, pyrite, Ni-rich pyrrhotite, chalcopyrite, molybdenite, alabandite	seawater	Loukola-Ruskeeniemi and Lahtinen, 2013
Germany	Oberpfalz, KTB drill hole	Sulfur and metals derived from sedimentary host-rock	Pentlandite Pyrrhotite, argentopentlandite, chalcopyrite, pyrite, sphalerite, galena, quartz	260°C	Kontny et al., 1994
Greece	Thrace, Maronia	Porphyry Cu-Mo system hosted by phallic and propylitic alteration of porphyritic microgranite. Fluid boiling is main process of ore formation.	Pentlandite Pyrite, chalcopyrite, cubanite, pyrrhotite, molybdenite, sphalerite, galena, bismuthinite, sulfosalts, magnetite	280-460°C, 150-510 bar, 5-55 wt.% NaCl equiv.	Melfos et al., 2002
New Zealand	South Island, Nelson	Talc carbonate alteration of ultramafic rocks during regional greenschist metamorphism	Pentlandite Gersdorffite, violarite, pyrrhotite	300-<100°C	Grapes and Challis, 1999
	South Island, Otago and Alpine Schists	subgreenschist metamorphosed metasediments	Locally pentlandite Pyrrhotite, chalcopyrite, sphalerite, galena, cobaltite	unknown	Pitcairn et al., 2006
Papua New Guinea	Doriri Creek	Hydrothermally altered ultramafic rocks	Minor pentlandite Ni-bearing chlorite and serpentinite, apatite, magnetite	120-180°C	González-Álvarez et al., 2013
Russia	Ural mountains, Ishkinino	Sub-seafloor hydrothermal system with massive sulfides associated with ultramafic rocks	Pentlandite, gold chalcopyrite, pyrrhotite, pyrite, gersdorffite, nickeline, arsenopyrite, sphalerite, Co-Ni-Fe-diarsenides	130-450°C 1.2-2.7 wt.% $NaCl_{eq}$ Highly reduced	Melekestseva et al., 2013
	Ural mountains, Ivanovka	Sub-seafloor hydrothermal system with massive sulfides associated with ultramafic rocks	Pentlandite, gold Pyrrhotite, mackinawite, chalcopyrite, pyrite, sphalerite, sulfarsenides, bismuth, Bi-tellurides	130-450°C 1.2-2.7 wt.% $NaCl_{eq}$ Highly reduced	Melekestseva et al., 2013

	Ural mountains, Talitsa	Porphyry Cu deposit	Rare pentlandite, gold Pyrite-quartz veins, Au-, Ag-, Pb-, and Ni-tellurides, rare pyrrhotite and Fe-Cu sulfides	235-280°C 4.9-6.5 wt. % NaCl eq.	Azovskova and Grabezhev, 2008
	Yana-Kolyma	Metamorphic fluids formed gold-quartz veins	Pentlandite, gold Millerite, breithauptite, pyrrotite, sulfarsenides, Pb-Sb-sulfosalts, fahlore, stibnite	unknown	Voroshin et al., 2014
South Africa	Limpopo belt, Hout River Shear Zone	Orogenic gold deposit formed from metamorphic fluids	Pentlandite, gold Löllingite, pyrrhotite, chalcopyrite, arsenopyrite, pyrite, sphalerite, biotite, amphibole, tourmaline, carbonate	600-620°C, 6 kbar	Kolb et al., 2015
Switzerland	Grisons, Platta nappe	Fossil hydrothermal vent system on ocean floor (now serpentinites)	Pentlandite Magnetite, pyrrhotite, chalcopyrite, isocubanite, sphalerite	seawater	Coltat et al., 2019
Zambia	Kabompo Dome, Kalumbila	Ni enrichment in copper shale style mineralization which then became metamorphically overprinted.	Pentlandite Siegenite, violarite, chalcopyrite, pyrrhotite, pyrite,	unknown	Steven and Armstrong, 2003
Zimbabwe	Filabusi greenstone belt, Epoch	Massive sulfide veins in ultramafic rocks	Minor pentlandite Pyrite, millerite, bravoite, chalcopyrite	unknown	Pirajno and González-Álvarez, 2013

Pentlandite ($(Ni_xFe_y)_9S_8$) is a mineral that typically forms from a mafic to ultramafic magmatic sulfide melt (Naldrett, 2004; Kitakaze et al., 2016; Mansur et al., 2019; Barnes et al., in press). High-form pentlandite, a precursor to pentlandite, crystallizes from a peritectic reaction of mono-sulfide solid-solution (MSS) with interstitial higher fractionated sulfide melt (Mansur et al., 2019; Barnes et al., in press). Pentlandite can also form from the exsolution from MSS or pyrrhotite during cooling (Durazzo and Taylor, 1982). Hydrothermal vein-style pentlandite, the topic of this contribution, forms through precipitation from an aqueous solution and is distinct from magmatic sulfide veins or physically mobilized magmatic pentlandite-bearing sulfides. Hydrothermal vein-style pentlandite is rare since Ni is typically incorporated into As- or Sb-bearing minerals (e.g. Staude et al., 2007; 2012; Scharrer et al., 2019), into pyrite; $(Fe,Ni)S_2$, (Harms, 2009), precipitates as millerite, NiS (Pirajno and González-Álvarez, 2013), or is minor constituent in chlorite and serpentine (González-Álvarez et al., 2013). Further, hydrothermal Ni-sulfides such as heazlewoodite (Ni_3S_2) are typically formed in reduced low-S serpentinized environments (Tzamos et al., 2016) or are weathering products of magmatic pentlandite (violarite; $FeNi_2S_4$, Tenailleau et al., 2006).

Only two non-magmatic pentlandite-rich occurrences have been reported in the literature so far. (1) Avebury (Tasmania; Keays and Jowitt, 2013) is hosted in serpentinites and adjacent skarns which are interpreted to be hydrothermal in origin and (II) the iron-oxide copper gold (IOCG) GT-34 deposit (Brazil, Garcia et al., 2020), which formed through metasomatic crystallization at high temperatures (>700 °C). While hydrothermal pentlandite is rare and has only been reported to occur in very few mineral association types worldwide, orogenic gold deposits (Pitcairn et al., 2006; Tomkins and Grundy, 2009; Bath et al., 2013; Lawrence et al., 2013; Molnár et al., 2017; El Monsef et al., 2018) as well as some IOCG deposits (Garcia et al., 2020; Veloso et al., 2020) frequently contain small amounts of pentlandite (Table 1). Physiochemical conditions of the fluids forming pentlandite and the formation processes in general are poorly understood and thus, a better understanding of pentlandite formation from aqueous fluids can help to understand and better characterize these types of gold deposits.

Kambalda (Western Australia; WA) is host to world class orogenic gold (Bath et al., 2013; McGoldrick, et al., 2013) and magmatic nickel deposits (Gresham and Loftus-Hills, 1981; Marston, 1984; Naldrett, 2011, Staude et al., 2017a). In addition to magmatic pentlandite, hydrothermal veins containing

pentlandite were observed and are the topic of this study. On the eastern limb of the Kambalda Dome (Fig. 1) three contrasting types of pentlandite-hosting veins occur: (1) Pentlandite-rich, pyrrhotite- and biotite-bearing veins, (2) quartz-rich scheelite-bearing veins with frequent pentlandite, and (3) carbonate-rich veins with significant Ni-arsenides and minor pentlandite. Interestingly, no gold was observed in type (1) and (2) veins, whereas type (3) veins contain gold in association with Ni minerals. Therefore, these veins in Kambalda will be used to decipher fluid conditions favourable for pentlandite formation – with and without associated gold.

2. Occurrences of hydrothermal vein-style pentlandite

Hydrothermal vein-style pentlandite occurrences are summarized in Table 1. They are typically spatially close to either a magmatic Ni sulfide body and/or mafic to ultramafic rocks (e.g., Avebury in Tasmania; Keays and Jowitt, 2013). The only exception to this are porphyry Cu systems (e.g., Thrace in Greece; Melfos et al., 2002). Major hydrothermal pentlandite is only reported in the Avebury deposit (Tasmania, Keays and Jowitt, 2013), the GT-34 deposit (Brazil, Garcia et al., 2020), and in type (1) veins described here from Kambalda. In all other occurrences, it is a minor or accessory mineral that forms together with more frequent and abundant base-metal sulfides and/or (Ni-) arsenides and sulfarsenides - similar to type (3) vein described here from Kambalda. Gold is associated with some of the reported pentlandite occurrences, but is more frequent in occurrences where hydrothermal veins cut through magmatic sulfide deposits and re-precipitate Ni-arsenides (Table 1).

3. Geology of Kambalda and formation of hydrothermal veins

The volcanic-sedimentary succession of the Kambalda Dome is part of the Kalgoorlie Terrane in the Archean Yilgarn Craton (Goscombe et al., 2009). The oldest rocks form the lava flows of the tholeiitic Lunnon Basalt which is followed by thin (<10 m) chert-rich sediments and the up to 1 km thick sequence of the 2710-2700 Ma Kambalda Komatiite (Kositcin et al., 2008). The magmatic Ni-sulfide deposits are found at the base of these komatiites and contained >3,000,000 tonnes of Ni prior to mining (Gresham and Loftus-Hills, 1981; Lesher et al., 1981; Barnes, 2006; Staude et al., 2017a). The komatiite is

followed by the komatiitic Devon Consols and Paringa Basalts and further volcanic and sedimentary units. A sedimentary layer (Kapai Slate) between the two basalts was dated at 2692±4 Ma (Claoué-Long et al., 1988). The sequence was intruded by felsic to intermediate dykes, sills and stocks, with a trondhjemite pluton at the centre of the Kambalda Dome. Hill et al. (1992) reported the age of the trondhejemite pluton to be 2662±6 Ma. The rocks were subsequently metamorphosed, but despite this overprint, many igneous textures in the sulphides and surrounding lithologies are still preserved (Staude et al. 2016, 2017b, 2020a, 2020b; Barnes et al. 2018; Staude and Markl, 2019) and hence the prefix 'meta' is omitted in literature. Regional metamorphism around 2680 Ma and again between 2665-2655 Ma caused folding and greenschist facies conditions (Mueller et al., 2016). Based on mineral assemblages, regional peak metamorphic conditions were reported to be 510 °C ±20 °C at 2.5±1 kbar (Bavinton, 1979).

The Kambalda St. Ives Au district, directly to the south of the Kambalda Dome, is related to the NNW-SSE striking Boulder-Lefroy Fault which is connected to the Kalgoorlie Au district by the Golden Mile fault system; both combined are host to >2200 tonnes of Au (Mueller et al., 2020). Two contrasting Au deposits occur along the faults, telluride-bearing epithermal deposits (e.g., Golden Mile; Mueller et al., 2020) and orogenic gold deposits (e.g., St. Ives; Neumayr et al., 2008). The orogenic gold is associated with biotite-sericite alteration and is thought to have formed during orogenic deformation in 11±4 km depth during sinistral strike-slip tectonics at 2678-2663 Ma and folding at 2665-2655 Ma (Mueller et al., 2016). A dextral strike-slip event at 2655-2640 Ma that controls Au formation in Kalgoorlie barren in Kambalda (Mueller et al., 2016).

The fluid, responsible for Au deposition in Kambalda-St. Ives, was investigated by several studies. Neall and Phillips (1987) investigated alteration profiles at the Hunt mine in Kambalda, which is only 3 km (Moran) to 8 km (Long North) south of the samples investigated in this study. Their studies showed an increase in sulfidation of host rock magnetite (forming pyrrhotite) with increasing Au contents in associated quartz veins and biotite-ankerite-chlorite alteration halos. Ho et al. (1992) investigated fluid inclusions from several orogenic gold deposits in the Yilgarn Craton and from the Hunt mine reporting homogenization temperatures of 280-325°C, salinities <3 wt.%, X_{CO2} of 0.15-0.25, and ore deposition

123 from a near neutral reducing fluid. For Hunt, they assume a fluid/rock ratio of only 10 to 100, whereas
124 for the Mt. Charlotte deposit (Kalgoorlie) they give a ratio of 5,000-10,000.

125 In the St. Ives Camp, 10-30 km to the south of Kambalda, Polito et al. (2001) differentiate between three
126 different vein systems that formed during three distinct time periods. (1) Pre-gold molybdenite-bearing
127 quartz veins with fluid inclusion representing mixing of a >340°C brine with a low-saline 150°C fluid.
128 (2) Syn-gold fluid inclusions are 400°C and CO_2-bearing in the centre and are CH_4-bearing at the vein
129 margin, where the Au content is highest. Polito et al. (2001) explain the different carbon species with
130 either introduction of CH_4 into the vein or with reduction of CO_2. Neumayr et al. (2008) suggests
131 contrasting redox conditions to be responsible for gold deposition. A reduced alteration assemblage with
132 pyrrhotite, arsenopyrite and pyrite prevails in the southwest of the camp, whereas a more oxidized
133 assemblage with magnetite-pyrite or hematite-pyrite occurs in the central area and the northeast. In the
134 early assemblage, hydrothermal magnetite is synchronous with early gold and albite-carbonate-pyrite-
135 biotite-chlorite alteration. Later-stage assemblage comprise pyrite associate with gold is in equilibrium
136 with hematite. Neumayr et al. (2008) proposed that the highest gold grades are found where the redox
137 state of the alteration assemblage switches from reduced leading to the interpretation that gold
138 precipitation is due to mixing of contrasting fluids.

139 Bath et al. (2013) used biotite-apatite thermometry to estimate the gold-ore forming fluid temperature
140 at the St. Ives Camp resulting in 480±60 °C, which represents a minimum re-equilibrium temperature.
141 They differentiate between three alteration stages; an early albite-carbonate, main-stage biotite-
142 amphibole-carbonate, and late-stage carbonate alteration. Interestingly, the biotite alteration is
143 accompanied by trace pentlandite in the hangingwall of the ore zone, whereas sulfates (anhydrite, barite,
144 celestine) and scheelite accompany biotite in the ore zone and in the footwall.

145

146 **4. Description of hydrothermal vein-style pentlandite in Kambalda**

147 Different types of pentlandite-hosting veins have been observed on the eastern limb of the Kambalda
148 Dome. Type (1) occurs in the trondhjemite adjacent (3-10 m) to the Long North magmatic Ni deposit
149 (Fig. 1; Staude et al., 2017a), type (2) occurs along a subparallel structure to the Boulder-Lefroy Fault

cutting through the McLeay magmatic Ni deposit (Fig. 1; Staude et al., 2017a), and type (3) is cutting through and along the Moran magmatic Ni deposit (Fig. 1; Staude et al., 2016; 2017b).

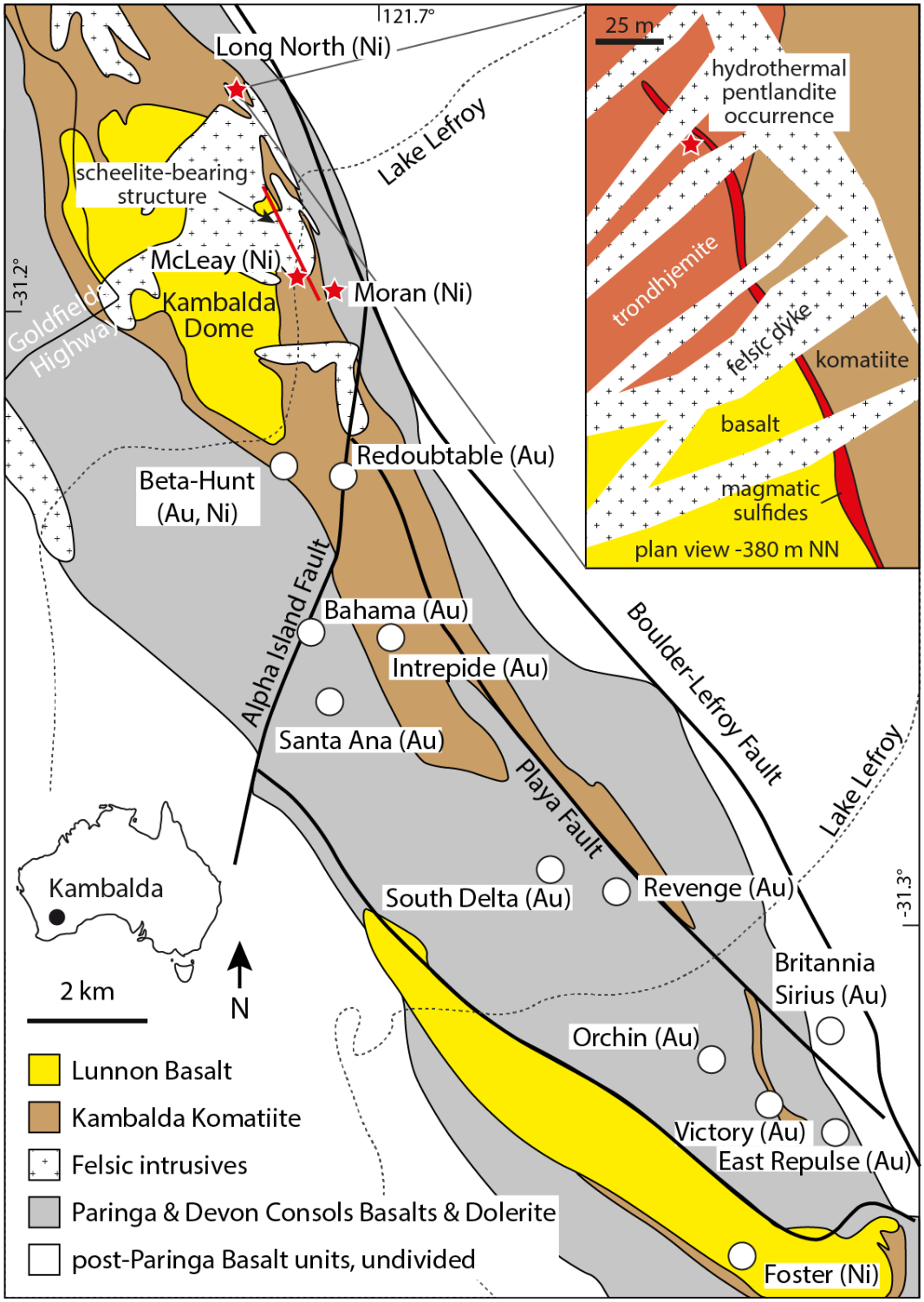

Figure 1

Map of Kambalda area including sample locations (Long North, McLeay, Moran) and gold deposits mentioned in the text.

Vein type (1): Thin (<2 cm) veins cut through the trondhjemite and exhibit an up to 5 cm thick alteration halo (Fig. 2a,b). Characteristic are 1-2 cm euhedral biotite crystals which are intergrown with pentlandite, pyrrhotite, other sulfides, calcite and quartz (Fig. 3a,b). The distribution of a sulfide-dominated assemblage and a quartz-dominated part in type (1) veins is irregular. Fig. 3 a shows a second order veinlet branching off and terminating within a few centimetres. In this area the largest area of alteration was observed.

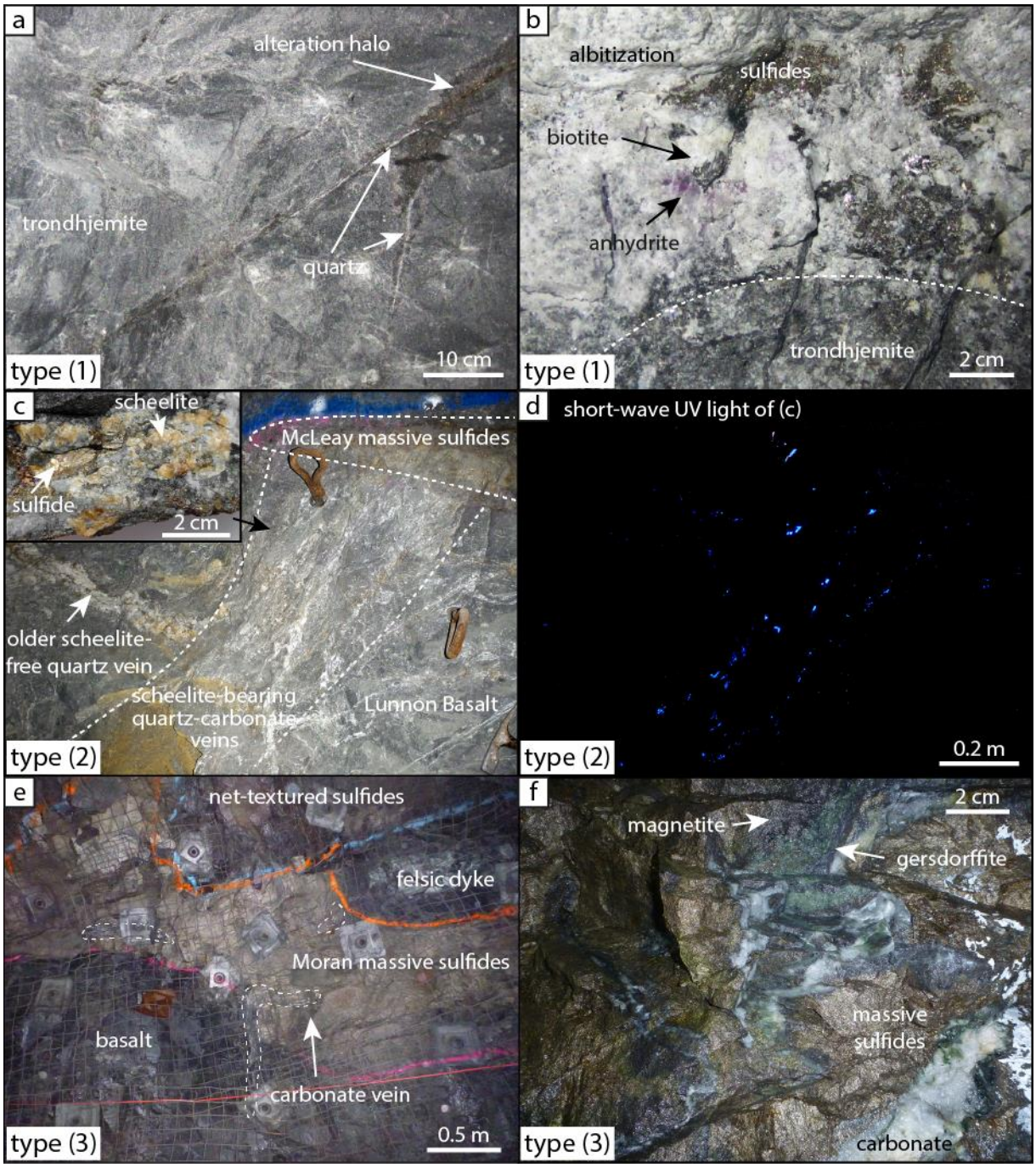

Figure 2

Photos of the pentlandite-bearing veins. (a) Vein type (1) Sulfide-quartz vein cutting through the trondhjemite. The widest alteration zone is observed where a second order structure branches off in the right of the photo. (b) Patchy sulfide distribution in an albite-biotite-altered trodnhjemite. (c) Multiple thin veinlets, Vein type (2), forming a scheelite-bearing structure cutting through the McLeay orebody. The inlet shows a large scheelite-sulfide aggregate from this vein network. (d) The same part under short-wave UV light highlighting the scheelite. (e) Lenses of pentlandite- and arsenide-bearing carbonate, Vein type (3), cutting through the Moran orebody. (f) Close-up photo of the pentlandite- and arsenide-bearing carbonate cutting through older magmatic sulfides.

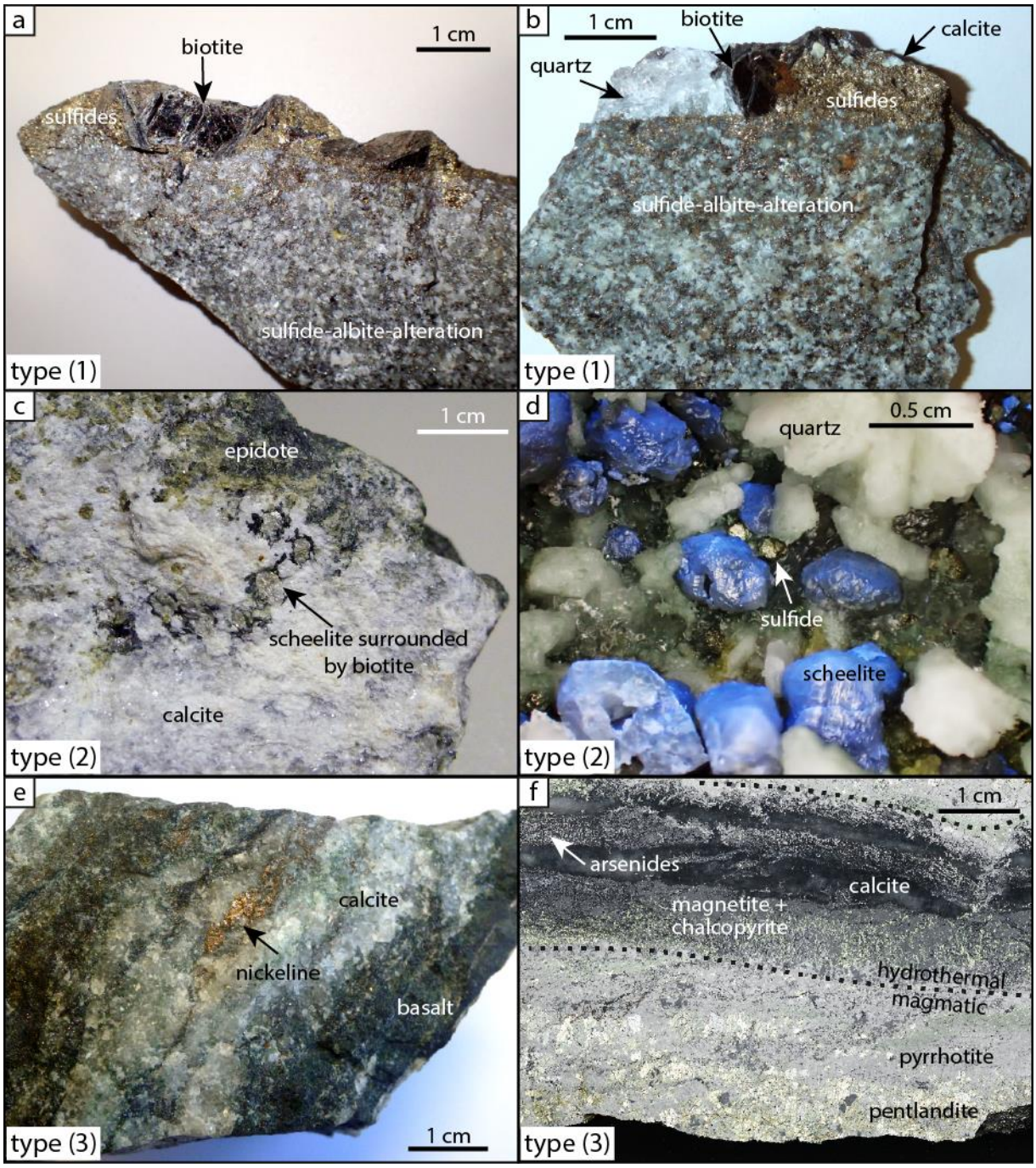

Figure 3

Photos of hand specimen of the pentlandite-bearing veins. (a) Contact of a biotite-rich sulfide vein to the alteration halo. (b) A similar hand specimen to (a), but the sulfide vein is here in irregular contact to massive quartz and calcite is visible in the sulfides. (c) Calcite-rich sample of the scheelite-bearing structure. Scheelite is here associated with large biotite and epidote alteration of the basalt. (d) Crystals of scheelite, highlighted with short-wave UV light, is associated with quartz, calcite (dissolved in acid), and sulfides. (e) Arsenide-bearing carbonate vein cutting through basalt originating from the footwall of the Moran orebody. (f) Polished slab of the arsenide-carbonate vein contact to the magmatic sulfides of Moran.

Vein type (2): Individual quartz-carbonate thin veinlets (<1 cm) and lenses, that are typically <1 cm in width can sometimes reach up to 50 cm. They form a vein network structure that can locally be up to 5 m wide cutting through Victor South-McLeay (Fig. 2c,d). The veins are characterized by their scheelite occurrence, which forms up to 10 cm large irregular masses and small (<0.5 cm) euhedral crystals. Associated minerals are pyrrhotite, epidote and biotite, with the latter representing the predominant alteration phase in the host basalt. The whole scheelite-bearing structure can be traced over 2 kilometres in NW-SE direction and is sub-parallel to the Boulder-Lefroy Fault (Fig. 1). Pentlandite was only observed in veins close to magmatic sulfides (<10 m), whereas samples further away do not contain pentlandite or other Ni-bearing phases.

Vein type (3): Carbonate-tremolite-chlorite veins hosted in the older magmatic Moran deposit occur as relic boudinaged and folded lenses of up to 10 cm thickness in massive sulfides and the neighbouring basalt in the NE of the deposit (Fig. 2e,f). They were also observed as thin (<2 cm) veins running parallel to the pinchout (where massive sulfides occur with older basalt underneath and above due to thermomechanical erosion during the formation of the magmatic deposit; Staude et al., 2016; 2017b) and in an area in the NE of Moran. The vein relics are bound by a diffuse zone of magnetite alteration in the magmatic sulfide orebody, whereas no alteration is visible where the vein is hosted in basalt. Pentlandite that is associated with carbonates occurs together with base metal sulfides, Ni-arsenides, and gold.

Physically mobilized pentlandite: In addition to hydrothermal pentlandite, samples from physically mobilized magmatic sulfides of Moran were investigated to compositionally compare them to hydrothermally formed pentlandite. The physically mobilized occurrences are mostly associated with

quartz veins, which are partly brecciated and cemented by the mobilized sulfides. Sulfides in non-brecciated quartz usually fill the central part of the vein (Fig. 4).

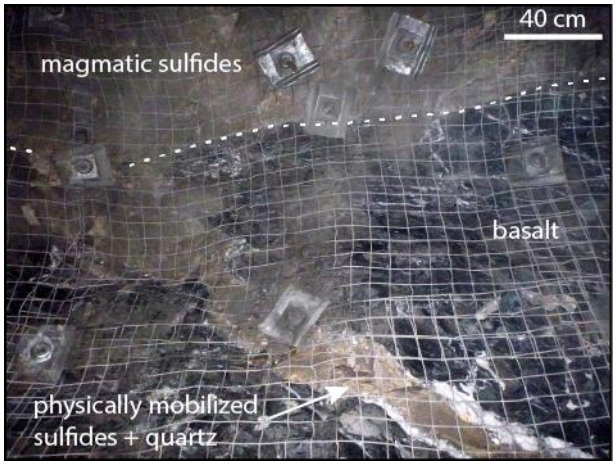

Figure 4

Photo of physically mobilized sulfides into the footwall of Moran. The mechanically mobilized sulfides cut through an older quartz vein.

5. Analytical methods

5.1. Electron microprobe analyses

Hydrothermal pentlandite, pyrrhotite and sulfarsenides have been analysed by electron microprobe analyses and compared to their magmatic counterparts. Analyses were carried out on a JEOL 8900 probe at the University of Tübingen (Germany) using wavelength-dispersive (WD) mode at an acceleration voltage of 25 kV, a probe current of 20 nA, and a focused beam. Biotite and feldspar were analysed using the same microprobe in WD mode with an acceleration voltage of 15 kV, a probe current of 20 nA, and a defocused beam of 2 µm. Counting time for sulfides and silicates was 15 s for major elements and 30 s for trace elements. The analysed elements with their respective energy line, detection limits, and results are listed in the electronic supplementary material (ESM) 1.

Field-Emission Scanning Electron Microscopy (FE-SEM)

Back Scattered Electron (BSE) images and semi-quantitative EDS analyses were collected with a TESCAN MIRA3 LMH Schottky Field Emission Scanning Electron Microscope (FE-SEM) in the Mineral and Materials Characterization (MMC) Facility in the Department of Geology and Geological Engineering at the Colorado School of Mines in Golden, Colorado, USA. The FE-SEM is equipped with a TESCAN motorized retractable annular, single-crystal YAG backscatter electron detector and a Bruker XFlash® 6/30 silicon drift detector for energy-dispersive x-ray (EDX) spectrometer, allowing for spectra acquisition and consequent mineral identification. BSE imaging and EDX analyses were performed at 15 keV and at 20keV acceleration voltage, respectively, a beam intensity of 11, and a working distance of 10 mm.

Optical Cathodoluminescence Microscopy (Katha/Isaac to write)

Cathodoluminescence (CL) imaging of samples was performed using a HC5-LM hot-stage CL microscope by Lumic Special Microscopes at Colorado School of Mines. The CL system is equipped with a high sensitivity, double-stage Peltier cooled Kappa DX40C CCD camera allowing for photographic acquisition of optical luminescence. The system was operated at an acceleration voltage of 14 kV and a current density of about 10 $\mu A/mm^2$ (Neuser, 1995).

Automated Mineralogy

False-colour mineral maps of samples were acquired using automated scanning electron microscopy. Automated mineralogy was performed at the Colorado School of Mines' Mineral and Materials Characterization (MMC) Facility, using a TESCAN-VEGA-3 Model LMU VP-SEM platform which is equipped with the TIMA3 control software program. Four energy dispersive X-ray spectrometers acquire spectra from each point or particle with a user defined beam stepping interval (i.e., spacing between acquisition points) of 15 μm, an acceleration voltage of 25 keV, a beam intensity of 14 and a working distance of 15mm. Interactions between the beam and the sample are modelled through Monte Carlo simulation. The EDX spectra are compared with spectra held in a look-up table allowing a mineral

or phase assignment to be made at each acquisition point without making a distinction between mineral species and amorphous grains of similar composition. Results are output by the TIMA software as a spreadsheet giving the area percent of each composition in the look-up table. This procedure allows a compositional map to be generated. Composition assignments will be grouped appropriately.

5.2. Thermodynamic modelling

Thermodynamic modelling was done using Geochemist's Workbench software package version 12 and 14. The application React was used for reaction path calculations and Phase2 for stability, predominance and solubility diagrams. The applied thermodynamic database is the Thermoddem database that was extrapolated from 0-300 °C (Blanc et al., 2012) to 0-600 °C and 2.5 kbar. This extrapolation and the added minerals where integrated into the database by Philippe Blanc, the creator and maintainer of the data base (Blanc et al., 2012) to keep internal consistency. The list of minerals considered in thermodynamic calculations are for silicates: actinolite, aegerine, albite, almandine, andalusite, andradite, annite, anorthite, antigorite, brucite, chlorite, diopside, eastonite, epidote, hedenbergite, jadeite, kyanite, microcline, muscovite (ordered), paragonite, phlogopite, quartz(alpha), quartz(betha), sanidine, sillimanite, staurolite, tremolite; oxides: bunsenite, corundum, hematite, magnetite, spinel, wustite; Native elements: nickel, arsenic, gold, graphite, iron, sulfur(alpha); sulfates: anhydrite, gypsum; sulfides and arsenides: arsenopyrite, löllingite, nickeline, millerite, vaesite, pyrite, pyrrhotite, troilite; carbonates: aragonite, calcite, dolomite, siderite.

Unfortunately, thermodynamic data for the main mineral of interest, pentlandite, is sparse in the literature. Both Gamsjäger (2005) and Robie and Hemingway (1995) suggest the use of the experimental enthalpy value by Cemič and Kleppa (1987) of -837.37 ± 14.59 kJ/mol, which is selected here. However, experimental values for the entropy of pentlandite of the composition $Ni_{4.5}Fe_{4.5}S_8$ (this study) is lacking. Thus, we have tried to estimate the entropy using several methods shown in Table 2. Four out of five methods are in good agreement with each other whereas one deviates significantly and thus is excluded. As a result, the value of 490 ± 20 kJ/mol K is selected for thermodynamic modelling. The temperature-dependent specific heat capacity (cp) was estimated by assuming Δcp reaction=0, according to the Neumann-Kopp rule for the reaction III in Table 2. The resulting temperature-dependent cp is: a = -

1956.6 J/molK, b = 4.9729 J/molK^2, c =80204000 J/mol/K. It is in good agreement with that of reaction IV at temperatures above 100 °C and with the experimental value of 442.7 J/mol K by Berezovskii et al. (2001) for $Ni_{4.6}Fe_{4.4}S_8$ at standard state conditions. The selected thermodynamic properties and sources are presented in Table 3.

Table 2: Estimation methodology for the entropy of pentlandite

	Resulting S^0 in J/mol K
(I) Ideal mixing on both octahedral and tetrahedral Fe/Ni position using entropy values from Waldner & Sitte (2008).	502,35
(II) Single ion method of Glasser (2013). Note that Fe^{2+} and S^{2-} ions where used, resulting in a charge imbalance.	483,70
(III) Additive method (ΔS=0): Ni_3S_2 + 1.5 NiS + 4.5FeS = $Ni_{4.5}Fe_{4.5}S_8$	484,35
(IV) Difference method (ΔS=0): Ni_9S_8 +4.5Fe = $Ni_{4.5}Fe_{4.5}S_8$ +4.5Ni	469,53
(V) Difference method using ΔS=0 for the following reaction: Ni_9S_8 +4.5FeS = $Ni_{4.5}Fe_{4.5}S_8$ +4.5NiS	514,03
(VI) Linear correlation with volume (Jenkins & Glasser 2003) Molar volume for $Ni_{4.5}Fe_{4.5}S_8$ from Robie & Hemingway (1995)	365,94

NiS = millerite, Ni_2S_3 = haezelwoodite, FeS = troilite, $Ni_{4.5}Fe_{4.5}S_8$ = pentlandite, Ni_9S_8 = Godlevskite, Fe = native iron

Table 3: Thermodynamic properties used in this study.

Mineral	ΔH^0_f	S^0	a	$b*10^3$	$c*10^{-5}$
	(kJ/mol)	(J/mol.K)	(J/mol.K)	(J/mol.K²)	(J/mol/K)
Ni4.5Fe4.5S8 (pentlandite)	-837.37 ±14.59[(1)]	490 ±20[(2)]	-1956.6[(2)]	4972.9[(2)]	802.0[(2)]

References: [(1)]Cemic & Keppla (1987), [(2)] this study

The extrapolation to higher temperature and pressure was achieved by coupling the Thermoddem database with the calculation tool ThermoZNS developed by Lassin et al. (2005). The latter allows calculating LogK(T) functions for T and P, based on the H_2O vapour curve, overcoming the H_2O critical point limit (Lassin et al. 2005). Within the course of the Geowell European project (http://geowell-h2020.eu/), this calculation process was applied successfully to the hydrothermal alteration of granite

based on calculations presented by Dolejš and Wagner (2008), and to phase relations in the CaO-SiO_2-Al_2O_3-H_2O chemical system, up to 600°C and 2 kbars (Lach et al., 2018). Using the HKF formalism for aqueous species (Helgeson et al., 1981), logK (T) calculations could theoretically reach 5 kbars and 1000°C. The database is formatted using the Thermobridge code to be compliant with the geochemical code of interest (Blanc et al., 2012) which provides the database for the Geochemist Workbench (Bethke, 2004) application.

The aqueous higher-order Ni-Cl complexes that are increasingly important at higher temperature were integrated from Liu et al. (2012) using the modified Ryzhenko–Bryzgalin model (Ryzhenko et al., 1985) for a pressure of 2.5 kbar. Introduced deviations from an internally consistent database is minimal since the fitting calculations from Liu et al. (2012) are based on the same thermodynamic data of HCl (Tagirov et al., 1997) that is also implemented into Thermoddem database.

6. Results

6.1. Petrography of hydrothermal veins

6.1.1. Petrography of vein type (1)

The alteration zone next to the vein is mostly composed of albite, replacing and overgrowing plagioclase, and a network of sulfides. In unaltered samples the trondhjemite contains about 30 % quartz, 5 % orthoclase, and 5 % biotite (Fig. 5). In the alteration zone these minerals are only found in traces (1-4 % quartz, 1-2 % orthoclase and <0.2 % biotite; Fig. 5). Pentlandite forms about 25-40 % of the sulfides in the alteration zone, whereas it represents 65-75 % of the sulfides in the vein.

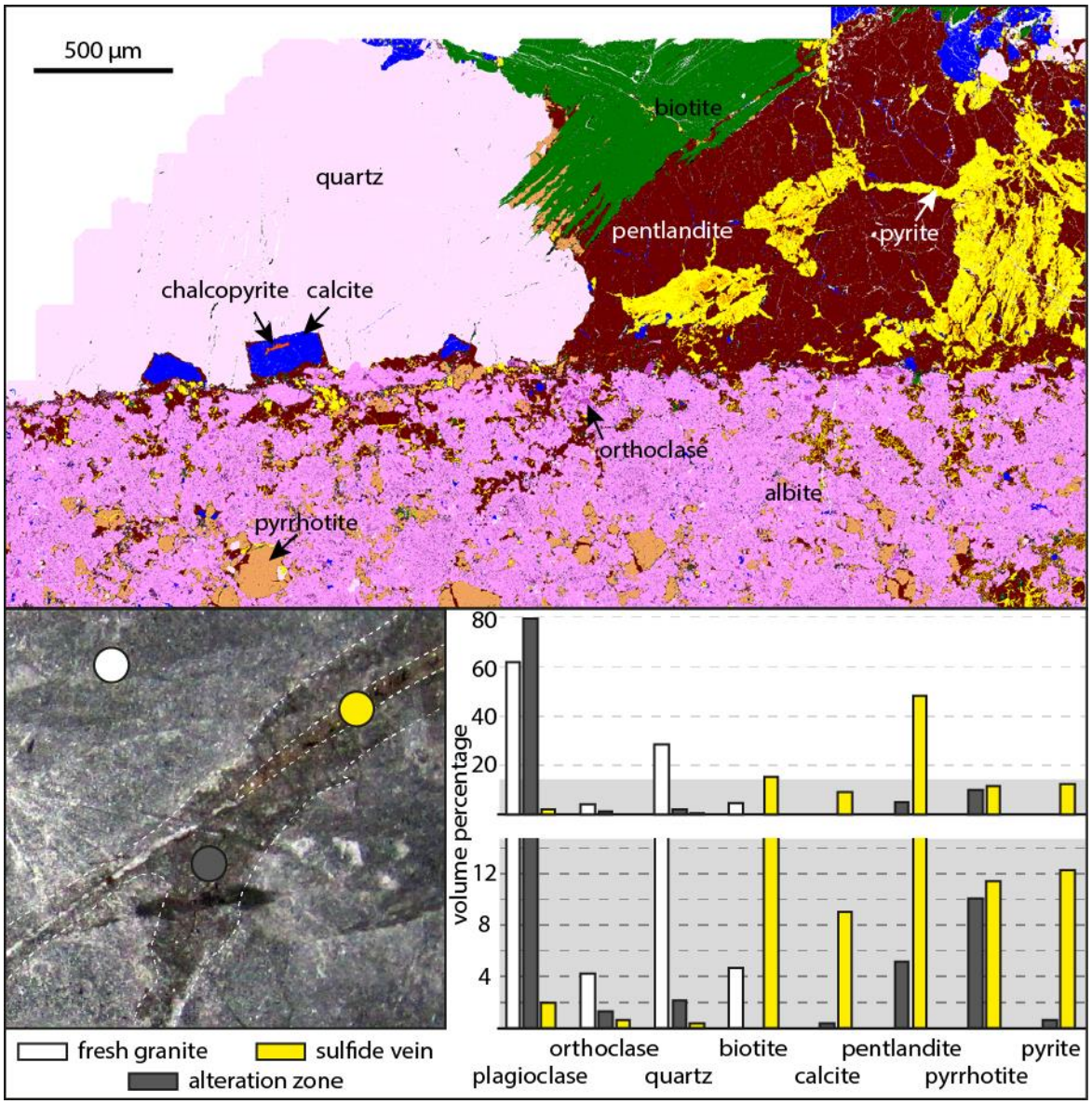

Figure 5

Mineral map of the contact of quartz with sulfide rich portion of the vein and the surrounding alteration. The mineral maps were used to quantify the modal mineral abundance with digital image processing. The fresh trondhjemite contains abundant quartz which is nearly absent in the alteration zone. Sulfide vein refers to the part of the vein where biotite and sulfides are intergrown; not including the irregular patches of quartz.

The vein is composed of euhedral biotite within pentlandite-dominated sulfides (Fig. 6). The sulfides also host anhedral calcite with minor amounts of albite, quartz and orthoclase. Quartz occurs as large patches in the vein (Fig. 5). It commonly overgrows the sulfides and biotite, but sometimes also shows contemporaneous growth. Vein-quartz overgrows euhedral calcite where it is in contact with altered

trondhjemite. Accessory phases are chalcopyrite, melonite, tetradymite, galena, a TiO_2 phase, apatite, chlorite, and muscovite.

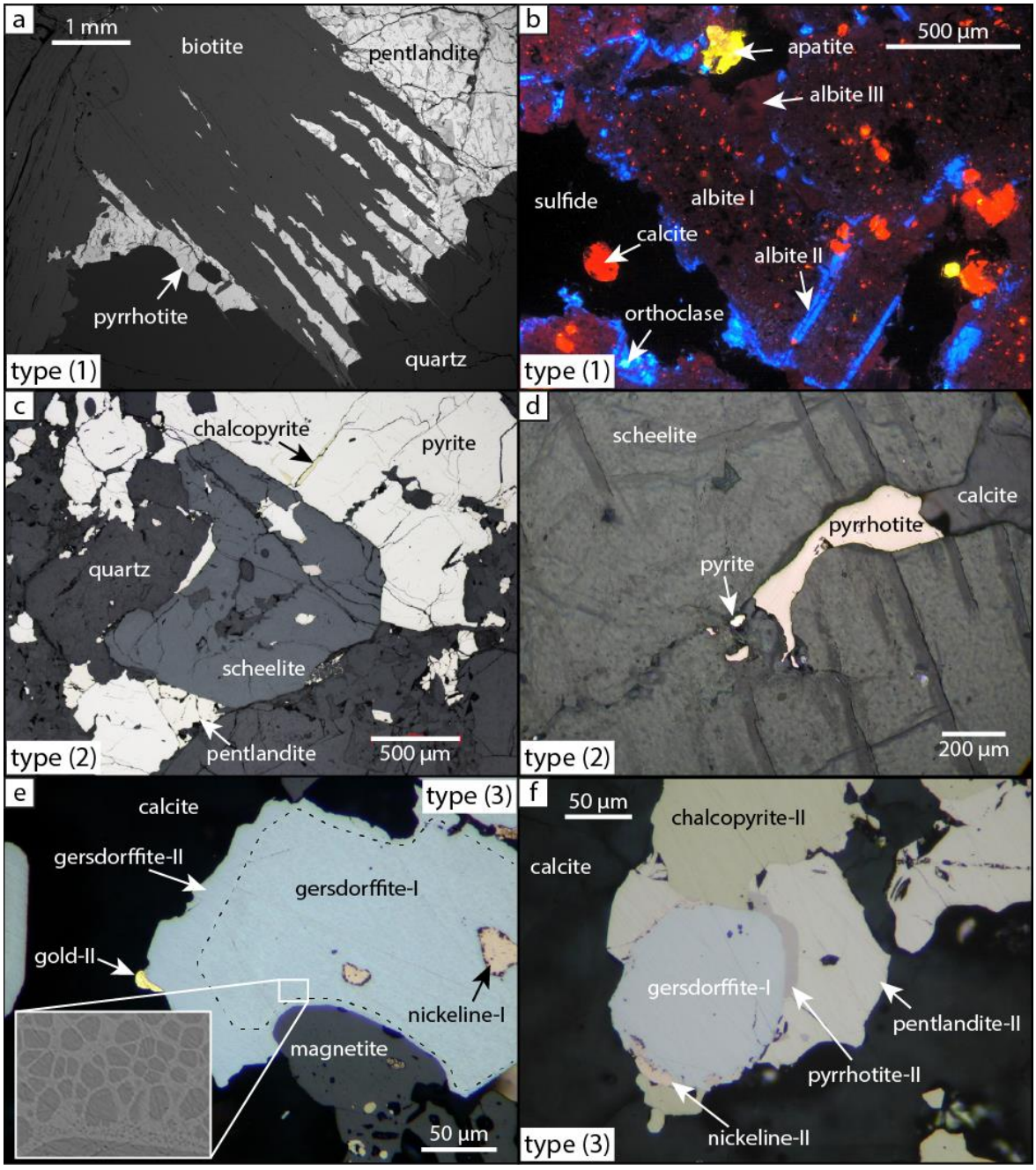

Figure 6

Photomicrographs of the pentlandite-bearing veins. (a) BSE image of a contact of quartz bearing part of the vein with biotite- and sulfide-rich part. Quartz overgrows the biotite-sulfide assemblage. (b) Cathodoluminescence image of the alteration zone in the trondhjemite showing three generations of albite. (c) Reflected light image (in air) of a poikilitic-like scheelite that overgrows sulfides and is overgrown by pentlandite-bearing sulfides. This sample originates from the vicinity of the McLeay deposit. (d) Reflected light image (in oil) of pyrite and pyrrhotite that are ovegrown by scheelite which is overgrown by

pyrrhotite and calcite. No pentlandite is observed in this sample from >100 m distance to a magmatic orebody. (e) and (f) Reflected light images (in oil) of the pentlandite-bearing arsenide assemblage cutting through Moran. Note the recrystallization of gersdorffite in the inlet in (e) (BSE image) where a S-rich gersdorffite is surrounded by a S-poor gersdorffite.

Evidence for a metamorphic overprint is common as many of the minerals show kinking and twinning and quartz has undulose extinction, a uniform cathodoluminescence signature and shows dynamic recrystallization. Furthermore, pyrrhotite is replaced by micrometre-sized pyrite-chalcopyrite symplectites, which has previously been interpreted to be a metamorphic phenomenon in the Moran deposit (Staude et al., 2017b).

6.1.2. *Petrography of vein type (2)*

Quartz-dominated veins of this type are accompanied by biotite, epidote, scheelite, sulfide, albite, carbonate and apatite alteration of the basalt, whereas it shows talc, carbonate and scheelite alteration in the komatiite. There are at least two generations of scheelite; one predating the felsic dykes and one being coeval or younger than the dykes. Scheelite is either <1 mm and disseminated in basalt, forms euhedral crystals (<5 mm) on the veins selvedge, or forms irregular masses (<10 cm) in veins and in the adjacent basalt. Disseminated scheelite and euhedral crystals are colourless to grey, whereas the masses are orange (Fig. 2c). In samples near the magmatic McLeay deposit, poikilitic-like scheelite overgrows an older hydrothermal sulfide assemblage which overgrows euhedral (but now recrystallized) quartz. This poikilitic-like scheelite is overgrown by younger hydrothermal sulfides. Both sulfide assemblages consist of euhedral pyrite, anhedral pyrrhotite, pentlandite, and chalcopyrite. However, due to recrystallization, the age relations between them are not possible to determine. Pentlandite is found only in samples close to older magmatic sulfides (<10 m). In samples further away from magmatic deposits (approximately 100 m to McLeay and 200 m to Moran South along strike of the scheelite-bearing structure) no pentlandite is observed and the sulfide assemblage consists only of pyrite, pyrrhotite, and chalcopyrite. Accessory minerals are muscovite, melonite, and molybdenite.

6.1.3. Petrography of vein type (3)

This type is characterized by a pervasive magnetite alteration of the magmatic sulfides next to the vein, as well as within the vein. On the direct contact to the vein the magmatic sulfides are partly replaced by gersdorffite and nickeline or are overgrown by hydrothermal calcite if not replaced by arsenides. Sometimes nickeline is overgrown by maucherite. Gersdorffite is the youngest arsenide phase, overgrowing nickeline/maucherite. Nickeline-gersdorffite associations have been observed in two generations. The first generation of nickeline-I (with maucherite) and gersdorffite-I is anhedral and show recrystallization with grain contact angles of 120°. The younger generation is euhedral, partly overgrows older arsenides, and does not show recrystallization. Gold is intergrown with nickeline-I and with gersdorffite-II, which it partly overgrows (Fig. 6e).

Hydrothermal pentlandite, in association with pyrrhotite and chalcopyrite, is generally anhedral and occurs in two generations. The first generation overgrows arsenides-I and is overgrown by the second arsenide generation. The larger proportion of pyrrhotite-pentlandite-chalcopyrite overgrows both arsenide generations.

Calcite is the dominant gangue mineral which occasionally hosts tremolite and chlorite causing a green colour of the samples (Fig. 2f). Distinctly contrasting to type (1) and (2), biotite is absent within this association. All calcite shows signs of strain and has grain boundaries of 120° and the arsenide-sulfide assemblage I is partly replaced by chalcopyrite-pyrite symplectite. Other rare symplectites are nickeline-chalcopyrite next to gersdorffite, nickeline-pyrrhotite between chalcopyrite and gersdorffite, and nickeline-gersdorffite within pyrrhotite. The relative ages of these symplectites are unclear. Other observed accessory minerals, without relative age determination, are bornite, arsenopyrite, löllingite, galena, sphalerite, argentopentlandite, nat. Ag, nat. Bi, undetermined Pd-Te and Bi-Pd-Te phases, famatinite, greenockite, mackinawite (as exsolution in chalcopyrite), tungstenite and ilmenite.

6.1.4. Petrography of physically mobilized sulfides

383 The mineral assemblage of physically mobilized sulphide orebodies are identical to the magmatic
384 mineral assemblage with the exception that magnetite is missing. Several sub-grains form larger clusters
385 of pyrrhotite and pentlandite, respectively, with the sub-grains having grain boundaries of about 120°.
386 The sulfides are overprinted by a symplectic pyrite-chalcopyrite assemblage. Trace amounts of
387 melonite, molybdenite and sphalerite are present.

388

389 *6.2. Mineral composition of sulfides and silicates*

390 Hydrothermal pentlandite generally differs in its Fe and Ni content relative to the neighbouring
391 magmatic pentlandite, although compositional overlapping is common (Fig. 7). This overlap is
392 especially pronounced for type (1) where the hydrothermal pentlandite shows a larger variation in Fe
393 and Ni and overlaps with the magmatic pentlandite. However, type (2) and (3) pentlandite display a
394 clearly higher Fe content at constant Ni compared to their magmatic counterpart (Fig. 7a). The average
395 molar Fe/Ni ratio for hydrothermal type (2) pentlandite is 0.92 and for magmatic pentlandite as well as
396 for the physically mobilized pentlandite it is 0.88. For type (3) hydrothermal pentlandite the average
397 molar Fe/Ni ratio is 0.89 and for the neighbouring magmatic pentlandite of McLeay it is 0.85.
398 Pentlandite of vein type (3) has a lower Co content (2000-2500 ppm) compared to most of the adjacent
399 magmatic pentlandite (4000-5500 ppm, but this is dependent on the spatial occurrence within the
400 orebody; Staude et al., (in press) as well as the physically mobilized pentlandite (3000-5000 ppm Co).
401 The other hydrothermal pentlandite types do not differ significantly with respect to trace element
402 concentrations relative to the respective magmatic pentlandite (Fig. 7b).

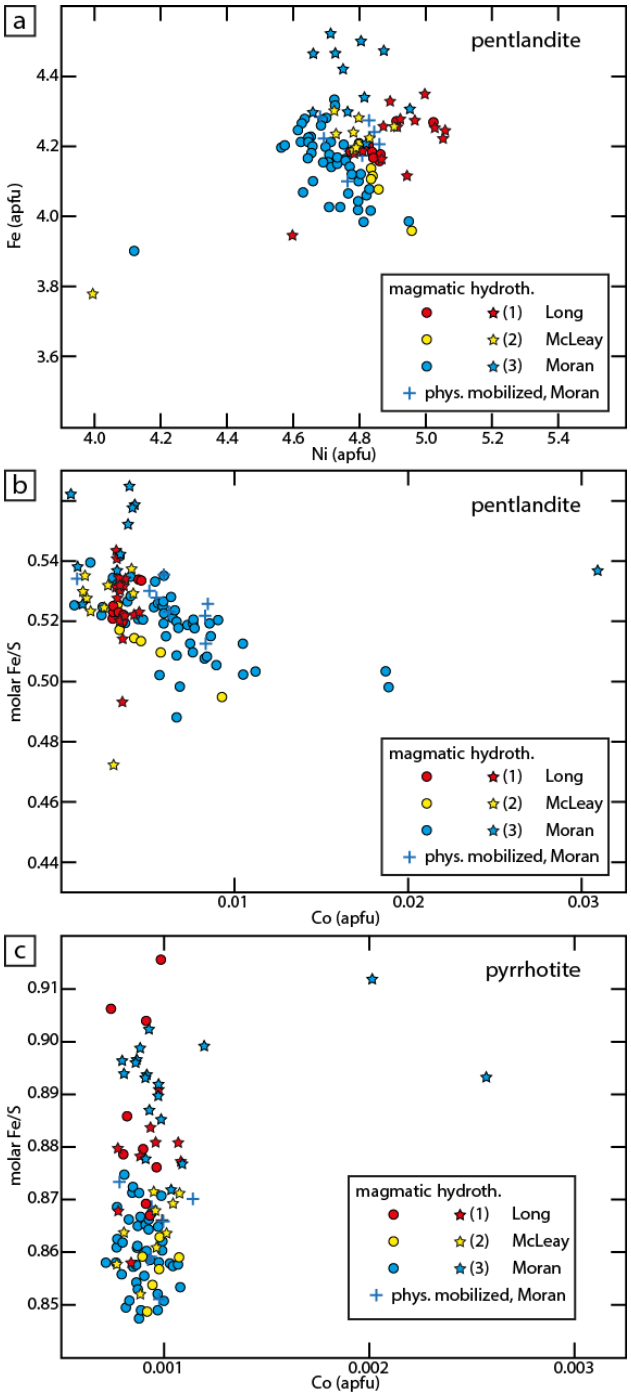

Figure 7

Chemical variation of pyrrhotite and pentlandite. (a) Fe versus Ni in atoms per formula unit (apfu) of magmatic and hydrothermal pentlandite. There is no clear variation between magmatic and hydrothermal at Long North, but for Moran and McLeay the hydrothermal pentlandite displays a higher Fe content. Note the similar composition of magmatic and physically mobilized pentlandite. (b) Molar Fe/S ratio versus Co concentration in pentlandite. Magmatic (from Moran and McLeay) and physically mobilized pentlandite show a higher Co content compared to hydrothermal pentlandite. There is no clear variation between magmatic and hydrothermal at Long North. (c) Molar Fe/S ratio versus Co concentration in pyrrhotite. With the exception of Long North display hydrothermal pyrrhotites a higher Fe/S ratio.

412

413 A similar variation between hydrothermal and magmatic is visible in the molar Fe/S ratio of pyrrhotite
414 (Fig. 7c). Type (1) again largely overlap with magmatic pyrrhotite, whereas the other hydrothermal
415 pyrrhotite types have characteristically higher molar Fe/S ratios compared to their magmatic pyrrhotite
416 counterparts. Type (2) pyrrhotite has an average ratio of 0.864 whereas for the neighbouring magmatic
417 it is 0.857. Type (3) pyrrhotite has an average molar Fe/S ratio of 0.892, whereas for the magmatic
418 pyrrhotite and the physically mobilized pyrrhotite it is 0.860 and 0.864 respectively. In type (3)
419 pyrrhotite, which occurs together with arsenides, the As content is always above the detection limit of
420 300 ppm and ranges between 900 and 2000 ppm, whereas in all the other hydrothermal pyrrhotite types
421 as well as the magmatic pyrrhotite it is below the detection limit.

422 The composition of the sulfarsenides also depend on their origin (Fig. 8a). Magmatic cobaltite
423 commonly is euhedral, overgrows sperrylite and is overgrown by tellurides (Staude et al., in press). It
424 contains up to 14.5 wt.% Ni and 7.0 wt.% Fe as well as up to 5000 ppm Bi, which is not detected in
425 hydrothermal sulfarsenides. The major elemental composition of the magmatic sulfarsenide in the
426 investigated ore bodies is similar to magmatic sulfarsenides reported from other komatiite-hosted sulfide
427 deposits (Fig. 8b) deposits. The composition of hydrothermal gersdorffite of type (3) is spatially
428 dependent and two groups can be classified, independently of the observed two generations. A high Co-
429 and Fe-bearing gersdorffite occurs on the direct contact to magmatic sulfides. In this gersdorffite the
430 highest Co concentration is located on grain boundaries and where the gersdorffite replaces the
431 magmatic sulfide (Fig. 8). A low Co- and Fe-bearing gersdoffite occurs everywhere in the vein which
432 is not in contact with magmatic sulfides. This phenomenon has previously been reported in similar cases
433 where Au-bearing mineralization cuts through the komatiitic sulfide deposit (Fig. 8c).

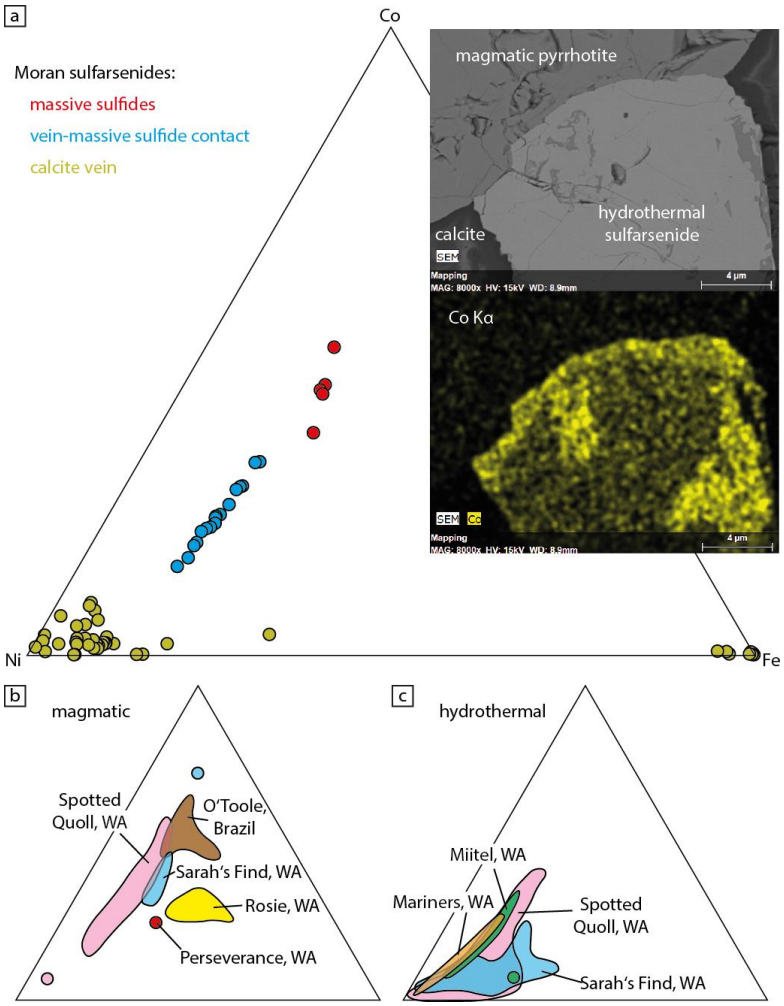

Figure 8

Gersdorffite (Ni)-cobaltite (Co)-arsenopyrite (Fe) triangle to discriminate between magmatic and hydrothermal sulfarsenides. (a) Magmatic sulfarsenide display the highest Co content, hydrothermal sulfarsenides on contact with magmatic sulfides an intermediate Co content, and hydrothermal sulfarsenide within the vein the lowest Co content. The inset shows magmatic sulfides overgrown by hydrothermal sulfarsenides. Cobalt is concentrated on the rim and on the contact to the magmatic sulfides. (b) Magmatic sulfarsenides from other komatiite-hosted sulfide deposits. They are similar to the composition of the Moran sulfarsendies with the exception of Spotted Quoll, which could be due to a hydrothermal overprint. (c) Composition of sulfarsenides from other komatiite-hosted deposits which formed from a hydrothermal overprint. They exhibit the same trend as observed for hydrothermal sulfarsenides from the Moran hydrothermal veins. O'Toole: Marchetto (1990), Rosie: Godel et al. (2012), Sarah's Find: (Le Vaillant et al., 2016), Perseverance: (Le Vaillant et al., 2018), Spotted Quoll: (Prichard et al., 2013), Mariners: Goodgame (1997), Miitel: (Le Vaillant et al., 2015).

Biotite of vein type (1) and (2) is similar in its composition (ESM 1). Magnesium varies between 1.4 and 1.9 atoms per formula unit (apfu) and Fe between 0.8 and 1.2 apfu. All biotite associated with

hydrothermal mineralization contain between 0.01 and 0.03 apfu Ni. Fluorine was only detected in biotite of vein type (1) with up to 0.16 apfu. Plagioclase in the alteration zone of vein type (1) is near end-member albite, independent of the observed generation, with a maximum Ca content of 0.02 apfu.

7. **Discussion**

7.1. Comparison of hydrothermal and magmatic mineralization

The mineralogy of the vein-type sulfides is distinct different to the magmatic sulfides. In the vein-type sulfides, chromite and magnetite are absent (except in type 3 vein) and minerals such as biotite, quartz and carbonate (type 1), quartz, biotite and scheelite (type 2), and carbonate, arsenides, base metal sulfides and gold (type 3) are common. Thus, they are easily to distinguish from the primary magmatic sulfides.

Hydrothermal pentlandite tends to be enriched in Fe compared to magmatic pentlandite (Fig. 7). However, there is a large overlap between both. A distinct difference between hydrothermal and magmatic pentlandite is also visible in the Co content (Fig. 7). Magmatic, and importantly physically mobilized pentlandite show a large variation (depending on its position within the orebody; Staude et al., in press), whereas hydrothermal pentlandites of all vein types have a low Co content. Therefore, the Fe and Co content of pentlandite can be used to discriminate between magmatic and hydrothermal origin if the typical indicator minerals for the respective vein type are absent. Similarly, the Fe/S ratio and the As content of pyrrhotite further helps to differentiate them.

In hydrothermal mineralization with arsenides the sulfarsenide habit and composition can be used to discriminate between hydrothermal and magmatic origin. Magmatic sulfarsenides from Moran, and from other reported occurrences, are euhedral and rich in Co (up to cobaltite composition). Contrarily, hydrothermally formed sulfarsenides, replacing magmatic sulfides, are anhedral and rich in Ni (gersdorffite; or rarely Fe: arsenopyrite) and are therefore easily to distinguish.

7.2. Timing of vein formation and fluid origin

The pentlandite-bearing vein type (1) in Long North cuts the 2662±6 Ma trondhjemite. The mineralization shows intense deformation (kinking of minerals, twinning, 120° grain boundaries) and is overprinted by chalcopyrite-pyrite symplectite and thus, has been metamorphically overprinted. This leaves only a short time gap for the vein formation between 2662 and 2655 Ma, considering the lower boundary of the youngest metamorphic event at Kambalda occurred at 2655 Ma. Vein types (2) and (3) cut through the basalt and komatiite and are metamorphically overprinted, which results in a formation period between 2700 and 2655 Ma. In addition, vein type (3) has an overgrowth of euhedral minerals without the indication of a metamorphic overprint. Thus, the late stage of vein type (3) formed past the peak metamorphism, but due to the similar mineralogy compared to orogenic gold deposits, most likely from the same fluid system as this deposit type. The quartz-carbonate-biotite-albite mineral assemblage in type (1) and quartz-carbonate- biotite-epidote assemblage in type (2) further indicate a metamorphic fluid origin. In summary, mineralogy and textures indicate that all three mineralization types formed in a narrow time period, during or after peak metamorphism, from metamorphic fluids. Hence, metamorphic temperatures and pressures of 500°C and 2.5 kbar are assumed to have prevailed during vein formation and thus these were chosen for thermodynamic calculations. In addition to the peak metamorphic conditions reported by Bavinton (1979), a similar temperature (480±60 °C) was found in biotite- and hydrothermal pentlandite-bearing mineralization in the St. Ives gold district (Bath et al., 2013).

7.3. Fluid conditions to form pentlandite-bearing veins

The structural setting and spatial occurrences of the pentlandite-rich vein type (1) as well as their mineral assemblages leads to the assumption that the veins formed by a fluid, probably in equilibrium with serpentinite, interacted with the massive sulfide orebody and precipitated the veins within the felsic host rock. Thus, it can be assumed that the Ni in the vein is largely sourced and remobilized from the older magmatic orebody. However, the exact nature of the fluid origin or composition, prior to reacting with the magmatic massive sulfide body is not well constrained. Furthermore, the fact that the komatiitic rock is highly variable with respect to mineralogy (variable proportions of serpentine, chlorite, magnetite, tremolite, talc and carbonates, depending on the degree of metamorphic-hydrothermal overprint; Arndt

et al., 2008) and the local presence of felsic to intermediate dikes makes the determination of an original fluid composition prior to reacting with the magmatic sulfide orebody difficult. Thus, we have selected several host rock endmember compositions that exist in the vicinity of the sulfide orebody and let a neutral ± 2 pH fluid at several steps along the whole lower redox range equilibrate with serpentinite as possible initial fluids. These fluids were then equilibrated with the sulfide orebody (Fig. 9a). The maximum fO_2 of the equilibrated fluid is defined by the magnetite stability of the serpentinite and the orebody. The resulting fluid compositions show an Fe:Ni ratio of >10 with the relative and absolute Fe- and Ni-content being strongly pH dependent and the S-content reaching up to ~1000mg/kg, which decreases with more reduced conditions. The highest Ni content of the fluids are in the order of 10 mg/kg, which is why the composition of 10, 100 and 1000 mg/kg of Ni, Fe and S, respectively, was chosen as a basis for further thermodynamic modeling.

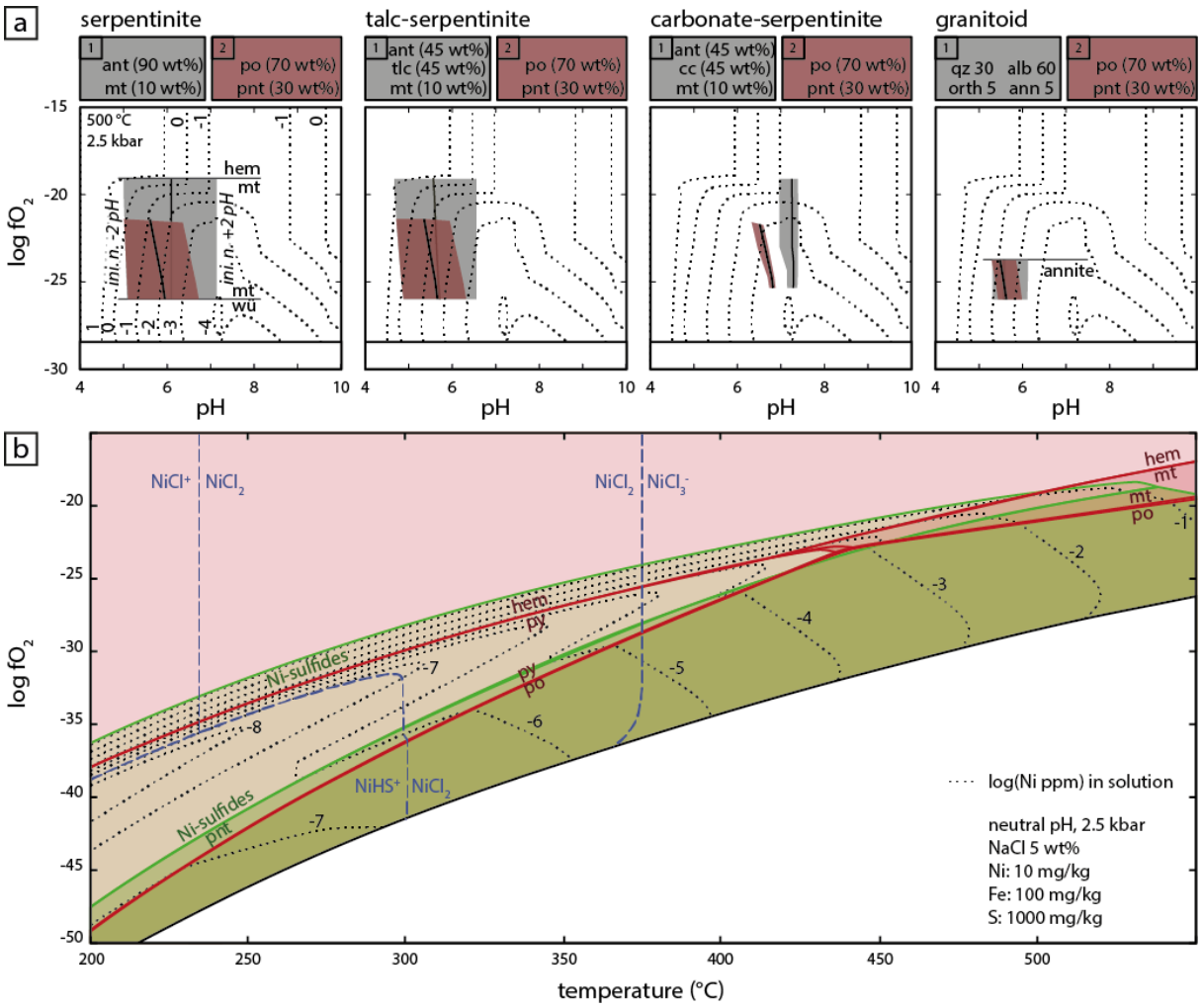

Figure 9

(a) Thermodynamic predictions at 500 °C of various possible initial fluid endmembers that resided in the region of the orebody (various types of serpentinites and a granite equilibrium fluid) and their resulting fluid conditions (with the contours for the log Ni ppm in solution) at equilibration with the orebody. (b) Temperature and fO2 dependent Ni-solubility at neutral pH and a fluid composition estimation based on the maximum soluble Ni and the relative contents of Fe and S, according to (a). Wüstite is disregarded. Abbreviations: mt=magnetite, hem=hematite, po=pyrhottite, pnt=pentlandite, Ni-sulfides=millerite and NiS_2.

With increasing fluid temperature, the stability of aqueous Ni-Cl species increases, conjointly with an increase in Ni coordination by Cl (Liu eta al. 2012; Fig. 9b). The higher temperatures facilitate the transport of Ni, even at reduced and roughly neutral conditions, for which Ni is fairly immobile. To enable the transport of significant amounts of Ni with these conditions, the metal bearing fluid must have been as acidic and/or as high in temperature as possible (Fig. 9b and 10). Thus, it is most likely that the initial fluid did not strongly interact with carbonate-rich regions of the serpentinite, but is more profoundly influenced by antigorite or talc rich sections (Fig. 9a). This enables a lower pH, and thus, a more pronounced ability to transport Ni at reduced conditions.

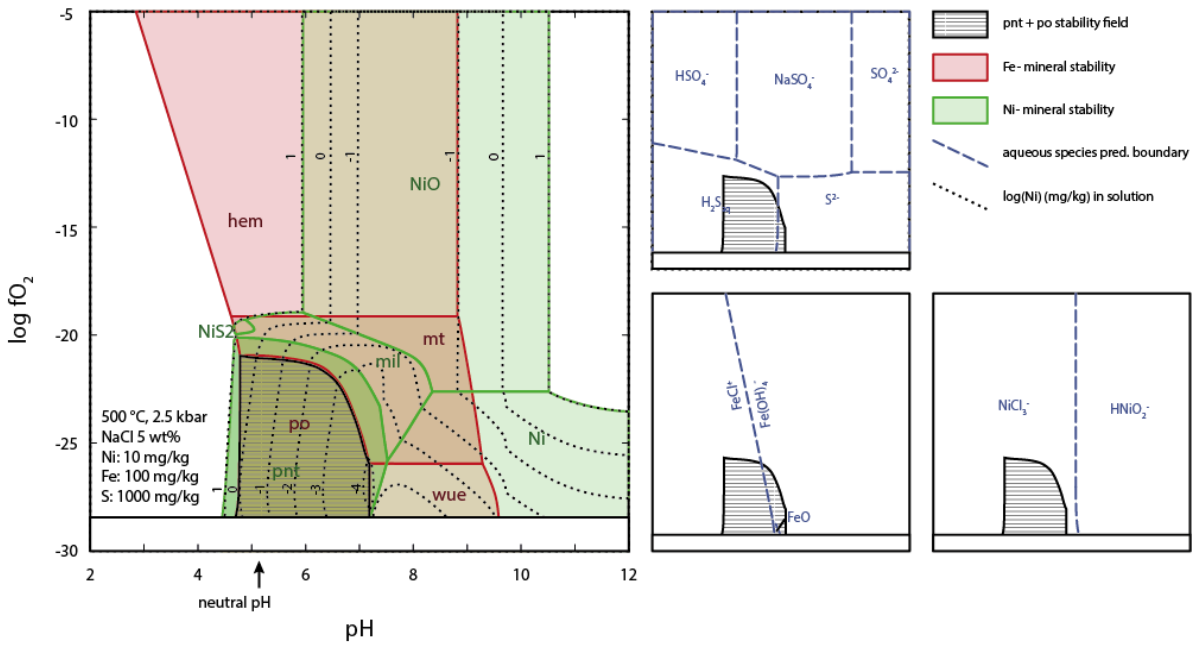

Figure 10

Thermodynamic calculations of the redox and pH dependence of the Ni-Fe-S-Na-Cl system at 500 °C for the fluid composition of calculated by modeling of Fig. 9. Hatched area represents overlapping stability field of pentlandite and pyrhottite which is

the mineral assemblage visible in the veins and host rock alteration zone. Abbreviations: mt=magnetite, hem=hematite, wue=wüstite, po=pyrhottite, pnt=pentlandite, mil=millerite, Ni=native Ni.

The most effective precipitation mechanism of a pentlandite and pyrrhotite assemblage without the formation of abundant pyrite, hematite and millerite (which are stable at slightly more oxidizing conditions) is by pH increase to slightly basic conditions of a reduced fluid. Additionally, fluid cooling favours the precipitation of the observed minerals. This can be achieved by neutralization of a slightly acidic and reduced Ni-bearing fluid by mixing (e.g. see active hydrothermal vents on the ocean floor; Table 1) or by interaction with, for example, the host rock. Due to the pentlandite-bearing alteration zone of the host rock next to the veins, a reaction-based precipitation mechanism is most likely for the granitoid-hosted pentlandite-bearing veins. The reaction of the pentlandite-forming fluid with the felsic host rock is strongly dependent on the fluid composition, especially with respect to pH and elemental composition such as, but not limited to Al, Si and K. However, the exact fluid composition is unknown and due to the high number of unknown variables, thermodynamic modelling of this replacement reaction was not possible. Mass balance calculations show that Al has to be introduced into the alteration halos around pentlandite veins by the fluid as the absolute albite content increases at the cost of mainly quartz and biotite (Fig. 5). The source of Al in the initial fluid may have been felsic dikes within the serpentinite.

Quartz dissolution in the alteration zones around the pentlandite-bearing veins in question shows an initial under-saturation of quartz and/or an increase in pH, where the latter is in accordance to the proposed pentlandite precipitation mechanism. Re-precipitation of quartz within the vein itself can be attributed to a decline in temperature and/or pressure as this is the most effective precipitation mechanism for quartz (Li et al., 2020). However, the importance of fluid mixing cannot be excluded. A high K concentration is needed for the stability of biotite to prevail over that of antigorite at neutral to slightly basic conditions (Fig. 11). If one assumes that the primary fluid originated from the serpentinite, it is expected to be rich in Mg but poor in K and thus significant granitic host rock alteration is needed before biotite formation can occur within the vein (Fig. 11). Thus, we suggest that K-enrichment of the

fluid during mica and alkali feldspar dissolution in the alteration zone of the host rock enables biotite formation within the vein.

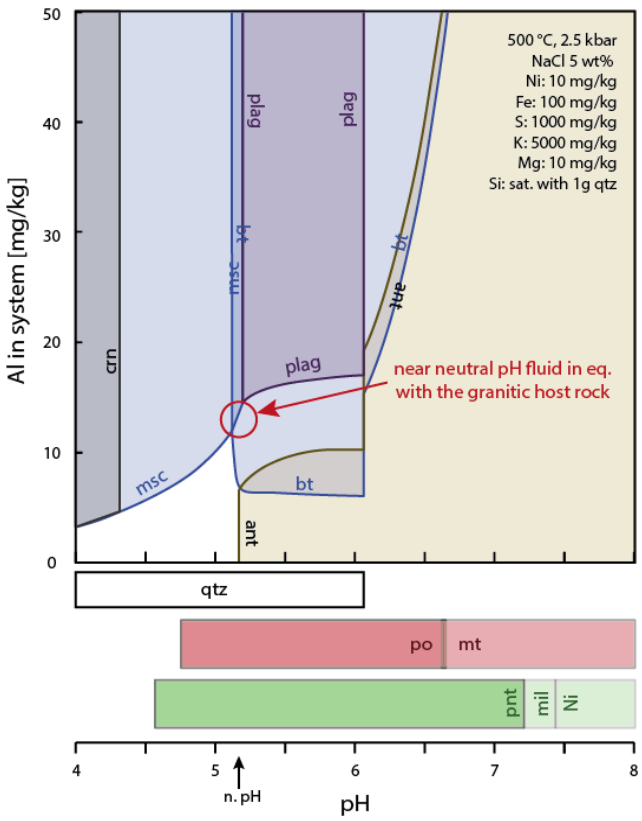

Fix 11. Thermodynamic modelling of the pentlandite-veins in the Ni-Fe-S-Na-K-Mg-Si-Cl system. Input variables for salinity, Ni, Fe, S are taken from Fig. 8 & 9. Magnesium concentration is taken from the serpentinite equilibrated fluid at neutral pH and Potassium from the granitic equilibrated fluid at near neutral conditions. This enables this diagram to represent the maximum pH-stability range of biotite, as Mg and K are not expected to be higher (more likely lower) than the concentrations shown here. The Silica is set by the fluid being in equilibrium with 1g of quartz, as the veins host abundant quartz and quartz saturation is achieved at roughly neutral pH. Mineral stabilities below the Al-dependent graph are only pH dependent and are not in the graph due to illustration purposes. Abbreviations: qtz=quartz, plag= albite, msc=muscovite, bt=phlogopite, ant=antigorite, crn=corundum, mt=magnetite, po=pyrhottite, pnt=pentlandite, mil=millerite, Ni=native Ni.

The stability of both the sulfide and silicate assemblage within the veins clearly indicates reduced formation conditions at neutral to slightly basic pH (Figs. 10 & 11). The silicate assemblage within the veins, as well as the alteration halo, show a strong interaction with the host rock, congruent with a K and Si increase within the fluid and thus enabling oversaturation of quartz and biotite.

In vein-type (2) a textural age relation between the minerals is mostly not possible. Due to the mineralogical similarity to vein-type (1) (e.g., quartz-biotite-carbonate-sulfide mineralization), with the exception of scheelite, thermodynamic modelling has not been separately preformed for these veins.

7.4. Fluid conditions to form pentlandite in arsenide-bearing veins

Type (3) veins have been frequently reported in literature (e.g., Prichard et al., 2013; Le Vaillant et al., 2015, 2018) and thermodynamic calculations have been performed for various arsenide minerals (e.g., Scharrer et al., 2019), and thus, type (3) veins are modelled to discriminate the differences to type (1) veins.

The reaction of an arsenic-bearing fluid with the magmatic sulfide body enables the oversaturation of initially nickeline, followed by millerite and/or pentlandite and pyrrhotite (Fig. 12). The formation of nickeline is however constrained to reducing conditions (depending on the As content of the fluid; Fig. 12). Although insufficient thermodynamic data exists for gersdorffite, preventing it to be quantitatively considered during modeling, its stability is bound to the transition between nickeline and millerite (qualitatively shown in Fig. 12). It is expected to form after nickeline, during successive sulfur enrichment of the fluid. As soon as pentlandite and pyrrhotite are saturated, the reaction with the host magmatic sulfides is halted. Subsequent fluid cooling and/or local variabilities in parameters such as pH will then continue to promote precipitation of these two minerals. Thus, the mineral sequence preserved in these veins (nickeline → gersdorffite → pentlandite + pyrrhotite) can be thermodynamically explained. Furthermore, the relative abundance of magnetite within and around these arsenide-bearing veins is congruent with thermodynamic predictions. If we assume a scenario, where Au is near saturation in the initial As-rich fluid prior to the reaction with the host rock, Au precipitation is expected to occur in association with the arsenide/sulfarsenide, as observed (Fig. 12). During progressing sulfur enrichment of the fluid, the stability of aqueous Au-sulfide complexes prohibits the formation of later Au.

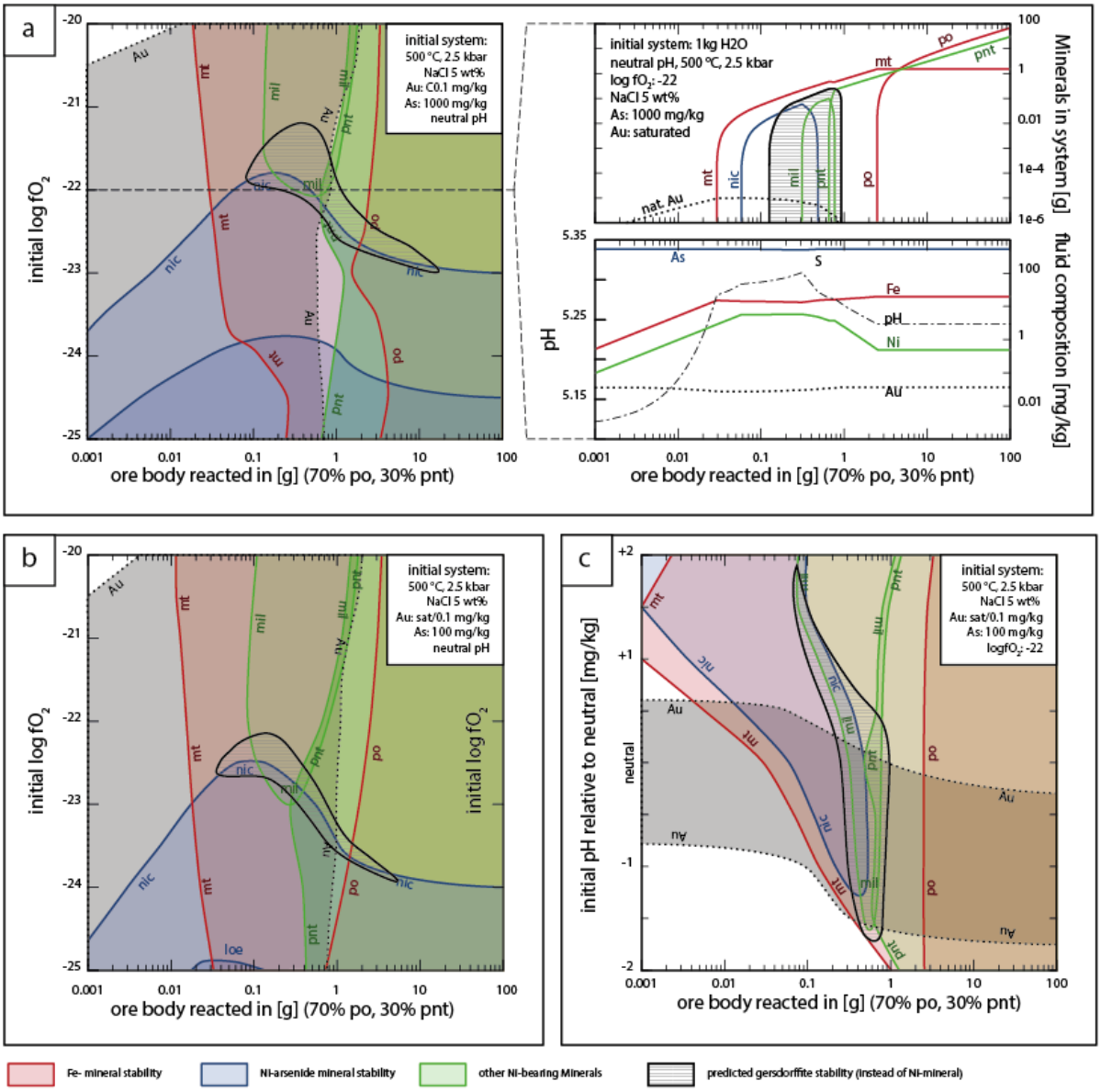

Fig. 12

Thermodynamic model of the reaction of an As bearing, Au saturated (max 0.1 mg/kg Au) fluid with the magmatic sulfide orebody. Variabilities concerning the initial redox (a), initial As content (b) and initial (pH) show the mineral sequence present in the arsenide veins formed from an initially roughly neutral pH fluid with reduced conditions where the exact redox state needed depends on the availability of As. Stability field diagrams are generated from reacted mass - mineral in system diagrams at logf_{O2} and pH steps of at least 0.5 with successive interpolation. The stability field of gersdorffite is qualitatively predicted and not thermodynamically modelled. mt=magnetite, hem=hematite, wue=wüstite, po=pyrhottite, pnt=pentlandite, mil=millerite, Ni=native Ni, nic=nickeline, loe=löllingite, Au=native Au.

7.5. Pentlandite in gold ore

Pentlandite often occurs as accessory mineral in orogenic gold deposits and have also been described from IOCG deposits (Table 1). There are several large gold deposits along the Boulder-Lefroy Fault which are thought to originate from either metamorphic (Phillips et al., 2017) or magmatic fluids (Bath et al., 2013; Mueller et al., 2020). In a recently published model, it is proposed that the metamorphic fluids forming orogenic gold deposits originate from the devolatilization of a subducted oceanic slab containing Au- and As-bearing sulfide-rich sediments (Groves et al., 2020). Some of the investigated veins also contain gold in combination with a contrasting mineralogy relative to the others. Since all these veins are interpreted to have formed from metamorphic fluids (see section 7.2), it needs to be discussed why similar fluids form differing vein types (minor pentlandite with gold vs. major pentlandite without gold).

Textures of all three types suggest they formed in a narrow time period during syn- to late-metamorphism, the mineralization is found in comparable small fluid pathways (cm-sized veinlets rather m-sized veins) and all fluids had to interact with magmatic sulfides to pick up Ni. Additionally, textures and the calculations in section 7.3. suggest that type (1) and probably type (2) fluids interacted with the local lithology (i.e., dissolve biotite in the alteration zone and re-precipitate it in the vein) and are probably sourced from the regional metamorphic reservoir. There are three possibilities to explain the absence of As and Au in type (1) veins, the lack of precipitation, different fluid and metal sources or that these veins represent different stages of an evolving fluid.

The lack of precipitation can be thermodynamically explained by the stability of pentlandite together with pyrrhotite and biotite, which spans a small field in which gold has a high solubility (Fig. 13a). Considering the fluid source, it is suggested that subducted sediments are the source of arsenic and gold in many orogenic gold deposits, whereas the regional lithology's are poor in arsenic and gold (Groves et al., 2020). However, a potential regional gold source may be present, as the metamorphically overprinted magmatic sulfides can contain gold (Figs. 13b and c). Although the theoretically possible pH range of formation of the type (3) veins is wider than the other veins as they are arsenide bearing and lack biotite (Fig. 11), a simple pH shift is not sufficient in explaining the mineralogical differences.

This is because if arsenic were present in the non-arsenide-bearing vein type (1) and (2) fluids, they would also have formed during vein precipitation. Thus, vein type (1) or (2) and (3) could not have formed from compositionally identical fluids at the time of formation.

This leaves the possibility of either two differently sourced fluids or a fluid evolution with type 3 veins forming prior to type 1 and 2 veins. Vein type (3) could represent the stage where the As- and Au-bearing fluid interact with the magmatic sulfides to form arsenides and gold, which become exhausted in the fluid during this stage and are not present in later mineralizing events. However, an evolutionary scenario would also have to explain the contrasting gangue mineralogy as vein type (3) is dominated by carbonate (>90 %; Figs. 2, 3) whereas vein type (1) is dominated by sulfides (>70 %) and quartz, and only minor carbonate, within the vein and albite (80 %) in the alteration zone (Fig. 5). Therefore, different fluids are most likely the reason for the contrasting mineralogy, although in all mineralization types metamorphic fluids formed the veins. Type (3) veins must have been hydraulically connected to larger deep-reaching structures, as the Boulder-Lefroy Fault, whereas this fluid pathway was not available for the formation of type (1) and (2), although at least type (2) vein is sub-parallel to the Boulder-Lefroy Fault.

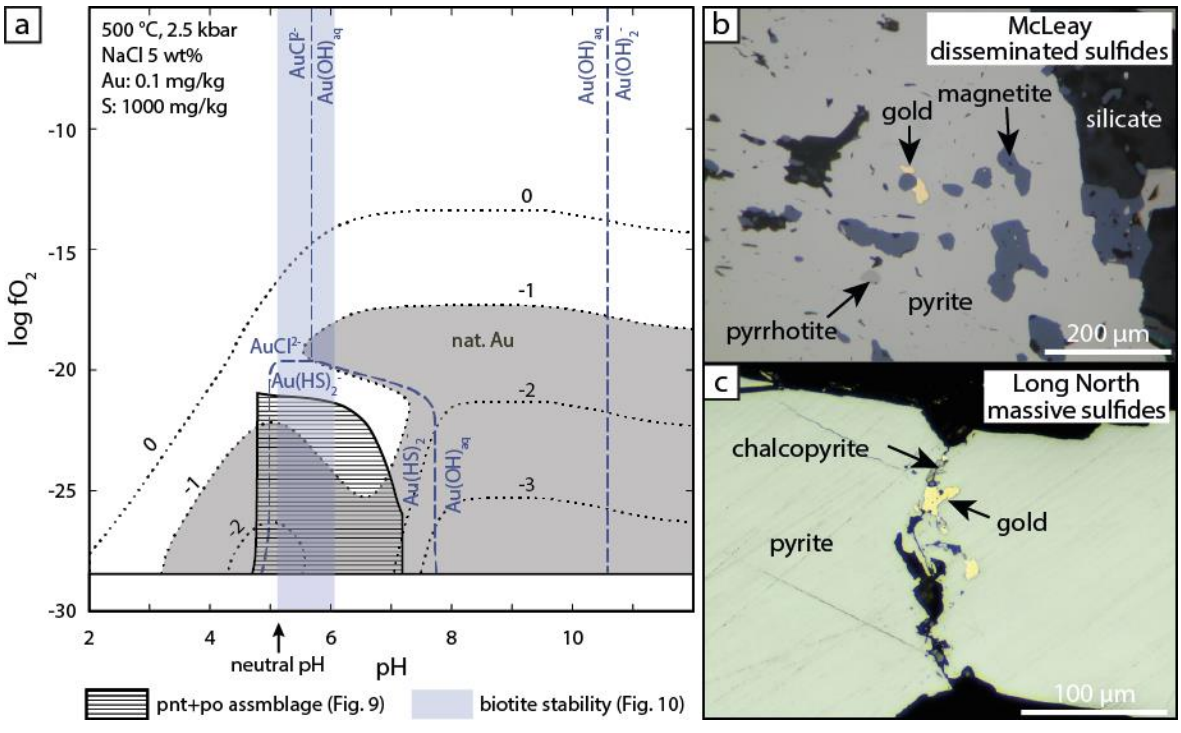

Fig. 13

(a) Modelled redox- and pH-dependencies of native Au and aqueous Au species for the fluid composition of Figure 9 and the solubility of up to 1 mg/kg Au. (b) Microphotograph of disseminated sulfides containing gold from McLeay. (c) Microphotograph of massive sulfides from long North containing gold. Both, (b) and (c), magmatic sulfides have been overprinted to form pyrite.

8. Summary

Pentlandite-bearing hydrothermal veins in Kambalda are found in close distance to older magmatic Ni-sulfide deposits. Three different types of pentlandite-bearing veins were identified: (1) pentlandite-rich biotite-bearing veins with albite alteration, (2) pentlandite- and scheelite-bearing quartz veins, and (3) pentlandite-poor arsenide and gold-bearing carbonate veins. All of them were formed from fluids during syn- to late regional metamorphism. Thermodynamic calculations show that a high temperature and a pH as low as possible are necessary to transport large quantities of Ni in these low-salinity reduced fluids. The formation of pentlandite requires reduced conditions around a neutral pH. Precipitation of pentlandite occurs due to an increase in pH and/or decrease in temperature and the precipitation of the associated silicates most likely occurred due to fluid-rock interaction. The occurrence of hydrothermal pentlandite points towards a proximal Ni source. An assemblage of pentlandite, pyrrhotite and biotite is stable where Au has a higher solubility and hence are unlikely to be associated with a gold deposit. The occurrence of arsenides with minor pentlandite on the other hand can be associated with Au deposits and hence may be useful as pathfinder minerals in conditions.

Acknowledgements

IGO Limited is thanked for the samples. The research was funded by the German Research Foundation (grant number.: 407352165) to SS. The Society of Economic Geologists is thanked for financial support through a Graduate Student Fellowship of the M.Sc. research performed, relating to this study. The Mineralogical Association of Canada is thanked for funding travel between Colorado School of Mines and University of Tübingen for collaborative research and Electron Probe Microanalyses.

686

References

Arndt, N.T., Lesher, C.M., Barnes, S.J., 2008. Komatiite. Cambridge University Press.

Ashley, P.M., 1973. Petrogenesis of sulphide-bearing reaction zones in the Coolac ultramafic belt, New South Wales, Australia. Mineralium Deposita 8, 370-378.

Azovskova, O.B., Grabezhev, A.I., 2008. The Talitsa porphyry copper-molybdenum deposit, the first object of a subalkaline porphyry system in the central Urals. Doklady Earth Sciences 418, 99-102.

Barnes, S.J., 2006. Komatiite-hosted nickel sulfide deposits: Geology, geochemistry, and genesis. Society of Economic Geologists Special Publication 13, 51-97.

Barnes, S.J., Staude, S., Le Vaillant, M., Piña, R., Lightfoot, P.C., 2018. Sulfide-silicate textures in magmatic Ni-Cu-PGE sulfide ore deposits: Massive, semi-massive and sulfide-matrix breccia ores. Ore Geology Reviews 101, 629-651.

Barnes, S.J., Taranovic, V., Schoneveld, L.E., Mansur, E.T., Le Vaillant, M., Dare, S., Staude, S., Vukmanovic, Z. (in press). The occurrence and origin of pentlandite-chalcopyrite-pyrrhotite loop textures in magmatic Ni-Cu sulphide ores. Economic Geology.

Barnicoat, A.C., Fare, R.J., Groves, D.I., McNaughton, N.J., 1991. Synmetamorphic lode-gold deposits in high-grade Archean settings. Geology 19, 921-924.

Bath, A.B., Walshe, J.L., Cloutier, J., Verrall, M., Cleverley, J.S., Pownceby, M.I., Macrae, C.M., Wilson, N.C., Tunjic, J., Nortje, G.S., Robinson, P., 2013. Biotite and apatite as tools for tracking pathways of oxidized fluids in the Archean East Repulse gold deposit, Australia. Economic Geology 108, 667-609.

Bath, A.B., Walshe, J.L., Cloutier, J., Rotherham, J., Hutchison, R., Hollebeck, E., Verrall, M., Schmitt, L., 2020. Alteration patterns and architecture linked to high-grade gold mineralization at the Wattle Dam deposit, Western Australia. Ore Geology Reviews 103471.

Bavinton, O.A., 1979. Interflow sedimentary rocks from the Kambalda ultramafic sequence: Their geochemistry, metamorphism and genesis. Unpublished PhD. Thesis, Australian National University Canberra, 196 p.

Berezovskii, G.A., Drebushchak, V.A. and Kravchenko, T.A., 2001. Low-temperature heat capacity of pentlandite. American Mineralogist 86, 1312-1313.

Bethke, C., 2004. GWB Reference Manual. RockWare Incorporated.

Blanc, P., Lassin, A., Piantone, P., Azaroual, M., Jacquemet, N., Fabbri, A. and Gaucher, E.C., 2012. Thermoddem: A geochemical database focused on low temperature water/rock interactions and waste materials. Applied Geochemistry 27, 2107-2116.

Borodaev, Y.S., Bryzgalov, I.A., Mozgova, N.N., Uspenskaya, T.Y., 2007. Pentlandite and Co-enriched pentlandite as characteristic minerals of modern hydrothermal sulfide mounds hosted by serpentinized ultramafic rocks (Mid-Atlantic Ridge). Moscow University Geology Bulletin 62, 85-97.

Cemič, L. and Kleppa, O.J., 1987. High temperature calorimetry of sulfide systems. Physics and Chemistry of Minerals 14, 52-57.

Claoué-Long, J.C., Compston, W., Cowden, A., 1988. The age of the Kambalda greenstones resolved by ion-microprobe: implications for Archaean dating methods. Earth and Planetary Science Letters 89, 239-259.

Coltat, R., Branquet, Y., Gautier, P., Rodriguez, H.C., Poujol, M., Pelleter, E., McClenaghan, S., Manatschal, G., Boulvais, P., 2019. Unravelling the root zone of ultramafic-hosted black smokers-like hydrothermalism from an Alpine analog. Terra Nova 31, 549-561.

De Almeida, C.M., Olivo, G.R., De Carvalho, S.G., 2007. The Ni-Cu-PGE sulfide ores of the komatiite-hosted Fortaleze De Minas deposit, Brazil: Evidence of hydrothermal remobilization. Canadian Mineralogist 45, 751-773.

Dolejš, D., Wagner, T., 2008. Thermodynamic modelling of non-ideal mineral–fluid equilibria in the system Si–Al–Fe–Mg–Ca–Na–K–H–O–Cl at elevated temperatures and pressures: Implications for hydrothermal mass transfer in granitic rocks. Geochimica et Cosmochimica Acta 72, 526-553.

Durazzo, A., Taylor, L.A., 1982. Exsolution in the Mss-Pentlandite System: Textural and Genetic Implications for Ni-Sulfide Ores. Mineralium Deposita 17, 313-332.

El Monsef, M.A., Slobodník, M., Salem, I.A., 2018. Hydrothermal evolution of granitoid-hosted gold mineralization in Gidami area: An example for orogenic-gold deposits in Egypt. Journal of African Earth Sciences 146, 132-149.

Gamsjäger, H., Bugajski, J. and Preis, W., 2005. Chemical thermodynamics of nickel. Amsterdam: Elsevier.

Garcia, V.B., Schutesky, M.E., Oliveira, C.G., Whitehouse, M.J., Huhn, S.R.B., Augustin, C.T., 2020. The Neoarchean GT-34 Ni deposit, Carajás Mineral Province, Brazil: an atypical IOCG-related Ni sulfide mineralization. Ore Geology Reviews, 103773

Glasser, L., 2013. Single-Ion Values for Ionic Solids of Both Formation Enthalpies, Δf H (298) ion, and Gibbs Formation Energies, Δf G (298) ion. Inorganic Chemistry, 52(2), pp.992-998.

Godel, B., González-Álvarez, I., Barnes, S.J., Barnes, S.-J., Parker, P., Day, J., 2012. Sulfides and Sulfarsenides from the Rosie Nickel Prospect, Duketon Greenstone Belt, Western Australia. Economic Geology 107, 275-294.

González-Álvarez, I., Sweetapple, M., Lindley, I.D., Kirakar, J., 2013. Hydrothermal Ni: Doriri Creek, Papua New Guinea. Ore Geology Reviews 52, 37-57.

Goodgame, V.R., 1997. The distribution and origin of arsenic and platinum group element mineralization in the Mariners nickel deposit Widgiemooltha, Western Australia. Unpublished PhD thesis, University of Oregon.

Goscombe, B., Blewett, R.S., Czarnota, K., Groenewald, P.B., Maas, R., 2009. Metamorphic Evolution and Integrated Terrane Analysis of the Eastern Yilgarn Craton: Rationale, Methods, Outcomes and Interpretation. Gedoscience Australia 2009/23, 270 p.

Grapes, R.H., Challis, G.A., 1999. Gersdorffite with pentlandite, violarite, pyrrhotite, and pyrite, northwest Nelson, New Zealand. New Zealand Journal of Geology and Geophysics 42, 189-204.

Gresham, J.J., Loftus-Hills, G.D., 1981. The Geology of the Kambalda Nickel Field, Western Australia. Economic Geology 76, 1373-1416.

Groves, D.I., Santosh, M., Deng, J., Wang, Q., Yang, L., Zhang, L., 2020. A holistic model for the origin of orogenic gold deposits and its implications for exploration. Mineralium Deposita 55, 275-292.

Harms, U., 2009. Nickeloan pyrite from Prangenhaus quarry, Niederberg area, Germany – A short communication. Chemie der Erde 69, 279-285.

Helgeson, H.C., Kirkham, D.H., Flowers, G.C., 1981. Theoretical prediction of the thermodynamic behavior of aqueous electrolytes by high pressures and temperatures; IV, Calculation of activity coefficients, osmotic coefficients, and apparent molal and standard and relative partial molal properties to 600 degrees C and 5kb. American Journal of Science 281, 1249-1516.

Hill, R.I., Chappell, B.W., Campbell, I.H., 1992. Late Archaean granites of the southeastern Yilgarn Block, Western Australia: age, geochemistry, and origin. Transactions of the Royal Society of Edinburgh: Earth Sciences 83, 211-226.

Ho, S.E., Groves, D.I., McNaughton, N.J., Mikucki, E.J., 1992. The source of ore fluids and solutes in Archaean lode-gold deposits of Western Australia. Journal of Volcanology and Geothermal Research 50, 173-196.

Huang, W., Wu, J., Liang, H., Chen, X., Zhang, J., Ren, L., 2020. Geology, Geochemistry and Genesis of the Longhua Low-Temperature Hydrothermal Ni-Co Arsenide Deposit in Sedimentary Rocks, Guangxi, South China. Ore Geology Reviews, 103393.

Jefferson, C.W., Thomas, D.J., Gandhi, S.S., Ramaekers, P., Delaney, G., Brisbin, D., Cutts, C., Quirt, D., Portella, P., Olson, R.A., 2007. Unconformity-associated uranium deposits of the Athabasca Basin, Saskatchewan and Alberta. Geological Association of Canada, Mineral Deposits Division, Special Publication 5, 273-305.

Jenkins, D. H. B. and Glasser, L., 2003. Standard Absolute Entropy, S 298, Values from Volume or Density. 1. Inorganic Materials. Inorg. Chem, 42, pp.8702-8708.

Kamenetsky, V.S., Lygin, A.V., Foster, J.G., Meffre, S., Maas, R., Kamenetsky, M.B., Goemann, K., Beresford, S.W., 2016. A story of olivine from the McIvor Hill complex (Tasmania, Australia): Clues to the origin of the Avebury metasomatic Ni sulfide deposit. American Mineralogist 101, 1321-1331.

Keays, R.R., Jowitt, S.M., 2013. The Avebury Ni deposit, Tasmania: A case study of an unconventional nickel deposit. Ore Geology Reviews 52, 4-17.

Kitakaze, A., Machida, T., Komatsu, R., 2016. Phase relations in the Fe–Ni–S system from 875 to 650 °C. Canadian Mineralogist 54, 1175-1186.

Kolb, J., Dziggel, A., Bagas, L., 2015. Hypozonal lode gold deposits: A genetic concept based on a review of the New Consort, Renco, Hutti, Hira Buddini, Navachab, Nevoria and The Granites deposits. Precambrian Research 262, 20-44.

Kontny, A., Friedrich, G., Herzig, P., Keyssner, S., 1994. Argentian-pentlandite-bearing assemblages in metamorphic rocks of the KTB pilot hole, Oberpfalz, Germany. Canadian Mineralogist 32, 803-814.

Kositcin, N., Brown, S.J.A., Barley, M.E., Krapež, B., Cassidy, K.F., Champion, D.C., 2008. SHRIMP U-Pb zircon age constraints on the Late Archaean tectonostratigraphic architecture of the Eastern Goldfields Superterrane, Yilgarn Craton, Western Australia. Precambrian Research 161, 5-33.

Lach, A., Wasch, L.J., Blanc, P., André, L., Pipilikaki, P., Durst, P., 2018. GeoWell: Geochemical assessment of cement durability in the supercritical domain, German Geothermal Congress, Essen, Germany.

Lassin, A., Azaroual, M., Mercury, L., 2005. Geochemistry of unsaturated soil systems: Aqueous speciation and solubility of minerals and gases in capillary solutions. Geochimica et Cosmochimica Acta 69, 5187-5201.

Lawrence, D.M., Theloar, P.J., Rankin, A.H., Harbridge, P., Holliday, J., 2013. The geology and mineralogy of the Loulo mining district, Mali, West Africa: Evidence for two distinct styles of orogenic gold mineralization. Economic Geology 108, 199-227.

Lesher, C.M., Lee, R.F., Groves, D.I., Bickle, M.J., 1981. Geochemistry of Komatiites from Kambalda, Western Australia: I. Chalcophile Element Depletion – a Consequence of Sulfide Liquid Separation from Komatiitic Magmas. Economic Geology 76, 1714-1728.

Le Vaillant, M., Barnes, S.J., Fiorentini, M.L., Miller, J., McCuaig, T.C., Mucilli, P., 2015. A Hydrothermal Ni-As-PGE Geochemical Halo Around the Miitel Komatiite-Hosted Nickel Sulfide Deposit, Yilgarn Craton, Western Australia. Economic Geology 110, 505-530.

Le Vaillant, M., Saleem, A., Barnes, S.J., Fiorentini, M.L., Miller, J., Beresford, S., Perring, C., 2016. Hydrothermal remobilisation around a deformed and remobilised komatiite-hosted Ni-Cu-(PGE) deposit, Sarah's Find, Agnew Wiluna greenstone belt, Yilgarn Craton, Western Australia. Mineralium Deposita 51, 369-388.

Le Vaillant, M., Barnes, S.J., Fiorentini, M.L., Barnes, S.-J., Bath, A., Miller, J., 2018. Platinum-group element and gold contents of arsenide and sulfarsenide minerals associated with Ni and Au deposits in Archean greenstone belts. Mineralogical Magazine 82, 625-647.

Li, X.-H., Klyukin, Y.I., Steele-MacInnis, M., Fan, H.-R., Yang, K.-F., Zoheir, B., 2020. Phase equilibria, thermodynamic properties, and solubility of quartz in saline-aqueous-carbonic fluids: Application to orogenic and intrusion-related gold deposits. Geochimica et Cosmochimica Acta 283, 201-221.

Liu, W., Migdisov, A. and Williams-Jones, A., 2012. The stability of aqueous nickel (II) chloride complexes in hydrothermal solutions: Results of UV–Visible spectroscopic experiments. Geochimica et Cosmochimica Acta 94, 276-290.

Loukola-Ruskeeniemi, K., Lahtinen, H., 2013. Multiphase evolution in the black-shale-hosted Ni-Cu-Zn-Co deposit at Talvivaara, Finland. Ore Geology Reviews 52, 85-99.

Mansur, E.T., Barnes, S.-J., Duran, C.J., 2019. Textural and compositional evidence for the formation of pentlandite via peritectic reaction: Implications for the distribution of highly siderophile elements. Geology 47, 351-354.

Marchetto, C.M.L., 1990. Platinum-Group minerals in the O'Toole (Ni-Cu-Co) deposit, Brazil. Economic Geology 85, 921-927.

Marques, A.F.A., Barriga, F., Chavagnac, V., Fouquet, Y., 2006. Mineralogy, geochemistry, and Nd isotope composition of the Rainbow hydrothermal field, Mid-Atlantic Ridge. Mineralium Deposita 41, 52-67.

Marston, R.J., 1984. Nickel mineralization in Western Australia. Geological Survey of Western Australia Mineral Resource Bulletin 14, 271 p.

McGoldrick, K.L., Squire, R.J., Cas, R.A.F., Briggs, M., Tunjic, J., Allen, C.M., Campbell, I.H., Hayman, P.C., 2013. The largest Au deposits in the St Ives Goldfield (Yilgarn Craton, Western Australia) may be located in a major Neoarchean volcano-sedimentary depo-centre. Mineralium Deposita 48, 861-881.

Melekestseva, I.Y., Zaykov, V.V., Nimis, P., Tret'yakov, G.A., Tessalina, S.G., 2013. Cu–(Ni–Co–Au)-bearing massive sulfide deposits associated with mafic–ultramafic rocks of the Main Urals Fault, South Urals: Geological structures, ore textural and mineralogical features, comparison with modern analogs. Ore geology Reviews 52, 18-36.

Melfos, V., Vavelidis, M., Christofides, G., Seidel, E., 2002. Origin and evolution of the Tertiary Maronia porphyry copper-molybdenum deposit, Thrace, Greece. Mineralium Deposita 37, 648-668.

Molnár, F., O'Brien, H., Lahaye, Y., Kurhila, M., Middleton, A., Johanson, B., 2017. Multi-stage hydrothermal processes and diverse metal associations in orogenic gold deposits of the Central Lapland greenstone belt, Finland. Mineral resources to Discover – 14th SGA Biennial Meeting 2017, Volume 1, 63-66.

Mueller, A.G., Hagemann, S.G., McNaughton, N.J., 2016. Neoarchean orogenic, magmatic and hydrothermal events in the Kalgoorlie-Kambalda area, Western Australia: constraints on gold mineralization in the Boulder-Lefroy-Golden Mile fault system. Mineralium Deposita, DOI 10.1007/s00126-016-0665-9.

Mueller, A.G., Hagemann, S.G., Brugger, J., Xing, Y., Roberts, M.P., 2020. Early Fimiston and late Oroya Au-Te ore, Paringa South mine, Golden Mile, Kalgoorlie: 4. Mineralogical and thermodynamic constraints on gold deposition by magmatic fluids at 420-300 °C and 300 MPa. Mineralium Deposita. DOI 10.1007/s00126-019-00939-8.

Naldrett, A.J., 2004. Magmatic sulfide deposits. Springer, 727 p.

Naldrett, A.J., 2011. Fundamentals of magmatic sulfide deposits. Reviews in Economic Geology 17, 1-50.

Neall, F.B., Phillips, G.N., 1987. Fluid-wall rock interaction in an Archean hydrothermal gold deposit: A thermodynamic model for the Hunt mine, Kambalda. Economic Geology 82, 1679-1694.

Neumayr, P., Walshe, J., Hagemann, S., Petersen, K., Roache, A., Frikken, P., Horn, L., Halley, S., 2008. Oxidized and reduced mineral assemblages in greenstone belt rocks of the St. Ives gold camp, Western Australia: vectors to high-grade ore bodies in Archaean gold deposits? Mineralium Deposita 43, 363-371.

Neuser, R. D., 1995. A new high-intensity cathodoluminescence microscope and its application to weakly luminescing minerals. Bochumer Geol. Geotech. Arb. 44, 116-118.

Novoselov, K., Belogub, E., Ermolina, O., Mikhailov, A., 2013. Gold-bismuth mineralisation in the orogenic gold occurrences of the Kuhmo greenstone belt (Finland). 12th Biennial SGA meeting, Uppsala, Volume 3, 1168-1171.

Pašava, J., Hladíková, J., Dobeš, P., 1996. Origin of Proterozoic metal-rich black shales from the Bohemian Massif, Czech Republic. Economic Geology 91, 63-79.

Peltonen, P., Kontinen, A., Huhma, H., Kuronen, U., 2008. Outokumpu revisited: New mineral deposit model for the mantle peridotite-associated Cu-Co-Zn-Ni-Ag-Au sulphide deposit. Ore Geology Reviews 33, 559-617.

Phillips, G.N., Hergt, J., Powell, R., 2017. Kalgoorlie goldfield – petrology, alteration and mineralisation of the Golden Mile Dolerite. *In*: Philips, G.N., (ed) Australian Ore Deposits. The Australian Institute of Mining and Metallurgy, Melbourne, 185-194.

Pirajno, F., González-Álvarez, I., 2013. A re-appraisal of the Epoch nickel sulphide deposit, Filabusi Greenstone Belt, Zimbabwe: A hydrothermal nickel mineral system? Ore Geology Reviews 52, 58-65.

Pitcairn, I.K., Teagle, D.A.H., Craw, D., Olivo, G.R., Kerrich, R., Brewer, T.S., 2006. Sources of metals and fluids in orogenic gold deposits: Insights from the Otago and Alpine Schists, New Zealand. Economic Geology 101, 1525-1546.

Polito, P.A., Bone, Y., Clarke, J.D.A., Mernagh, T.P., 2001. Compositional zoning of fluid inclusions in the Archaean Junction gold deposit, Western Australia: a process of fluid – wall-rock interaction? Australian Journal of Earth Science 48, 833-855.

Prichard, H.M., Fisher, P.C., McDonald, I., Knight, R.D., Sharp, D.R., Williams, J.P., 2013. The Distribution of PGE and the Role of Arsenic as a Collector of PGE in the Spotted Quoll Nickel Ore Deposit in the Forrestania Greenstone Belt, Western Australia. Economic Geology 108, 1903-1921.

Robie, R.A., Hemingway, B.S., 1995. Thermodynamic properties of minerals and related substances at 298.15 K and 1 bar (105 Pascals) pressure and at higher temperatures. US Geol. Survey Bull, 2131, p.461.

Ryzhenko, B.N., Bryzgalin, O.V., Artamkina, I.Y., Spasennykh, M.Y. and Shapkin, A.I., 1985. An electrostatic model for the electrolytic dissociation of inorganic substances dissolved in water. Geochem. Int, 22, pp.138-144.

Scharrer, M., Kreissl, S., Markl, G., 2019. The mineralogical variability of hydrothermal native element-arsenide (five-element) associations and the role of physicochemical and kinetic factors concerning sulfur and arsenic. Ore Geology Reviews 113, 103025.

Staude, S., Wagner, T., Markl, G., 2007. Mineralogy, mineral compositions and fluid evolution at the Wenzel hydrothermal deposit, southern Germany: Implications for the formation of Kongsberg-type silver deposits. Canadian Mineralogist 45, 1147-1176.

Staude, S., Werner, W., Mordhorst, T., Wemmer, K., Jacob, D.E., Markl, G., 2012. Multi-stage Ag–Bi–Co–Ni–U and Cu–Bi vein mineralization at Wittichen, Schwarzwald, SW Germany: geological setting, ore mineralogy, and fluid evolution. Mineralium Deposita 47, 251-276.

Staude, S., Barnes, S.J., Le Vaillant, M., 2016. Evidence of lateral thermomechanical erosion of basalt by Fe-Ni-Cu sulfide melt at Kambalda, Western Australia. Geology 44, 1047-1050.

Staude, S., Sheppard, S., Parker, P., Paggi, J., 2017a. Long-Victor nickel sulfide deposits, Kambalda. *In*: Philips, G.N., (ed) Australian Ore Deposits. The Australian Institute of Mining and Metallurgy, Melbourne, 107-112.

Staude, S., Barnes, S.J., Le Vaillant, M., 2017b. Thermomechanical erosion of ore-hosting embayments beneath komatiite lava channels: Textural evidence from Kambalda, Western Australia. Ore Geology Reviews 90, 446-464.

Staude, S., Markl, G., 2019. Remnant lenses of komatiitic dykes in Kambalda (Western Australia): Occurrences, textural variations, emplacement model, and implications for other komatiite provinces. Lithos, 342-343, 206-222.

Staude, S., Jones, T.J., Markl, G., 2020a. The textures, formation and dynamics of rare high-MgO komatiite pillow lavas. Precambrian Res 343:105729.

Staude, S., Barnes, S.J., Markl, G., 2020b. Interspinifex Ni sulfide ore from Victor South-McLeay: Evidence for post-ore formation. Miner Depos, doi.org/10.1007/s00126-020-00982-w.

Staude, S., Oelze, M., Markl, G., in press. Multi-stage sulfide evolution of the Moran Ni sulfide ore, Kambalda, Western Australia: Insights into the dynamics of ore forming processes of komatiite-hosted deposits. Mineralium Deposita.

Steven, N., Armstrong, R., 2003. A Metamorphosed Proterozoic Carbonaceous Shale-Hosted Co-Ni-Cu Deposit at Kalumbila, Kabompo Dome: The Copperbelt Ore Shale in Northwestern Zambia. Economic Geology 98, 893-909.

Symons, P.M., Anderson, G., Beard, T.J., Hamilton, L.M., Reynolds, G.D., Robinson, J.M., Staley, R.W., Thompson, C.M., 1990. Boddington gold deposit. Australasian Institute of Mining and Metallurgy, Monograph 14, 165-169.

Tagirov B. R., Zotov A. V. and Akinfiev N. N. (1997) Experimental study of dissociation of HCl from 350 to 500 C and 500 to 2500 bars; thermodynamic properties of HClo aq. Geochim. Cosmochim. Acta 61, 4267–4280.

Tenailleau, C., Pring, A., Etschmann, B., Brugger, J., Grguric, B., Putnis, A., 2006. Transformation of pentlandite to violarite under mild hydrothermal conditions. American Mineralogist 91, 706-709.

Thalhammer, O., Stumpfl, E.F., Panayiotou, A., 1986. Postmagmatic, hydrothermal origin of sulfide and arsenide mineralizations at Limassol Forest, Cyprus. Mineralium Deposita 21, 95-105.

Tomkins, A.G., Mavrogenes, J.A., 2001. Redistribution of gold within arsenopyrite and löllingite during pro- and retrograde metamorphism: Aplication to timing of mineralization. Economic Geology 96, 525-534.

Tomkins, A.G., Mavrogenes, J.A., 2002. Mobilization of gold as a polymetallic melt during pelite anataxis at the Challenger deposit, South Australia: A metamorphosed Archean gold deposit. Economic Geology 97, 1249-1271.

Tomkins, A.G., Grundy, C., 2009. Upper temperature limits of orogenic gold deposit formation: constraints from the granulite-hosted Griffin's Find deposit, Yilgarn Craton. Economic Geology 104, 669-685.

Tzamos, E., Filippidis, A., Michailidis, K., Koroneos, A., Rassios, A., Grieco, G., Pedrotti, M., Stamoulis, K., 2016. Mineral chemistry and formation of awaruite and heazlewoodite in the Xerolivado chrome mine, Vourinos, Greece. Bulletin of the Geological Society of Greece 50, 2047-2056.

927 Veloso, A.S.R., Monteiro, L.V.S., Juliani, C., 2020. The link between hydrothermal nickel mineralization and an
928 iron oxide-copper-gold (IOCG) system: constraints based on mineral chemistry in the Jatobá deposit, Carajás
929 Province. Ore Geology Reviews, 103555.

930 Voroshin, S.V., Tyukova, E.E., Newberry, R.J., Layer, P.W., 2014. Orogenic gold and rare metal deposits of the
931 Upper Kolyma District, Northeastern Russia: Relation to igneous rocks, timing, and metal assemblages. Ore
932 Geology Reviews 62, 1-24.

933 Waldner, P. and Sitte, W., 2008. Thermodynamic modelling of Fe–Ni pentlandite. Journal of Physics and
934 Chemistry of Solids, 69(4), pp.923-927.

935

Appendix IX

Accepted publication

Study 9

Epp, T., Walter, B. F., Scharrer, M., Lehmann, G., Henze, K., Heimgärtner, C., & Markl, G. (2019). Quartz veins with associated Sb-Pb-Ag±Au mineralization in the Black Forest, SW Germany: a record of metamorphic cooling, tectonic rifting, and element remobilization processes in the Variscan belt. Mineralium Deposita, 54(2), 281-306.

Mineralium Deposita
https://doi.org/10.1007/s00126-018-0855-8

ARTICLE

Quartz veins with associated Sb-Pb-Ag±Au mineralization in the Schwarzwald, SW Germany: a record of metamorphic cooling, tectonic rifting, and element remobilization processes in the Variscan belt

T. Epp[1] · B. F. Walter[1] · M. Scharrer[1] · G. Lehmann[1] · K. Henze[1] · C. Heimgärtner[1] · W. Bach[2] · G. Markl[1]

Received: 3 May 2018 / Accepted: 1 November 2018

Abstract

A combination of textural observations from 38 Permian Sb-Pb-Ag±Au-bearing quartz veins in the Schwarzwald (SW Germany) with isotopic, fluid inclusion, and geochemical data allows to refine genetic models for this common type of mineralization, to understand the origin of mineralogical diversity and the correlation with large scale tectonic events. Textures record four main mineralization stages: (I) Fe-As(-Sb±Au), (II) Pb-Zn-Cu, (III) Pb-Sb, and (IV) Ag-Sb. Stage I sulfides, dominated by pyrite and arsenopyrite, formed due to cooling of low-salinity metamorphic fluids during the Permian with maximum homogenization temperatures of 400 °C. Invisible gold in arsenopyrite, pyrite, marcasite, and stibnite was remobilized and locally precipitated as electrum at the end of stage I. Minerals of stages II and III comprise a rich diversity of Sb-bearing sulfosalts including, e.g., bournonite, zinkenite, and jamesonite. This assemblage formed during Jurassic times due to mixing of high-salinity, mid- and upper-crustal fluids (up to 27 wt% NaCl+$CaCl_2$) with homogenization temperatures between 50 and 250 °C. Stage III is marked by a rich variety of Pb-Sb sulfosalts. Its local abundance is directly related to the presence of stage I mineralization and its extent of remobilization during a significant influx of Pb in the Jurassic-Cretaceous. The formation of the Upper Rhine Graben during the Tertiary reactivated especially NE-SW-oriented veins. Percolating Ag-rich fluids reacted with earlier stage III Pb-Sb sulfosalts forming Ag-rich minerals (stage IV) such as miargyrite, pyrargyrite, and stephanite. The transition from metamorphic fluids to basinal, saline (e.g., Pb-bearing) brines over hundreds of millions of years as is shown in this study and present in other Variscan occurrences indicates a possibly typical poly-stage characteristic of Sb deposits worldwide, which has, however, not been investigated in detail so far.

Keywords Stibnite · Gold · Remobilization · Fluid cooling · Fluid mixing

Introduction

Shear zone-hosted, mesothermal (Au-)Sb vein deposits are arguably the most important source for Sb. Such Sb deposits occur worldwide and comprise either monotonous stibnite deposits (e.g., Lake George deposit, Canada, Lentz et al. 2002; Sentachan and Sarylakh deposits, Russian Federation, Baltukhaev and Solozhenkin 2009; Schwarz-Schampera 2014) or polymetallic Sb-(Pb-Ag±Au-W-Sn-As-Zn) deposits (e.g., Dúrico-Beirã region, Portugal, Neiva et al. 2008; Bournac deposit, France, Munoz and Shepherd 1987). The quartz vein associated with Sb-Pb-Ag±Au deposit type is common in Europe, where it is strongly associated with the Variscan Orogen. Examples of former (more or less) important European mining districts are Rheinisches Schiefergebirge,

Editorial handling: J. Gutzmer

Electronic supplementary material The online version of this article (https://doi.org/10.1007/s00126-018-0855-8) contains supplementary material, which is available to authorized users.

✉ T. Epp
tatjana.epp@uni-tuebingen.de

[1] Department of Geosciences, Eberhard Karls University Tübingen, Wilhelmstraße 56, 72074 Tübingen, Germany

[2] Department of Geosciences, University of Bremen, Klagenfurter Straße 4, 28359 Bremen, Germany

Published online: 21 November 2018

Harz, Schwarzwald, and Erzgebirge in Germany, Massif Central and Vosges mountains (France), Lombardy, Piemont, and Sardinia (Italy), and some regions in Slovakia, Czech Republic, Spain, Portugal, Austria, and Great Britain (e.g., Walenta 1957; Clayton et al. 1990; Ortega et al. 1991; Munoz et al. 1992; Dill 1993; Wagner and Cook 2000; Cidu et al. 2014; Burisch et al. 2018, this issue).

Previous studies dealt with the structural history and fluid evolution in the context of the Variscan Orogen of Sb(±Au)-quartz veins (Behr et al. 1984; Matte 1991; Schroyen and Muchez 2000; Kroner and Romer 2013; Chicharro et al. 2016). These studies clearly relate these veins to late-Orogenic, post-compressive brittle tectonic events which explains why they are commonly situated within late-Variscan extensional shear zones (Bril 1982; Munoz et al. 1992; Ortega and Vindel 1995; Wagner and Cook 2000). They formed during the transition from the Variscan compressive stress regime to post-Variscan strike slip tectonics (Arthaud and Matte 1977; Malavieille et al. 1990; Doblas et al. 1994; Wagner and Cook 2000). Several models have been proposed for stibnite precipitation in these vein-type deposits of the European Variscan belt and these comprise convective fluid cooling (Bril and Beaufort 1989; Munoz et al. 1992), segregation of H_2O-NaCl-CO_2-CH_4-N_2 fluids (Clayton et al. 1990; Ortega et al. 1991; Ortega and Vindel 1995), fluid boiling (Ortega et al. 1991), and dilution of CO_2-rich metamorphic fluids by near-surface H_2O-NaCl fluids (Bril 1982; Boiron et al. 1990; Couto et al. 1990). It is, however, generally assumed that the precipitation process is dominantly triggered by fluid cooling, either conductively or by fluid mixing with a low temperature fluid (Wagner and Cook 2000). The salinity of the hydrothermal fluid has no apparent influence on the solubility and the precipitation, because, in contrast to Pb and Ag, which are mostly transported as Cl complexes in hydrothermal solutions, the dominant Sb species in reduced hydrothermal fluids presumably is $Sb(OH)_3$ (Wood et al. 1987). However, the common polystadial mineral assemblage is generally not considered when these formation mechanisms were proposed and is therefore investigated more in detail in this study. Furthermore, this study comprehensively investigates the details of ore mineral associations and their evolution over a 300-Ma time span, using 38 localities in the Schwarzwald, a well-known mining district in the Variscan Orogen. Interestingly, the otherwise spatially separated Sb-Ag-sulfide and Sb-sulfide assemblages typical of such veins (Burisch et al. 2018, this issue) are intimately intergrown in the localities investigated in the Schwarzwald. The careful textural analysis of these ores sheds further light on the temporal evolution and major formation mechanisms of four distinct mineralization stages. Stages I and II do not only occur in the Variscan Orogen but worldwide (e.g., Guillemette and Williams-Jones 1993; Dill et al. 1995; Baltukhaev and Solozhenkin 2009). Due to the similarities between this mineralization type in Europe and other worldwide Sb-Au localities, the process of formation investigated in this study is pertinent also to larger, economically significant deposits.

Geological setting

The Schwarzwald in SW Germany (Fig. 1 and ESM Table 1) is part of the Central European Variscan Orogen and dominated by partially migmatized ortho- and paragneisses (Kalt et al. 2000). Variscan crystalline basement units are separated by the Baden-Baden-Zone (BBZ) in the north and the Badenweiler-Lenzkirch-Zone (BLZ) in the south, containing metamorphosed greywackes and conglomerates. The metamorphic rock units were intruded by post-collisional granites between 335 and 315 Ma (e.g., Todt 1976; Altherr et al. 2000; Hann et al. 2003). This crystalline basement was then covered by a Palaeozoic and Mesozoic sedimentary sequence on top of a prominent erosion surface of Permian age (Geyer et al. 2011 and references therein). During the Middle Triassic (Muschelkalk), limestones, shales, and evaporites (carbonates, anhydrite, gypsum and halite; Geyer et al. 2011) were deposited. Clastic and gypsum-bearing sediments followed during the Upper Triassic (Keuper) and further carbonates and shales were deposited during the Jurassic (Geyer et al. 2011). Cretaceous sedimentary rocks are lacking in the region. Since the initiation of rifting in the Upper Rhine Graben and the uplift of the Schwarzwald, Paleogene to Quaternary sediments of up to 4000 m thickness filled the graben structure, including Oligocene halite-sylvite-bearing evaporites, anhydrite, gypsum, and organic-rich claystones (Geyer et al. 2011).

Peaks of hydrothermal activity in the Schwarzwald

In general, most hydrothermal mineralizations in the Schwarzwald are hosted by veins. Most veins are gneiss-hosted, due to pre-existing deep tectonic fault patterns, which, in case of reactivation, offer sufficient pathways for fluid circulation (Knipe 1993; Werner and Franzke 2001). Repeated Permian and Tertiary volcanic activity and the ongoing basement subsidence during the Jurassic due to far-field effects of the opening of the North Atlantic promoted hydrothermal activity and the formation of mineralized veins (e.g., Wetzel et al. 2003; Staude et al. 2007, 2009, 2010a; Walter et al. 2016, 2017, 2018a). Numerous aspects of fluid flow and hydrothermal vein formation in the Schwarzwald are well documented in the published literature: this includes studies on fluid inclusion microthermometry (e.g., Behr and Gerler 1987; Staude et al. 2009; Walter et al. 2015), stable and

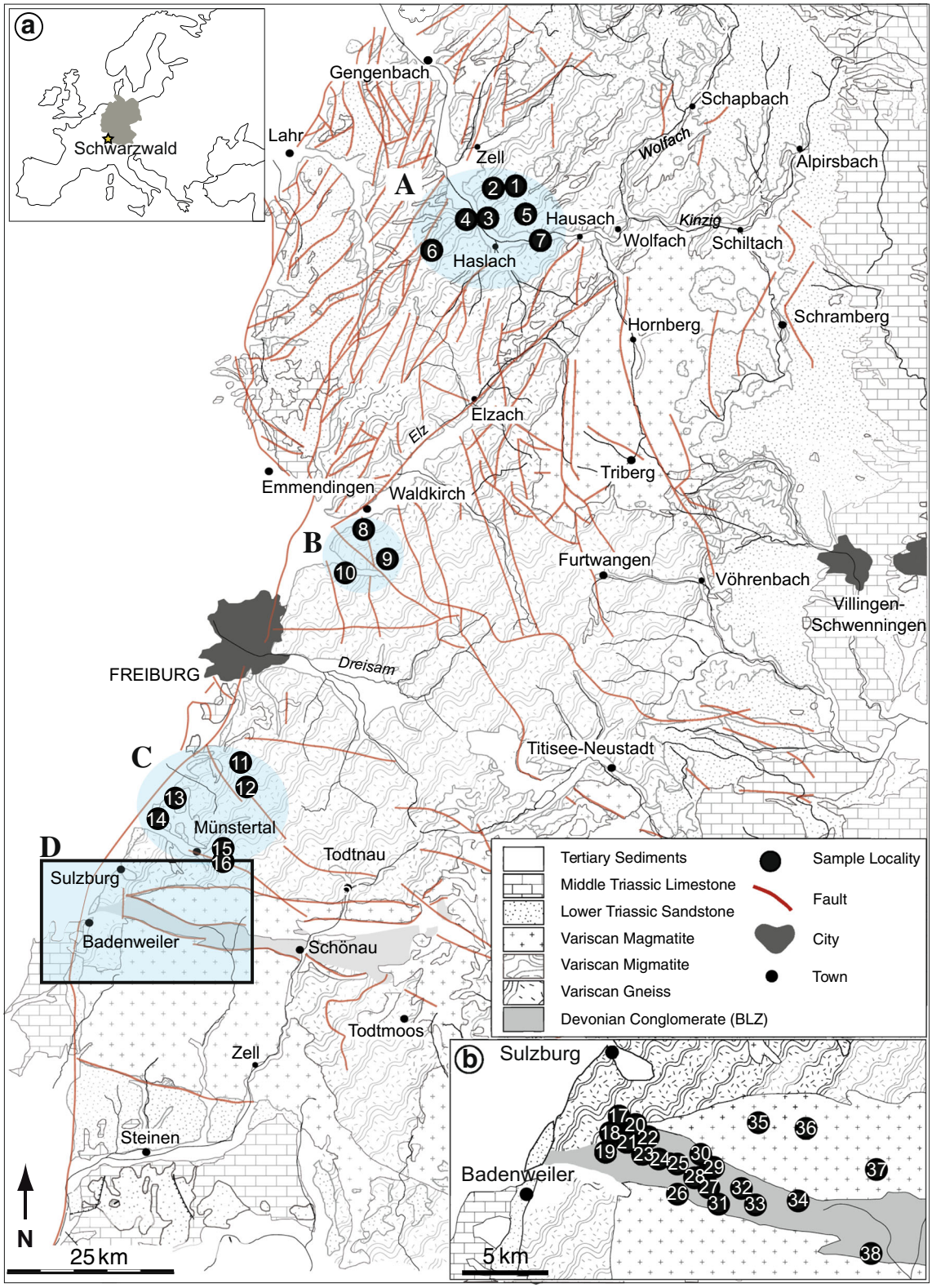

Fig. 1 **a** Geological overview of the Schwarzwald (SW Germany). The blue fields mark regions of quartz veins with associated Sb-Ag-Au mineralization in the Schwarzwald: (A) Kinzigtal, (B) Freiburg, (C) Münstertal, and (D) Badenweiler & Bad Sulzburg. **b** Close-up of area D, the Badenweiler-Lenzkirch-Zone (BLZ). Sample localities 1–38 (for more information refer to ESM Table 1). Map modified after Pfaff et al. (2011)

radiogenic isotopes of O, C, H, S, Sr, Pb, Cu, Fe, and Mg (Staude et al. 2010b; Walter et al. 2015), paleo- and modern fluid models and aquifer data (e.g., Stober and Bucher 1999; Pfaff et al. 2010; Bons et al. 2014; Walter et al. 2016), leaching experiments on basement and cover rocks (Bucher and Stober 2002; Burisch et al. 2016), and regional geological setting (Geyer et al. 2011). This comprehensive knowledge provides a suitable framework to decipher the complex history of vein-type Sb-quartz mineralization.

Hydrothermal veins in the Variscan crystalline basement formed continuously between about 310 Ma and today, but certain peaks in hydrothermal activity exist (e.g., Pfaff et al. 2009; Staude et al. 2009; Walter et al. 2016). Five formation stages are distinguished based on structural, mineralogical, and microthermometric arguments (e.g., Behr and Gerler 1987; Pfaff et al. 2009; Staude et al. 2009; Walter et al. 2016); these are in accordance with observations from other central European districts (e.g., Bril 1982; Chovan et al. 1995; Krolop et al. 2018; Burisch et al. 2018, this issue):

1. Late Carboniferous quartz-tourmaline veins with small amounts of wolframite, scheelite, and cassiterite precipitated from magmatic low-salinity fluids (< 4.5 wt%, up to 550 °C; Marks et al. 2013; Walter et al. 2016).
2. Permian Sb±Ag±Au-bearing quartz veins (277.6 Ma; Walter et al. 2018c, submitted) precipitated from a low-salinity, high-temperature (up to 440 °C) late-Variscan metamorphic basement fluid (Wagner and Cook 2000; Baatartsogt et al. 2007; Staude et al. 2009). This is the group the current contribution is concerned with.
3. Triassic-Jurassic quartz-hematite±barite veins precipitated from medium temperature, high- and low-salinity fluids (Brander 2000; Walter et al. 2016).
4. Jurassic-Cretaceous veins with variable amounts of fluorite, barite, quartz, and carbonates. This complex mineralization type contains either Ag-Bi-Co-Ni-U, Fe-Mn, or Pb-Zn-Cu ores. In contrast to (1)–(3), a deep-seated highly saline brine (20–28 wt% NaCl+$CaCl_2$) was mobilized and precipitation occurred due to binary fluid mixing between deep-seated and shallow brines (e.g., Metz and Richter 1957; Meyer et al. 2000; Werner 2002; Pfaff et al. 2009; Staude et al. 2010a; Walter et al. 2015). Moreover, the formation of fractures in this stage was probably linked to far-field effects from the opening of the North Atlantic (Wetzel et al. 2003; Pfaff et al. 2009; Staude et al. 2009).
5. Post-Cretaceous veins with variable amounts of barite, quartz, fluorite, and carbonates, which were mainly associated with Pb and less commonly Zn and Ag mineralization (Staude et al. 2009), showing large mineralogical and fluid compositional heterogeneities (1–23 wt% NaCl+$CaCl_2$) (Walter et al. 2015, 2016).

Sample description

The following sections give an overview of the local geological setting and also shortly introduce different occurring vein types in the investigated area. Furthermore, the sample locations and a detailed petrographic description were given.

Local geological setting

Antimony-bearing veins in the Schwarzwald exclusively occur in crystalline basement rocks and meta-conglomerates. Currently, the Clara barite-fluorite mine (ESM Table 1) is the only ore deposit exploited in the Schwarzwald, whereas most of our sampling sites were mined during medieval and early modern times (800 AC to 17th century; Dennert 1993). From 17th to the 20th century, minor exploitation took place but ended in the middle of the 20th century (Dennert 1993). Based on field evidence, the veins investigated in this study can be divided into three groups:

1. Veins of the areas A–C (Fig. 1) are a few centimeters to 1 m thick and consist of several massive quartz generations of various crystal sizes with minor amounts of ore minerals. The (outcropping) length of these veins varies between tens and hundreds of meters, and in rare cases (such as the Baberast locality), the mineralized structure can be traced for up to 3 km. The strike orientation is bimodal, either NW-SE or NE-SW, and the dip is near vertical (see ESM Table 1). In direct contact to the veins, the host rock is strongly silicified and host rock clasts are commonly embedded. Bleached zones around the sampled veins are commonly observed in the field and pyrite impregnation of the host rock is typical. Small occurrences of this vein type are located in the vicinity of the Elztal fault in the central Schwarzwald, the Kinzigtal area (area A, Fig. 1), and the area around Freiburg (area B, Fig. 1). Paragneisses, migmatites, and rarely granites are the host rocks in this region (see Fig. 1 and ESM Table 1).
2. The up to 1-m-thick Segen Gottes vein in the Kinzigtal area (area A, Fig. 1) takes a special position, as it comprises various vein generations of different gangue minerals. The (15 cm thick) Sb-bearing quartz veins (identical to group 1, see above) are locally brecciated and the clasts are cemented by successive fluorite-barite-bearing assemblages.
3. The veins of area D (Fig. 1) are part of the longest Sb-bearing mineralized zone in the Schwarzwald, ranging from the Holderpfad in the west to the Kälbelescheuer in the east. The whole set of structures comprises a total length of 5 km. Generally, the veins have a NW-SE-striking orientation and are frequently displaced by Upper Rhine Graben-parallel faults (Markl 2017). The

mineralogy of the veins changes from east to west. In the east, veins with Fe-As-Zn-Cu-bearing assemblages (i.e., arsenopyrite, marcasite, pyrite, sphalerite, chalcopyrite) dominate, whereas in the west, the assemblage is dominated by more Pb-Sb-rich minerals including stibnite, zinkenite, jamesonite, boulangerite, fülöppite, and semseyite. Interestingly, Cu-rich Sb sulfosalts such as chalcostibite and meneghinite and Ag-bearing andorite only occur in the central and western part; bournonite becomes progressively more common towards the east. The minerals contain invisible gold (see below), and one grain of native gold/electrum was found in the central part of the zone. In the same area (particularly in the central and eastern part), a gold-enriched zone (reaching up to 5 ppm in some outcrops) with small native gold-bearing quartz veinlets (together with pyrite/marcasite, galena, sphalerite, arsenopyrite) strikes subparallel to the Sb-bearing quartz veins. Both gold-bearing vein systems are about 200 m apart from each other and can be traced over a few kilometers between Bad Sulzburg and Weiherkopf/Münsterhalden. The conspicuous co-occurrence of the Sb-dominated and the Au-rich mineralization is considered in the present study.

Sample locations and petrographic observations

For this study, 148 representative samples from 38 veins, including both recently sampled and collection specimens, were investigated (Fig. 1 and ESM Table 1). The samples were chosen for their representative character (e.g., textures, mineralogy, structural position in the host rocks, and crystal size for fluid inclusions and isotopes). A specific focus was placed on the eastern Sulzburg Sb-veins in the BLZ (group 3, area D, Fig. 1), hosted by Devonian meta-conglomerates. In this area, the Sb-Au mineralization is found over a large area (about 20 by 5 to 10 km).

Petrographic description

Tangible petrographic attributes of the studied Sb-Pb-Ag±Au-quartz veins are collated below:

Not all investigated veins display the entire paragenetic sequence in samples. Therefore, the detailed petrographic description of the vein mineralogy focuses on veins and samples that show the most complete mineralogical succession to produce a generalized paragenetic scheme (Fig. 2). The detailed mineral assemblage of all investigated localities is reported in ESM Table 1.

In general, the evolution of the veins can, by combining the variable mineral sequence of all veins, be classified into four successive mineralization stages, according to mineral assemblages and textural relations:

Stage I: Fe-As (-Sb±Au) mineralization
Stage II: Pb-Zn-Cu mineralization
Stage III: Pb-Sb mineralization
Stage IV: Ag-Sb mineralization

Stage I was found at all localities, whereas stage II was identified only very locally. Stages III and IV are, in contrast, rather dominant. Quartz, either gray and coarse-grained (quartz I) or white and microcrystalline (quartz II–V, ESM 3a), is the dominant gangue mineral throughout. The ore minerals are intergrown with or grown into voids within the quartz. Locally, lath-shaped pyrrhotite crystals initiate mineralization stage I; these are followed by euhedral Au-bearing arsenopyrite, pyrite, and marcasite (Fig. 3a, b), which form aggregates in quartz I (Fig. 3a, b and ESM 3 1a-c) and often show porous grain surfaces. This association is followed by a succession of berthierite, stibnite (Fig. 3c), and electrum. Electrum (with a maximum diameter of 24 μm) is present as small inclusions in minerals of stage II or around marcasite (Figs. 3b, d and 4d–f). Some samples show that electrum is partially dissolved due to weathering. At the end of this stage, calcite occurs in minor quantities, surrounding stibnite and, at few localities, electrum. Numerous sub-generations of barren, white microcrystalline quartz are recognized.

Stage II is typically initiated by tetrahedrite (I) and galena (I), followed by chalcopyrite and sphalerite (I) (Fig. 3d–f and ESM 3 1d-f). Small electrum grains or stibnite (stage I) are locally found as inclusions in tetrahedrite (I) (Fig. 3d, e). Tetrahedrite I may also be replaced by tetrahedrite II (Fig. 4d, f) and is often very porous. Galena (I) is less abundant in stage II but occurs as anhedral masses (ESM 3 1d) or tiny inclusions in chalcopyrite, sphalerite, or tetrahedrite (freibergite) II. Sphalerite (I) commonly appears as reddish to brownish anhedral crystals (ESM 3 1e). Stage II is predominantly accompanied by fine crystalline quartz.

More variable and complex Sb mineralization marks mineralization stage III. The whole mineral succession was not observed (and is probably not present) at any of the sampling sites. The stage typically commences with the crystallization of bournonite ($PbCuSbS_3$), locally needle-shaped zinkenite ($Pb_9Sb_{22}S_{42}$) which is mostly pseudomorph after stibnite (stage I, Fig. 4a), and jamesonite ($Pb_4FeSb_6S_{14}$). This is followed by the crystallization of andorite ($AgPbSb_3S_6$) and chalcostibite ($CuSbS_2$), which is intergrown with zinkenite and partly replaced by meneghinite ($Pb_{13}CuSb_7S_{24}$). Boulangerite ($Pb_5Sb_4S_{11}$) replaces zinkenite and locally fizélyite ($Pb_{14}Ag_5Sb_{21}S_{48}$) was observed, replacing andorite. Fülöppite ($Pb_3Sb_8S_{15}$) replaces stibnite and is replaced by

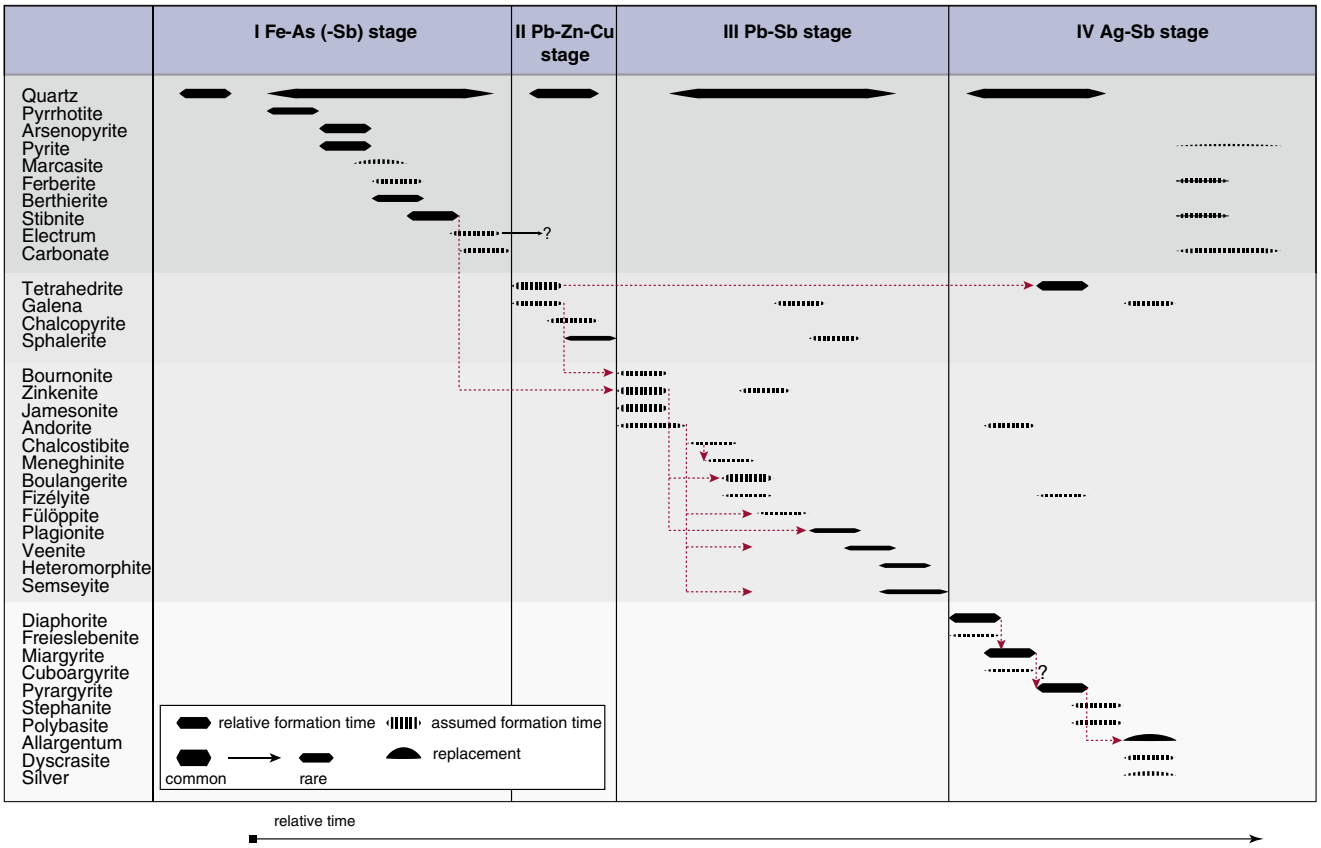

Fig. 2 Paragenetic sequence of all studied Sb-Ag±Au-quartz mineralization in the Schwarzwald with four mineralization stages. Note, not every vein shows the complete sequence. Various gray shades separate different mineralization stages (I to IV). Red dashed arrows indicate replacement reactions

plagionite ($Pb_5Sb_8S_{17}$), which in turn is replaced by veenite ($Pb_2(Sb,As)_2S_5$). Heteromorphite ($Pb_7Sb_8S_{18}$) and semseyite ($Pb_9Sb_8S_{21}$) mark the end of this stage (Fig. 4b). Distinctive replacement reactions between these minerals are common (Figs. 2 and 4a, b). During this stage, quartz is the only gangue mineral.

The silver-dominated assemblage of mineralization stage IV starts with the crystallization of diaphorite ($Pb_2Ag_3Sb_3S_8$) (Fig. 4 d) and freieslebenite ($AgPbSbS_3$). Subsequently, miargyrite ($AgSbS_2$) (ESM 3 2c-e), cuboargyrite ($AgSbS_2$), and pyrargyrite (Ag_3SbS_3) (Fig. 4c, d) form due to variable replacement reactions (i.e., diaphorite ➔ miargyrite, miargyrite ➔ pyrargyrite, tetrahedrite I (stage II) ➔ tetrahedrite/freibergite II (stage IV, Figs. 3f and 4d), pyrargyrite ➔ allargentum, Fig. 4c): pyrargyrite grows around miargyrite, tetrahedrite (II, freibergite) replaces tetrahedrite (I) from stage II and contains inclusions of miargyrite, chalcopyrite, and galena. Furthermore, jamesonite (stage III) grains are enclosed by tetrahedrite II (stage IV). These replacement textures show clearly that Pb-Sb-dominated minerals of stages II and III are replaced by Ag-Sb-rich minerals of stage IV. Stage IV ends with the precipitation of stephanite (Ag_5SbS_4), polybasite ($(Ag,Cu)_{16}Sb_2S_{11}$), allargentum ((Ag,Sb), Fig. 4c), dyscrasite (Ag_3Sb), and native silver (ESM 3 2f). Transparent quartz with pyrite II, berthierite II, and stibnite II is overgrown by a sequence of calcite, ankerite, and less frequently very late quartz during stage IV.

The petrography of the Au-rich impregnations and disseminations near Bad Sulzburg were considered separately, since these form no macroscopically distinct mineralization but occur rather as microscopic veinlets. However, the mineralogy of these veinlets is the same as the stage I mineralization of the Sb-Pb-Ag±Au-quartz veins (described above) and thus are assumed to have formed contemporaneously. Gold grains contain a significant amount of Ag and are, therefore, referred to as electrum. Generally, two associations of electrum with sulfides are observed (Fig. 4e, f; see also Krützfeldt 1985). The first association shows electrum either in pores/free space of weathered pyrite and/or quartz or on altered and silicified host rock minerals (e.g., feldspar, clay minerals, iron (hydro-) oxide mixture, Fig. 4e). This association was found at the Weiherkopf southeast of Bad Sulzburg and is interpreted to be of supergene origin, formed during oxidation of Au-bearing pyrite. Grain sizes of electrum range between 0.2 and 0.6 mm. The second association, found in the Felsengrund southeast of Bad Sulzburg, shows primary, hydrothermally formed electrum within sulfides (especially galena and marcasite) in quartz veinlets (Fig. 4f). Late barite is a

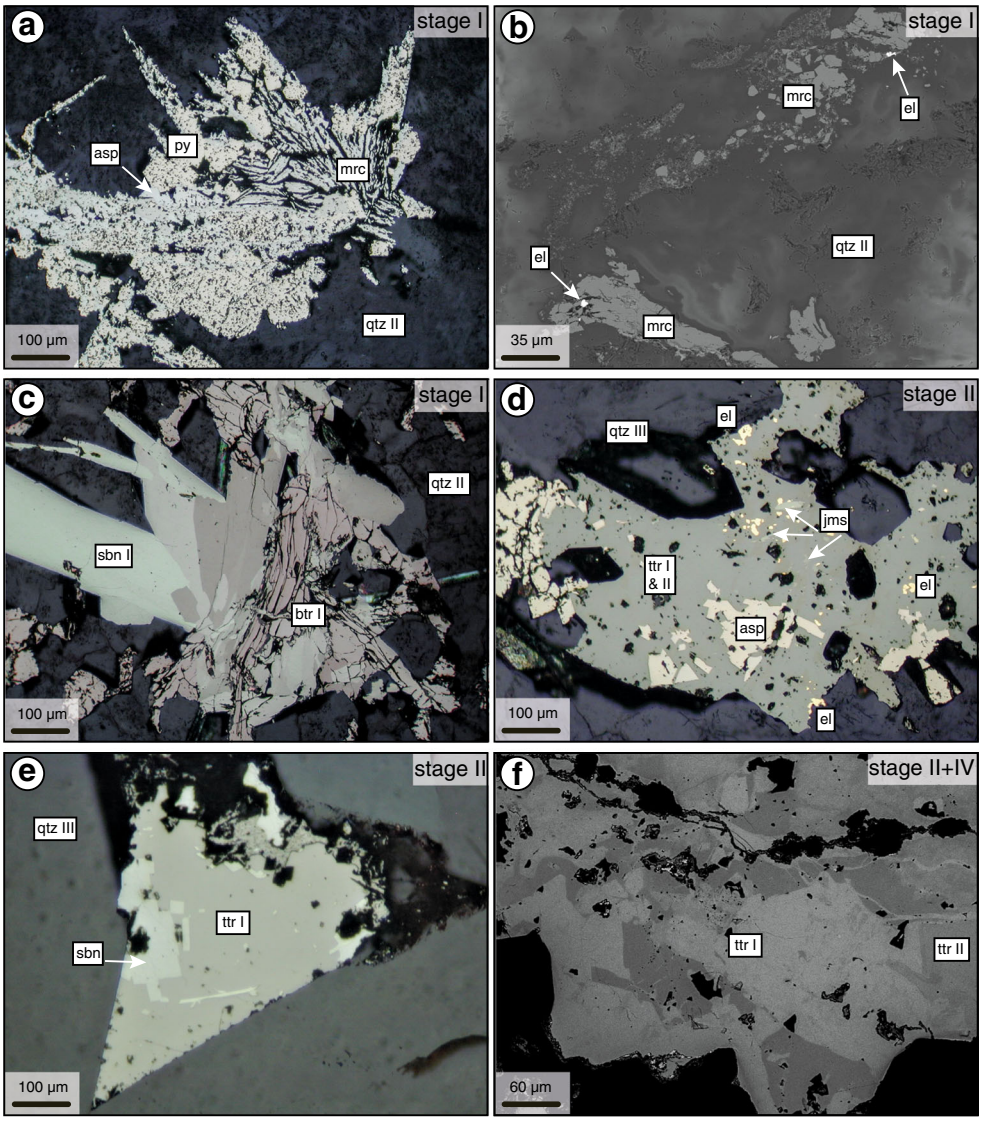

Fig. 3 Photomicrographs illustrating typical relations between ore minerals. RL - reflected light microscopy; BSE - backscattered electron images. **a** RL image in oil illustrating the association of arsenopyrite, pyrite, and marcasite, which replaces pyrrhotite; Artenberg, GL-Ar4. **b** BSE image of marcasite with electrum grains enclosed in quartz II; Segen Gottes, GL-Sg1. **c** RL image in oil berthierite I overgrown by stibnite I in quartz II; Goldengründle, GL-Go1. **d** RL image in oil of quartz III-hosted tetrahedrite I and II with inclusions of arsenopyrite, electrum and jamesonite; Hornbühl, GL-Ho1. **e** RL image in oil of quartz III-hosted tetrahedrite I with numerous stibnite inclusions; Münstergrund, GL-Mü3. **f** BSE image of tetrahedrite I which is replaced by tetrahedrite II (high contrast); Flammeck, TE-FE01E

rare member of this assemblage. Electrum from the other investigated veins in the Schwarzwald is either associated with altered marcasite, which fits with the first association of the Sulzburg veinlets, or occurs as inclusions in sulfides, mainly in tetrahedrite I and II of stage II.

Methods

Electron microprobe analysis

The chemical composition of the ore minerals was determined using a JEOL Superprobe JXA-8900RL at the University of Tübingen. Acceleration voltage of the focused beam was 25 kV at a beam current of 20 nA. Counting times for major elements were 16 s for the element peak and 8 s for each background and for minor elements 30 and 15 s, respectively. A detailed description of the method, detection limits (2σ) and standard deviation are provided in ESM 5.

Fluid inclusion analyses by optical, IR, CL microscopy, and micro-Raman

Relative chronological sequences of fluid inclusions (fluid inclusion assemblages (FIAs)) after Goldstein and Reynolds (1994) were investigated by optical microscopy. A "hot cathode" CL microscope (type HC1–LM) with an acceleration voltage of 14 kV and a beam current density of ~ 9 µA mm^{-2} on the sample surface was applied at the University of Tübingen to retain additional information on the fluid inclusion petrography (Kolchugin et al. 2016).

Microthermometric investigations on quartz were performed using a Linkham (THMS 600) fluid inclusion stage on a Leica DMLP microscope with an optical CCD camera at the University of Tübingen. For the analysis of fluid inclusions in

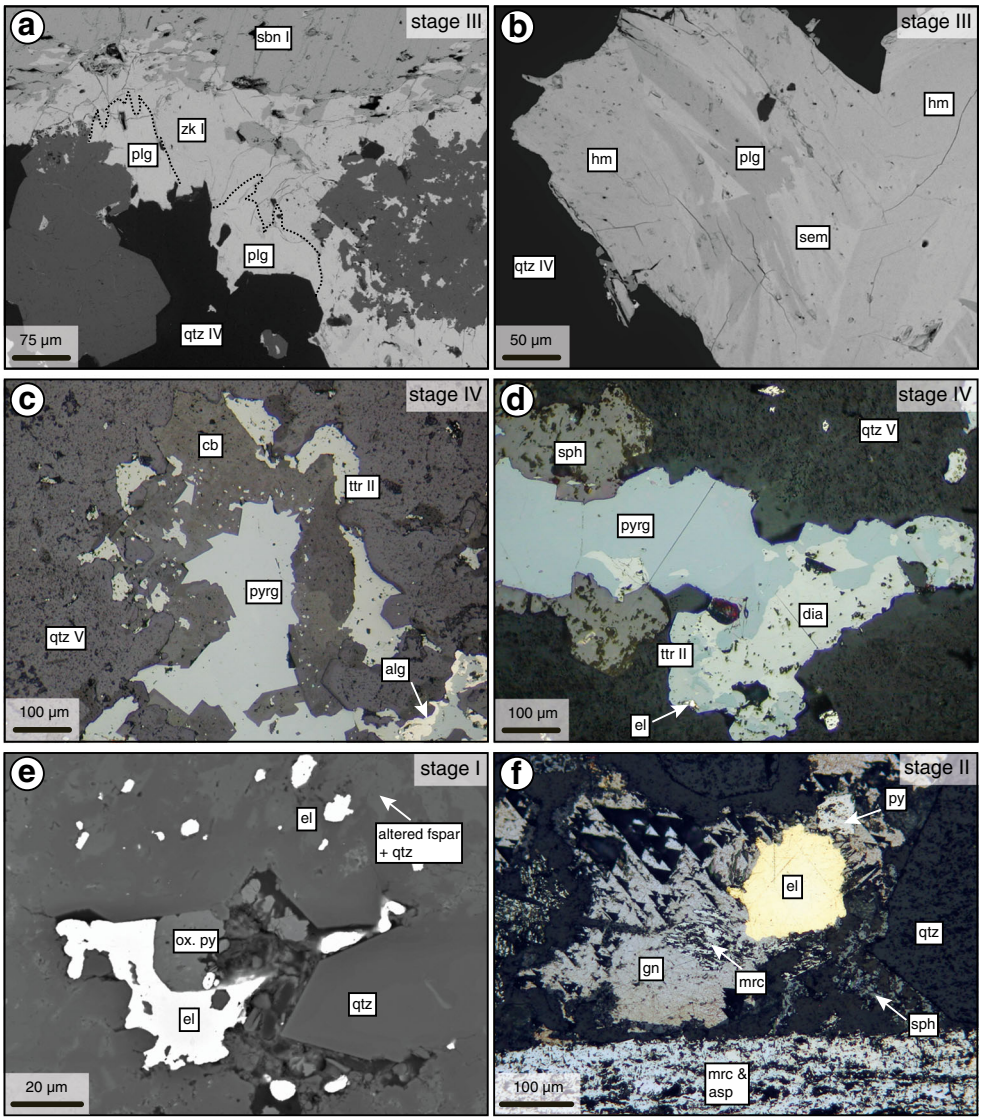

Fig. 4 Photomicrographs illustrating typical relations between ore minerals. RL - reflected light microscopy; BSE - backscattered electron images. **a** BSE image of stibnite replaced by zinkenite I, which is then replaced by plagionite. Black dashed lines show the grain boundaries between zinkenite and plagionite; Ludwig, GL-Lu8. **b** BSE image of plagionite overgrown by co-genetic heteromorphite and semseyite, accompanied by quartz IV; Hornbühl, GL-Ho4. **c** RL image in oil of tetrahedrite (freibergite) II in a quartz V void. Carbonate and pyrargyrite initially grew co-genetically, pyrargyrite precipitated later. Allargentum partly replaces pyrargyrite; Baberast, GL-Ba2. **d** RL image in oil of diaphorite replaced by pyrargyrite and tetrahedrite (freibergite) II with electrum inclusions and overgrown by sphalerite; Barbara, GL-Br2. **e** BSE image of electrum on oxidized pyrite in quartz and altered feldspar; Weiherkopf, CH-70. **f** RL image of a large electrum grain associated with galena and marcasite, pyrite, and sphalerite but mostly overgrown by galena; Felsenloch, CH-54

sphalerite and stibnite, the same setup with an IR camera Retiga 2000R (λ up to 1000 µm) was used at the TU Bergakademie Freiberg. For each inclusion, the ice melting temperature (T_m, ice), the hydrohalite melting temperature (T_m, hh), and the homogenization temperature (T_h) were measured.

For the calculation of salinity in the ternary NaCl-$CaCl_2$-H_2O system, the Excel-based program of Steele-MacInnis et al. (2011) was used. Pressure correction was done using the program HOKIEFLINCS_H2O-NACL (Steele-MacInnis et al. 2012) in combination with estimates on basement and sedimentary overburden based on Geyer et al. (2011 and references therein). A maximum overburden of 1000 m, corresponding to 300 bar, was estimated. For the correction of the homogenization temperature, this maximum pressure results in maximum temperature differences of + 45 °C, the median of all analyses being 15 °C. Further interpretation was done with the raw data to avoid estimation errors. The uncertainties of this approach are discussed by Walter et al. (2015).

Micro-Raman measurements were conducted using a confocal Raman spectrometer Renishaw InVia Reflex at the University of Tübingen. A laser wavelength of 532 nm, with a laser output of 50%, was a numerical aperture of 0.55 and an opening angle of 66.7° was used. With a three-rate accumulation, the measurement time was set to 30 s, a beam diameter of 2 µm, and the slit diaphragm was automatically adjusted and corrected.

Oxygen isotope chemistry

A suite of 50 quartz samples from 30 sites was analyzed for oxygen isotope compositions. Oxygen isotope analyses were performed using a laser extraction procedure that follows the techniques described by Sharp (1990) and Rumble and Hoering (1994) and the $^{18}O/^{16}O$ isotope ratio was measured on a Finnigan MAT-252 gas source mass spectrometer at the University of Tübingen. By combining oxygen isotope

analyses of quartz samples and homogenization temperatures from fluid inclusion studies of primary inclusions, the oxygen isotope composition of the fluid was determined according to the equation of Ligang et al. (1989). ESM 6 reports all minimum and maximum homogenization temperatures, $\delta^{18}O$ quartz, and the calculated $\delta^{18}O$ H_2O values of each sample.

Thermodynamic modelling

For thermodynamic modelling, "The Geochemist's workbench (GWB)" package was used with a tailor-made thermodynamic database for a uniform pressure of 50 MPa and temperatures between 0 and 400 °C. Information about the database is detailed in Burisch et al. (2018, this issue) and in the electronic supplement ESM 4.

Results

In the following section, the results of all applied methods in this study will be presented, within the context of the different mineralization stages described above.

Mineral chemistry

Representative chemical compositions of all analyzed minerals are listed in ESM Table 2. Individual analyses are provided in the ESM 7.

Stage I: Fe-As (-Sb±Au)

Arsenopyrite has a non-stoichiometric composition, which can be explained by varying Sb and As concentrations, whereas the other minerals (marcasite, pyrite, and stibnite) of this stage show almost ideal compositions. Of particular importance are noble metal contents of ore minerals of this stage. Arsenopyrite, marcasite, and pyrite contain invisible gold with maximum values of 3100, 2100, and 710 ppm, respectively (Fig. 5a and ESM Table 2). Some berthierite grains show maximum Au concentrations of 730 ppm. The dominant mineral stibnite contains up to 1800 ppm Au and 1000 ppm Ag. Electrum grains range between 50 and 85 wt% Au (Fig. 5b) and contain up to 2 wt% Pb and 1500 ppm Hg (ESM Table 2). Compositions below the 1:1 line have lower totals and cannot be explained by exchange with other elements such as Cu, Bi, or Hg, overlap corrections or reference material, but by variable porosities. Furthermore, analyses from areas in the central Schwarzwald (i.e., Freiburg, Kinzigtal) show a distinctly higher Ag content of up to 50 wt%, whereas analyses from Bad Sulzburg and Badenweiler have maximum Ag values of 35 wt%.

Stage II: Pb-Zn-Cu

The minerals of this stage show compositions close to their stoichiometric formulae, with the only exception of chalcopyrite, which shows a minor Cu deficit. Tetrahedrite I is the most common mineral in this stage with Cu contents between 15 and 30 wt% (average 23 wt%), whereas the Ag content ranges from 11 to 30 wt% with an average value of 19 wt%. Chalcopyrite incorporates significant amounts of As (up to 3.7 wt%) and Sb (up to 1400 ppm). Galena has Ag concentrations up to 1.2 wt% and Sb up to 2.7 wt%. Important minor elements in sphalerite are Cd and Ag, with maximum amounts of 7700 ppm and 1.7 wt%, respectively. High amounts of Ag have previously been attributed to nano-inclusions of fahlore solid solution (Pfaff et al. 2010).

Stage III: Pb-Sb

Different to the previous two mineralization stages, ore minerals of stage III usually have non-stoichiometric compositions. Highest Ag and Au concentrations were observed in zinkenite with maximum Ag values of 3700 ppm and in jamesonite, with up to 3300 ppm Ag and 1 wt% Au. Andorite and bournonite show exceptionally high Se concentrations of up to 2 and 1.5 wt%, respectively. High Cu concentrations were measured in zinkenite (< 7000 ppm) and jamesonite (< 1 wt%). Besides, andorite and semseyite show the highest Fe content (up to 1600 ppm), whereas only up to 550 ppm were measured in fizélyite, heteromorphite, plagionite, and zinkenite. Highest As concentrations were detected in bournonite (up to 1 wt%), jamesonite (up to 1200 ppm), and zinkenite (up to 1000 ppm).

Stage IV: Ag-Sb

All minerals of this stage contain large amounts of As (up to 4700 ppm), Se (up to 2000 ppm), and Fe (up to 3.3 wt%). Au was detected with maximum amounts of 850 ppm in diaphorite, miargyrite, and pyrargyrite. Tetrahedrite/freibergite II shows Cu concentrations between 12 and 18 wt% (average 15 wt%), whereas the Ag content ranges from 26 to 37 wt% with an average value of 32 wt%. Diaphorite and freieslebenite show a non-ideal Pb site occupancy, with not fully occupied Pb (1.87 a.p.f.u. instead of 2 and 0.61 a.p.f.u. instead of 1, respectively), whereas the Ag and Sb contents are close to ideal. The opposite holds true for pyrargyrite, where the Ag site is not completely filled (2.85 a.p.f.u. instead of 3). Miargyrite and stephanite analyses result in compositions close to their ideal formulae.

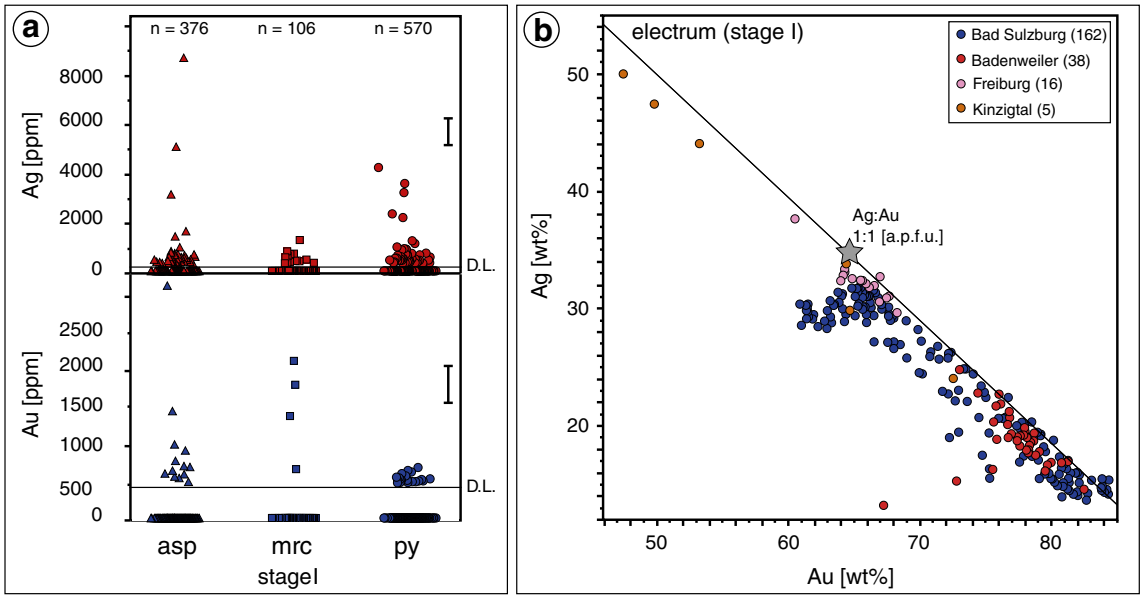

Fig. 5 **a** Ag and Au content in ppm of arsenopyrite, marcasite, and pyrite of all localities of stage I. Black bars show the uncertainty of each measurement, D.L. = detection limit. **b** Ag versus Au (wt%) of all electrum analyses, classified by the areas in the Schwarzwald. Gray star represents the stoichiometric electrum. Variations below the 1:1 line can be explained by lower totals due to porosity

Fluid compositions

Considering the salinity and homogenization temperature of fluid inclusion analyses from both ore and gangue minerals in all stages of the mineralization, three clusters were identified. These are briefly described in the following section. Detailed results are provided in ESM 8. The sum of all presented fluid inclusion analyses records the whole range of fluids involved, as they are composed of fluid inclusions from various quartz generations throughout the entire succession of mineral assemblages (Fig. 6). For temporal interpretation, only primary and pseudo-secondary inclusions were considered and the analyzed secondary inclusions serve only a statistical purpose in fluid composition-homogenization temperature space. Due to the polyphase nature of mineralization (e.g., multistage reaction and overgrowth textures), we were only in rare instances able to directly correlate individual fluid inclusions to ore mineral assemblages (Fig. 6a–d). These include (1) quartz-ore mineral-quartz with a clear temporal succession (Fig. 6c), (2) quartz-ore mineral clusters with a paragenetic association (Fig. 6d), and (3) fluid inclusions in stibnite and sphalerite with a direct age correlation.

Fluid type A: low salinity, high to medium temperature

This fluid type was found in quartz and stibnite from mineralization stage I. Primary, secondary, or pseudo-secondary inclusions of this type are in most cases irregularly shaped; pseudo-secondary ones typically occur in healed cracks in quartz and stibnite. Measured homogenization temperatures (T_h) range from 100 to 400 °C (Fig. 7a), but most analyses show temperatures above 250 °C. Fluids freeze in the range of − 30 to − 45 °C and the first melting can be observed above − 20 °C, providing evidence for a binary NaCl-H_2O system (Steele-MacInnis et al. 2011, Fig. 7b). The final melting temperature of ice is between 0 and 5 °C, resulting in calculated salinities of 0 to 5 wt% (NaCl+$CaCl_2$, Steele-MacInnis et al. 2011). Only H_2O, HCO_3^-, or CO_3^{2-}, but no SO_4^{2-} was detected in micro-Raman analyses.

Fluid type B: high salinity, moderate to low temperature

Fluid type B was recognized in sphalerite from and quartz associated with mineralization stage II and in quartz from stage III. Similar to fluid type A, most primary (Fig. 6f), secondary, or pseudo-secondary inclusions are irregularly shaped (Fig. 6f), but they occur on primary growth zones and well-healed fractures in quartz and sphalerite. Homogenization temperatures vary between 50 and 250 °C into the liquid (Fig. 7a). Above − 50 °C, a first melting is visible, indicating a ternary NaCl-$CaCl_2$-H_2O system (Fig. 7b). Last dissolving phases are ice and hydrohalite. Observations show that the final melting temperature of ice ranges between − 29 and 18.5 °C and of hydrohalite between − 28.5 and − 17.5 °C, which results in calculated salinities of 20 to 26 wt% (NaCl+$CaCl_2$, Steele-MacInnis et al. 2011). The molar Ca/(Ca+Na) ratio ranges between 0.00 and 0.80. In all FIAs, H_2O (Raman bands between 2750 and 3900 nm) was the only Raman-

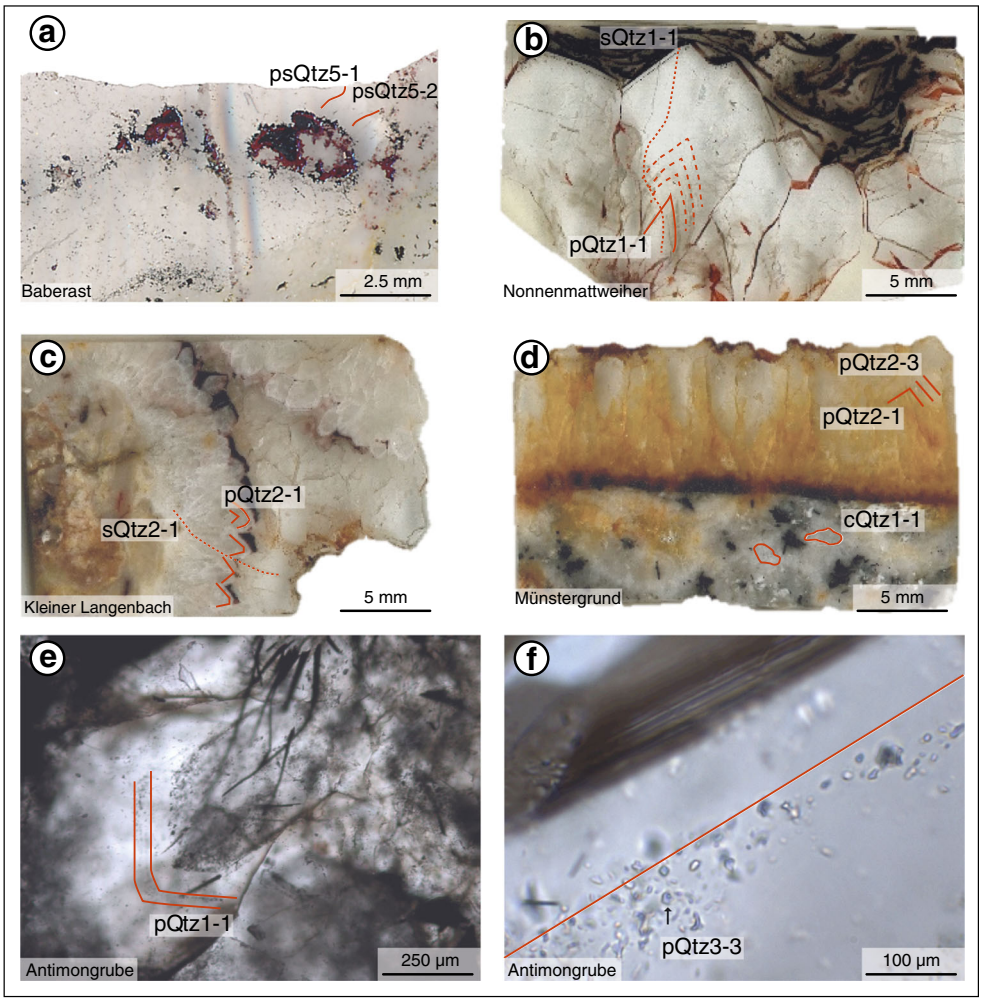

Fig. 6 Photomicrographs illustrating the characteristic attributes of fluid inclusions in different samples and different mineralization stages. **a** Silver mineralization (stage IV) in voids of and intergrown with quartz V (stage IV) and measured pseudo-secondary fluid inclusions in quartz. **b** Various primary fluid inclusions on growth zones in quartz and a secondary inclusion trail, cutting across the whole quartz I crystal, prior to stage I. **c** Several quartz generations, with ore minerals in between two quartz generations (II and III). Analyzed primary and secondary inclusions in quartz II are shown. **d** Clustered fluid inclusions and ore minerals in quartz I overgrown by quartz II with primary inclusions. **e**, **f** Representative microscope images of typical primary fluid inclusion trails in quartz II

active species detected in all analyses. Further, minor NaCl-dependent modifications of the H_2O-bands were recognized (Frezzotti et al. 2012).

Fluid type C: variable salinity, moderate to low temperature

This fluid type was found in inclusions in quartz, associated with stage IV sulfide mineral assemblages. Inclusions of this fluid type have variable sizes and shapes and occur along trails and in clusters. Homogenization temperatures vary between 50 and 200 °C (Fig. 7a). Compared to fluid types A and B, two different clusters of fluid compositions can be distinguished: one with a eutectic temperature of − 21.2 °C and another one with a eutectic temperature of − 52 °C. Final melting temperatures of ice range between − 2.6 and − 18 °C, and hydrohalite melts between − 20.9 and − 25.8 °C. The calculated salinity ranges between 7.5 and 20 wt% ($NaCl+CaCl_2$, Fig. 7a, Steele-MacInnis et al. 2011) and the molar Ca/(Ca+Na) ratio ranges from 0.00 to 0.80. In all FIA, H_2O was the only Raman-active species detected in all analyses with significant NaCl-dependent H_2O-band modifications.

Oxygen isotope data

All oxygen isotope data is reported relative to the SMOW standard. The $\delta^{18}O$ values of quartz vary greatly, quartz (stage I–III) from the Bad Sulzburg area (area D, Fig. 1) showing a range from − 1 to + 18‰, from Ehrenkirchen (area C, Fig. 1) a range from + 12 to + 18‰, and from Münstertal a range from − 3.5 to + 19‰ (area C, Fig. 1). The analyzed range of $\delta^{18}O$ values greatly exceeds the range reported by Baatartsogt et al. (2007) who related $\delta^{18}O$ values of quartz to Variscan (− 12.5 to + 4.4‰) and post-Variscan fluids (− 7.1 to + 2.1‰).

The large dataset of formation temperatures was combined with oxygen isotope data of quartz to calculate $\delta^{18}O$ values of the fluid responsible for vein formation (according to Ligang et al. 1989). For analyses from samples, where no respective fluid inclusion data was available, the $\delta^{18}O$ fluid values were calculated at 50 and 400 °C, representing the minimum and

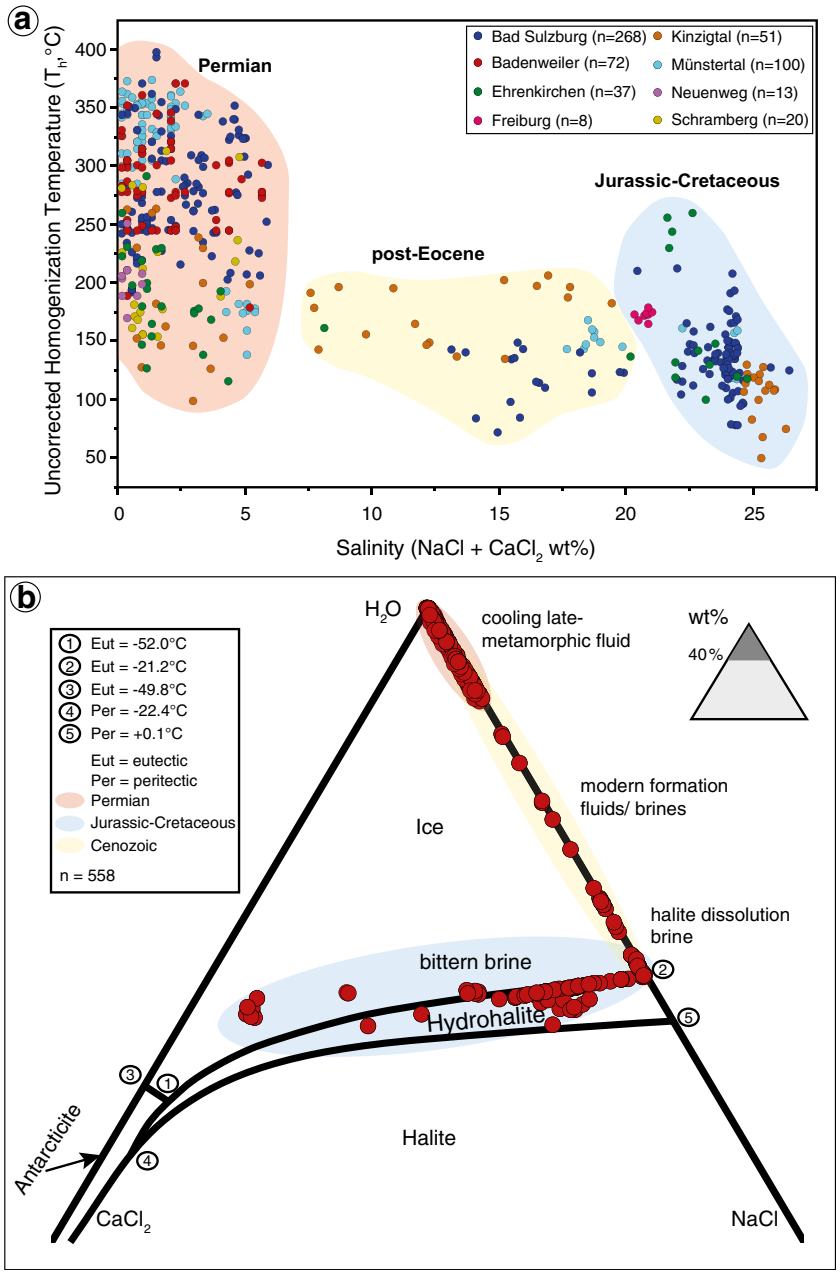

Fig. 7 **a** Homogenization temperature versus calculated fluid salinity (NaCl+$CaCl_2$) in wt%. The different box colors refer to various time periods of mineralization (Walter et al. 2016, 2018a). **b** Phase diagram of the ternary H_2O-$CaCl_2$-NaCl fluid system. Different colors show the same classification as in (**a**)

maximum homogenization temperatures observed in all veins. Unfortunately, the large number of intergrown quartz generations and the commonly lacking textural evidence prevented an exact temporal correlation of a specific quartz generation from one locality to a specific quartz generation from other localities and/or mineralization stages. However, relative trends from initial quartz (I) to successive quartz (II, III) generations are visible within individual localities from which several, temporally distinguished quartz generations were analyzed; also, the overall range of the isotopic ratios serves as a solid base for interpretation. The analyses illustrate that the calculated $\delta^{18}O$ values of fluids associated with Sb-Pb-Ag ±Au veins overlap with magmatic/metamorphic and meteoric fluids, with peaks at ca. − 5‰ and + 6 to + 11‰. Metamorphic fluids typically have $\delta^{18}O$ values of ~ + 3 to + 20‰, magmatic fluids + 5.5 to + 9.5‰, and meteoric water shows variations from − 25 to 0‰ (e.g., Craig 1961; Sheppard 1986; Taylor and Barnes 1997; Kendall and Coplen 2001). The evolutionary trend for a specific locality with several quartz generations indicates an increasing importance of meteoric fluids for successively younger quartz generations. For example, at the Wonnen locality (Münstertal, Area C Fig. 1), the fluid which formed the early quartz I shows a typical magmatic/metamorphic signature (max. +13‰), whereas the subsequent quartz generations (II + III) indicate a meteoric fluid composition (on average − 2.4‰).

Discussion

The discussion section is subdivided into two parts. The first part deals with fluid compositions and age constraints for Sb-Pb-Ag±Au-quartz veins in the Schwarzwald. In the second part, the mineralogical and chemical evolution of the different mineralization stages is discussed in detail, as well as the occurrence of gold and the comparison to other Sb- (Au) occurrences in the Variscan Orogen and worldwide.

Fluid compositions and age constraints

Textural observations correlated to fluid inclusion data, fluid salinities, and oxygen isotopes can be used here to invoke a Permian age for mineralization stage I, whereas stage II and III formed during Jurassic and stage IV during Tertiary times.

With an age of 277.6 Ma (Walter et al. 2018c, submitted), Permian veins are significantly younger than the last magmatic event in the Schwarzwald, which was the intrusion of post-collisional granites between 335 and 315 Ma (e.g., Todt 1976; Altherr et al. 2000; Hann et al. 2003). The rare and local occurrence of ferberite ($FeWO_4$; at the Segen Gottes locality) in the Permian veins is tentatively attributed to the proximity of this locality to the Nordrach pluton from which W-bearing minerals are well-known (Walenta et al. 1970) and which may have been remobilized. Such post-Variscan mobilization processes are common in the Schwarzwald and were described in detail by Werner et al. (1990). Oxygen isotope analyses for quartz from stage I mineralization point to a magmatic/metamorphic fluid signature. Very variable homogenization temperatures (100 to 400 °C, Fig. 7a) and low salinities (0 to 5 wt% NaCl + $CaCl_2$, Fig. 7a) show fluid compositions typical for Permian veins in the Schwarzwald (e.g., Wagner and Cook 2000; Baatartsogt et al. 2007; Walter et al. 2016). The temperature fluctuation is due to fluid cooling and not due to evaluating primary vs. secondary inclusions. This large temperature (cooling) range is similarly observed in many large Sb deposits worldwide, e.g., in Australia, Bolivia, Russian Federation, or China (e.g., Comsti and Taylor 1984; Ashley et al. 1990; Dill et al. 1995; Bortnikov et al. 2010; Zhai et al. 2014). However, individual localities from all over the world generally do not show such a broad temperature range (commonly < 200 °C), which may be linked to factors such as the difference in tectonic setting and/or size of the mineralization (fluids in small fractures in the Schwarzwald may cool down faster than larger volumes of fluids in the large deposits).

The intensive brecciation of stage I minerals and the overgrowth by minerals of stage II indicates significant tectonic processes during the initiation of stage II. In combination with a strong change in fluid composition and formation temperature, this suggests the presence of a significantly different fluid reservoir during stages II and III. During Late Permian to Triassic times, the central European basin was flooded by seawater and evaporites were deposited (e.g., Roscher and Schneider 2006; Geyer et al. 2011). This marine influence is reflected in the fluid composition of the successive stages, which contains increased salinities up to 27 wt% NaCl+$CaCl_2$ (Fig. 7a, b), compared to Permian low-salinity fluids (max. 5 wt%). Furthermore, the recorded fluid composition is in agreement with fluids from other Jurassic-Cretaceous veins that typically show salinities between 20 and 28 wt% (Walter et al. 2016). The presence of significant Pb in the mineralized system is probably related to the high chlorinity of these fluids (as Pb is transported als Cl complexes, Yardley 2005; Wagner et al. 2016), since the sudden increase in Pb is directly correlated with a significant salinity increase, whereas the possible source rocks have remained constant. Moreover, the calculated oxygen isotope values of the fluid show (at some localities) that the younger quartz generations formed from a fluid with increasing influx of meteoric water and/or seawater (Weissert and Erba 2004).

A second significant change in fluid composition is visible for the transition to stage IV, which is also recorded by a change in tectonic regime. Fluid inclusion analyses of quartz directly associated with the Ag-bearing minerals of stage IV show variable salinities ranging between 7.5 and 20 wt% (NaCl+$CaCl_2$). These values are typical of post-Cretaceous fluids in veins of the Schwarzwald district (Walter et al. 2016). This stage and the newly formed Ag-bearing minerals are only locally present, especially in the Central Schwarzwald district, and are generally lacking in the Southern Schwarzwald. Interestingly, stages I to III occur in all veins independent of their strike direction (ESM 3 3), whereas predominantly NE-SW striking veins (i.e., parallel to the Rhine Graben rift) contain a large variety of Ag minerals (ESM 3 3). Thus, there is a correlation between vein orientation and the presence of stage IV. Because it is regarded as unlikely that the tectonic regime changed significantly during a single mineralization event, it is assumed that the Ag mineralization is related to a separate tectonic setting and fluid influx. The orientation of these veins parallel to the Rhine Graben is thus thought to be related to a reactivation of pre-existing Permian veins during the course of the Upper Rhine Graben opening, and hence, a Tertiary age of the Ag-rich stage IV mineralization is deemed very likely.

Mineralogical and chemical evolution

Fe-As(-Sb±Au) stage (stage I)

Initially, this stage is strongly dominated by Fe- and As-bearing minerals, but this transitions to an abundance of Sb-rich sulfides. The initial minerals do, however, contain Sb (as well as Au and Ag) as a minor or trace element. The best example is the As-Sb zoning of arsenopyrite (ESM 3 1b). Antimony was, hence, present in the fluid from the beginning

and this mineral sequence does not record a compositional evolution from an Fe-As- to a Sb-dominated fluid. Rather, the mineral succession records a decrease in temperature (e.g., Wagner and Cook 2000; Krolop et al. 2018; Burisch et al. 2018, this issue).

The fluid inclusions of the first stage (in quartz and in stibnite) record a large temperature range from 400 to 100 °C (Fig. 7a), which further strengthens the argument of fluid cooling. The process of fluid cooling can be thermodynamically modelled by using a fluid of low salinity (5 wt% NaCl) in equilibrium with a granitic host rock (assumed composition, comprised of 5 wt% muscovite, 5 wt% annite, 10 wt% anorthite, 10 wt% albite, 35 wt% quartz, and 35 wt% K-feldspar) at neutral pH (6.55 at 400 °C). Granitic host rocks buffer a fluid at near-neutral conditions (Bucher and Stober 2002; Bucher and Stober 2010; Fig. 8c, d). Starting at 400 °C, the minimum temperature estimate of the source fluid produces a sequence of early pyrite and later stibnite during simple cooling (Fig. 8a, b). However, without additional water-rock interaction during cooling, the quantity

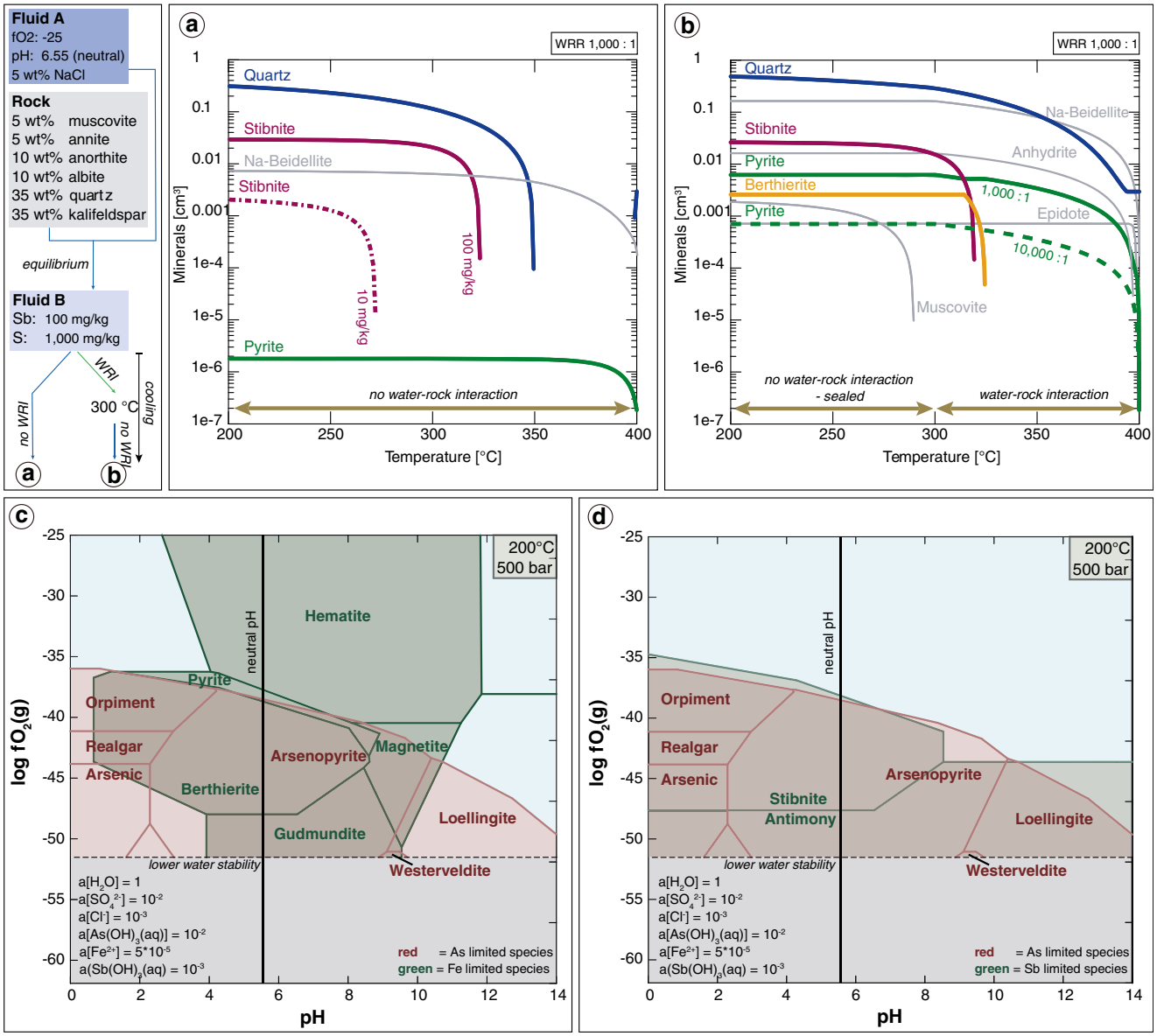

Fig. 8 **a, b** Mineral stability diagram during cooling of a fluid initially in equilibrium with a granitic host rock. WRR = water-rock ratio, WRI = water-rock interaction, gray minerals = not found in samples of this study. **a** No WRI during cooling with Sb concentrations of 100 and 10 mg/kg. **b** WRI during cooling drastically increases the amount of pyrite precipitation. Shown is an example of WRI (1000:1) between 400 and 300 °C and a sealed system from 300 to 200 °C. **c, d** Predominance fO_2-pH diagrams at 200 °C, 500 bar, where the Fe species are shown in **c** and the Sb species in **d**. For a simplified comparison between the predominance field, the As species are shown in both **c** and **d**. Both **c** and **d** represent overlapping predominance fields of the same fluid

of pyrite relative to stibnite and quartz would be too low to match the observed relative phase volumes, since only minor amounts of Fe can be transported at near-neutral conditions. We thus assume that additional Fe was derived near the place of pyrite precipitation from the host rocks. Bleached zones around the veins support this notion. However, in our model, water-rock interaction was only assumed to happen between 400 and 300 °C, as quartz precipitation seals the veins and prevents further reactions. Still, relatively little fluid-rock interaction suffices to explain the observed amounts of pyrite.

The hydrothermal fluid must initially have been relatively reduced and sulfur-rich, otherwise, hematite and/or magnetite would form and deplete the fluid of Fe before pyrite saturation is reached. Graphite- and sulfide-bearing host rocks favor reduced fluids (Kontny et al. 1997) and the Schwarzwald gneisses contain both (e.g., Bucher et al. 2009; Markl et al. 2016; Walter et al. 2018b). Further, the formation of arsenopyrite together with pyrite during the initial fluid stage requires an As/Sb ratio of 10 (Fig. 8c, d). This is at first glance surprising since we are dealing with an Sb-dominated mineralization, but it is thermodynamically essential.

Finally, the mineral berthierite, which based on the observed textures precipitated between pyrite and stibnite, is not thermodynamically stable (data from Seal et al. 1992) in our calculations with a realistic fluid composition (see Fig. 8a–d). It only becomes stable if the stability of berthierite is increased by 2 log$K$ values, which represents twice the estimated uncertainty given by Seal et al. (1992). We have no conclusive explanation of the non-stability of berthierte in our calculations.

Pb-Zn-Cu stage (stage II)

The chemical variability increases during this second stage, where Pb-, Zn-, and Cu-bearing minerals dominate. Tetrahedrite (I) is the only Sb- and Ag-bearing (up to 30 wt% Ag but prevalently < 20 wt%) mineral in this stage. The formation of galena instead of Pb-Sb sulfides (in contrast to stage III) indicates a higher S/Sb activity ratio of the fluid. Mineral textures show that some stibnite of stage I is replaced by tetrahedrite (I) of stage II, indicating a remobilization of stibnite (Fig. 3e). Available aqueous Sb is incorporated in tetrahedrite (I) and, thus, base metal sulfides (i.e., sphalerite, galena, and chalcopyrite) can precipitate. This implies that only minor amounts of stibnite were dissolved and re-precipitated and thus the ore-forming fluid only contained minor Sb, which fits with textural observations. Furthermore, to form tetrahedrite and chalcopyrite in the large quantities observed, increased amounts of Cu in the fluid or more effective precipitation mechanisms need to be invoked. We speculate that rather an increased amount of Cu is probable since no Cu-bearing minerals are present before the occurrence of these minerals and besides, Cu can be more effectively transported in highly saline fluids (Yardley 2005; Wagner et al. 2016), which formed stage II.

Pb-Sb stage (mineralization stage III)

This mineralization stage is characterized by a large variety of chemically very similar minerals. Interestingly, textures show a clear inverse relationship: samples with large modal amounts of stage I-stibnite typically do not show a well-developed stage III and the mineral assemblage ends with the Pb-Zn-Cu stage II; samples with a distinct stage III Pb-Sb mineralization, on the other hand, do not show any or only minor amounts of stage I-stibnite. If it occurs at all, it is present as small relics (stage III minerals intensively replace stibnite, Fig. 4a). Hence, formation of the stage III minerals depends on the existence of an earlier Sb mineralization and remobilization especially of stibnite by Pb±Fe-Ag-bearing fluids (Fig. 9). Locally, these reaction textures are preserved (e.g., stibnite ➔ zinkenite, zinkenite ➔ plagionite, Fig. 2). Thermodynamic calculations show that the Pb-Sb sulfides can precipitate from fluids of variable composition and pH, as long as sufficient Pb is present (Fig. 9). Some reactions (e.g., stibnite ➔ zinkenite) show approximately volume constant textures (Fig. 4a) which indicates a steady Pb increase with simultaneous Sb and S decrease during the evolution of this stage. Although these calculations hold an uncertainty since a constant volume cannot be guaranteed in most cases, it is the only method to investigate the mobility of elements (influx vs. discharge), as the fluid composition (relative elemental content) is unknown. Concluding, an additional Pb influx and replacement of pre-existing stibnite has been essential for ore stage III (Fig. 9).

Apart from Pb, Ag is a conspicuous element in stage III, as shown by the occurrence of the Ag-rich minerals andorite and fizélyite in all investigated occurrences. Ag may have been added by the Pb-rich stage III fluid, or it was remobilized from stage II tetrahedrite and stage I electrum. As there is no textural evidence for tetrahedrite and electrum dissolution, it is plausible that the stage III fluid must have transported some Ag besides Pb.

Ag-Sb stage (stage IV)

Mineral composition and mineral sequence in stage IV record a successive Ag enrichment (Fig. 10): the minerals with the highest Ag contents precipitate at the end of this stage. Textures record abundant replacement processes of stages II and III Pb-Sb minerals by minerals of stage IV (e.g., tetrahedrite I ➔ tetrahedrite II (freibergite), andorite ➔ tetrahedrite II (freibergite), galena ➔ pyrargyrite, andorite ➔ miargyrite, Fig. 2). Stage IV Pb-bearing minerals (i.e., diaphorite and freieslebenite, Fig. 2) only crystallize at the beginning of stage IV. Common reaction textures show that the strongly porous

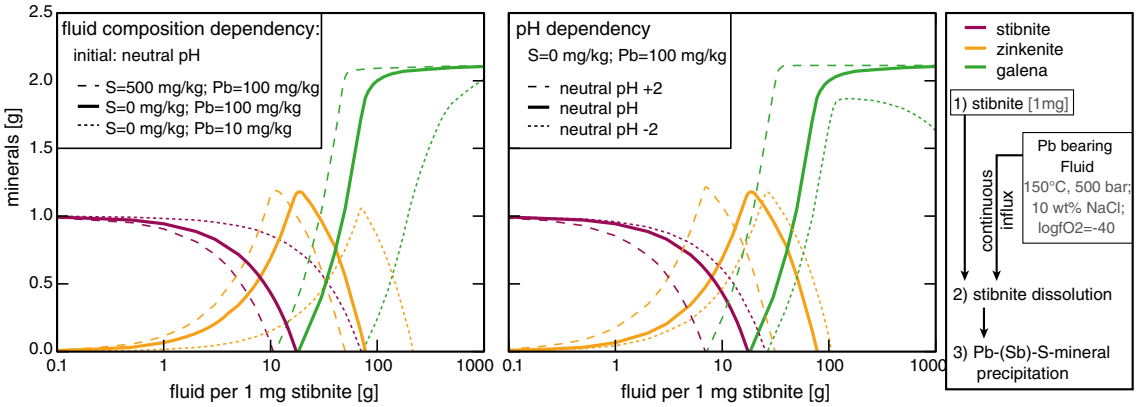

Fig. 9 Mineral stability diagrams at 150 °C (average homogenization temperature) and 500 bar (database condition) showing variable fluid-stibnite ratios during the reaction of a Pb-bearing fluid with pre-existing stibnite. Depicted are the compositional dependency of the fluid and the initial pH dependency of the mineral stability relative to fluid-stibnite ratios. Note that the stability of zinkenite is estimated by the assumption that $\Delta G_f = 0$ for the formation from stibnite and galena

tetrahedrite I is replaced irregularly by tetrahedrite II (freibergite; Fig. 3d, f). Tetrahedrite I of the Pb-Zn-Cu stage II (Figs. 10 and 11) is obviously remobilized and re-precipitated with a Ag-enriched composition (tetrahedrite II (freibergite); Figs. 10 and 11). During this reaction, excessive Cu could not be removed from the system, and hence, local oversaturation leads to the precipitation of chalcopyrite inclusions in tetrahedrite II (freibergite). Moreover, small grains of miargyrite form locally during this process due to the high Ag content of the fluid. Interestingly, there is a correlation of Ag content in tetrahedrite and homogenization temperature of fluid inclusions (Fig. 12): higher homogenization temperatures are

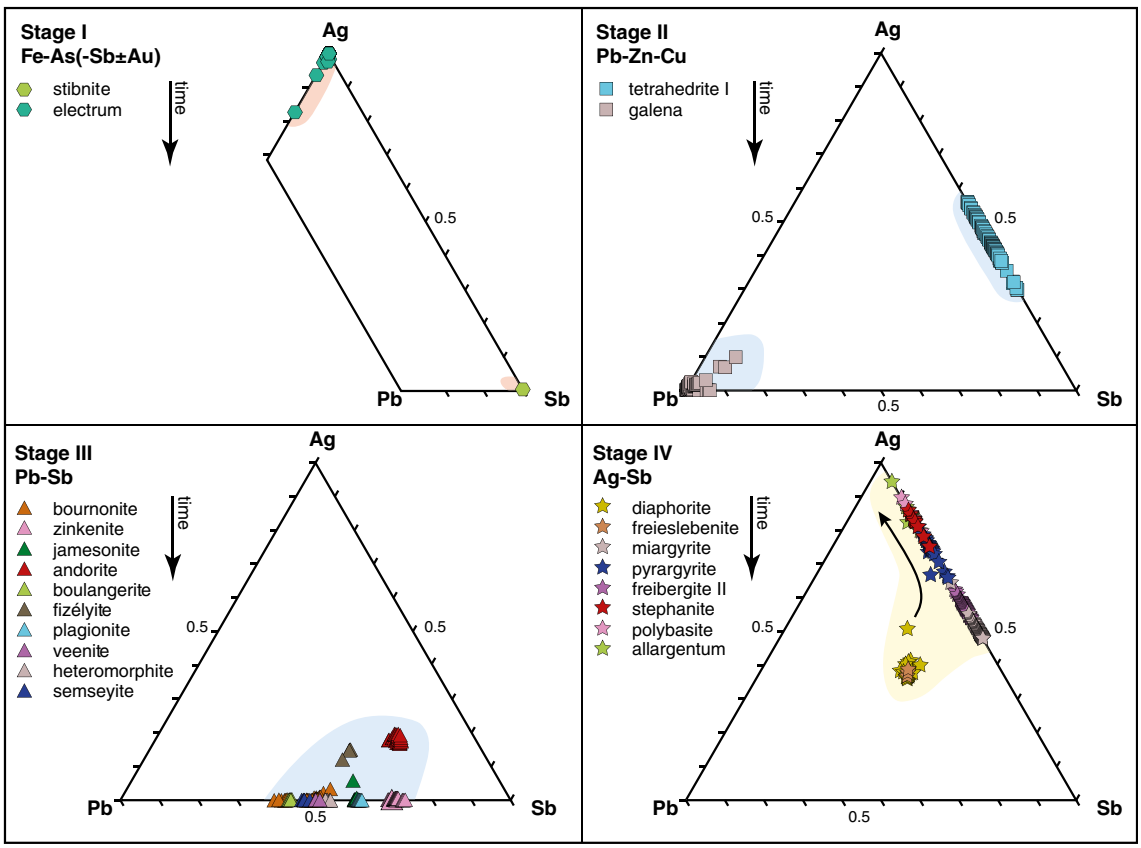

Fig. 10 Composition of all Pb±Ag±Sb-bearing minerals, separated by each mineralization stage and time of crystallization. Red fields show Permian minerals (stage I), blue fields Jurassic-Cretaceous minerals (stage II and III), and the yellow field shows minerals of the Tertiary mineral stage IV. The black arrow indicates a strong Ag enrichment during stage IV, where the youngest minerals show the highest Ag content

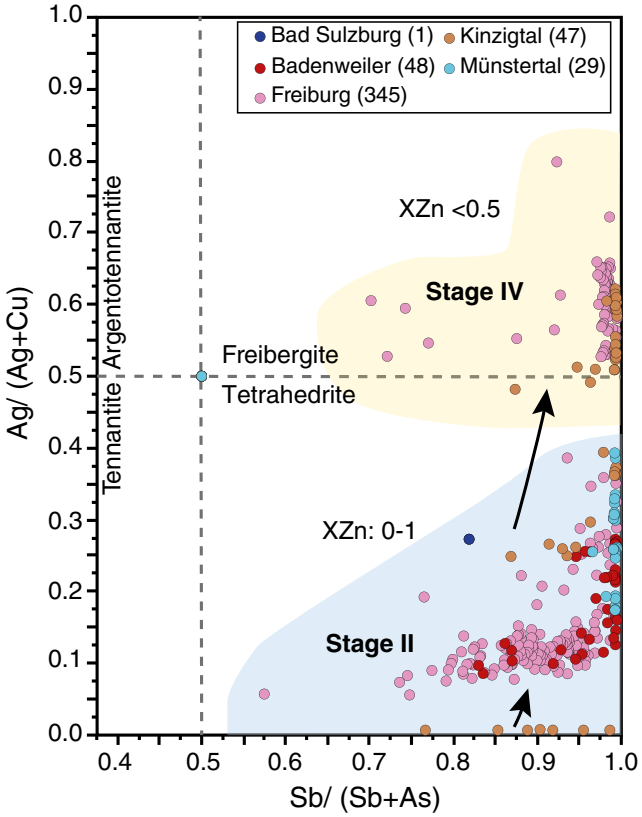

Fig. 11 Ag/(Ag+Cu) versus Sb/(Sb+As) plot of all tetrahedrite analyses, colored according to the different areas sampled. Blue field shows compositions of Jurassic-Cretaceous tetrahedrite I (stage II) and the yellow field those of Tertiary tetrahedrite (freibergite) II (stage IV). Black arrows indicate the evolution of the tetrahedrite composition, oldest at the bottom, youngest at the top

associated with lower Ag content in tetrahedrite, i.e., this is due to a higher Ag content in later stage fluids and not due to crystallographic effects. Precipitation mechanisms for this stage are fluid mixing (indicated by the large spread in salinities even for individual samples) as well as reaction with pre-existing sulfides.

The occurrence of gold

Gold is rather widespread in the studied Sb-quartz vein type mineralization in the Schwarzwald either as invisible gold and/or as native gold/electrum. Invisible gold is present in significant concentrations in minerals of stage I, in pyrite, arsenopyrite, marcasite, and stibnite. Invisible Au concentrations of some samples in this study (up to 3100 ppm) are similar to concentrations commonly observed in large economically significant structurally controlled Au-Sb deposits (~ 100–5000 ppm; e.g., Dill et al. 1995; Ashley et al. 2000; Baltukhaev and Solozhenkin 2009; Kovalev et al. 2011). Generally, changes of physicochemical parameters such as pressure, temperature, Cl concentration, pH, oxygen, or sulfur fugacity provide effective mechanisms for gold precipitation (e.g., Williams-Jones et al. 2009; Zhu et al. 2011).

Due to the intimate correlation between gold and sulfide abundances (i.e., Au as invisible gold in sulfides), one can presume a common precipitation mechanism. Similar to the sulfides, the solubility of gold in the presence of sulfide and chloride complexes (as are present in such hydrothermal systems; Gammons and Williams-Jones 1997; Zhu et al. 2011) decreases with temperature (Seward 1973) indicating that both

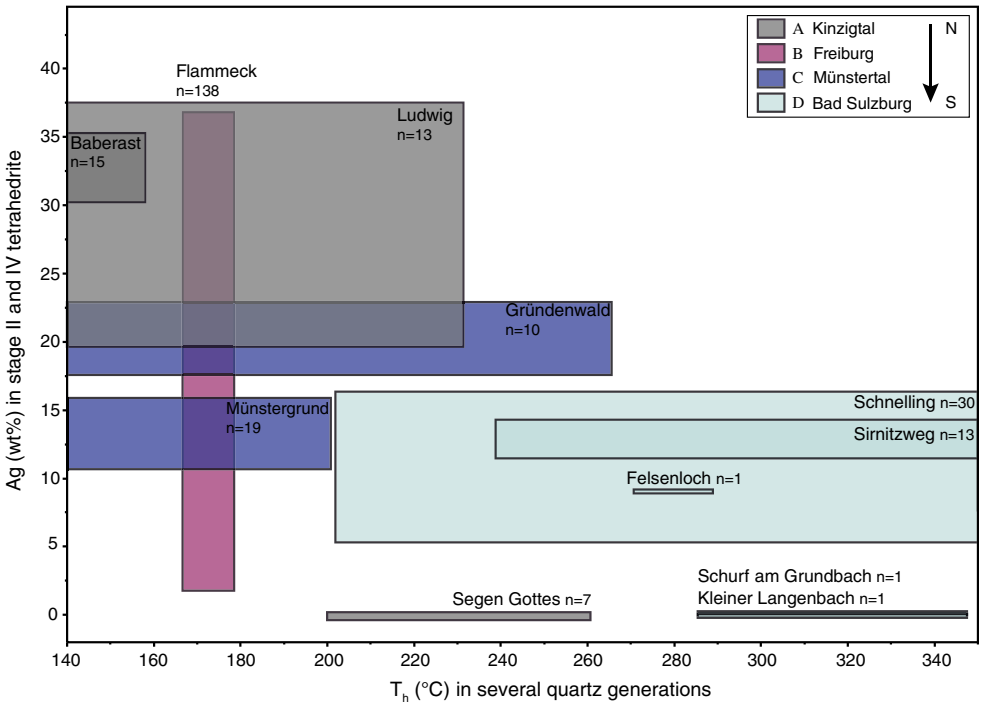

Fig. 12 Ag content (wt%) of tetrahedrite (stage II and IV) versus the homogenization temperature of all four investigated areas in the Schwarzwald. The boxes of each locality represent the temperature range between the minimum and maximum homogenization temperature and the minimum to maximum Ag content

can form by fluid cooling (e.g., Gammons and Williams-Jones 1997; Hagemann and Lüders 2003; Zhu et al. 2011). Furthermore, ongoing sulfide precipitation decreases the sulfide activity and gold-sulfide complexes are de-stabilized (Williams-Jones et al. 2009). Thus, the association between Au and Sb sulfides in quartz veins is typical and has been observed in a large number of deposits (e.g., Distanov et al. 1975; Bril and Beaufort 1989; Clayton et al. 1990; Ortega and Vindel 1995; Obolensky et al. 2007; Zhu et al. 2011).

According to Romer and Kroner (2017), major sources for hydrothermal Au (independent whether it forms discrete grains or is incorporated as invisible gold) in the Variscan basement are Cambrian to Ordovician sedimentary rocks and magmatic arcs; re-distribution in the crust during metamorphism is common in the entire Variscan basement and Au-bearing mineralization is found in many parts of central Europe (e.g., in Germany: Goldkronach, Fichtelgebirge, Pascher 1985, Irber and Lehrberger 1993; Korbach, Rheinisches Schiefergebirge, Lehrberger 1995, Kulick et al. 1997; in France le Bourneix, Laurieras, Saint Yrieix district, Bouchot et al. 1989; in the Czech Republic, Bohemian Massif, Moravek and Pouba 1987, Zachariáš et al. 2014).

Gold also occurs as discrete electrum grains. These are rarely observed in direct association with stage I but occur as small inclusions within minerals of the second, third, and fourth ore stage. Textures show marcasite (stage I) directly associated with electrum (Figs. 3b and 7b), which either formed by direct precipitation during fluid cooling (i.e., primary gold) or, more likely, by remobilization when primary pyrrhotite reacted to pyrite or marcasite. This hypothesis is strengthened by the porous appearance of, e.g., marcasite (Fig. 3b). Some electrum associated with the later stages also could have formed by Au and Ag remobilization of invisible gold during replacement of sulfides from ore stage I during later stages. Since the concentration of invisible gold is extremely low (on average < 0.05 wt% in ore minerals of stage I), the remobilized amount of these ore minerals needed to form electrum is significant. Thus, the probability and abundance of discrete gold grains in individual samples in the Schwarzwald are very low.

Comparison to other occurrences of this mineralization type in the Variscan belt

Sb-(Au)-bearing quartz veins of the type studied here are widespread throughout the Variscan Orogenic belt (ESM 3 4 and Table 1) (e.g., Walenta 1957; Dill 1985; Dill 1986; Gumiel and Arribas 1987; Ortega and Vindel 1995; Dill 1998; Wagner and Cook 2000; Krolop et al. 2018; Burisch et al. 2018, this issue). According to literature, four typical metal associations can be distinguished in these deposits: (1) Fe-As ±Sb-Au, (2) Pb-Zn-Cu±Au, (3) Pb-Sb±Au-Ag, and (4) Ag-Sb which is broadly similar to mineralization stages recognized in this study. However, only the first three metal associations are widespread (e.g., Boiron et al. 1990; Clayton et al. 1990; Munoz et al. 1992; Wagner and Cook 2000; Pochon et al. 2016; Krolop et al. 2018).

The initial stage of mineralization at many deposits is characterized by the mineral succession pyrrhotite, arsenopyrite, pyrite, and late-stage berthierite and stibnite. Only small mineralogical variations are documented, such as the presence of Ag-Sb minerals in the primary ore stage in the Erzgebirge (Burisch et al. 2018, this issue). This indicates a common formation mechanism due to fluid cooling of a, commonly described as a primarily late-metamorphic, Sb-bearing fluid, as has been previously suggested for other localities by, e.g., Wagner and Cook (2000), Neiva et al. (2008), and Krolop et al. (2018). Thus, a similar fluid composition can be invoked in all these Variscan occurrences, indicating a relatively similar fluid regime/source over thousands of kilometers largely independent of host rock. The same holds true for the subsequent stages II and III, suggesting extensive remobilization processes throughout the Variscan belt.

The fourth stage (Ag-Sb), which is abundant in several veins of the Schwarzwald, has only been documented at few other localities in the Variscides (see Table 1 for references), i.e., Urbeis and Charbes (France, No. 6, ESM 3 4), Erzgebirge and Fichtelgebirge (Germany, No. 5 + 8, ESM 3 4), Pribram and Kutná Hora (Czech Republic, No. 9, ESM 3 4), Kremnica (Slovakia, No. 12, ESM 3 4), and the Diógenes mine (Spain, No. 18, ESM 3 4). Local tectonic processes such as the Upper Rhine Graben or the Eger Graben rifting in the course of the Cenozoic tectonic evolution of Europe (Ziegler 1992; Rajchl et al. 2009) may tentatively invoked to explain these late reactivation and remobilization processes.

International context—Sb-Au deposits worldwide

Compared to the small size of structurally controlled Sb-(Au) deposits in Europe, similar deposits in, e.g., China, Canada, Bolivia, Australia, or the Russian Federation are much larger and have great economic significance (e.g., Dill et al. 1995; Kontak et al. 1996; Ashley et al. 2000; Baltukhaev and Solozhenkin 2009). However, independent of deposit size, the mineralogy of the initial stages appears generally similar (e.g., Dill et al. 1995; Ashley et al. 2000; Hagemann and Lüders 2003), and for this reason, similar formation processes and parameters (e.g., fluid chemistry, cooling) may be assumed. Hence, the evolution of stages I through III of the Variscan occurrences is an analogy to many large deposits, the main difference being size and the absence of a distinct late-stage silver-rich assemblage (stage IV) in the large deposits. Our study shows that the characteristic ore succession of the primary mineralization (stage I) can be exclusively explained by fluid cooling. Boiling or fluid mixing, which have been described for some economically significant deposits

Table 1 Overview of characteristic structural, mineralogical, and fluid inclusion data of late-Orogenic Sb-Pb-Ag±Au-quartz mineralization in the European Variscan Orogen

	Country	District	Host rocks	Structural position	Mineralized structures	Mineral assemblage	Th of fluid inclusion types			Formation	Reference
							A	B	C		
1	England	Cornwall	Middle Devonian to Upper Carboniferous volcanite, slates carbonate	Variscan folded sequences, anticlinal zones	Systems of dilational veins, transsecting cleavage and folds	asp[1], py[1], ccp[2], sph[2], gn[3], sbn[3], jms[3], bno[3], bou[3], fhl[3]	250–350 °C	270–290 °C	170–230 °C	Cooling, fluid unmixing	Clayton et al. (1990)
2	Germany	Harz Mountains	Carboniferous, Devonian schist, greywacke			sbn, chalcostibite, bno, zk, plg, bou, jms, sms, dadsonite, heteromorphite, fhl					Dill (1993)
3	Germany	Rheinisches Schiefergebirge	Lower Devonian to Lower Carboniferous slate, sandstone, quartzite, carbonate, greywacke	Variscan major anticlinal zones	Extensional veins, bedding-concordant mineralization	py[1], qtz[1], chlorite[1], sbn[2], zk[2], plg[2], sms[2], sph[2], chalcostibite, bno, jms, btr, bou, fhl, gold (in py)	160–390 °C	110–180 °C		Fluid cooling (boiling)	Dill (1993) Wagner and Cook (2000)
4	Germany	Thüringer Wald	Ordovician to lower Carboniferous slate, greywacke	NE-SW Variscan fault zones		py[1], asp[1], sph[1,4], qtz[1,2,4], sbn[2], zk[3], plg[3], sms[3], bou[3,4], gn[4], ankerite[3,4], siderite[3,4], bno, jms, btr, fhl, gold, antimonides				Fluid cooling, late-stage mixing	Dill (1993) Krolop et al. (2018)
5	Germany	Erzgebirge	Ordovician to Carboniferous phyllite, slate, black shale, volcanite	Variscan anticlinal zones	Dilational veins, cleavage-concordant mineralization	py[1], asp[1], gold[1], sbn[2], qtz[2], sph[3], gn[3], carbonate[3], Pb-Sb-Ag sulfosalts[3], zk, bno, bou, btr, dys, fhl, freibergite					Dill (1993) Wagner and Cook (2000) Burisch et al. (2018)
6	France	Vosges Mountains, Charbes	Gneiss, granite, phyllite, schist			sbn, asp, bou, freieslebenite, fülöppite, dys, pyrg, falor, py, zk, sph, silver, btr, ramdohrite, stibiconite, qtz, cal, dolomite					Wittern and Journée (1997)
6	France	Vosges Mountains, Urbeis	Silurian-Cambrian schist			e.g. sbn, freibergite, asp, btr, cal, ccp, bno, bou, ferberite, gn, pyrg, py, silver, scheelite, sph, stibiconite, fhl, qtz					Meyer and Hohl (1994)
7	Germany	Schwarzwald	Devonian metamorphic conglomerate, Variscan paragneiss and migmatite	Late-Variscan extensional shear zones	Late-orogenic, post-compressive brittle tectonic events	See Fig. 2 for details	100–400 °C	50–250 °C	50–170 °C	Fluid cooling, fluid mixing	Staude et al. (2007, 2010a, 2010b, 2012)) Walter et al. (2016, 2017, 2018a) This study
8	Germany	Fichtelgebirge	Ordovician to Devonian slate, phyllite, diabase, keratophyr			sbn, chalcostibite, zk, plg, sms, bou, jms, menehinite, antimony, Ag-tetrahedrite, gold					Dill (1993)
8	Germany	Oberpfälzer Wald	Ordovician phyllite								Dill (1993)

Table 1 (continued)

	Country	District	Host rocks	Structural position	Mineralized structures	Mineral assemblage	Th of fluid inclusion types			Formation	Reference
							A	B	C		
						chalcostibite, bno, bou, jms, geocronite, antimony, fhl					
9	Czech Republic	Bohemian Massif; Pribram, Kutná Hora	Cambrian to Precambrian slate, granite, sandstone, schist, conglomerate, diabase, gneiss, lamprophyr			sbn, bou, geocronite, bno, sms, jms, btr, pyrg, stephanite, diaphorite, Ag-sulfosalts, aurostibite, antimony, fhl, gold					Dill (1993)
10–13	Slovakia	West-Carpathians, Kremnica	Devonian to Permian, Miocene, migmatite, gneiss, granite, phyllite, schist, andesite			jms, fhl, gold, btr, Ag-Sb sulfosalts, bou, antimony, chalcostibite, zk, dys, cinnabar					Dill (1993)
		West-Carpathians; Dúbrava, Tatra Mountains				scheelite, py[1–3], qtz[1–5], molybdenite[1], asp[2], sph[3], zk[3], dolomite[3–5], fhl[4], bno[4], chalcostibite[4], Pb-Sb-Bi sulfosalts[4], barite[5], cal[5], strontianite[5]	315–355 °C[1]; 305–350 °C[2]	105–170 °C[3]	118–162 °C[4]; 105–158 °C[5]		Chovan et al. (1995)
14-15	France	Massif Armoricain, Massif Central	Upper Precambrian to Silurian shale, sandstone, micaschist, gneiss, granite	Variscan folded and thrusted sequences, major anticlinal zones	Veinlet networks, satellites of extensional shear zones	asp[1],py[1], gold[1], qtz[1–3], cal[1], sph[2], gn[2], ccp[2], sulfosalts[2,3], sbn[3]	280–410 °C	260–390 °C	100–280 °C	Simple cooling, fluid dilution	Bril (1982) Bril and Beaufort (1989) Boiron et al. (1990) Munoz et al. (1992) Pochon et al. (2016)
16	Portugal	Dúrico-Beirao district	Pre-Ordovician to Silurian conglomerate, quartzite, schist	Variscan anticline	N-NE subvertical fractures	asp[1,4], py[1,2,4], gold[1], cassiterite[1], wolframite[1], qtz[1–3], sph[2,3], ccp[2], pyrrhotite[2], fhl[2], jms[3], bou[3], gn[3], carbonate[3,4], btr[4], sbn[4]	290–340 °C	230–320 °C	128–225 °C	Fluid mixing, dilution, and cooling	Couto et al. (1990)
17	Spain	Spanish Hercynian Massif; Mari Rosa	Upper Precambrian greywacke, phyllite, slate	Variscan anticline core	Dilational veins	asp[1], py[1,3], qtz[1,2,3], sbn[2], gold[2], pyrrhotite[3], sph[3], sulfosalts[3], btr	270–390 °C	180–330 °C	150–270 °C	Fluid mixing	Gumiel and Arribas (1987) Ortega et al. (1991) Ortega and Vindel (1995)

Mineralization stages according to the respective reference are shown with superscripts 1–5

asp arsenopyrite, *py* pyrite, *ccp* chalcopyrite, *sph* sphalerite, *gn* galena, *sbn* stibnite, *jms* jamesonite, *bno* bournonite, *bou* boulangerite, *fhl* fahlore, *zk* zinkenite, *plg* plagionite, *sms* semseyite, *btr* berthierite, *qtz* quartz, *pyrg* pyrargyrite, *dys* dyscrasite, *cal* calcite

(e.g., Hillgrove Au-Sb deposit in Australia, Ashley et al. 1990; Ashley et al. 2000; Lake George Sb deposit in Canada, Yang et al. 2004; Woxi deposit in China, Zhu and Peng 2015), may further aid ore formation at some localities, but due to the lack of features such as boiling in fluid inclusions from many localities and a general presence of cooling indicators, further processes are not essential.

Although the vast difference in size between deposits may be attributed to processes such as boiling further aiding precipitation, it is likely that it is predefined by the tectonic setting/absolute fluid volume and is thus structurally controlled. For example, the formation of frequent small scale deposits in Europe may be related to the presence of abundant former micro-continents and predefined small scale fractures (Kalt et al. 2000; Geyer et al. 2011).

Due to the economic insignificance of late-stage sulfosalts in economically important worldwide deposits, their formation is commonly not investigated in sufficient detail. However, all deposits generally show an evolution from an Fe-Sb stage to a Pb-enriched stage (e.g., Kaiman et al. 1980; Ashley et al. 1990; Dill et al. 1995; Bortnikov et al. 2010), where the formation of the commonly occurring Pb- rich sulfosalts (e.g., Hagemann et al. 1994; Chovan et al. 1998; Tomkins et al. 2004) is not linked to the initial cooling process but to remobilization processes of stibnite (e.g. Schwarzwald, this study; Kharma ore deposit in Bolivia, Dill et al. 1995). This could indicate a polystage nature of other deposits around the globe with a typical and common evolutionary process representing a transition from initial cooling of a late-metamorphic fluid system (stage I) to a system dominated by a typical Pb-rich saline basinal brine of initial seawater/meteoric fluid origin (subsequent stages). Hence, this study can be used as an example for future investigations of remobilization processes within hydrothermal Sb deposits worldwide.

Conclusions

Quartz rich Sb-Pb-Ag±Au veins in the Schwarzwald can be seen as representative examples of this ore type with a high mineralogical diversity. They typically show four mineralization stages that can be related to distinct mineralization events,

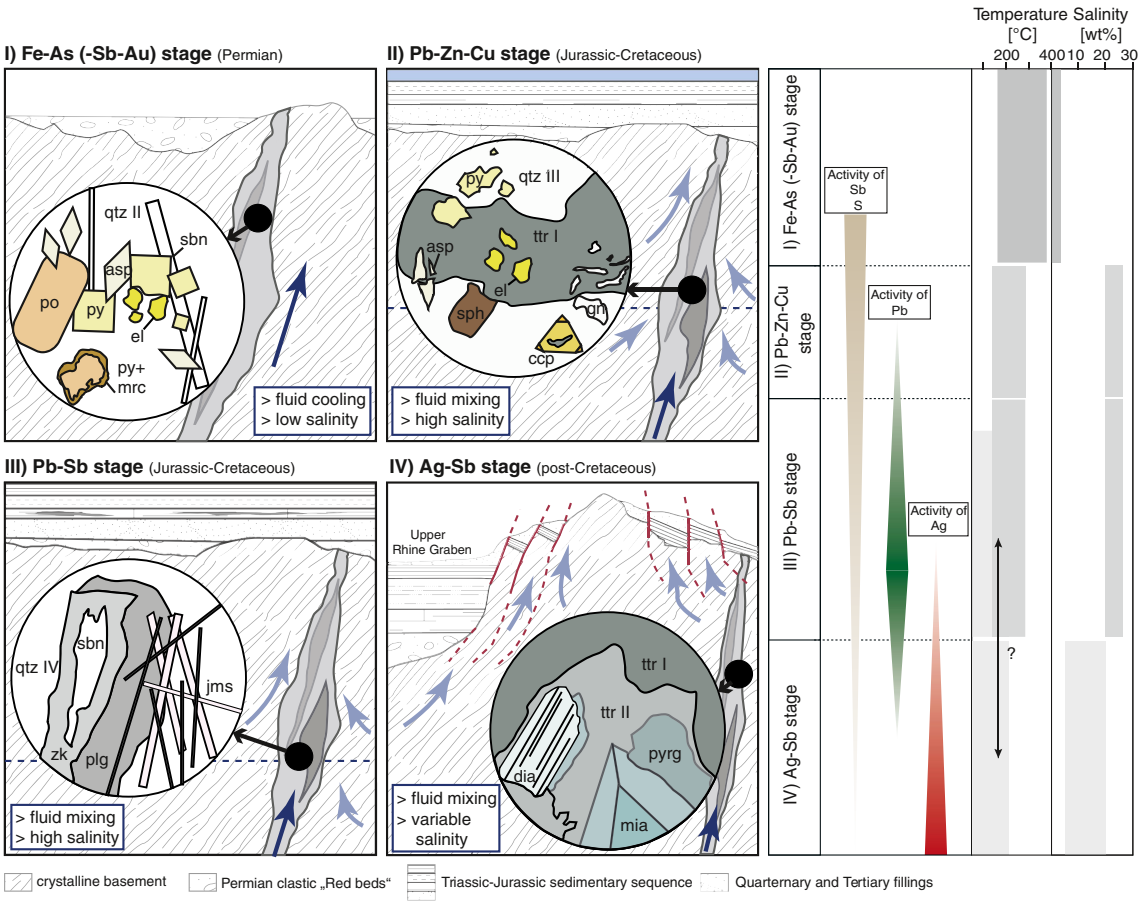

Fig. 13 Summary of all mineralization stages I–IV with representative mineral sketch of each stage, schematically illustrating geological setting, corresponding fluid temperature and salinity, as well as activities of important elements. Po = pyrrhotite, py = pyrite, mrc = marcasite, asp = arsenopyrite, sbn = stibnite, qtz = quartz, sph = sphalerite, ccp = chalcopyrite, ttr = tetrahedrite, gn = galena, zk = zinkenite, plg = plagionite, jms = jamesonite, dia = diaphorite, mia = miargyrite, and pyrg = pyrargyrite. Gray boxes show the ranges of each parameter

metal and fluid source, and precipitation mechanisms: The characteristic mineral sequence of the primary ore stage I is formed by cooling of late-metamorphic (400–100 °C), low-salinity fluids with maximum salinities of 5 wt% (NaCl eq.) (Fig. 13). A remobilization of early minerals which incorporate significant amounts of invisible gold, such as arsenopyrite, pyrite, marcasite, and stibnite, leads to the precipitation of electrum, which is observed at Sb-Au-deposits worldwide. The development and thus the character of later mineralization stages is strongly dependent on the abundance and remobilization of pre-existing Sb minerals. The fluid composition evolved to high-salinity (up to 28 wt% NaCl eq. and < 250 °C) and Pb-rich fluids which remobilized stibnite and formed a complex Pb-Sb mineral assemblage (Fig. 13). This transition from an initially late-metamorphic fluid system to a saline basinal brine fluid system is also evident for many other examples of this deposit type. During the influx of Pb, remobilization of stibnite leads to the formation of various Pb-Sb-bearing sulfosalts, whereas during limited remobilization, galena forms. The last mineralization stage is locally confined to only some localities in the Variscan belt affected by Tertiary tectonic events (e.g., Upper Rhine Graben and Eger Graben). A rift-related hydrothermal fluid with variable salinity and low temperature (7–20 wt%, 150 °C) combined with an influx of Ag into the pre-existing mineralization leads to the replacement of Pb-Sb minerals and formation of a distinct Ag-rich assemblage during this stage.

Acknowledgements We would like to thank Steffen Hagemann and Wolfgang Werner for their constructive comments that improved this manuscript significantly. Bernd Lehmann and Jens Gutzmer are thanked for careful and thoughtful editorial handling of this manuscript. We are grateful to Thomas Wenzel for the assistance with the electron microprobe. Simone Schafflick and Per Jeiseke are thanked for sample preparation. We would also like to thank Bernd Steinhilber and Gabriele Stoschek for isotope measurements and their help with crush leach analyses and technical support. Further thanks go Thomas Seifert for the possibility to analyze fluid inclusions in stibnite and sphalerite at the TU Bergakademie Freiberg and to Matthias Bauer and Lisa Richter for their help and supervision. Olga Apukhtina is thanked for data acquisition at the Münstergrund locality.

References

Altherr R, Holl A, Hegner E, Langer C, Kreuzer H (2000) High-potassium, calc-alkaline I-type plutonism in the European Variscides: northern Vosges (France) and northern Schwarzwald (Germany). Lithos 50:51–73. https://doi.org/10.1016/S0024-4937(99)00052-3

Arthaud F, Matte P (1977) Late Paleozoic strike-slip faulting in southern Europe and northern Africa: result of a right-lateral shear zone between the Appalachians and the Urals. Geol Soc Am Bull 88:1305–1320. https://doi.org/10.1130/0016-7606(1977)88<1305:LPSFIS>2.0.CO;2

Ashley P, Cook N, Hill R (1990) Occurrence and significance of aurostibite in Sb-Au ore from Hillgrove, New-South-Wales, Australia. Neues JB Mineral Monat:537–551

Ashley P, Creagh C, Ryan C (2000) Invisible gold in ore and mineral concentrates from the Hillgrove gold-antimony deposits, NSW, Australia. Mineral Deposita 35:285–301

Baatartsogt B, Schwinn G, Wagner T, Taubald H, Beitter T, Markl G (2007) Contrasting paleofluid systems in the continental basement: a fluid inclusion and stable isotope study of hydrothermal vein mineralization, Schwarzwald district, Germany. Geofluids 7:123–147. https://doi.org/10.1111/j.1468-8123.2007.00169.x

Baltukhaev GI, Solozhenkin PM (2009) Concentration of gold-antimony ores in the Sakha Republic (Yakutia). Russ J Non-Ferr Met+ 50:199–205. https://doi.org/10.3103/S106782120903002X

Behr H-J, Gerler J (1987) Inclusions of sedimentary brines in post-Variscan mineralizations in the Federal Republic of Germany—a study by neutron activation analysis. Chem Geol 61:65–77. https://doi.org/10.1016/0009-2541(87)90028-3

Behr H-J, Engel W, Franke W, Giese P, Weber K (1984) The Variscan belt in Central Europe: main structures, geodynamic implications, open questions. Tectonophysics 109:15–40. https://doi.org/10.1016/0040-1951(84)90168-9

Boiron M, Cathelineau M, Dubessy J, Bastoul A (1990) Fluids in Hercynian Au veins from the French Variscan belt. Mineral Mag 54:231–243

Bons PD, Fusswinkel T, Gomez-Rivas E, Markl G, Wagner T, Walter B (2014) Fluid mixing from below in unconformity-related hydrothermal ore deposits. Geology 42:1035–1038. https://doi.org/10.1130/G35708.1

Bortnikov N, Gamynin G, Vikent'eva O, Prokof'ev VY, Prokop'ev A (2010) The Sarylakh and Sentachan gold-antimony deposits, Sakha-Yakutia: a case of combined mesothermal gold-quartz and epithermal stibnite ores. Geol Ore Deposit+ 52:339–372

Bouchot V, Gros Y, Bonnemaison M (1989) Structural controls on the auriferous shear zones of the Saint Yrieix District, Massif Central, France; evidence from the Le Bourneix and Laurieras gold deposits. Econ Geol 84:1315–1327. https://doi.org/10.2113/gsecongeo.84.5.1315

Brander T (2000) U/HE-chronologische Fallstudien an Eisen-und Manganerzen Department of Geoscience. Ruprecht-Karls University Heidelberg, pp 275.

Bril H (1982) Fluid inclusions study of Sn–W–Au, Sb– and Pb–Zn mineralizations from the Brioude-Massiac district (French Massif Central). Tscher Miner Petrog 30:1–16. https://doi.org/10.1007/BF01082422

Bril H, Beaufort D (1989) Hydrothermal alteration and fluid circulation related to W, Au, and Sb vein mineralization, Haut Allier, Massif Central, France. Econ Geol 84:2237–2251. https://doi.org/10.2113/gsecongeo.84.8.2237

Bucher K, Stober I (2002) Water-rock reaction experiments with Black Forest gneiss and granite Water-rock interaction Springer, pp 61–95.

Bucher K, Stober I (2010) Fluids in the upper continental crust. Geofluids 10:241–253. https://doi.org/10.1007/s00531-008-0328-x.

Bucher K, Zhu Y, Stober I (2009) Groundwater in fractured crystalline rocks, the Clara mine, Black Forest (Germany). Int J Earth Sci 98:1727–1739. https://doi.org/10.1111/j.1468-8123.2010.00279.x.

Burisch M, Marks MA, Nowak M, Markl G (2016) The effect of temperature and cataclastic deformation on the composition of upper crustal fluids—an experimental approach. Chem Geol 433:24–35. https://doi.org/10.1016/j.chemgeo.2016.03.031

Burisch M, Hartmann A, Bach W, Krolop P, Krause J, Gutzmer J (2018, this issue) Genesis of hydrothermal silver-antimony-sulfide veins of the Bräunsdorf sector of the Freiberg District, Germany. Mineral Deposita

Chicharro E, Boiron M-C, López-García JÁ, Barfod DN, Villaseca C (2016) Origin, ore forming fluid evolution and timing of the Logrosán Sn–(W) ore deposits (Central Iberian Zone, Spain). Ore Geol Rev 72:896–913. https://doi.org/10.1016/j.oregeorev.2015.09.020.

Chovan M, Hurai V, Sachan H, Kantor J (1995) Origin of the fluids associated with granodiorite-hosted, Sb-As-Au-W mineralisation at Dúbrava (Nízke Tatry Mts, Western Carpathians). Mineral Deposita 30:48–54. https://doi.org/10.1007/BF00208876

Chovan M, Majzlan J, Kristin J, Ragan M, Siman P (1998) Pb-Sb and Pb-Sb-Bi sulfosalts and associated sulphides from Dúbrava antimony deposit, Nízke Tatry Mts Acta Geologica Universitatis Comenianae.

Cidu R, Biddau R, Dore E, Vacca A, Marini L (2014) Antimony in the soil–water–plant system at the Su Suergiu abandoned mine (Sardinia, Italy): strategies to mitigate contamination. Sci Total Environ 497:319–331. https://doi.org/10.1016/j.scitotenv.2014.07.117.

Clayton R, Scrivener R, Stanley C (1990) Mineralogical and preliminary fluid inclusion studies of lead-antimony mineralisation in north Cornwall. Proc Ussher 7:258–262

Comsti E, Taylor G (1984) Implications of fluid inclusion data on the origin of the Hillgrove gold-antimony deposits. NSW Proceedings of the Australasian Institute of Mining & Metallurgy 289:195–203

Couto H, Roger G, Moëlo Y, Bril H (1990) Le district à antimoine-or Dúrico-Beirão (Portugal): évolution paragénétique et géochimique; implications métallogéniques. Mineral Deposita 25:S69–S81. https://doi.org/10.1007/BF00205252

Craig H (1961) Isotopic variations in meteoric waters. Science 133:1702–1703. https://doi.org/10.1126/science.133.3465.1702

Dennert V (1993) Der Bergbau vom Mittelalter bis heute im Auftrag der Stadt Sulzburg von der Anna Hugo Bloch-Stiftung Red Anneliese Müller and Jost Grosspietsch Bd 1:119–221.

Dill H (1985) Antimoniferous mineralization from the Mid-European Saxothuringian Zone: mineralogy, geology, geochemistry and ensialic origin. Geol Rundsch 74:447–466. https://doi.org/10.1007/BF01821205

Dill H (1986) Die Vererzung am Westrand der Böhmischen Masse. Geologisches Jahrbuch Reihe D 500:73

Dill HG (1993) Die Antimonvorkommen der mitteleuropäischen Alpiden und Varisziden. Z Dtsch Geol Ges:434–450

Dill H (1998) Evolution of Sb mineralisation in modern fold belts: a comparison of the Sb mineralisation in the Central Andes (Bolivia) and the Western Carpathians (Slovakia). Mineral Deposita 33:359–378. https://doi.org/10.1007/s001260050155

Dill H, Weiser T, Bernhardt I, Kilibarda CR (1995) The composite gold-antimony vein deposit at Kharma (Bolivia). Econ Geol 90:51–66. https://doi.org/10.2113/gsecongeo.90.1.51

Distanov E, Stebleva A, Obolenskii A, Kochetkova K, Borisenko A (1975) Origin of the Uderei gold-antimony field in the Yenisei Ridge area. Geol Geofiz 16:19–27

Doblas M, López-Ruiz J, Oyarzun R, Mahecha V, Moya YS, Hoyos M, Cebriá J-M, Capote R, Enrile JH, Lillo J (1994) Extensional tectonics in the Central Iberian Peninsula during the Variscan to Alpine transition. Tectonophysics 238:95–116. https://doi.org/10.1016/0040-1951(94)90051-5.

Frezzotti ML, Tecce F, Casagli A (2012) Raman spectroscopy for fluid inclusion analysis. J Geochem Explor 112:1–20. https://doi.org/10.1016/j.gexplo.2011.09.009.

Gammons C, Williams-Jones A (1997) Chemical mobility of gold in the porphyry-epithermal environment. Econ Geol 92:45–59. https://doi.org/10.2113/gsecongeo.92.1.45

Geyer OF, Gwinner MP, Geyer M, Nitsch E, Simon T (2011) Geologie von Baden-Württemberg. 626.

Goldstein RH, Reynolds TJ (1994) Fluid inclusion microthermometry.

Guillemette N, Williams-Jones A (1993) Genesis of the Sb-W-Au deposits at Ixtahuacan, Guatemala: evidence from fluid inclusions and stable isotopes. Mineral Deposita 28:167–180

Gumiel P, Arribas A (1987) Antimony deposits in the Iberian Peninsula. Econ Geol 82:1453–1463

Hagemann SG, Lüders V (2003) PTX conditions of hydrothermal fluids and precipitation mechanism of stibnite-gold mineralization at the Wiluna lode-gold deposits, Western Australia: conventional and infrared microthermometric constraints. Mineral Deposita 38:936–952. https://doi.org/10.1007/s00126-003-0351-6

Hagemann SG, Gebre-Mariam M, Groves DI (1994) Surface-water influx in shallow-level Archean lode-gold deposits in Western, Australia. Geology 22:1067–1070

Hann H, Chen F, Zedler H, Frisch W, Loeschke J (2003) The Rand Granite in the southern Schwarzwald and its geodynamic significance in the Variscan belt of SW Germany. Int J Earth Sci 92:821–842. https://doi.org/10.1007/s00531-003-0361-8

Irber W, Lehrberger G (1993) Das Gold-Erzrevier von Goldkronach-Brandholz im Fichtelgebirge: Ein modifiziertes Genesemodell. Eur J Mineral 5:225

Kaiman S, Harris D, Dutrizac J (1980) Stibivanite, a new mineral from Lake George antimony deposit, New Brunswick. Can Mineral 18:329–332

Kalt A, Altherr R, Hanel M (2000) The Variscan basement of the Schwarzwald. Eur J Mineral 12:1–43

Kendall C, Coplen TB (2001) Distribution of oxygen-18 and deuterium in river waters across the United States. Hydrol Process 15:1363–1393. https://doi.org/10.1002/hyp.217

Knipe R (1993) The influence of fault zone processes and diagenesis on fluid flow. In: Horbury AD and Robinson AG (ed) Diagenesis and Basin Development, Vol 36, American Association of Petroleum Geologists, pp 135-151

Kolchugin A, Immenhauser A, Walter B, Morozov V (2016) Diagenesis of the palaeo-oil-water transition zone in a Lower Pennsylvanian carbonate reservoir: constraints from cathodoluminescence microscopy, microthermometry, and isotope geochemistry. Mar Pet Geol 72:45–61

Kontak DJ, Horne RJ, Smith PK (1996) Hydrothermal characterization of the West Gore Sb-Au deposit, Meguma Terrane, Nova Scotia, Canada. Econo Geol 91(7):1239–1262. https://doi.org/10.2113/gsecongeo.91.7.1239

Kontny A, Friedrich G, Behr H, Hd W, Horn E, Möller P, Zulauf G (1997) Formation of ore minerals in metamorphic rocks of the German continental deep drilling site (KTB). Journal of Geophysical Research: Solid Earth 102:18323–18336. https://doi.org/10.1029/96JB03395

Kovalev K, Kalinin YA, Naumov E, Kolesnikova M, Korolyuk V (2011) Gold-bearing arsenopyrite in eastern Kazakhstan gold-sulfide deposits. Russ Geol Geophys 52:178–192

Krolop P, Burisch M, Richter L, Fritzke B, Seifert T (2018) Antimoniferous vein-type mineralization of the Berga Antiform, Eastern-Thuringia, Germany: A fluid inclusion study. Chem Geol. https://doi.org/10.1016/j.chemgeo.2018.02.034

Kroner U, Romer R (2013) Two plates—many subduction zones: the Variscan orogeny reconsidered. Gondwana Res 24:298–329. https://doi.org/10.1016/j.gr.2013.03.001

Krützfeldt B (1985) Beobachtungen an Vererzungen in Sedimenten der Zone Badenweiler-Lenzkrich. Der Aufschluss 36:261–265

Kulick J, Meisl S, Theuerjahr A-K (1997) Die Goldlagerstätte des Eisenberges: südwestlich von Korbach. Hessisches Landesamt für Bodenforschung

Lehrberger G (1995) The gold deposits of Europe Prehistoric gold in Europe. Springer, pp 115–144.

Lentz DR, Thorne K, Yang X-M (2002) Preliminary analysis of the controls on the various episodes of gold mineralization at the Lake George antimony deposit, New Brunswick Current research:02–01

Ligang Z, Jingxiu L, Huanbo Z, Zhensheng C (1989) Oxygen isotope fractionation in the quartz-water-salt system. Econ Geol 84:1643–1650. https://doi.org/10.2113/gsecongeo.84.6.1643

Malavieille J, Guihot P, Costa S, Lardeaux J, Gardien V (1990) Collapse of the thickened Variscan crust in the French Massif Central: Mont Pilat extensional shear zone and St. Etienne Late Carboniferous basin. Tectonophysics 177:139–149. https://doi.org/10.1016/0040-1951(90)90278-G

Markl G (2017) Schwarzwald - Lagerstätten und Mineralien aus vier Jahrhunderten. Band 4 - Südlicher Schwarzwald., Bode

Markl G, Burisch M, Neumann U (2016) Natural fracking and the genesis of five-element veins. Mineral Deposita 51:703–712. https://doi.org/10.1007/s00126-016-0662-z

Marks MA, Marschall HR, Schühle P, Guth A, Wenzel T, Jacob DE, Barth M, Markl G (2013) Trace element systematics of tourmaline in pegmatitic and hydrothermal systems from the Variscan Schwarzwald (Germany): the importance of major element composition, sector zoning, and fluid or melt composition. Chem Geol 344:73–90. https://doi.org/10.1016/j.chemgeo.2013.02.025

Matte P (1991) Accretionary history and crustal evolution of the Variscan belt in Western Europe. Tectonophysics 196:309–337. https://doi.org/10.1016/0040-1951(91)90328-P

Metz R, Richter M (1957) Die Blei-Zink-Erzgänge des Schwarzwaldes. Beihefte zum Geologischen Jahrbuch Beiheft 29:277

Meyer J, Hohl J-L (1994) Minerals engineering Reviews in mineralogy and geochemistry. Editions du Rhin

Meyer M, Brockamp O, Clauer N, Renk A, Zuther M (2000) Further evidence for a Jurassic mineralizing event in Central Europe: K–Ar dating of hydrothermal alteration and fluid inclusion systematics in wall rocks of the Käfersteige fluorite vein deposit in the northern Black Forest, Germany. Mineral Deposita 35:754–761. https://doi.org/10.1007/s001260050277

Moravek P, Pouba Z (1987) Precambrian and Phanerozoic history of gold mineralization in the Bohemian Massif. Econ Geol 82:2098–2114. https://doi.org/10.2113/gsecongeo.82.8.2098

Munoz M, Shepherd T (1987) Fluid inclusion study of the bournac polymetallic (Sb-As-Pb-Zn-Fe-Cu...) vein deposit (montagne noire, France). Mineral Deposita 22:11–17

Munoz M, Courjault-Radé P, Tollon F (1992) The massive stibnite veins of the French Palaeozoic basement: a metallogenic marker of Late Variscan brittle extension. Terra Nova 4:171–177. https://doi.org/10.1111/j.1365-3121.1992.tb00468.x

Neiva A, Andráš P, Ramos J (2008) Antimony quartz and antimony–gold quartz veins from northern Portugal. Ore Geol Rev 34:533–546. https://doi.org/10.1016/j.oregeorev.2008.03.004

Obolensky A, Gushchina L, Borisenko A, Borovikov A, Pavlova G (2007) Antimony in hydrothermal processes: solubility, conditions of transfer, and metal-bearing capacity of solutions. Russ Geol Geophys 48:992–1001. https://doi.org/10.1016/j.rgg.2007.11.006

Ortega L, Vindel E (1995) Evolution of ore-forming fluids associated with late Hercynian antimony deposits in central/western Spain; case study of Mari Rosa and El Juncalon. Eur J Mineral 7:655–673 0935–1221/95/0007–0655

Ortega L, Vindel E, Beny C (1991) COHN fluid inclusions associated with gold-stibnite mineralization in low-grade metamorphic rocks, Mari Rosa mine, Caceras, Spain. Mineral Mag 55:235–247. https://doi.org/10.1180/minmag.1991.055.379.12.

Pascher G (1985) Gold aus dem Fichtelgebirge. Ein montanhistorischer und mineralogischer Überblick. Lapis 10:25–42

Pfaff K, Romer RL, Markl G (2009) U-Pb ages of ferberite, chalcedony, agate, 'U-mica'and pitchblende: constraints on the mineralization history of the Schwarzwald ore district. Eur J Mineral 21:817–836. https://doi.org/10.1127/0935-1221/2009/0021-1944

Pfaff K, Hildebrandt LH, Leach DL, Jacob DE, Markl G (2010) Formation of the Wiesloch Mississippi Valley-type Zn-Pb-Ag deposit in the extensional setting of the Upper Rhinegraben, SW Germany. Mineral Deposita 45:647–666. https://doi.org/10.1007/s00126-010-0296-5

Pfaff K, Koenig A, Wenzel T, Ridley I, Hildebrandt LH, Leach DL, Markl G (2011) Trace and minor element variations and sulfur isotopes in crystalline and colloform ZnS: incorporation mechanisms and implications for their genesis. Chem Geol 286:118–134. https://doi.org/10.1016/j.chemgeo.2011.04.018.

Pochon A, Gapais D, Gloaguen E, Gumiaux C, Branquet Y, Cagnard F, Martelet G (2016) Antimony deposits in the Variscan Armorican belt, a link with mafic intrusives? Terra Nova 28:138–145. https://doi.org/10.1111/ter.12201

Rajchl M, Uličný D, Grygar R, Mach K (2009) Evolution of basin architecture in an incipient continental rift: the Cenozoic Most Basin, Eger Graben (Central Europe). Basin Res 21:269–294. https://doi.org/10.1111/j.1365-2117.2008.00393.x

Romer RL, Kroner U (2017) Paleozoic gold in the Appalachians and Variscides. Ore Geol Rev 92:475–505. https://doi.org/10.1016/j.oregeorev.2017.11.021

Roscher M, Schneider JW (2006) Permo-Carboniferous climate: Early Pennsylvanian to Late Permian climate development of Central Europe in a regional and global context. Geol Soc Lond, Spec Publ 265:95–136. https://doi.org/10.1144/GSL.SP.2006.265.01.05

Rumble D, Hoering TC (1994) Analysis for oxygen and sulfur isotope ratios in oxide and sulfide minerals by spot heating with a carbon dioxide laser in a fluorine atmosphere. Acc Chem Res 27:237–241

Schroyen K, Muchez P (2000) Evolution of metamorphic fluids at the Variscan fold-and-thrust belt in eastern Belgium. Sediment Geol 131:163–180. https://doi.org/10.1016/S0037-0738(99)00133-5

Schwarz-Schampera U (2014) Antimony. Critical metals handbook:70–98.

Seal I, Robert R, Robie RA, Barton Jr PB, Hemingway B (1992) Superambient heat capacities of synthetic stibnite, berthierite, and chalcostibite: revised thermodynamic properties and implications for phase equilibria.

Seward TM (1973) Thio complexes of gold and the transport of gold in hydrothermal ore solutions. Geochim Cosmochim Acta 37:379–399. https://doi.org/10.1016/0016-7037(73)90207-X

Sharp ZD (1990) A laser-based microanalytical method for the in situ determination of oxygen isotope ratios of silicates and oxides. Geochim Cosmochim Acta 54:1353–1357. https://doi.org/10.1016/0016-7037(90)90160-M

Sheppard SM (1986) Characterization and isotopic variations in natural waters. Rev Mineral Geochem 16:165–183

Staude S, Wagner T, Markl G (2007) Mineralogy, mineral compositions and fluid evolution at the Wenzel hydrothermal deposit, Southern

Germany: implications for the formation of Kongsberg-type silver deposits. Can Mineral 45:1147–1176. https://doi.org/10.2113/gscanmin.45.5.1147

Staude S, Bons PD, Markl G (2009) Hydrothermal vein formation by extension-driven dewatering of the middle crust: an example from SW Germany. Earth Planet Sci Lett 286:387–395. https://doi.org/10.1016/j.epsl.2009.07.012

Staude S, Dorn A, Pfaff K, Markl G (2010a) Assemblages of Ag–Bi sulfosalts and conditions of their formation: the type locality of schapbachite (Ag0. 4Pb0. 2Bi0. 4S) and neighboring mines in the Schwarzwald ore district, southern Germany. Can Mineral 48:441–466. https://doi.org/10.3749/canmin.48.3.441

Staude S, Mordhorst T, Neumann R, Prebeck W, Markl G (2010b) Compositional variation of the tennantite–tetrahedrite solidsolution series in the Schwarzwald ore district (SW Germany): the role of mineralization processes and fluid source. doi: https://doi.org/10.1180/minmag.2010.074.2.309.

Staude S, Werner W, Mordhorst T, Wemmer K, Jacob DE, Markl G (2012) Multi-stage Ag–Bi–Co–Ni–U and Cu–Bi vein mineralization at Wittichen, Schwarzwald, SW Germany: geological setting, ore mineralogy, and fluid evolution. Mineral Deposita 47:251–276. https://doi.org/10.1007/s00126-011-0365-4

Steele-MacInnis M, Bodnar R, Naden J (2011) Numerical model to determine the composition of H2O–NaCl–CaCl2 fluid inclusions based on microthermometric and microanalytical data. Geochim Cosmochim Acta 75:21–40. https://doi.org/10.1016/j.gca.2010.10.002

Steele-MacInnis M, Lecumberri-Sanchez P, Bodnar RJ (2012) HOKIEFLINCS_H2O-NACL: a Microsoft Excel spreadsheet for interpreting microthermometric data from fluid inclusions based on the PVTX properties of H2O–NaCl. Comput Geosci 49:334–337

Stober I, Bucher K (1999) Deep groundwater in the crystalline basement of the Black Forest region. Appl Geochem 14:237–254. https://doi.org/10.1016/S0883-2927(98)00045-6.

Taylor H, Barnes H (1997) Oxygen and hydrogen isotope relationships in hydrothermal mineral deposits. Geochemistry of hydrothermal ore deposits 3:229–302

Todt W (1976) Zirkon U/Pb-Alter des Malsburg-Granits vom Südschwarzwald. Neues Jb Miner Abh 12:532–544

Tomkins AG, Pattison DR, Zaleski E (2004) The Hemlo gold deposit, Ontario: an example of melting and mobilization of a precious metal-sulfosalt assemblage during amphibolite facies metamorphism and deformation. Econ Geol 99:1063–1084

Wagner T, Cook N (2000) Late-Variscan antimony mineralisation in the Rheinisches Schiefergebirge, NW Germany: evidence for stibnite precipitation by drastic cooling of high-temperature fluid systems. Mineral Deposita 35:206–222. https://doi.org/10.1007/s001260050016

Wagner T, Fusswinkel T, Wälle M, Heinrich CA (2016) Microanalysis of fluid inclusions in crustal hydrothermal systems using laser ablation methods. Elements 12:323–328. https://doi.org/10.2113/gselements.12.5.323

Walenta K (1957) Die antimonerzführenden Gänge des Schwarzwaldes. Jahreshefte des Geologischen Landesamtes Baden-Württemberg 2:13–67

Walenta K, Sawatzki G, Dayal R (1970) Die Wolframerzvorkommen im Gebiet des Nordracher Granitmassivs und seiner Umgebung. Jahresh Geol Landesamt Baden-Wuerttemberg 12:207–226

Walter BF, Immenhauser A, Geske A, Markl G (2015) Exploration of hydrothermal carbonate magnesium isotope signatures as tracers for continental fluid aquifers, Schwarzwald mining district, SW Germany. Chem Geol 400:87–105. https://doi.org/10.1016/j.chemgeo.2015.02.009

Walter BF, Burisch M, Markl G (2016) Long-term chemical evolution and modification of continental basement brines—a field study from the Schwarzwald, SW Germany. Geofluids 16:604–623. https://doi.org/10.1111/gfl.12167

Walter BF, Burisch M, Marks MAW, Markl G (2017) Major element compositions of fluid inclusions from hydrothermal vein-type deposits record eroded sedimentary units in the Schwarzwald district, SW Germany. Mineral Deposita 52:1191–1204. https://doi.org/10.1007/s00126-017-0719-7

Walter BF, Burisch M, Fusswinkel T, Marks MAW, Steele-MacInnis M, Wälle M, Apukhtina OB, Markl G (2018a) Multi-reservoir fluid mixing processes in rift-related hydrothermal veins, Schwarzwald, SW-Germany. J Geochem Explor 186:158–186. https://doi.org/10.1016/j.gexplo.2017.12.004

Walter BF, Kortenbruck P, Zeitvogel C, Wälle M, Mertz-Kraus R, Markl G (submitted 2018b) Chemical evolution of ore-forming brines—basement leaching, metal provenance, and the redox link between barren and ore-bearing hydothermal veins. Chem Geol

Walter BF, Gerdes A, Kleinhanns IC, Dunkl I, von Eynatten H, Kreissl S, Markl G (2018c) The connection between hydrothermal fluids, mineralization, tectonics and magmatism in a continental rift setting: fluorite Sm-Nd and hematite and carbonates U-Pb geochronology from the Rhinegraben in SW Germany. Geochim Cosmochim Acta. https://doi.org/10.1016/j.gca.2018.08.012

Weissert H, Erba E (2004) Volcanism, CO2 and palaeoclimate: a Late Jurassic–Early Cretaceous carbon and oxygen isotope record. J Geol Soc 161:695–702. https://doi.org/10.1144/0016-764903-087

Werner W (2002) Die Erzlagerstätte Schauinsland bei Freiburg im Breisgau: Bergbau, Geologie, Hydrogeologie, Mineralogie, Geochemie, Tektonik und Lagerstättenentstehung. Aedificatio-Verlag.

Werner W, Franzke HJ (2001) Postvariszische bis neogene Bruchtektonik und Mineralisation im südlichen Zentralschwarzwald. Z Dtsch Geol Ges:405–437.

Werner W, Schlaegel-Blaut P, Rieken R (1990) Verbreitung und Ausbildung von Wolfram-Mineralisationen im Kristallin des Schwarzwaldes. Jahreshefte des Geologischen Landesamtes Baden-Württemberg 32:17–61

Wetzel A, Allenbach R, Allia V (2003) Reactivated basement structures affecting the sedimentary facies in a tectonically “quiescent” epicontinental basin: an example from NW Switzerland. Sediment Geol 157:153–172. https://doi.org/10.1016/S0037-0738(02)00230-0

Williams-Jones AE, Bowell RJ, Migdisov AA (2009) Gold in solution. Elements 5:281–287. https://doi.org/10.2113/gselements.5.5.281

Wittern A, Journée J-R (1997) Mineralien finden in den Vogesen: ein Führer zu über 40 Fundstellen. Sven Von Loga, Köln

Wood SA, Crerar DA, Borcsik MP (1987) Solubility of the assemblage pyrite-pyrrhotite-magnetite-sphalerite-galena-gold-stibnite-bismuthinite-argen-tite-molybdenite in H2O-NaCl-CO2 solutions from 200 degrees to 350 degrees C. Econ Geol 82(7):1864–1887. https://doi.org/10.2113/gsecongeo.82.7.1864

Yang X-M, Lentz DR, Chi G, Kyser TK (2004) Fluid–mineral reaction in the Lake George Granodiorite, New Brunswick, Canada: implications for Au–W–Mo–Sb mineralization. Can Mineral 42:1443–1464

Yardley BW (2005) 100th Anniversary Special Paper: metal concentrations in crustal fluids and their relationship to ore formation. Econ Geol 100:613–632. https://doi.org/10.2113/gsecongeo.100.4.613

Zachariáš J, Moravek P, Gadas P, Pertoldova J (2014) The Mokrsko-West gold deposit, Bohemian Massif, Czech Republic: mineralogy, deposit setting and classification. Ore Geol Rev 58:238–263. https://doi.org/10.1016/j.oregeorev.2013.11.005

Zhai W, Sun X, Yi J, Zhang X, Mo R, Zhou F, Wei H, Zeng Q (2014) Geology, geochemistry, and genesis of orogenic gold–antimony mineralization in the Himalayan Orogen, South Tibet, China. Ore Geol Rev 58:68–90

Zhu Y-N, Peng J-T (2015) Infrared microthermometric and noble gas isotope study of fluid inclusions in ore minerals at the Woxi orogenic Au–Sb–W deposit, western Hunan, South China. Ore Geol Rev 65: 55–69

Zhu Y, An F, Tan J (2011) Geochemistry of hydrothermal gold deposits: a review. Geosci Front 2:367–374. https://doi.org/10.1016/j.gsf.2011.05.006

Ziegler PA (1992) European Cenozoic rift system. Tectonophysics 208: 91–111. https://doi.org/10.1016/0040-1951(92)90338-7